UNIVERSITÉ DE REIMS CHAMPAGNE-ARDENNE

ÉCOLE DOCTORALE MATHEMATIQUES PHYSIQUE SCIENCES DU NUMERIQUE ET DE L'INGENIEUR n°620

# THÈSE

Pour obtenir le grade de

**DOCTEUR DE L'UNIVERSITÉ DE REIMS CHAMPAGNE-ARDENNE**

***Discipline*** : Génie des procédés

***Spécialité : Génie des procédés environnementaux***

Présentée et soutenue publiquement par


## ADELE POIRIER


Le 15 décembre 2025

---

## Composites biosourcés à base de PP, PLA et de drêches de bière : impact des procédés de transformation et de modification sur les propriétés des composites

---

Thèse dirigée par **SEBASTIEN ALIX**, co-dirigée par **PEDRO E.D. AUGUSTO**

**JURY**

| | | | |
|---|---|---|---|
| M. Joël Bréard, | Professeur, | Université de Caen Normandie, | **Président et Examinateur** |
| Mme Sophie Duquesne, | Professeur, | Centrale Lille Institut, | **Rapporteur** |
| Mme Nathalie Leblanc, | Maître de Conférence HDR, | UniLaSalle Rouen, | **Rapporteur** |
| Mme Sandrine Hoppe, | Chargée de recherche, | ENSIC - Université de Lorraine, | **Examinateur** |
| M. Sébastien Alix, | Professeur, | Université de Reims Champagne-Ardenne, | **Directeur de thèse** |
| M. Pedro E.D. Augusto, | Professeur, | CentraleSupélec - CEBB, | **Co-Directeur de thèse** |
| Mme Catherine Lacoste, | Maître de Conférences HDR, | Université de Reims Champagne-Ardenne, | **Co-encadrante** |
| Patrick Perré, | Professeur, | CentraleSupélec - CEBB, | **Invité** |

# Remerciements

Une thèse, trois ans et quelques pages plus tard, je suis fière d'annoncer à ma famille et mes amis que ça y est : je décroche le tant attendu titre de docteure. Une chose est sûre, ce grand projet n'aurait pas abouti sans le soutien, les conseils et la générosité de nombreuses personnes que je souhaite remercier ici.

Pour commencer, j'aimerais adresser un grand remerciement à mes directeurs, Sébastien et Pedro, pour leur encadrement et leur confiance tout au long de ces années de recherche. Sébastien, sa bienveillance et sa disponibilité lorsque j'en avais besoin et les échanges que nous avons eus ont été précieux. Il m'a également laissé une grande autonomie dans la conduite de mes recherches, ce qui m'a permis de développer pleinement mon indépendance scientifique. Pedro, sa rigueur scientifique, son exigence et sa patience m'ont beaucoup apporté et ont été particulièrement formatrices et essentielles à ce travail. Ses nombreux conseils m'ont aidé à garder le cap dans la conduite de ce projet.

Je tiens à remercier chaleureusement Catherine, mon encadrante, pour son soutien constant au cours de ce doctorat. Elle a toujours su trouver du temps pour m'accompagner, m'encourager et valoriser mon travail. Sa bienveillance, son soutien dans les moments plus délicats et les nombreuses attentions dont elle a fait preuve ont rendu ces années bien plus agréables et enrichissantes.

Je remercie également Patrick Perré pour son accompagnement, ses remarques pertinentes et les échanges scientifiques qui m'ont enrichie ainsi que ce projet.

Merci beaucoup aux membres du jury d'avoir accepté d'évaluer ce travail et d'y avoir consacré leur temps et leur attention, plus particulièrement à mes rapporteurs Sophie Duquesne et Nathalie Leblanc qui ont examiné avec une grande attention ce manuscrit.

Je souhaite également remercier chaleureusement Phillipe, pour son aide précieuse tout au long de ce doctorat. Sa grande maîtrise des équipements du laboratoire, ainsi que sa capacité à en expliquer le fonctionnement avec clarté et précision m'ont énormément apporté. Grâce à lui, j'ai pu mieux comprendre les instruments que j'utilisais et découvrir l'envers du décor de nombreuses machines du laboratoire, (j'ai eu l'honneur d'assister à quelques dissections du DMA). Sa rigueur et son sens du détail ont été particulièrement inspirants, et les nombreuses discussions que nous avons eues pour résoudre certains casse-tête expérimentaux ont été aussi enrichissantes qu'agréables. Je lui suis également très reconnaissante pour son écoute et sa disponibilité, qui ont largement contribué au bon déroulement de ce travail.

Je remercie également Samuel, compagnon de nombreuses aventures doctorales. Entre les cours que nous avons assurés ensemble, les expériences montées au laboratoire et les nombreuses manipulations partagées (malgré des sujets de recherche différents), nous avons souvent eu l'occasion de réfléchir ensemble à divers problèmes scientifiques. Sa capacité à toujours trouver une solution, son aide précieuse et son soutien dans les moments difficiles ont été particulièrement importants pour moi. Les nombreux trajets jusqu'à Charleville resteront également parmi les souvenirs marquants de ces années de doctorat.

Je remercie tous les techniciens, ingénieurs, doctorants et jeunes (et moins jeunes) docteurs du CEBB (Nicolas, Jules, Arthur, Sarah, Franco, Sylvain, Wendie, Brahim, Cédric, Cristobal, Ning et

tant d'autres) je garderai en souvenir les soirées, les barbecues et les différentes sorties qui ont rythmé ma vie à Reims.

Merci à tous les membres de l'ITheMM côté Charleville-Mézière qui m'ont toujours accueillie très chaleureusement et tout particulièrement à ma "sœur" doctorante (on a les mêmes encadrants) Coraline avec qui j'ai eu la chance de partager plusieurs moments marquants de ce doctorat, notamment la conférence en Tunisie. Ces expériences, ponctuées de fous rires, resteront d'excellents souvenirs.

Je souhaite enfin adresser un immense merci au formidable groupe de doctorants (et de non-doctorants évidemment) de l'ITheMM, qui ont largement contribué à rendre ces années de doctorat aussi enrichissantes qu'agréables. Vous avez été un public formidable pour écouter mes histoires souvent insolites, merci pour votre aide toujours proposée avec spontanéité et les nombreux moments partagés au laboratoire comme en dehors. Entre les innombrables repas, les pauses café, les longues discussions, les fous rires et quelques bêtises (toujours réparées) vous avez créé une ambiance unique au quotidien. J'aimerais citer chacun d'entre vous, mais de peur d'oublier quelqu'un, je préfère vous laisser vous reconnaître dans ces quelques mots.

Enfin, merci à chaque personne qui, de près ou de loin, ont contribué à ce travail que ce soit par un conseil, une parole sympathique ou un coup de main.

Merci à mon frère, Jules, pour son soutien moral sans égal.

Cette thèse marque l'aboutissement d'un projet mais je crois surtout qu'elle marque le commencement d'une belle aventure qu'il me tarde de vivre.

## Table of contents (EN)

*Table des matières (FR)* ..... *iv*

*Table of figures* ..... *viii*

*List of Tables* ..... *xiv*

*List of symbols* ..... *xvi*

*Introduction générale (FR)* ..... *1*

*General introduction (EN)* ..... *5*

*RÉSUMÉ DU CHAPITRE 1* ..... *9*

*Chapter 1 : Literature review* ..... *11*

**1. Introduction** ..... **11**

**2. Thermoplastic polymers as matrix for bio-based composites** ..... **13**

2.1. Introduction ..... 13

2.2. Petro-based polymers ..... 14

2.3. Bio-based and biodegradable polymers ..... 18

2.4. Studies comparing PLA and PP ..... 23

**3. Natural filler for composites materials** ..... **26**

3.1. Natural fibers ..... 26

3.2. Brewer's spent grain ..... 32

**4. Filler treatment** ..... **39**

4.1. Filler preparation ..... 39

4.2. Filler modification/compatibilization strategies ..... 48

**5. Processing of particulate composites** ..... **59**

5.1. Process steps ..... 59

5.2. Internal mixing ..... 60

5.3. Extrusion ..... 61

5.4. Injection molding ..... 62

5.5. Conclusion ..... 63

**6. Particulate composites properties: experiment and theory** ..... **63**

6.1. Introduction ..... 63

6.2. Rheological behavior ..... 64

6.3. Thermal characteristics ..... 69

6.4. Mechanical behavior: tensile test ..... 72

6.5. Water absorption ..... 80

**7. Conclusion: objectives and challenges** ..... **82**

*RÉSUMÉ CHAPITRE 2* ..... *85*

*Chapter 2 : Material and methods* ..... *87*

**1. Overview of the research strategy / study design** ..... **87**

**2. Material** ..... **89**

2.1. PP and PLA ..... 89

2.2. Brewer's spent grain ..... 89

**3. Characterization methods ..... 90**
3.1. Chemical and microstructural characterization techniques ..... 90
3.2. Rheological properties ..... 92
3.3. Mechanical properties ..... 93
3.4. Thermal characterizations ..... 94
3.5. Water related behavior ..... 96
3.6. Statistical analysis ..... 98

**4. Material production ..... 98**
4.1. Thesis first part: composites elaboration with Internal Mixer ..... 98
4.2. Thesis second part: BSG drying via extrusion ..... 103
4.3. Thesis third part: bridging strategies for composites optimization ..... 108
4.4. Alkaline treatment of BSG to improve interfacial adhesion ..... 111

***RÉSUMÉ DU CHAPITRE 3 ..... 115***

***Chapter 3 : Development of bio-based materials ..... 117***

**1. Introduction ..... 117**

**2. Material preparation ..... 118**
2.1. Internal mixing ..... 118
2.2. Injection molding ..... 119

**3. Thermal degradation behavior ..... 121**

**4. Thermal transition behavior ..... 126**

**5. Rheological behavior ..... 130**
5.1. Strain sweep ..... 130
5.2. Frequency sweep ..... 133

**6. Interface morphology ..... 137**
6.1. Cryofracture ..... 137
6.2. Tensile fracture ..... 140

**7. Mechanical behavior ..... 141**
7.1. Young's modulus ..... 141
7.2. No-adhesion model ..... 143

**8. Water absorption behavior ..... 145**

**9. Conclusions ..... 149**

***RÉSUMÉ DU CHAPITRE 4 ..... 151***

***Chapter 4 : Integrated drying and grinding of brewer's spent grain via extrusion process ..... 153***

**1. Introduction ..... 153**

**2. Setting the objective: moisture content ..... 155**

**3. Preliminary study ..... 157**
3.1. Introduction ..... 157
3.2. First set of trials - Defining a window of parameters ..... 158
3.3. Second set of trials – Modified screw profile ..... 162

**4. Extrusion trial methodology ..... 169**
4.1. Extrusion profile ..... 169

4.2. Extrusion parameters ..... 170
4.3. Effects of the parameters on BSG moisture content ..... 170

**5. Results ..... 171**
5.1. Effects of the parameters on Particle Size Distribution (PSD) ..... 171
5.2. Particles aspect (SEM) ..... 176
5.3. Thermal stability of extruded particles ..... 180
5.4. Energy consumption involved in conventional method vs extrusion ..... 182

**6. Conclusions ..... 185**

***RÉSUMÉ DU CHAPITRE 5 ..... 187***

***Chapter 5 : Bridging strategies for composites optimization ..... 189***

**1. Introduction ..... 189**

**2. Producing composites with extruded BSG via internal mixing ..... 190**
2.1. Presentation of the composites ..... 190
2.2. Effect of the extruded BSG on PP and PLA composites ..... 190
2.3. Conclusion ..... 206

**3. Upscaling the process ..... 207**
3.1. Introduction ..... 207
3.2. Composites compounding: from internal mixing to extrusion ..... 208
3.3. Composites injection: from manual injection press to industrial injection press ..... 219
3.4. Conclusion about injection methods ..... 228

**4. Conclusions ..... 228**

***RÉSUMÉ DU CHAPITRE 6 ..... 231***

***Chapter 6 : Alkaline Treatment of BSG to improve interfacial adhesion with polymer matrices ..... 233***

**1. Introduction ..... 233**

**2. BSG NaOH treatment ..... 234**
2.1. Introduction ..... 234
2.2. Effect of the treatment on BSG chemical functions ..... 235
2.3. Effect of the treatment on BSG thermal stability ..... 239
2.4. Effect of the treatment on BSG particles' aspect ..... 241
2.5. Conclusion ..... 246

**3. Composites manufacture ..... 246**
3.1. Introduction ..... 246
3.2. BSG density ..... 247
3.3. Effect of the treatment on composites thermal stability ..... 248
3.4. Effect of the treatment on composites rheological behavior ..... 251
3.5. Effect of the treatment on composites thermal transitions ..... 254
3.6. Effect of the treatment on composites morphology ..... 257
3.7. Effect of the treatment on composites tensile properties ..... 259
3.8. Effect of the treatment on composites water absorption behavior ..... 261
3.9. Conclusion on the composite manufacture with treated BSG ..... 262

**4. Conclusion ..... 262**

***General conclusion (EN) ..... 265***

*Conclusion générale (FR)..... 268*

*References ..... 271*

# Table des matières (FR)

**Liste des figures**
**Liste des tableaux**
**Liste des symboles**
**Introduction générale (FR)**

**General introduction (EN)**

**RÉSUMÉ DU CHAPITRE 1**
**Chapitre 1 : État de l'art**

1. **Introduction**
2. **Polymères thermoplastiques comme matrices pour les composites biosourcés**
   2.1. Introduction
   2.2. Polymères d'origine pétrochimique
   2.3. Polymères biosourcés et biodégradables
   2.4. Études comparatives entre PLA et PP
3. **Charges naturelles pour matériaux composites**
   3.1. Fibres naturelles
   3.2. Drêche de brasserie
4. **Traitement des charges**
   4.1. Préparation des charges
   4.2. Stratégies de modification/compatibilisation des charges
5. **Procédés de fabrication des composites particulaires**
   5.1. Étapes du procédé de fabrication
   5.2. Mélangeur interne
   5.3. Extrusion
   5.4. Moulage par injection
   5.5. Conclusion
6. **Propriétés des composites particulaires : expérimentation et théorie**
   6.1. Introduction
   6.2. Comportement rhéologique
   6.3. Caractéristiques thermiques
   6.4. Comportement mécanique : Test de traction
   6.5. Absorption d'eau
7. **Conclusion : objectifs et défis**

**RÉSUMÉ DU CHAPITRE 2**
**Chapitre 2 : Matériaux et méthodes**

1. **Vue d'ensemble de la stratégie de recherche / conception de l'étude**

2. **Matériaux**
   2.1. PP et PLA
   2.2. Drêche de brasserie

3. **Méthodes de caractérisation**
   3.1. Caractérisations chimiques et microstructurales
   3.2. Propriétés rhéologiques
   3.3. Propriétés mécaniques
   3.4. Caractérisations thermiques
   3.5. Comportement vis-à-vis de l'eau
   3.6. Analyse statistique

4. **Production des matériaux**
   4.1. Première partie de la thèse : élaboration des composites par mélangeur interne
   4.2. Deuxième partie de la thèse : séchage de la drêche par extrusion
   4.3. Troisième partie de la thèse : stratégies d'optimisation des composites
   4.4. Traitement alcalin de la drêche pour améliorer l'adhésion à l'interface

**RÉSUMÉ DU CHAPITRE 3**
**Chapitre 3 : Développement de matériaux biosourcés**

1. **Introduction**

2. **Préparation des matériaux**
   2.1. Mélangeur interne
   2.2. Moulage par injection

3. **Comportement à la dégradation thermique**

4. **Comportement de transition thermique**

5. **Comportement rhéologique**
   5.1. Balayage en déformation
   5.2. Balayage en fréquence

6. **Morphologie à l'interface**
   6.1. Cryofracture
   6.2. Fracture de traction

7. **Comportement mécanique**
   7.1. Module de Young
   7.2. Modèle en l'absence d'adhésion

8. **Comportement d'absorption d'eau**

9. **Conclusions**

**RÉSUMÉ DU CHAPITRE 4**
**Chapitre 4 : Séchage et broyage intégrés de la drêche de brasserie par extrusion**

1. **Introduction**

2. **Objectif : réduction de la teneur en humidité**

3. **Étude préliminaire**
   3.1. Introduction
   3.2. Première série d'essais – Définition d'une fenêtre de paramètres
   3.3. Deuxième série d'essais – Profil de vis modifié

4. **Méthodologie des essais d'extrusion**
   4.1. Profil d'extrusion
   4.2. Paramètres d'extrusion
   4.3. Effets des paramètres sur la teneur en humidité de BSG

5. **Résultats**
   5.1. Effets des paramètres sur la distribution granulométrique
   5.2. Aspect des particules (MEB)
   5.3. Stabilité thermique des particules extrudées
   5.4. Consommation énergétique : méthode d'origine vs extrusion

6. **Conclusions**

**RÉSUMÉ DU CHAPITRE 5**
**Chapitre 5 : Stratégies de pontage pour l'optimisation des composites**

1. **Introduction**

2. **Production de composites à base de drêche extrudée par mélangeur interne**
   2.1. Présentation des composites
   2.2. Effet de la drêche extrudée sur les composites PP et PLA
   2.3. Conclusion

3. **Changement d'échelle du procédé : de laboratoire à pilote**
   3.1. Introduction
   3.2. Mélange des composites : du mélangeur interne à l'extrusion
   3.3. Moulage des composites : de la presse manuelle à la presse industrielle
   3.4. Conclusion sur les méthodes d'injection

4. **Conclusions**

**RÉSUMÉ DU CHAPITRE 6**
**Chapitre 6 : Traitement alcalin de la drêche pour améliorer l'adhésion à l'interface avec les matrices polymères**

1. **Introduction**

2. **Traitement de la drêche à la soude (NaOH)**
   2.1. Introduction
   2.2. Effet du traitement sur les fonctions chimiques de BSG
   2.3. Effet du traitement sur la stabilité thermique de BSG
   2.4. Effet du traitement sur l'aspect des particules de BSG
   2.5. Conclusion

3. **Fabrication des composites**
   3.1. Introduction
   3.2. Densité de BSG
   3.3. Effet du traitement sur la stabilité thermique des composites

3.4. Effet du traitement sur le comportement rhéologique des composites
3.5. Effet du traitement sur les transitions thermiques des composites
3.6. Effet du traitement sur la morphologie des composites
3.7. Effet du traitement sur les propriétés mécaniques en traction
3.8. Effet du traitement sur l'absorption d'eau des composites
3.9. Conclusion sur la fabrication des composites à base de drêche traitée

**4. Conclusion**

**General conclusion (EN)**

**Conclusion générale (FR)**
**Références**

# Table of figures

*Figure 1.1: Classification of biocomposites* ..... *12*
*Figure 1.2: General formula of PP* ..... *14*
*Figure 1.3: Schematic representation of the isotacticity of polypropylene and common PP copolymer, red circles for $CH_3$, blue circles for $CH_3$, $CH_2$ or CH, and green circles for $CH_2$ from ethylene monomers.* ..... *15*
*Figure 1.4: Schematic of the production of three forms of lactide* ..... *19*
*Figure 1.5: Classification of Natural fibers including some examples* ..... *27*
*Figure 1.6: Global production trends of natural fibers and fiber-rich crops from 2015 to 2023. Data collected on FAO website (consulted in May 2025).* ..... *28*
*Figure 1.7: Structural organization of the plant cell wall, highlighting the arrangement of the three main components (cellulose -green-, hemicellulose -yellow-, and lignin (G-guaiacyl, S-syringyl, H-p hydroxyphenyl) focusing on the secondary cell wall* ..... *31*
*Figure 1.8: Brewing process* ..... *32*
*Figure 1.9: Production quantities of Beer from barley (kg) of the top five beer-producing countries and Production shares of Beer from barley - average 2015-2023, extracted from the FAO (consulted in May 2025).* ..... *33*
*Figure 1.10: Current disposal methods of BSG in Europe and their drawbacks [94]* ..... *35*
*Figure 1.11: Picture of dry BSG and the schematic representation of a barley grain in longitudinal section* ..... *35*
*Figure 1.12: Overview of the main research teams (grouped by color) contributing to the development of brewer's spent grain (BSG) composites, with main results of studies published by each.* ..... *38*
*Figure 1.13: Comparison of drying methods based on their energy consumption and processing time* ... *41*
*Figure 1.14: Multiscale structure of lignocellulosic biomass and corresponding milling technologies with their global energy consumption; color gradient indicates relative energy consumption, with green representing lower energy requirement.* ..... *43*
*Figure 1.15: Different types of screw element* ..... *45*
*Figure 1.16: FTIR spectra of untreated and alkali treated walnutshell flour from [182].* ..... *56*
*Figure 1.17: Fibrillation effect, SEM images of untreated flax fiber and 10% NaOH treated flax fibers from [185].* ..... *57*
*Figure 1.18: Schematic representation of Internal mixer along with typical curve of torque against time when introducing a thermoplastic material.* ..... *60*
*Figure 1.19: Scheme of a twin-screw extruder used as compounder for bio-based composites.* ..... *61*
*Figure 1.20: Scheme of an injection molding machine extracted from [310]* ..... *62*
*Figure 1.21: Scheme of a plate-plate oscillatory rheometer* ..... *64*
*Figure 1.22: Plot of Log G' and Log G" vs. Log strain of hypothetical polymer* ..... *65*
*Figure 1.23: (a) Log G' and Log G" vs. Log angular frequency with highlighted crossover point (b) Common shear rates occurring in different processes extracted from [311]* ..... *66*
*Figure 1.24: Viscosity curves for ideally viscous, shear thinning and shear thickening flow behavior.* ..... *67*
*Figure 1.25: (**a**) Typical dynamic moduli plots (G' solid line, G" dashed line) for increasing wood flour content $\phi$.; (**b**) Typical complex viscosity plot at increasing wood flour content, extracted from [312].* ..... *69*
*Figure 1.26: Typical DSC curve of the different thermal events of a thermoplastic material.* ..... *70*
*Figure 1.27: Stress-Strain curve of a typical tensile test displaying four stages* ..... *73*
*Figure 1.28: Stress-strain curve of rice husks-PP composites at different filler content extracted from [212].* ..... *74*
*Figure 1.29: Young's modulus prediction models derived from parallel and series models with Elastic modulus of composites ($E_c$), Elastic modulus of the matrix ($E_m$), Ekastic modulus of particles ($E_p$), Volume content of the matrix ($v_m$), and Volume content of the particles ($v_p$).* ..... *75*
*Figure 1.30: Young's modulus prediction models derived from Einstein's model Shear modulus of composites ($\eta_c$), Shear modulus of the matrix ($\eta_m$), Elastic modulus of composite ($E_c$), Elastic modulus of matrix ($E_m$), and Volume content of the particles ($v_p$).* ..... *76*

*Figure 1.31: More recent Young's modulus prediction models with Elastic modulus of composite ($E_c$), Elastic modulus of matrix ($E_m$), η is Halpin-Tsai constant parameter, A and B being Nielsen constant parameters.* ..... *77*
*Figure 1.32: Determination of HDPE composite modulus containing rice hulls. Using some of the presented models, extracted from [223]* ..... *78*
*Figure 1.33: Moisture absorption mechanism creating degradation of the interfacial adhesion and fiber-matrix debonding, grey rectangles represent the matrix.* ..... *81*
*Figure 1.34: Water absorption curves of rice husk-PP composites at different loadings of rice husks extracted from [313]* ..... *82*

*Figure 2.1: Flowchart representing all the methods used to elaborate the different materials of this PhD work.* ..... *88*
*Figure 2.2: PLA pellets on the left and PP pellets on the right* ..... *89*
*Figure 2.3: Wet Brewer's spent grain* ..... *90*
*Figure 2.4: Malvern 3000 laser particle size apparatus* ..... *90*
*Figure 2.5: Schematic procedure to determine BGS composition* ..... *91*
*Figure 2.6: Rheometer AR2000ex equipped with a parallel plate geometry and its scheme.* ..... *92*
*Figure 2.7: Strain sweep test showing storage modulus versus Strain with the limit of LVR and selected strain* ..... *93*
*Figure 2.8: TG analyzer along with temperature program* ..... *95*
*Figure 2.9: Moisture analyzer Kern DAB* ..... *96*
*Figure 2.10: Water activity analyzer Labswift* ..... *97*
*Figure 2.11: Water absorption experiment on BSG composites.* ..... *98*
*Figure 2.12: Schematic summary of thesis first part experiments to elaborate and characterize BSG-PP/PLA composite materials.* ..... *99*
*Figure 2.13: Rotor miller and BSG after and before grinding.* ..... *99*
*Figure 2.14: Rheomix 600 QC internal mixer and Holishred plastic crusher* ..... *100*
*Figure 2.15: Holipress, circular mold, and rectangle mold* ..... *101*
*Figure 2.16: Schematic illustration of the injection press with distances and applied force indicated for pressure calculation.* ..... *102*
*Figure 2.17: Die-cut equipment and dog-bone shape die* ..... *102*
*Figure 2.18: Schematic description of BSG drying grinding by extrusion study* ..... *103*
*Figure 2.19: Correlation between the volumetric feeder motor load (percentage of maximum capacity, Q BSG (%)) and BSG feed rate (Q BSG in kg/h)* ..... *104*
*Figure 2.20: Screw profile selected for further drying grinding investigations.* ..... *105*
*Figure 2.21: Screw profile used for material composites compounding* ..... *111*
*Figure 2.22: Schematic diagram for alkaline chemical pretreatment of BSG.* ..... *112*

*Figure 3.1: Schematic summary of chapter 3 experiments to elaborate and characterize BSG-PP/PLA composite materials* ..... *117*
*Figure 3.2: Torque and temperature as function of time during processing of PLA and BSG-PLA composites at different BSG loadings in internal mixer at 180°C and 50 rpm* ..... *118*
*Figure 3.3: Torque and temperature as function of time during processing of PP and BSG-PP composites at different BSG loadings in internal mixer at 180°C and 50 rpm* ..... *118*
*Figure 3.4: Log G' and Log G" vs. Log angular frequency of pure PP at 180 and 200°C and PLA at 180 °C, with highlighted crossover points* ..... *120*
*Figure 3.5: Thermogravimetric Analysis of dry and ground BSG. Relative mass loss and its derivative curves showing decomposition rate as a function of temperature (10 K/min under nitrogen flow). Average of three experiments.* ..... *122*

*Figure 3.6: Thermogravimetric analysis of biocomposites made with BSG and PP. DTG curves showing decomposition rate as a function of temperature (10 K/min under nitrogen flow). Average of three experiments.* ..... *123*
*Figure 3.7: Thermogravimetric analysis of biocomposites made with BSG and PLA. DTG curves showing decomposition rate as a function of temperature (10 K/min under nitrogen flow). Average of three experiments.* ..... *125*
*Figure 3.8: Detection of PLA molecules using refractive index as function of elution time (a) and comparison of the number average molecular weight (Mn) of PLA composites (b) after internal mixing and injection molding. Different letters (a,b,c) indicate statistically significant differences between samples.* ..... *125*
*Figure 3.9: Differential scanning calorimetry curves of pure BSG, injected PP and composites at 10 K/min, under nitrogen atmosphere* ..... *127*
*Figure 3.10: Differential scanning calorimetry curves of injected PLA and composites at 10 K/min, under nitrogen atmosphere.* ..... *128*
*Figure 3.11: Log G' vs Log strain and 10 rad/s in plate-plate rheometer at 180 °C for PP and PP composites processed at 180 °C in internal mixer at 180 °C and injected at 200 °C, plate-plate gap = 2200 µm, plate diameter = 25 mm* ..... *131*
*Figure 3.12: Log G' vs Log strain and 10 rad/s in plate rheometer at 180°C for PLA and PLA composites processed at 180°C in internal mixer and injected at 180°C, plate-plate gap = 2200 µm, plate diameter = 25mm*..... *132*
*Figure 3.13: Effects of BSG ratio on storage modulus (Pa) vs. angular frequency (rad/s) in plate-plate rheometer at 180 °C for PP and PP composites processed at 180 °C in internal mixer at 180 °C and injected at 200°C $\Phi$= volume fraction of BSG, s= slope of the curve, plate-plate gap = 2200 µm, plate diameter = 25 mm, strain = 10 % for PP, PPBSG10, PPBSG20, 0.05 % for composites with 30, 40 and 50 %(m/m) BSG. Average of three experiments.* ..... *133*
*Figure 3.14: Effects of BSG ratio on complex viscosity (Pa.s) vs. angular frequency (rad/s) in plate-plate rheometer at 180 °C for PP and PP composites processed at 180 °C in internal mixer at 180 °C and injected at 200 °C $\Phi$= volume fraction of BSG, plate-plate gap = 2200 µm, plate diameter = 25 mm, strain = 10 % for PP, PPBSG10, PPBSG20, 0.05 % for composites with 30, 40 and 50 %(m/m) BSG. Average of three experiments.* ..... *134*
*Figure 3.15: Effects of BSG ratio on storage modulus (Pa) vs. angular frequency (rad/s) in plate rheometer at 180 °C for PLA and PLA composites processed at 180 °C in internal mixer and injected at 180 °C, $\Phi$ = volume fraction of BSG, plate-plate gap = 2200 µm, plate diameter = 25 mm, strain = 10 % for PLA, PLABSG10, and PLABSG20, 0.05 % for composites with 30, 40 and 50 %(m/m) BSG. Average of three experiments.*..... *135*
*Figure 3.16: Effects of BSG ratio on complex viscosity (Pa.s) vs. angular frequency (rad/s) in plate rheometer at 180 °C for PLA and PLA composites processed at 180 °C in internal mixer and injected at 180 °C, $\Phi$ = volume fraction of BSG, plate-plate gap = 2200 µm, plate diameter = 25 mm, strain = 10 % for PLA, PLABSG10, and PLABSG20, 0.05 % for composites with 30, 40 and 50 %(m/m) BSG. Average of three experiments.*..... *136*
*Figure 3.17: SEM micrographs taken from the cryofracture surface of PP composites obtained using internal mixing (180 °C, 50 rpm, 5 min) and injection molding (200 °C) x50*..... *138*
*Figure 3.18: SEM micrographs of cryofracture surface of PLA composites obtained using internal mixing (180 °C, 50 rpm, 5 min) and injection molding (180 °C) x50*..... *139*
*Figure 3.19: SEM micrographs of samples fractured cross-section of tensile specimens: Neat PP ; Neat PLA ; PPBSG30x200 ; PLABSG30x200 ; PPBSG50x500 ; PLABSG30x500*..... *141*
*Figure 3.20: Comparison of Young's modulus for different BSG mass fraction in PLA and PP composites.* ..... *142*
*Figure 3.21: Comparison of maximum tensile strength predicted form Nicolais-Narkis model for BSG reinforced PP and PLA composite* ..... *145*
*Figure 3.22: Water absorption curve for BSG/PP or PLA composites drown in water at room temperature, means of duplicates.*..... *146*

*Figure 3.23: Water absorption of PP and PLA composites after two days as a function of BSG volume fraction* ..... *147*
*Figure 3.24: Water absorption of PP and PLA composites after 21 days as a function of BSG volume fraction* ..... *148*
*Figure 3.25: PLABSG50 and PPBSG50 samples after 21 days of water immersion* ..... *149*
*Figure 3.26: Schematic overview summarizing the key results and interpretations of Chapter 3* ..... *150*

*Figure 4.1: Structure of the chapter and experimental workflow.* ..... *155*
*Figure 4.2: Moisture sorption isotherm of BSG showing experimental moisture content (dots) and GAB model prediction (dash line)* ..... *156*
*Figure 4.3: Screw profile 1 of the twin-screw extruder designed to grind and dry BSG* ..... *158*
*Figure 4.4: Average residence time recorded as function of screw speed for profile 1, considering all feed rates (10-70%) and all temperatures (110-190°C)* ..... *159*
*Figure 4.5: Moisture content (% wet basis) of BSG after extrusion using Screw Profile 1 as a function of screw speed (100, 250, and 450 rpm), feed rate (10, 25, 55, and 70 % motor load), and barrel temperature (110, 150, and 190 °C). Means of triplicates. Initial BSG moisture = 75 % (wet basis).* ..... *160*
*Figure 4.6: Summary of preliminary process results using Profile 1. Crosses indicate unprocessable parameter combinations, red circles correspond to the highest moisture contents (> 55 %), and green circles are used for the lowest values (<40%).* ..... *161*
*Figure 4.7: Pearson correlation matrix showing the relationship between processing parameters (Temperature, Screw Speed, Throughput), Residence Time and BSG moisture content for Profile 1. The size and color intensity of the circles indicate the strength and direction of the correlations.* ..... *162*
*Figure 4.8: Screw profile 2 of the twin-screw extruder designed to grind and dry BSG incremented by one grooved reverse element* ..... *163*
*Figure 4.9: Screw profile 3 of the twin-screw extruder designed to grind and dry BSG incremented by two grooved reverse elements* ..... *164*
*Figure 4.10: Screw profile 4 of the twin-screw extruder designed to grind and dry BSG incremented by one grooved and one full reverse element* ..... *164*
*Figure 4.11: Residence time of BSG at a feed rate of 10 % and 150 °C, for four screw profiles and three screw speeds* ..... *165*
*Figure 4.12: Average moisture content of BSG at a feed rate of 10 % and temperatures of 150 °C, for four screw profiles and three screw speeds* ..... *166*
*Figure 4.13: Moisture content of BSG vs residence time at 150 °C and a feed rate of 10 %, each shape and color representing a screw profile, the intensity of the color corresponds to the screw speed as displayed in the legend* ..... *167*
*Figure 4.14: Moisture content of BSG against screw speed for different screw profiles (1,2,3,4) at 150°C (on the left) and 190°C (on the right) for a feed rate of 25%* ..... *168*
*Figure 4.15: Visual comparison of BSG after processing by two different methods: (A) BSG extruded using Profile 3 at 150 °C, 10 % feed rate, and 250 rpm; (B) BSG dried and ground following the method described in Chapter 3* ..... *169*
*Figure 4.16: Screw profile 5 of the twin-screw extruder designed to grind and dry BSG incremented by two grooved and two full reverse elements* ..... *170*
*Figure 4.17: Average moisture content (wet basis) of BSG after extrusion process as function of Temperature (°C) and Screw speed (rpm) at 1.8kg/h using Profile 5* ..... *171*
*Figure 4.18: Particle size distribution of BSG dried and ground using method of Chapter 3 next to its SEM image x80* ..... *172*
*Figure 4.19: Particle size distribution of extruded BSG at three barrel temperatures (150 °C, 170 °C, and 190 °C) and three screw speeds (200, 300, and 400 rpm) using Profile 5* ..... *172*
*Figure 4.20: Particle size distribution of extruded BSG at three screw speeds (200, 300, and 400 rpm) and three barrel temperatures (150 °C, 170 °C, and 190 °C) using Profile 5* ..... *175*
*Figure 4.21: Effect of processing variable conditions (temperature and screw speed) on median size ($D_{50}$) of extruded BSG particles.* ..... *176*

*Figure 4.22: SEM images of conventional BSG (from chapter 3) (x80 and x200) compared to extruded BSG at 150 °C 400 rpm Profile 5(x80 and x800)* ..... *177*
*Figure 4.23:SEM images of extruded BSG using Profile 5 at: a) 190 °C and 400 rpm x 200 b) 150 °C and 300 rpm x800* ..... *178*
*Figure 4.24: SEM images of extruded BSG at 150 °C, 200 rpm using Profile 5, magnifications a) x80 and b) x2000* ..... *178*
*Figure 4.25: SEM images of extruded BSG at 190 °C, 200 rpm using Profile 5, magnifications a) x80 and b) x200* ..... *179*
*Figure 4.26: Thermogravimetric curves (a,c,e) and their derivatives (b,d,f) of BSG made with conventional method and extruded BSG with profile 5 at 200 rpm (a,b) ; 300 (c,d) ; 400 rpm (e,f)* ..... *181*
*Figure 4.27: Schematic overview of Chapter 4.* ..... *186*

*Figure 5.1: Structure of the Chapter and experimental workflow.* ..... *190*
*Figure 5.2: Thermogravimetric analysis of biocomposites made with 30 %(m/m) of extruded BSG (Profile5) or BSG conv with 70 %(m/m) of PP (a,c) or PLA (b,d) (MI 180 °C, 50 rpm, 5 min) TG and DTG curves. Average of three experiments for TG curves and most representative of the three samples for DTG curves.* ..... *191*
*Figure 5.3: Particle size distribution of BSGconv and BSGext (Profile 5 at 150°C_200rpm, 170°C_300rpm and 190°C_400rpm)* ..... *192*
*Figure 5.4: Differential scanning calorimetry curves of injected PP and PLA composites containing 30 %(m/m) of extruded BSG or BSGconv, at 10K/min, under nitrogen atmosphere.* ..... *194*
*Figure 5.5: Effect on BSG process on storage modulus and complex viscosity vs. angular frequency (rad/s) in plate-plate rheometer at 180 °C for PP composites processed at 180 °C in internal mixer and injected at 200 °C, plate-plate gap = 2200 µm, plate diameter = 25mm; strain = 0.05 %. Average of three experiments, error bars fall within the symbols.* ..... *198*
*Figure 5.6: Effect on BSG process on storage modulus, loss modulus and complex viscosity vs. angular frequency (rad/s) in plate-plate rheometer at 180 °C for PLA composites processed at 180 °C in internal mixer and injected at 180 °C, plate-plate gap = 2200 µm, plate diameter = 25 mm, strain= 0.05 % [200-1rad/s] and 0.4% [1-0.1 rad/s]. Average of three experiments, error bars fall within the symbols. Blue arrow indicating crossover point.* ..... *199*
*Figure 5.7: SEM micrographs of PP composites filled with 30 %(m/m) BSGconv and extruded BSG, made with IM 180°C 50 rpm 5 min and injected at 200 °C observation of the tensile fractured cross-section x100* ..... *201*
*Figure 5.8: SEM micrographs of PP composites with BSGconv and extruded BSG, observation of the tensile fractured cross-section x500* ..... *202*
*Figure 5.9: SEM micrographs of PLA composites with BSGconv and extruded BSG, observation of the tensile fractured cross-section x100 and x500* ..... *203*
*Figure 5.10: Effect of BSG processing on PP composites (Internal mixing 180 °C 50 rpm 5 min) mechanical properties (Young's modulus and yield tensile strength)* ..... *204*
*Figure 5.11: Effect of BSG processing on PLA composites mechanical properties (Young's modulus and yield tensile strength), 2 mm/min.* ..... *205*
*Figure 5.12: Overview of scale-up approaches evaluated.* ..... *208*
*Figure 5.13: Thermogravimetric analysis of PP obtained through extrusion compared to PP obtained through internal mixing (TG and DTG curves, 10 K/min under nitrogen flow. Average of three experiments.* ..... *209*
*Figure 5.14: Thermogravimetric analysis of PP composites containing 30 %(m/m) of BSG obtained through extrusion compared to PP composites obtained through internal mixing (180 °C, 50 rpm, 5 min), 10 K/min under nitrogen flow. Average of three experiments.* ..... *209*
*Figure 5.15: Effects of compounding method (internal mixing a) c) or extrusion b) d)) on storage modulus (Pa) (a,b) and complex viscosity (Pa.s) (c,d) vs. angular frequency (rad/s) in plate rheometer at 180°C for Polypropylene (PP) composites made with 30 % of different BSG injected at 200 °C using laboratory*

*press, plate-plate gap = 2200 µm, plate diameter = 25 mm, strain 0.05%. Average of three experiments* ..... *211*
*Figure 5.16: SEM micrographs of PP70BSGconv composites compounded using either extrusion or internal mixing, observation of the tensile fractured cross-section x100 and x500* ..... *212*
*Figure 5.17: SEM micrographs of PP70BSGext150 composites compounded using either extrusion or internal mixing, observation of the tensile fractured cross-section x100 and x500* ..... *213*
*Figure 5.18: SEM micrographs of PP70BSGext190 composites compounded using either extrusion or internal mixing, observation of the tensile fractured cross-section x100 and x500* ..... *214*
*Figure 5.19: Comparison of Young's modulus for different processing methods in PP composites containing 30% of BSG (conv or extruded). Average of five experiments.* ..... *215*
*Figure 5.20: Comparison of maximum tensile strength for different processing methods in PP composites containing 30 % of BSG (conv or extruded). Average of five experiments.* ..... *216*
*Figure 5.21: Effect of compounding method on water absorption of PP and PP composites containing 30% of BSGconv and injected with laboratory press, means of two replicates.* ..... *218*
*Figure 5.22: Effect of processing methods to obtain BSG on water absorption of extruded PP composites containing 30% of BSG and injected with laboratory press, means of two replicates.* ..... *219*
*Figure 5.23: Differential scanning calorimetry curves of extruded pure PP and PP composites containing 30 %(m/m) of BSGconv, comparison of the injection method, at 10 K/min, under nitrogen atmosphere.* ..... *221*
*Figure 5.24: Comparison of the cross-fractured surface of pure PP and PP composites filled with 30 %(m/m) of BSG conv obtained with two different methods (1-extrusion + industrial injection ; 2- Internal mixing + manual injection)* ..... *223*
*Figure 5.25: Picture of extruded PP specimens from two different injection methods after tensile test* . *224*
*Figure 5.26: SEM micrographs of extruded PP composites filled with 30 %(m/m) of BSG injected using either industrial or manual injection press, observation of the tensile fractured cross-section x80 and x200* ..... *225*
*Figure 5.27: Tensile test specimens obtained from two different injection molding process after industrial injection before (a1) and after tensile test (a2); after manual injection and after tensile test (b)* ..... *226*
*Figure 5.28: Tensile strength of extruded pure PP and PP composites injected via two methods. Different letters indicate statistically different TS.* ..... *227*
*Figure 5.29: Schematic overview of Chapter 5.* ..... *229*

*Figure 6.1: Structure of the Chapter and experimental workflow.* ..... *234*
*Figure 6.2: Alkali pretreatment of BSG particles* ..... *235*
*Figure 6.3: FTIR spectra of our BSG and lignin, cellulose and holocellulose extracted from [208] (4000 to 500 $cm^{-1}$)* ..... *237*
*Figure 6.4: FTIR profiles of untreated BSG and after treatment a) at ambiant temperature b) at 70 °C, circle showing the zones of interest purple for lignin, orange for cellulose and green for hemicellulose belonging bands and arrows showing missing bands.* ..... *238*
*Figure 6.5: Derivative thermogravimetric curves of untreated and treated BSG at ambiant temperature (a) 30min and 1h and b) 4h and 8h) and at 70 °C (c). Average of three experiments.* ..... *241*
*Figure 6.6: SEM images of (a) Raw BSG before grinding x30 and x800, (b) Untreated BSG after grinding x800, (c) Alkali-treated (4 h-70 °C) BSG before grinding x30 and x800, and (d) alkali-treated (4 h-70 °C) BSG after grinding x800* ..... *242*
*Figure 6.7: SEM images of treated BSG particles at two temperatures (room temperature and 70 °C and three different times (30 min, 1h and 4h) after grinding x200* ..... *244*
*Figure 6.8: SEM images of BSG conv and treated BSG particles at two temperatures (room temperature and 70 °C and two times 30min and 4h after milling x80* ..... *245*
*Figure 6.9: Visual comparison of ground BSG after alkaline treatment (4h-70°C) and BSGconv* ..... *247*
*Figure 6.10: Thermogravimetric analysis of PP and PLA biocomposites made with 10 %(m/m) and 30 %(m/m) of traited BSG and BSGconv. TG and DTG curves. Average of three experiments for TG curves and most representative of the three samples for DTG curves.* ..... *249*

*Figure 6.11: Effect of BSG alkaline treatment on storage modulus (G') and complex viscosity vs angular frequency in plate rheometer at 180 °C for PLA and PP composites processed at 180 °C in internal mixer and injected at 180 °C and 200 °C respectively, = volume fraction of BSG, plate-plate gap = 2200 µm, plate diameter = 25 mm, strain = 10 % for PP, PP90BSGconv, PLA and PLA90BSGconv, and 0.05 % for composites with BSGNaOH and 30 % (m/m) BSG. Average of three experiments. ..... 253*
*Figure 6.12: DSC curves of injected PP, PLA composite with BSGconv and BSGNaOH (10 %(m/m) and 30 %(m/m)) at 10 K/min under nitrogen flow. ..... 254*
*Figure 6.13: SEM images of PP and PLA composites with BSGNaOH (internal mixing 180 °C, 50 rpm, 5 min + injection molding lab press 200 °C for PP and 180 °C for PLA), cryofractured surface, x200 ..... 257*
*Figure 6.14: SEM images of PP and PLA composites with BSGNaOH (internal mixing 180 °C, 50 rpm, 5 min + injection molding lab press 200 °C for PP and 180 °C for PLA), tensile fractured surface, except for PLA70BSGNaOH x200 ..... 258*
*Figure 6.15: Comparison of Young's modulus for PP and PLA composites with untreated and alkaline treated BGS. Average of at least 3 replicates at 2 mm/min. ..... 259*
*Figure 6.16: Comparison of max tensile strength for PP and PLA composites with untreated and alkaline treated BGS. Average of at least 3 replicates. 2 mm/min. ..... 260*
*Figure 6.17: Water absorption curves for PP and PLA composites with BSGconv and BSGNaOH drown in water at room temperature, means of duplicates. ..... 262*
*Figure 6.18: Schematic overview of Chapter 6. ..... 263*

## List of Tables

*Table 1.1: PP general properties ..... 17*
*Table 1.2: PLA general properties ..... 22*
*Table 1.3: PLA vs PP main properties ..... 25*
*Table 1.4: Chemical composition of some agro-waste fibers ..... 31*
*Table 1.5: Composition of Brewer's spent grain according to the literature ..... 36*
*Table 1.6: Alkaline treatments used for modifications of natural fibers in polymer composites. ..... 55*
*Table 1.7: Different combinations of internal mixing parameters used in literature to process composites with PP and PLA matrices. ..... 61*
*Table 1.8: Summary of the effects of fillers on the rheology of thermoplastic composite systems. ..... 69*
*Table 1.9: Summary of DSC thermal properties of polypropylene (PP) and polylactic acid (PLA) composites filled with various natural fibers. ..... 72*
*Table 1.10: Tensile strength prediction models ..... 80*

*Table 2.1: Geometric dimensions and schematic representation of the internal mixer used in this Ph.D work. ..... 100*
*Table 2.2: PP and PLA - BSG composites formulations and sample codes. PP density = 0.9 g/cm$^3$; PLA density = 1.24 g/cm$^3$; BSG density = 1.35 g/cm$^3$ ..... 101*
*Table 2.3: Clextral BC21 extruder information and extruder picture ..... 104*
*Table 2.4: Extruder screw geometry and dimensions selected for further drying grinding investigations 106*
*Table 2.5: List of variables and variance ..... 107*
*Table 2.6: PP and PLA- BSG composites formulations made and characterized in Chapter 5 and their sample codes. ..... 109*
*Table 2.7: PP-BSG composites formulations made with extruder and sample codes. ..... 109*
*Table 2.8: Extruder screw geometry and dimensions used to compound composites blends ..... 110*
*Table 2.9: PP and PLA- alkali treated BSG composites formulations made using internal mixer and characterized in chapter 6 and their sample codes. ..... 113*

*Table 3.1: Temperatures reached at maximum degradation rates for biocomposites made with BSG and PP or PLA. The values represent the mean of triplicate measurements, with standard deviations indicated. Different letters (a, b, c) indicate statistically significant differences.* ..... *121*
*Table 3.2: DSC data of PP, PLA and their composites after internal mixing and injection molding. Different letters (a,b,c) indicate statistically significant differences between samples.* ..... *130*

*Table 4.1: GAB parameters of the moisture sorption of BSG and determination of coefficients of the regression ($R^2$)*..... *157*
*Table 4.2: Median size ($D_{50}$) of BSG particles obtained after extrusion for the 9 experimental runs and after drying and grinding following Chapter 3 method. Different letters represent statistically different values.* ..... *175*
*Table 4.3: Multiple regression equation and regression coefficient of median size (µm) of BSG particles after extrusion for various parameters sets* ..... *176*
*Table 4.4: Results of thermogravimetric analysis of extruded BSG samples using Profile 5 and BSGconv, different letters mean significative difference*..... *182*
*Table 4.5: Values of specific mechanical energy required for extrusion drying grinding of BSG under different conditions.* ..... *184*

*Table 5.1: Temperatures reached at maximum degradation rates for biocomposites made with 30 % (m/m) of extruded BSG or BSGconv and 70 %(m/m) of PP or PLA. The values represent the mean of triplicate measurements, with standard deviations indicated. Different letters indicate statistically significant differences*.* ..... *193*
*Table 5.2: DSC data of PP, PLA and their composites with extruded BSG and BSGconv after internal mixing and injection molding. Different letters indicate statistically significant differences between samples.* ..... *197*
*Table 5.3: Temperatures reached at maximum degradation rates for biocomposites made with PP and extruded BSG or BSGconv through two different processing methods (extrusion and internal mixing). The values represent the mean of triplicate measurements, with standard deviations indicated.* ..... *210*
*Table 5.4: Mechanical tensile test results for PP composites comparing two compounding methods. Average of five replicates. Statistical tests were performed pairwise according to the compounding method. Different letters within a row indicate statistically significant differences ($p < 0.05$).*..... *216*
*Table 5.5: Comparison between laboratory and semi-industrial injection presses used for PP composite processing.*..... *220*
*Table 5.6: DSC data of extruded PP and PP composites with 30 %(m/m) of BSGconv, comparison of injection methods (manual (man) vs industrial (ind) with subscript "1" for 1$^{st}$ heating step. Different letters indicate statistically significant differences between samples.* ..... *222*

*Table 6.1: Assignments of FTIR peaks in BSG, lignin, cellulose and holocellulose samples [208,295–298].* ..... *237*
*Table 6.2: Bulk and true densities of BSGNaOH and BSGconv with their calculated maximum packing fraction. Different letters mean statistical differences.* ..... *248*
*Table 6.3: Temperatures reached at maximum degradation rates for biocomposites made with 30 %(m/m) and 10 %(m/m) of alkali-treated BSG 70 %(m/m) and 90 %(m/m) of PP or PLA. The values represent the mean of triplicate measurements, with standard deviations indicated. Different letters indicate statistically significant differences*.* ..... *250*
*Table 6.4: DSC data of PP, PLA and their composites with BSGNaOH and BSGconv after internal mixing and laboratory injection molding. Different letters inidcate statistically significant differences between samples.* ..... *256*

*Table 6.5: Mechanical tensile test results for PP and PP composites with untreated and alkaline treated BSG. Average of at least 3 replicates. 2 mm/min. Different letters indicate statistically significant differences (p-value < 0.05)..... 261*

# List of symbols

**Abbreviations**

ATR: Attenuated Total Reflectance

BSG: Brewer's spent grain

DSC: Differential Scanning Calorimetry

DTG: Derivative Thermogravimetry

EVD: Eilers-Van Dijk

FAO: Food and Agriculture Organization of the United Nations

FTIR: Fourier transform infrared spectroscopy

GAB: Guggenheim-Anderson-de Boer

GPS: 3-glycidyloxypropyl)trimethoxysilane

GTR: Ground Tire rubber

IR: Infra-red

LLDPE: Linear Low-density polyethylene

LVR: Linear Viscoelastic Region

MAPP: Maleated Polypropylene

NREL: National Renewable Energy Laboratory

PA: Polyamids

PBS: Polybutylene succinate

PCL: Polycaprolactone

PDLA: Poly-D-lactic acid

PDLLA: Poly-D-L-lactic acid

PE: Polyethylene

PET: Polyethylene terephtalate

PHA: Polyhydroxyalkanoates

PHB: polyhydroxybutyrate PHB

PHBV : polyhydroxybutyrate-valerate

PLA : Poly lactic Acid

PLLA: Poly-L-lactic Acid

PP : Polypropylene

PSD: Particle size distribution

PTFE: Polytetrafluoroethylene

PVC: Polyvinyl chloride

RSM: Response surface methodology

SEC : Size Exclusion Chromatography

SEM : Scanning Electron Microscopy

SGW: Stone groundwood

SME: Specific Mechanical Energy

TG: Thermogravimetric

TS: Tensile strength

USA: United State of America

UV: Ultraviolet

YM: Young's modulus

**Latin Symbols**

A: parameter of Nielsen equation (Figure 1.31)

Aw: water activity

B: parameter of Nielsen equation (Figure 1.31)

C: Guggenheim constant related to the heat of absorption (Equation 2.4)

C: Average torque of extruder (Equation 2.7)

$C_{max}$: Max torque of extruder (Equation 2.7)

Cos(ϕ): Power factor (Equation 4.2)

D: Inner diameter of extruder

$D_1$: Distance from lever to handle (Figure 2.16)

$D_2$: Distance from lever to force transmitted (Figure 2.16)

$D_{50}$: Median particle size

$E_c$: Elastic modulus of composite (Figure 1.30)

$E_m$: Elastic modulus of matrix (Figure 1.30)

$E_p$: Elastic modulus of particles (Figure 1.30)

f: shape factor (Figure 1.30)

F: load applied during tensile test (Equation 2.1)

$F_m$: Manual force (estimated) (Figure 2.16)

$F_t$: Transmitted force (Figure 2.16)

G': Storage modulus

G": Loss modulus

I: Current intensity (Equation 4.2)

K: Constant related to temperature effect (Equation 2.4)

k: crowding factor (Figure 1.30)

L: Total length of extruder

$L_0$: Gauge length

$M_0$: Mass of dry sample (Equation 2.5)

Mn: Molecular mass

$mP_I$: First melting peak

$mP_{II}$: Second melting peak

$M_t$: mass of absorbed water at t (Equation 2.5)

n: number of monomers

N: Rotor speed (Equation 3.1)

N: Screw speed (Equation 2.7)

$N_{max}$: Max screw speed of the extruder (Equation 2.7)

p: aspect ratio (Figure 1.30)

P: Power consumption (Equation 4.2)

Q: Mass feedrate (Equation 2.7)

r: motor efficiency (Equation 2.7)

$R_e$: Largest rotor radius (Equation 3.1)

$R_i$: Smallest rotor radius (Equation 3.1)

S: Screw speed (Equation 2.6)

S: Section area of the specimen (Equation 2.2)

s: crowding factor (Figure 1.30)

S: stress concentration function (Table 1.10)

$S_{G'}$: Slope of G' curve

$S_{G''}$: Slope of G" curve

T: Temperature of the barrel (Equation 2.6)

$T_{1\%}$ : Temperature reached at 1% of mass loss

$T_{50\%}$ : Temperature reached at 50% of mass loss

$T_c$ : Crystallization temperature

$T_{cc}$ : Cold crystallization temperature

$T_g$ : Glass transition temperature

$T_m$: Melting temperature

$T_{m1}$: Melting temperature (First heating curve)

$T_{m2}$: Melting temperature (Second heating curve)

$T^{\infty}$: $T_g$ at infinite molecular weight

$T_{peak1}$: Degradation temperature of DTG peak 1

$T_{peak2}$: Degradation temperature of DTG peak 2

U: Nominal voltage (Equation 4.2)

V: sedimentation vs true volume ratio of the filler (Table 1.10)

$v_m$: Volume of matrix (Figure 1.30)

$v_p$: volume of particle (Figure 1.30)

w: weight fraction of polymer (Equation 1.4)

W: moisture content of BSG on a dry basis (g water/ g dry BSG) (Equation 2.4)

W: nominal power (Equation 2.7)

$W_m$: Monolayer moisture content (dry basis) (Equation 2.4)

X: state of adhesion (Figure 1.29)

Y: Predicted response (Equation 2.6)

**Grek Symbols**

$\dot{\gamma}$: shear rate (Equation 3.1)

α: state of parallel (Figure 1.29)

β: state of series (Figure 1.29)

$\beta_0$: intercept (Equation 2.6)

$\beta_1$: linear coefficient (Equation 2.6)

$\beta_2$: linear coefficient (Equation 2.6)

$\beta_3$: quadratic coefficient (Equation 2.6)

$\beta_4$: quadratic coefficient (Equation 2.6)

$\beta_5$: interaction coefficient (Equation 2.6)

$\Delta H^0_m$: Enthalpy of melting for a 100 % crystalline sample (Equation 1.4)

$\Delta H_{cc}$ : Enthalpy for the cold crystallisation (Equation 1.4)

$\Delta H_m$: Enthalpy for melting transition (Equation 1.4)

$\Delta L$: Deformation of initial elongated gauge length

$\varepsilon_c$: Elongation at break of composite

$\varepsilon_m$: Elongation at break of matrix

$\eta$: Viscosity

$\eta$: Halpin-Tsai constant parameter

$\eta^*$: Complex viscosity

$\eta_c$: Viscosity of composite (Figure 1.30)

$\eta_m$: Viscosity of matrix (Figure 1.30)

$\sigma_c$: Tensile strength of composite

$\sigma_m$: Tensile strength of matrix

$\chi c$ : degree of crystallinity

$\chi c_1$: degree of crystallinity (First heating curve)

$\chi c_2$: degree of crystallinity (Second heating curve)

$\Phi$: Volume fraction

$\Phi_m$: Maximum packing fraction

$\Phi_p$: Particle volume fraction

$\omega$: Angular frequency

$\psi$ : Parameter considering maximum packing fraction (Figure 1.31)

# INTRODUCTIONS

# Introduction générale (FR)

Nous le savons tous, le plastique est omniprésent et il a contribué à la révolution de nos activités quotidiennes. En effet, il serait difficile, pour ne pas dire impossible, de passer une journée sans entrer en contact avec un objet en plastique, tant ce matériau a pénétré tous les aspects de notre quotidien. Néanmoins, son héritage se mesure en million de tonnes de déchets persistants, à la fois dans les sols et dans les océans. Face à cette crise, la question n'est plus de savoir s'il faut repenser ces matériaux mais comment accélérer la transition vers des alternatives plus durables. Parmi les solutions envisageables permettant de conjuguer exigences industrielles et enjeux environnementaux, se trouvent les biocomposites. En associant polymères et biomasse lignocellulosique, ils représentent une alternative sérieuse et prometteuse aux plastiques d'origine fossile.

Un biocomposite désigne de manière générale un matériau composite constitué, en tout ou en grande partie, de biomasse. Les fibres naturelles (souvent lignocellulosiques) y sont associées à des polymères d'origine pétrochimique ou biosourcée, conférant au matériau de bonnes propriétés mécaniques, souvent particulièrement adaptées aux applications semi-structurelle. Lorsqu'une matrice pétrochimique est utilisée, l'incorporation de biomasse permet en outre de réduire la part de composés d'origine fossile dans le matériau final. Dans ce dernier cas, l'objectif en termes de performance est d'obtenir des propriétés similaires à celle de la matrice seule.

Ainsi, le potentiel de ces biocomposites repose sur l'exploitation de la biomasse lignocellulosique, renouvelable et souvent sous-valorisée, dans l'objectif de diminuer la consommation de plastique dérivé du pétrole. À cela s'ajoute une deuxième qualité, ces matériaux ne sont pas seulement plus durables mais ils représentent également une opportunité de valorisation pour les co-produits agricoles et agro-industriels. C'est le cas des drêches de brasserie, résidus majoritaires de la filière brassicole.

Encore trop souvent considérées comme un déchet, les drêches de brasserie représentent 85 % des résidus solides d'une brasserie. Actuellement, elles sont évacuées de trois manières majoritaires : par incinération, épandage dans les champs, ce qui donne lieu à la génération de gaz à effet de serre, ou encore données aux animaux mais peuvent être refusées en raison de leur contamination par des pathogènes. En effet, du fait de leur composition très riche en sucres et très humide, les drêches sont fortement exposées à la colonisation

microbienne. Par ailleurs, cet aspect les rend difficilement valorisables tant elles sont périssables rapidement et de fait difficilement stockables. Nous soulevons ici l'une des problématiques majeures de ce travail : concevoir un procédé continu à l'échelle laboratoire de séchage et de broyage permettant à la fois leur conservation et leur utilisation directe dans les composites et qui présente un potentiel d'industrialisation.

Plus largement, ce défi illustre les verrous scientifiques et techniques auxquels se heurtent les biocomposites. Parmi ceux-ci figure la variabilité des fibres lignocellulosiques : si les biocomposites ont montré de bons résultats avec les fibres de bois, il reste pertinent d'élargir le champ des expérimentations et des connaissances à d'autres charges lignocellulosiques et d'en évaluer leur potentiel. L'un des obstacles les plus fréquemment soulignés dans la littérature concerne par ailleurs, l'incompatibilité entre les fibres lignocellulosiques, de nature hydrophile, et les matrices polymères, majoritairement hydrophobes. Répondre à ces défis exige une approche intégrée, croisant science des matériaux, procédés et traitement de la biomasse.

C'est dans ce cadre que s'inscrit ce travail de thèse. L'objectif est multiple :

(i) Explorer et caractériser le potentiel des drêches de brasserie comme charge dans les composites thermoplastiques, en particulier le polypropylène (PP) et l'acide polylactique (PLA)

(ii) Développer un procédé adapté afin d'améliorer la stabilité et la compatibilité des drêches obtenues.

(iii) Initier un changement d'échelle, en passant des essais de laboratoire à des procédés pilotes, constituant une première étape vers une possible industrialisation.

(iv) Développer un traitement adapté en vue d'améliorer la compatibilité entre la drêche et les matrices thermoplastiques (PP et PLA)

Pour y parvenir la recherche s'est déployée en 4 axes complémentaires constituant 6 chapitres.

Le chapitre 1 est consacré à une étude de l'état de l'art autour de cinq axes principaux. Les deux premiers axes se focalisent sur les deux constituants d'un biocomposite : la matrice, avec une attention particulière portée sur le PP et le PLA et sur les études récemment réalisées comparant ces deux matrices, ainsi que la charge, présentée progressivement partant d'une perspective plus large, les fibres naturelles, pour converger jusqu'aux drêches de brasserie en passant par les fibres lignocellulosiques dérivées des co-produits agro-industriels. Le troisième axe aborde la préparation de ces fibres en vue d'une application composite. Cet axe est scindé

en deux parties, l'une se concentre sur les prétraitements indispensables des fibres tels que le séchage et le broyage ; l'autre discute des traitements dont l'objectif est d'améliorer la compatibilité des renforts lignocellulosiques avec la matrice. Le quatrième axe permet d'introduire les principales méthodes de mise en œuvre des composites associant matrices thermoplastiques et charges particulaires lignocellulosiques. Chacune des méthodes présentées est accompagnée d'un aperçu des paramètres couramment retenus dans la littérature pour les composites à matrices PP et PLA. Enfin, le cinquième axe présente les principales méthodes de caractérisation utilisées pour évaluer les propriétés des biocomposites ainsi que le niveau d'interaction entre la charge et la matrice, en s'appuyant sur les résultats expérimentaux et les approches théoriques. Cet état de l'art permet d'identifier les défis actuels et de définir les objectifs liés au développement de composites intégrant des sous-produits agro-industriels.

Le chapitre 2 est consacré à la description de la démarche expérimentale. Il commence par la description de chacune des méthodes de caractérisation utilisées. Puis, il décrit les procédés de fabrication des différents matériaux étudiés, organisés selon les axes de recherche.

Le chapitre 3 a pour objectif d'évaluer le potentiel des drêches de brasserie comme charges dans des composites thermoplastiques. Les deux matrices sélectionnées sont le PLA et le PP car elles diffèrent non seulement par leur structure chimique et leur origine, mais aussi par leurs segments de marché et leurs applications, ce qui permet d'élargir la portée de l'étude. Ce chapitre se concentre sur le développement et la caractérisation de composites thermoplastiques à base de drêches respectueux de l'environnement. Les formulations étudiées incluent des charges de drêches allant de 0 % à 50 %, et l'impact de la matrice et du taux de charge sur les propriétés mécaniques, physiques, thermiques et morphologiques est évalué afin d'identifier le meilleur compromis entre performance et durabilité.

Le chapitre 4 présente le développement d'un procédé thermo-mécanique permettant de sécher et de broyer la drêche de manière continue en utilisant l'extrusion. Ce chapitre permet de répondre au défi de la périssabilité et de concevoir une méthode de prétraitement indispensable des drêches afin de les utiliser en tant que charge dans un composite. L'extrusion combine chauffage, cisaillement et mise en forme. Elle apparaît donc comme une technique particulièrement adaptée pour un séchage et un broyage en continu de la drêche. Sa flexibilité, via des paramètres ajustables tels que la température, la vitesse et le profil de vis, permet un contrôle précis des conditions de traitement, avantageux pour le prétraitement de la biomasse. Bien que traditionnellement peu utilisée pour le séchage, l'extrusion a montré son potentiel pour

fragmenter les fibres, réduire l'humidité et améliorer l'homogénéité du mélange. Elle constitue donc une approche prometteuse pour préparer la drêche tant pour son stockage que pour son incorporation dans les composites. Ce chapitre étudie l'effet des paramètres d'extrusion sur la teneur en humidité, la distribution granulométrique, la forme et la surface des particules de drêches, ainsi que sur leur stabilité thermique et l'énergie mécanique spécifique nécessaire au broyage et au séchage. Ce chapitre est divisé en deux parties. La première consiste en une étude préliminaire permettant de déterminer la faisabilité de l'approche extrusion-séchage et d'identifier la plage de paramètres appropriée. Sur cette base, un plan expérimental de type Box-Behnken est mis en place, utilisant un profil de vis et un débit d'alimentation sélectionnés, avec trois niveaux de températures et trois vitesses de vis. Les effets de ces paramètres sur la teneur en eau, la taille et la forme des particules de drêches sont évalués, et la consommation énergétique de la méthode par extrusion est comparée à celle du procédé de séchage-broyage décrit au chapitre 3.

Le chapitre 5 se situe à l'interface des développements présentés dans les chapitres 3 et 4, combinant les études sur l'incorporation des drêches dans les composites thermoplastiques et les procédés de séchage et de broyage par extrusion. Dans une première partie, la drêche extrudée en utilisant trois combinaisons de paramètres différentes est incorporé à 30 % dans les matrices PP et PLA. Les composites résultants sont caractérisés selon leur propriétés thermiques, rhéologiques, mécaniques et morphologiques. Dans une seconde partie, le passage de l'échelle laboratoire à l'échelle pilote est discuté selon deux étapes de la mise en forme de biocomposites : le mélange et le moulage par injection.

Le chapitre 6 ouvre la voie du traitement chimique pour améliorer la compatibilité des drêches de brasserie avec les matrices PP et PLA. Ce chapitre se concentre sur le traitement alcalin (mercerisation) des drêches, reconnu pour son efficacité et son faible coût. Dans une première partie, les effets de la durée et de la température de traitement sont étudiés sur les caractéristiques structurelles, la stabilité thermique et la morphologie de la drêche. Dans une seconde partie, la condition de traitement optimale est appliquée pour produire de la drêche traitée en plus grande quantité, ensuite incorporée dans des composites PP et PLA à la hauteur de 10 % et 30 %. Ces composites sont alors caractérisés en termes de propriétés thermiques, rhéologiques, morphologiques, mécaniques et d'absorption d'eau.

Enfin, ce manuscrit se termine par les conclusions générales issues de ce travail de thèse, ainsi que par les perspectives et objectifs futurs à envisager.

## General introduction (EN)

As we all know, plastic is omnipresent and has played a major role in transforming our daily activities. Indeed, it would be difficult, if not impossible, to go through a single day without coming into contact with a plastic item, as this material has penetrated every aspect of modern life. However, its legacy can also be measured in millions of tons of persistent waste, polluting both soil and oceans. Faced with this crisis, the question is no longer whether we should rethink these materials, but how to accelerate the transition toward more sustainable alternatives. Among the possible solutions that meet both industrial requirements and environmental concerns are biocomposites. When combining polymers with lignocellulosic biomass, they represent a serious and promising alternative to fossil-based plastics.

A biocomposite is generally defined as a composite material composed, wholly or partly, of biomass. Natural fibers (often lignocellulosic) are combined with petro- or bio-based polymers, giving the material good mechanical properties, often well suited for semi-structural applications. When a petro-based matrix is used, incorporating biomass also helps reducing the proportion of fossil-based compounds in the final material. In this case, the performance objective is to achieve properties comparable to those of the pure polymer matrix.

Thus, the potential of these biocomposites lies in the use of renewable and often underutilized lignocellulosic biomass, with the aim of reducing the consumption of petro-based plastics. Beyond being more environmentally friendly, these materials also create opportunities to valorize agricultural and agri-food by-products. This is the case for brewers spent grain (BSG), the main solid residue from the brewing industry.

Still too often regarded as waste, BSG accounts for about 85 % of a brewery's solid residues. Currently, it is mainly disposed of in three ways: incineration, discarded in landfills (which generates greenhouse gases) or as animal feed, though this last option is sometimes rejected due to potential contamination by microorganisms. Indeed, because of its high sugar and moisture content, BSG is highly susceptible to microbial colonization. These same characteristics make it difficult to preserve and store, as it deteriorates rapidly. This issue highlights one of the main challenges of this work: to design a continuous laboratory-scale drying and grinding process that enables both preservation and direct use of BSG in composite materials.

More broadly, this challenge illustrates the scientific and technical barriers facing biocomposites. One of these is the variability of lignocellulosic fibers: while biocomposites reinforced with wood fibers have shown promising results, it remains relevant to extend studies to other lignocellulosic fillers and to assess their potential. Another frequently cited obstacle in

the literature concerns the incompatibility between hydrophilic lignocellulosic fibers and hydrophobic polymer matrices. Addressing these challenges requires an integrated approach that combines material science, processing technology, and biomass treatment.
This thesis is part of that framework. Its objectives are multiple:

(i) To explore and characterize the potential of brewers' spent grain as a filler for thermoplastic composites, particularly PP and PLA.
(ii) To develop a suitable process to improve the stability and compatibility of the obtained BSG.
(iii) To initiate a scale-up: from laboratory trials to pilot-scale processes as a first step toward possible industrialization.
(iv) To develop a specific treatment to enhance compatibility between BSG and thermoplastic matrices (PP and PLA).

To achieve these goals, the research was structured into four complementary axes, presented across six chapters.

Chapter 1 presents a literature review organized around five main axes. The first two focus on the two components of a biocomposite: the matrix (emphasizing PP and PLA and the recent comparative studies between them) and the filler, introduced from natural fibers to lignocellulosic agro-industrial by-products, ending with brewers' spent grain. The third axis discusses the preparation of these fibers for composite applications, divided into two parts: one on essential pre-treatments such as drying and grinding, and another on modification strategies aiming at improving fiber-matrix compatibility. The fourth axis introduces the main processing methods for lignocellulosic particulate filled thermoplastic composites, providing a literature overview of typical processing parameters for PP and PLA composites. Finally, the fifth axis summarizes the key characterization techniques used to assess biocomposite properties and the fiber-matrix interactions, drawing on both experimental and theoretical approaches. This review identifies current challenges and helps define objectives for developing composites incorporating agro-industrial by-products.

Chapter 2 details the experimental methodology, beginning with the description of each characterization technique, followed by the fabrication processes of the studied materials, structured according to the research axes.

Chapter 3 aims to evaluate the potential of brewers' spent grain as a filler in thermoplastic composites. The two matrices selected (PLA and PP) differ not only in chemical structure and origin but also in market segment and application, thereby broadening the study's scope. This chapter focuses on the development and characterization of environmentally friendly thermoplastic composites containing BSG. Formulations include BSG contents ranging from 0 % to 50 %, and the effects of matrix type and filler content on mechanical, physical, thermal, and morphological properties are analyzed to identify the best balance between performance and sustainability.

Chapter 4 presents the development of a thermo-mechanical process for continuous drying and grinding of BSG using extrusion. This chapter addresses the perishability issue and establishes an essential pre-treatment method for using BSG as a composite filler. Extrusion, which combines heating, shearing, and shaping, is particularly well suited for continuous BSG drying and grinding. Its flexibility, through adjustable parameters such as temperature, screw speed, and screw configuration, allows precise control of processing conditions, an advantage for biomass pretreatment. Although traditionally not used for drying, extrusion has shown potential for fiber breakdown, moisture reduction, and improved mixing uniformity. It therefore represents a promising approach for preparing BSG both for storage and for composite use. This chapter studies the effects of extrusion parameters on moisture content, particle size distribution, particle morphology and surface, thermal stability, and specific mechanical energy. It is divided into two parts: a preliminary study assessing feasibility and defining the process window, and a Box–Behnken experimental design used to optimize temperature and screw speed. The effects of these parameters on BSG characteristics are evaluated, and extrusion energy consumption is examined along with that of conventional drying-grinding (Chapter 3).

Chapter 5 bridges the developments presented in Chapters 3 and 4, combining the studies on BSG incorporation into thermoplastic composites with the extrusion drying and grinding process. In the first part, BSG extruded under three different parameter combinations is incorporated at 30 % into PP and PLA matrices. The resulting composites are characterized for their thermal, rheological, mechanical, and morphological properties. The second part discusses the transition from laboratory to pilot scale, focusing on two key processing steps: compounding and injection molding.

Chapter 6 explores the use of chemical treatment to improve the compatibility of BSG with PP and PLA matrices. The chapter focuses on alkaline treatment (mercerization), known for its efficiency and low cost. The first section studies the effects of treatment duration and temperature on BSG structural, thermal, and morphological characteristics. The second applies the optimized treatment condition to produce larger quantities of treated BSG, which are then incorporated into PP and PLA composites at 10 % and 30 %. These composites are characterized in terms of their thermal, rheological, morphological, mechanical, and water absorption properties.

Finally, the manuscript concludes with a general summary of the findings, followed by future perspectives and research directions.

# CHAPTER 1:

## Literature review

# RÉSUMÉ DU CHAPITRE 1

Ce chapitre présente un état de l'art consacré aux biocomposites à matrices thermoplastiques renforcées par des fibres naturelles ou lignocellulosiques, avec une attention particulière portée sur le polypropylene (PP), l'acide polylactique (PLA), ainsi que sur les drêches de brasserie (BSG), coproduit agro-industriel abondant et sous-valorisé. Il décrit les types de matrices thermoplastiques couramment utilisées, notamment le PP et le PLA dont l'étendue du marché et les propriétés sont abordés en détail. Ensuite, différentes études ayant comparé le PLA et le PP en tant que matrices dans les biocomposites sont présentées. Il apparaît que, malgré son origine fossile, le PP présente l'avantage d'être recyclable et peut désormais être produit à partir du craquage de la biomasse. De plus, son utilisation est en pleine expansion, avec une production mondiale estimée à près de 11 millions de tonnes d'ici 2030. Dès lors, travailler sur cette matrice conserve tout son sens, puisqu'elle s'inscrit dans la transition vers des matériaux plus durables et circulaires. Le PLA, lui, est formé à partir d'un monomère bio-sourcé : l'acide lactique. Ce dernier est en effet produit par les mammifères mais aussi par des micro-organismes lactobacilles lors d'une fermentation anaérobique de sucres extraits de la biomasse. En comparant ces deux matrices aux propriétés différentes, ce travail nous permettra d'élargir les champs d'applications de nos composites et de mieux comprendre les interactions entre biomasse et matrice thermoplastique.

Les fibres naturelles utilisées en tant que charges dans les composites sont ensuite présentées en détail en définissant progressivement les limites de cette étude. Les fibres naturelles englobent aussi bien les fibres animales que minérales et végétales. Cependant, le chapitre se réduit dans un premier temps aux fibres végétales lignocellulosiques. La place faite aux fibres végétales par les consommateurs et les opportunités de marché sont étudiées. Il est montré que de nombreuses marques célèbres telles que Coca-Cola ou Ford ont déjà introduit des fibres végétales dans leurs produits. De plus la croissance de la population induit une croissance de la production de nourriture et de fait une croissance des co-produits agricoles contenant des fibres lignocellulosiques. Tout cela suggère un potentiel croissant pour développement de composites à base de co-produits agricoles. Le chapitre se réduit à s'intéresser à l'utilisation des co-produits dans les composites et plus particulièrement sous la forme de farine de co-produits avec des fibres d'aspect particulaire. Enfin, une dernière partie dédiée à la présentation des drêches de brasserie, co-produit majoritaire de l'industrie brassicole.

Les méthodes de préparation de co-produits agricoles en vue de les incorporer dans les matrices thermoplastiques sont abordées. Elles comprennent le séchage et le broyage mais s'étendent aussi à l'extrusion, procédé thermomécanique souvent utilisé pour transformer la biomasse dans les procédés alimentaires. L'extrusion est donc mise en avant comme procédé prometteur permettant de sécher et broyer la biomasse. Puis les méthodes de traitements physiques, biologiques et chimiques des fibres sont également passées en revue, en mettant en évidence leur rôle sur la compatibilité interfaciale, la morphologie et les performances mécaniques des futurs composites. L'accent est porté sur un traitement chimique en particulier : le traitement alcalin. En combinant, faible coût et facilité de mis en œuvre, celui-ci permet d'éliminer les composés hydrophiles tels que les hémicelluloses et ceux diminuant l'adhésion entre les fibres et la matrice comme les cires et les lignines. Il rend les fibres plus rugueuses avec un plus grand potentiel d'accroche pour la matrice et améliore la compatibilité entre charge et matrice.

Trois méthodes de mise en œuvre des composites à matrices thermoplastiques sont présentées : le mélangeur interne, l'extrusion et le moulage par injection. Chacune est accompagnée d'un échantillon de paramètres utilisés dans la littérature avec les matrices PP et PLA.

Enfin, les propriétés thermiques, rhéologiques, mécaniques et liées à l'absorption d'eau des composites à charges particulaires sont discutées et les effets de l'augmentation du pourcentage de charges sont détaillés en s'appuyant sur des exemples concrets tirés de la littérature.

Ce chapitre aborde les limitations des matériaux existants, telles que la variabilité des propriétés des fibres, la sensibilité à l'humidité et l'incompatibilité avec les matrices hydrophobes. Enfin, il nous permet d'identifier les principaux défis scientifiques et techniques pour la valorisation des drêches, notamment l'optimisation des procédés de séchage et de réduction granulométrique, l'amélioration de l'adhésion charge-matrice et le passage à l'échelle supérieure permettant une valorisation plus étendue. Ce panorama permet de cadrer les objectifs des chapitres suivants et de définir les axes de recherche pour le développement de biocomposites performants et durables.

# Chapter 1 : Literature review

## 1. Introduction

Green composites made of natural fibers and polymers are expected to play a **major role** in the 21$^{st}$ century, as they offer a possible solution to the waste-disposal problems associated with conventional petroleum-derived plastics. Therefore, in recent decades, remarkable progress has been achieved in the development of green materials science, particularly through the emergence of biocomposites. Driven by **environmental** and **sustainability concerns**, global production of high-performance materials derived from renewable resources continues to rise. To better understand the **role** and **potential** of such sustainable materials, it is essential to first clarify the concept of "composite" and, more specifically, "biocomposite".

A **composite** material results from the **combination** of at least two immiscible materials whose properties synergistically enhance the overall performance. In some cases, composites are also designed to lower **environmental impact**, for example by reducing the amount of polymer used and thus the overall carbon footprint. In general, a rigid and strong material, called **filler** or reinforcement, is embedded in a continuous component known as the **matrix**. Where there is a general consensus on the definition of composite, the term "biocomposite" embodies a multitude of concepts. For instance, some researchers posit that a biocomposite must be **biocompatible**. Others suggest that a biocomposite should be defined as **bio-based** and/or **biodegradable**, or in which at least one constituent is bio-based [1]. In this study, we will define a biocomposite as the combination of **natural filler** with a matrix that is either biodegradable and/or bio-based or petroleum-based (Figure 1.1).

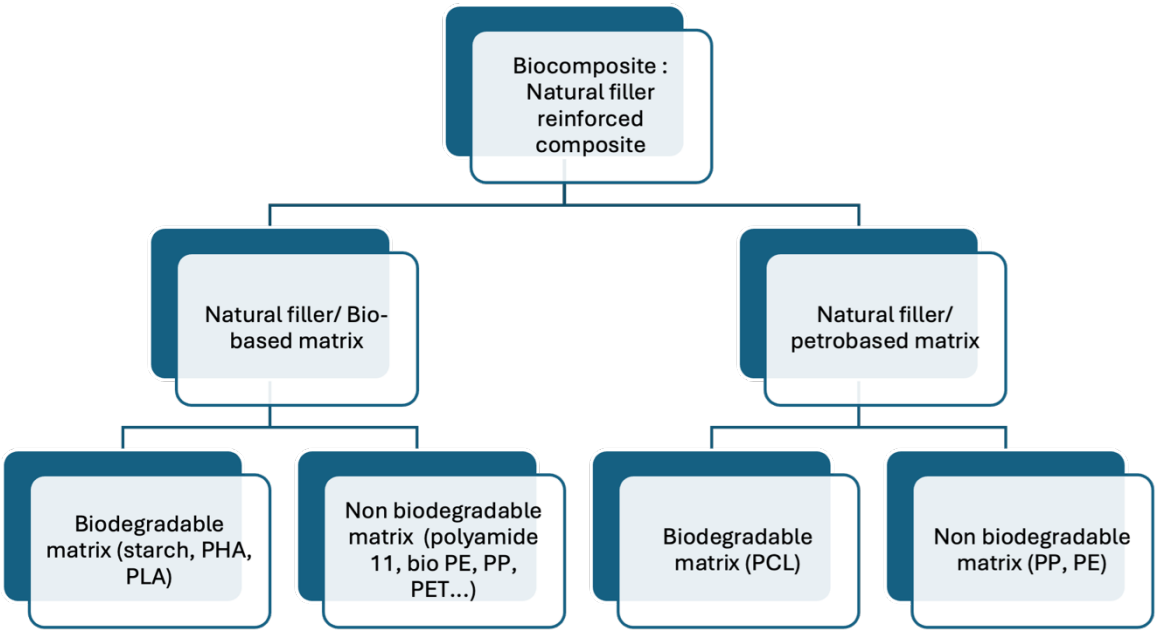


*Figure 1.1: Classification of biocomposites*

Fillers are commonly incorporated into polymers to modify their properties and to reduce the overall cost of final products. Traditionnally, these fillers have included glass fiber, graphite, silica, calcium carbonate, clay, graphene, etc. In recent years, however, driven by the purpose of the sustainable development, increasing attention has been directed towards replacing such traditional fillers with **natural fibers**. In this work, the focus is placed on fillers derived from **renewable sources**, particularly those based on **lignocellulosic** biomass. Given their abundance, renewability, and performance-enhancing potential, natural fibers have attracted significant interest. Nowadays, a wide range of plant-based fibers have been investigated. These include jute, hemp, kenaf, and sisal [2], fibers obtained from recycled wood or waste paper, regenerated cellulose fibers, as well as by-products from food crops (wheat straw, rice straw, rice husk, etc.) and other agro-industrial residues (nutshell, cherry stones, tea mill). They have shown success in being incorporating in **polymer matrices** and find applications in various sectors such as automotive panels, furniture, and interior decoration.

However, a **major challenge** remains in the **variability** of their properties, which depend on numerous factors such as fiber type, growth conditions, processing techniques, and possible modifications. Due to the large variability of lignocellulosic resources for biocomposite production, ongoing research is essential to **expand the knowledge** on the multifactorial relationship among fiber properties, formulation, processing, and the resulting composite performance.

The use of thermoplastics as matrices for natural fiber-reinforced composites has expanded substantially, in line with the **rising demand** for plastics, more than 80% of which are thermoplastics [2]. The most commonly used thermoplastics as matrices are polypropylene (PP), polyethylene (PE), and poly vinyl chloride (PVC) [3]. Research is also conducted on renewable polymers as matrix such as starch, polycaprolactone (PCL), polyhydroxybutyrate (PHB), polylactic acid (PLA) and polyester amide [4]. Natural fiber–reinforced thermoplastic composites are increasingly considered for structural applications, highlighting their potential as sustainable alternatives to petroleum-based materials.

This chapter presents a state of the art on biocomposites, dissecting their different constituents and processing routes. The **first part** focuses on the thermoplastic **matrix**, considered as a material on its own, with particular emphasis on polypropylene (PP) and polylactic acid (PLA). We then turn to **natural fibers**, their classification, and the lignocellulosic resources available for composite manufacture, with an approach focusing on consumer demand and market opportunities. Among the different types and morphologies of lignocellulosic fillers, this review will narrow its scope to **particulate lignocellulosic fillers**, described in terms of their structure and composition. Special attention will be given to one specific agricultural by-product, **Brewer's Spent Grain** (BSG). Its market opportunities, current disposal methods, and chemical composition will be examined in order to establish why it could represent an **ideal filler** for polymer composites.

Subsequently, we will address **filler treatment**, beginning with **preparation** steps (conversion from raw material to usable filler) following with **modification** techniques designed to enhance **compatibility** with the matrix. Once the filler is ready, the focus will shift to **processing methods** for obtaining composite materials. Finally, the **impact** of incorporating particulate lignocellulosic fillers on the rheological, mechanical, and water-related **properties** of composites will be discussed.

This state of the art will make it possible to identify the **current challenges** and define the **objectives** related to the development of composites filled with agro-industrial by-products.

## 2. Thermoplastic polymers as matrix for bio-based composites

### 2.1. Introduction

Due to their flexible designs and fairly straight-forward processing, thermoplastic polymers make good candidates for composites manufacturing. Indeed, they offer ease of processing, which includes the ability to be **reshaped** multiple times without significant

degradation, making them suitable for various manufacturing techniques. As a matter of fact, in recent years, their usage has been considered for high performance engineering applications. Contrary to some assumption, carbon footprint of polymers is usually lower than that of materials used for similar applications such as glass or metal. Consider a glass bottle. For a given volume, it is significantly heavier than its plastic counterpart. Thus, the energy required for its transport is greater than that of a plastic bottle. Moreover, the high temperatures needed for its production (approximately 1000°C for glass and metals) further contribute to its higher carbon footprint. Given the advantages of thermoplastic materials in composites manufacturing, it is worth taking a closer look at specific categories based on the source of the matrix as suggested in Figure 1.1.

## 2.2. Petro-based polymers

### *2.2.1. Introduction*

Due to their predominant consumption in the global market, thermoplastics derived from petroleum feedstock were extensively studied as matrices for natural filler reinforced composites. The most frequently used thermoplastic polymer matrices are **PP** and **PE** which are classified as polyolefins [5]. Due to their **cost-effectiveness**, petrochemical-based polymers are more commercially viable as matrix materials. In the next sections, we will focus on polypropylene (PP) as it is the matrix of choice for this work.

### *2.2.2. PP structure*

Polypropylenes are synthetized from the polymerization of the **propylene monomer** resulting in the formation of homopolymers or via copolymerization of propylene with ethylene leading to copolymers. Figure 1.2 shows the general formula of PP with *n* being between 5 000 and 10 000.

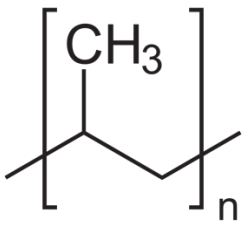


*Figure 1.2: General formula of PP*

Depending on the position of the methyl group along the chain, the homopolymers exhibit three different structural configurations. The **isotactic** structure is characterized by all the

methyl groups being on the same side of the plan. **Syndiotactic** PP are composed of methyl groups that alternate position from one side to the other of the plan. Finally, the **atactic** PP, is characterized by random position of the methyl groups. These three forms of PP are represented in Figure 1.3. Industrial PP shows an isotactic rate of 92 to 98 % [6]. Their **crystallinity** varies from 60 to 70 %. In common usage, polypropylene is used as a general term that also encompasses **copolymers** with ethylene groups. Hence, statistic copolymers present a structure comparable to that of homopolymers with a random distribution of the ethylene groups. Commercial copolymer PP contains 1.5 to 7 % of ethylenic motives [6]. Moreover, PP can also exist in the form of bloc-copolymers which consist of small segments of poly(ethylene/propylene) up to 35 % embedded in a PP homopolymer matrix [6]. This confers high impact strength to the material. Figure 1.3 displays a representative scheme of a PP copolymer.

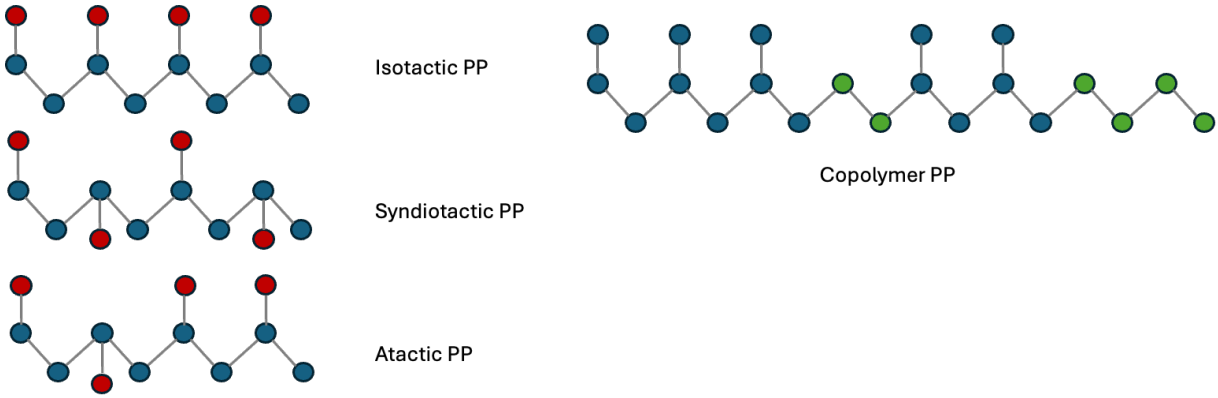


*Figure 1.3: Schematic representation of the isotacticity of polypropylene and common PP copolymer, red circles for $CH_3$, blue circles for $CH_3$, $CH_2$ or CH, and green circles for $CH_2$ from ethylene monomers.*

After polymerization, PP is found in powder form and is then extruded to obtain **pellets** which are easier to store, distribute, and process.

### *2.2.3. PP Feedstock*

Currently, propylene is extracted from **fossil raw** materials, 50 % is obtained from crude oil via **steam cracking** of hydrocarbons. The rest of it comes from **fluid catalytic cracking**, steam enhanced catalytic cracking, from natural gas via propane dehydrogenation, from metathesis process, and from olefin catalytic cracking [7]. Thus, propylene is a **non-renewable** monomer, and its use contributes to environmental pollution [8]. To mitigate polypropylene's (PP) environmental impact, it is essential to address its end-of-life phase, as PP can take up to 30 years to degrade naturally [9]. **Recycling** offers a viable solution, helping to reduce waste, lower the demand for raw materials, and create financial opportunities. Many studies have focused on PP waste recycling and reuse. For instance, it has been shown that **recycled PP** can

reduce its carbon footprint by 42.8 % compared to virgin PP [10]. In their study, Galve *et al.* showed that recycled PP mechanical properties were slightly reduced, by 5 % for the tensile modulus and by 15 % for the tensile strength at yield, compared to virgin PP [10]. Moreover, recycled material can replace **entirely or partially** a virgin material in order to maintain good mechanical performance. Therefore, PP remains of interest due to its potential for **reuse** as a matrix material after recycling.

Moreover, recently, processes to produce propylene from renewable materials have been developed. The most advanced process is called **Biopropylene** from bioethanol, it consists of dehydration ethanol to ethylene, dimerization and metathesis of the bioethanol made from renewable resources. Biopropylene can also be produced from cracking of biomass. Propylene is one of the products of **biomass catalytic pyrolysis** which consists of two stages. The first one is a **fast pyrolysis** and second one a **pyrolysis vapor catalytic** conversion [11]. However, the separation process to purify polypropylene is costly. In 2010, Braskem, a huge chemical company, which is the leading manufacturer of bio-ethylene, announced to produce bio-propylene from bioethanol [11]. To conclude, PP production **derived from biomass** and **recycled** PP will become an important progress of plastic industry in the near future. It is therefore important to keep investigating the use of PP in innovative materials.

*2.2.4. PP general properties*

The main advantage of PP is its relatively low melt temperature (160 -170 °C) [6] which allows for energy saving during its processing compared to other thermoplastics such as polyamids (PA) or polyethylene terephthalate (PET). Moreover, it has the **lowest density** among plastics (0.905 g/cm$^3$) and its high-strength-to-weight ratio makes it a good candidate for automotive applications that seek for light-weight materials. PP can bear **sterilization** temperature without any structural deformation. Its mechanical properties are influenced by its crystallinity, molecular weight, and molecules orientation. A PP film with oriented molecules would be twice less permeable than a non-oriented PP [6]. PP is a **semi-crystalline** polymer with a crystallinity rate between 50 and 70 %. Hence, its properties will be driven by its crystalline structure and the relative amounts of amorphous and crystalline phases. Its crystals are mostly organized in an $\alpha$-form with a helicoidal structure [12]. **Crystal formation** of PP depends on the shear rates and temperatures occurring during its processing. Hence, the structure of an injection is particularly interesting. **High shear** and **thermal conditions** give rise to a multilayered structure, characterized by a continuous variation in the type, size, and orientation of crystalline and amorphous phases from the outer layers toward the core [13]. The highly

sheared layers contain a significant number of ß-spherulites which make these layers weak and prompted to cracks [14]. Table 1.1 displays PP's main properties.

*Table 1.1: PP general properties*

| Properties | | Refs |
|---|---|---|
| Degradation temperature | 457-477 °C | [15] [16] [17] |
| Glass transition | -10-+5°C | [13] |
| Melt temperature | 173 °C | [13] |
| Tensile modulus | 0.9-1.35 GPa | [18] [19] [20] [3] |
| Tensile strength | 26-41 MPa | [21] [20] [3] |
| Water absorption rate (%) | 0.01 to 0.03 % in 24 hours | [22] |

### *2.2.5. Market and Applications*

PP is a very common plastic accounting for 16 % of the total plastics industry. According to Chemanalyst industry report, in 2022, the global PP market was approximately 74 million tons [23]. It is projected to reach 114 million tons by 2030 at an annual growth rate of 5.54 %. Asia pacific dominates the market due to a high demand in **packaging** and **automotive** sector, particularly in China, India and Japan. North America and Europe are also significant markets, due to food packaging and automotive sector. Its market growth is driven by several factors such as the increase demand for **light-weight** vehicles in the automotive industry, innovative technologies in polymerization process have led to the development of **new PP grades** with enhanced properties, and recyclability of PP is a key driver aligned with industry's efforts to improve recyclability infrastructure [23]. Nowadays, **bio-PP** hold 1.9 % shares of the market of bio-based polymers [24]. Moreover, the market of sustainable PP is expected to significantly increase at a 5.42 % annual growth rate in the recent and following years from 2021 to 2028 and reach USD 76.92 million by 2028 [24]. PP is used in numerous industrial and household applications such as packaging, carpets, electrical insulators, etc. Among these, **packaging** is a leading sector, representing 47 % of the demand for PP in 2022 [23]. Given its widespread use, good properties, and growing sustainability, pursuing the investigation of PP as a matrix for composite applications is both relevant and necessary.

## 2.3. Bio-based and biodegradable polymers

### *2.3.1. Introduction*

Consumer concern about the environment, **climate change** and the extensive use of **fossil fuel** resources are the driving factors towards the use of more sustainable products. To create such products, their entire life cycle must be considered, from the source to the disposal. **Bio-based** plastics are plastics obtained from natural, renewable resources. They can be divided in several classes. Among these, there are natural biopolymers such as proteins, including collagen or gluten, as well as microbial polymers which can be synthetized by microorganisms from sugar resources, such as Polyhydroxyalkanoates (PHA). However, most of the commercially available bio-based polymers are chemically synthetized. Most of these are **polyesters**, aliphatic and aromatic; characterized by ester bonds that are easily hydrolysable which makes them suitable for **biodegradation**. Within this category, **Polylactic acid** (PLA) is a notable **biodegradable** and **biocompatible** thermoplastic polyester, derived from renewable resources such as corn starch, cassava, roots, or sugarcane. In the next parts, we will focus only on PLA.

### *2.3.2. PLA presentation*

PLA is a **linear polyester** obtained by polymerization of **lactic acid**. This monomer can be extracted using **anaerobic fermentation** of sugars by lactobacillus microorganisms which makes it bio-based. Indeed, the fermented carbohydrates are derived from **agricultural products**. For example, glucose and maltose come from corn or potatoes starch, sucrose from cane and beet sugar and lactose are extracted from cheese whey [25]. Lactic acid (2-hydroxy propionic acid) contains an **asymmetric** carbon atom. Consequently, it exists in two optically active forms: the L-isomer which is produced by mammals including humans and microorganisms whereas the D-isomer is exclusively synthetized by bacterial systems. Due to the presence of both acid and hydroxyl functional groups, the polymerization of lactic acid can be achieved through a classic **polycondensation process**. However, the molecular weight of obtained PLA chains is relatively low leading to an unusable polymer in most of the applications [25]. Based on this approach, the most common method to obtain a high-molecular weight PLA consists of depolymerizing the low-molecular-weight PLA to reach a cyclic dimer called **lactide**. Then a **catalytic ring opening** of the lactide results in the production of a high-molecular-weight polymer. This method was used by Cargill, one of the main producers of PLA [26]. Another method to obtain the high-molecular-weight PLA is to use an **azeotropic dehydrative condensation** of the lactic acid monomer. It is worth noting now that the stereochemistry of the

initial monomer has great influence of the final properties of PLA. The cyclic dimer formed during the depolymerization stage exists in **three forms**: the L and D forms, which are optically active, and the meso form, composed of L and D lactic acid, which does not exhibit optical activity (Figure 1.4). Thus, **crystallinity** and **crystallization kinetics** differ significantly depending on the racemization of the monomer constituting PLA. This variation can greatly influence the process conditions. For instance, meso lactide results in lower crystalline melting points, thereby allowing lower melt-processing temperatures of the polymer. Finally, this permits the reduction of hydrolytic and oxidative degradation of PLA during the process.

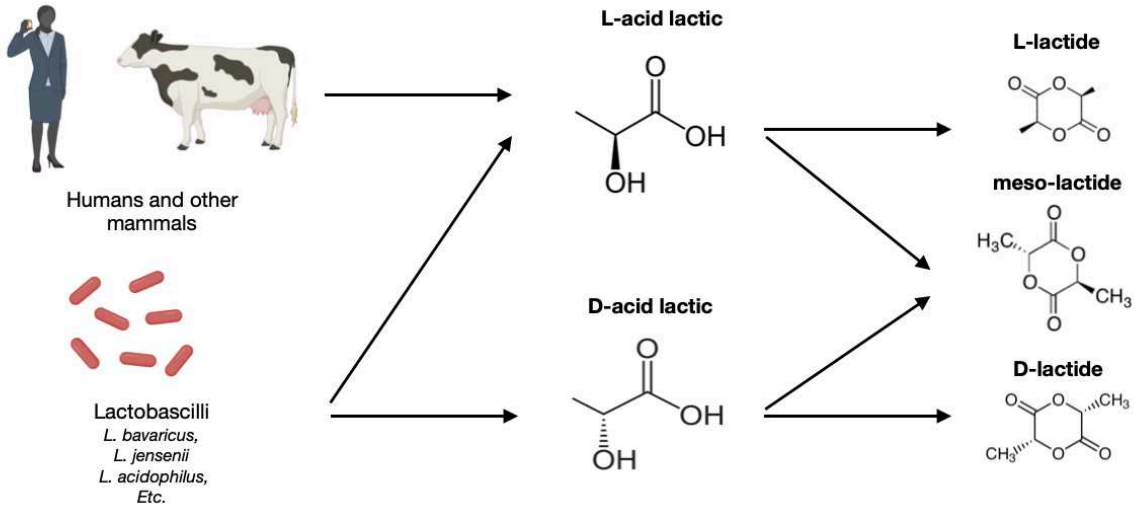


*Figure 1.4: Schematic of the production of three forms of lactide*

### *2.3.3. PLA degradation behavior*

Beyond processing conditions, the sensitivity of PLA to **degradation** is a critical factor that may result in deterioration of its properties. As for the majority of aliphatic polyesters, thermo-mechanical stability of PLA is limited due to **vulnerable** linkages. Consequently, this sensitivity has been extensively studied. The main issues during processing are the high temperatures, moisture and shear rates. As a result, PLA must be processed within a narrow range of parameters to balance the smoothest conditions minimizing degradations and obtaining good melting and homogeneity. The action levers to prevent degradation include the **moisture** of the polymer, processing **temperature**, residence time, and shear forces [27]. However, to better control the quality of PLA during processing, it is important to understand the undergone degradation mechanisms, all of which result in **shortening** of the polymer chains and a consequent decrease in molecular weight [28]. Thus, three mechanisms are involved: hydrolytic,

thermal and thermomechanical degradations [27]. The **hydrolytic** degradation involves the cleavage of ester linkages in PLA when it is exposed to moisture which results in the formation of carboxyl and hydroxyl polymers or oligomers. This number of degraded ester linkages depends on the water content present. Thermal degradation occurs when temperatures exceed 100 °C via ester bonds scission [29]. Six degradation reactions may occur including hydrolysis, inter- and intra-molecular transesterification, homolysis, radical degradation, and pyrolytic elimination [27]. Lastly, there is thermomechanical degradation which causes the scission of long polymer chains due to **shear heating** and **oxidation** [29].

All together, these degradations cause changes in molecular weight which has great influence on rheological, mechanical, and thermal properties of the PLA. Indeed, **rheological properties** of polymers are directly connected to the **molecular weights** of the chains. Researchers that investigated the effects of processing on the degradation observed a decrease in the complex viscosity with the increase of number of processing cycles [30,31]. A similar decrease of storage modulus and loss modulus was observed. Velghe *et al.* concluded that rheology and especially complex viscosity could be a good **indicator** of PLA degradation [27].

Regarding mechanical properties, a change in the elastic modulus has been reported in previous studies. Many authors reported a decrease in stiffness and tensile strength of PLA after several processing cycles [30,32,33]. This can be explained by the fact that when the length of PLA chains is reduced, the number of entanglements decreases, leading to a reduction in tensile strength.

The molecular weight directly influences the thermal transitions of PLA such as glass transition ($T_g$) or melt ($T_m$) and crystallization ($T_c$ and $T_{cc}$) temperatures. The Flory-fow equation gives the relationship between $T_g$ and molecular weight [34]:

$$T_g = T^{\infty} - K/M_n \quad (1.1)$$

with $T^{\infty}$ being the $T_g$ at the infinite molecular weight, $K$ a constant representing the free volume present at the end of polymer chains, and $M_n$ is the number average molecular weight. The values of $T^{\infty}$ and $K$ are around ~58 °C and (5.5–7.3) × $10^4$, respectively, as reported in the literature for PDLLA and PLLA [34].

Most of the literature does not report a significant influence of the degradation on $T_g$ or $T_m$. This observation may be attributed to the fact that these properties are also influenced by optical purity which differ significantly with the PLA grade used [35]. However, a **double melting** peak has been observed in Differential Scanning Calorimetry (DSC) [31] which was attributed to

several possible factors: the development of a disordered **α-phase** caused by low crystallization temperatures, the coexistence of **multiple** crystalline structures, or variations in lamellar morphology formed before heating [31]. The decrease in $T_c$ and $T_{cc}$ is also reported [31,32]. Indeed, a decrease in molecular weight increases the mobility of polymer chains, enhancing the crystallization kinetics.

### *2.3.4. PLA properties*

- Crystallinity

As presented earlier, PLA crystallization is strongly connected to its degradation. Controlling the **crystallization rate** of PLA could also permit to control the degradation rates, thermal resistance, mechanical and barrier properties. Highly crystalline PLA proved to be harder to degrade compared to amorphous ones [36,37]. PLA crystallization behavior is influenced by its chain structure. As seen earlier (Figure 1.4), the three forms of lactides allow for the production polymers made of pure L-, pure D-, and a random racemisation referred to as PLLA, PDLA, and PDLLA, respectively. By changing the ratio of the D-lactide and L-lactide content, it is possible to influence the **crystallinity** of the PLA. When the D-lactide content exceeds 10 %, the PLA likely becomes amorphous. Most of the PLA used in industry contain 95-99 % L-lactides which gives them a crystalline structure, thereby enhancing strength properties of the material [38]. Crystallization consists of the self-organization of the polymer chains into ordered three-dimensional structures. In contrast to amorphous region, crystalline regions are tightly packed and organized. For PLA, **different crystals structures** have been observed depending on the crystallization conditions. PLA can crystallize in **α-, α'-, β-, and γ- forms** [35]. Under normal melt conditions, the most common and **stable form** observed is α which crystallized at temperatures above 120 °C [39,40]. It consists of a $10_3$ helical chain conformation where two chains are interacting in an orthorhombic unit cell [35]. A slightly different crystal form with a looser chain packing is observed when PLA crystallized below 120 °C [40]. When crystallization occurs between 110 and 130 °C, the coexistence of α- and α'- forms is observed [41] which leads to a double melting peak observed in DSC thermograms [40]. The lower melting peak is attributed to the **α'-form** while the higher melting peak is attributed to the more stable form of crystals (α-form). Upon heating, an exothermic peak is observed corresponding to the transition of the less ordered α'- crystal structures to α-type [40]. A consequence of the presence of α' looser structure is a lower elastic modulus and higher elongation at break [39]. **β-forms** are obtained under high drawing conditions and high temperatures [41]. The β-form is obtained from the stretching of the α-form, containing three chains in a trigonal cell, it is less thermally stable than the previous form. Finally, **γ-forms** are orthorhombic crystal systems which consists of two

chains oriented antiparallel in a $3_1$ helical conformation. This form is a result of epitaxial crystallization occurring around 140 °C [42]. Due to its slow crystallization rate, PLA often remains amorphous under conventional processing speeds; however, crystallization effects must still be considered given their significant impact on mechanical properties.

- General properties

Beyond its ecofriendly properties (biodegradability, recyclability, and composability), PLA is also **biocompatible**, meaning that it can be used for biomedical applications. Indeed, the degradation products of PLA do not interfere with biological tissues and do not produce toxic effects. PLA is approved for direct contact with biological fluids, making it a suitable candidate for drug encapsulation. Additionally, PLA can be processed at **lower** temperatures compared to other polyolefins, which offers advantages in terms of production costs. It is suitable for large scale production lines such as injection molding, film extrusion, thermoforming or blow molding which enable a large variety of applications. Its tensile strength and elastic modulus are comparable to other petro-based polymers such as PET [43]. However, with a glass transition of 60 °C, it is **very brittle** with a poor elongation limiting its use in application that require plastic deformations. Industrials mix it with **plasticizers** agent to overcome its brittleness [38]. Table 1.2 displays PLA main properties.

*Table 1.2: PLA general properties*

| Properties | | Refs |
|---|---|---|
| Degradation temperature | ~350 °C | [44] |
| Glass transition | 60 °C | [45] |
| Melt temperature | 155 °C | [45] |
| Tensile modulus | 0.6-2.3 GPa | [46,47] |
| Tensile strength | 58 MPa | [45,48] |
| Water absorption rate (%) | 1 % after 30 days | [49] |

*2.3.5. Market and Applications*

Initially, the production **costs of PLA** were prohibitively high, limiting its use to biomedical applications only. However, the cost of PLA has significantly **decreased** over the years, allowing it to be used in a broader range of applications. In October 2025, PLA price index was around 2-2.5 $/kg while PP price index was between 1 and 1.5 $/kg. According to the *Bioplastics Market Development Update 2024 report,* global biobased plastic production is expected to increase

significantly from 2.47 million tons in 2024 to about 5.73 million tons by 2029 [50]. PLA, along with PHA, is a **leading polymer** driving this growth. Its production keeps increasing due to an increasing variety of application. Flexible and rigid packaging are the largest market segment for PLA. However, it is also used in agriculture, electric, consumer goods and fiber sectors. Bio-based plastics are currently produced at only 60 % of the total capacity.

## 2.4. Studies comparing PLA and PP

### *2.4.1. Comparison of PP and PLA in the literature*

Considering the propensity of lignocellulosic material to degrade with temperature, Rowell suggests that processing temperatures lower than 180 °C are necessary if a biomass material is utilized as a filler [51]. Thermoplastics with a **high melt flow index** and **low softening** temperatures are typically used. Due to its moderate melting temperature (160 °C), **PLA** presents a suitable option for blending with lignocellulosic fillers. Furthermore, PLA is a **versatile** polymer derived from renewable agricultural materials, which enables the production of a **fully bio-based** material when combined with natural fillers. It has gained attention as one of the most promising polymers as an alternative to conventional petro-based polymer. Thus, many research articles investigated the potential of natural filler-PLA composites, for example cassava flour, pineapple flour, rice husk, sugar beet pulp, pine wood flour have been blended with PLA [48,52–54]. However, it has been shown that fibers like rice husk act more as **filler** than fibers with a decrease in mechanical properties due to irregular filler shapes [52]. Moreover, tensile strength tends to decrease with increase flour addition because of weak bonding between PLA and flour [48]. Nonetheless, natural fillers such as sugar beet pulp might serve as low-cost filler for PLA composites decreasing the overall cost of the material [53]. While some natural fibers may **negatively** impact mechanical properties, the potential for **cost reduction** and **sustainability** benefits keeps on driving research into optimizing natural filler-reinforced PLA composites for various applications. Nonetheless, PLA, due to its low thermal stability and brittleness, exhibits **restricted use** in high-performance application. Therefore, it was chosen to also investigate the potential of **PP**, a non-biodegradable and petroleum-based matrix, in order to address the limitations of PLA. Indeed, PP is known for its excellent mechanical properties and its longevity making it a suitable option for a whole range of applications where **strength** and **durability** take priority over biodegradability. Although PP does not provide the same environmental benefits as PLA, its performance meets the requirements of industries which demand for cost-effectiveness and mechanical strength. Moreover, replacing a portion of the PP matrix with lignocellulosic material may enhance the sustainability of the resulting material by **sequestering carbon** and

reducing the use of petroleum-based materials. Many studies of natural fillers reinforced PP-composites are observed throughout the literature. Among the fillers used, one can find: pineapple leaf, kenaf, cherry stones, acacia bark residues or wheat straw fibers [19,55–58]. It is shown that natural filler such as wheat straw fibers up to 30 %(m/m) tend to enhance the mechanical properties of virgin polypropylene. Nonetheless, it is also observed that **poor dispersion** of the filler and **variability** within the particles may affect composite strength [58].

With the objective of comparing a fully biobased composite with a conventional PP-composite, researchers have investigated the mechanical, thermal, and processability properties, as well as the morphology of the resulting composites under similar conditions. Regarding the mechanical aspect, studies such as that of Jaszkiewicz *et al*. have directly compared mechanical properties of **PP** and **PLA** composites with **abaca** and man-made cellulose, offering significant insights into their behavior. They observed that **PLA** exhibits superior mechanical properties compared to PP, primarily due to **better adhesion** with the fibers [59]. Although they also found **good adhesion** between **PP** and short **sisal fibers**, similar results with enhanced interaction with PLA were observed by Mofokeng *et al*. [60]. **FTIR** tests were performed to demonstrate hydrogen bonding between PLA and sisal fibers. Overall, a need for the improvement of interfacial adhesion for better mechanical performance has been highlighted by researchers [4,61,62]. Regarding thermal stability, most of the studies indicate a better thermal stability of the composites when increasing fiber content and especially in the case of PP-composites [4,60]. Jaszkiewicz *et al*. investigated notably the flowability of PLA based composites compared to PP based composites. The **melt flow** characteristics of the corresponding materials were evaluated using melt flow rate measurements and real-time flow spiral testing. Although, they emphasized the need for industrial-scale processing comparisons, it was found that PLA's flowability was lower than PP's flowability. They also showed that the mass flow rate of PLA was reduced with the addition of abaca fibers. It could be explained by the fact that compounds resulting from the **partial degradation** of the fibers during processing could interact with PLA leading to a reduction of its **molecular weight** and a smaller than expected decrease in the melt flow rate [59].

This comparison of PLA and PP matrices highlights the complexity involved in selecting the suitable matrix for a natural filler. The findings emphasize the need to carefully balance the processability, mechanical performance and environmental impact when choosing a polymer as matrix.

*2.4.2. Comparison of intrinsic properties of PP and PLA*

In this PhD work, **Polylactic acid** (PLA) is investigated as a first matrix due to its **renewability**, and the ability to form composites with desirable properties for a wide range of applications. A second matrix is selected to enhance the possibility for developing composites. In this regard, **polypropylene** (PP) is examined. PP exhibits balanced properties between mechanical strength and low density, making it suitable for many applications, such as in the automotive industry where lightweight materials are sought after. By comparing these two matrices, one **biodegradable** and **bio-based** (PLA) the other **durable** but **non-biodegradable** (PP), this research aims to provide insights into the trade-offs between **sustainability** and material **performance** in natural fiber reinforced composites. Table 1.3 compares the main thermal, mechanical, and physical properties of PLA and PP. PLA exhibits a lower **degradation temperature** (~350 °C) compared to PP (457-477 °C), which indicates lower **thermal stability**. Its glass transition temperature (60 °C) is significantly higher than that of PP (-10 °C), while its melting point (155 °C) is slightly lower than PP (173 °C). In terms of **mechanical performance**, PLA displays a broader tensile modulus range (0.6-2.3 GPa) than PP (0.9-1.35 GPa), and a considerably higher tensile strength (58 MPa versus 26-41 MPa). Both polymers are low sensitive to **water up-take**.

*Table 1.3: PLA vs PP main properties*

| Properties | PLA | PP |
|---|---|---|
| Degradation temperature | ~350 °C | 457-477 °C |
| Glass transition | 60 °C | -10 °C |
| Melt temperature | 155 °C | 173 °C |
| Tensile modulus | 0.6-2.3 GPa | 0.9-1.35 GPa |
| Tensile strength | 58 MPa | 26-41 MPa |
| Water absorption rate (%) | 1 % after 30 days | 0.01 to 0.03 % in 24 hours |
| Density ($g/cm^3$) | 1.2 | 0.9 |

The comparison of these two matrices is particularly relevant for composite development: while PLA offers the advantage of being bio-based and mechanically strong, its thermal sensitivity and brittleness limit its applications. Conversely, PP provides excellent thermal stability and water resistance but is petro-based. Studying both matrices in parallel

therefore **broadens** the understanding of how different polymer characteristics influence composite performance, ultimately helping to adapt materials for a **wider range of applications**.

## 3. Natural filler for composites materials

### 3.1. Natural fibers

#### *3.1.1. Natural fibers classification*

To place this in context, we must first consider its **origin**. Natural fibers reinforced composites have been used in manufacturing since ancient times, long before their adoption by 21st-century industries. As early as the third millennium B.C., the Mesopotamians constructed roads using composites reinforced with **chopped straw** [63]. Similarly, the early Egyptians used to combine crop straw and mud to create an effective **building composite**. Another significant example is The Great Wall of China, whose construction began in 121 B.C.. It was fortified with red willow reeds and later with clay stones, willow branches, and sand [64]. Despite its significant role in construction over millennia, the term "composite" was first used during the Renaissance era [63]. The **first industrial biocomposite**, known as "celoron," emerged in the 1930s, consisting of a phenolic resin reinforced with cotton fibers and used in the **automotive** industry. The concept of a matrix reinforced with discontinuous elements became widely recognized in the 1950s. Building on this foundation, recent developments have brought natural fibers reinforced composites back into focus. This advancement is driven by the remarkable properties. Indeed, their stiffness, high strength, low cost, renewability and lightweight make them suitable for **high-performance** applications in many sectors such as aerospace, automobile, marine, and construction industry [1]. Natural filler can be subdivided based on their origins, coming from **plants** (grass fibers, straw fibers, seed fibers, wood fibers, etc.), **animals** (wool, silk, chickens feathers, etc.) or **minerals** (Brucite, wollastonite, basalt, etc.) (Figure 1.5). Basalt fibers have emerged as natural fibers showing good mechanical properties with high strength, comparable to glass fibers [65]. Plant fibers can be divided upon their uses, whether they are **primary** fibers, grown for their fiber content (such as flax, kenaf or ramie) or **secondary** fibers (by-products such as rice husks, wheat straw fibers, etc.). Given the wide variability of plant fibers, their composites suit various industrial applications. Indeed, they can be used as structural bio-composites such as bridge, or as non-structural components like panels, window frame, laptop case, furniture, fencing, etc. [1]. In next parts, we will be focusing only on **plant fibers**.

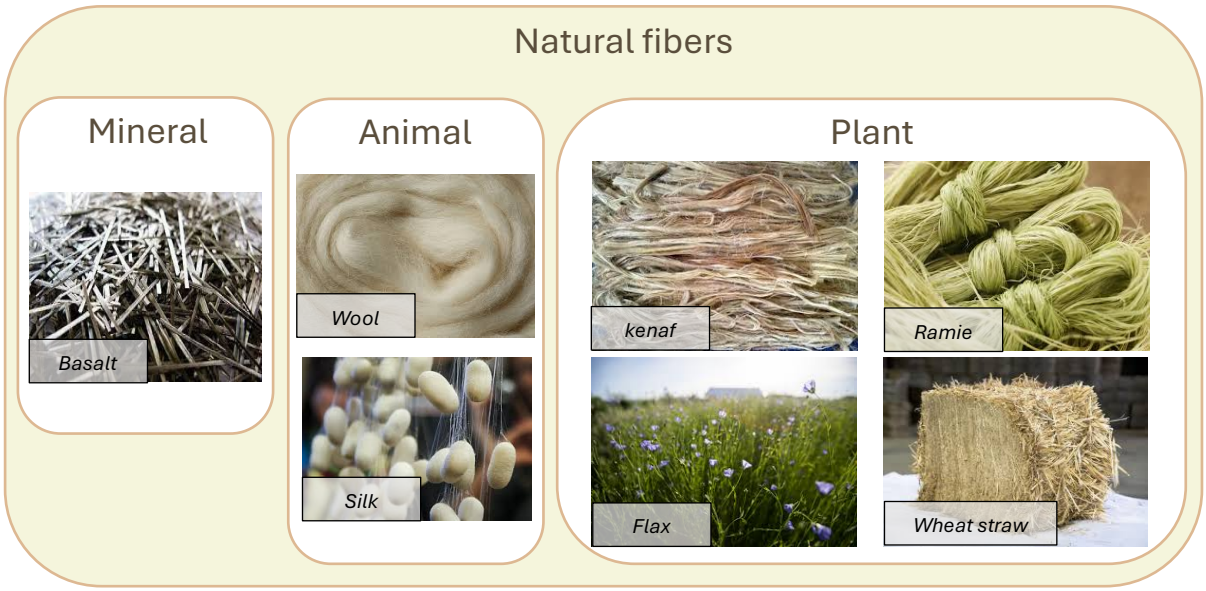


*Figure 1.5: Classification of Natural fibers including some examples*

### *3.1.2. Lignocellulosic resources for composites applications*

- Consumers demand

Although the current economy is predominantly dependent on fossil resources, there is a noticeable transition towards a **bioeconomy**, leading to a society that efficiently uses resources from both land and sea. Growing consumer demand for sustainable products is prompting industrial to seek for **alternative** materials. In this way, many global brands try to convince the consumers by adding bio-based materials to their products. For example, recently Coca-cola introduced a bottle made from 30 % renewable material from sugar canes. [66]. Moreover, natural fibers such as flax or sisal have been widely used in the automotive sector by companies like Ford, Mercedes-Benz, and Audi [67]. Many studies show **positive attitudes** toward products like bio-based packaging, hygiene goods, and personal care items [68,69]. However, consumers were least likely to purchase products such as sports equipment or children's toys [68]. Genencor *et al.* showed that consumers would likely buy bio-based products if their cost and performance were similar to these of conventional products [70]. Thus, willingness to pay for bio-based products instead of petro-based ones varies significantly across product categories. Research also showed the **environmental awareness** among customers promotes purchase [71]. Once informed, studies showed that consumers would actively choose a bio-based product over a petroleum one [67]. Together, these trends highlight the shift in consumers mindset and industrials practices which accelerates the transition towards a more sustainable economy. Thus, the growing awareness of the public increases the market potential for bio-based composites.

♦ Market opportunities (supply)

As demonstrated earlier, the natural fiber composite market shows substantial potential to increase in the following years. According to the natural fibers global report 2025 from the Business Research Company [72], the market for Natural fibers across various applications (automotive, textile, medical, etc.) is anticipated to **grow rapidly** over the coming years, reaching $100.39 billion in 2029 with a compound annual growth rate of 6.5 %. Figure 1.6 displays the world production growth percentage from 2015 to 2023 of **technical fibers** crops and other agricultural crops which **by-products are rich in fibers**. Data were extracted from the Food and Agriculture Organizations of the United Nations website. This analysis shows contrasting trends between both groups. Indeed, technical fibers such as flax (-5.5 %), kenaf (-2.4 %), and sisal (-23,3 %) present noticeable decline in their production. On the other end, crops with potential for **valorizing by-product** as reinforcing filler into composites have shown significant increase over the past decade. Coffee (25.3 %), Coconut (6.4 %), maize (17.8 %), Rice (9.0 %), and wheat (7.7 %) exhibited high growth over the same period. The decline in technical fiber crops can be explained by competition with low-cost synthetic fibers, reduced demand in traditional applications, and shifts in agricultural land use toward **food crops** with higher economic returns. However, since global **food production** is expected to keep increasing with **population growth**, the availability of **agricultural residues** will also rise, offering a promising and sustainable source of fibers for composite development. This suggests potential and **opportunities** for the development of bio-based composites derived from **agricultural by-products**.

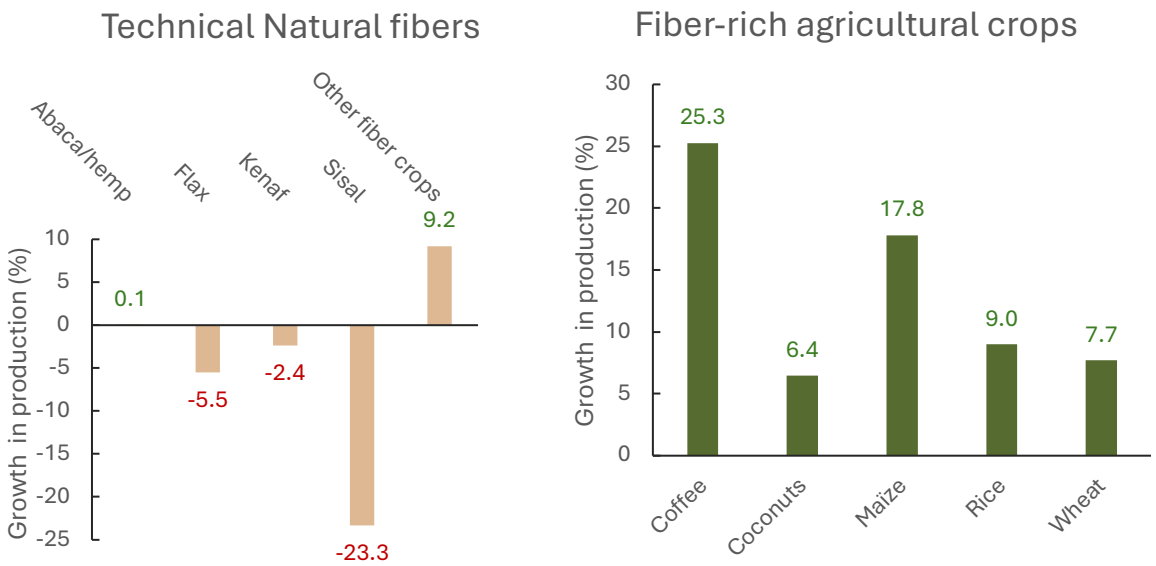


*Figure 1.6: Global production trends of natural fibers and fiber-rich crops from 2015 to 2023. Data collected on FAO website (consulted in May 2025).*

*3.1.3. Type of lignocellulosic filler (long fiber vs particulates)*

For several decades, **wood fibers** have demonstrated technical and economic viability as an alternative to traditional **synthetic reinforcements** such as glass and carbon fibers. However, the use of wood fibers may raise concerns about deforestation and sustainability, especially if not sourced responsibly. These drawbacks have led some researchers and industries to explore **other plant-based alternatives**. Lignocellulosic fibers are a key component of sustainable composite materials, as these natural reinforcements provide unique properties and environmental benefits. Given their predominant derivation from agro-industry, their use could contribute substantially to organic waste recycling and to the **circular economy**. Furthermore, they provide a diverse raw material base adapted to the region in which they are cultivated. In tropical zones, lignocellulosic fibers obtained from **kenaf** or **abaca** are common [73,74], whereas temperate regions rely on **hemp**, **wheat straw** or **sugar beet pulp** [18,53,75]. Moreover, the versatility of lignocellulosic fillers extends beyond their geographical adaptability, offering a **wide range** of chemical composition and exhibit a considerable variation in length and diameter which significantly influence the processing conditions required for their utilization and their properties. Whereas **long fibers** reinforcing composite materials have been extensively studied, fewer research articles focus on agricultural waste in the form of smaller particles (< 1 mm) such as **lignocellulosic flour**, even though these represent a widely exploitable resource that does not compete with food production. These filler particles offer distinct advantages, such as improved **dispersion** within matrices and potential to enhance specific material properties. Furthermore, particle reinforcement, such as flour, offers **ease of processing** as it degrades less compared to fibers during blending with a thermoplastic. Consequently, numerous studies focus on using biomass flour rather than fiber [51]. However, considering the **substantial variety** of co-products generated by the agri-food industry that can be reduced to fine particles, only a **limited portion** has been evaluated as potential filler for biocomposite in the literature among these: rice husk flour, olive stones flour, peach stones or oat and barley flour [19,76–78]. When reduced to flour, grain husks can show similar effect as wood flour by improving mechanical properties of thermoplastic matrix [78]. In general, lignocellulosic flours appear to be viable reinforcement for composites by enhancing flexural and impact strength, as it is shown for barley husk and coconut shell reinforced polypropylene composites where coconut shell and barley husk composites showed 20 % and 35 % better Charpy impact strength than soft wood composites [79]. Up to 50 %(m/m) of the matrix can be replaced by particle fillers, which allows for a reduction in the overall cost of the composite and/or a decrease in the resulting material's weight. Despite a well-established industry in the case of wood composites, several challenges remain before this

technology reaches its full potential for other lignocellulosic fillers. Indeed, the combination of two distinct materials (one hygroscopic biomass and one hydrophobic thermoplastic) leads to issues concerning the **interfacial adhesion**. Moreover, biocomposites technology gathers two unrelated domains: **agri-food sector** and **plastic industry**. A balance must be found between achieving the high temperatures and shear forces necessary for plastic processing and maintaining the integrity of biomass fillers.

*3.1.4. Structure and composition*

**Plant cell wall's structure** and chemical composition are influenced by several factors such as climate conditions, agricultural practices, plant type and age, and the origin of plant tissue. Commonly, the plant cell wall is constituted of three layers: the **middle lamella**, the **primary** cell wall, and the **secondary** cell wall. **Cellulose** is the most abundant polysaccharide in nature and the main plant cell wall component. It is a macromolecule consisting of chains of **glucose** monomers with a degree of polymerization of about 10 000 [80]. These long-stretched chains linked with each other through hydrogen bonds and Van der Waals forces to form a compact and orderly structure constituting the crystalline part of the cellulose. Cellulose presents several advantages regarding the structure. Firstly, its mechanical strength allows the plant to grow against gravity. Secondly it is very deformable which reduces the risk of breaking and allows, for example, the turgescence phenomena to take place. Finally, the cellulose permits gas and water exchanges thanks to the microfibrils structure. The second most abundant component of the plant cell wall after cellulose is the **lignin**. It is an amorphous polymer that contains three monomeric units: syringyl (S), guaiacyl (G) and p-hydroxy-phenyl (H) [81]. Lignin consists of aromatic and aliphatic hydrocarbon forming a three-dimensional network. Its aim is to reinforce woody plant rigidity and their mechanical resistance to compression. Lignins are mostly hydrophobic. At the interface of the two compounds, we have just presented is the **hemicellulose**. It is a polysaccharide heterogeneous polymer with a branched linear structure composed of several monomers such as xylan, glucuronoxylan, arabinoxylan, glucomannan, and xyloglucan. Hemicellulose makes hydrogen bonds with cellulose and covalent bonds with lignin either directly or via phenolic acids which are part of the extractives (Figure 1.7). Hemicelluloses are not crystalline which makes them more susceptible to chemical attack than cellulose such as hydrolysis and oxidation [80]. In addition to these three main compounds, biomass is composed of **extractives**. They gather a wide variety of chemical compounds such as terpenes, aromatics, or waxes; it is therefore difficult to classify them. One of the main components of the extractives are the pectins. **Pectins** are water soluble and

abundant in the middle lamella and primary wall. They are made up of different chemical entities whose structure and proportions vary greatly. These molecules act as intercellular cement.

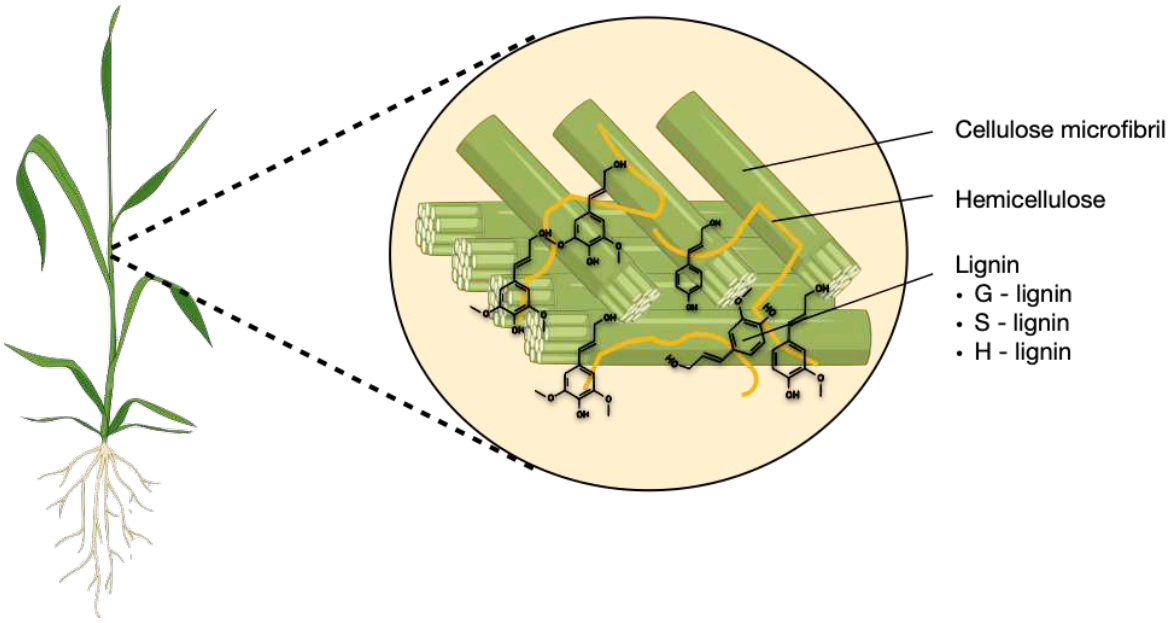


*Figure 1.7: Structural organization of the plant cell wall, highlighting the arrangement of the three main components (cellulose -green-, hemicellulose -yellow-, and lignin (G-guaiacyl, S-syringyl, H-p hydroxyphenyl) focusing on the secondary cell wall*

The proportion of the **three primary components** of lignocellulosic products varies from plant to plant and significantly affects the characteristic of the fillers and especially their physico-mechanical properties, their ability to retain moisture. Consequently, these factors may impact the performance of composites reinforced with lignocellulosic fillers. Table 1.4 displays the composition of various natural fillers focusing on lignocellulosic material derived from agro-wastes that can be reduced to particle size.

*Table 1.4: Chemical composition of some agro-waste fibers*

| Filler | Cellulose (wt.%) | Hemicellulose (wt.%) | Lignin (wt.%) | Ref |
|---|---|---|---|---|
| Rice straw | 41-51 | 19-25 | 20 | [2] |
| Spent grain | 17.1 | 34.4 | 19.1 | [82] |
| Oat husks | 50 | 25 | 3-5 | [83] |
| Wheat straw | 38-45 | 15-31 | 12-20 | [2] |
| Corncob | 26.1 | 45.9 | 11.3 | [82] |
| Rice husk | 35-45 | 19-25 | 20 | [2] |
| Wood | 45-50 | 23 | 27 | [84] |

While many types of **agro-waste** share a common lignocellulosic composition, this work is going to focus on a prominent industrial example: brewer's spent grain (BSG), the main by-product of the brewing process and one very abundant lignocellulosic residues worldwide.

## 3.2. Brewer's spent grain

### *3.2.1. Brewing process*

A typical **brewing process** shows several steps. The first one is the malt milling to open the shell and expose the starch for transformation. Conventionally in Europe, beer is produced from **barley**, and sometimes from wheat. However, in other continents the cereal supplies can be different, such as rice in Asia [85], or maize in America [86]. The grains are then dried. During the second step, the crushed malt is soaked into warm water, this process is called mashing. The starch present in malt is converted to fermentable sugars and non-fermentable sugars which are then released in the water. To stop the enzymatic activity, the mash temperature is raised before next steps. Then the solid residue, called the **brewer's spent grain** (BSG) is washed and removed by filtration. The liquid part called the wort is boiled to stop enzymatic processes and to induce caramelization and Maillard reaction. Then it is cooled down before adding yeast which will ferment sugars to produce alcohol, carbon dioxide, and other components. Figure 1.8 shows the different steps of brewing process.

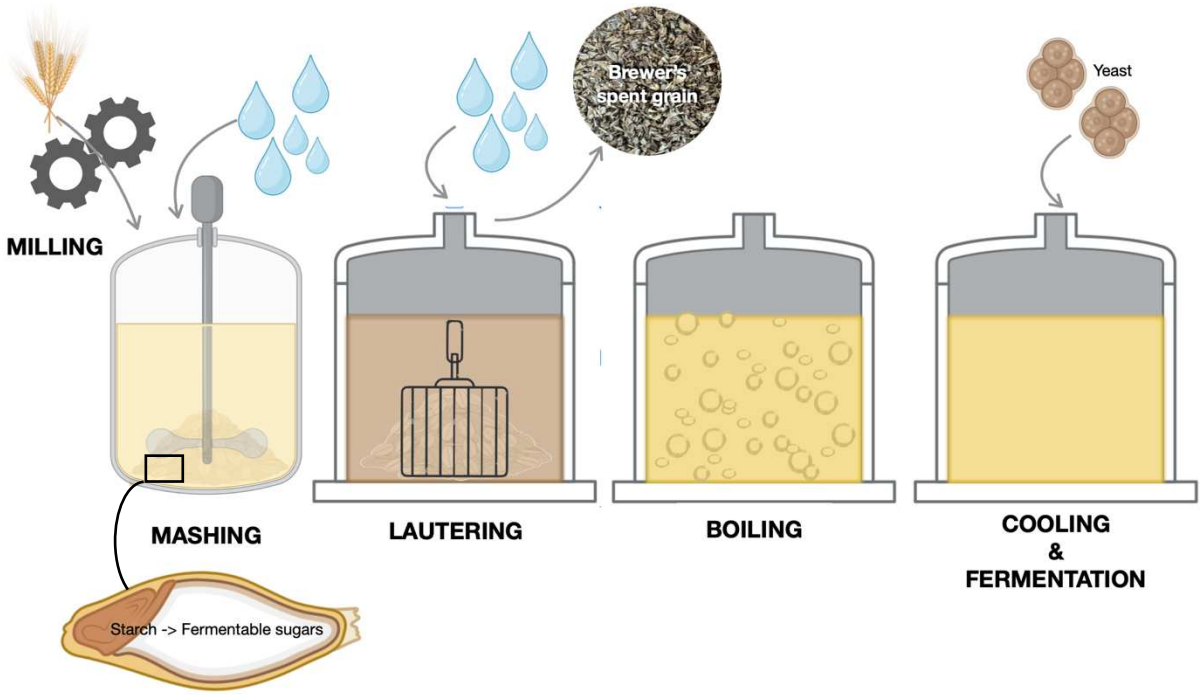


*Figure 1.8: Brewing process*

### *3.2.2. Market potential*

Beer consumption came as early as 7000 years ago in China [87]. From this time, brewing has been spreading all around the world. The overall growth of brewing industry emerged when commercial breweries replaced monasteries. During the 90s, European and American breweries started to extend their business across the world which led to an increasing blossom of breweries. Finally, at the beginning of the twenty-first century, a new generation of small-scaled breweries begun. **Microbreweries** were designed to produce a limited amount of beer and to be part of local markets. Therefore, the generation of brewing by-products has become **widespread**. Nowadays, beer is still one of the most popular beverages in the world. According to the Food and Agriculture Organization of the United Nations (FAO), the global beer production reached **185.6 million** kilograms in 2022. China led the market with an average annual production of 39.6 million kilograms from 2015 to 2023, followed by United states of America, Brazil, Mexico and Germany (Figure 1.9). Global beer market is mainly divided between America, Asia and Europe; Africa representing only 7.2 % of the market shares. We can observe that beer is widely spread around the world.

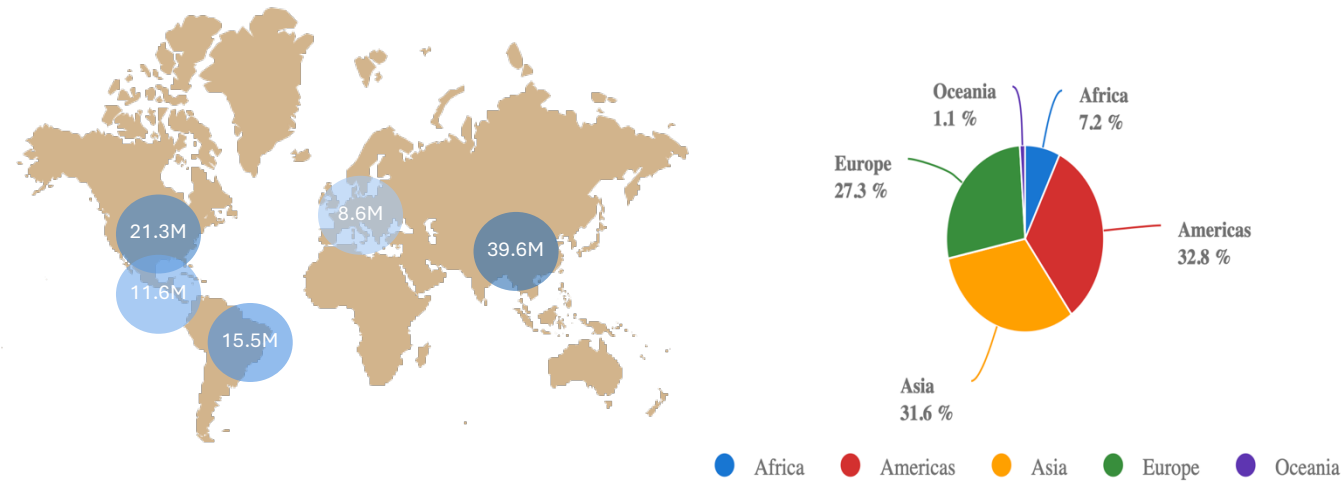


*Figure 1.9: Production quantities of Beer from barley (kg) of the top five beer-producing countries and Production shares of Beer from barley - average 2015-2023, extracted from the FAO (consulted in May 2025).*

Accounting for **85 %** of the by-product generated by the brewing process, Brewer's spent grain is the main and most abundant by-product [88]. Considering that the production of hundred liters of beer necessitates 20 kg of malt, 6.2 kg of dry BSG are generated [88]. Consequently, BSG is globally generated in high amounts, almost **12 million tons of BSG** are produced annually in

the world. Therefore, research activities concerning the valorization of beer production by-product are crucial because these aspects may impact a substantial number of people worldwide.

*3.2.3. Current disposal methods*

As seen earlier, the quantity of generated BSG is very large, considering only Europe the production of BSG reaches 3 million tons each year [89]. Hence, there are different current methods of disposal. The main use of BSG consists of **animal feedstock** [90] which reduces the cost of feeding. BSG provides many essential amino acids which encourage farmers to feed cattle, poultry, pigs and fish [90]. However, the **high moisture content** of BSG makes it susceptible to **spoilage** which shorten its usable period. Moreover, a stabilization of BSG may add costs that outweigh the potential benefits. When there is a lack of animals to be fed, BSG can be **landfilled** where, in small amounts, it may act as natural fertiliser. However, the extensive application of spent grain over the fields generates several **greenhouse gases** [91] such as methane and $CO_2$ due to decomposition. In addition, using only BSG produces an unbalanced compost leading to a bad fertilisation of soils. Moreover, the cost of transport for wet BSG are high and for this reason BSG can be only supplied to local farmers [90]. From this point, one of the solutions may be to use BSG for **energy production** directly in the brewery through combustion [90]. Studies have reported the potential of producing biogas, ethanol and thermochemical conversion from BSG [90]. According to the biomass cascade model of the Copenhagen Institute of Technology [92], the utilization of biomass for energy purposes exhibits the **lowest value**. Besides being of interest as material for animal feed and energy production, BSG has been considered for incorporation in human diet [90]. Considering it is derived from food, BSG can be added the composition to bakery products as flour and snacks [90,93]. Finally, a growing interest for agricultural derived materials has been observed over the past decades. Being one of the strategies for food industry waste management, they meet the demand of a bio-economy market. Also, the development of this kind of materials represents a good opportunity to add value to the agricultural wastes.

To sum up, numerous valorization strategies have been reported. Currently in Europe, 70 % of BSG are used to **feed animals**, 20 % are discarded in **landfills**, and 10 % is used for **biogas production** [94] (Figure 1.10). The rest of discussed valorization pathways have not been implemented on an industrial scale. Thus, over the past decade, research efforts have intensified to explore the reuse of BSG for valuable applications. The advances suggest the potential for an imminent industrial scaling of some of the applications.

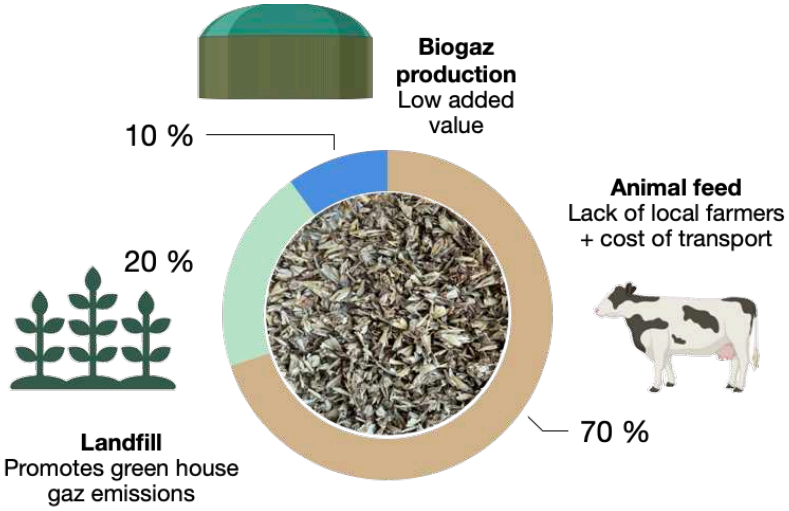


*Figure 1.10: Current disposal methods of BSG in Europe and their drawbacks [94]*

### *3.2.4. Structure and composition*

Barley is a cereal rich in **starch** and **proteins** which is constituted of three main parts: the embryo, the endosperm (including aleurone layer) which contains starch, and the pericarp covered by the husk (Figure 1.11) [95]. With 80 % moisture content, BSG is composed of layers of peel, pericarp, and seeds with residues of undigested starch and aleurone from barley [96]. Hence, **BSG** is mainly made of **cell wall** component, which are lignified and rich in arabinoxylans [96]. A smaller part is constituted by proteins. As for any lignocellulosic products, the composition of BSG is contingent upon barley type, harvest conditions and mashing conditions [92].

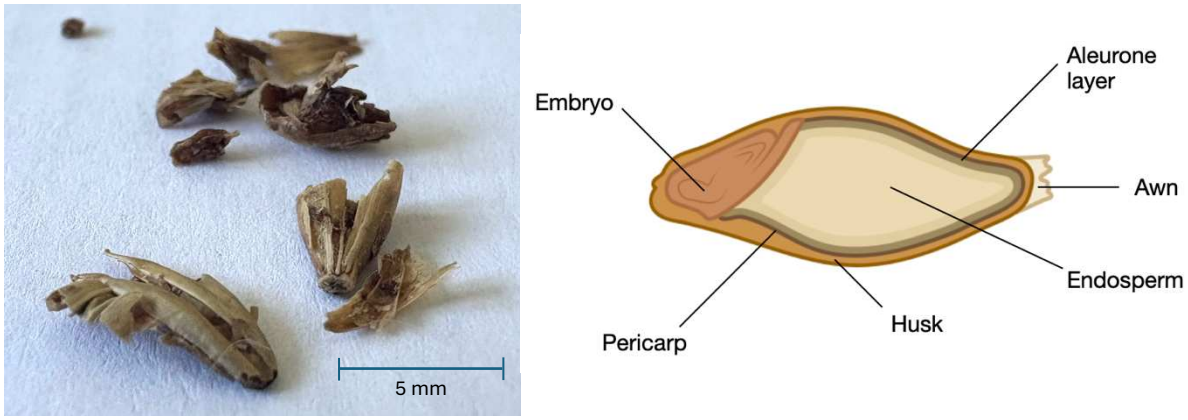


*Figure 1.11: Picture of dry BSG and the schematic representation of a barley grain in longitudinal section*

Since the major constituents are cellulose, hemicellulose, lignin, and proteins, BSG is considered as a **lignocellulosic material**. Hemicellulose mainly consisting of arabinoxylans is the main constituent which can account for up to 41.9 % of BSG dry basis (Table 1.5). Then, cellulose is the second most abundant component reaching 25.3 % of BSG dry basis. The **sugars** found in BSG mainly consist of arabinose, xylose, mannose, galactose and glucose [95]. Besides sugars, lignins and proteins are also found in significant amounts, up to 28 and 30 % respectively.

BSG is also an excellent **source of minerals** including Ca, Mg, K, Na, Cl, P, and S. It has been found that the profile of BSG minerals was of interest as they were used as cofactors in enzymes reactions [97]. Husks contains high amounts of silica, indeed 25 % of the minerals in barley are silicates [98].

*Table 1.5: Composition of Brewer's spent grain according to the literature*

| Component | Content (%dry basis) | | | | | | | |
|---|---|---|---|---|---|---|---|---|
| Cellulose | 16.8 | 25.4 | 21.9 | 25.3 | 21.7 | 26.0 | 12-25 | 22.2 |
| Hemicellulose | 28.4 | 21.8 | 29.6 | 41.9 | 19.2 | 22.2 | 20-25 | 26.8 |
| Lignin | 27.8 | 11.9 | 21.7 | 16.9 | 19.4 | - | 12-28 | 14.1 |
| Proteins | 15.3 | 24.0 | 24.6 | - | 24.7 | 22.1 | 19-30 | - |
| Extractives | 5.8 | - | - | 9.5 | 10.7 | - | - | - |
| Ash | 4.6 | 2.4 | 1.2 | 4.6 | 4.2 | 1.1 | 2-5 | - |
| Ref | [95] | [99] | [100] | [101] | [102] | [103] | [104] | [92] |

*3.2.5. A filler for composites*

Considering its composition with a relatively high fiber content and similar to **wood fiber**, BSG could be a potential raw material for the manufacturing of polymer composites. Moreover, the content of **proteins** in BSG could be a source of additional properties for composite application. Indeed, proteins may be used as plasticizers [105]. Indeed, Hejna *et al.* showed that BSG proteins caused partial plasticization of polycaprolactone matrix [106]. According to them, amino acids located on the surface of BSG are low-molecular-weight compounds, which can act as plasticizers [106]. As a matter of fact, very small molecules could penetrate and keep polymer chains apart which could facilitate their movement rendering them more plastic. Few papers to date have investigated the use of BSG as a filler for composite.

In 2015, Berthet *et al.* explored the potentialities of using **alkali-treated BSG** as constituents of biocomposites for **food packaging** applications. Experiments were conducted

on a twin-screw extruder with polyhydroxybutyrate-valerate (**PHBV**) polymer and grinded BSG. They reported that BSG fibers were aggregating at the entrance of the extruder causing an uncontrolled feeding of the fibers inside the mix. Thus, the preparation of such a composite was not possible [107]. Later in 2017, also using an extrusion method with **PHBV** polymer, Cunha *et al.* developed a composite made of PHBV and BSG. For the experiments PHBV was cryo-grinded into powder and BSG was ball-milled. Up to 20 % of BSG content were investigated but 10 % was the biggest content that was processed in the extruder. Regarding the mechanical tests, the maximum tensile modulus increases with BSG content up to 5 wt.%. The addition of BSG increases the permeability of the films to $O_2$, $CO_2$ and water vapor [108].

Another polymer that tends to be used in the making of BSG composite foams is the polyurethane. Hejna et al. explored the properties of a polyurethane-polyisocyanurate (**PUR-PIR**) foams filled with BSG. Approximately 16.7 wt.% of BSG was introduced into the composite. This paper reported that BSG can be successfully used to prepare foamed PUR-PIR composites [109]. In another study, Formela *et al.* worked on a rigid polyurethane **foam** reinforced with two fillers: BSG and **ground tire rubber** (GTR). GTR and BSG were grinded to obtain small particles size and then added to a polyol mix by stirring in different ratios. They reported a better compatibility between GTR and the polymer than between BSG and the polymer which can be observed by the size of the polyurethane cells which were smaller and more regular with a higher GTR content compared to BSG. It was shown that a combination of BSG and GTR fillers was a good low-cost and environment-friendly alternative as fillers in **polyurethane foam composites** [110]. These two fillers were also used by Zedler *et al.* to reinforce **natural rubber composite**. They also reported a better compatibility between GTR and the matrix than with BSG because of the polarity and the particles size of the fillers [111]. In their studies, Bledzki *et al.* compared the impact of two different fillers into a **polypropylene** matrix to replace wood fibers. In this paper, coconut shell fibers and barley husk were investigated. Experiments were conducted by mixing the fibers (40 wt.%) with polypropylene into a high-speed cascade mixer. They reported that the elongation at break of barley husk composite was 40 wt.% better than soft wood composites. The impact strength was also higher for barley husk than for wood fibers composites [112].

Figure 1.12 summarizes the different studies contributing to the development of BSG composites. The research efforts are mainly concentrated within three teams identified on the figure by different colors.

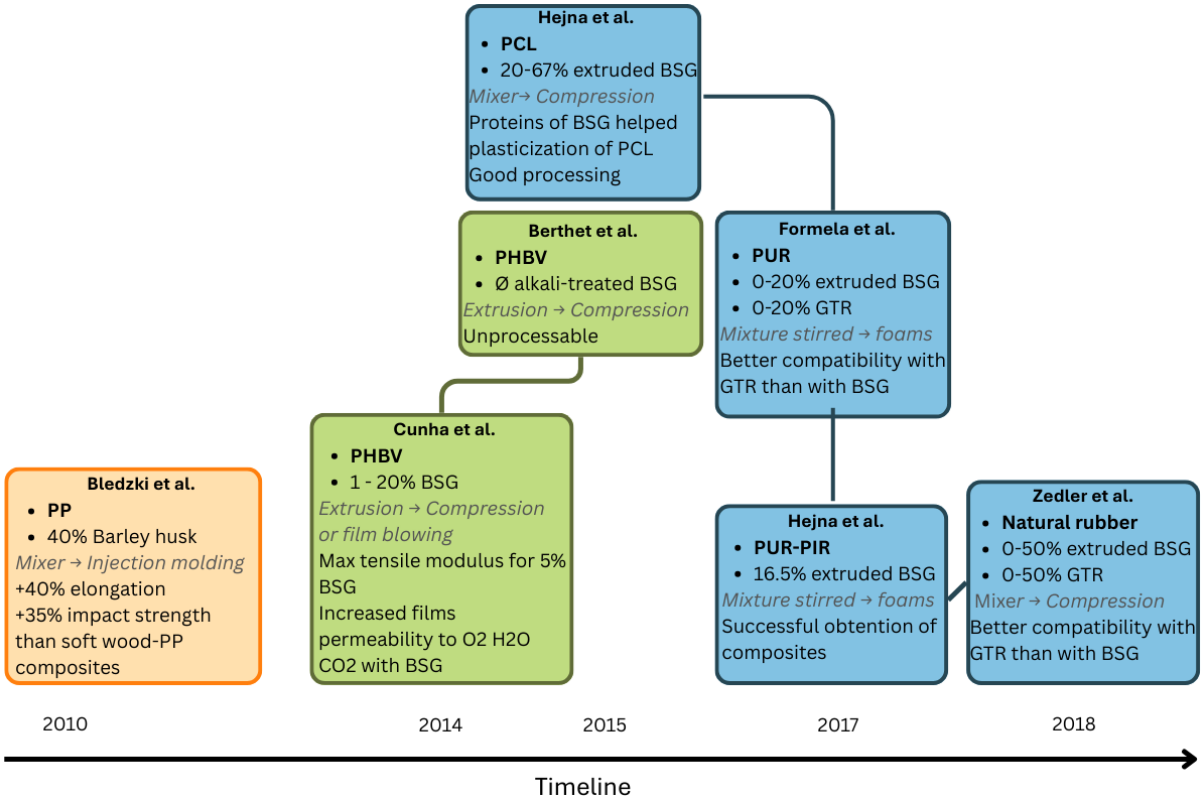


*Figure 1.12: Overview of the main research teams (grouped by color) contributing to the development of brewer's spent grain (BSG) composites, with main results of studies published by each.*

BSG show substantial potential as reinforcement for composites material. Their low cost and the fact that they are safer to process in terms of toxicity make them good candidates for this use. In response to a strong marketing trend toward alternative lignocellulosic sources, BSG have some advantages but need to overcome several drawbacks to permit such a replacement. BSG are wet bio-products which means that they are perishable. In this way, optimal storage parameters must be identified. Furthermore, their **poor compatibility** with the matrix needs to be enhanced, for instance by modifying the fibers or adjusting processing parameters/conditions. To do this, a comprehensive investigation of BSG is necessary. As seen earlier, BSG is rarely used in its **raw form**. Instead, it generally requires specific **preparation** and/or treatments before incorporation into composite materials. The following section therefore focuses on the pretreatment strategies commonly applied to biomass to improve its suitability for composite applications.

# 4. Filler treatment

## 4.1. Filler preparation

### *4.1.1. Introduction*

Producing composites from natural fibers presents **two main challenges** due to fibers inherent properties which are different from those of synthetic fibers like glass and carbon. The **primary** drawback comes from the **initial moisture content** of these fibers. Due to their hydrophilic nature, most of the fibers show a high equilibrium moisture content. For instance, abaca, jute or sisal fibers present a moisture content of 15, 12, 11 % respectively, at 65 % of relative humidity and 21 °C [113] and it is even higher for food industry waste. This amount of moisture can cause issues during processing, with shrinkage and swelling of the fibers [51], and during the use, it has been shown that the moisture can negatively impact the **mechanical behavior** of natural fiber composites [113]. Moisture content should be reduced to less than **3 %** to produce composites of good quality [5]. The **secondary** challenge when processing natural fiber composite is mastering the **fiber aspect** throughout the compounding with polymers. It has been shown that fibers are losing length, width, and aspect ratio during the compounding [51]. Moreover, as demonstrated earlier, reducing the fiber to **flour** (aspect ratio less than 10, [51]) increases their potential use by improving their **dispersibility** within the polymer matrix and enabling more uniform mechanical properties in the resulting composite material. Therefore, the comminution of lignocellulosic biomass has become a key operation for bio-based composite application. In this part, we will discuss about the common **drying and grinding** methods to process lignocellulosic biomass and increase its usability as filler of polymeric matrices.

### *4.1.2. Drying treatments*

**Biomass drying** is a pretreatment process that requires a lot of **energy**. Consequently, the efficiency of the process greatly influences the economic viability and sustainability of bio-based composites. Many drying systems have been designed and implemented. They can be classified according to the **heat transfer**: convective drying, conductive drying, radiation drying, and microwave drying [114]. The drying process of biomass occurs in **two stages**: a steady drying-rate period, and one or more falling drying-rate period [115]. The first period consists of the evaporation of **free water**; the second period occurs after **internal diffusion** of water to the surface of biomass [114].

The most applied method to dry biomass uses **convective drying**, they can be batch or continuous processes. To diffuse the heat, different medium can be used: hot air/gas, or steam.

To prepare the biomass, numerous drying techniques are used including solar drying, hot air drying, fluidized bed, microwave drying, drum drying, and freeze drying.

♦ Solar drying – Hot air drying

One of the oldest systems consists of using solar energy. Despite being the **cheapest** mean, it has very **long drying times** and possible contaminations and **lack of control** over drying conditions. Therefore, **hot air convection drying** systems are commonly implemented to dry food residue. They allow a precise control of the temperature and gas velocity. However, the drying time is extensive (up to 23 hours at 100 °C, [116]) and there is a low thermal conductivity leading to performance loss [117]. Therefore, this method is sometimes combined with other systems such as microwave and infrared [117].

♦ Rotary drum dryer

Combining both convective and conductive heat, rotary drum dryer is also a method commonly used to dry **dust** and **husks**. It consists of a cylindrical inclined rotating drum which dries biomass by exposing it to hot gas or steam. It allows large amounts and extensive range of particle size. The energy consumption per ton of dry beet pulp of a drum dryer is about 815 kWh [118].

♦ Fluidized bed dryer

Fluidized bed type of dryer benefits from a high heat transfer rate with a good mixing of the solid and a uniform temperature distribution due to high velocity gas flow. In this technique, the heating fluid is forced through a bed of particles. These dryers are commonly used to dry small particles; however, the operating cost is high [117]. The energy consumption of fluidized bed dryer is 3.1 to 4 MJ/kg of water [118].

♦ Pneumatic or flash drying

Pneumatic drying or flash drying is a very fast process where biomass is dried with a continuous flow of hot air at very high velocity. The drying time is usually about half a minute. However, the installation cost is high [117]. The net dryer energy consumption is 3 to 3.5 GJ per ton of pulp when using air [118]. Steam drying and especially **super-heated steam** drying shows significant advantages compared to other convective methods such as **low energy** consumption, and low carbon emissions [117]. Super-heated steam can be **combined** with a lot of other drying systems. This technique usually reduces the energy consumption by **recovering** the latent heat of vaporization of water. For instance, when associated with flash drying, the energy consumption is reduced by approximately 80 % [118]. Nonetheless, this technique is not widely implemented at larger scale. All the drying methods are gathered in Figure 1.13.

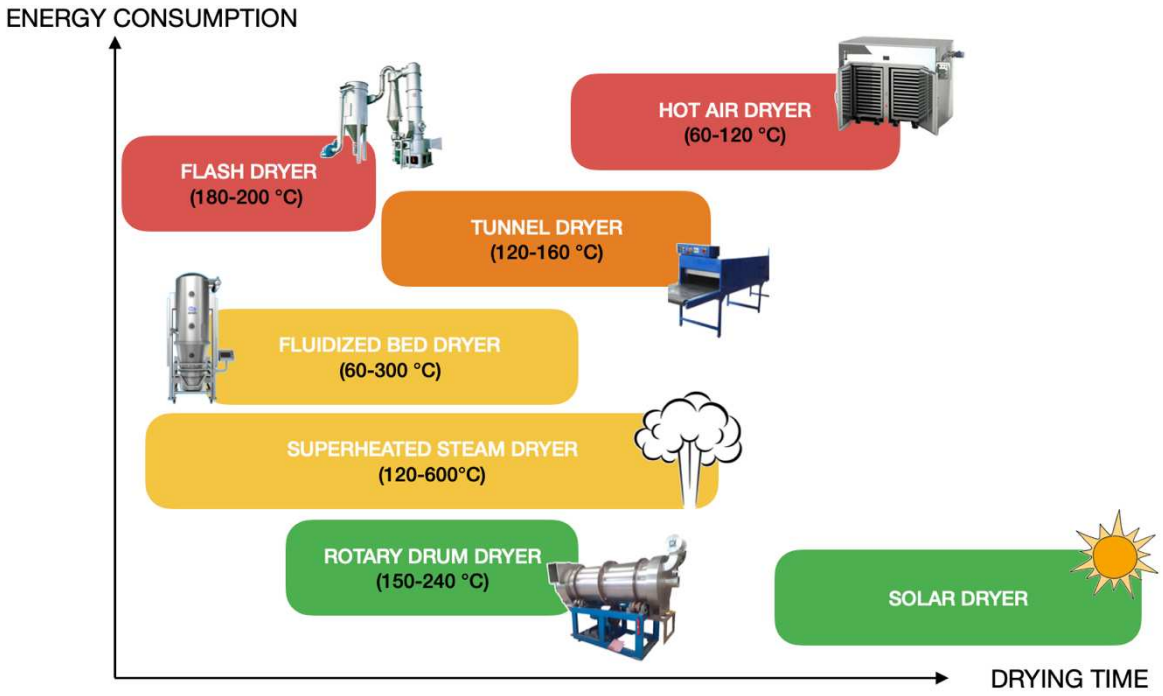


*Figure 1.13: Comparison of drying methods based on their energy consumption and processing time*

### *4.1.3. Conventional milling treatments*

As reported earlier, the **milling of lignocellulosic biomass** for material applications is a key operation. This process is subjected to challenges such as costs, energy consumption or ground powder properties. Size reduction can be described in terms of either particle dimensions or structural breakdown of plant tissue. Given the complex nature of biomass, milling typically starts from crushing plants, typically from meter to centimeter, then an intermediate milling happens at the tissue scale from 1 mm to 100 µm using shearing process. Finally, a finer milling can be reached at the cell-wall scale to 100 nm [119]. Mechanical stress generated during milling process can be classified in **four groups**: Impact, compression, shear, and attrition [119]. Depending on this mechanical stress, it has been shown that lignocellulosic particle breaks differently [120]. Therefore, the **grinder type** will influence not only the **size distribution** but also the **aspect ratio** of the particles. Then, these properties have direct influence on rheological properties of the powder as well as on mechanical properties and water absorption capacity of the composites [121,122].

There is a wide diversity of grinders including hammer mills, knife mills, disk mills, ball mills, colloid mills, jet mills, centrifugal mills, extruder, etc [123]. Thus, in this section, we will try to be as inclusive as possible by dividing them in **four categories**.

♦ Impact milling

The impact-mill grinder such as hammer-mills or knife-mills is a tool that turns at high speed (10 000 to 20 000 rpm) which projects particles through a **sieving grid** against a screen to obtain particles with the size of hundreds of micrometers [124]. This kind of grinder generates shear and impact mechanical stress to the particles.

♦ Disc milling

The pin-mill consists of two discs usually one stationary and one rotating. Particles are eventually struck by the pins which breaks them apart through **shear mechanical stress**.

♦ Ball-milling

To obtain, even finer particles, one can use ball-milling which combines **compression and attrition** by the ball usually made of ceramic.

♦ Jet milling

Finally, jet mill grinds particles by **projecting** them with air-compressed nozzles. Then particles are selected by a sieving grid rotating between 3000 and 20 000 rpm. This grinder permits to obtain particles **smaller than 20 µm**.

Only ball milling is a **batch process**, the others can operate under continuous mode. Most of the techniques presented here are only suitable for biomass up to **20 % moisture content**. The performance and **energy consumption** are influenced by several factors such as initial moisture content of lignocellulosic biomass, the feed rate, or size of particles before and after. Several studies showed that the grinding energy increases with the moisture content of the biomass [125,126]. Consequently, an optimization of these parameters and an adjustment of the target size to the value of intended applications are necessary. Figure 1.14 illustrates various milling technologies positioned according to the **particle range size** they target along with the hierarchical structure of lignocellulosic biomass impacted. The color gradient indicates relative energy consumption, green indicating low energy consumption while red indicates higher energy consumption. These are relative consumption as it depends on several factors such as moisture content and composition of ground material, screen size, or grinding speed.

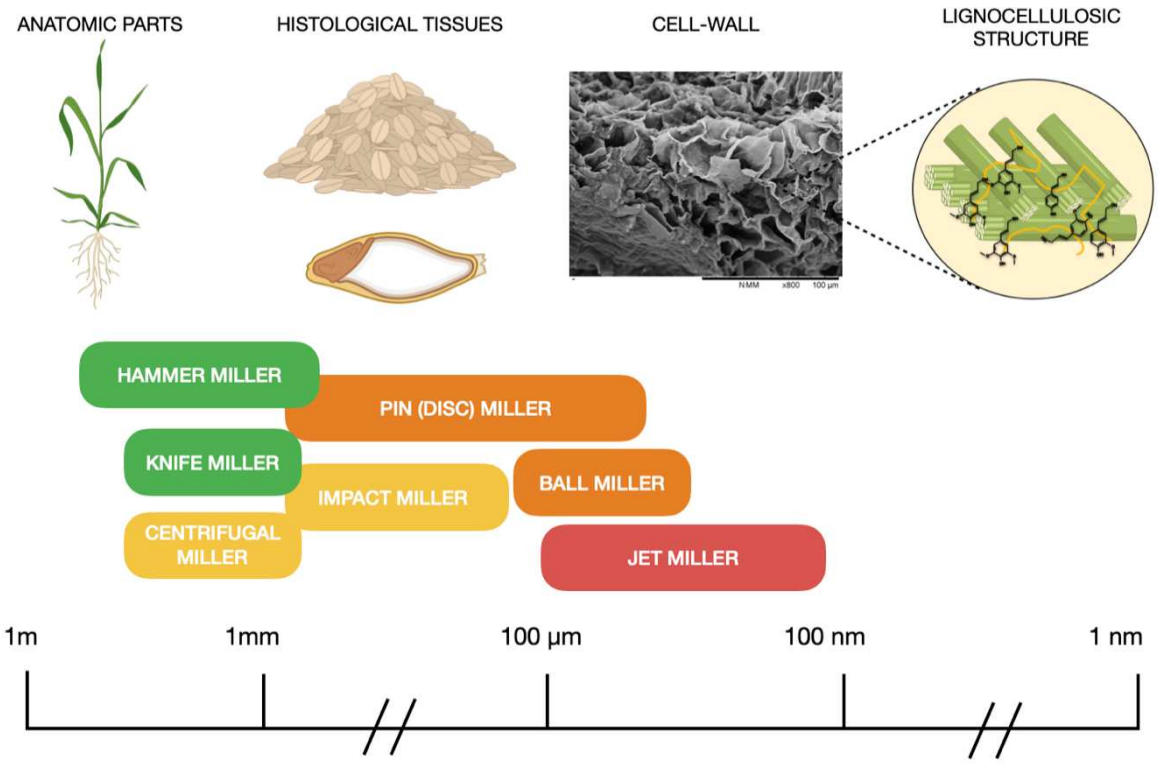


*Figure 1.14: Multiscale structure of lignocellulosic biomass and corresponding milling technologies with their global energy consumption; color gradient indicates relative energy consumption, with green representing lower energy requirement.*

To lower the energy consumption, a **thermal pretreatment** step prior or during the grinding process can be added [124]. Both **heat and cold** (cryogenic milling) treatments can be considered. However, this discussion will only focus on heat treatment, as drying the biomass is a prerequisite for subsequent composite processing. Hence, **heat treatment**, as presented earlier, can be used to modify chemical and physical properties of the fibers. At temperatures below 200 °C, it can be used to simply dry the fibers since it has been proved to **reduce the energy consumption** [125]. In this case, the plasticizing effect of water is removed, Young's modulus of the fibers tends to be higher for lower moisture contents [127]. Between 200 and 300 °C, torrefaction occurs which removes the condensable volatiles and degrades hemicellulose which is the most reactive component in the cell wall [80]. The material undergoes modification of its structure due to molecular rearrangements with, for instance, ramifications of the lignin network [128]. This reduces the possibility of the re-absorption of the water. Moreover, the relative amount of crystalline cellulose increases [128]. The material after **torrefaction** becomes more **brittle and rigid**, and consequently more susceptible to grinding. Therefore, we need to keep in mind that torrefied biomass will exhibit modified properties compared to non-torrefied one.

At industrial scale, a balance must be found between the energy used to dry and heat the biomass and the gain in grinding performance. However, integrating drying and grinding in a continuous process remains challenging due to equipment limitations. Thus, combined technologies could offer a promising approach to optimize operations and improve overall energy efficiency.

*4.1.4. The extrusion process treatment*

**Extrusion** is a **thermo-mechanical** process based on the action of one or two screws that rotate into a barrel, which is equipped with temperature control. In this section, we are focusing on **twin-screw** extrusion. During this manufacturing process, the material is subjected to simultaneous mixing, heating, shearing. It involves forming raw materials into specific cross-sectional shapes using a die. This process uses heat and pressure to soften or melt the material for processing. This results in physical and chemical changes in the material as it is conveyed along the screw. Extrusion is used across various industries. In the **construction sector**, it is used to create aluminium beams and window frames. In the **consumer goods industry**, it helps in manufacturing bike frames and oven components. In the **food industry**, extrusion is commonly employed for making pet food and crispy snacks. Extruders are not typically used to pretreat the biomass. However, due to its ubiquity across sectors and versatility, they have often been tested for biomass processing. The main advantage of extrusion is that it is a **continuous process** and can easily be used in **large-scale** production. Extrusion can generate **high shear forces** which facilitate the break-down of the feedstock, fast heat exchange, and effective mixing [126]. Moreover, extrusion is a highly adaptable process due to its numerous adjustable parameters such as temperature, screw speed, feed rate, and screw configuration, allowing it to be precisely customized for specific processing objectives. Therefore, extrusion has the potential to become a viable biomass pretreatment process. Many studies have been reported the use of extrusion to pretreat the biomass for sugar recovery. Only a few focused on dry and milling on the biomass.

**Screw configuration** can deeply affect pretreatment efficiency. It can be modified by associating different type of screw elements such as forward **conveying**, forward **kneading**, neutral kneading, or **reverse** conveying and reverse kneading. For example, N'Diaye *et al*. used an extruder to extract hemicellulose from poplar wood. They used kneading elements to ensure homogenization and impregnation of the alkali, and reverse elements to facilitate the separation of the liquid through a filter and conveying elements to transport the solid [129].




*Figure 1.15: Different types of screw element*

**Screw speed** has been reported to control the **shear rate** and the mean **residence time** [130]. In their study on extrusion pretreatment of corn stover for sugar extraction, Zhang *et al*. observed that increasing the screw speed enhanced shear forces, which facilitated lignin softening up to an optimal threshold of 80 rpm [131]. This speed, however, the reduced residence time limited the extent of lignin sheath disruption. The energy consumption for fiber breakage is increasing with the screw speed [130]. In this way, the applied shear forces impact the comminution of the fibers.

Finally, **barrel temperature** is another important extrusion parameter which facilitates the melting or the **drying** of the feedstock. It generally fluctuates between 40 and 200 °C [132]. It has been showed that increasing the extruder temperature would promote the **moisture evaporation** which develops more friction and thereby, a higher reduction of the fiber size.

The main source of energy for extrusion is electricity. The **energy consumption** can be divided in thermal energy to keep the operating temperature and mechanical energy ensuring the rotation of the screws. Regarding the **mechanical energy**, one factor provides insights into the amount required: the **torque**. Indeed, the torque is directly associated to the power consumption of the extruder, it is also influenced by the **screw speed**, the **feed rate** and **fill**, and the **viscosity** of the material [130]. Torque is inversely proportional to screw speed and higher temperatures of the barrels lead to lower torque values [132]. Even if the torque seems to be a good indicator of the mechanical energy requirement, it varies depending on the size of the equipment or the extrusion conditions. Therefore, specific mechanical energy seems to be more adequate to compare processes. It can be deduced from torque measurement using the following Equation (1.2) [133]:

$$SME = \frac{1}{Q} \frac{N}{N_{max}} r \frac{C}{C_{max}} W \qquad (1.2)$$

With $Q$ the mass feed rate, $N$ is the screw speed, $N_{max}$ is the maximum screw speed, $r$ is the motor efficiency, $C$ is the torque, $C_{max}$ is the maximum torque, and $W$ is the nominal power.

*4.1.5. The case of BSG*

With a moisture content ranging from **70 % to 80 %**, along with the presence of polysaccharides and proteins, BSG is susceptible to **microbial growth**, limiting its shelf life to a maximum of **7 days** in the fridge. This microbial contamination is characterized by a wide range of microorganisms, including aerobic mesophilic bacteria, aerobic thermophilic bacteria, and anaerobic bacteria [91]. **Water activity** plays a key role, in various aspect of food preservation. It is defined as the ratio of the vapor pressure of water in the food to the vapor pressure of pure water at a given temperature. It is commonly known that microorganisms cannot grow in dried food systems with a water activity ranging between **0.6 and 0.7**. Therefore, to ensure long-term storage of BSG, it is suggested to lower its moisture content down to 10 %. The relationship between material moisture content and its water activity is known as the sorption isotherm. It is a crucial parameter that can affects many aspects of drying and storage. Moreover, to make it suitable for composite applications, it is necessary to dry it prior to grind it. As a result, several studies focused on investigating the **drying kinetic**s of BSG [134–136]. Indeed, drying kinetics is a prerogative work to design efficient valorization methods. Mallen *et al.* studied BSG drying mechanism under isothermal conditions at four different temperatures (60, 70, 80 and 90 °C) using a thermogravimetric analyser. From the diffusion coefficients they obtain an activation energy of 26.6 $kJ.mol^{-1}$ [136]. Arranz *et al.* studied the drying of BSG at three different temperatures and three air velocities. They found an activation energy similar to that of Mallen *et al.* which was 24.88 $kJ.mol^{-1}$ for an air velocity of 1.2 $m.s^{-1}$ [134]. Santos *et al.* modelled the moisture sorption isotherms using Guggenheim, Anderson, and deBoer (**GAB**) equation to establish the maximum acceptable residual moisture content un BSG after drying to avoid the growth of bacteria [135]. They obtained three equations for the three tested temperatures (10, 20 and 40 °C) and concluded the BSG should be dried up to **13 % moisture content in wet basis** to avoid the proliferation of *Bacillus cereus* [135].

Currently, several processes are used for food drying. The traditional process for drying BSG using **rotary-drum dryers**. It is considered to be energy intensive compared with other drying methods for BSG because of their heat transfer mechanism. Stroem *et al.* reported an energy efficiency ranging between 60 and 76 % with a feed rate of 14 to 23 kg/h [137]. The second most common method is **oven drying**. This method is time consuming, in their study, Santos *et al.* oven-dried BSG during 18 h at 60 °C. Moisture content of BSG was between 8.7 and 10.8 %. They

compared this method with **freeze drying**, which is a less-harsh preservation method but conducts to higher cost of utilization [138]. In another study, BSG oven drying was compared with a natural convection **solar drying** [139]. The drying time was increased by ten with the solar drying system. However, regarding the energy consumption, the electric dryer consumption was about 1.68-1.88.$10^{-3}$ (kWh)/kg for temperatures between 60 and 95 °C, and it emitted 294.80-410.73 kg $CO_2$/(kWh). The solar drying system consumption and CO2 emissions were considered as null [139]. Mosqueda showed that solar drying took 5.5 to 6 h. **Super-heated steam drying** was studied on a thin layer of BSG at different temperature (from 110 to 180 °C) with no significant difference in dried BSG protein content. The drying rate was reported to increase linearly with steam temperature [140]. It should be noted that super-heated steam drying requires a more complex equipment than oven drying which can be a drag on its implementation at bigger scale. Another study employed **infrared** (IR) drying and **hot air-drying** methods [141]. IR drying was performed during 41 min (for the longer amount of time) on BSG placed on a performed tray at temperatures around 350-380 °C. Hot air drying was used during 2 hours at 85 °C. They reported that the moisture content and water activity were significantly lower for hot air drying than for IR drying. The drying method didn't seem to affect the **BSG composition**. Thai et al concluded that energy-saving could be done using the IR drying method [141]. While several studies have investigated drying systems for BSG, further research is needed to develop more energy-efficient and sustainable processes suited for large-scale applications.

Moreover, to our knowledge, too few studies have specifically addressed the **grinding process of BSG**. This highlights a gap in the literature that commands further exploration, particularly for its use in composite materials. One pertinent study examines **grinding BSG using extrusion**. In this study, Hejna *et al.* present the upcycling of **dry BSG** through thermomechanical processing using twin-screw extruder examines how extrusion conditions such as temperature (30-180 °C), throughput (1-5 kg/h), and screw speed (75-375 rpm) affect the specific mechanical energy needed for reducing BSG particle size. They found out that the color of BSG was particularly affected by the extend of Maillard reaction occurring during extrusion. Such browning was the result of melanoids production which enhances antioxidant activity of BSG. Thermal stability of BSG was increased when extrusion temperature was the highest (120 and 180 °C). They conclude that proper adjustment of the extrusion parameters could tailor BSG properties for composites applications [105].

## 4.2. Filler modification/compatibilization strategies

### *4.2.1. Introduction*

Natural fillers have gained increasing attention in industrial applications, particularly as reinforcement for polymer composites. However, their use presents several challenges. Beyond their **inherent moisture content** and the need of mastering their **aspect ratio** during manufacturing, a major drawback, particularly emphasized when using in thermoplastic composites, is their **low compatibility** with the polymer matrix. This incompatibility often results in reduced mechanical performance and durability, as well as a significant variability in quality [142]. To address this particular issue, extensive research has been focusing on the **surface treatment of natural fibers** that enhance the interactions at fiber/matrix interface [143–147].

A **strong interfacial bonding** is essential for effective **stress transfer** between matrix and the reinforcing filler in composite materials. However, lignocellulosic fibers are **polar** and **hydrophilic** due to the high content of structural hydrophilic groups, while most thermoplastics are **hydrophobic** and **non-polar**, leading to **poor compatibility** [142]. Thus, while incompatibility is clear for non-polar polymers such as PP, the case of partially polar bioplastics like PLA seems less evident. Studies on natural fiber/PLA composites report that at fiber loadings below 30 %(m/m), the tensile modulus increases but the tensile strength decreases, it has been mostly attributed to **weak interfacial adhesion** [148]. Hence many research studies have explored treatments methods to improve the adhesion between PLA and natural fibers [148–150].

Moreover, natural fibers show high propension to moisture absorption leading to a **reduced dimensional stability** and reduced mechanical properties which make their composites less suitable for **outdoor applications**.

Many treatment strategies have been studied, they include polymer-matrix modifications through **chemical** or **physical processes**, natural filler modifications (chemical, physical, biological or combination of these methods), and the use of additive coupling agents and obviously any combination of the mentioned methods. In this section, the focus is placed on **natural fiber treatments**.

Most fiber treatments, that are adapted for composite applications, are derived from the textile and wood industries to improve the quality of biomass derived products and are mainly based on retting processes [151]. Such treatments aim to reduce the **hydrophilic character** of the fibers and the crystalline index of the cellulose [142]. They primarily alter fiber surface topography, enhancing **roughness** and surface physico-chemistry (free surface energy, polarity,

and chemical functionality) by removing **non-cellulosic compounds** from the middle lamellae and plant cell walls. This can also weaken the cohesion within **fiber bundles**, splitting them from the surrounding cortical tissues [152], thereby promoting bundles dispersion within the polymer matrix and increasing the **specific interfacial area**. According to Paridah *et al.*, the biochemical composition, fineness, cleanliness, and mechanical strength of extracted fiber are highly dependent on the type and conditions of retting [153]. Indeed, natural fibers treatments vary widely in their mechanisms and effects. Therefore, next section will explore the principal fiber treatment methods.

*4.2.2. Comparative overview of the methods*

♦ Physical methods

Physical methods modify the structural and surface properties of natural fibers, influencing their reinforcing effect through enhanced mechanical interlocking at the fiber-matrix interface, without significantly changing their chemical composition. Their main effects on the fibers include the removal of the **weak surface layers**, the formation of new functional groups which increases hydrophobicity and improves interfacial adhesion. According to Mukhopadhyay and Fangueiro [154], physical treatment has two objectives: the **separation** of the fiber's bundles and the **surface modification** for composites applications [154]. Common approaches include plasma treatments, electric field discharges, radiations (UV or $\gamma$), and ultrasound treatments.

**Thermal treatments** were briefly discussed in Section 4.1.2. . These processes are called torrefaction and retification which were originally developed in wood industry. They aimed to reduce the **water content** and swelling of wood fibers. Treatment parameters such as heating temperature and rate, the residence time and the atmosphere drive the extent of fiber modification. Unlike most physical methods, heat treatments also induce **chemical changes** in the cell wall constituents [155]. Indeed, **hemicelluloses**, which are amorphous and of low molecular weights, undergo hydrolytic depolymerization [156], a process that can be catalyzed by the degradation products formed such as acetic acid or heterocyclic aldehydes and furfural [157]. At higher temperatures, around 220 °C, **lignins** are also modified releasing compounds such as vanillin, eugenol, guaiacol [158], while cellulose shows a small increase in crystallinity due to the preferential degradation of amorphous regions. **Crystalline cellulose** degrades above 300°C. A study on wood fiber/PP composites showed that pre-heat treatment of fibers (175-205 °C) improved interfacial adhesion and mechanical properties, particularly at higher fiber loadings (50%). The best results were obtained at 190 °C for strength and 205 °C for stiffness, with MAPP further enhancing fiber–matrix bonding [159].

**Plasma treatment** exposes fibers to an ionized gaseous medium able to react with the natural fibers. The plasma discharge can be generated by either **corona treatment** or **cold plasma** treatment. High frequency cold plasma can be produced by **microwave energy**, whereas corona plasma is produced at atmospheric pressure by a lower frequency alternation current discharge [160]. Depending on the working gas, the plasma atmosphere may contain atoms, ions, free electrons, and radicals that interact with fiber surfaces, leading to numerous surface reactions [161]. Reported effects include enhanced **roughness** [162], improved **wettability** by the matrix[163], and enhanced **hydrophobicity** [164]. However, **long exposures** can severely **damage** the fiber microstructure, making control of processing conditions crucial. In their study, Gibeop *et al.* showed that plasma treatment of jute fibers significantly improved their adhesion with a PLA matrix, leading to notable increases in tensile (28%), flexural (20%), and Young's modulus (17%) values compared to untreated fibers. The enhanced interfacial bonding was confirmed through micro-droplet tests and SEM analysis, highlighting plasma treatment as an effective, eco-friendly modification method [163].

**High energy radiations** including $\gamma$-rays, e-beams or X-rays have also been used to modify lignocellulosic material. The energy brought by these radiations generates highly reactive intermediary species (mostly ions and free radicals), which initiate reactions at the surface such as break and rearrangement of some chemical bonds, ablation, grafting or crosslinking. Although low radiation doses are generally sufficient to achieve desired modifications, **prolonged irradiations** lead to in depth polymeric chain scissions and accumulation of free radicals at the surface [161].

**Ultrasound treatment** method consists of using sound waves with frequency over 20 kHz [161]. The vibrations promote **saccharides depolymerization** [155]. This treatment is widely applied in pulp industry for debarking, defibration, pulping, bleaching, etc [154]. Ultrasounds were reported to increase the **fiber wall porosity** and inducing changes in the fiber morphology with partial defibrillation when secondary wall layer is exposed, with treatment's effects depending on power and duration. In a study on bamboo fiber-reinforced PLA composites, ultrasonic welding was used to fabricate strong lap joints. Tensile tests showed that the maximum load was achieved at a welding time of 3000 ms, holding time of 9000 ms, and welding pressure of 3 bars. The results also indicated that increasing the welding time beyond 3000 ms led to a decrease in tensile strength, with an 18.4 % reduction observed at 9000 ms [165].

Despite their high energy input, physical treatments are limited to **surface modification** since they do not deeply penetrate fibers. These methods are generally safer than chemical

methods and offer high flexibility. However, they are **energy intensive** methods and their cost may limit large-scale application for the modification of lignocellulosic fibers.

♦ Biological pretreatment

Biological methods use biological agents such as **fungi, enzymes, and bacteria** to modify the surface properties of natural fibers. Their main effects include **separating fibers** from non-fibrous components, producing **cleaner fiber surfaces**, and improving overall **fiber appearance.** As evocated earlier, lignocellulosic material is a complex mix of components composed primarily of cellulose, hemicellulose, lignin, and pectin. On the other hand, enzymatic and microbiocidal materials are very specific and exclusive. Because enzymes and microorganisms are typically **highly specific** in their activity, the complete destructuration of such complex biomass requires a consortium of enzymes. At least four groups of enzymes have been investigated: **cellulases** which are used to hydrolyze the cellulosic substrate to glucose monomers, **hemicellulases** that act similarly on hemicellulose through common ß-1,4 glycosidic, ligninolytic enzymes which oxidize the phenylpropanoid linkages in lignin, and pectinases which depolymerize and de-esterify pectin.

For enzymatic treatment to occur, enzymes must come into direct contact with substrates. This process involves the enzyme diffusing through physical barriers like lignin, adhering to the substrate's surface, and facilitating the hydrolysis reaction. These treatments primarily degrade the **surrounding non-cellulosic** polymer, resulting in **higher cellulose** content with **increased surface roughness**. As a result, the available surface for interfacial adhesion with the matrix is improved. Some studies have reported enhanced **mechanical performance** of the composites although the intrinsic mechanical properties of enzymatically treated fibers were reduced [166,167]. In a study on hemp fiber-PP composites, enzymatic treatment of hemp fibers with pectinase has been shown to improve fiber-matrix interaction in polypropylene composites. Although the treatment reduced the fiber **cross-sectional area** and tensile strength of individual fibers, it led to **better dispersion** and separation of fibers within the PP matrix. As a result, composites reinforced with pectinase-treated fibers exhibited increased tensile and flexural strength, as well as higher moduli, particularly when maleic anhydride grafted PP was used as a compatibilizer [166].

Compared with chemical treatments, biological approaches have **no harmful effects** and are not energy intensive like physical methods. However, the processing rates are **low**, and the treatment require a lot of space to grow and use enzymes and a **strict control** of growth conditions. Moreover, some microorganisms are not always highly selective and may attack

cellulose in addition to hemicellulose and lignin. Enzymatic treatment is further limited by biomass characteristics such as **lignin content** which strongly restricts the action of hemicellulolytic enzymes probably due to the number of ester linkages between lignin and carbohydrates. Furthermore, **particles size** could be a limiting factor as it was shown that the mechanical reduction of particle size facilitates the enzymatic hydrolysis of different feedstock. Taken together, these limitations contribute to the **low economic viability** of enzymatic treatments and to the high price of enzymes.

♦ Chemical treatment

Chemical treatment methods use chemical reagents to reduce the natural fibers hydrophilic properties and consequently improve their compatibility with the hydrophobic polymer matrices. Such surface modifications strategies introduce new functional groups on the fiber surface, facilitating chemical coupling with matrices. These treatments are commonly used to remove the **wax** and **lignin** from the surface, thereby improving the mechanical interlocking while also providing bifunctional molecules that bridge the hydrophilic nature of lignocellulosic fiber with the hydrophobic plastic matrix.

**Chemical modification** of natural fibers is recognized as one of the **most effective** methods for improving the fiber-matrix interfacial adhesion. It involves a chemical reaction between some reactive groups of lignocellulosic substrates and a specific chemical reagent, often forming covalent bonds. The **hydroxyl groups** located in hemicellulose, lignin and amorphous cellulose are the main reactions sites, since the hydroxyl groups in crystalline regions (highly ordered structure of cellulose fibrils) are densely packed and less accessible to chemical reagents [168]. In literature, a wide range of chemicals has been investigated including peroxide, silane, sodium hydroxide, calcium hydroxide, organic and inorganic acids, anhydrides and acrylic monomers.

**Peroxide treatment** relies on the breakage of the divalent ion bond O-O generating highly reactive **free radicals**. These radicals can graft onto cellulose molecules by bonding with the hydrogen groups and polymer matrix [148].

**Acetylation** of plant fibers is an esterification method implying the acetyl functional group CH3COO-. The main principle of the reaction is to **substitute** hydrophilic hydroxyl groups (OH) of the cell wall with **acetyl group** from an acetic anhydride. This renders the surface more **hydrophobic**. Acetylation of flax fibers has been shown to improve fiber surface morphology and moisture resistance, enhancing fiber-matrix adhesion in polypropylene composites. Composites with 30 %(m/m) modified flax fibers exhibited increased tensile and flexural

strengths, particularly at an optimal degree of acetylation (18 %), while the addition of maleated polypropylene further improved these mechanical properties by 20-35 %. However, Charpy impact strength decreased with higher degrees of acetylation, indicating a trade-off between stiffness and toughness [168].

**Silane** coupling agents bear two reactive groups, one end of silane agent with alkoxysilane which **bonds with hydroxyl groups** at fiber surface, whereas the other end interacts with the polymer matrix, creating a molecular bridge. Silane-coupling modification of stone groundwood (SGW) pulp has been shown to enhance fiber-matrix adhesion in PLA-based biocomposites. Incorporation of 20-30 %(m/m) SGW, partially modified with (3-glycidyloxypropyl)trimethoxysilane (GPS), led to significant improvements in tensile strength (up to 27 %) and thermo-mechanical properties. Optimal GPS contents of 5-7 %(m/m) provided the best performance by improving interface bonding and processability, demonstrating that chemical fiber modification can bring PLA-based biocomposites to properties comparable with conventional polypropylene composites [169].

The **maleic anhydride** treatment reduces fiber **hydrophilicity** by reaction with hydroxyl groups. Moreover, it can be grafted to plastic polymers forming **C-C bonds** that strengthen fiber-matrix compatibility [170]. Whereas this treatment is more a matrix treatment, it has been shown earlier that maleic anhydride is often associated with a fiber treatment [166,168].

The objective of **alkaline treatment** is to remove **hemicellulose and lignin** from the cell walls of plant fibers while reducing the number of hydrophilic hydroxyl groups. This process increases fiber surface **roughness** and disrupts the **hydroxyl groups** in the fiber network. Structural rearrangements occur in crystalline cellulose, leading to the formation of amorphous regions [171]. Among the various chemical treatments, alkaline treatment is one of the most **widely applied** and **effective** approaches. The following section therefore focuses on alkaline treatment and its role in improving the performance of natural fiber composites.

The overall effects of chemical treatments on the fiber include **cleaner** fiber surface, reduced moisture absorption, increased surface roughness, enhanced **interfacial adhesion**, and improved **fiber strength**. Their advantages are ease of process, applicability across diverse systems, industrial scalability. It is also the most commonly used method because of the wide availability of chemical reagents. However, drawbacks include the use of hazardous chemicals with handling and disposal issues, potential health and safety risks, and added costs in composite production.

*4.2.3. Alkaline treatment*

Among chemical treatments, alkaline treatment of fibers has proven to be the most efficient methods [148,155,172]. Often referred to as **mercerization**, it is widely seen as the chemical treatment method of choice because of its combination of effectiveness and low cost. This treatment is usually performed using **NaOH**. Soaking in NaOH aqueous solution breaks fibres bundles and reduces crystallinity by converting densely packed cellulose into more amorphous regions. The key modification is the disruption of hydrogen bonds within the network structure. During the treatment, the hydroxyl groups (OH) are **cleaved** and react with water leaving the ionized reactive molecules to form alkoxide with NaOH. As a result, it takes out a certain portion of hemicelluloses, lignin, proteins, pectin, wax, and oil covering material [143,146].

Alkali treatment effectively **cleans** the fibers surface of impurities, thereby reducing moisture absorption by removing the coating of -OH groups in the fiber. The **waxy layer** which contributes towards ineffective fiber bonding and poor surface wetting, is removed [173]. After alkali treatment, surfaces of the fibers become rougher which results in a decrease in diameter leading to a higher **aspect ratio**. The removal of hemicellulose during the treatment breaks down the tightly packed alignments of the fibers into **smaller fibrils**. Together, these modifications increase the effective **surface area** available for matrix contact and penetration into the fiber cells and promotes better interfacial adhesion in composites.

The **concentration** of NaOH, treatment **time** and **temperature** are critical parameters to achieve optimal effectiveness in fiber mercerization [174]. Excessively high alkali concentration may cause a too **severe elimination** of covering materials from the cellulose surface and delignify the fibre extremely, which negatively affect their mechanical strength [146,175–177]. For this reason, researchers investigated a wide range of values for each parameter (time, temperature and NaOH concentration). Reported values in the literature include the concentrations of NaOH between **0.5 and 30 %**, temperatures from **room temperature to 100 °C** and treatment durations ranging from **1 h to 24 h**. Table 1.6 shows some examples of the use of natural fibers subjected to the chemical modification by mercerization with aqueous NaOH solution and their effects.

*Table 1.6: Alkaline treatments used for modifications of natural fibers in polymer composites.*

| Type of natural fiber | Polymer matrix | Specific conditions | Main results | Ref |
|---|---|---|---|---|
| Bamboo fiber | Polyester resin | 1, 3, 5% NaOH 24h, room temperature | Interfacial shear strength was improved with higher NaOH concentrations | [178] |
| Pineapple leaf fibers | Polyester resin | Fibers were dewaxed then treated with 5, 10% NaOH, 1h at 30 °C | All tensile, flexural, and impact strengths of the composites were improved compared to the untreated one. 5% NaOH was found to promote better mechanical properties than 10% NaOH. | [177] |
| Rice husk | PP | 1M NaOH 80°C 4h | Treated fibers showed improved interlocking and possible aggregation due to shorter fiber lengths. | [179] |
| Kenaf fibers | PLA | 60 °C 4h | Alkali treated fibers exhibited a rough surface which improved compatibility with PLA traduced by a reduced number of voids and gap between kenaf and PLA, most of the treated fiber were embedded in the matrix compared to untreated which showed pull-out. | [180] |
| Alfa fiber | PP | 10% NaOH 24h at room temperature | Alkali treatment enhanced the tensile properties compared to untreated material about 16% for tensile strength. The treatment promoted string interfacial bond between fiber and matrix. Degradation caused by moisture uptake were less important for treated material. | [181] |
| Walnut shell | PLA | 2% NaOH 12h at room temperature, 7.5% NaOH 90min at 100 °C | Alkali treatment improved adhesion between filler and PLA matrix, tensile strength was improved for treated samples. | [182] |
| Sisal fibers | Rubber | 0.5, 1, 2, 4, 10% NaOH, 1h at room temperature | Maximum tensile strength of composite resulted from the 4% NaOH treatment | [183] |

An important point in evaluating the effectiveness of a treatment is to **characterize** both the treated fibers and the composites made from them.

Fourier transform infrared spectroscopy (**FTIR**) is a useful technique for analyzing the surface of natural fiber and to assess chemical modifications. When comparing untreated fibres with alkali-treated fibres, changes in absorbance bands are typically observed: several **characteristics peaks** present in untreated fibers disappear after treatment, reflecting the removal of cementing substances like hemicellulose, lignin, pectin and moisture. For instance, the disappearing of peaks in the range of 1735 $cm^{-1}$ is commonly associated with the **removal of hemicellulose** [175,182]. Anuar *et al.* confirmed the **removal of lignin** from oil palm empty fruit bunches in the absence of 1740 $cm^{-1}$ and 1513 $cm^{-1}$ [184]. As an example, Figure 1.16 represents the FTIR spectra of untreated and alkali treated walnut shell which evidences the occurrence of the structural changes in lignocellulosic components.

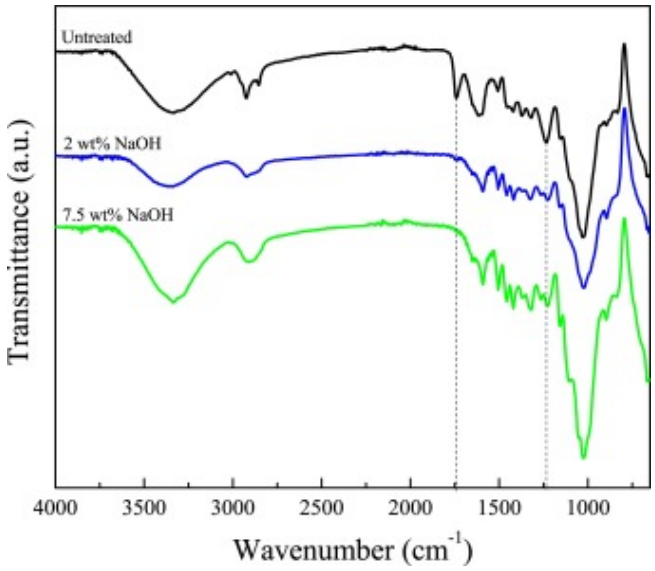


*Figure 1.16: FTIR spectra of untreated and alkali treated walnutshell flour from [182]*

**Scanning electron microscopy** is also frequently used to characterize the surface topography of the fibers and to evaluate the influence of the treatment. The alkali treated fibers were found to undergo fibrillation which is splitting of a single-fibre bundles into smaller fibrils which becomes more pronounced with increasing alkali concentration. For instance, Aydin et al. observed that the fibrillation effect on flax fibers intensified as the alkali concentration was increased to 30% [185]. Fibrillation can be observed from their SEM images on Figure 1.17 [185].

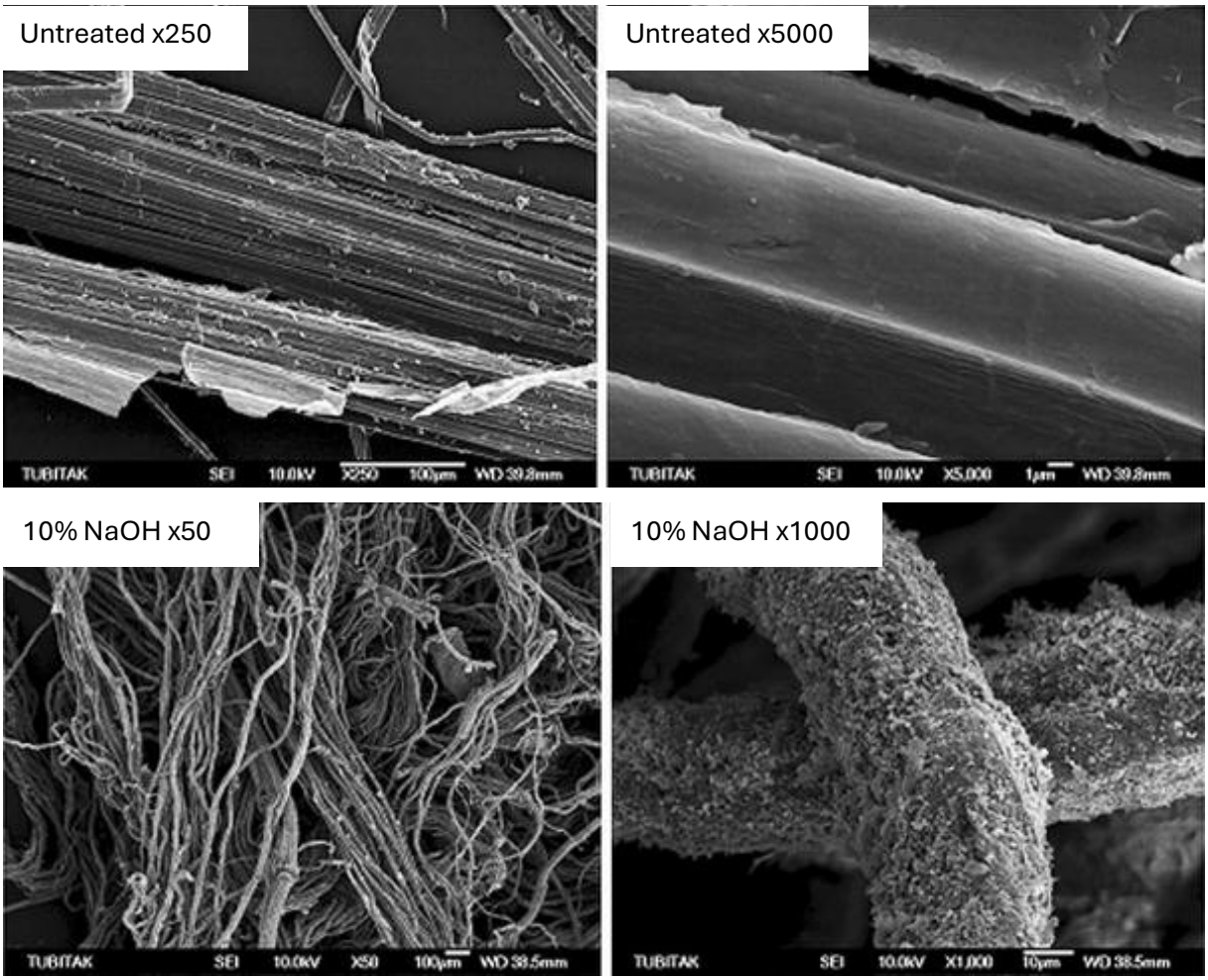


*Figure 1.17: Fibrillation effect, SEM images of untreated flax fiber and 10% NaOH treated flax fibers from [185]*

In conclusion, alkali treatment is one of the most **effective** and **widely** used methods for modifying natural fibers. It removes impurities, disrupts hydrogen bonding, and induces fibrillation, thereby increasing surface roughness, aspect ratio, and reactivity. These changes improve **fiber-matrix adhesion** and **stress transfer**, making the treatment both simple and cost-effective. However, because the chemical composition of natural fibers varies considerably, it is essential to optimize treatment conditions for each new fiber type.

*4.2.4. The case of BSG*

As previously discussed, BSG has received **limited attention** as a reinforcement in polymer composites, therefore studies addressing treatments to improve its interfacial adhesion with matrices remain limited. However, within the context of **biorefinery** with an objective of extracting its compounds, BSG has been the subject of various extraction strategies. From the

literature, **three strategies** have been particularly relevant to our study: the extraction of cellulose to recover and use it, the extraction of lignin to remove it, and the extraction of hemicellulose to remove it as well.

To **recover nano-cellulose**, Mishra *et al.* reported a multi-stage process involving alkali treatments and bleaching, yielding nanosized fibers with an average diameter of 4.6 nm, as observed via atomic force microscopy. A first, milder alkali treatment, **4 % NaOH, at 60 °C for 60 min**, followed by a bleaching step using sodium chlorite and sodium bisulphite which removed protein-based components and partially delignified the material, and a second, stronger alkali treatment, **17.5 % NaOH at room temperature for 8 h**, completed lignin removal. Thermo-gravimetric Analysis (TGA) and SEM were performed to evaluate the modification at each step [171]. Similarly, performed one step of alkaline treatment, **2 % NaOH for 2h at 90 °C**, followed by a bleaching step in order to extract cellulose. Chemical composition of BSG after different stages of the treatment revealed a reduction of the hemicellulose and lignin contents from 25.78 % to 17.09 % and from 30.48 % to 11.85 %, respectively, after alkali treatment. These contents decreased to 5.97 % and 3.23 %, respectively, following bleaching treatments [186].

The main objective of pulping process is to **remove lignin** from the cellulose fibers. In this way, Mussatto *et al.* investigated the optimum operating conditions for brewer's spent grain soda pulping. They studied only the removal of lignin as they worked on pretreated BGS material where hemicellulose was removed using dilute sulfuric acid. They evaluated the effects of soda concentration (**1-2 %**), temperature (**80-120 °C**), and pulping time (**30-90 min**) on the resulting pulp cellulose and lignin content of the pulp. They identified optimal conditions which were **2 % soda, 120 °C, 90 min** to yield a pulp with 72.1 % cellulose and only **10.4 % residual lignin** [187].

In addition to cellulose and lignin, **hemicellulosic arabinoxylans** have been extracted from BSG. Moreirinha *et al.* extracted hemicelluloses from BSG using **0.5 M KOH** solution whereas Reis *et al.* used a **3 M KOH** solution to extract hemicelluloses from BSG, they reported that the size of BSG is an important parameter to control the extraction as each size of sieving resulted in different arabinoxylans structures [188,189].

Although direct chemical modifications of BSG for composite application are rare, with only a few examples such as isocyanate treatment [190], the literature shows that alkaline treatments are consistently used. Strategies like fiber isolation, lignin recovery, and arabinoxylan extraction provide key insights into the chemical and structural changes needed to make BSG suitable for composite reinforcement, as we need to remove amorphous components.

#### *4.2.5. Conclusion*

The review of natural fiber treatment methods highlights that chemical treatments, particularly alkaline (NaOH) treatment, are among the **most effective** strategies to improve fiber-matrix compatibility. By removing surface impurities, reducing crystallinity, and inducing fibrillation, alkali treatment increases fiber surface roughness, aspect ratio, and hydrophobicity all of which contribute to enhanced interfacial adhesion and mechanical performance in composites. Compared with physical and biological approaches, alkaline treatment offers a combination of simplicity, cost-effectiveness, and industrial scalability. However, the **optimal treatment parameters** such as NaOH concentration, temperature, and treatment duration must be carefully adjusted depending on the type of fiber to prevent excessive degradation. Given these advantages, NaOH treatment represents a promising strategy to enhance the compatibility of brewer's spent grain (BSG) with polymer matrices, which will be the focus of **Chapter 6**.

## 5. Processing of particulate composites

### 5.1. Process steps

Plastic material transformation processes are essentially thermomechanical. To manufacture bio-based composites, the same techniques that are based on the conventional techniques for processing plastics are used. They include open and close mold techniques such as hand lay-up, extrusion, injection molding, compression molding, sheet mold compounding, etc. [191]. Considering that thermoplastics matrices must be processed above their **melting temperature**, special care must be taken to minimize the **exposure of lignocellulosic fillers**. Indeed, the fillers start to degrade in the range of **150-220 °C** [158] which generates volatiles and lower mechanical properties of the resulting composites. Consequently, polymer **with lower melting point** such as PLA, PP, PE, PBS are preferred to be used as matrix. Another challenge is that **high shear rates** involved in these processes are likely to reduce filler aspect and size. This is why using filler in powder shape can be advantageous depending on the process. Regarding composites, manufacturing techniques generally involve 6 steps: polymer fusion, compounding, cooling, composite fusion, composite manufacture, and cooling. **Compounding** consists of dispersing the filler in the molten polymer. The compounded material can then be **pressed or injected** into a shaped item or can be processed into pellets to be shaped later. In this part, only two methods of compounding are presented, one is a **batch** process very often found in laboratories (**internal mixing**) and the other is a **continuous** lab-scale and industrial scale

process (**extrusion**). One method of final shaping will be presented: **injection molding**. These three methods are the most utilized for thermoplastic processing.

### 5.2. Internal mixing

**Internal mixers** are extensively used in **academical** research to produce especially small polymer blends. Indeed, they allow scientists to work with lab quantities of thermoplastics, thermosets and elastomers, even of food products. The first batch mixer prototype was attributed to Fernley Banbury in the beginning of the 20th century [192]. This equipment consists of two parallel rotating screws in a **close chamber** with free volume. This volume varies from 5mL to 5L. Laboratory mixers can be operated according to several parameters such as the temperature, the rotor speed or time. The software device linked to the mixer records the temperature and the torque of the rotors against time. Usually, a batch mixing lasts until the components are fully mixed that is when there is no additional change in material properties. Visually, it is when the torque remains low and constant. Then, the resulting material can be pelletized to be shaped later. Figure 1.18 displays a typic scheme of internal mixer with the **torque versus time** curve recorded during an experiment.

Table 1.7 gathers different combinations of parameters used in internal mixing of thermoplastic composites seen in literature.

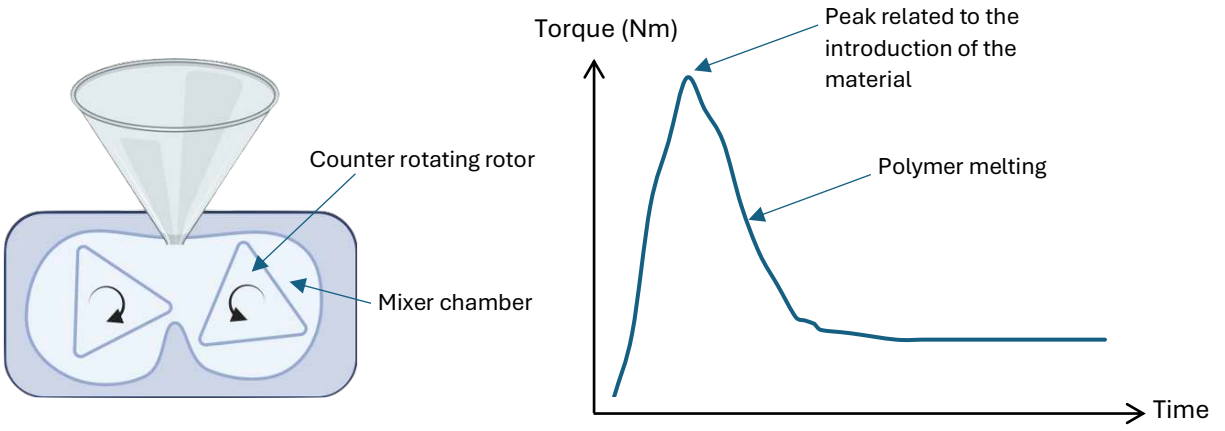


*Figure 1.18: Schematic representation of Internal mixer along with typical curve of torque against time when introducing a thermoplastic material.*

*Table 1.7: Different combinations of internal mixing parameters used in literature to process composites with PP and PLA matrices.*

| Matrix | Temperature (°C) | Speed (rpm) | Time (min) | Ref |
|---|---|---|---|---|
| PLA | 185 | 50 | 5 | [182] |
| PLA | 170 | 60 | 15 | [193] |
| PP | 180 | 50 | 8 | [57] |
| PP | 180 | 60 | 5 | [18] |
| PP | 180-190 | 90 | 10-15 | [179] |

### 5.3. Extrusion

As **extrusion** has been briefly presented in the filler preparation part in 4.1.4. . As shown in Figure 1.19, it consists of forcing melted polymer through a die inside a thermoregulated barrel. The material is transported using one or two screws. For enhanced mixing efficiency, **twin-screw extruders** are preferred over **single-screw extruders**. This preference is due to their ability to obtain a homogeneous distribution of fillers, which are effectively wetted within the thermoplastic melt [2]. Plastic pellets are introduced at the beginning of the screws when they are melted, the fillers are added to the screws and then the material is mixing inside the barrel. At the end of the extruder the composite material exits through a die and is immediately cooled into a cooling tank. It can also be pelletized for further processing thanks to die-face pelletizing.

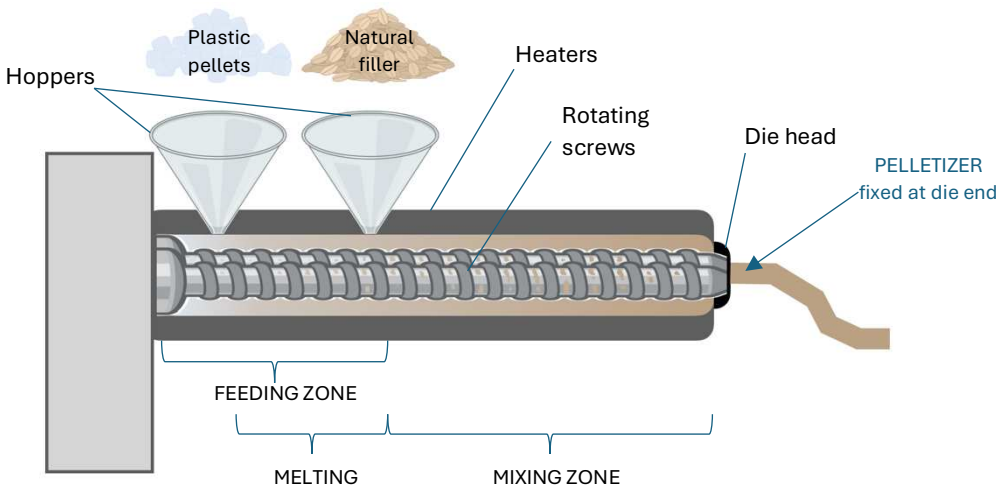


*Figure 1.19: Scheme of a twin-screw extruder used as compounder for bio-based composites.*

In the composites sector, numerous studies have investigated extrusion using different screw profiles, screw speeds, and temperature settings, resulting in a wide spectrum of experimental conditions for composite manufacturing. Since natural fillers are sensitive to thermal degradation, processing temperatures must be adjusted in accordance with their thermal stability [194]. Hence, for PLA composites, extrusion temperatures are between 175 and 200 °C [62,195,196]. For PP which presents a slightly higher melting temperature, extrusion temperature is set between 170 and 215 °C [194,196]. Screw rotation may vary from 40 to 300 rpm leading to soft or more severe processes [194,196]. However, according to Cisneros *et al.*, too high screw speed could trap some air in the material resulting in bad material properties [197].

### 5.4. Injection molding

This process is the most widely used molding method in the industry. Using **injection molding**, it is possible to obtain complex geometric items at high production rate [2]. Injection is particularly suitable for **particle reinforced composites** since the **nozzle** does not allow long fibers transport. The injection press is divided into three sections including injection unit, mold, and ejection unit. The injection unit contains a heated screw barrel which provides heat to melt the material before injection while the screw carries and compress the material. It allows a precise control of the **pressure** and **speed of injection** and the **holding pressure**. The mold has the product final shape; it can be cooled or heated. Finally, the ejectors permit to eject the final product outside the mold at the end of the process. Figure 1.20 displays the scheme of an injection press.

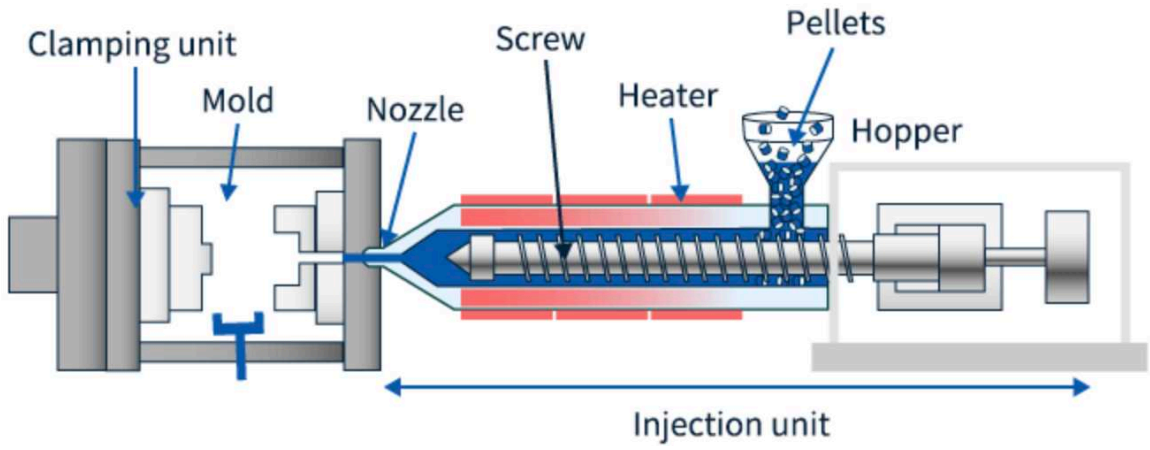


*Figure 1.20: Scheme of an injection molding machine extracted from [310]*

As for extrusion parameters, the injection molding parameters are highly variable. For instance, the injection pressure is set between **60 and 900 bar** [21,182,198,199], the mold temperature is usually set to room temperature but sometimes it is heated at **40-75 °C** [21,182,200].

### 5.5. Conclusion

To conclude, **processing thermoplastic** over thermoset presents several advantages such as process cycle time **very short** because there is no chemical reaction during processing, therefore thermoplastic composites production can reach high volume. Moreover, thermoplastics composites can be reshaped and reformed with heat and pressure which makes them easy to **recycle**. However, it is important to note that **inherent properties** of the final material are greatly influenced by **the production methods**. For example, Clemons studied the moisture sorption of wood plastic composite containing 50 % of wood flour processed by various methods. They observed that compression molded composites reached the equilibrium moisture of 4.1 % in 5 weeks, whereas extruded composites reached 3.9 % moisture content in 9 weeks and injection molded specimens barely reached a moisture content at equilibrium of 2 % [201]. This notably indicates that depending on the process, the amount of biomass at the surface varies. Given the wide range of possible processing parameters and techniques reported in the literature, it is clear that processing parameters can be tailored to enhance the blending of natural filler and thermoplastic matrix. With this in mind, next part focuses on particulates composites properties and characterization methods that allows to evaluate the interactions between filler and matrix.

## 6. Particulate composites properties: experiment and theory

### 6.1. Introduction

The properties of natural particle composites depend not only on processing techniques but also on other parameters, including **filler size**, filler **treatment** (as discussed in Section 4.2. ), and matrix type. Most importantly, they are influenced by the **filler content** and the **interactions** between the filler and the matrix. Accordingly, this section examines the **impact** of incorporating particulate lignocellulosic fillers on the rheological, thermal, mechanical, and water-related properties of composites.

## 6.2. Rheological behavior

### *6.2.1. Introduction*

In order to design and anticipate the behavior of the composite during processing, it is crucial to study the rheological properties of the composites. Understanding the flow behavior of the material not only enables a better control of the manufacture but also ensure consistency and good quality of the final product. **Rheology** is the study of the **deformation** and **flow** of materials when external forces are applied. An important aspect of polymer rheology is the study of how **viscoelastic behavior** changes with respect to **shear stress**, **molecular weight** and material **microstructure**. These parameters give insights into the behavior of the polymer during industrial processing. Polymer melts have a **dual behavior**, acting as **viscous liquids** by dissipating energy as heat when a stress is applied, and acting as **solids** by storing applied energy. Consequently, they are defined as viscoelastic materials. A common approach to characterize the rheological properties of a sample involves using a **two-plate** tool in which the upper plate applies a shear force with oscillatory movements on the sample inserted between the two plates (Figure 1.21). The lower plate remains stationary.

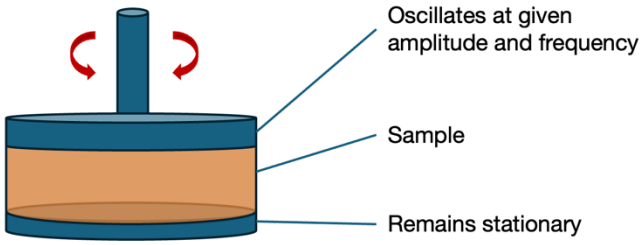


*Figure 1.21: Scheme of a plate-plate oscillatory rheometer*

While rotational rheology is limited to low shear rates, it offers a more fundamental insight into the **dispersion**, **structure**, and **interactions** among components. Rheology can be divided into two fields of study: linear and non-linear rheology. **Linear** rheology is used to study structure-properties relationship and the state of dispersion. To remain in the **linear viscoelastic region** (*LVR*), the moduli (storage modulus G' and loss modulus G") must not vary with the deformation amplitude, also known as strain, as shown in Figure 1.22.

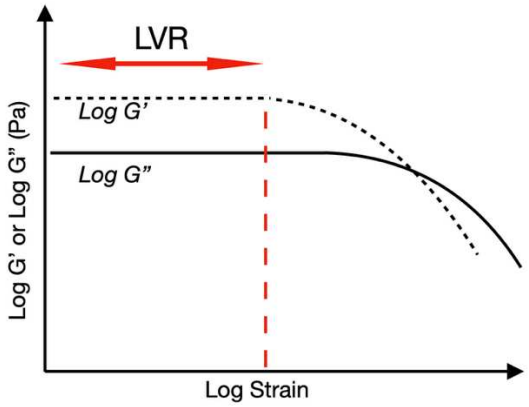


*Figure 1.22: Plot of Log G' and Log G" vs. Log strain of hypothetical polymer*

### *6.2.2. Rheological behavior: key factors*

Among many results possible to obtain, some key rheological quantities are commonly analyzed. The **elastic and viscous moduli** (*G', G"*) are of particular interest. Elastic modulus (*G'*) refers to the **solid-like** behavior whereas viscous modulus (*G"*) is related to the **liquid-like** behavior. *G'* is also called the storage modulus and G" is alternatively referred to as loss modulus. The material behavior is influenced by which of these two moduli **predominates** at a given temperature or shear rate. Hence, at low temperature, polymer material shows solid response with *G'* dominating over *G''*. Moreover, when the shear rate decreases, the deformation time increases allowing polymer chains to relax and dissipate the energy. Consequently, *G"* dominates over *G'* and the material shows a liquid-like behavior. These behaviors are displayed in Figure 1.23a. In addition, the **shear rates** experienced by the material during manufacture are directly linked to the **processing technique** used as shown in Figure 1.23b. It is therefore essential to understand the viscoelastic behavior of the composite under the shear rate conditions characteristic of the selected manufacturing process. Moreover, it should be noted that shear rate ranges span several orders of magnitude, which must be taken into account when evaluating a composite.

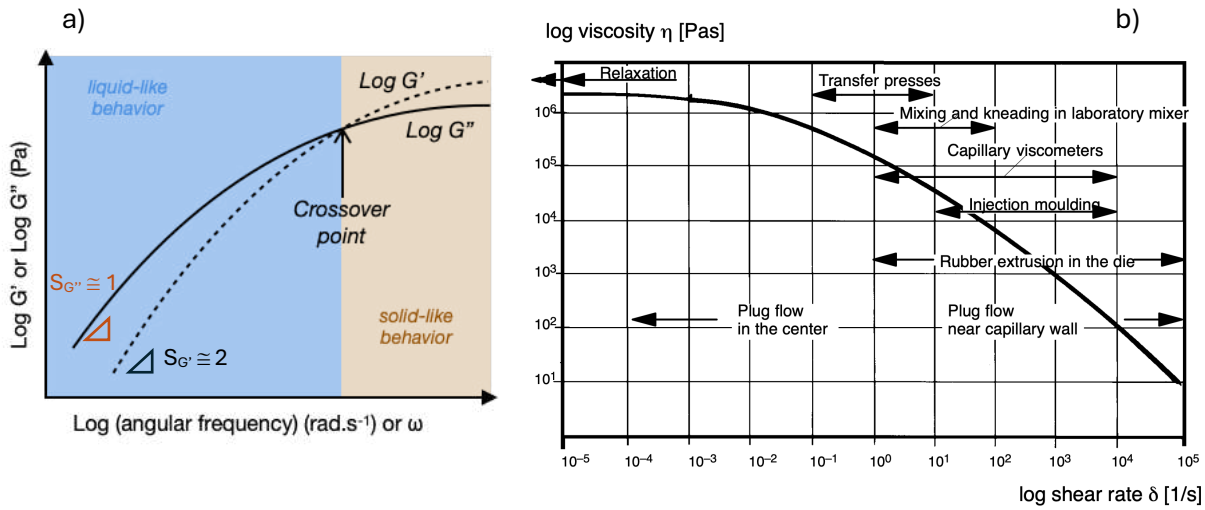


*Figure 1.23: (a) Log G' and Log G" vs. Log angular frequency with highlighted crossover point (b) Common shear rates occurring in different processes extracted from [311]*

Finally, **complex viscosity** is also a key parameter that reflects **dissipation rate** of the strain into flow. This property involves resistance to continuous deformation. When the polymer shows **Newtonian flow** behavior, the viscosity is independent of shear rate. However, non-Newtonian fluids present a viscosity depending on the shear rate. **Shear-thinning** polymers, also known as pseudoplastic liquids, display a decreasing viscosity with increasing shear rate whereas **shear-thickening** behavior is represented by a decrease of the viscosity with increasing shear rate. Figure 1.24 displays the viscosity response of these three types of polymer behavior against shear rate. No fewer than **5 parameters** might influence viscosity, they include temperature, pressure, shear rate, shear history, and electrical field. Therefore, when studying viscosity as function of one parameter, it is important that the others remain controlled.

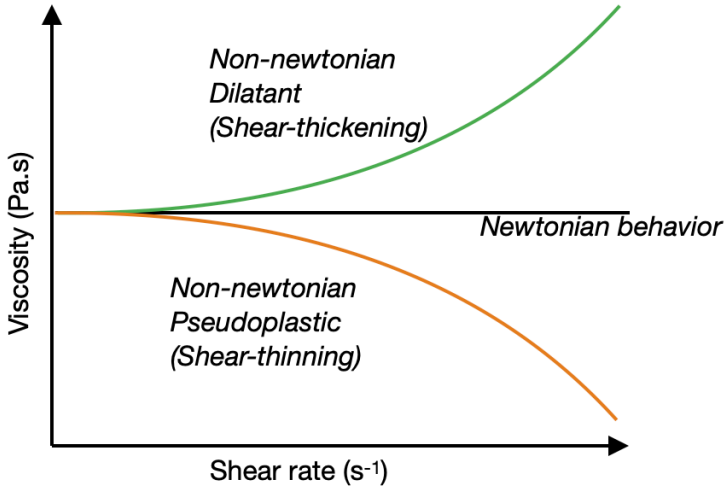


*Figure 1.24: Viscosity curves for ideally viscous, shear thinning and shear thickening flow behavior*

*6.2.3. General trends for particulate composites*

The incorporation of particles strongly affects the flow properties of the materials. Parameters such as **shape**, **size**, and **concentration of the filler** ($\Phi$) might influence the rheological behavior of the matrix. Particles are subjected to two types of interactions. Stability of the dispersion is controlled by the intensity of these interactions.

At **low concentration**, **matrix-particle** interactions dominate and restrict the mobility of the chains [202]. Hydrodynamic forces are applied by the fluid on the particles which are carried along at the same speed as the fluid. This provokes the rotation of the particle which disturbs the flow.

At **higher filler loadings**, particles are closely packed, the hydrodynamic forces are increased between fluids and particles. Moreover, **inter-particles interactions** of a non-hydrodynamic nature are observed within the system. These include Van der Waals interactions, electrical double layer interaction, and steric repulsions which can lead to particles agglomerations. The formation of **aggregates** through particle-particle adhesion results from collisions driven by Brownian motion.

At **low volume fractions**, the aggregates move freely through the fluid, and the suspension shows a **liquid-like behavior**. In contrast, above a **critical concentration** ($\Phi_m$) corresponding to the percolation threshold, clusters of particles become interconnected forming a network, and the system presents a **solid-like behavior**. If the repulsive barrier is

sufficiently high, shear forces can provide enough energy to break these aggregates, resulting in shear-thinning behavior. Friction between particles causes energy dissipation which traduces in a greater viscosity mixture [202,203]. With even higher particles content, the **maximum packing fraction** ($\Phi_m$) is approached. It is when the system reaches a limit where the particles can no longer move freely within the matrix. This significantly affects rheological properties of the suspension. It has been shown that when particles content approached $\Phi_m$, *G'* and *G"* became **independent** of shear rate ($\omega$). The maximum packing fraction depends on the geometry of the filler. For spherical unimodal size particles, the value of $\Phi_m$ is 0.64. For other type of particles, it can be defined as [204]:

$$\phi_m = \frac{Bulk\ density\ of\ particles}{True\ density\ of\ particles} \quad (1.3)$$

The **bulk density** is defined as the mass of a powder divided by its volume which includes the gaps between particles and the voids within them whereas **true density** does not include voids between particles and open pores of the particles.

It has been demonstrated that the higher the filler loading, the **shorter** the LVR is. In linear rheology, the incorporation of filler, most of the time, increases *G'* and *G"*. Indeed, adding solid filler would definitively increase the storage modulus reflecting the elasticity of the material. *G"* is also increased due to a more evident dissipation process with more **friction between particles**. A change in viscosity may be an effect of a structural organization of particles and polymer chains, formation of a filler network, interaction between particles or degradation [202]. Figure 1.25 displays the main effects of increasing filler content ($\Phi$) on wood fiber polymer composites rheological behavior. The crossover points (red dots, Figure 1.25 a) shift at lower frequencies as the wood content ($\phi$) increases. Complex viscosity curves (Figure 1.25 b) show the Newtonian-like plateau disappearing as the wood content $\phi$ increase (curves A, B, and C). Yield may appear at very high wood flour content (curve D).

Table 1.8 summarizes these effects.

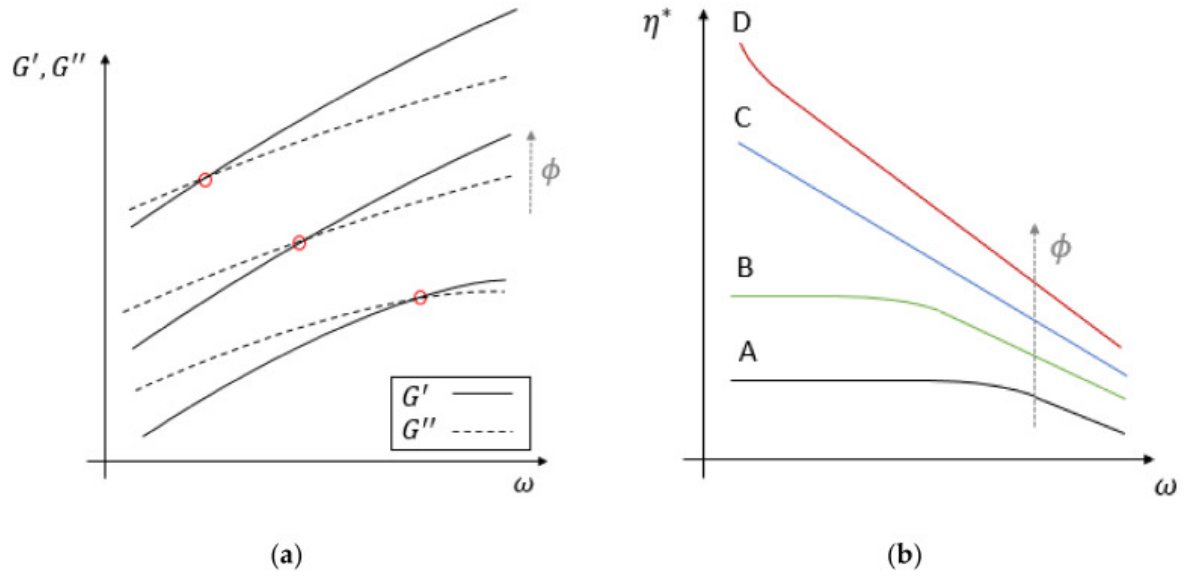


*Figure 1.25: (**a**) Typical dynamic moduli plots (G' solid line, G" dashed line) for increasing wood flour content ϕ.; (**b**) Typical complex viscosity plot at increasing wood flour content, extracted from [312]*

*Table 1.8: Summary of the effects of fillers on the rheology of thermoplastic composite systems.*

| General trends | Comments | Ref |
|---|---|---|
| $\Phi\uparrow \Rightarrow$ LVR$\downarrow$ | In the *LVR*, chains have time to relax. With the addition of particles, *LVR* is reduced because of the hindrance and interactions generated among polymer and fillers. | [202] |
| $\Phi\uparrow \Rightarrow$ G', G", $\eta^*\uparrow$ | Moduli and $\eta^*$ increase with the same shape when no interactions among fillers are observed. | [203] |
| $\Phi\uparrow \Rightarrow$ Crossover point $\downarrow$ | Samples highly filled reach the crossover point faster than less filled system. | [203] |
| $\Phi$ $\Phi_m \Rightarrow$ G', G" = insensitive to $\omega$ | Composites present a solid-like behavior. | [203] |
| $\Phi\uparrow \Rightarrow$ slope (G') < 1<br>$\Phi\uparrow \Rightarrow$ slope (G") < 2 | A low frequency plateau in *G'* reflects a percolated network with restricted relaxation due to physical interactions. This extra effect is due to network-type interactions. | [203] |

### 6.3. Thermal characteristics

Differential Scanning Calorimetry is widely used to characterize **thermal properties** of bio-based composites. It measures important thermoplastic properties such as melting temperature, glass transition temperature, crystallization rate and degree of crystallinity. The

thermal response of the composites is obtained by plotting the heat flow against temperature as seen in Figure 1.26.

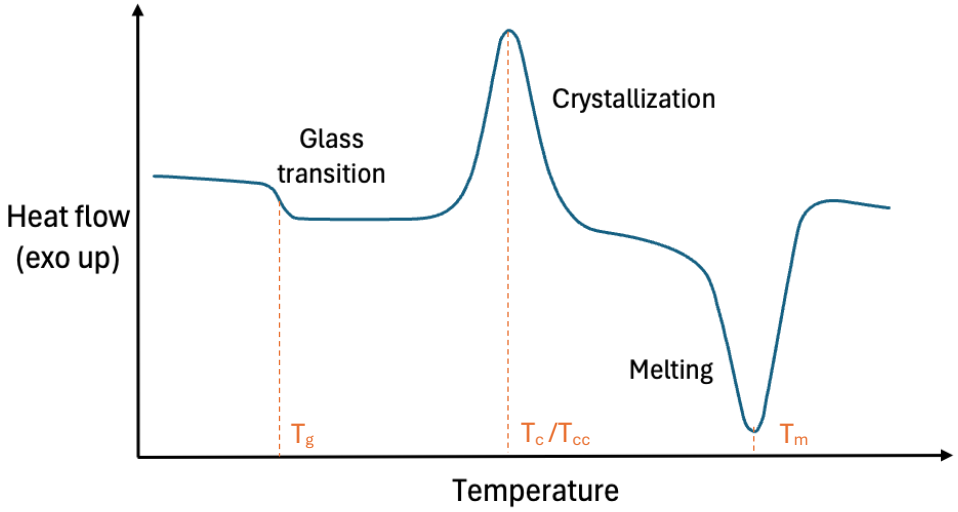


*Figure 1.26: Typical DSC curve of the different thermal events of a thermoplastic material.*

**Glass transition** temperature ($T_g$) is a crucial aspect of polymer composites. It indicates the temperature at which the polymer shifts from a **glassy brittle** state to a more **flexible and rubber-like** state due to changes in chain mobility. $T_g$ happens over a range of temperatures and is seen as a step on the DSC curve. It is not always easy to observe in DSC. In applications like **automotive** parts or urban furniture, where materials are subjected to varying temperatures during usage, understanding $T_g$ is very important. This knowledge ensures that the material maintains mechanically integrity and does not undergo undesirable changes in its physical properties.

**Crystallization** is an **exothermic** phenomenon that can occur during the cooling phase ($T_c$) or during heating phase, it is then called cold crystallization ($T_{cc}$). This phenomenon happens when polymer chains form an orderly pattern releasing energy. Crystallization can be impacted by the presence of fillers that either hinders the chain movement delaying the crystallization or provides nucleation sites which may induce crystallizations. When the filler plays the role of nucleating agent, crystallization tends to occur earlier [205,206].

**Melting** is an **endothermic** process where the heat is absorbed by the polymer to break its crystalline structure. Therefore, melting is seen in crystalline and semi-crystalline polymers only. It is common to see that the addition of filler shifts the melting temperature ($T_m$) to higher values. This is due to the thermal insulating effect of the filler which hinders heat conductivity. Therefore, the polymer matrix needs more heat to melt.

As most of crystalline polymers are not entirely crystalline, it is useful to calculate the **percentage of crystallinity** ($\chi c$). As seen earlier in section in PLA crystallinity section, crystallinity is a crucial parameter that affects storage modulus, mechanical properties, density and melting point. Crystallinity is obtained by calculating the normalized heat of melting and comparing it with a fully crystalline sample of the same polymer. When calculating for composites material, we only use the polymer weight fraction to calculate it. Also, when there is cold crystallization happening, its enthalpy is removed from the calculation. Hence, the equation (1.4) is written as followed:

$$\chi c = \frac{\Delta H_m - \Delta H_{cc}}{\Delta H_m^0} x \frac{100}{w} \qquad (1.4)$$

$\Delta H_{cc}$ is the enthalpy for the cold crystallisation in J/g,
$\Delta H_m$ is the enthalpy for melting transition in J/g,
$\Delta H^0_m$ is the enthalpy of melting for a 100 % crystalline sample in J/g,
w is the weight fraction of polymer in the sample.

It has been shown that when fillers provide **nucleation sites**, the crystallinity increases. However, when the filler volume is too high, it could **hinder** the development of polymer spherulites, resulting in a **reduction** of crystallinity.

Table 1.9 summarizes thermal properties for different PP and PLA composites filled with natural fibers. The arrows represent the effect of particles addition on matrix thermal transitions.

*Table 1.9: Summary of DSC thermal properties of polypropylene (PP) and polylactic acid (PLA) composites filled with various natural fibers.*

| Composite *Process* | Tg (°C) | | Tm (°C) | | χc (%) | | Refs |
|---|---|---|---|---|---|---|---|
| | Matrix | Composite | Matrix | Composite | Matrix | Composite | |
| **PLA**-coir (30%) *Compression molding* | 54.8 | ↓51.5 | 153.0 | ↓147.8 | 6.93 | ↑8.45 | [207] |
| **PLA**-olive pits (10%) *Injection molding* | 65.8 | ↓62.6 | 155.1 | ↓153.2 | 8.5 | ↑12.5 | [200] |
| **PLA**-hemp (30%) *Injection molding* | 58.8 | ≈58.6 | 149.6 | ≈150.3 | 5.7 | ↓4.1 | [199] |
| **PLA**-Cotton burr (40%) *Extrusion* | 56.8 | ↓52.3 | 156.4 | ↓145.2 | 1 | ↑8 | [46] |
| **PLA-**Chicken feather (10%) *Injection molding* | 58.7 | ↓57.5 | 163.4 | ↑166.7 | - | - | [208] |
| **PP**-rice husk (30%) *Injection molding* | - | - | 149.3 | ≈149.3 | 39.9 | ↑56.3 | [209] |
| **PP**-olive pits (30%) *Injection molding* | - | - | 149.3 | ≈149.3 | 39.9 | ↑56.0 | [209] |
| **PP-**sisal (3%) Injection molding | - | - | 165.9 | ↑167.7 | - | - | [60] |
| **PP**-rice husk (60%) *Injection molding* | - | - | - | - | 68.8 | ↓51.0 | [210] |
| **PP-**Wood flour (40%) *Injection molding* | - | | 164.4 | ≈165.2 | 41.6 | ↓36.2 | [211] |

## 6.4. Mechanical behavior: tensile test

### *6.4.1. Introduction*

The **tensile test** is of prior interest for industrial when designing a composite. The properties extracted from this test are crucial factors to select the right filler and loading for a selected application. Hence, to ensure bio-based composites viability for practical use, it is critical to investigate their mechanical behavior before they can be applied in specific fields. Two main mechanical properties are usually extracted from a tensile test: **Young's modulus** and **tensile**

**strength at yield** or **at break**. When a filler is incorporated into a polymer matrix, it should ideally maintain or improve its properties. If the filler is intended as a reinforcement, both the tensile modulus and tensile strength are expected to increase with its addition.

Tensile test can be divided into **4 stages**. The first one is represented by a **linear elastic deformation** of the material. It is during this stage that the Young's modulus or elastic modulus is calculated. It is defined as the **slope** of the linear part of the curves at very small deformations. The second one is characterized by a **plastic permanent deformation**, as the specimen elongates significantly, its section is reduced, and less load is needed to deform the specimen. Plastic deformation stage ends when the **highest point** is reached. Beyond this point, the specimen experiences the third stage characterized by a **localized necking**. At this stage, elongation occurs preferentially around a small region called the neck. In this region, there is a significant reduction of the cross-sectional area and the force required for further elongation decreases rapidly. The end of the tensile test is marked by the **rupture of the specimen**. These four stages are displayed in Figure 1.27.

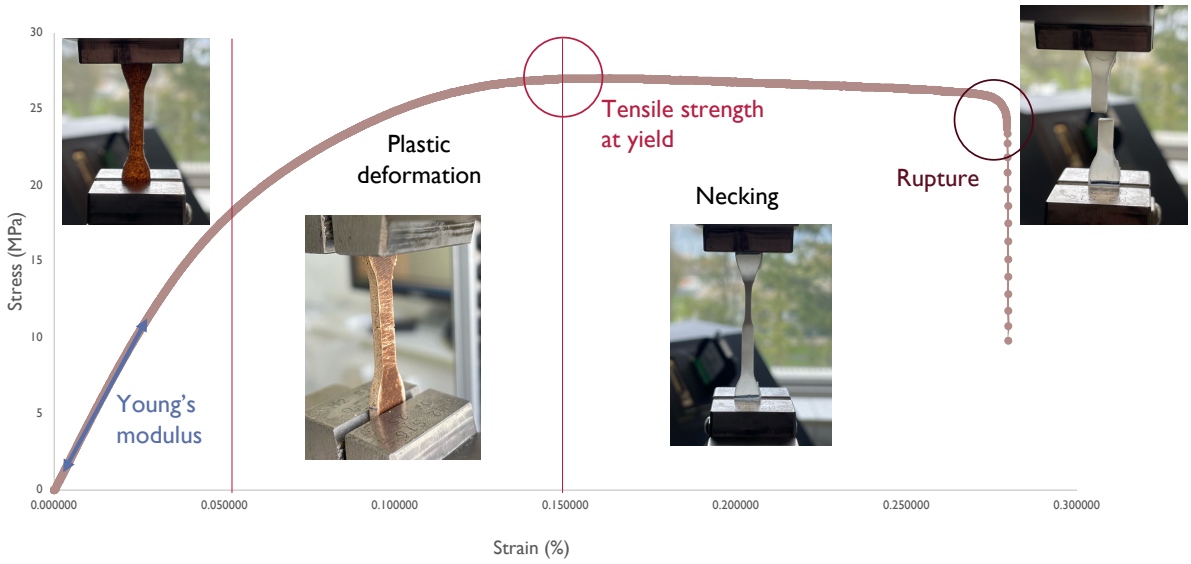


*Figure 1.27: Stress-Strain curve of a typical tensile test displaying four stages*

Many parameters may affect the mechanical properties of the composites, including the filler **length-weight ratio**, filler **orientation**, and interfacial **adhesion** between the matrix and fillers. Most importantly, filler content has a significant influence on both tensile strength and Young's modulus. Usually, the addition of natural filler is supposed to enhance Young's modulus by making the composites stiffer [18,73,212]. On the contrary, it is mostly observed that tensile strength decreases with the addition of natural filler due to **poor compatibility** between natural

filler and hydrophobic polymer matrix [46,212,213]. This trend is represented for rice husk polypropylene composites in Figure 1.28 reprinted from [212].

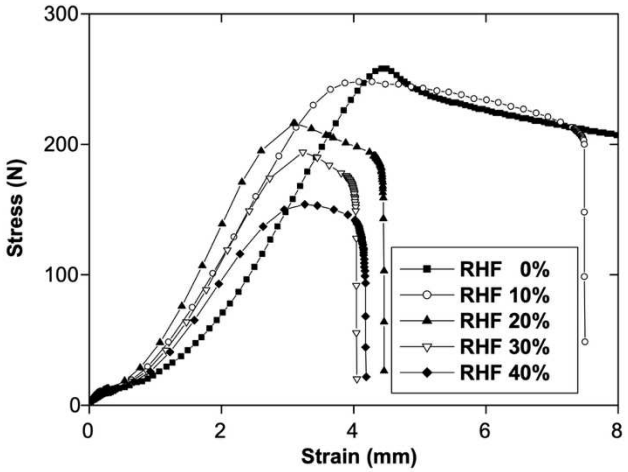


*Figure 1.28: Stress-strain curve of rice husks-PP composites at different filler content extracted from [212].*

Considering these parameters, numerous theories have been developed to **predict** the Young's modulus and tensile strength as a function of the filler volume fraction. **Micromechanics** is a subfield of mechanics that focuses on the behavior and interactions of materials at the microscopic scale, considering the influence of constituents such as particles on the overall mechanical properties and behavior of the material. This field seeks to elucidate deformation and damage mechanisms at the microstructural level using **theoretical models** and **experimental** techniques.

*6.4.2. Young's modulus*

The concept of Young's modulus, which describes the relative **stiffness of a material**, was first introduced by Thomas Young in the late 18$^{th}$ century. This parameter can be calculated using the slope of a strain-stress graph. A wide variety of equations for predicting the modulus have been developed over the years. Whereas most of the advances occurred in the 1960s and the 1970s, the earliest models were based on **Voigt** (1889) and **Reuss** (1929), who provided two of the most basic cases for a **biphasic material**: a parallel arrangement case where a uniform strain was assumed and a series arrangement case where stress was assumed to be uniform (Figure 1.29). These two models are also called, the **rule of mixture** and the **inverse rule of mixture**, respectively. Nowadays, Voigt's model (rule of mixture) is a widely applied in the biocomposites field to predict their tensile modulus.

In 1962, Hirsh **combined** both these equations and introduced a parameter (x) to represent the proportion of filler perfectly bonded (x=1) and the proportion poorly bonded (x=0) [214]. In 1964, Takayanagi also combined the Voigt and Reuss equations to propose a model in which part of the fillers follow the parallel model and some of them follow the series arrangement. The two parameters $\alpha$ and $\beta$ represent the proportions of particles in parallel and series states, respectively. The main problem is that $\alpha$ and $\beta$ are difficult to determine [214]. The same year, Counto took inspiration from Hirsh's model assuming that the particle and matrix are **perfectly bonded**, and that the height-width ratio of the particles is the same for the composite shape [215].

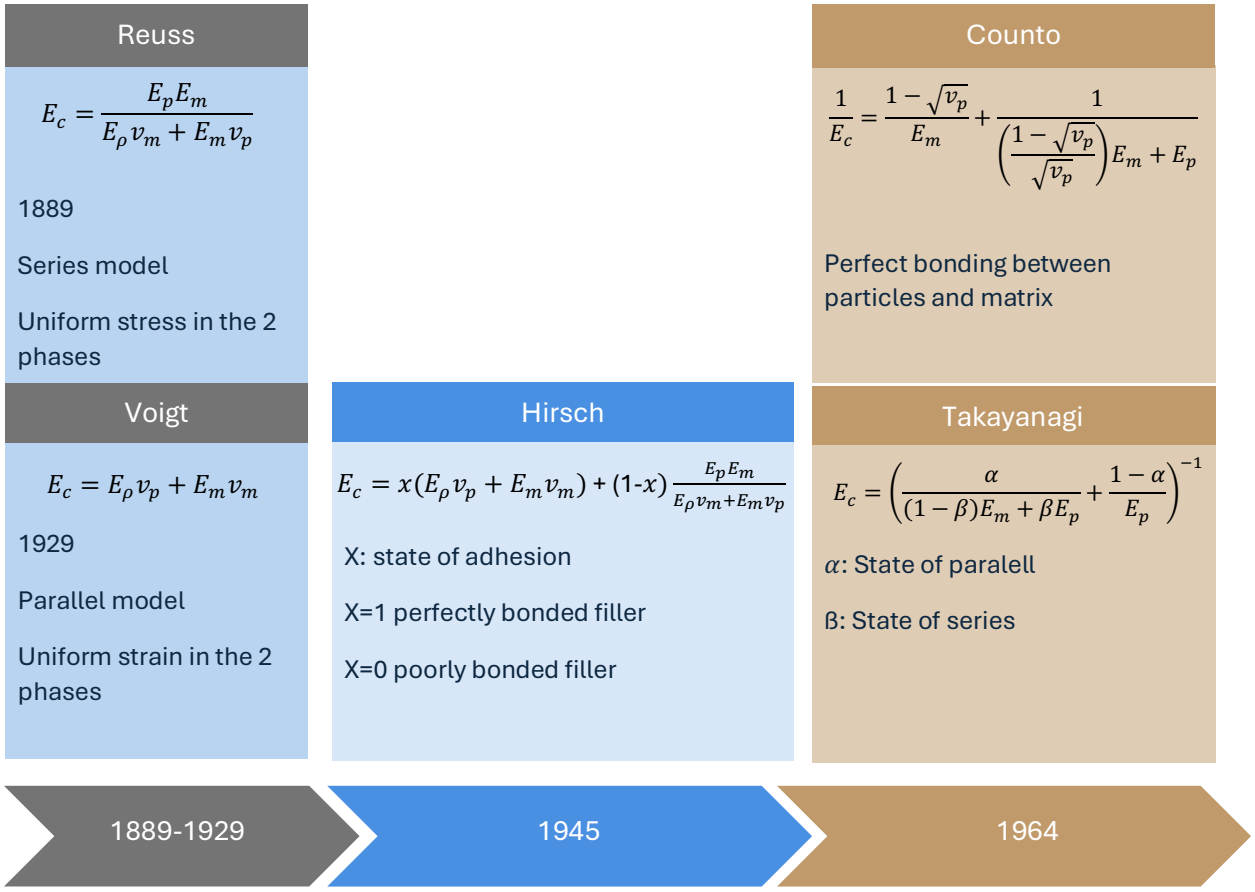


*Figure 1.29: Young's modulus prediction models derived from parallel and series models with Elastic modulus of composites ($E_c$), Elastic modulus of the matrix ($E_m$), Ekastic modulus of particles ($E_p$), Volume content of the matrix ($v_m$), and Volume content of the particles ($v_p$)*

Albert Einstein formulated a foundational theory in the early 20th century, which predicts the effects of fillers in a composite system. In his study, the model enabled the prediction of the **viscosity** of a filled elastomer (Figure 1.30). In 1945, Guth generalized Einstein's equation for **ellipsoidal filler particles** which demonstrate a greater increase in modulus compared to

spherical particles, as per the prediction [216]. Later, in 1951, Mooney modified Einstein's equation to consider the first-order interaction between particles at a **high-volume fraction**. His equation reduces to Einstein's equation at **low concentrations**. Mooney introduced parameter k to represent the **crowding effect**, based on the Kepler conjecture, which posits that the maximum volume fraction of densely packed spheres would be 0.74, and the maximum volume fraction of the densest packing of the spheres, which allows movement, would be 1.91. Hence, *k*, the crowding factor, must remain between these values [217]. Smallwood's research on rubber composites demonstrated that Einstein's equation could also be applied to determine the shear modulus of composites. The equation was verified under several assumptions: the filler particles were assumed to be **spherical**, the adhesion between the filler and matrix was **perfect**, the elongation was small, the filler was completely dispersed, the volume loading was small, and the filler was large enough to consider the molecular structure of the matrix to be negligible [218]. Therefore, Mooney's equation could also be applied to the tensile modulus. To date, only a few researchers have studied **non-spherical particles**. In 1959, Brodnyan introduced parameter p, referring to the axial ratio of ellipsoidal particles, to Mooney's equation. Hence, Brodnyan's equation reduces to Mooney's equation for *p*=1, which applies to spherical particles [219].

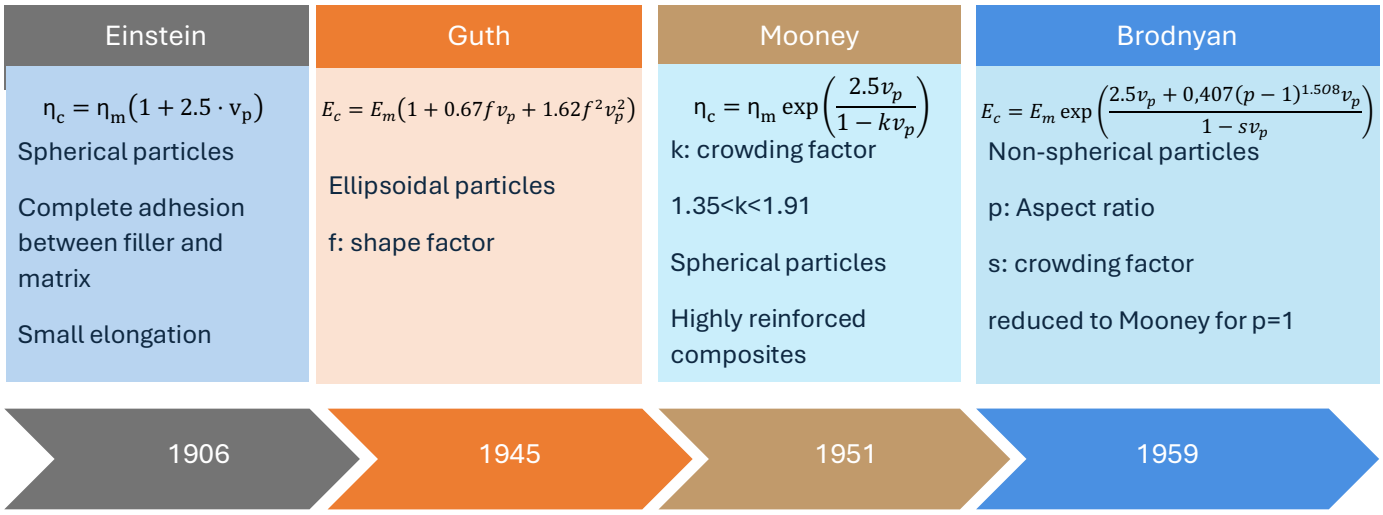


*Figure 1.30: Young's modulus prediction models derived from Einstein's model Shear modulus of composites ($\eta_c$), Shear modulus of the matrix ($\eta_m$), Elastic modulus of composite ($E_c$), Elastic modulus of matrix ($E_m$), and Volume content of the particles ($v_p$)*

More recently, Kerner employed a different approach by considering **spherical particles** as fillers that are perfectly bonded with the matrix and randomly distributed. He introduced the **Poisson ratio** of the matrix. The Poisson ratio influences the material's response to stress and is integral to the accurate calculation of the tensile modulus, which is a measure of a material's

stiffness or resistance to elastic deformation under tension [220] (Figure 1.31). More recent research conducted by Halpin and Tsai has primarily focused on the development and refinement of analytical models for predicting the mechanical properties of composite materials. Drawing upon Kerner's equation, the researchers proposed a new equation with modified parameters and coefficients to enhance the accuracy of predictions. This equation includes the **length-width ratio** of fibers and the **elastic modulus of the fibers** within $\eta$. The assumption underlying this equation is that the fibers are **perfectly aligned**, and for larger length-width ratios, the equation reduces to the parallel model discussed earlier. Subsequently, the work of Halpin and Tsai aimed to improve the predictive capabilities of the Halpin-Tsai equations for various types of composite materials [221]. By incorporating new analytical methods and considering factors such as porosity, particle shape, and interfacial effects, these studies have contributed to a more accurate and comprehensive understanding of composite behavior, which is crucial for material design and optimization. In 1970, Nielsen observed that the Halpin-Tsai equation failed to account for crucial elements, such as the **maximum packing fraction** ($\phi_m$) previously considered by Mooney and other researchers. To address this deficiency, Nielsen *et al.* developed a revised equation that extended the Halpin-Tsai equation by incorporating an additional parameter, $\phi_m$, which considers the maximum packing fraction [222]. In Nielsen's equation, the constants *A* accounts for the **geometry of the filler and Poisson's ratio** of the matrix and *B* takes into account the **relative moduli of filler and matrix**.

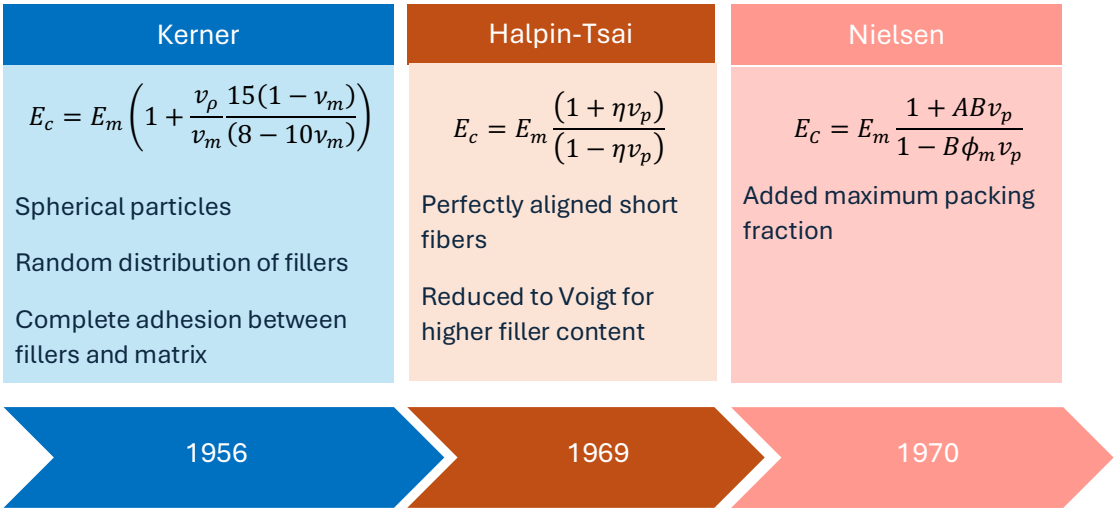


*Figure 1.31: More recent Young's modulus prediction models with Elastic modulus of composite ($E_c$), Elastic modulus of matrix ($E_m$), $\eta$ is Halpin-Tsai constant parameter, A and B being Nielsen constant parameters.*

Figure 1.32 shows some of the presented models used to predict Young's modulus for **HDPE-rice hulls** composites reprinted from [223]. Most models tend to overestimate the tensile

modulus, likely due to poor fibre–matrix adhesion. In composites with hydrophilic natural fibres and hydrophobic polymer matrices, interfacial slip reduces fibre stress transfer. Model accuracy could also be enhanced by accounting for fibre orientation, aspect ratio and distributions, as current assumptions of perfect alignment and uniform geometry oversimplify real conditions.

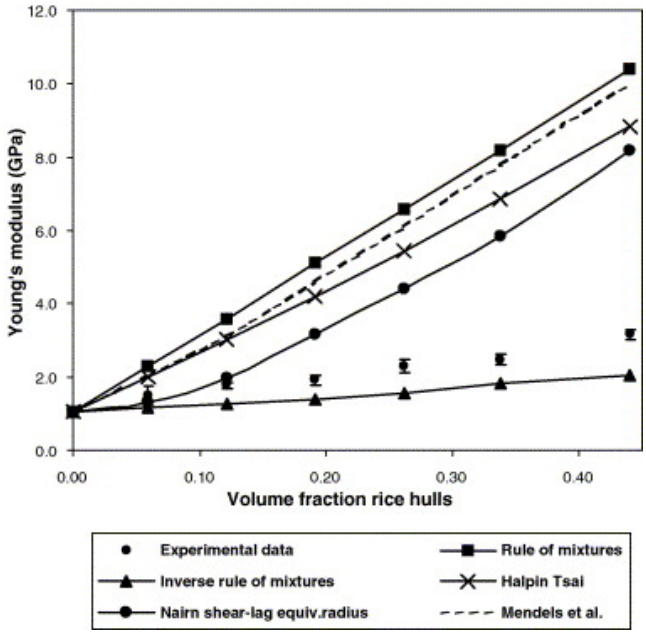


*Figure 1.32: Determination of HDPE composite modulus containing rice hulls. Using some of the presented models, extracted from [223]*

### *6.4.3. Tensile strength*

The **prediction of strength** in particle-reinforced composites is a multifaceted problem that is influenced by various factors, such as the mechanical properties of the constituent materials, particle size, volume fraction, and interfacial strength. The complexity arises from the stress fields generated within the composite, which are affected by the presence of particles and their interaction with the matrix material. For instance, the tensile strength of a particle-reinforced polymer composite is notably challenging to predict due to the complicated stress fields and the **significant impact of interfacial strength**, which is difficult to measure directly. Contradictory findings are evident in the literature, highlighting the nuanced relationship between particle content and mechanical properties. While some studies report an increase in certain mechanical properties with the addition of particles, others observe a decrease. According to Fu *et al.*, when the reinforcing effect is more prominent, the strength of the composite tends to be lower than that of the neat polymer, particularly when the weakening effect is more pronounced [224]. To simplify the estimation of the strength, many researchers assumed that there is **no stress transfer** nor bonding between the polymer and the particles.

One of the approaches for predicting the strength of a system involves assuming that the stress is distributed across the effective available area of the matrix due to the presence of the filler. Thus, the strength can be easily described by:

$$\sigma_c = \sigma_m(1 - \phi_p) \qquad (1.5)$$

$\sigma_c$: composite tensile strength,
$\sigma_m$: matrix tensile strength,
$\Phi_p$: particle volume fraction.

The presented model illustrates that the **tensile strength** exhibits a linear decrease as the **volume fraction** of particles increases. Drawing on Bueche's work on elongation of plastic, Nielsen predicted the stress-strain behavior of a filler polymer based on the filler concentration in the case of **no adhesion** between the filler and matrix. He introduced parameter S related to the weakness in the composite structure, with a maximum of 1 to represent no stress concentration. He highlighted that in the **absence of adhesion**, the particles cannot **bear any of the load** applied to the composite system, and thus, the matrix must carry the load entirely on its own [225]. Later, unlike Nielsen, Eilers-Van Dijk (EVD) worked with the assumption of **perfect adhesion** between filler and matrix. He developed a model to determine the viscosity of filler material, which can be utilized to forecast the strength of composite systems. At high filler ratio, Nielsen and Eilers-Van Dijk tend to strongly differ, indeed, **EVD's model** predicts an **increase of the tensile strength** for composites with a volume fraction of filler greater than 0.1 [225]. In 1971, Nicolais and Narkis conducted research to investigate the behavior of Styrene-Acrylonitrile glass bead composites in the glassy region. They created a simple model that demonstrated the relationship between the volume fraction and yield stress in the absence of adhesion. Nicolais and Narkis assumed that the filler was **uniformly distributed** and of **spherical shape**. Their findings revealed that the yield stress decreased substantially with an increase in bead concentration, and the yield strain also decreased with an increase in the volume fraction of filler, which is consistent with previous research on elastomeric PVC composites [226]. The three equations presented here are displayed in Table 1.10.

*Table 1.10: Tensile strength prediction models*

| Model | Equation | Nomenclature |
|---|---|---|
| Nielsen | $\sigma_c = \sigma_m \left(1 - \phi_p^{2/3}\right) S$ | $\sigma_c$: composite tensile strength<br>$\sigma_m$: matrix tensile strength<br>$\Phi_p$: particle volume fraction<br>S: stress concentration function<br>V: sedimentation vs true volume ratio of the filler<br>$\varepsilon$: elongation at break |
| Eilers-Van Dijk | $\sigma_c = \sigma_m \frac{\varepsilon_c}{\varepsilon_m}\left(1 + \frac{1{,}25\Phi_p}{1 - V\Phi_p}\right)^2$ | |
| Nicolais-Narkis | $\sigma_c = \sigma_m\left(1 - 1{,}21{\phi_p}^{2/3}\right)$ | |

*6.4.4. Conclusion*

In summary, the models discussed previously provide valuable insights into the impact of incorporating fillers within a polymer matrix. **Tensile strength** modeling gathers two distinct scenarios, either characterized by **perfect adhesion** or the complete absence of adhesion. The influence of filler shape and size on the prediction of tensile strength in composite systems is expected to be significant. These factors not only impact the surface of the interface, but also affect the state of the interface, which is challenging to measure.

To sum up, the general experimental and theoretical conclusions for composites are that Young's modulus and tensile strength both depend on the **shape of the fillers**, the **volume fraction** occupied by them, and the **interface** among components. Whereas **Young's modulus** is predicted to **increase with filler loading**, tensile strength is **negatively affected** by filler content usually due to **poor adhesion** between filler and matrix. Tensile strength is likely to increase when filler is chemically treated to improve interface. Aspect ratio and filler size and orientation can greatly influence the mechanical properties; therefore, these factors must remain under consideration. However, they are very difficult to evaluate in composites filled with lignocellulosic particles.

## 6.5. Water absorption

Besides having impressive properties, lignocellulosic fillers are **inherently hydrophilic** which makes them, as seen earlier, incompatible with hydrophobic polymer matrices. This results in lower filler dispersion, poor matrix-filler interfacial adhesion and moisture absorption which limits their end use applications. The abundance of **polar hydroxide groups** (-OH) in

cellulose and hemicellulose results in high moisture absorption. Cellulose has a high hydroxide groups-to-carbon ratio and only small quantity of -OH are exposed to water molecule due to crystalline structure of the cellulose. In contrast, hemicellulose being amorphous is more susceptible to water uptake. When water is absorbed by the lignocellulosic filler, it swells up due to water occupying the **microfibril network**. The absorbed water molecules can form a monolayer associated with the -OH groups or a multilayer with some water molecules not in contact with these groups [227]. The occupation of the hydrogen sites by water molecules leads to weakening the hydrogen bonds inside lignocellulosic material which decreases its stiffness [228]. This constitutes an undesired property since filler are likely to carry the load inside polymer matrix under mechanical stress.

In lignocellulosic filler reinforced composites, moisture absorption is driven by one main mechanism called **diffusion**. Understanding the effect of moisture uptake on natural filler composites is an important aspect for these materials to be used in a humid environment. Water molecules diffuse into the material breaking hydrogen bonds and creating **additional space** inside the lignocellulosic fibers. This creates swelling and softening [228]. **Swelling** is significantly larger in radial direction than in axial direction due to cellulose microfibrils direction that do not swell. This change in filler **structural integrity** might induce **micro-cracks** within the surrounding matrix. Then **capillary forces** transport water into gaps at the interface between fibers and polymer [229]. This is particularly emphasized when there is a **poor adhesion** and wetting of the matrix on the filler. In the end, swelling leads to **dilapidation** and **debonding** of the filler [227]. The different stages of moisture absorption in composites are displayed in Figure 1.33.




*Figure 1.33: Moisture absorption mechanism creating degradation of the interfacial adhesion and fiber-matrix debonding, grey rectangles represent the matrix.*

The hydrophilic nature of lignocellulosic filler makes that their addition to a composite increase the water absorption as shown on Figure 1.34.

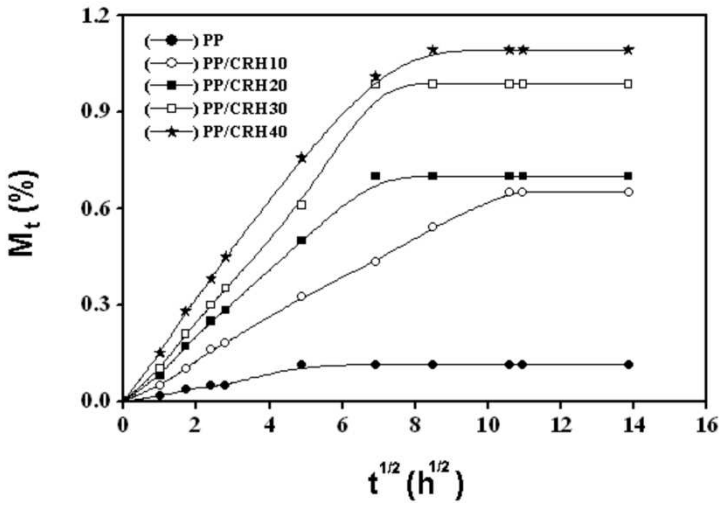


*Figure 1.34: Water absorption curves of rice husk-PP composites at different loadings of rice husks extracted from [313]*

## 7. Conclusion: objectives and challenges

This literature chapter has reviewed the state of art on biocomposites, with a particular focus on **polypropylene** and **polylactic acid** reinforced with particulate lignocellulosic fillers. Special attention was given to Brewer's spent grain, abundant agro-industrial by-product which is currently under-valorized and whose valorization would meet the goals of sustainable development.

Several key points emerge from this review. First, BSG represents a **low-cost**, **widely available** filler, but its **high moisture content** and **poor compatibility** with hydrophobic polymer matrices are particularly challenging. **Drying and particle size reduction** are critical pretreatment steps at laboratory scale, optimizing these operations for time and energy efficiency remains an open research question. Second, chemical modifications such as **alkali-treatment** represent a promising approach to improve filler-matrix adhesion. Although, the optimal treatment parameters are to be determined.

It has been discussed that the incorporation of lignocellulosic fillers such as BSG impact or alter the rheological, thermal, mechanical, and water related properties of composites in ways that depend strongly on filler morphology treatment, and matrix type. Although a variety of theoretical models exist to predict composite mechanical properties, their applicability to fillers such as BSG remains limited due to the **irregular nature of the particles** and the lack of data concerning their intrinsic properties, such as modulus.

Key challenges ahead include:

- Assessing the potential of BSG as a suitable filler for PP and PLA composites.
- Understanding and identifying the role of BSG in defining the composite performance.
- Developing a scalable drying and size reduction process for BSG.
- Understanding the influence of BSG particle morphology and surface on composite properties.
- Scaling up the entire composite development chain to unlock the commercial potential of BSG-based composites.
- Optimizing chemical treatments to enhance compatibility between BSG and PP and PLA matrices.

Altogether, this chapter draws the lines to understand the opportunities and challenges associated with incorporating BSG filler into PP and PLA based composites. Next chapter presents the **research strategy** designed to address the limitations identified and provides a detailed report of the materials, devices, and techniques employed in this work.

# CHAPTER 2:

## Material & methods

# RÉSUMÉ CHAPITRE 2

Ce chapitre est consacré à la description de la démarche expérimentale mise en œuvre dans le cadre de cette étude. Il présente d'abord les différentes méthodes de caractérisation utilisées pour évaluer les propriétés physiques, thermiques, mécaniques et morphologiques des biocomposites, ainsi que les interactions entre la charge et la matrice. Ces techniques incluent notamment la thermogravimétrie, la calorimétrie différentielle à balayage, la rhéologie dynamique, les essais de traction et la microscopie électronique à balayage. Ensuite, le chapitre détaille les protocoles de fabrication des différents matériaux, chapitre par chapitre, depuis la préparation des drêches de brasserie jusqu'à leur incorporation dans les matrices thermoplastiques de polypropylène (PP) et d'acide polylactique (PLA). Les étapes de séchage, de broyage, de mélange et d'injection y sont décrites, en précisant les paramètres de procédés retenus pour assurer la reproductibilité et la comparabilité des résultats. Ce chapitre expose l'organisation expérimentale du travail, structurée selon plusieurs axes de recherche visant à explorer l'effet de la nature du polymère, du traitement de la charge et des conditions de mise en œuvre sur les performances globales des biocomposites.

# Chapter 2 : Material and methods

## 1. Overview of the research strategy / study design

This chapter is essential for this PhD thesis research. It provides a detailed report of materials, devices and techniques employed in this work. The research strategy was designed to address the objectives and challenges identified in previous chapter and is structured into three interconnected parts, complemented by a fourth part which also contributes to meet these objectives and challenges. These parts are described in Figure 2.1.

The first part (Chapter 3) aims to explore the potential of BSG as a valuable filler in composite materials using two different thermoplastic polymer matrices: PP and PLA. This section is focused on material formulation and characterization to evaluate the compatibility and performance of BSG composites.

The second part (Chapter 4) addresses the issue of BSG perishability. To ensure its storage, processability, and to enable a broader range of sustainable material applications, a novel method of drying and grinding is developed and evaluated for efficiency.

The third part (Chapter 5) integrates knowledge from the first and second parts to develop improved composites materials. This is approached in two ways: first, by using dried and ground BSG from the second part (Chapter 4) with the methods of Chapter 3. Second, by investigating upscaled processing methods. The ultimate goal would be to meet both performance and sustainability requirements, aligning with the objective of sustainable innovation. This part also acts as an open window for further improvements, laying the groundwork for future research on process optimization and industrial applications.

Finally, the fourth and last part (Chapter 6) aims to address the compatibility issue between BSG and PP and PLA polymer matrices using alkali treatments. First, different treatment times and temperatures were investigated in order to determine the optimal conditions to enhance BSG suitability for composite applications. Then, the selected treatment parameters were applied to BSG, which was subsequently incorporated into PP and PLA composites.

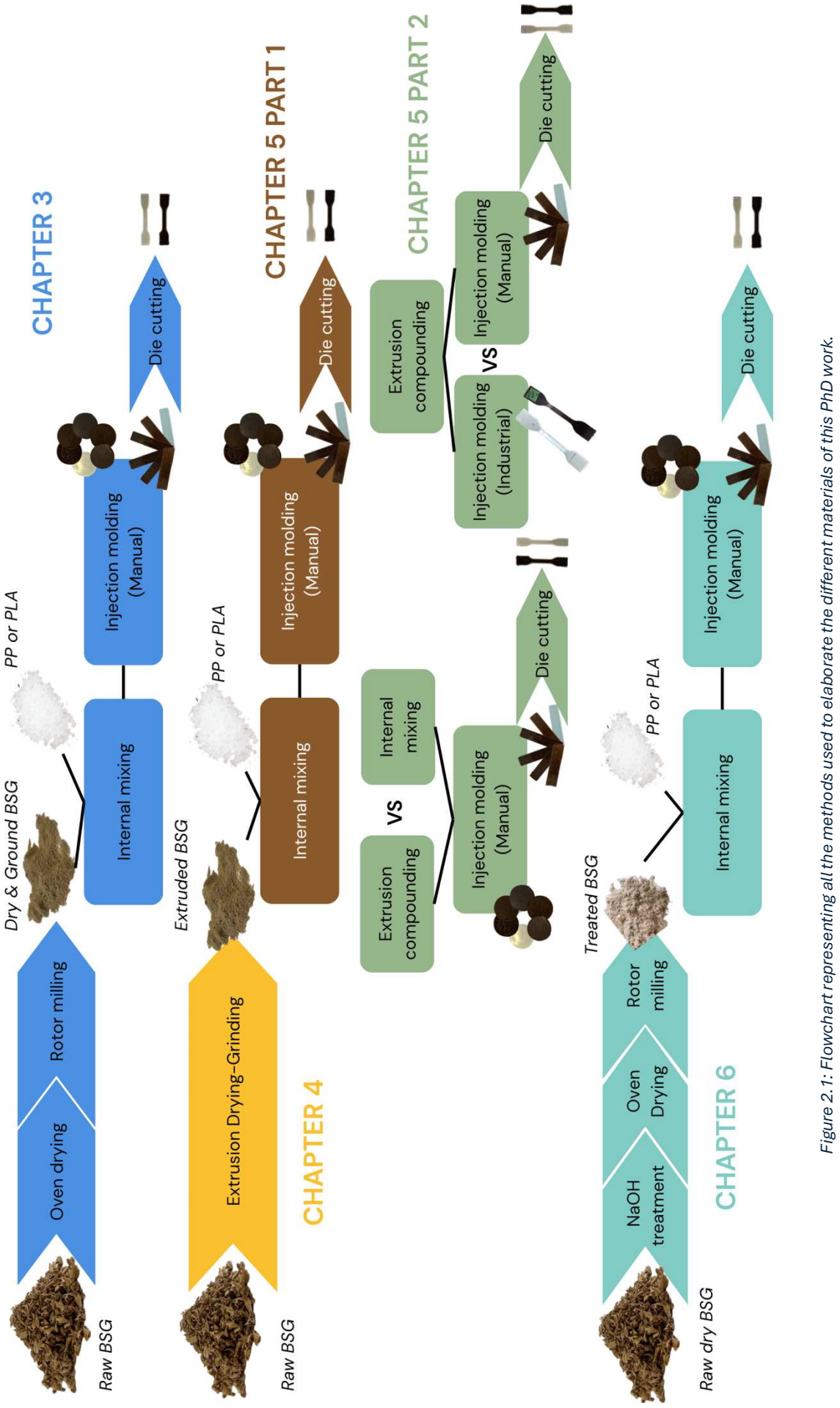


*Figure 2.1: Flowchart representing all the methods used to elaborate the different materials of this PhD work.*

# 2. Material

## 2.1. PP and PLA

PLA (PLE001, Figure 2.2 ) was supplied by NaturePlast with a density of 1.24 g/cm$^3$ and melt flow index of 6 dg/min (ASTM D1238, 210 °C / 2.16 kg). PLA is fully biobased and biodegradable according to NF EN 13432 : 2000.

PP (PP H357-09RSB, Figure 2.2) was supplied by Braskem with density of 0.900 g/cm$^3$ and melt flow index of 9.5 dg/min (ISO 1133, 230 °C / 2.16 kg). This PP is a petro-based polymer.

Technical sheets of PLA and PP used in this work are in annexes 1 and 2.

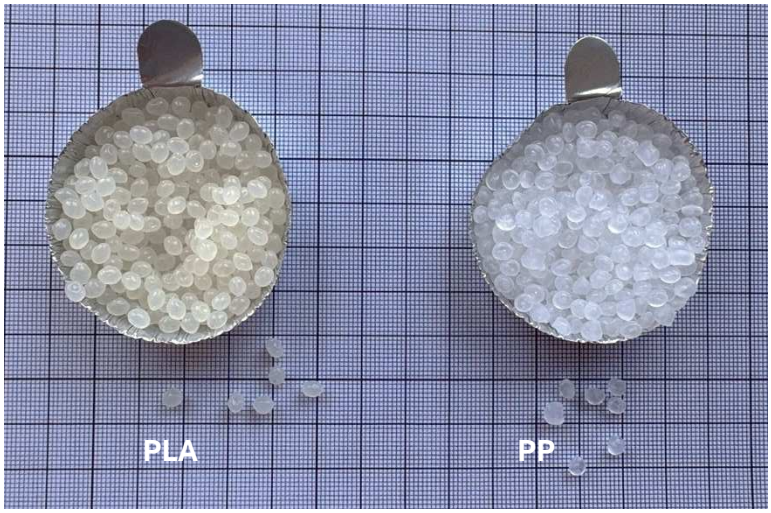


*Figure 2.2: PLA pellets on the left and PP pellets on the right*

## 2.2. Brewer's spent grain

Brewer's spent grain (Figure 2.3) used in this study was kindly provided by Senses Brewing (Reims, France). It was a by-product from the production of light beer consisted of 9 % of Best Caramel Pils, 45.5 % of Pilsen and 45.5 % of Pale Ale barley malts, the technical sheet is available in annexe 3. BSG was collected from one batch of beer production and then frozen at -18 °C to prevent any microbiological degradation. To prepare BSG before drying, it was defrosted at 17 °C during 48 h.




*Figure 2.3: Wet Brewer's spent grain*

## 3. Characterization methods

### 3.1. Chemical and microstructural characterization techniques

*3.1.1. Scanning electron microscopy*

Scanning electron microscopy was used to observe BSG particles, the fracture surfaces after tensile testing, and cryo-fractured sections of composites. The samples were sputter-coated with a 13 nm layer of gold/palladium. The sputtering was generated with a Leica EM SCD050 under Argon atmosphere at 60 mA during 30 s. The microstructures of composites fractures were analyzed using a Hitachi TM3030Plus tabletop microscope (granted access by the Physic department of Université de Reims Champagne-Ardenne) under mix mode (backscattered and secondary electrons) at accelerating voltage of 15 kV.

*3.1.2. BSG particle size distribution*

Prior to measurement, BSG was submerged in distilled water and agitated overnight. Particle size distribution (PSD) was conducted using a Malvern 3000 laser particle sizer apparatus (Figure 2.4), operating within a range of 0.01-2000 µm. The results are given in volume percentage of particles. Each sample was prepared in triplicate, and each replicate was measured twice by the sizer apparatus.

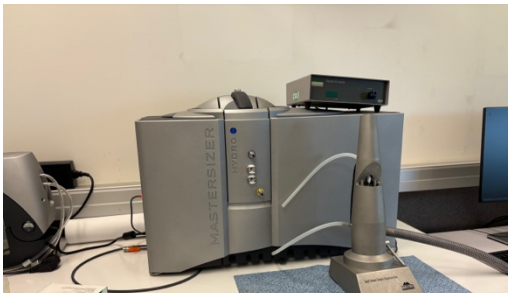


*Figure 2.4: Malvern 3000 laser particle size apparatus*

### 3.1.3. BSG true density

BSG true density was obtained using a pycnometer with isopropanol to prevent swelling effects of the particles. The pycnometer was first weighed empty, then filled with a known volume of isopropanol (d = 0.786 at 20 °C) and weighed again to determine the mass of the liquid. A know mass of BSG was then added to the pycnometer, the pycnometer was reweighed. Then isopropanol was added. Using these mass differences and the known density of isopropanol, the volume occupied by BSG was calculated. The density of the fibers was then determined by dividing their mass by the displaced volume. All measurements were performed at room temperature and repeated at least three times.

### 3.1.4. BSG composition analysis

BSG cellulose, hemicellulose, lignin, extractives, and ashes contents were determined using National Renewable Energy Laboratory (NREL) standard procedure [230]. The simplified procedure is displayed in a schema below, see Figure 2.5.

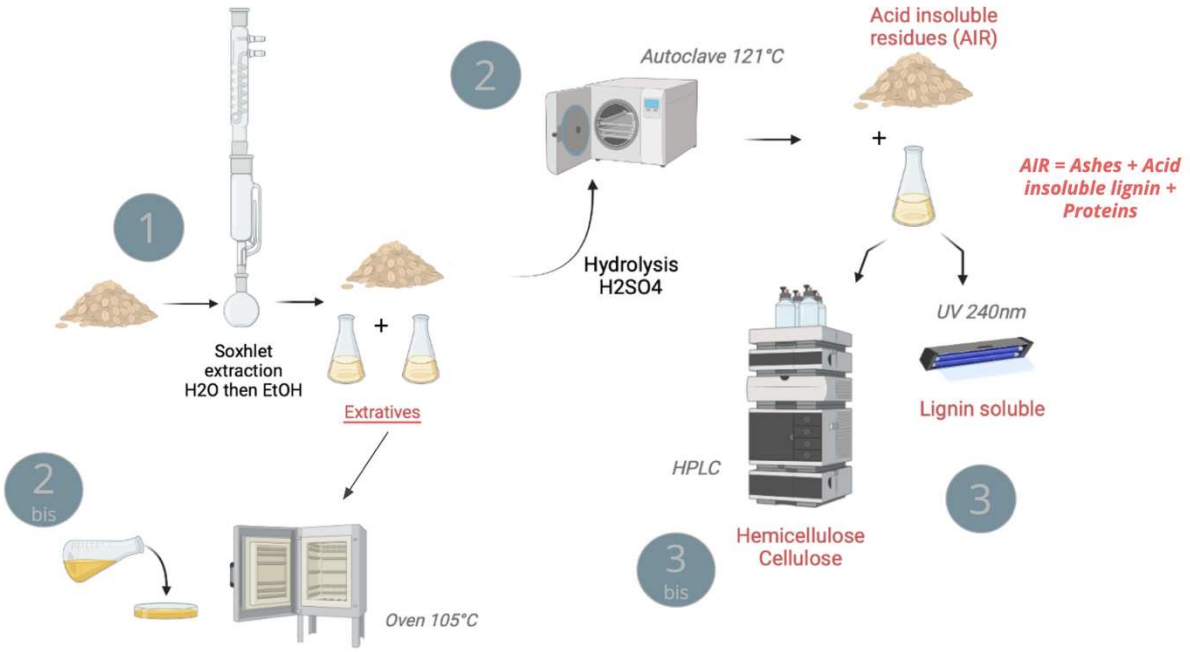


*Figure 2.5: Schematic procedure to determine BGS composition*

### 3.1.5. Size exclusion chromatography

Given our hypothesis and what was observed in the literature regarding potential PLA degradation during compounding, molecular weight of PLA samples was measured using Shodex K-804 L mixed gel styrene-divinylbenzene copolymer column (Shimadzu, USA) (8 mm internal diameter, 300 mm length, 7 µm particle size). Prior to analysis, the PLA composites were

dissolved in chloroform at a concentration of 3-4 mg/mL and filtered with 0.45 µm PTFE filters to separate the filler phase from polymeric phase. The injection volume was 20 µL and chloroform was used as mobile phase at a flow rate of 1 mL/min. Column temperature was maintained at 50 °C. A refractive index detector was used to detect the studied samples. The system was calibrated using polystyrene standards with molecular weight ranging from 12 630 to 388 500 g/mol.

### *3.1.6. Fourier Transform InfraRed spectroscopy (FTIR)*

FTIR analysis on BSG samples was performed using Spectrum Two FTIR spectrometer (Perkinelmer) under ATR mode. The wavelength of spectrometer was set to 500-4000 $cm^{-1}$ accumulating 64 scans with resolution of 4 $cm^{-1}$. The BSG sample was placed directly onto the ATR crystal and secured using the pressure screw to ensure good contact.

## 3.2. Rheological properties

### *3.2.1. Rheological test*

Oscillatory shear rheological properties of neat polymers and each blend were measured using a smooth parallel plate (diameter = 25 mm) in a Rheometer AR2000ex (TA Instrument), Figure 2.6. Tests were performed at 180 °C, the gap was adjusted to 2200 µm two minutes after the sample has been loaded to let it melt. All measures were carried out in oscillatory mode.

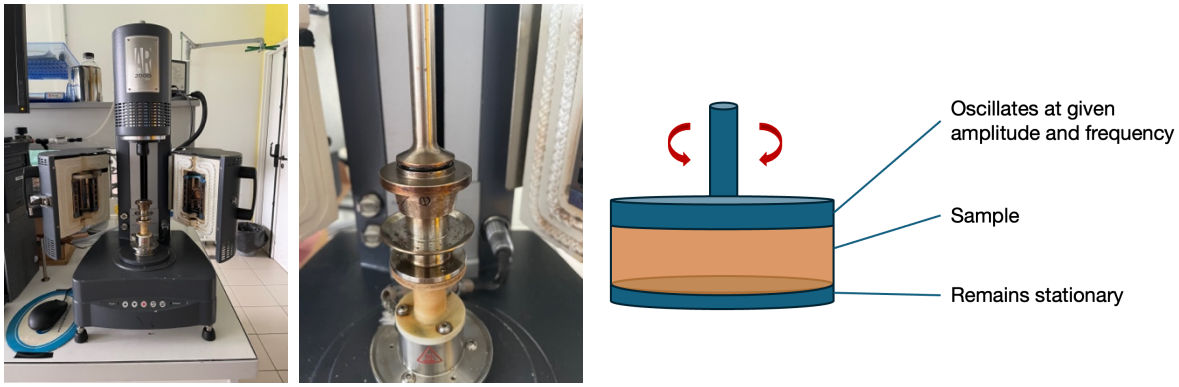


*Figure 2.6: Rheometer AR2000ex equipped with a parallel plate geometry and its scheme.*

### *3.2.2. Strain sweep*

In order to determine the limit of linear viscoelastic region (LVR) of the samples, strain sweeps were conducted from 0.01 to 100 % at angular frequency of 10 rad/s and of 0.1 rad/s. To ensure reliable data within the linear viscoelastic region (LVR), the strain was chosen at a level

corresponding to a few data points prior to the end of the LVR as shown in Figure 2.7. It ensures that the polymer chains have enough time to relax prior to the following measurement.

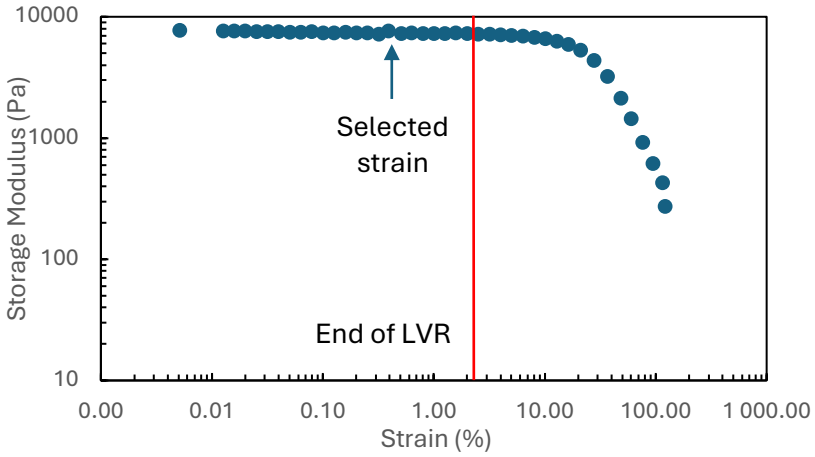


*Figure 2.7: Strain sweep test showing storage modulus versus Strain with the limit of LVR and selected strain*

### *3.2.3. Frequency sweep*

Frequency sweeps were conducted at 180 °C from 200 rad/s to 0.1 rad/s and at the maximum strain the material can withstand in the LVR. Thus, the selected strain was 10 % for the pure polymers and composites with BSG fractions 10 and 20 %(m/m), while it was 0.5 % for more highly filled composites (30, 40, and 50 %(m/m)) to remain in the LVR. Frequency sweep tests were performed at least three times to obtain a mean curve and standard deviation.

## 3.3. Mechanical properties

### *3.3.1. Tensile test*

Samples were prepared according to the ASTM D638 standard [231]. Samples were conditioned for at least 48 h at ambient temperature (20 - 25 °C) and 55 ± 5 % relative humidity before tensile testing.

For samples cut into dog-bone shape with a total length of 50 mm and a working length of 17 mm, and a width of 4 mm and for samples injected with the injection press Boy 22A (type 5A) the method was as following: tensile tests were performed using an Instron K1188 5544 universal testing machine equipped with a loadcell of 2 kN. Prior to testing, the specimen was securely mounted onto the testing machine's grips, ensuring proper alignment. A preload of 10 N was applied at a speed of 1 mm/min before the test to eliminate any slack in the specimen and ensure proper contact between the grips and the specimen. Then the crosshead speed was 2 mm/min. For samples injected with the injection press Boy 22A, the crosshead speed was

adjusted to 5 mm/min due to higher elongation of the specimen, it ensures breakage within a required time.

The tests were conducted until rupture, and data, including maximum load, load at rupture, and elongation at rupture, were recorded. Each test was conducted five times to assess the reproducibility of results.

### *3.3.2. Young's modulus calculations*

Young's modulus is calculated from the slope of stress-strain curve obtained during tensile test. Firstly, stress ($\sigma$, in MPa) is calculated from the load applied ($F$, in N) on the section area of the specimen ($S$, in $mm^2$). Secondly, strain is the deformation ($\Delta L$) of the initial elongated section of the specimen ($L_0$), it is given in mm/mm or without unit. Deformation is measured either using an extensometer or by tracking the grip displacement. When an extensometer is used, the initial gauge length ($L_0$) is defined according to the recommendations of ISO 527-2. When deformation is measured via grip displacement, $L_0$ refers to the total length of the section undergoing deformation. Finally, the slope is calculated between 0.0005 and 0.0025 mm/mm.

$$\sigma = \frac{F}{S} \qquad (2.1) \qquad\qquad \varepsilon = \frac{\Delta L}{L_0} \qquad (2.2)$$

### *3.3.3. Tensile strength and elongation at break*

Other results can be extracted from the stress-strain curves. For example, the elongation at break is the elongation in mm/mm reached when the specimen breaks. The yield tensile strength (MPa) is the stress at which the material begins to deform plastically (Figure 1.27). Beyond this point the deformation occurring is irreversible. Finally, there is tensile strength at break (MPa) which is the stress obtained when the specimen breaks.

## 3.4. Thermal characterizations

### *3.4.1. Thermogravimetric (TG) analysis*

- Program

TG analyses were conducted using a thermogravimetric analyzer (TG209F3, Netzsch) in nitrogen atmosphere. A three-step heating rate was applied: 40 K/min from 20 °C to 100 °C, an isotherm for 30 min at 100 °C to remove the residual water, then 10 K/min from 100 °C to 600 °C. The temperature program and apparatus are displayed in Figure 2.8. Samples, weighing

approximately 10 mg, were loaded into alumina ($Al_2O_3$) pans. Key parameter derived from TGA curves was the derivative temperature peak, which was indicative of the temperature reached for the highest degradation rate. Control experiments were performed for all experimental procedures, with each test replicated three times. To eliminate the influence of the crucible mass on heat capacity measurements, the results were adjusted by deducting data from a control test conducted using identical protocols and crucibles. This calibration process ensured the accuracy of the raw data.

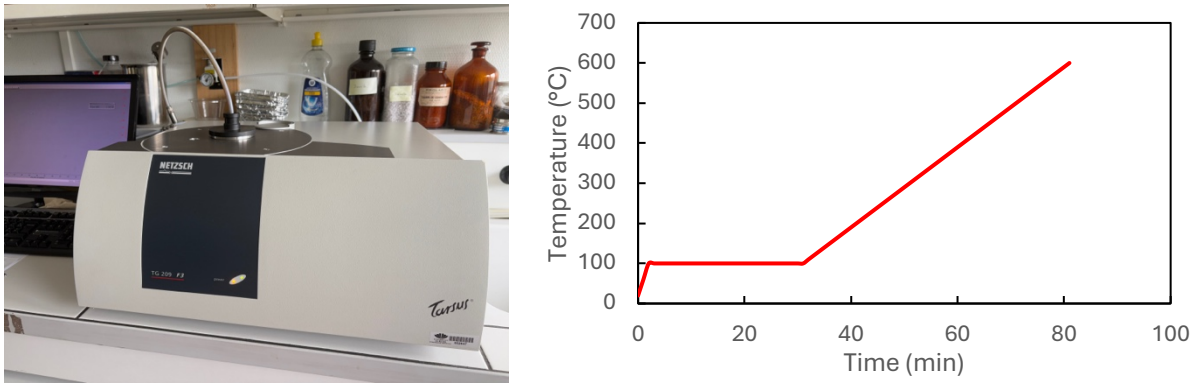


*Figure 2.8: TG analyzer along with temperature program*

- Model-based kinetics and deconvolution procedure

BSG pyrolysis behavior was studied using TG Analysis conducted at 10 K/min. DTG curves of BSG samples were used to determine the elementary pyrolysis decomposition stages. A multi-component kinetic model was employed to describe the thermal decomposition of BSG. Each distinct mass loss was assumed to correspond to a pseudo-component of BSG such as hemicellulose, cellulose, lignin and extractives as Sobek *et al*. suggested in their study [232]. Thus, BSG decomposition kinetic was treated as the superposition of 3 individual decomposition steps (hemicellulose, cellulose and lignin+extractives). Each step was modelling using a Gaussian-like peak shape. Deconvolution was performed using the software Fityk and the optimisation of the gaussian parameters was based on the minimisation of the residual least squares.

### *3.4.2. Differential scanning calorimetry*

DSC analyses were conducted using a DSC Q20 (TA instrument) using three ramps at 10 K/min: a first heating ramp from -60 °C to 200 °C, a cooling ramp, and a second heating ramp. Samples, weighing approximately 12 mg, were loaded into aluminium pans. The DSC analysis was performed under nitrogen purge with a flow rate of 50 mL/min. Temperatures of different

thermal events such as glass transition ($T_g$), crystallization ($T_c$), cold crystallization ($T_{cc}$) and melting ($T_m$) were recorded. The degree of crystallization ($\chi_c$) was calculated using the following equation [233]:

$$\chi c = \frac{\Delta H_m - \Delta H_{cc}}{\Delta H_m^0} x \frac{100}{w} \quad (2.3)$$

$\Delta H_{cc}$ is the enthalpy for the cold crystallisation in J/g,

$\Delta H_m$ is the enthalpy for melting transition in J/g,

$\Delta H^0_m$ is the enthalpy of melting for a 100 % crystalline PLA or PP sample in J/g,

taking $\Delta H^0_m$ = 93.6 J/g for PLA [234] and $\Delta H^0_m$ = 209 J/g for PP [81].

*w* is the weight fraction of PLA or PP in the sample.

### 3.5. Water related behavior

#### *3.5.1. Moisture content measurement*

Immediately after extrusion, moisture content of the BSG samples was measured with a moisture analyser Kern DAB, Kern & Sohn (Figure 2.9). The mass (close to 1 g) of BSG is heated at constant temperature of 105 °C. Measurement stops when sample mass is steady. The reported moisture content values are calculated on a wet basis representing the percentage of water relative to BSG initial weight. Three measurements were performed on each set of extrusion parameters.




*Figure 2.9: Moisture analyzer Kern DAB*

#### *3.5.2. Water activity measurement*

The water activity of BSG was measured using a water activity analyzer Labswift, Novasina (Figure 2.10). Approximately 1.5 g of samples were placed and sealed in the measurement chamber. The sample was equilibrated until a steady reading was obtained for 4 min, typically within 20 min. The measurements were carried out at room temperature.




*Figure 2.10: Water activity analyzer Labswift*

### *3.5.3. Modelling using Guggenheim-Anderson-de Boer (GAB) equation*

To determine the optimal drying conditions for BSG to be stored, the moisture sorption isotherm of BSG was constructed using experimental data. The GAB equation was used to describe the relationship between water activity and equilibrium moisture content. GAB equation is written in the following form [235]:

$$W = \frac{CKW_m a_w}{(1-Ka_w)(1-Ka_w+CKa_w)} \qquad (2.4)$$

With:

*W*: moisture content of BSG on a dry basis (g water/ g dry BSG)

$a_w$: water activity

$W_m$: Monolayer moisture content (dry basis)

*C*: Guggenheim constant related to the heat of absorption

*K*: Constant related to temperature effects

The obtained data were fitted using Microsoft Excel Solver, the optimisation of the parameters $W_m$, *C* and *K* was based on the minimisation of the residual least squares

### *3.5.4. Water absorption behavior*

Liquid water absorption of composites specimen was measured. To do that, initial mass of the composite samples was recorded. Then, two identical specimens of each formulation were soaked in distilled water at room temperature as per Figure 2.11. At different time, specimens were taken out from the water and surface water droplets were carefully removed with a dry

cloth. Then specimens were placed again in the water. Stainless steel nuts were placed on the samples with a density lower than that of water in order to keep them submerged.

$$M_t(\%) = \frac{M_t - M_0}{M_0} \times 100 \qquad (2.5)$$




*Figure 2.11: Water absorption experiment on BSG composites.*

### 3.6. Statistical analysis

The means and standard deviations were calculated, and the data were statistically analyzed for comparison using R Studio software (version 3.6.3). To evaluate differences between the sample groups, a t-test was performed. Statistical significance was determined using a p-value of 0.05. The results were annotated with letters to indicate statistical groupings. The results sharing the same letters were not significantly different from one another and results with different letters were considered to show significances differences in their means. GPC was performed in duplicates. Moisture content, BSG density, TGA, rheology and DSC measurements were performed in triplicates. Tensile tests were performed 5 times per composites formulations.

## 4. Material production

### 4.1. Thesis first part: composites elaboration with Internal Mixer

#### *4.1.1. Introduction*

This part deals with the development and characterization of BSG- PP/PLA composites material using internal mixing and injection molding. The schematic summary of this part is displayed in Figure 2.12.

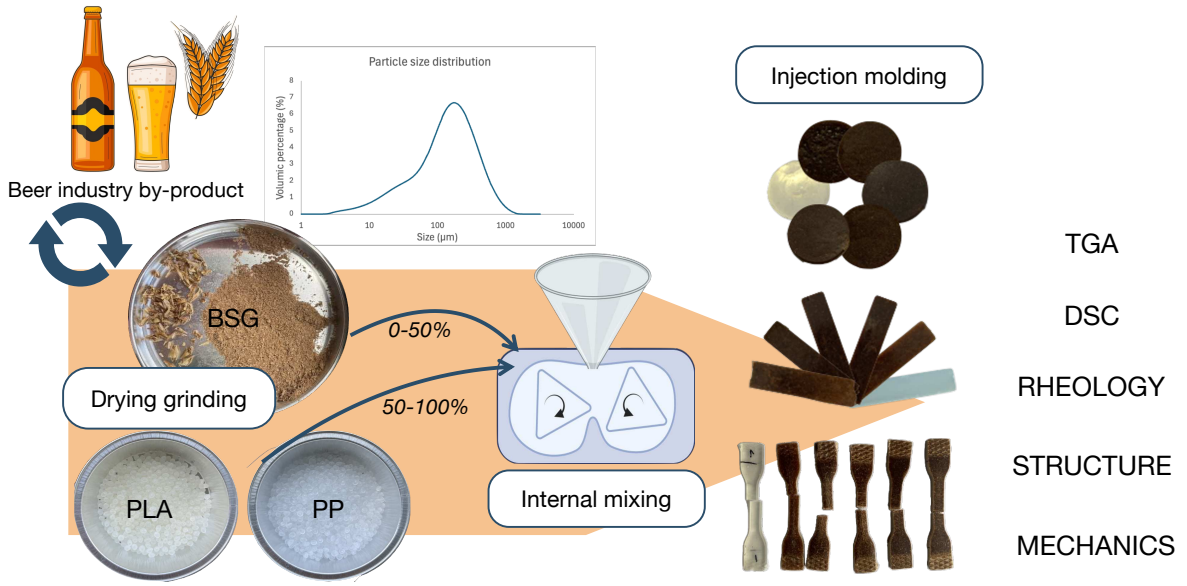


*Figure 2.12: Schematic summary of thesis first part experiments to elaborate and characterize BSG-PP/PLA composite materials.*

### *4.1.2. Conventional drying and grinding of BSG*

To make it suitable for composite manufacturing, BSG was dried at 70 °C for 44 h (MMM Medcenter Venticell 55 - ECO line – drying oven) from 74 % to 3 % moisture, then grinded (RETSCH Ultra Centrifugal Mill ZM 1000) for 5 minutes at 15000 rpm (Figure 2.13).



*Figure 2.13: Rotor miller and BSG after and before grinding*

### 4.1.3. Internal mixing

Blends of 50 g of polymer pellets (PLA or PP) and dry grinded BSG with different ratios (0, 10, 20, 30, 40, 50 % (m/m)),Table 2.2 ) were mixed at 180 °C for 5 min using a Rheomix 600 QC (Thermo Fisher Scientific) equipped with two counter roller rotors R600. Mixing was conducted at 50 rpm screw speed to compound all the blends. Blends were pelletized using a plastic crusher HoliShred (Holimaker). Figure 2.14 displays internal mixer and crusher used.




*Figure 2.14: Rheomix 600 QC internal mixer and Holishred plastic crusher*

*Table 2.1: Geometric dimensions and schematic representation of the internal mixer used in this Ph.D work.*

| | |
|---|---|
| Volume of the chamber (cm3) | 120 |
| Largest rotor radius (*Re*) (mm) | 20.0 |
| Smallest rotor radius (*Ri*)* (mm) | 17.6* |
| *Ri/Re* ratio (>0.85 required for narrow gap approximation) | 0.88 |

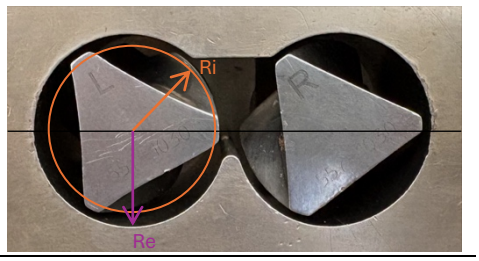


**Value extracted from Bousmina et al. who worked using the same equipment [236].*

*Table 2.2: PP and PLA - BSG composites formulations and sample codes. PP density = 0.9 g/cm$^3$; PLA density = 1.24 g/cm$^3$; BSG density = 1.35 g/cm$^3$*

| Polymer | Sample Code | Weight ratio of polymer (%) | Weight ratio of BSG (%) | Volume ratio of BSG (%)* |
|---|---|---|---|---|
| Polypropylene (PP) | PP | 100 | 0 | 0 |
| | PPBSG10 | 90 | 10 | 7.0 |
| | PPBSG20 | 80 | 20 | 14.4 |
| | PPBSG30 | 70 | 30 | 22.4 |
| | PPBSG40 | 60 | 40 | 31.0 |
| | PPBSG50 | 50 | 50 | 40.2 |
| Polylactic acid (PLA) | PLA | 100 | 0 | 0 |
| | PLABSG10 | 90 | 10 | 9.3 |
| | PLABSG20 | 80 | 20 | 18.8 |
| | PLABSG30 | 70 | 30 | 28.5 |
| | PLABSG40 | 60 | 40 | 38.2 |
| | PLABSG50 | 50 | 50 | 48.1 |

### *4.1.4. Injection molding: Laboratory press*

The injection was processed at 180 °C for PLA composite materials and 200 °C for PP composite materials to ensure optimal flow and molding using the Holipress (Holimaker), Figure 2.15. The pellets were melted in the barrel of the injection press for 6 min before injection. Two shapes of specimens were used: a circular one (diameter of 26 mm and a thickness of 2 mm) used for rheological tests; a rectangle one (length of 60 mm, thickness of 2.5 mm and 13.5 mm width). The circular-mold temperature was set at 80 °C, the rectangle-mold temperature was set at 120 °C.

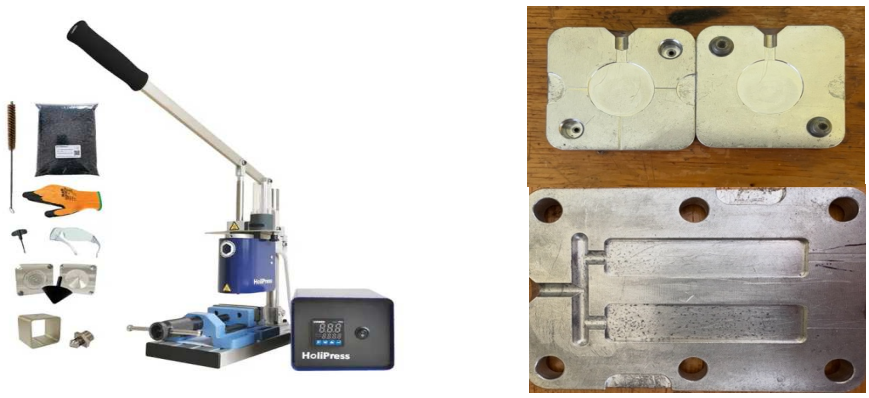


*Figure 2.15: Holipress, circular mold, and rectangle mold*

The pressure applied on the material was estimated from the force manually exerted on the injection press handle. As shown in Figure 2.16, an estimated force ($F_m$) between 200 and 600 N was applied at the end of the handle ($D_1$ = 0.474 m from the lever junction). Considering the piston located at 0.101 m ($D_2$) from the junction, the transmitted force ($F_t$) was calculated using the lever law. This force was then divided by the piston surface area (2 $cm^2$), corresponding to an applied pressure in the range of 46–120 bar.

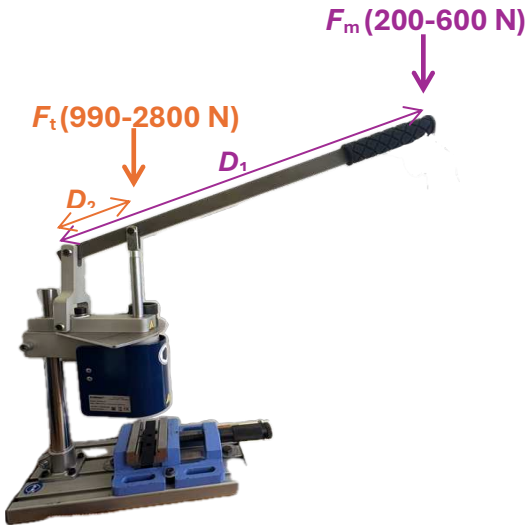


*Figure 2.16: Schematic illustration of the injection press with distances and applied force indicated for pressure calculation.*

### *4.1.5. Specimens die-cutting*

A dog-bone shape ISO527-2 type 5A [237] was used for tensile tests. The specimen was cut from the previously injected rectangle-shaped specimen which was heated on a heated plate for three minutes at a temperature of 60 °C, after which it was die-cut, using the dog-bone shape die, Figure 2.17.



*Figure 2.17: Die-cut equipment and dog-bone shape die*

## 4.2. Thesis second part: BSG drying via extrusion

### *4.2.1. Introduction*

In this part, we introduce the methods used to complete our study on developing a new drying grinding strategy of BSG. Hence, this part focuses on a thermomechanical treatment involving extrusion where we study the effect of extrusion parameters such as screw profile, throughput, screw speed, and temperature on BSG properties. In a preliminary study, many parameters were studied including screw profile of the extruder, screw speed, BSG feed rate, and temperature. This preliminary study was conducted to evaluate the processability of the experiment and to verify whether the moisture (< 10 % wet basis) and particle size reductions were sufficient. These assessments constituted essential checkpoints to ensure that the experiment met the minimum requirements, namely moisture content reduction and particles size reduction, for deeper investigations. Once the criteria were confirmed, one screw profile and one feed rate were selected to pursue the experiments, allowing variation of screw speed and temperature. Schematic description of this part is displayed in Figure 2.18.`

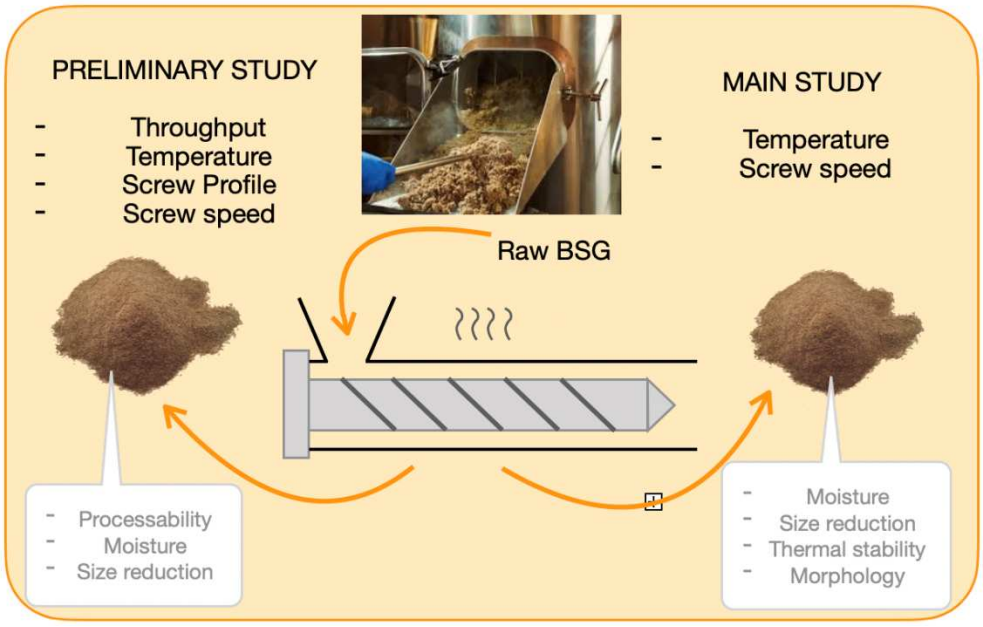


*Figure 2.18: Schematic description of BSG drying grinding by extrusion study*

### *4.2.2. Extrusion drying and grinding of BSG*

♦ Introduction

Extrusion drying and grinding were performed with a Clextral BC21 (L = 900 mm, L/D = 36) co-rotating twin-screw extruder. The extruder has 9 heating/cooling zones with a screw diameter

of 25 mm. Two venting zones for water steam evacuation are located in zones 4 and 7. All the information about this extruder are gathered in Table 2.3.

*Table 2.3: Clextral BC21 extruder information and extruder picture*

| | |
|---|---|
| **Inner diameter (D)** | 25 mm |
| **Total length (L)** | 900 mm |
| **L/D ratio** | 36 |
| **Center-to-center distance** | 21 mm |
| **Number of heating/cooling zones** | 9 |
| **Maximum screw speed** | 680 rpm |
| **Motor power** | 9.2 kW |



Since we used a **volumetric feeder**, it must be calibrated to obtain the mass feed rate for further calculations. Figure 2.19 depicts the **equivalence** between **volumetric feeder motor load** in percentage of the maximum and **BSG mass feed rate**. The strong linear relationship ($R^2 = 0.9972$) confirms the reliability of motor load settings to estimate BSG mass input rate during extrusion.

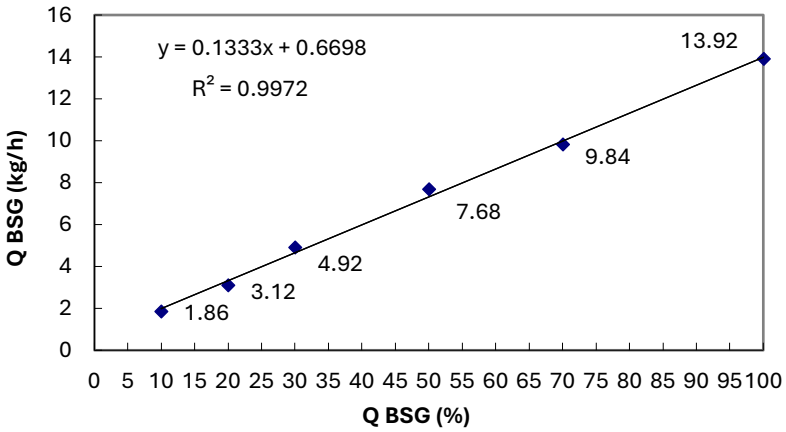


*Figure 2.19: Correlation between the volumetric feeder motor load (percentage of maximum capacity, Q BSG (%)) and BSG feed rate (Q BSG in kg/h)*

The residence time in the extruder was determined using a tracer method. A portion of BSG was pre-colored with a food-grade blue dye and introduced into the extruder. The elapsed time between tracer addition and its first appearance at the die was measured with a stopwatch and recorded as the residence time.

♦ Preliminary study

The preliminary study consisted of finding the right profile that allow the obtention of fine powder and low moisture content. In this way, four screw profiles were investigated; they will be detailed in Chapter 4. Moreover, different feeding rates of BSG (1.8, 4, 8, 10 kg/h), screw speeds (100, 250, 450 rpm) and temperatures (110, 150, 190 °C) were explored.

♦ Main study

For the main study, only one screw profile and one feed rate were selected. This selected screw profile for the main is displayed in Figure 2.20 and described in Table 2.4. Raw wet BSG was introduced into the extruder via a volumetric feeder with a constant throughput of 1.82 ± 0.06 kg/h. Throughput was measured before each trial. Screw speed was set at 200, 300, and 400 rpm, and barrel temperature in all zones was set at 150, 170, and 190 °C. For each set of parameters, extrusion was conducted for a minimum of 20 minutes after stabilization of the extruder's motor load, indicating process stabilization, and prior to BSG sampling. Humidity and water activity were measured directly at die exit of the extruder. Samples were designated as BSGext_a_b, where *a* represents the processing temperature, and *b* indicates the screw speed, for example BSGext_150_200 for BSG extruded at 150 °C and 200 rpm.

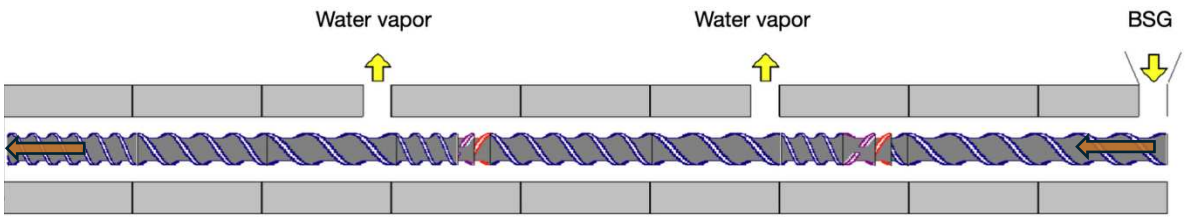


*Figure 2.20: Screw profile selected for further drying grinding investigations.*

*Table 2.4: Extruder screw geometry and dimensions selected for further drying grinding investigations*

| Zone | Screw number | Screw type | Screw length (mm) | Pitch | Thread type | Helix angle (°) |
|---|---|---|---|---|---|---|
| 1 | 1 | Convoying | 50 | Forward | Solid | 33 |
| | 2 | Convoying | 50 | Forward | Solid | 33 |
| 2 | 3 | Convoying | 50 | Forward | Solid | 33 |
| | 4 | Convoying | 50 | Forward | Solid | 33 |
| 3 | 5 | Convoying | 12.5 | Forward | Solid | 25 |
| | 6 | Convoying | 12.5 | Reverse | Solid | 25 |
| | 7 | Convoying | 25 | Reverse | Grooved | 25 |
| | 8 | Convoying | 50 | Forward | Solid | 16 |
| 4 | 9 | Convoying | 50 | Forward | Solid | 33 |
| | 10 | Convoying | 50 | Forward | Solid | 33 |
| 5 | 11 | Convoying | 25 | Forward | Solid | 25 |
| | 12 | Convoying | 25 | Forward | Solid | 25 |
| | 13 | Convoying | 50 | Forward | Solid | 25 |
| 6 | 14 | Convoying | 25 | Forward | Solid | 25 |
| | 15 | Convoying | 12.5 | Reverse | Solid | 25 |
| | 16 | Convoying | 12.5 | Reverse | Grooved | 25 |
| | 17 | Convoying | 50 | Forward | Solid | 16 |
| 7 | 18 | Convoying | 50 | Forward | Solid | 33 |
| | 19 | Convoying | 50 | Forward | Solid | 33 |
| 8 | 20 | Convoying | 50 | Forward | Solid | 25 |
| | 21 | Convoying | 50 | Forward | Solid | 25 |
| 9 | 22 | Convoying | 25 | Forward | Solid | 16 |
| | 23 | Convoying | 25 | Forward | Solid | 16 |
| | 24 | Convoying | 25 | Forward | Solid | 16 |
| | 25 | Convoying | 25 | Forward | Solid | 16 |

*4.2.3. Design of experiment: Response surface methodology*

Once, suitable screw profile and throughput were selected, a Response Surface Methodology (RSM) was used to find the optimal set of extrusion parameters allowing the obtention of a material suitable for storage and composite material applications. Thus, RSM was employed to optimize extrusion drying grinding by investigating the effects of two independent parameters: Temperature (*T*) of the barrels (150-190 °C) and Screw speed (*S*) (200-400 rpm). Each parameter was studied at three different levels and a Box-Behnken design was used comprising 9 experimental runs. All the variables and their variances are listed in Table 2.5. The response variables, BSG humidity at die-exit and granulometry, were measured in triplicate for each parameters set. Then, the data were analyzed using a second-order polynomial regression model to estimate the relationship between the parameter's variables (*T, S*) and the response variables. Regression analysis was performed using Microsoft excel. The model used was:

$$Y = \beta_0 + \beta_1 T + \beta_2 S + \beta_3 T^2 + \beta_4 S^2 + \beta_5 TS \quad (2.6)$$

With

*Y*: Predicted response

$\beta_0$: intercept

$\beta_1$, $\beta_2$: linear coefficients

$\beta_3$, $\beta_4$: quadratic coefficients

$\beta_5$: interaction coefficient

*S*: Screw speed

*T*: Barrel temperature

*Table 2.5: List of variables and variance*

| **Variable** | **Variance** | | |
|---|---|---|---|
| Temperature (°C) | 150 | 170 | 190 |
| Screw speed (rpm) | 200 | 300 | 400 |

*4.2.4. Extrusion Specific Mechanical Energy (SME) calculations*

To quantify the energy efficiency of the process, the drive motor torque was recorded, and SME was calculated using Equation 1:

$$SME = \frac{1}{Q}\frac{N}{\mathrm{Nmax}} r \frac{C}{Cmax} W \qquad (2.7)$$

with

*Q*: mass feed rate (kg/h)

*N*: screw speed (rpm)

*N*max: mass screw speed of the extruder (here, 680 rpm)

*r*: motor efficiency (here, 0.93)

*C*: average torque

*C*max: maximum torque (here, 100 %)

*W*: Nominal power (here, 9.2 kW)

## 4.3. Thesis third part: bridging strategies for composites optimization

*4.3.1. Introduction*

This part deals with the obtention of composite material with, first, extruded BSG from chapter 4 using internal mixing, second, using an up-scaled compounding method using extrusion for compounding BSG and PP and in the end, using an up-scaled injection press to obtain dog-bone shape specimens for tensile tests. For clarity, Figure 2.1 provides a schematic representation of the methods.

*4.3.2. Composites elaboration using internal mixing*

In the first part of chapter 5, extruded BSG was incorporated at 30 %(m/m) in our two matrices (PP and PLA) using internal mixing with the same parameters as in chapter 3. Hence, blends of 50 g of polymer pellets and extruded BSG were mixed at 180 °C, 50 rpm for 5 min using Rheomix 600 QC (Thermo Fisher Scientific) equipped with two counter roller rotors R600. The formulations are displayed in Figure 2.6. These blends were injected for characterization using method of Section 4.1.4.

*Table 2.6: PP and PLA- BSG composites formulations made and characterized in Chapter 5 and their sample codes.*

| Sample Code | Weight ratio of polymer (%) | Weight ratio of BSGext_150_200 (%) | Weight ratio of BSGext_170_300 (%) | Weight ratio of BSGext_190_400 (%) |
|---|---|---|---|---|
| **PP**70BSG ext_150_200 | 70 | 30 | - | - |
| **PP**70BSGext_170_300 | 70 | - | 30 | - |
| **PP**70BSGext_190_400 | 70 | - | - | 30 |
| **PLA**70BSGext_170_300 | 70 | - | 30 | - |

*4.3.3. Extrusion of composites*

Four blends of PP pellets and different extruded and non-extruded BSG with different ratios (0, 30 % (m/m), Table 2.7) were compounded at 200 °C in all zones and 150 rpm using two volumetric feeders and a Clextral BC21 (L = 900 mm, L/D = 36) co-rotating twin-screw extruder. The screw profile used is detailed in Table 2.8 and shown in Figure 2.21. PP volumetric feeder was set at 3.9 kg/h for every formulation while BSG gravimetric feeder was adjusted to obtain the target formulations. We chose to operate at a constant feed rate of PP, despite knowing that the filling level of the extruder would increase with the addition of BSG. This decision was made because adjusting the volumetric feeder during processing proved to be challenging, and the potentiometer controlling the feed rate did not provide sufficient accuracy. At the exit of the die, the blending was cooled using a water bath and then pelletized to be processed later. Materials prepared by extrusion are annotated with the suffix “EXT” in the sample code. When a direct comparison with extruded samples is required, materials prepared by integral mixing are annotated with the suffix “IM”. In all other cases, no suffix is included.

*Table 2.7: PP-BSG composites formulations made with extruder and sample codes.*

| Sample Code | Weight ratio of polymer (%) | Weight ratio of BSGconv (%) | Weight ratio of BSGext_150_200 (%) | Weight ratio of BSGext_190_400 (%) |
|---|---|---|---|---|
| PPext | 100 | 0 | 0 | 0 |
| PP70BSGconvEXT | 70 | 30 | - | - |
| PP70BSGext_150_200EXT | 70 | - | 30 | - |
| PP70BSGext_190_400EXT | 70 | - | - | 30 |

*Table 2.8: Extruder screw geometry and dimensions used to compound composites blends*

| Zone | Screw number | Screw type | Screw length (mm) | Pitch | Thread type | Helix angle (°) |
|---|---|---|---|---|---|---|
| 1 | 1 | Convoying | 50 | Forward | Solid | 33 |
| | 2 | Convoying | 50 | Forward | Solid | 33 |
| 2 | 3 | Convoying | 50 | Forward | Solid | 33 |
| | 4 | Convoying | 50 | Forward | Solid | 25 |
| 3 | 5 | Convoying | 50 | Forward | Solid | 16 |
| | 6 | Kneading | 25 | - | Solid | 45 |
| | 7 | Convoying | 50 | Forward | Solid | 33 |
| 4 | 8 | Convoying | 50 | Forward | Solid | 33 |
| | 9 | Convoying | 25 | Forward | Solid | 25 |
| 5 | 10 | Convoying | 25 | Forward | Solid | 25 |
| | 11 | Convoying | 25 | Forward | Solid | 25 |
| | 12 | Convoying | 50 | Forward | Solid | 16 |
| 6 | 13 | Kneading | 50 | - | Solid | 45 |
| | 14 | Kneading | 25 | - | Solid | 45 |
| | 15 | Convoying | 50 | Forward | Solid | 33 |
| 7 | 16 | Convoying | 25 | Forward | Solid | 16 |
| | 17 | Convoying | 25 | Forward | Solid | 16 |
| | 18 | Convoying | 25 | Forward | Solid | 25 |
| 8 | 19 | Convoying | 50 | Forward | Solid | 25 |
| | 20 | Convoying | 50 | Forward | Solid | 25 |
| 9 | 21 | Convoying | 50 | Forward | Solid | 16 |
| | 22 | Convoying | 25 | Forward | Solid | 16 |
| | 23 | Convoying | 25 | Forward | Solid | 25 |

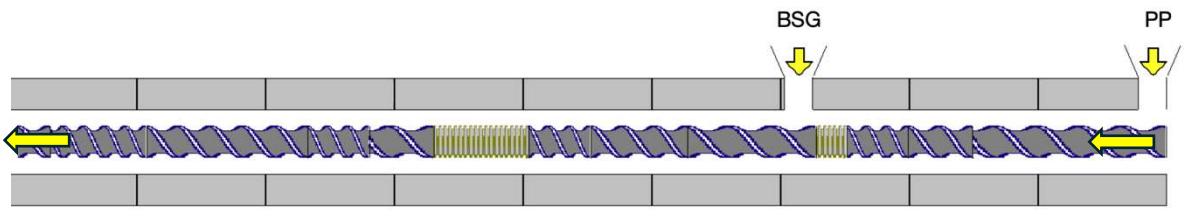


*Figure 2.21: Screw profile used for material composites compounding*

*4.3.4. Injection molding: Industrial press*

We were granted access to the injection molding machine by ESIREIMS. All four formulations obtained by extrusion were injected using the injection press BOY22A (BOY) with a screw diameter of 22 mm. Temperature of the five heating zones was set to 185, 185, 185, 200, and 200 °C, respectively from the feeder to the nozzle. Injection speed was set to 100 mm/s with a pressure of 50 bar. The mold was a 5A type from ISO 527-2, it was heated at 20 °C. The holding time and pressure were 10 s and 25 bar, respectively.

For comparison of the injection methods, these four extruded formulations were also injected using the laboratory press following the method of Section Chapter 24.1.4. .

Materials injected with industrial press are annotated with the suffix “ind” in the sample code. When a direct comparison with industrially injected samples is required, composites injected using laboratory press (which is manual) are annotated with the suffix “man”. In all other cases, no suffix is included.

## 4.4. Alkaline treatment of BSG to improve interfacial adhesion

*4.4.1. BSG alkaline treatment*

To improve the interactions between BSG and polymers, we treated BSG using alkaline treatment. An aqueous solution of 5 %(w/v) of NaOH was prepared. 2.5 %(m/v) of BSG was soaked and stirred using a magnetic stirrer at 500 rpm in this solution. After treatment, BSG was filtered using a 1 mm sieve and washed with distilled water until a neutral pH was reached. It was then dried at 55 °C in an oven for 12 h. The alkali treated BSG samples were then milled using the rotor miller under the same condition as non-treated BSG (section 4.1.2. ) and stored in polyethylene zipper bag. Seven treatment conditions including time (30 min, 1 h, 4 h, 8 h) and temperature (Room temperature and 70 °C) were explored (except 8 h at 70 °C). A schematic diagram of the treatment steps is displayed in Figure 2.22.

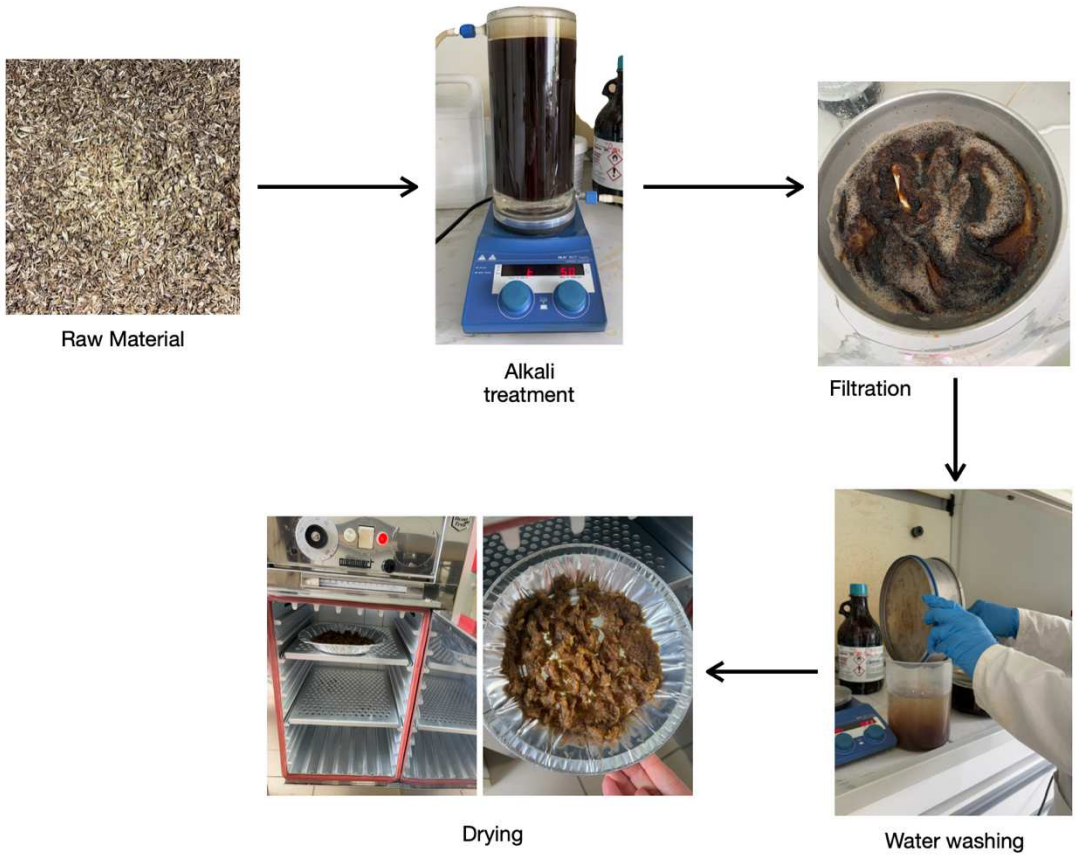


*Figure 2.22: Schematic diagram for alkaline chemical pretreatment of BSG.*

### *4.4.2. Composites elaboration*

Alkali treated BSG (during 4 h at 70 °C), referred to as BSGNaOH, was incorporated at 10 and 30 %(m/m) in our two matrices (PP and PLA) using internal mixing with the same parameters as in chapter 3. Hence, blends of 50 g of polymer pellets and treated BSG were mixed at 180 °C, 50 rpm for 5 min using Rheomix 600 QC (Thermo Fisher Scientific) equipped with two counter roller rotors R600. The formulations are displayed in Table 2.9. These blends were injected for characterization using laboratory press with method of Section Chapter 24.1.4. .

*Table 2.9: PP and PLA- alkali treated BSG composites formulations made using internal mixer and characterized in chapter 6 and their sample codes.*

| Polymer | Sample Code | Weight ratio of polymer (%) | Weight ratio of BSG (%) | Volume ratio of BSG (%) |
|---|---|---|---|---|
| Polypropylene (PP) | PP90BSGNaOH | 90 | 10 | 6 |
| | PP70BSGNaOH | 70 | 30 | 20 |
| Polylactic Acid (PLA) | PLA90BSGNaOH | 90 | 10 | 8 |
| | PLA70BSGNaOH | 70 | 30 | 25 |

# CHAPTER 3:

## Development of bio-based materials

# RÉSUMÉ DU CHAPITRE 3

Ce chapitre porte sur le développement de composites à base de drêches de brasserie (BSG), un coproduit issu du brassage de la bière, incorporé dans deux matrices thermoplastiques aux propriétés différentes : le PLA et le PP. L'effet du pourcentage de BSG dans les composites a été étudié par analyses thermogravimétrique et calorimétrique différentielle, rhéologie, test de traction, microscopie électronique à balayage et absorption d'eau. Les résultats de TGA ont montré que la drêche interagit avec le PLA, en particulier à haute température lors du mélange, accélérant la dégradation du polymère et favorisant la coupure de chaînes, ce qui est confirmé par chromatographie d'exclusion stérique. Cette interaction influence les transitions thermiques et les propriétés mécaniques des composites, ce qui se traduit par un comportement ductile observé en MEB. À l'inverse, dans le PP, la drêche agit comme une charge essentiellement inerte. L'analyse rhéologique a mis en évidence une floculation des particules au-delà de 30 %(m/m) dans le PLA, tandis que le PP a conservé un comportement d'écoulement stable malgré l'augmentation du pourcentage de charges. Ceci est grandement favorable dans les procédés d'extrusion et d'injection. La résistance à la traction a diminué pour les deux matrices avec l'ajout de la drêche, probablement en raison d'une faible adhésion à l'interface. Cependant, le module de Young est resté stable, démontrant le potentiel de ces composites à maintenir leur intégrité mécanique lorsqu'ils sont soumis à un stress. Cette étude contribue à une meilleure compréhension du comportement des composites drêches-PLA et drêches-PP et ouvre des perspectives pour la conception de matériaux durables destinés aux secteurs de l'emballage, du mobilier ou de l'automobile.

# Chapter 3 : Development of bio-based materials

## 1. Introduction

As it has been evocated in Chapter 1, thermoplastic polymers are a good match for lignocellulosic filler reinforced composites, since they offer ease of processing, which includes the ability to be reshaped multiple times without significant degradation. Thus, this chapter aims to assess the potential of BSG as a suitable filler in thermoplastic composites. Among different possibilities, polylactic acid (PLA) and polypropylene (PP) are interesting alternatives. Differing not only in chemical structure and origin but also in their market segments and applications, these two distinct polymers will maximize the relevance and increase the scope of the investigation. This chapter focuses on the development and characterization of environmentally friendly BSG thermoplastic composite materials using PLA and PP. Although both polymers have been extensively studied as matrix in biocomposite materials, comparative studies specifically involving BSG as a filler have not been yet reported. Addressing this lack, this chapter explores the interactions between BSG particles and each matrix, aiming to valorize BSG while contributing to the ongoing efforts to develop more sustainable composite materials. BSG loadings per matrix were made from 10 % (m/m) to 50 % (m/m). The effect of the matrix and filler loading on mechanical, physical, thermal and morphological properties were evaluated to determine which of the matrices and the loadings offer the better balance between performance and sustainability as describes on Figure 3.1.

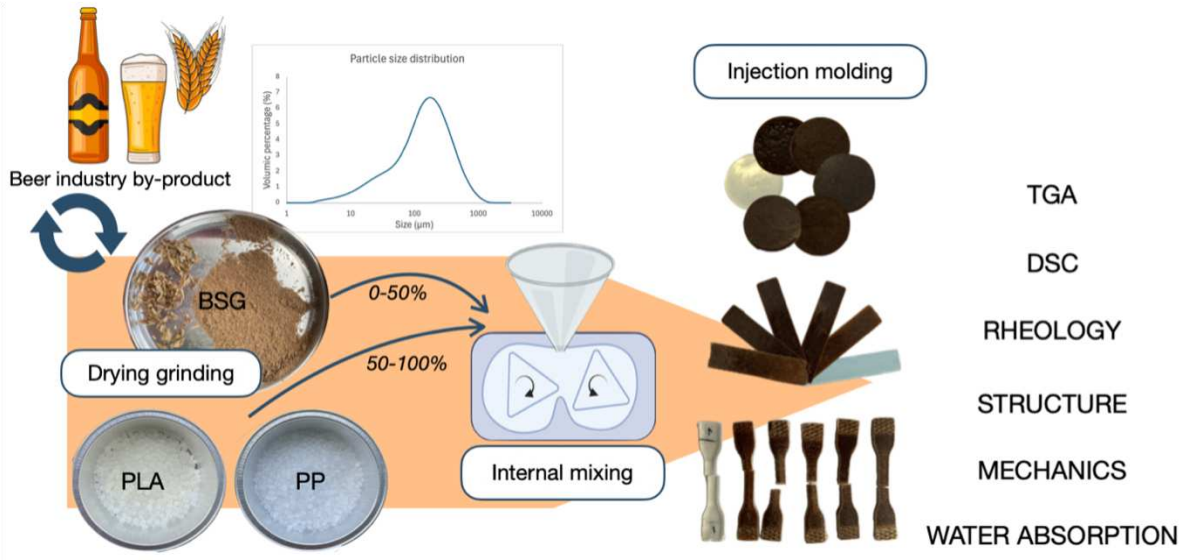


*Figure 3.1: Schematic summary of chapter 3 experiments to elaborate and characterize BSG-PP/PLA composite materials*

## 2. Material preparation

### 2.1. Internal mixing

**Six formulations** per polymer (PLA and PP), including both pure polymers, were processed in the **internal batch mixer** operated at 50 rpm which is a medium speed usually used in literature [57,238,239] and 180°C, a temperature allowing the melting and mixing of both PLA and PP. Torque and temperature were recorded as function of time. Figure 3.3 and Figure 3.2 display the torque and temperature for PP blends and PLA blends, respectively.

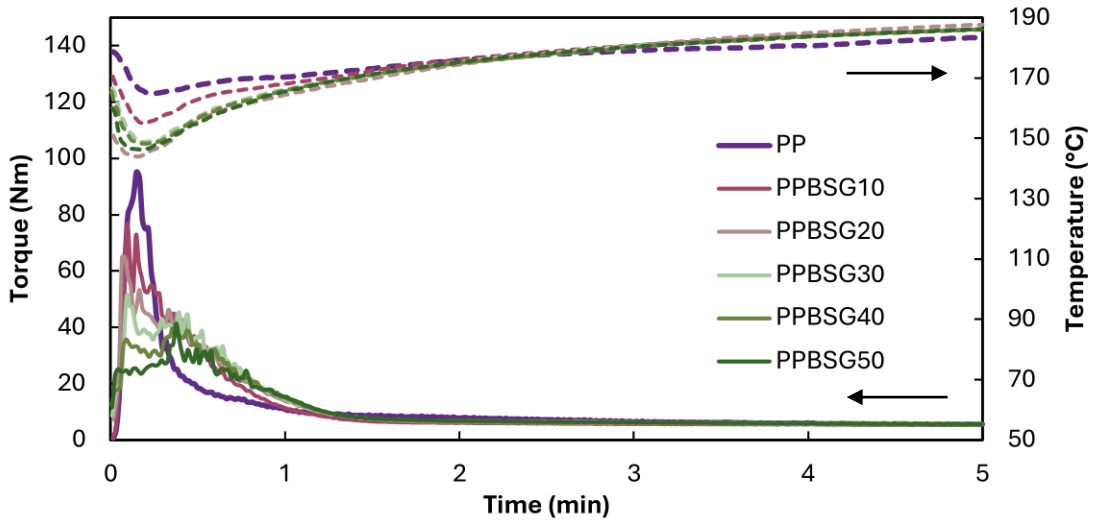


*Figure 3.3: Torque and temperature as function of time during processing of PP and BSG-PP composites at different BSG loadings in internal mixer at 180°C and 50 rpm*

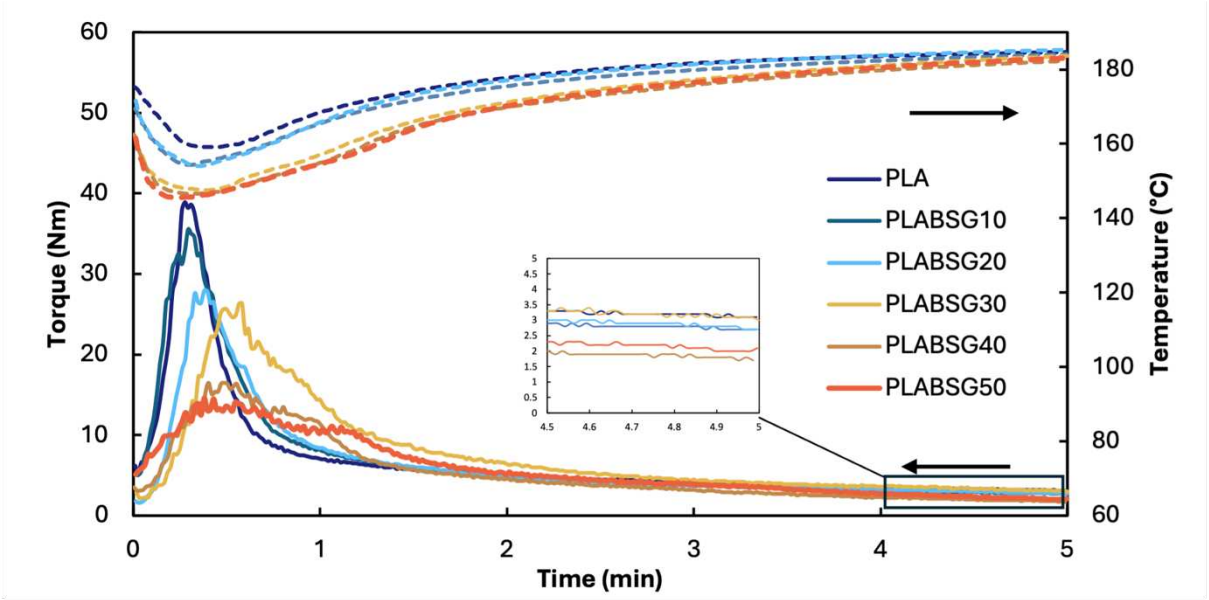


*Figure 3.2: Torque and temperature as function of time during processing of PLA and BSG-PLA composites at different BSG loadings in internal mixer at 180°C and 50 rpm*

On both figures, we can observe an abrupt **increase of the torque** corresponding to the feeding of cold material into the mixer. As time progresses, torque decreases as the polymer melts and attains a **steady state** indicating that homogeneity of the mixture should be reached. The torque fluctuation is related to the work required to **melt, mix**, and **mill** the material [240]. The final torque is an indicator of the resistance of the resulting material. Hence, we expect a bigger final torque for composites with higher content of BSG.

However, on both figures, we can observe that the values of maximum torque are decreasing with BSG content. These results are in accordance with findings reported by Abdoos *et al*. in their work on polypropylene, paraffin wax and stearic acid mix. [240]. One can also acknowledge the presence of shoulder peak (on the right of the main peak) for the sample containing BSG. The width of this shoulder peak increases with BSG content. In their study, Dolezal *et al*. attributed this peak to the breakdown of the filler agglomerates [241]. In our case, the **first peak** corresponds to the **milling and melting** of the matrix and the **shoulder peak** to the **incorporation of the fillers** inside the matrix that lasts until the matrix has entirely melted. Indeed, we can observe that the **torque** decreases at the same as the **temperature** is increasing. Once the temperature reaches the melting temperature of the matrix, the torque becomes steady. In the last two minutes on Figure 3.3 for PP composites, we can observe that the torque is not influenced by the composition since all the curves overlap, suggesting that BSG addition does not greatly influence the energy needed to produce the biocomposites. However, on Figure 3.2 for PLA composites, we can see that steady state seems to be not entirely reached at the end of the process, as the curves do not overlap as in Figure 3.3. This may be due to the internal mixer being **more filled** than in the other formulations. Moreover PLA, being **polar** and having a relatively lower melt viscosity compared to PP, can lead to **stronger interactions** with the filler, which contains numerous hydroxyl groups. This prevents good dispersion and exacerbate **flow irregularities**.

### 2.2. Injection molding

The injection molding temperatures for PLA and PP composites were selected to meet both rheological and thermal properties of each polymer matrix. Indeed, we need to ensure **optimal flow** of the material and thermal stability since the material remains for 6 min in the injection press barrel.

For PP-composites an injection temperature of 200°C was chosen. Indeed, PP exhibits a relatively high melting temperature (~170 °C) compared to PLA (~150 °C) and has a good thermal stability within this range. Thus, processing PP at **200 °C** ensures a sufficient melt flow to

accommodate the high filler loadings. Moreover, as previously observed in chapter 1, the **shear forces** applied during **injection molding** are significantly higher than these generated during **internal mixing**. In our case, we used internal mixing at 50 rpm, average shear rate can be calculating by using the Couette analogy presented in Equation 3.1 [236]:

$$\dot{\gamma} = \frac{2\pi N}{\ln\left(\frac{R_e}{R_i}\right)} \quad (3.1)$$

Where $N$ is the rotor speed (50 rpm), $R_e$ and $R_i$ are the extern and intern rotor radius (20.0 mm and 17.6 mm, respectively, using narrow gap approximation ($(R_e\text{-}R_i)/R_i$ <<1) [236]. Therefore, the average shear rate is ~40 $s^{-1}$. In comparison, shear rates experienced by the material during injection molding reach high shear rates up to $10^4$ $s^{-1}$ when injected through small diameter holes [242].

Hence, at 180 °C, the shear rates experienced by PP during injection are too high compared to the **crossover point** (angular frequency where the loss modulus is equal to the storage modulus). Above this crossover point, the storage modulus is higher than the loss modulus indicating a predominantly elastic behavior of the PP. By increasing the temperature to 200 °C, the **viscoelastic response of PP** is shift towards higher angular frequencies (or higher shear rates), thereby improving processability because the shear window where loss modulus is higher than elastic modulus is extended. On Figure 3.4 shows the crossover point of PP. This value increases with increasing temperature, notably from 180° to 200°, demonstrating improved processability.

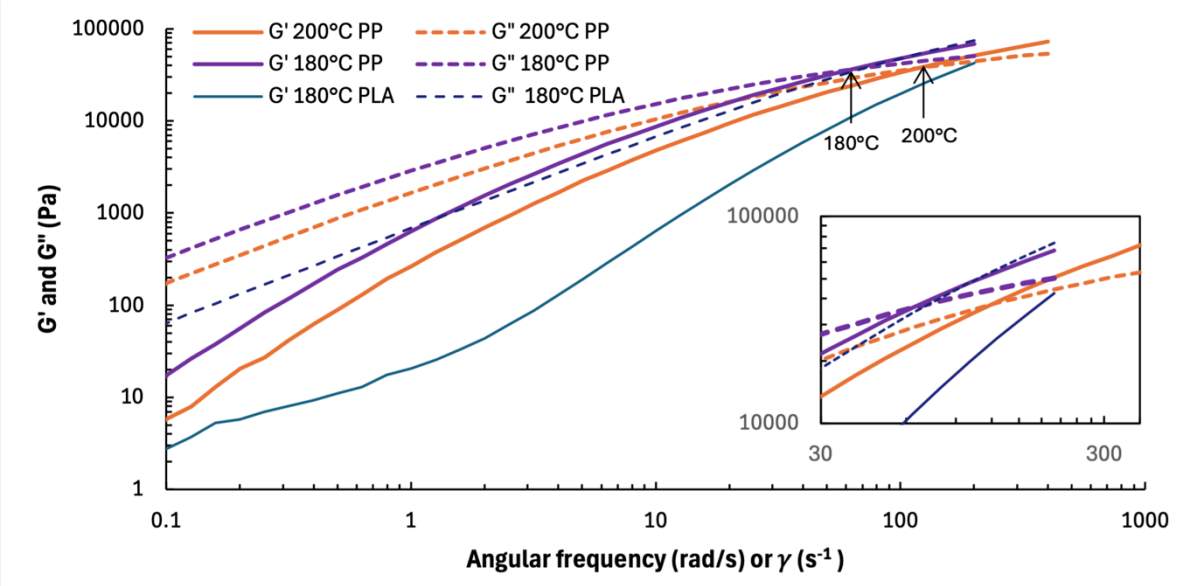


*Figure 3.4: Log G' and Log G" vs. Log angular frequency of pure PP at 180 and 200°C and PLA at 180 °C, with highlighted crossover points*

Conversely, PLA-composites injection temperature was maintained to 180 °C. Indeed, as discussed in chapter 1, PLA has a lower thermal stability. Hence, PLA composites were injected at a lower temperature which corresponds to the internal mixing temperature to **preserve thermal integrity**. Moreover, the crossover point of PLA does not appear within the studied range of frequencies as seen in Figure 3.4, its processability remains good at 180 °C. This behavior for pure PLA has been observed in literature [243].

## 3. Thermal degradation behavior

To obtain information on composition and thermal resistance to degradation, thermogravimetric analyses were carried out on all formulations. Table 3.1 gathers the temperatures reached at maximum mass loss rates for BSG, PP, PLA, and composites.

*Table 3.1: Temperatures reached at maximum degradation rates for biocomposites made with BSG and PP or PLA. The values represent the mean of triplicate measurements, with standard deviations indicated. Different letters (a, b, c) indicate statistically significant differences.*

| Material | Sample Code | Temp 1st peak (°C) *Hemicellulose* | Temp 2nd peak (°C) *Cellulose* | Temp 3rd peak (°C) *Matrix* |
|---|---|---|---|---|
| BSG (ground) | BSG | **297.6**$^{a}$ ± 0.6 | **347.1**$^{a}$ ± 6.3 | - |
| Polypropylene (PP) | PP | - | - | **444.5**$^{a}$ ± 10.2 |
| | PPBSG10 | **294.0**$^{b}$ ± 0.6 | - | **452.5**$^{ab}$ ± 3.2 |
| | PPBSG20 | **294.4**$^{b}$ ± 0.7 | **355.4**$^{a}$ ± 1.4 | **461.5**$^{bc}$ ± 2.3 |
| | PPBSG30 | **296.3**$^{ab}$ ± 0.9 | **354.8**$^{a}$ ± 1.6 | **460.7**$^{bc}$ ± 3.2 |
| | PPBSG40 | **295.3**$^{ab}$ ± 1.1 | **354.9**$^{a}$ ± 0.7 | **460.2**$^{bc}$ ± 3.3 |
| | PPBSG50 | **293.9**$^{b}$ ± 1.0 | **355.5**$^{a}$ ± 1.1 | **467.8**$^{c}$ ± 0.6 |
| Polylactic acid (PLA) | PLA | - | - | **366.4**$^{a}$ ± 1.8 |
| | PLABSG10 | - | - | **365.0**$^{a}$ ± 1.2 |
| | PLABSG20 | - | - | **364.4**$^{a}$ ± 0.9 |
| | PLABSG30 | - | - | **362.6**$^{ab}$ ± 0.9 |
| | PLABSG40 | - | - | **359.3**$^{b}$ ± 1.1 |
| | PLABSG50 | **299.0**$^{a}$ ± 2.0 | - | **359.2**$^{b}$ ± 1.0 |

Regarding pure BSG thermal degradation profile displayed on Figure 3.5, the **initial pyrolysis step** begins at around **175 °C** and is characterized by a shoulder corresponding to the

**lightest volatile compounds** in BSG. Sobek *et al*. conducted research on BSG pyrolysis kinetics and observed a similar profile attributed to the lightest volatile fractions of BSG [232]. Using a deconvolution procedure, these authors identified three pseudo-components, attributed respectively to hemicelluloses, cellulose and lignins, from the most volatile to the least volatile. These results on BSG are perfectly consistent with the pyrolysis of the **three primary components** of lignocellulosic biomass [232,244,245]. All these works suggest then that the first shoulder of Figure 3.5 represents the volatilization of lightest components. This shoulder extends until the **first sharp peak**, which represents the maximum mass loss rate reached at 297.6 ± 0.6 °C, clear signature of the fast decomposition of **hemicellulose** [244,245]. Following this, a **second sharp peak** detaches, attaining its optimal point at 347.1 ± 6.3 °C, related to **cellulose** [232]. The significant overlapping of the peaks highlights the intricacy of BSG composition. Nevertheless, BSG starts to degrade at a low temperature regarding the temperatures reached during thermoplastic material processing. Indeed, we observed **1 % mass loss at 180 °C** after 40 min and **3 % at 210 °C** after 43 min.

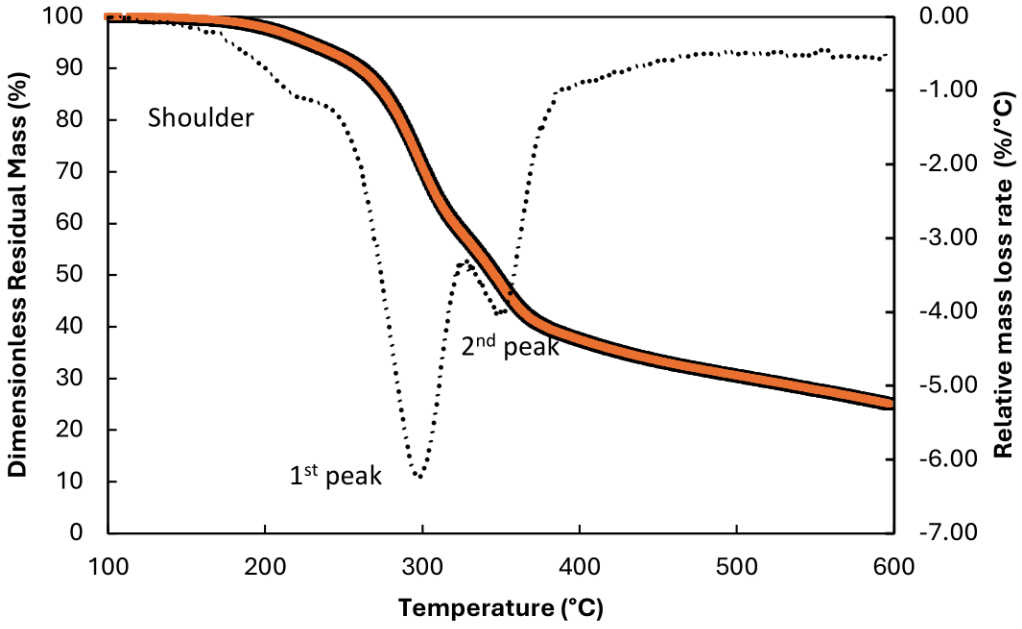


*Figure 3.5: Thermogravimetric Analysis of dry and ground BSG. Relative mass loss and its derivative curves showing decomposition rate as a function of temperature (10 K/min under nitrogen flow). Average of three experiments.*

Only a **single degradation** peak, consequence of the homogeneous nature of the polymers, was observed for **PP** and **PLA**. PP reaches its maximum degradation rate at 444.5 ± 10.2 °C while PLA degradation peak occurs at 366.4 ± 1.8 °C which is consistent with published

studies [246–248]. Surprisingly, PP exhibits a highly variable degradation temperature, as indicated by its large standard deviation compared to PLA. This suggests greater inconsistency in the thermal stability of PP whereas PLA shows more consistent thermal behavior. A similar dispersity between PP degradation temperatures was also observed by Stawski [249].

Analysis of Figure 3.6 reveals an interesting **degradation pattern** of PP-composites. Firstly, the degradation temperatures of BSG exhibit relative consistency across the composites, indicating that PP does not significantly influence the thermal stability of BSG. Indeed, the first peak occurs at similar temperatures, irrespective of the presence or content of PP. The **hemicellulose** of BSG appears to degrade marginally **earlier** in the composites compared to pure BSG. However, this difference is minimal and may be attributed to the composite **manufacturing process**, which could have **weakened** the BSG.

Secondly and in contrast, the degradation behavior of PP is substantially affected by the presence of BSG. As observed in the third peak, the degradation temperature of PP **increases** with **higher BSG** content, suggesting that BSG provides a **protective effect**. Specifically, the PPBSG50 composite exhibits a maximum degradation temperature of 467.8 °C, which is significantly higher than the 444.5 °C of pure PP. This implies that the BSG filler acts as a thermal barrier, **delaying the onset of PP degradation** and enhancing the **thermal stability** of the composite. This trend is in line with previous studies with other biomasses [60]. Such behavior could be attributed to the **char layer formation** from BSG during thermal degradation, which impedes heat transfer to the polymer matrix, thus protecting PP from premature degradation.

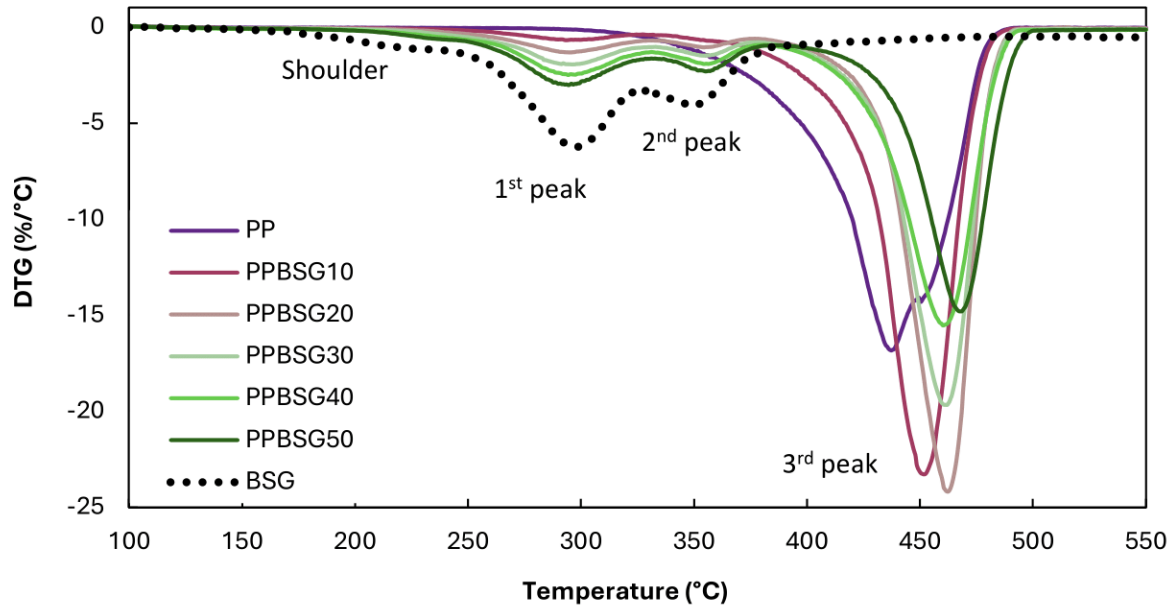


*Figure 3.6: Thermogravimetric analysis of biocomposites made with BSG and PP. DTG curves showing decomposition rate as a function of temperature (10 K/min under nitrogen flow). Average of three experiments.*

Furthermore, the standard deviations associated with the third peak for PP degradation demonstrate a marked decrease as the BSG content increases (Table 3.1). For pure PP, the degradation temperature exhibits relatively high variability (± 10.2 °C, 2.3 %), whereas in the composites with higher BSG content, the variability reduces significantly (± 0.6 °C, 0.1 % for PPBSG50). This reduction in variability suggests that BSG contributes to standardizing the degradation temperature of PP, likely by creating a more uniform thermal environment within the composite during heating. This stabilization effect highlights the potential of BSG to enhance the thermal consistency of PP-based composites, making them more reliable under thermal stress. The enhanced thermal consistency may lead to improved quality control during manufacturing and more predictable performance in end-use applications. It can also enable the use of higher temperatures for processing to allow an easier flow and better mold filling for example in the case of injection molding.

On Figure 3.7, PLA composites reveal a **different trend** of degradation. In the composite samples, particularly at lower content of filler, the first peak of BSG degradation appears as a shoulder that tends to overlap and partially fuse with PLA degradation peak. As the BSG content increases in the composites, the first peak of BSG degradation becomes more pronounced and starts to separate from the main PLA degradation peak. For example, in PLABSG50, BSG degradation 1$^{st}$ peak becomes distinct and appears at 359.2 °C. The standard deviations for PLA degradation peak (3$^{rd}$ peak) are relatively small and consistent across the samples. Furthermore, the PLA degradation temperature decreases as the BSG content increases. In the PLABSG50 composite, PLA degrades at 359.2 °C, compared to 366.4 °C for pure PLA. This behavior has been observed in literature where it was observed that potassium present in the filler acted as catalyser for PLA degradation [199]. It is plausible that BSG acts as a **catalyst**, facilitating the **breakdown of PLA** during thermal degradation by providing reactive sites or transferring heat more effectively. This behavior might be exacerbated under air atmosphere for example during internal mixing. This hypothesis has been confirmed through **SEC analysis**, which reveals clear evidence of PLA chain scission when mixed with BSG. Indeed, upon adding 10 %(m/m) of BSG, the number-average molecular mass (*Mn*) of PLA decreased by 27 %, and at 50 %(m/m) incorporation, the reduction in PLA's *Mn* reached 48 % (Figure 3.8).

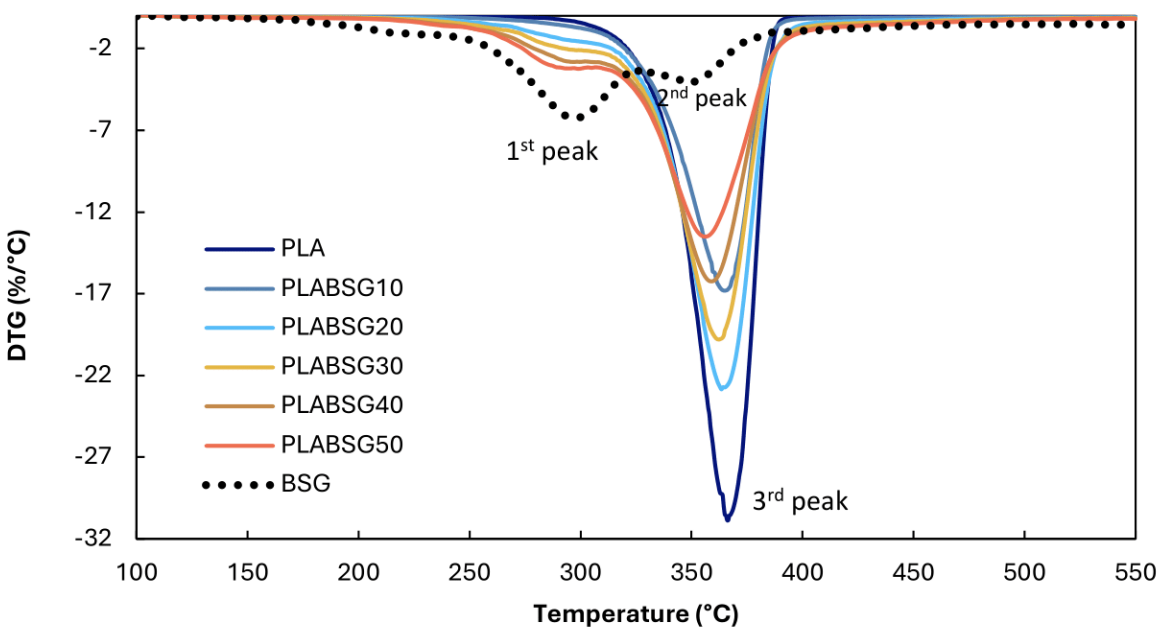


*Figure 3.7: Thermogravimetric analysis of biocomposites made with BSG and PLA. DTG curves showing decomposition rate as a function of temperature (10 K/min under nitrogen flow). Average of three experiments.*

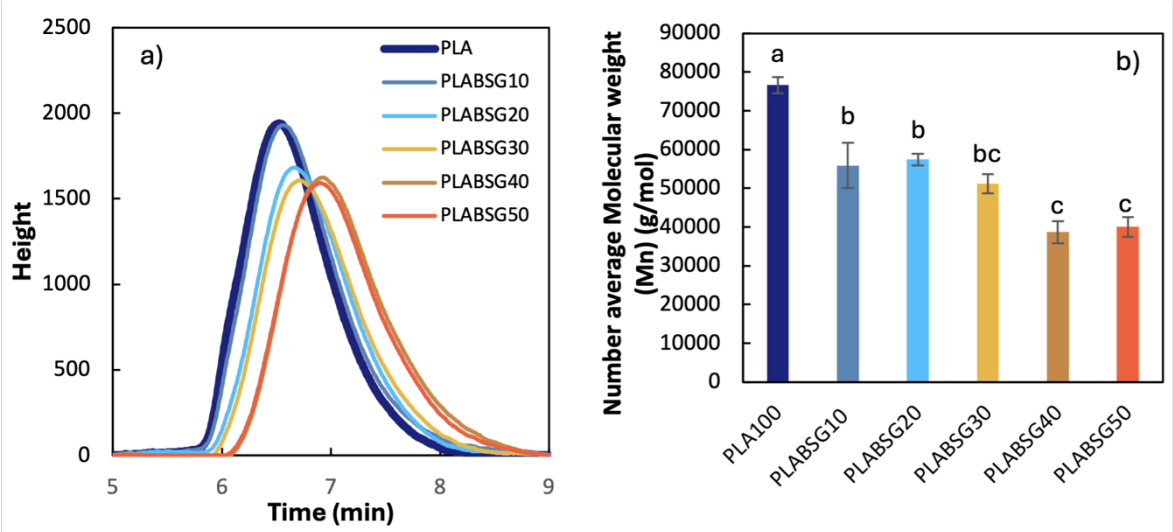


*Figure 3.8: Detection of PLA molecules using refractive index as function of elution time (a) and comparison of the number average molecular weight (Mn) of PLA composites (b) after internal mixing and injection molding. Different letters (a,b,c) indicate statistically significant differences between samples.*

To conclude, while **PP** seems to be preserved by the **char layer** formed by BSG, **PLA** degradation seems to be enhanced by some **thermal degradation products** of BSG. This is likely due to the very different degradation temperature of both polymers, PP degrading far beyond BSG while PLA degrades within the same range of temperature. Moreover, PLA shows **reactive sites**, which contribute both to its **biodegradability** and to its **susceptibility to depolymerization**. Its polymer chains can be easily cleaved, leading to decomposition into carbon dioxide, water, or

methane under the influence of inducers and heat. In contrast, PP lacks such easily cleavable bonds, its degradation proceeds via free radicals, which require more energy to form.

## 4. Thermal transition behavior

DSC analyses were carried out to determine characteristic temperatures and obtain information on the microstructure of the different formulations. Figure 3.9 and Figure 3.10 shows the DSC curves of PP and PLA composites.

For PP (Figure 3.9), both first cooling and the second heating curves were analyzed to show its crystallization and melting behavior, respectively. During the heating cycle, the melting temperature ($T_m$) and the degree of crystallinity ($\chi_c$) were determined. The cooling curve was used to determine the crystallization temperature ($T_c$).

In contrast, PLA exhibits a different thermal behavior characterized by the absence of crystallization under typical cooling rates. Thus, only the second heating curve was used to assess its glass transition temperature ($T_g$), its melting temperature ($T_m$), and its cold crystallization temperature ($T_{cc}$) (Figure 3.10).

Table 3.2 presents the results of measured $T_c$, $T_m$, $T_{cc}$, $T_g$ and $\chi_c$ for the pure polymers and BSG composites.

During cooling, as seen in Figure 3.9, the neat PP exhibits an exothermic peak corresponding to its crystallization occurring at **117.4 °C** which is consistent with previous studies [250]. With the addition of fillers, the **crystallization temperature** tends to decrease, and for PP with 50 %(m/m) BSG, crystallization occurs around **113.5 °C**, indicating a **delayed crystallization**. The crystallization process of PP might be hindered by an increased BSG content, causing a shift to lower temperatures. This phenomenon may be attributed to the restriction of polymer chain mobility by BSG [60,251].

Although the comparison of $T_m$ did not reach statistical significance (Table 3.2), a noticeable trend is observed for the temperature of melting, where fillers seem to have a negative impact on $T_m$. Pure PP melts around **167.0 °C**, while PP with 50 %(m/m) fillers melts around **164.2 °C**, indicating **lower interactions between PP chains** due to the presence of BSG. In the end, crystallization rate of PP and of its composites does not appear to differ significantly.

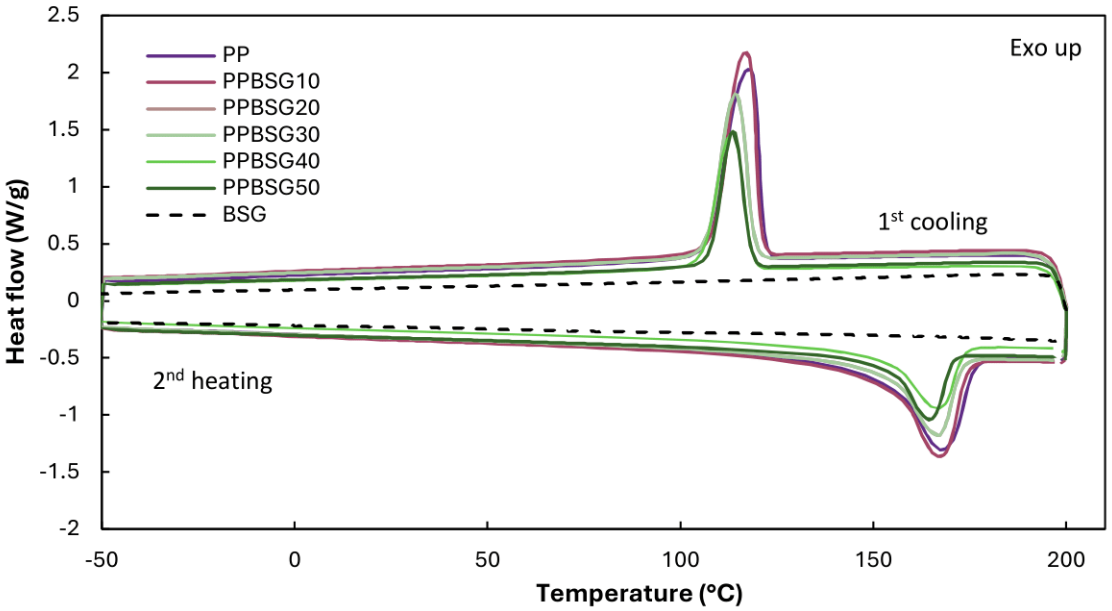


*Figure 3.9: Differential scanning calorimetry curves of pure BSG, injected PP and composites at 10 K/min, under nitrogen atmosphere*

Regarding PLA thermal transitions, the accurate determination of crystallization rates from DSC data needs distinct and well-separated crystallization and melting peaks. In the current study, the thermal events corresponding to cold crystallization and melting were closely overlapped, making it difficult to accurately define the onset and end temperatures for these transitions. Consequently, the integration limits for calculating the enthalpy of crystallization were not well-defined, leading to imprecise quantification of the crystallization rate. Thus, it led to anomalous crystallization rates close to 0 but yielding slightly negative values which is physically impossible. Therefore, these values were set to zero.

The $T_g$ for neat PLA was observed at **59.9 °C**, whereas with the incorporation of BSG, the $T_g$ decreased, reaching **54.6 °C** for PLABSG50. This reduction in $T_g$ suggests that BSG enhances the **ductility of PLA matrix**, by spacing PLA chains apart, potentially increasing the polymer chain mobility of the amorphous regions by reducing weak interactions.

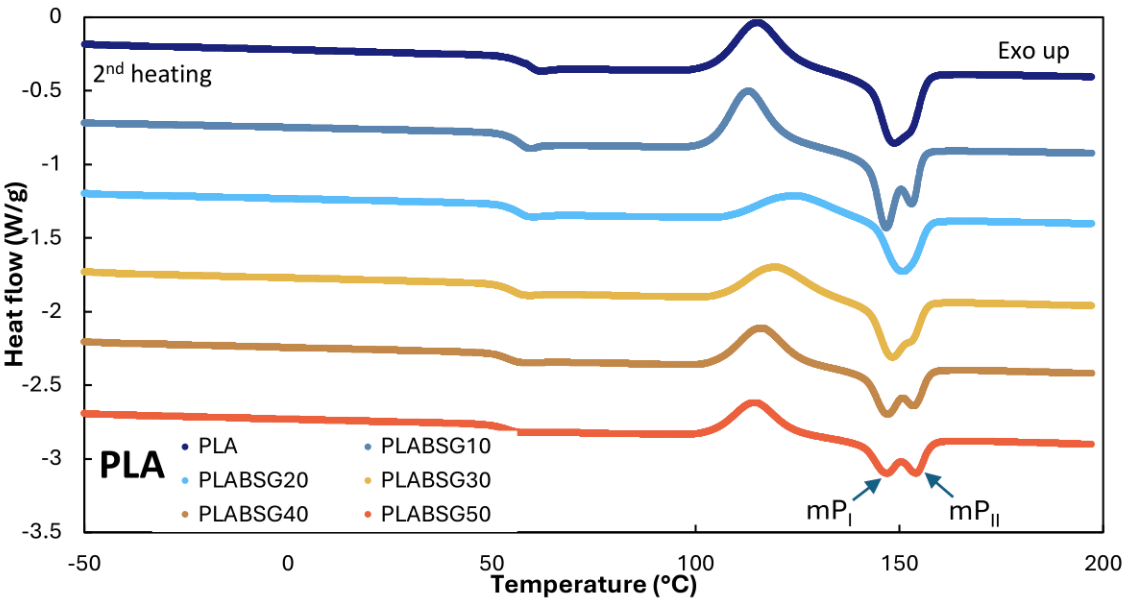


*Figure 3.10: Differential scanning calorimetry curves of injected PLA and composites at 10 K/min, under nitrogen atmosphere.*

An additional factor contributing to the lower $T_g$ could be that early thermal decomposition products of BSG could have initiated PLA chains hydrolysis during internal mixing process [59]. This hypothesis has been confirmed through SEC analysis, which reveals clear evidence of **chain scission** (Figure 3.8). Moreover, residual moisture in BSG may have also induced hydrolytic degradation of the PLA chains, resulting in chain scission and a consequent reduction in the molecular weight of the PLA. Decreased molecular weight typically leads to enhanced chain mobility and a corresponding decrease in $T_g$. Indeed, a higher number of chain ends causes the existence of a **higher free volume** enhancing chains mobility [39]. This effect is particularly pronounced at higher BSG loadings, as observed in the PLABSG40 and PLABSG50 composites. As the decrease in $T_g$ may be attributed to BSG thermal degradation products enhancing PLA chain scission, higher BSG concentrations could amplify this effect. Along the same lines, Zhang *et al.* showed the molecular weight dependence of glass transition temperature in their study on amorphous Poly-L-Lactic Acid system [252]. This correlation has also been highlighted by others [35].

The $\boldsymbol{T_{cc}}$ of PLA composites also varied with BSG content (Table 3.2). Indeed, for pure PLA, the $T_{cc}$ was observed at **115.9 °C**. In the PLABSG10 composite, the $T_{cc}$ decreased to **113.4 °C,** but surprisingly, it increased to **124.7 °C** in PLABSG20, before slightly decreasing again for composites with higher BSG content, such as PLABSG50, where $T_{cc}$ was recorded at **115.7 °C**. There is likely a **dual effect** of BSG on the crystallization behavior of PLA. First, BSG's thermal

degradation products tend to **reduce the molecular weight** of PLA during processing, which in turn lowers the $T_{cc}$ [35]. Second, BSG may physically **hinder the propagation of crystals** delaying the $T_{cc}$. At **low BSG content**, the **chain scission** effect seems to dominate, leading to a probable reduction in molecular weight and lowering $T_{cc}$. At **moderate BSG content**, the **physical barrier** hindering crystals propagation becomes more prominent, causing delays in $T_{cc}$. At **high BSG content**, the composite system might experience a **"phase separation" with the agglomeration of the excess particles** which could lead to localized regions where PLA crystallization behavior resembles the behavior seen in PLABSG10. This highlights the dual effect of BSG on thermal events of the composites. Mofokeng *et al.* also observed a dual effect of sisal on PLA chain mobility and stated that fibres can contribute to both nucleation and immobilization of PLA chains [60].

Turning now to the **melting transition**, Figure 3.10 shows the presence of **double melting** peaks for some PLA composite formulations. This indicates that the presence of BSG may amplify the formation of a **second type of crystal** within the PLA matrix. The **first** melting peak ($mP_I$) is associated with the melting of **less stable** crystals, while the **second** melting peak ($mP_{II}$) corresponds to **more stable** crystals that likely form through **recrystallization** (corresponding to exothermic peak between $mP_I$ and $mP_{II}$) [234].

However, in PLABSG20, where cold crystallization is **delayed** (as evidenced by higher $T_{cc}$ values), a different behavior is observed and highlighted by the appearance of a **single melting peak** seen in all replicates. In these cases, the $mP_I$ **overlaps** with the $mP_{II}$. A crystallization happening at higher temperature suggests the formation of more stable crystal forms named **α- crystals** [39]. In PLABSG30, the double melting peak is present but less distinct, indicating that the formation of the second type of crystal is **partially hindered**, possibly due to the overlapping melting transitions of the two types of crystals. In their study on Poly-L-Lactic Acid crystallization behavior, Lorenzo *et al.* highlighted the dependence between $T_{cc}$ and the presence of the first melting peak [253]. They stated that $T_{cc}$ > 120 °C (as it is the case for PLABSG20 and PLABSG30) induces a merge between the two melting peaks and recrystallization peak due to the lower extend of the recrystallization process. Moreover, they found that a $\boldsymbol{T_{cc}}$ **< 120 °C** leads to **imperfect crystals** that show tendency to **reorganize** through an exothermal peak between the two melting transition peaks [253].

While we did not observe a significant crystal rate in PLA composites (Table 3.2), although it is important to note that crystallization behavior may have consequences on mechanical properties. Indeed, crystal structure can affect the overall material properties. As we observed,

some composites showed the presence of two types of crystals highlighted by the two melting peaks. Less stables crystals reflect a looser and less ordered chain packing which consequences lead to a lower modulus and barrier properties [39]. However, in the present conditions, PLA remains amorphous in the solid state which prevents any mechanical consequences due to crystals.

As for PLA the influence of BSG content on crystallization rate of PP composites was negligible. However, PP composites appeared to show an increasing delay in their transition temperatures with increasing BSG content suggesting a physical effect of BSG which could act as a **barrier** hindering polymer chain mobility [60]. Such hinderance could be especially noticeable in the rheological behavior of the composites, which is examined in detail in the following section. Special care must be taken when choosing the process conditions especially the **cooling rate** to optimize processing parameters for desired material performance.

*Table 3.2: DSC data of PP, PLA and their composites after internal mixing and injection molding. Different letters (a,b,c) indicate statistically significant differences between samples.*

| Material | Sample Code | $T_g$ (°C) | $T_{cc}$ (°C) | $T_c$ (°C) | $T_m$ (°C) | $\chi c$ (%) |
|---|---|---|---|---|---|---|
| BSG | BSG | - | - | - | - | - |
| PP | PP | - | - | **117.4**$^{a}$ ±0.5 | **167.0**$^{a}$ ±0.8 | **40.9**$^{a}$ ±1.1 |
| | PPBSG10 | - | - | **117.5**$^{ab}$ ±0.4 | **166.2**$^{a}$ ±1.0 | **42.8**$^{a}$ ±0.7 |
| | PPBSG20 | - | - | **116.4**$^{b}$ ±0.9 | **165.5**$^{a}$ ±1.1 | **40.3**$^{a}$ ±6.3 |
| | PPBSG30 | - | - | **114.7**$^{c}$ ±0.4 | **165.6**$^{a}$ ±1.0 | **40.9**$^{a}$ ±2.4 |
| | PPBSG40 | - | - | **113.4**$^{c}$ ±0.3 | **166.0**$^{a}$ ±0.5 | **41.7**$^{a}$ ±4.3 |
| | PPBSG50 | - | - | **113.5**$^{c}$ ±0.1 | **164.2**$^{a}$ ±0.5 | **43.0**$^{a}$ ±2.0 |
| PLA | PLA | **59.9**$^{a}$ ± 0.7 | **115.9**$^{a}$ ±0.9 | - | **150.2**$^{a}$ ±2.3 | **0.6** |
| | PLABSG10 | **57.3**$^{b}$ ±0.3 | **113.4**$^{b}$ ±0.2 | - | **147.3**$^{a}$ ±0.5 | **~0** |
| | PLABSG20 | **56.7**$^{bc}$ ±0.1 | **124.7**$^{c}$ ±0.4 | - | **150.4**$^{a}$ ±0.4 | **~0** |
| | PLABSG30 | **55.5**$^{cd}$ ±0.1 | **120.5**$^{d}$ ±0.3 | - | **148.5**$^{a}$ ±0.2 | **~0** |
| | PLABSG40 | **54.0**$^{e}$ ±0.4 | **115.9**$^{a}$ ±0.9 | - | **146.6**$^{a}$ ±0.8 | **~0** |
| | PLABSG50 | **54.6**$^{de}$ ±0.5 | **115.7**$^{a}$ ±0.6 | - | **148.0**$^{a}$ ±0.7 | **~0** |

## 5. Rheological behavior

### 5.1. Strain sweep

To ensure that frequency sweep experiments are done in the linear viscoelastic domain, strain sweep test were assessed. On Figure 3.11and Figure 3.12 we can see the storage modulus of PP and PLA composites, respectively, against strain in percentage.

On figure, the storage modulus (G') exhibits a significant decrease as the strain amplitude increases. Moreover, as frequently presented in the literature, the linear viscoelastic domain diminishes as the filler content increases. The linear viscoelastic domain extends to 20 % for pure and to 0.05 % for PPBSG50.

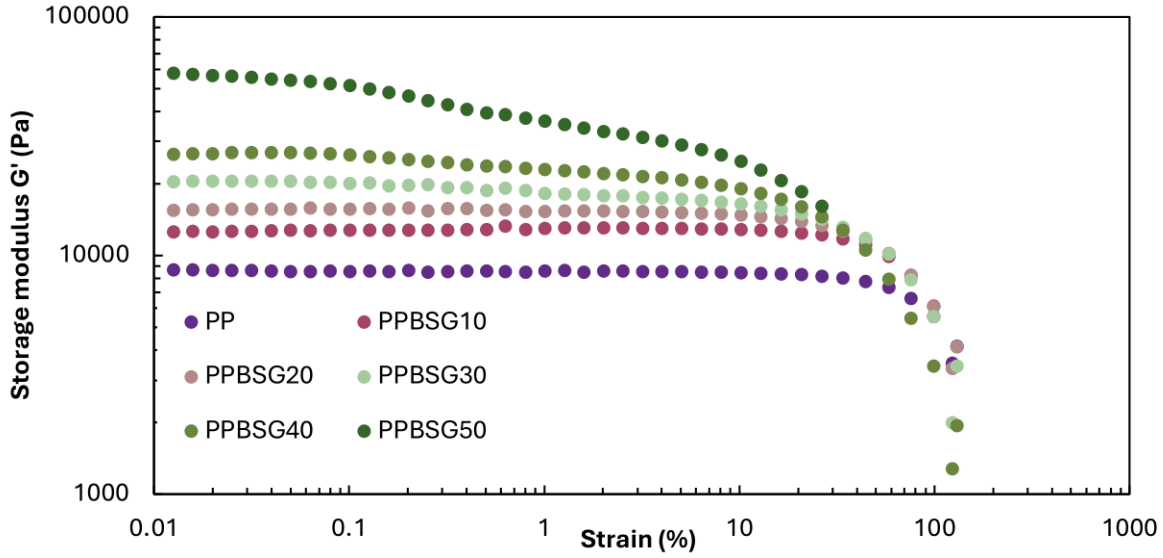


*Figure 3.11: Log G' vs Log strain and 10 rad/s in plate-plate rheometer at 180 °C for PP and PP composites processed at 180 °C in internal mixer at 180 °C and injected at 200 °C, plate-plate gap = 2200 µm, plate diameter = 25 mm*

Conversely to PP, there is a **strong cleavage** in the rheological behavior of PLA blends. On the one hand, neat PLA, PLABSG10 and PLABSG20 curves show the **same trend** with a very **long** linear viscoelastic domain which covers the whole investigated strain amplitude range. On the other hand, PLABSG30, PLABSG40, and PLABSG50 present a **short plateau** since G' drops drastically from 0.1 % strain. The critical strain values of each composite slightly decrease as the amount of BSG content increases. For instance, PLABSG50 and PLABSG40 show a critical value of 0.05 %, PLABSG30 presents a maximal critical strain value of 0.1 % while PLABSG20 maximal critical strain value is 10 %. In their study on PLA/lignin biocomposites, Anuar *et al.* chose 10 % as a maximal critical strain value for composite filled with 1 % lignin to remain in the linear viscoelastic region [184].

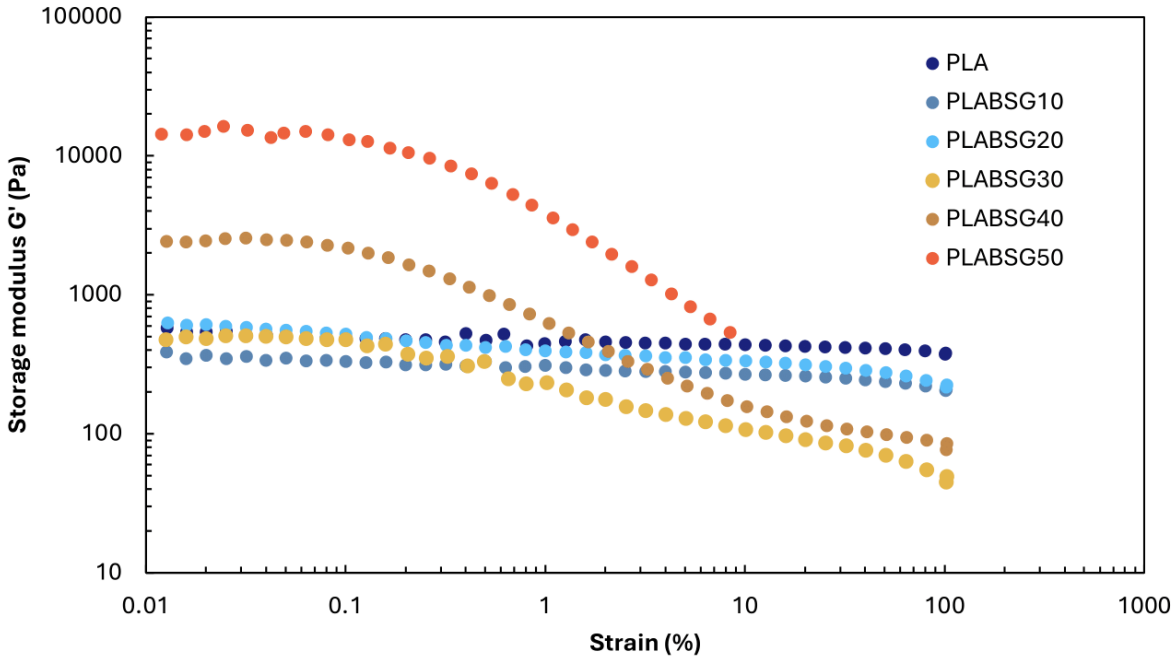


*Figure 3.12: Log G' vs Log strain and 10 rad/s in plate rheometer at 180°C for PLA and PLA composites processed at 180°C in internal mixer and injected at 180°C, plate-plate gap = 2200 µm, plate diameter = 25mm*

From the strain sweep analysis of PLA (Figure 3.12), three groups of behavior can be distinguished: PLA filled with 40–50 % (m/m) BSG, PLA with 30 %(m/m) BSG, and PLA filled with 0–20 %(m/m) BSG. These groups reflect the trends observed during internal mixing, particularly in the torque versus time curves, where a clear distinction appears for the highly filled composites (PLABSG40 and PLABSG50).

As discussed in Chapter 1 (Equation 1.3), the **maximum packing fraction** can be estimated using true density (1.353 ± 0.019 g/cm$^3$) and bulk density (0.540 ± 0.016 g/cm$^3$) of BSG. Hence, the calculated maximum packing fraction ($\Phi_m$) is approximately **39.9 ± 1.3 vol.%.** Referring to Chapter 2 (Table 2.1), the particle volume fraction of PLABSG40 and PLABSG50 are **38.2** and **48.1 vol.%** respectively. This indicates that PLABSG50 is above the maximum packing fraction, and PLABSG40 is near it. It is still possible to mix such a high filler content in an internal mixer, but this may lead to some inhomogeneity in the dispersion. Therefore, both formulations can result in **disturbance of the flow** of the material.

These behaviors will be further discussed in the following section (5.2. ).

Having defined the linear viscoelastic domain will allow us to proceed with the frequency sweep tests in which we select a strain compatible to remain in the linear-viscoelastic domain.

### 5.2. Frequency sweep

To better understand the interactions between BSG and the polymer chains in our biocomposites, it is very useful to observe the behavior of their elastic moduli and complex viscosity in the molten state at low frequencies, in the so-called flow zone. Figure 3.13, Figure 3.14, Figure 3.15 and Figure 3.16 present the evolution of *G'* and complex viscosity with frequency for PP-BSG and PLA-BSG composites at different filler contents.

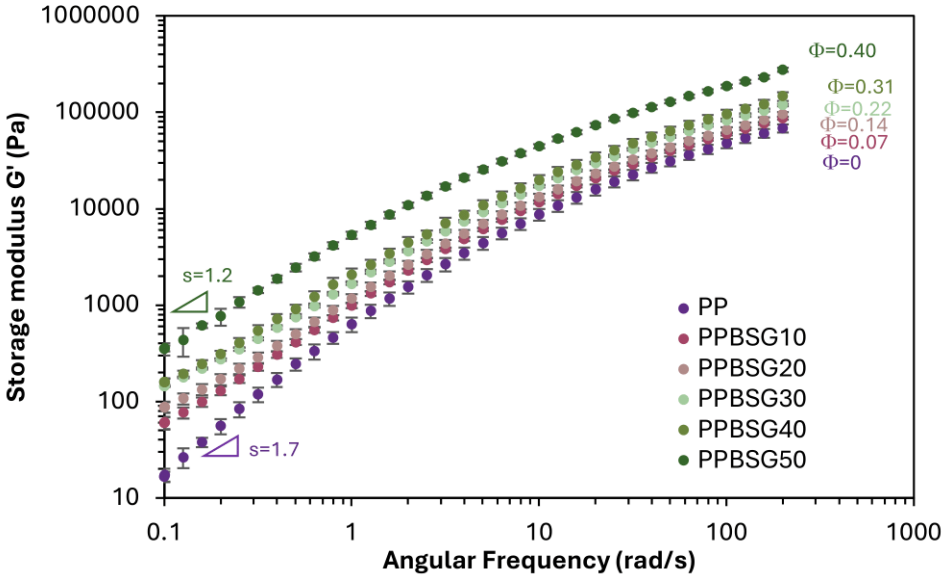


*Figure 3.13: Effects of BSG ratio on storage modulus (Pa) vs. angular frequency (rad/s) in plate-plate rheometer at 180 °C for PP and PP composites processed at 180 °C in internal mixer at 180 °C and injected at 200°C Φ= volume fraction of BSG, s= slope of the curve, plate-plate gap = 2200 µm, plate diameter = 25 mm, strain = 10 % for PP, PPBSG10, PPBSG20, 0.05 % for composites with 30, 40 and 50 %(m/m) BSG. Average of three experiments.*

For the PP-BSG composites, ***G'* systematically increased** with increasing filler fraction, indicating enhanced stiffness due to the presence of BSG (Figure 3.13). This behavior has also been observed by Guo *et al.* in similar filler loadings for glass fibers reinforced LLDPE [254]. Moreover, at low frequencies, pure PP exhibits a slope of 1.7 whereas PP filled with 50 %(m/m) has slope of 1.2. This decrease reflects the impact of the filler on the elasticity response of the composites.

Looking at the **complex viscosity** (Figure 3.14), a shear-thinning behavior is observed [255–258]. In all PP composites, irrespective of the BSG content, the **onset of shear thinning** occurs at approximately the **same frequency** (in the range 0.2 to 0.5 rad/s). It was shown in literature that the incorporation of particles systematically increases the storage modulus, as well as the loss modulus and complex viscosity [255,256,259,260]. This increase is attributed to the

particles acting as obstacles, resisting the recovery of the polymer chains under strain and thus enhancing the overall stiffness of the system.

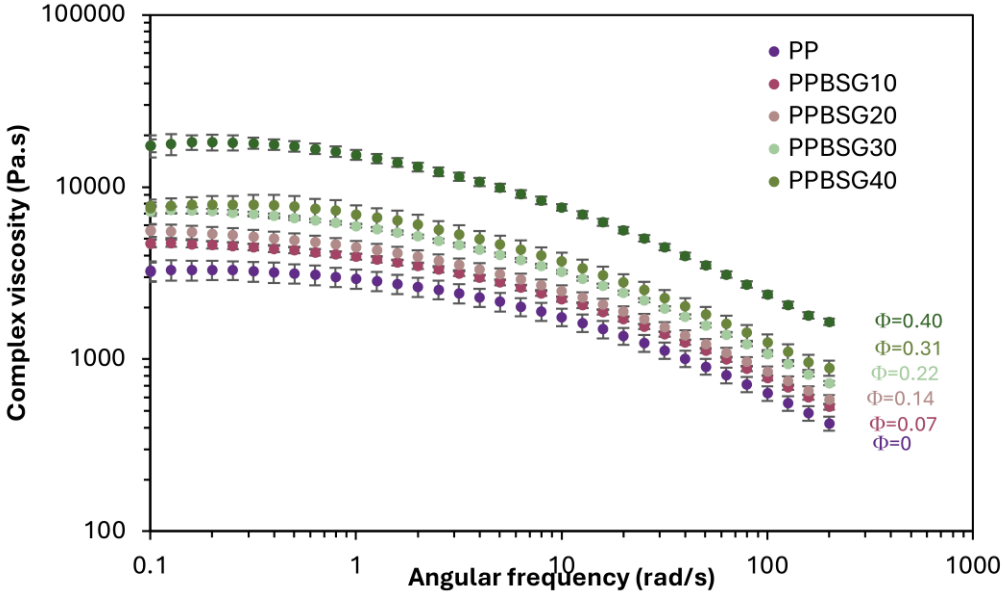


*Figure 3.14: Effects of BSG ratio on complex viscosity (Pa.s) vs. angular frequency (rad/s) in plate-plate rheometer at 180 °C for PP and PP composites processed at 180 °C in internal mixer at 180 °C and injected at 200 °C Φ= volume fraction of BSG, plate-plate gap = 2200 µm, plate diameter = 25 mm, strain = 10 % for PP, PPBSG10, PPBSG20, 0.05 % for composites with 30, 40 and 50 %(m/m) BSG. Average of three experiments.*

Lastly, it's worth noting that the incorporation of BSG does **not alter the overall shape** of the *G'* and viscosity curves of PP composites suggesting **little interactions** between BSG and PP.

In contrast, the behavior of **PLA-BSG composites** differs significantly (Figure 3.15 and Figure 3.16). While a decreasing *G'* with decreasing frequency is still observed, a **two-stage behavior and a plateau** in between at intermediate frequencies (1-10 rad/s) can be observed for pure PLA, PLABSG10, and PLABSG20. Although the plateau in the PLA curve is very limited, it becomes more pronounced and shifted to higher frequencies upon the incorporation of 10 % and 20 % BSG. This behavior has been observed in literature, although not described [184]. It may be related to **temporary entanglements** or **interactions** between the BSG filler and the PLA matrix. With increasing BSG content this plateau shifts to lower frequencies where it may be indicative of a **percolated network**, where the filler concentration reaches a critical level close to the **percolation threshold**, forming a continuous structure throughout the polymer matrix [255,260,261]. This percolated network restricts the mobility of the polymer chains, preventing their complete relaxation and maintaining a constant G' at low frequencies. This plateau may also be indicative of the state of dispersion since **flocculation of particles** is observable through

a *G'* plateau at very low frequency [203]. This aligns with our DSC and internal mixing observations and supports the hypothesis of particles flocculation leading to a phase separation at higher filler content. One can also observe a brutal change in the *G'* slope at high frequencies between low-filled composites (PLA, PLABSG10, PLABGS20) and high-filled systems (PLABSG330, PLABSG40, PLABSG50) which is evidence of a **structural change** in the composite system.

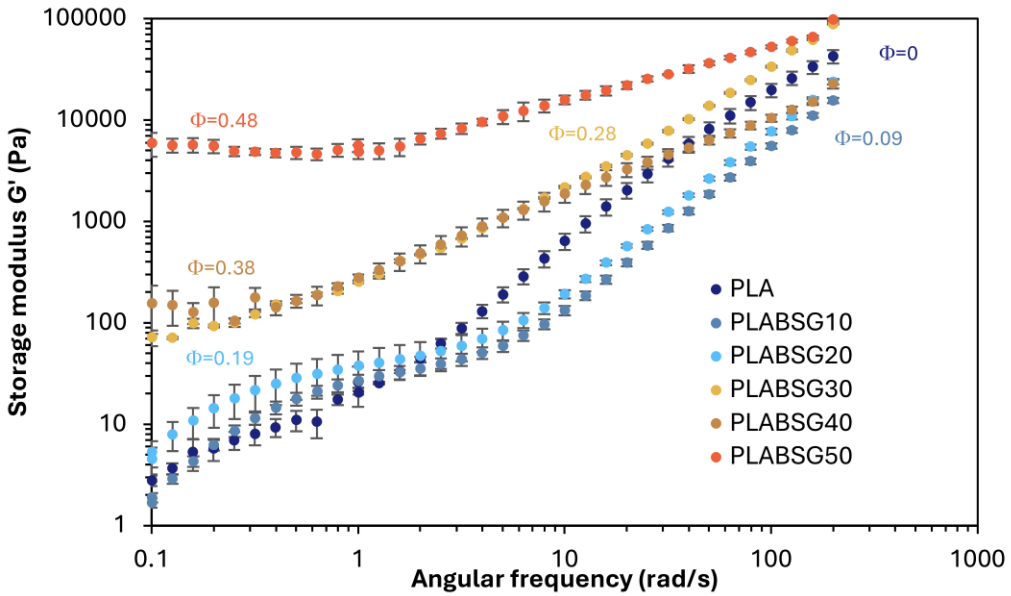


*Figure 3.15: Effects of BSG ratio on storage modulus (Pa) vs. angular frequency (rad/s) in plate rheometer at 180 °C for PLA and PLA composites processed at 180 °C in internal mixer and injected at 180 °C, Φ = volume fraction of BSG, plate-plate gap = 2200 µm, plate diameter = 25 mm, strain = 10 % for PLA, PLABSG10, and PLABSG20, 0.05 % for composites with 30, 40 and 50 %(m/m) BSG. Average of three experiments.*

Contrary to PP composites, PLA-BSG composites exhibit markedly different complex viscosity curves (Figure 3.16). At low filler concentrations (<30 %(m/m)), the composites demonstrate quasi-Newtonian behavior, wherein the viscosity remains almost constant over the entire frequency range, with no discernible shear-thinning effect. This suggests that at particle concentrations under 30 %(m/m), the filler may interact with PLA which restricts its chain mobility extending the Newtonian plateau and delaying a possible shear-thinning effect. However, the content is insufficient to significantly alter the flow properties of the PLA matrix which keeps its fluid-like behavior. We observe that the overall curves of PLABSG10 and PLABSG20 fall below that of pure PLA, which may be related to a reduction in the molecular weight of PLA (Figure 3.8), knowing that viscosity is strongly dependent on polymer molecular weight. Moreover, similar effects have been reported with other natural particles-reinforced PLA composites. For instance, in PLA composites, the addition of abaca fibers was found to reduce

less than expected the melt flow rate of the composite [59]. This effect was attributed to a reduction in PLA molecular weight due to chain scission happening during material processing. Indeed, the thermal decomposition of the natural fibers during processing releases residues such as water, waxes, and other volatiles. These decomposition byproducts likely interacted with the PLA matrix, initiating hydrolysis and scissions within the polymer chains and leading to a **reduction in molecular weight** [59]. This degradation process in PLA-BSG composites could similarly contribute to the observed **reduction in complex viscosity**. SEC analysis allowed us to confirm that PLA after internal mixing and injection molding showed a *Mn* of 76604 ± 2053 g/mol while *Mn* of PLABSG10 and PLABSG20 were respectively reduced to 55899 ± 5807 g/mol and 57459 ± 1510 g/mol (Figure 3.8).

However, at higher BSG content, the complex viscosity begins to follow a **power-law** behavior at low frequencies. Such a behavior indicates molten composite system reaching the **percolation threshold** which we could also observe on *G'* curve. The rheological response at this stage reflects the presence of a **filler network** that resists to flow, causing the system to behave almost like a solid under low-shear conditions. Moreover, these results confirm that **particle-particle interactions** dominate the behavior of composite at low frequencies [260–263]. These results are not surprising since, both PLABSG40 and PLABSG50 have a BSG content above or reaching the maximum packing fraction ($\Phi_m$) of BSG (0.399 ± 0.013).

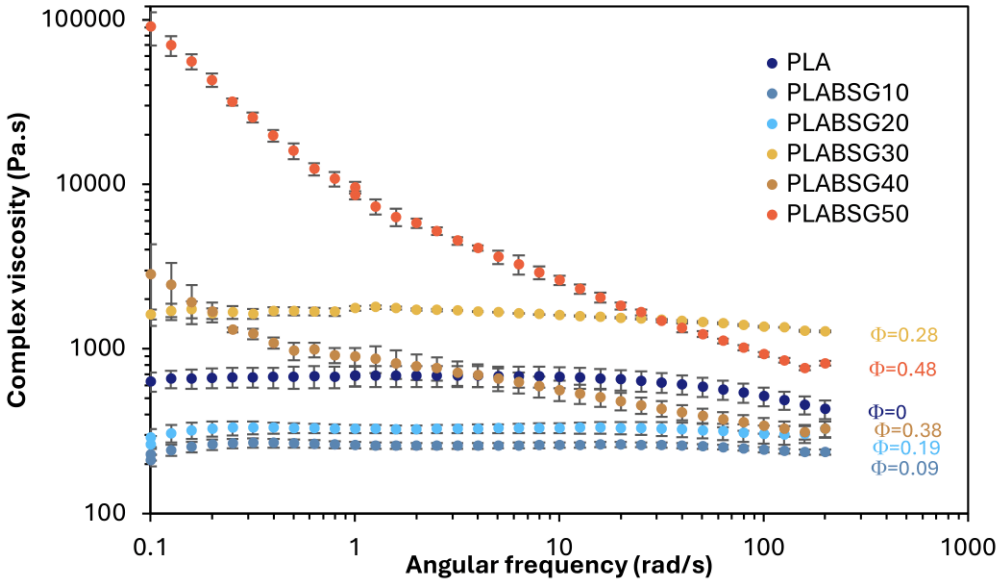


*Figure 3.16: Effects of BSG ratio on complex viscosity (Pa.s) vs. angular frequency (rad/s) in plate rheometer at 180 °C for PLA and PLA composites processed at 180 °C in internal mixer and injected at 180 °C, Φ = volume fraction of BSG, plate-plate gap = 2200 µm, plate diameter = 25 mm, strain = 10 % for PLA, PLABSG10, and PLABSG20, 0.05 % for composites with 30, 40 and 50 %(m/m) BSG. Average of three experiments.*

In both polymer systems BSG seems to exacerbate matrix flow behavior. The difference in behavior between PLA and PP composites highlights the stronger influence of particle-particle and particle-matrix interactions in the PLA system. These interactions significantly shape the curves across frequencies, reflecting their impact on composite's response to shear stress. These analyses highlight the importance of particle/matrix interactions on the flow behavior of a composite.

Studying the insights of interfacial bonding between particles and matrix could provide crucial information on physical, mechanical or rheological behavior of the composite material. Indeed, weak interaction between the matrix and particles can result in phase separation, fragile interfacial bonding, and a decline in the composite properties. Hence, scanning electron microscopy can provide qualitative information on the sample surface allowing a deeper understanding of the reaction between matrix and particles surface.

## 6. Interface morphology

In this part, we will consider firstly the composite section obtained by cryofracture which allows an easier observation of the filler dispersion due to cleaner cleavage. Cryofracture also allows a clearer observation of debonding between filler and matrix with voids at interface.

Secondly, we will study the composites sections obtained after tensile fracture which permits to see signs of matrix deformation either ductile tearing or brittle cracks. We will also perceive evidence of adhesion or non-adhesion under through filler pull-out.

### 6.1. Cryofracture

Figure 3.17 shows the **cryofracture** profiles of PP composites from pure PP to the higher filled PP. The small magnification use allows a better view on the **filler dispersion**. It is possible to observe that the PP shows a **brittle and smooth surface**. PPBSG10 and PPBSG20 show the same surface profile with few visible BSG particles. PPBSG30 and PPBSG40 display a surface with more particles but also more filler **pull-out and voids** indicating **poor bonded** interfacial area between BSG particles and PP. At 50 %(m/m) filler loading, **worse dispersion** of BSG particles is seen, the fillers are more likely to be in contact with each other.

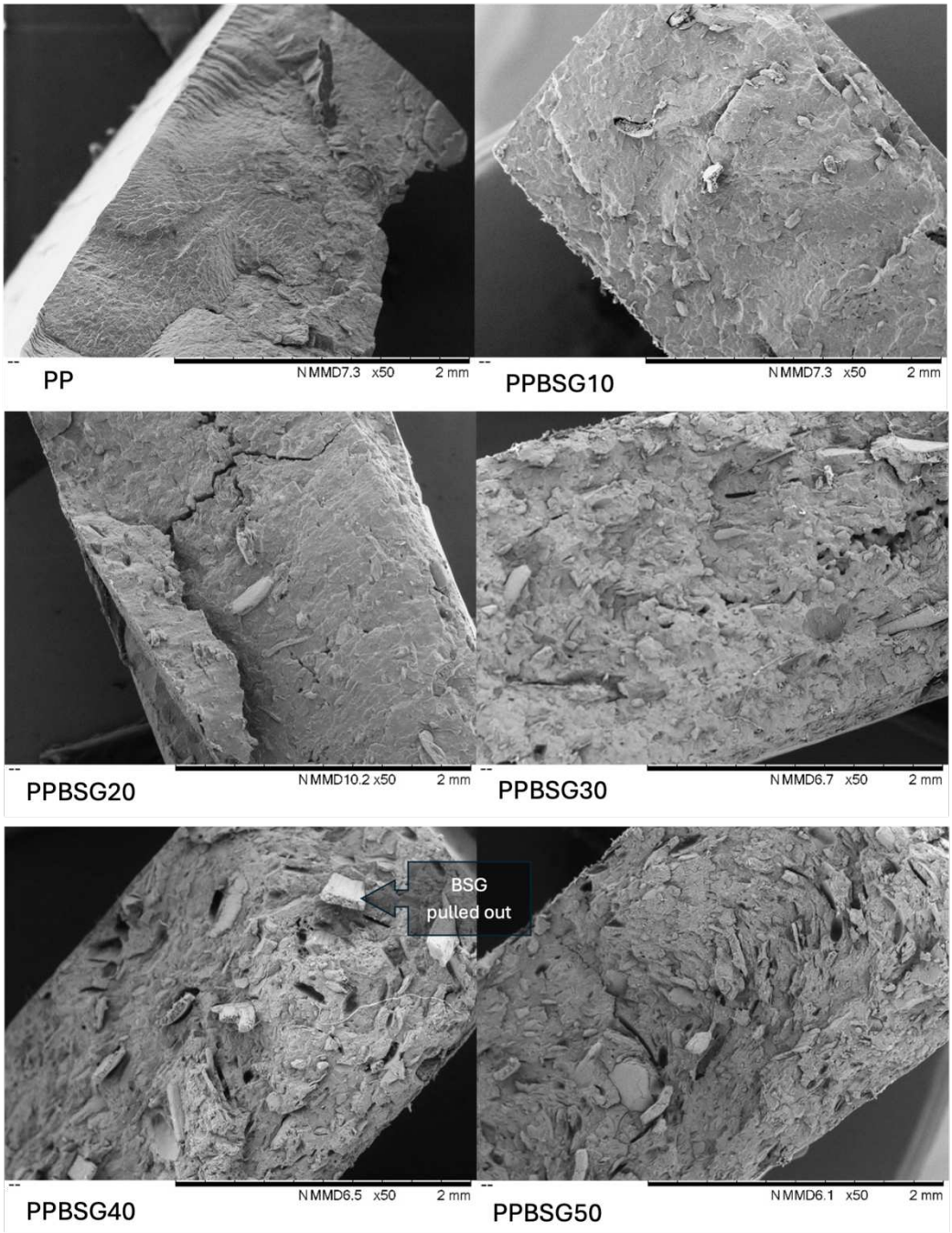


*Figure 3.17: SEM micrographs taken from the cryofracture surface of PP composites obtained using internal mixing (180 °C, 50 rpm, 5 min) and injection molding (200 °C) x50*

Figure 3.18 displays the cryofracture profiles of PLA composites from pure PLA to the higher filled PLA. Comparatively to PP, pure PLA shows a smooth and brittle surface. However, when filled with 10 %(m/m) BSG, signs of **BSG agglomeration** are seen as well as pulled-out traces. This traduces a poor matrix wetting where PLA fails to **break** the agglomerates. It could be due to the **lower viscosity** of PLA (~600 Pa.s at Newtonian Plateau) compared to PP (~2000 Pa.s at Newtonian Plateau) as seen in Figure 3.14 and Figure 3.16.

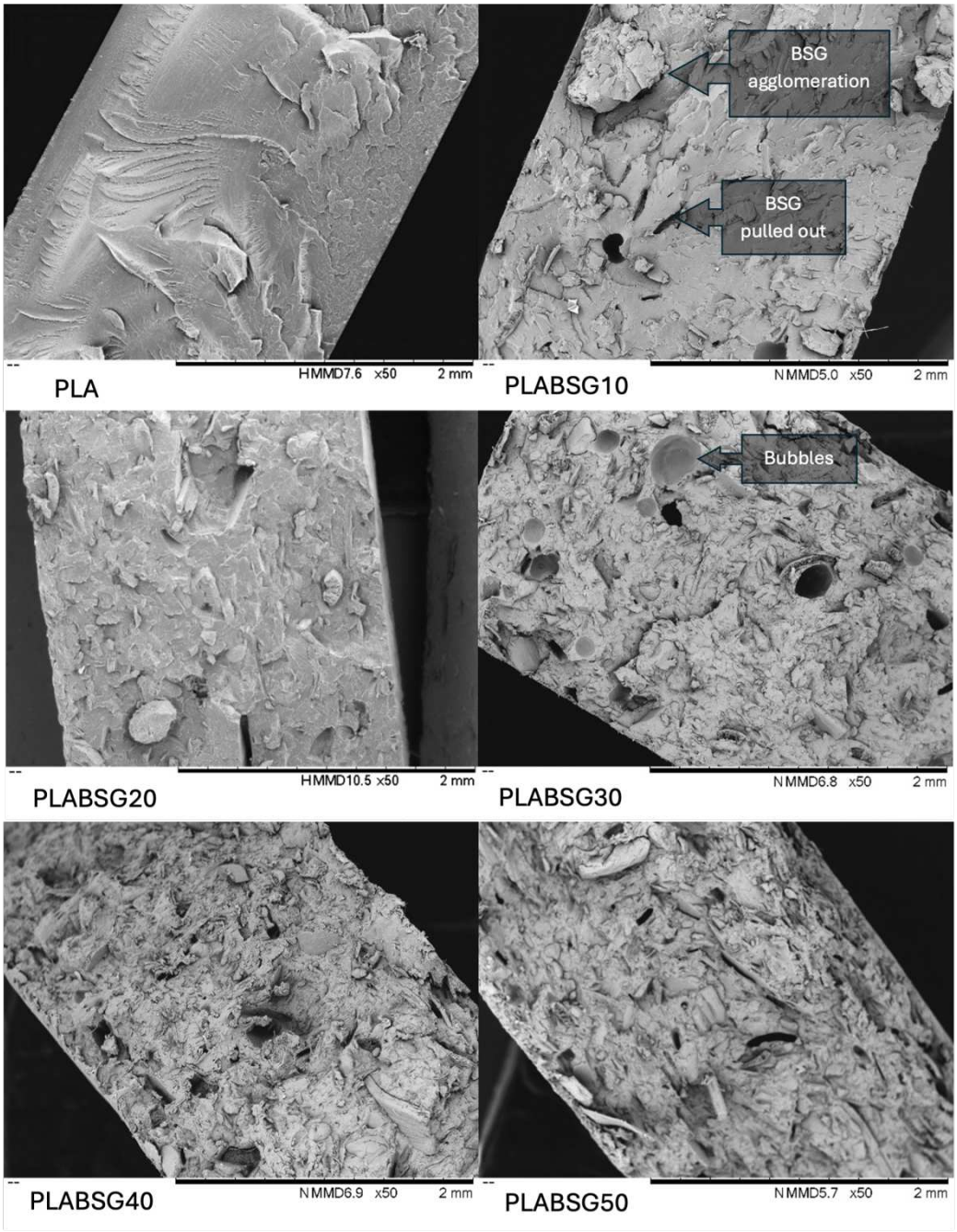


*Figure 3.18: SEM micrographs of cryofracture surface of PLA composites obtained using internal mixing (180 °C, 50 rpm, 5 min) and injection molding (180 °C) x50*

At higher BSG loadings, same signs of **poor interfacial adhesion** are seen with filler pulled out. PLABSG30 shows bubbles within the matrix which can compromise mechanical properties. PLABSG40 and PLABSG50 composites exhibit significantly different microstructures compared to lower filler loadings. In these samples, BSG particles appears **densely packed** and in direct contact with one another, indicating poor dispersion. PLABSG40 is close to the theoretical maximum packing fraction, while PLABSG50 exceeds it, meaning the available PLA matrix is no longer sufficient to **fully encapsulate** or separate the filler particles. As a result, the particles are forced into **direct particle-particle** contact, as clearly seen in the SEM images, Figure 3.18.

### 6.2. Tensile fracture

Examination of the tensile-fractured sections of both PLA and PP composites reveals distinct differences in fracture behavior, particularly at the interface between BSG and the polymer matrices.

In Figure 3.19, SEM micrographs of PP composites show a shift in fracture morphology, from the **uniform stretching** seen in neat PP to **shorter and focused stretching points** around the fillers (PPBSG30 and PPBSG50, Figure 3.19). This shift reflects stress concentration at the filler-matrix interface, which results in **localized weaknesses** and indicates that BSG may disrupt the propagation of tensile stress.

Pure PLA exhibits a predominantly brittle fracture profile (Figure 3.19), whereas the incorporation of BSG introduces **stress concentration points** characterized by ductile deformation around the filler particles (PLABSG30 and PLABSG50, Figure 3.19). These points of **ductility** increase with BSG content, suggesting that BSG reduces **the brittleness** of PLA which is a favorable improvement since PLA applications is limited by its high brittleness.

Additionally, both PLA and PP composites exhibit **voids at the interface** between BSG and the matrix, as well as particles **pull-out** under tensile stress, indicating poor adhesion, which is further worsened by the low elongation ratio of BSG particles. This **lack of adhesion**, likely due to the hydrophilic nature of BSG and the hydrophobic nature of the matrices, exacerbates the formation of microvoids around the interface. These microvoids seem to act as **crack-blunting sites**, allowing the material to deform **more plastically before failure**, as seen in the micrographs.

In PLA, this enhanced ductility is supported by DSC results, where a reduction in $T_g$ with BSG addition suggests increased flexibility in the polymer. Together, these observations underscore that BSG may alter the mechanical behavior of PLA and PP by **enhancing ductility rather than stiffness**, with microvoids and stress concentration points contributing to plastic deformation before fracture. The absence of adhesion likely contributes to a geometrical deformation of the polymer matrix due to the reduction of the polymer section.

Although PLA possesses good properties, its inherent brittleness can limit its applications. Therefore, enhancing its ductility remains of great interest, as they can improve its suitability for practical use.

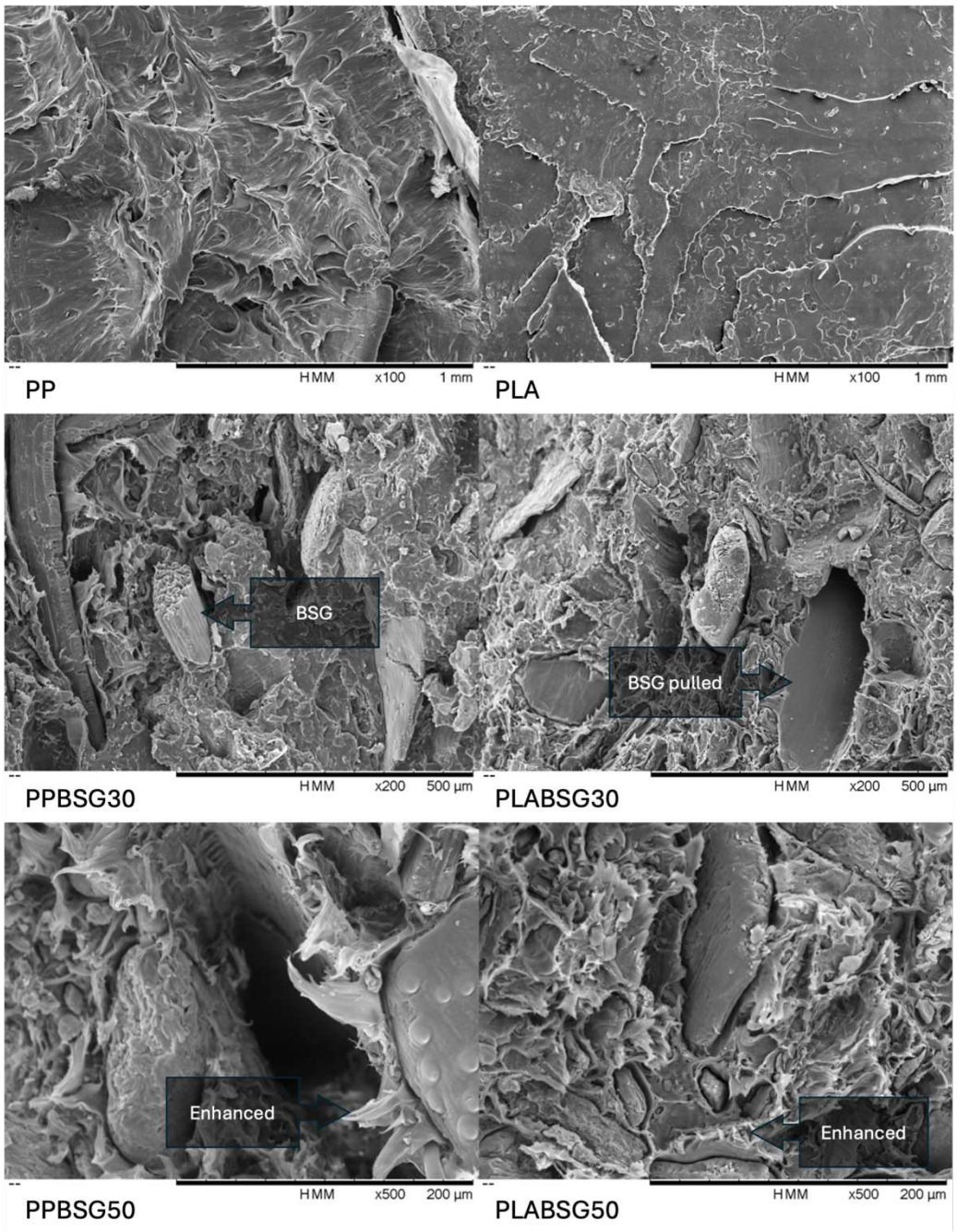


*Figure 3.19: SEM micrographs of samples fractured cross-section of tensile specimens: Neat PP ; Neat PLA ; PPBSG30x200 ; PLABSG30x200 ; PPBSG50x500 ; PLABSG30x500*

## 7. Mechanical behavior

### 7.1. Young's modulus

The **Young's modulus** values of PP and PLA composites calculated from the **slope** of stress versus small strain (0.5-1.5%) plotted against BSG mass content are gathered in Figure 3.20. As

can be observed, the elastic modulus of PP and PLA composites remains steady with increasing volume fraction of BSG.

Pure PP which was mixed by internal mixing and injected shows a tensile modulus of 1497 ± 140 MPa which is consistent with previous studies [18,19,264] whereas PP composites with 50%(m/m) has a modulus of 1556 ± 122 MPa.

Pure PLA showed a Young's modulus of 2301 ± 442 MPa aligning with previous studies [47,265] whereas PLA composites with 50%(m/m) has a modulus of 2169 ± 139 MPa.

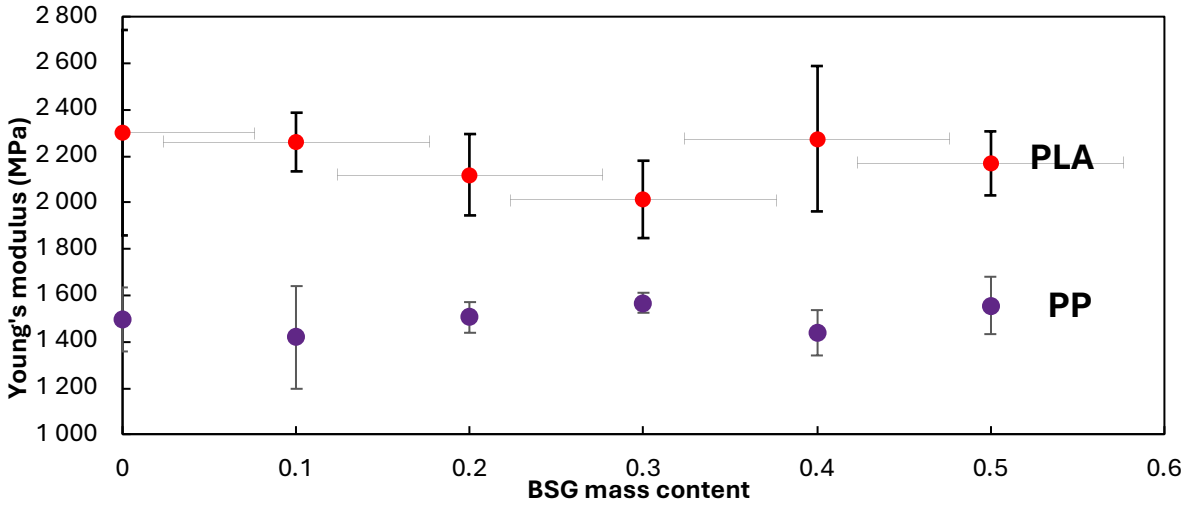


*Figure 3.20: Comparison of Young's modulus for different BSG mass fraction in PLA and PP composites.*

These trend results deviate from those in literature demonstrating the incorporation of fillers leads to an increase of the Young's modulus [55,58,73], being similar to those describing the biomass fillers not influencing or jeopardizing the composites mechanical properties [46]. For instance, the addition of wheat straw fibers to polypropylene increases the modulus of the composites from 1.21 GPa for PP to 2.99 GPa for 30 % reinforced PP, the fibers were mechanically defibrillated and sieved (500 µm) [18]. Similarly, the addition of rice husk flour to PP have been found to increase the Young's modulus continuously with increasing flour loading (0 % to 40 %(m/m) [212]. Moreover, 50 %(m/m) peach stone particles with small particles size (<80 mesh) reinforced composites have demonstrated superior tensile modulus (2.49 GPa) compared to the pure PP (1.35 GPa) [19]. However, in the same study, Nunez-Decap *et al.,* observed that 50 % peach stone particles composites with large particles size (80-140 mesh) demonstrated a tensile modulus which was not significantly different from the modulus of pure PP [19].

For PLA, the addition of 30 % pineapple skin flour was found to increase tensile modulus of the composite [18]. Similarly, wood fibers reinforced PLA composites exhibited increased tensile modulus, with 40 %(m/m) of wood fibers reaching a Young's modulus of 6.3 GPa against 2.7 GPa for the pure PLA [150]. However, not all fillers can enhance the tensile modulus of all polymers. Sutivisedsak *et al.* reported a decrease in elastic modulus of cotton burr/PLA composite with 0.609 GPa for pure PLA after extrusion and punch press cutting and 0.239 GPa for 10 % cotton purr filled PLA [46].

This **less influence or weaking of biomass** in the composites can be attributed to several factors. First, the **size of our filler** can negatively impact the Young's modulus of our composites. Indeed, bigger filler could result in a reduced tensile section inducing more stress concentration at the voids. Secondly, the steady modulus with increasing BSG content may be indicative of a **limited stress transfer** between BSG and the polymer. Lastly, while fillers extracted from biomass like BSG are often reported to act as nucleating agents, promoting crystallization and subsequently enhancing the stiffness et reducing elasticity of materials [264,266] our DSC results suggest that the addition of BSG did **not significantly affect the crystallization** rate of neither PP nor PLA matrix which is amorphous. This may explain the lack of reinforcement observed in the mechanical properties of our BSG composites. However, it is possible to conclude that since the Young's modulus remains stable with the addition of BSG, the mechanical behavior of the composites toward mechanical stress are maintained.

### 7.2. No-adhesion model

To quantify the **adhesion at the interface**, Nicolais and Narkis proposed an equation for a lower-bound strength of the composite, defining the tensile strength of the composites as function of volume fraction for the filler, based on the hypothesis that there is **no adhesion** between filler and polymer and that the load is sustained solely by the polymer. An upper-bound could be obtained by considering that for perfect adhesion, the strength of the composite is simply equal to the strength of the polymer matrix [224]. Nicolais and Narkis created a simple model that demonstrated the relationship between the filler volume fraction, the tensile strength of the pure polymer and tensile strength of the composite and yield stress in the absence of adhesion. Nicolais and Narkis assumed that the filler was uniformly distributed and of spherical shape, demonstrating the yield stress decreased substantially with an increase in bead concentration, and the yield strain also decreased with an increase in the volume fraction of filler. This is consistent with previous research on elastomeric PVC composites [226]. According to their model, the strength can be described by:

$$\sigma_c = \sigma_m\left(1 - 1.21{\phi_p}^{2/3}\right) \qquad (3.2)$$

$\sigma_c$: composite tensile strength

$\sigma_m$: matrix tensile strength (pure polymer)

$\Phi_p$: particle volume fraction

The constants are associated with stress concentration and the filler's geometric properties. They are equal to 1.21 and 2/3 for fillers that are spherical and uniformly dispersed into the matrix [226]. This model has only been established for this type of filler.

Figure 3.21 displays the tensile strength of PP and PLA composites as a function of BSG volume fraction. For reference, a conversion table between mass and volume content is provided in Chapter 2 (Table 2.2). Unlike the elastic modulus, tensile strength was **strongly and negatively** affected by the filler for both polymer matrices. For instance, by reinforcing PP with 40.2 vol.% of BSG, the tensile strength is **halved.** For pure PLA the tensile strength equals 57.4 ± 17.8 MPa which is consistent with the literature [46,213] whereas for 48.1 vol.% BSG reinforcing PLA, the tensile strength was dropped to 30 %. This trend was also **reported by several researchers** in both polymer systems [46,47,57,213], being connected with the **poor adhesion** of the BSG filler to both thermoplastic matrices [75,267,268]. This weak interfacial adhesion suggests that stress cannot be efficiently **transferred** from the polymer matrix to the filler.

The Nicolais-Narkis model (Equation 3.2), describes the tensile strength of composites under the assumption of no adhesion between filler and matrix, appears to be a good fit to our data (Figure 3.21). Upon comparison of the two matrices, PLA **aligns more closely** with the model of no adhesion, whereas PP exhibits **tensile strengths slightly above the model's predictions**. This observation suggests that PP may demonstrate stronger adhesion to BSG than PLA, facilitating enhanced stress transfer between matrix and filler. These results are in agreement with those observed on the micrographs of the fracture surfaces. Considering the adhesion between BSG and both matrix remains low, future research may focus on improving the interfacial interaction between BSG and the matrix. However, BSG thermoplastic composites can still perform well in injected application where the strength is not a critical requirement or where the mechanical solicitation remains in its linear elastic region, offering a sustainable alternative for less mechanically demanding usages.

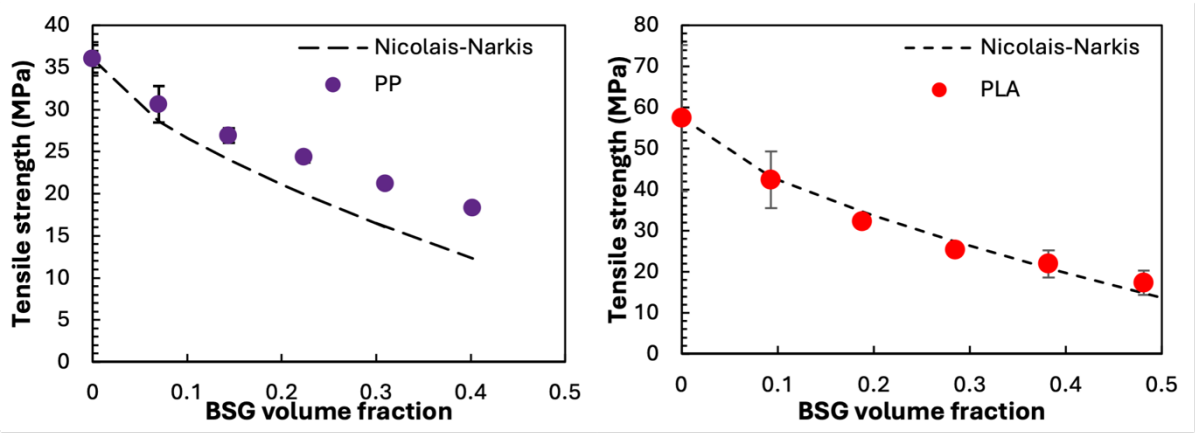


*Figure 3.21: Comparison of maximum tensile strength predicted form Nicolais-Narkis model for BSG reinforced PP and PLA composite*

Beyond mechanical performance, the durability of composites is also strongly influenced by their interaction with water. Therefore, the water absorption behavior of the materials was investigated.

## 8. Water absorption behavior

Because of the **hydroscopic behavior** of the lignocellulosic fillers, water absorption of composites containing such fillers can be a limiting parameter for a final application. Moreover, water absorption can give insight into the interactions between fillers and between filler and matrix.

The amount of water absorbed by the composites was calculated by the weight difference between samples at the beginning of the experiment and after water immersion. For composites with high BSG content, the water uptake experiment could not be extended to reach a stable mass due to the visible growth of microorganisms on the sample surface. Therefore, the mass measurement was compromised, and the experiment was stopped in the 21 days.

Figure 3.22 displays the water absorption kinetics for both pure polymers, BSG-PP composites and BSG-PLA composites respectively. What can be observe at first sight is that pure PP and PLA show a **very low water uptake** with 0.66 ± 0.06 % and 0.87 ± 0.11 %, respectively after 21 days of immersion. These results are closed to published values [49,269]. Their hydrophobicity makes their water uptake **negligible**. Thus, the water sorption in composites is limited to the sorption of BSG. Indeed, the hydroxyl groups present in BSG interact well with water molecules via hydrogen bonding.

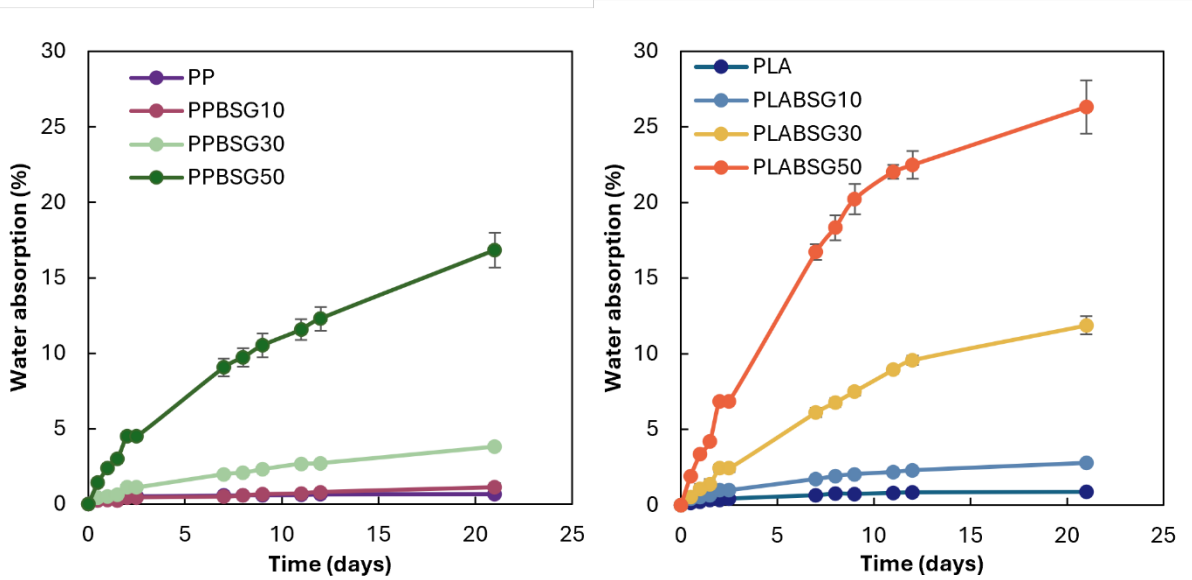


*Figure 3.22: Water absorption curve for BSG/PP or PLA composites drown in water at room temperature, means of duplicates.*

The incorporation of BSG inside both matrices leads to an increase of the water absorption. The water absorption rates for PP and PLA composites varied between 0.66 ± 0.06 % and 16.82 ± 1.16 % and 0.87 ± 0.11 % to 26.30 ± 1.76 %, respectively, after 21 days of immersion in water. Pure PP curve is hidden behind PPBSG10 curve. It is possible to observe that all composites display the **same absorption trend** with higher absorption for higher content of BSG. The highest values of absorption rates were obtained with composites filled with 50 %(m/m) which is due to the hydrophilic behavior of the BSG.

Since PLA and PP have different densities, formulations prepared by mass ratio do not correspond to the same volume fraction of BSG. Because the specimens are injection-molded with the same volume, the actual mass of BSG differs between samples at the same nominal formulation. For instance, an injected composite of PLABSG50 does not contain the same amount of BSG as PPBSG50. Therefore, a comparison based on **BSG volume content** should be more accurate (Chapter 2 Table 2.2, for the volume content). Next figure present data as function of BSG volume content.

Two immersion times (2 days and 21 days) were selected in order to investigate different stages of the water absorption process. The **short-term uptake** (2 days) reflects the initial diffusion of water into the composite, and **long-term immersion** (21 days) allows us to get closer to the equilibrium state and potential degradation effects.

Figure 3.23 displays the water absorption of PLA and PP composites as function of BSG volume content after 2 days of immersion. It possible to see that until 22 vol.% and 30 vol.%, PP and PLA, respectively, show a linear increase of water absorption proportional to filler content as it could be seen in literature [270–272]. At higher filler loadings (40 vol.% and 48 vol.%), composites show a different trend with no longer linear but higher water absorption rates. Tajvidi and Ebrahimi also observed a similar trend above 35 %(m/m) in wood fiber-PP composites. They attributed this phenomenon to filler agglomeration, that occurred during compounding, leading to extra voids and surface roughness [272]. It is possible that BSG show some agglomeration. However, another possible explanation for this behavior is that, at 40 vol.% and 48 vol.%, composites exceeded the theoretical maximum packing fraction (which was 39.9 ± 1.3 %. As a result, BSG fillers create a **network** where filler connectivity is high. As it could be seen in rheology experiments, for PLABSG40 and PLABSG50 where BSG network led to a plateau of the storage modulus at low frequencies. This network might **enhance water diffusion** inside the composites.

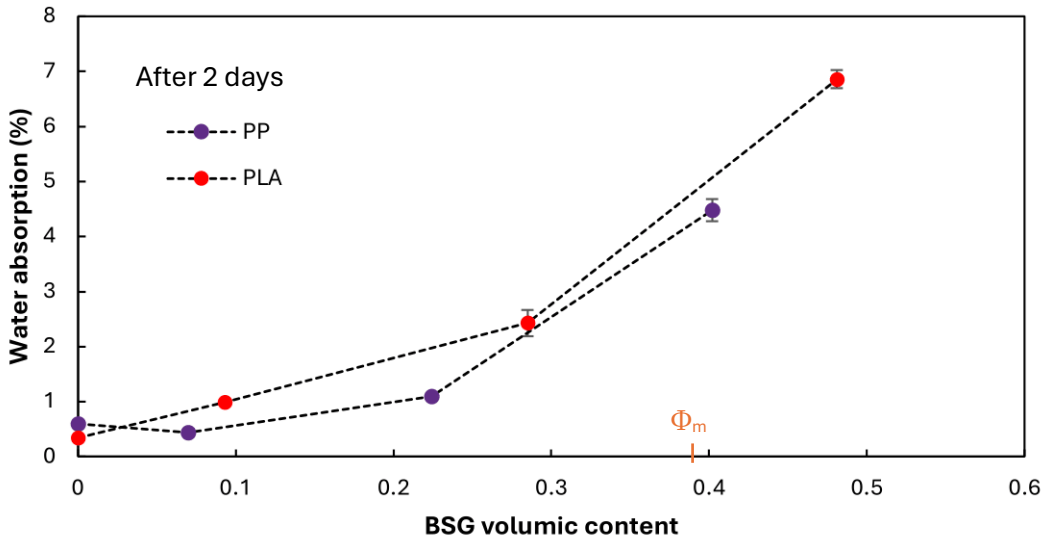


*Figure 3.23: Water absorption of PP and PLA composites after two days as a function of BSG volume fraction*

After 21 days of water immersion, it is possible to clearly distinguish PP and PLA composites behavior regarding water absorption. Figure 3.24 displays the water absorption of PLA and PP composites as function of BSG volume content after 21 days of immersion. Overall and especially at high BSG contents, PLA composites show higher water absorption rates than PP composites. This could be explained by the inherent brittleness of PLA causing more cracking

issues compared to PP, being more ductile as we saw on SEM images. Indeed, many authors acknowledged that differential swelling between filler and matrix creates high levels of stress inducing cracking and delaminating [269,273]. Moreover, PLA **cracking** has been visually observed at the end of the experiment as seen in Figure 3.25.

Additionally, the lower adhesion between PLA and BSG acknowledged during tensile assays and visible through the voids at the interface can enhance water entrapment in the matrix. Moreover, poor dispersion of the filler leads to agglomeration which weakens the composite structure and introduces extra voids which absorb water and promote filler swelling.

Overall, the combination of PLA's **brittleness** and the presence of **stress-concentrating voids** leads to a higher tendency for cracking compared to PP composites, where the ductile nature of PP helps to mitigate these effects.

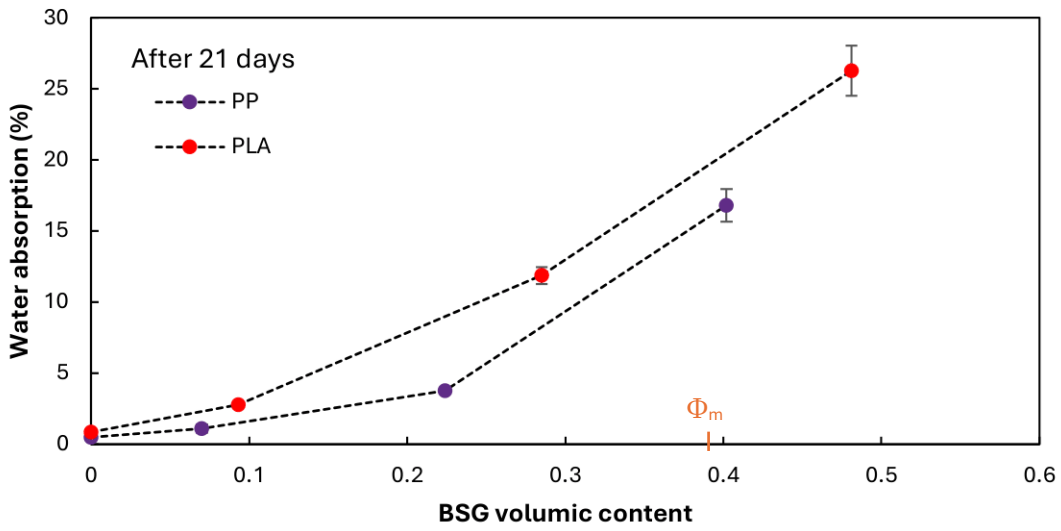


*Figure 3.24: Water absorption of PP and PLA composites after 21 days as a function of BSG volume fraction*

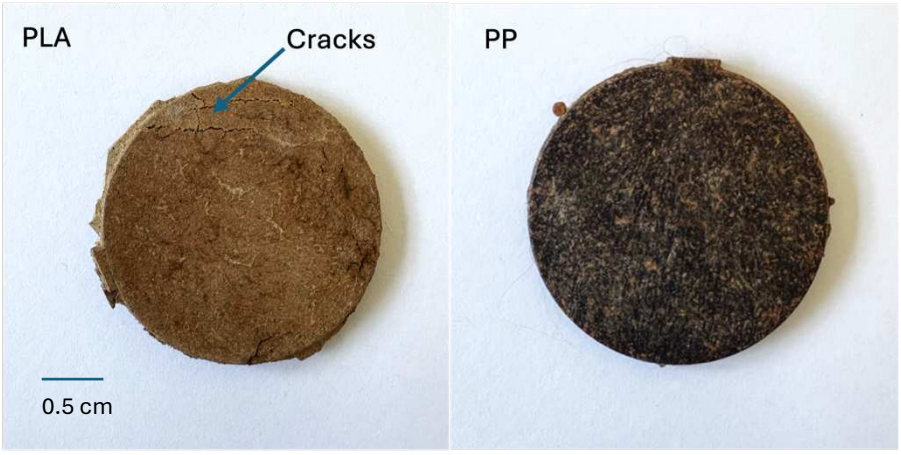


*Figure 3.25: PLABSG50 and PPBSG50 samples after 21 days of water immersion*

## 9. Conclusions

The aim of this chapter was to conduct a comparative approach to explore the potential of BSG as a filler in thermoplastic composites. Therefore, the chapter focused on the description of the rheological, thermal, and mechanical behavior of the BSG-PLA and BSG-PP composites containing 0 to 50 %(m/m) of BSG. The findings were correlated with SEM images of cross-sections of the samples revealing the interface of the filler and matrix. One key result was that BSG impacted thermal stability of both composites, but with complete opposite effects. Indeed, whereas BSG acted as a degradation buffer probably through the formation of a char layer around PP, standardizing and delaying its degradation, BSG tended to provoke PLA degradation. As a result, the flow behavior of PLA composites and their thermal transition temperatures were affected. It was shown that this also affected the mechanical properties of the composites, as evidenced by the ductile behavior observed in the micrographs. Rheological analysis showed that highly filled PLA composites were challenging to obtain. Indeed, their rheological profile under low shear rates might be the sign of particle flocculation above 30 %(m/m) of BSG. In contrast, PP demonstrated consistent flow behavior with increasing BSG content, suggesting the potential for higher filler loadings without compromising processability. Finally, the tensile strength of both polymers was negatively affected by BSG, likely due to poor interfacial adhesion, as indicated by the microvoids in the SEM images. These microvoids not only act as stress concentrators but also facilitate water uptake, particularly in PLA composites. Due to PLA's brittle nature and water sensitivity, microcracking enhanced by filler swelling can further amplify the available pathways for water penetration, making it more susceptible to water absorption

than PP, which has a more ductile matrix and better crack resistance. The main outcomes of this chapter are summarized in Figure 3.26.

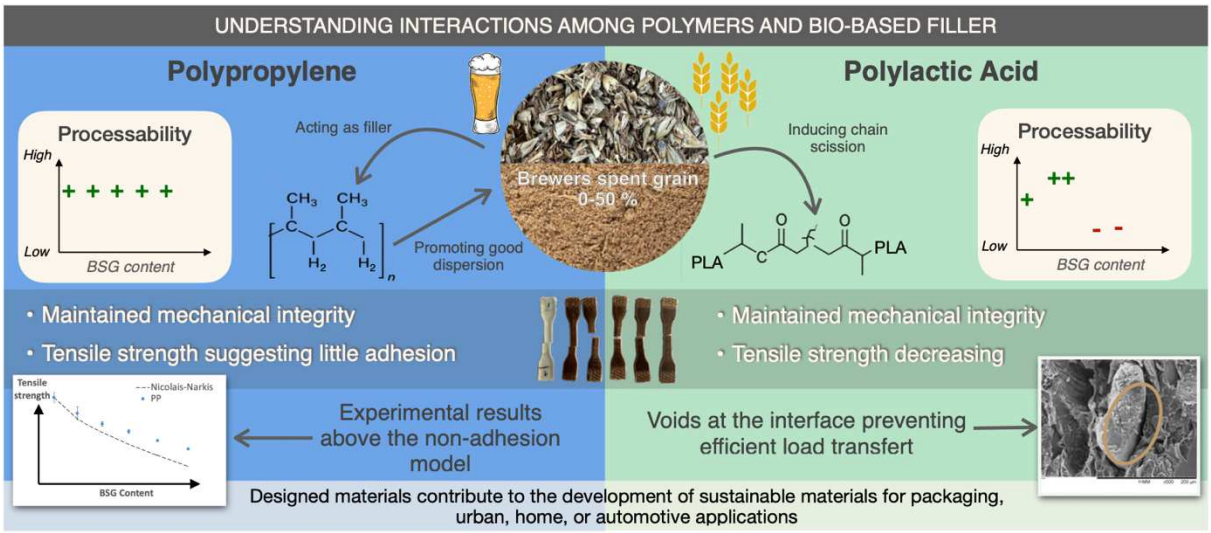


*Figure 3.26: Schematic overview summarizing the key results and interpretations of Chapter 3*

Future research may focus on improving the interfacial interaction between BSG and the matrix in order to fully develop the potential of BSG as a filler. However, a steady elastic modulus with increasing BSG content for both polymers demonstrated their potential to maintain mechanical integrity when subjected to stress. Despite, their mechanical limitations, BSG-composites offer advantages such as eco-friendliness and low price which make them attractive for specific fields where the strength requirements are moderate, but the environmental impact of the material is of significant concern. In conclusion, this study sheds light on the behavior of BSG-filled PLA and PP composites, particularly regarding their mechanical and rheological properties. The composites were successfully processed via injection molding, highlighting their suitability for indoor applications where high strength is not essential.

Having established that BSG can be effectively processed as a filler in PLA and PP composites, attention must now turn to another key challenge: ensuring its preservation and preparation for large-scale applications.

# CHAPTER 4:

# Integrated drying and grinding of Brewer’s spent grain via extrusion process

# RÉSUMÉ DU CHAPITRE 4

Les drêches de brasserie sont un co-produit lignocellulosique abondant, offrant un fort potentiel comme charge dans les composites polymères d'après les résultats du chapitre 3. Cependant, sa forte teneur en humidité, la mauvaise dispersion des particules et l'adhésion interfaciale limitée limitent sa valorisation à grande échelle. De plus, les méthodes de stockage utilisées dans ce travail (congélation) et le séchage-broyage (séchage au four pendant 48 h, broyage à environ1 kg/h) s'avèrent impraticables à plus grande échelle en raison de leur surconsommation d'espace, d'énergie et de temps. Cette partie étudie l'extrusion bi-vis comme alternative continue et évolutive, capable de sécher et de broyer simultanément les drêches afin de répondre aux exigences de stockage à long terme et de fabrication de composites.

Une conception expérimentale à deux étapes a été adoptée : tout d'abord, la température d'extrusion et le débit d'alimentation ont été optimisé afin de garder les conditions permettant un meilleur séchage et un broyage plus fin. Puis, la première optimisation ayant atteint ses limites, un affinement de la configuration du profil de la vis a été mené avec l'étude de 3 autres profils de vis permettant de définir un dernier profil de vis (Profil 5). Les conditions les plus efficaces (190 °C, 400 r/min, profil 5) ont permis de réduire la teneur en humidité de la drêche à 1,57 % (bien en dessous du seuil requis pour le stockage (10 %) et la fabrication des matériaux (3 %)) et d'obtenir une taille médiane de particule de 95,8 µm, plus petite et plus homogène que celle obtenue par la méthode de séchage broyage d'origine (≈ 150 µm). L'analyse au microscope électronique à balayage a mis en évidence des surfaces plus rugueuses et un type de fracture bimodal des drêches au broyage, indiquant un ramollissement de la lignine et une cristallinité accrue de la cellulose, tandis que les passages à températures plus élevées ont montré une légère agrégation, probablement due à des réactions de type Maillard. L'analyse thermogravimétrique a démontré une stabilité thermique améliorée de la drêche extrudée, attribuable à l'élimination partielle des composés volatils susceptibles de générer des gaz à l'interface polymère.

Du point de vue opérationnel, l'extrusion a surpassé l'approche d'origine en termes d'efficacité. À plus grande échelle, elle pourrait offrir des avantages supplémentaires : consommation énergétique mécanique plus faible pour le broyage, possibilité de récupération de la vapeur libérée, et suppression des besoins de stockage humide, ce qui simplifie la logistique. Ainsi, l'extrusion bi-vis constitue une voie techniquement robuste et énergétiquement favorable pour la valorisation des drêches, à l'échelle laboratoire dans un premier temps,

ouvrant des perspectives au-delà des composites polymères, notamment vers des stratégies de bioraffinerie (extraction de protéines) à l'aide de l'extrusion réactive et des applications dans le secteur de l'énergie.

# Chapter 4 : Integrated drying and grinding of brewer's spent grain via extrusion process

## 1. Introduction

In the previous chapter, BSG was successfully incorporated as a filler in PLA and PP composites via internal mixing. The results also highlighted some **limitations,** particularly linked to **moisture content, particle dispersion,** and **interfacial adhesion**, impacting composite properties. However, to move toward large-scale application, it is essential to address a second major challenge: the **perishability** of BSG and the need for **good storage** and **preparation** for composite application.

In the previous chapter, BSG was stored in a **freezer** to preserve it. However, at **larger scale**, this approach becomes **impractical** due to increased space requirements and **high energy consumption** associated with both **storage** and **transport**. Moreover, to make BSG **suitable for composite processing**, it was previously dried in a laboratory oven for **two days** and ground using a rotor mill at a rate of approximately **1 kg/h**. While effective for small-scale trials, this batch approach was **time-consuming** and **not viable for industrial-scale** production. Therefore, developing continuous, efficient drying and grinding processes is critical to ensure BSG's long-term storage stability and optimize its use in composite applications.

As presented in chapter 1, **extrusion** is a **continuous** thermo-mechanical process that enables simultaneous **mixing, heating, shearing,** and **shaping** of materials, making it highly suitable for **larger-scale** applications. Its **adaptability** through adjustable parameters such as temperature, screw speed, and screw configuration allows for precise control over processing conditions, which is particularly **advantageous for biomass pretreatment**. Although traditionally not used to dry biomass, extrusion has shown potential in facilitating **fiber breakdown, moisture removal**, and improved mixing efficiency, due to the **high shear forces** it generates [126,132]. Moreover, biomass extrusion is a widely implemented technique to pretreat lignocellulosic biomass especially for energy production or sugar recovery [274]. For instance, Karunanithy *et al.* studied the effects of screw speeds, barrel temperatures and enzymes levels on sugar yield recovery from different grasses, they observed that higher screw speed leads to reduced particle size which allows for better sugar recovery. Indeed, it was attributed to the increased accessible surface area for enzymes during hydrolysis [130]. Given its **industrial scalability and versatility**, extrusion presents a promising approach to prepare BSG for both storage and composite applications.

This chapter focuses on the **effect** of extrusion parameters on the **humidity content of** BSG, its **particle size distribution**, its **shape** aspect and **surface** roughness, its thermal stability and the specific mechanical energy required to mill and dry BSG. This study is built upon the innovative approach proposed by Hejna *et al.,* who suggested a thermo-mechanical treatment of BSG using twin-screw extruder to grind BSG. While their work primarily focuses on grinding BSG, this research extends their concept by introducing the drying process as well [105].

Firstly, this chapter begins with laying down the objectives in terms of drying, as drying represented the most critical output parameter. A **preliminary study** was then conducted to **assess the feasibility** of drying and grinding BSG via extrusion and to **narrow down** the suitable processing window. Based on these findings, a **Box-Behnken experimental design** was made using one selected screw profile and feed rate, with three levels of temperature and three screw speeds. The effects of these parameters on BSG particle **moisture content, size,** and **shape** were evaluated. Finally, the **energy consumption** of the extrusion-based method was compared to the drying grinding method presented in chapter 3. Figure 4.1 summarizes the presented experimental workflow.

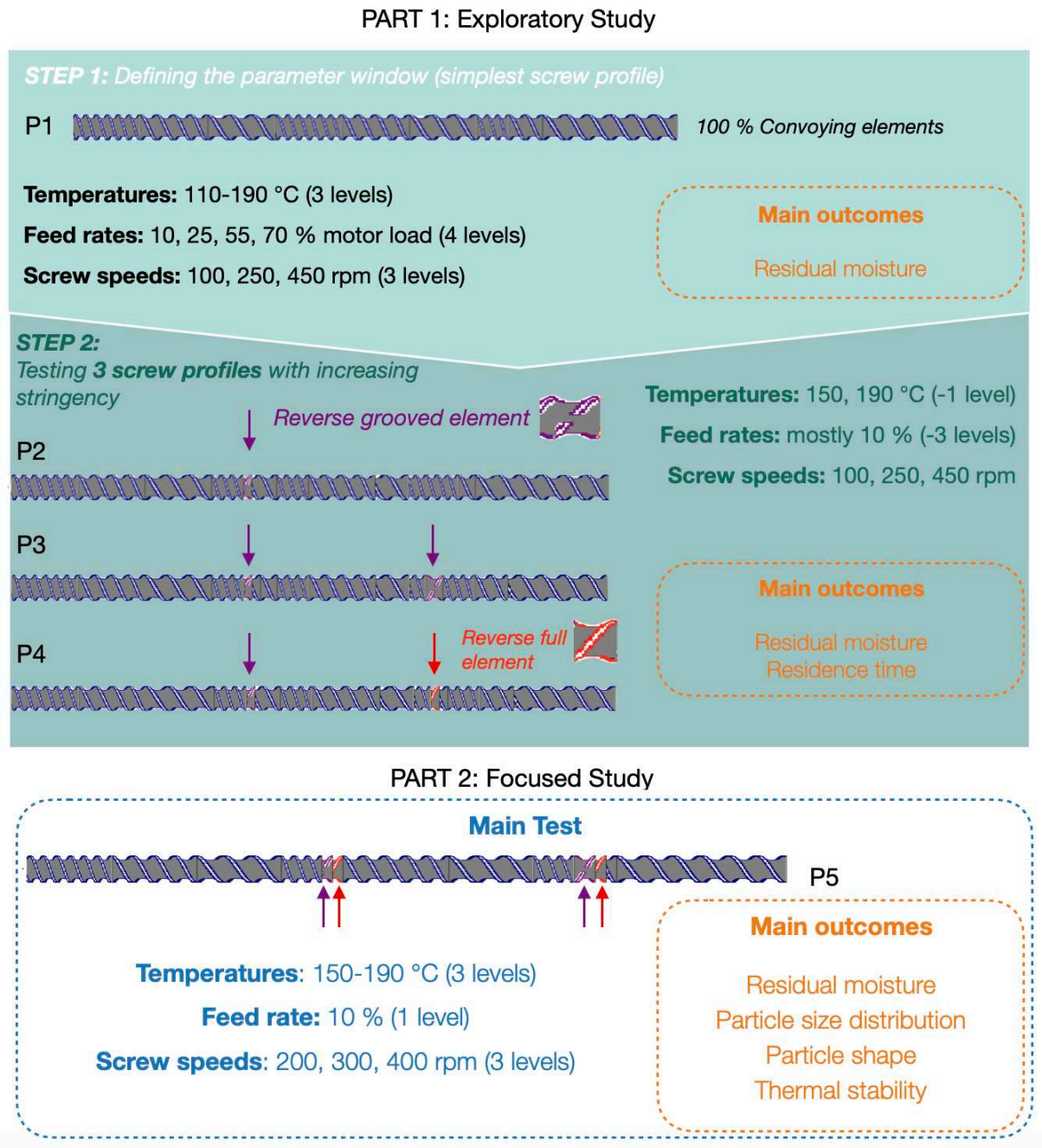


*Figure 4.1: Structure of the chapter and experimental workflow.*

## 2. Setting the objective: moisture content

Figure 4.2 displays **moisture content of BSG** and **corresponding water activity** at 25 °C. Although the samples were dried to varying moisture contents and their corresponding water activity was measured at 25 °C, this approach does not conform to the standard method to obtain a moisture sorption isotherm. Indeed, sorption isotherms are typically determined by equilibrating dry samples at controlled relative humidity levels and measuring the moisture uptake at equilibrium. Therefore, the present data cannot be interpreted as a true isotherm but

rather provides **indicative information on the relationship** between **moisture content** and **water activity of BSG** under non-equilibrium conditions.

Looking at Figure 4.2, it is still possible to observe **a trend** that could fit a sorption isotherm having a type III form (Brunauer's classification) since it does not show points of inflexion [235]. Therefore, the fitted **GAB model** parameters displayed in Table 4.1 were used to predict the moisture content required to achieve a low water activity (**aw < 0.6**), a critical threshold for inhibiting **microbial growth** and ensuring **storage** stability [275]. This model was previously used to predict moisture adsorption isotherms for BSG [135]. The model showed a good fit with experimental measurements. Based on this prediction, the **target** storage moisture content was identified as **0.12 g water/g dry BSG** corresponding to **10.7 %(m/m)** moisture content in wet basis. Moreover, for composite material applications, a much lower moisture content (**< 3 % wet basis**) is required to ensure optimal material performance.

Achieving lower moisture improves material quality but requires higher energy input. Therefore, depending on the **drying efficiency** and **energy considerations**, one mandatory target is be considered: we will call it the storage moisture content (**~10 %, wet basis**) ensuring microbiological safety [135]. Preferably, we will target an even lower moisture content (**~3 %, wet basis**) suitable for direct use in composite manufacturing [5]. As advised by Puglia *et al.* the moisture content of natural fiber should be reduced to less than 3 % to produce a good-quality molded-part [5].

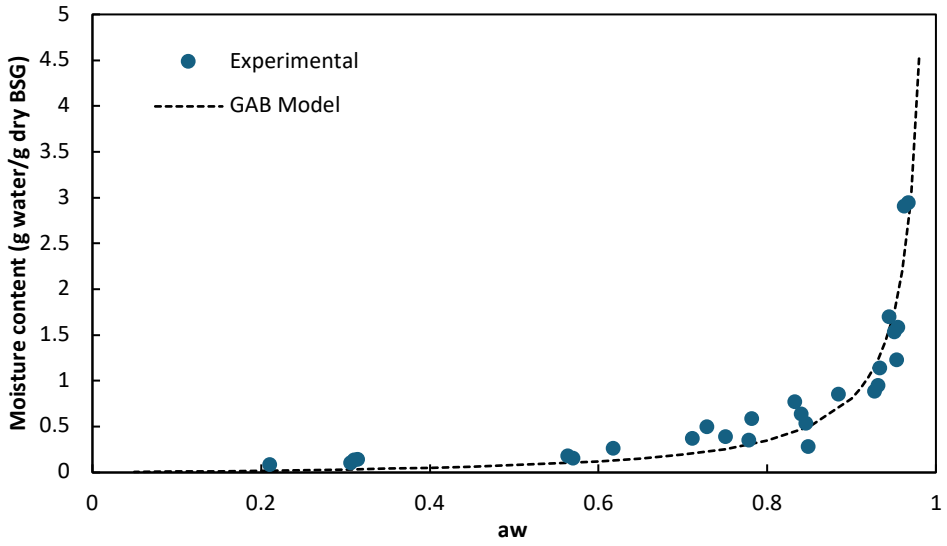


*Figure 4.2: Moisture sorption isotherm of BSG showing experimental moisture content (dots) and GAB model prediction (dash line)*

$$W = \frac{CKW_m a_w}{(1-Ka_w)(1-Ka_w+CKa_w)} \qquad (4.1)$$

with

*W*: moisture content of BSG on a dry basis (g water/ g dry BSG)

$a_w$: water activity

$W_m$: Monolayer moisture content (dry basis)

*C*: Guggenheim constant related to the heat of absorption (1.54)

*K*: Constant related to temperature effects (1)

*Table 4.1: GAB parameters of the moisture sorption of BSG and determination of coefficients of the regression ($R^2$)*

| GAB model parameters | | | Statistics |
|---|---|---|---|
| $W_m$ (g water/g of dry matter) | *C* | *K* | $R^2$ |
| 0.039 | 1.54 | 1 | 0.90 |

## 3. Preliminary study

### 3.1. Introduction

This preliminary study was essential to define a **narrow window** given the large number of adjustable parameters (temperature, screw speed, screw profile, feed rate) as seen in Figure 4.1. Initially, a **simplified** screw profile containing **only straightforward convoying** elements was used while varying barrel **temperature, throughput** and **screw speed** to observe general trends. The results will demonstrate that moisture content could not be reduced below **27 %(m/m) wet basis**, therefore, the **temperature** settings were adjusted later. Moreover, the **absence of significant particle size reduction** indicated that the **grinding was ineffective** under these conditions. Therefore, **screw profile** was also revised by adding several **reverse** screw elements to increase shear rates.

## 3.2. First set of trials - Defining a window of parameters

### *3.2.1. Introduction*

The screw profile selected firstly (**Profile 1**) is constituted only by **straightforward convoying** elements to minimize **shear rates** and **burning of BSG**. As seen on Figure 4.3, two venting zones were opened along the barrel to facilitate **water vapor extraction** and thereby BSG drying. The selection and arrangement of screw elements were designed to optimize **both grinding** and **water vapor extraction** during extrusion. At the beginning of the screw profile, **wide pitch** conveying elements facilitated **smooth feeding** of the wet BSG (75 %(m/m) of water). Prior to each venting zone, **narrower pitch** conveying elements were positioned to **slow down BSG flow**, thereby increasing residence time and internal pressure. This configuration enhanced **shear and compression**, promoting **particle size reduction** and facilitating **moisture release**. Immediately after each venting zone, **wider-pitch** elements were introduced to rapidly convey the material forward. This **prevented backflow** or **material accumulation** at the vent, minimizing the risk of BSG escaping through the venting aperture.

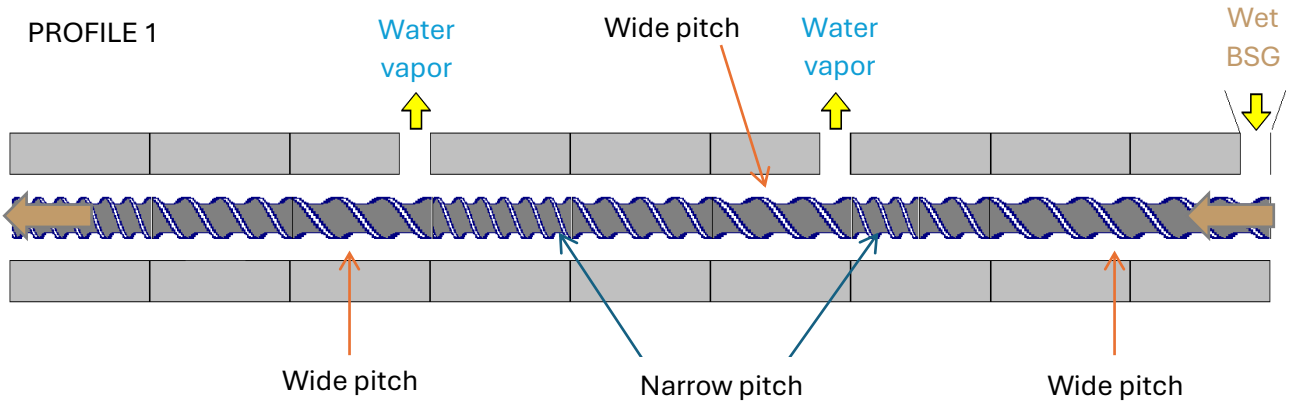


*Figure 4.3: Screw profile 1 of the twin-screw extruder designed to grind and dry BSG*

### *3.2.2. Temperature*

Using **screw profile 1**, a wide range of temperatures was studied. Considering the short residence time (between 25 and 70 s), it was chosen to start with temperature above the vapor transition temperature of water. So, the **lowest temperature** for the trial was set to **110 °C**. Then two other temperatures were investigated: **150 °C** and **190 °C**. Considering that BSG is subjected to temperatures up to 200 °C during composite manufacturing process, it is acceptable to dry it up to 190 °C. Under these conditions, volatiles compounds identified in chapter 3 as responsible for PLA chain scission are expected to be removed as seen in TGA (Figure 3.5). To explore the effect of processing temperature, 150 °C was chosen as intermediate point.

*3.2.3. Throughput*

Feed rates corresponding to **10 %, 25 %, 55 %**, and **70 %** of the maximal feeder motor load were selected to investigate a **broad range of BSG input**. These feed rates correspond to **1.86 kg/h, 4.00 kg/h, 8.00 kg/h**, and **10.00 kg/h**, respectively. These levels were chosen to evaluate the influence of increasing feed rates on drying efficiency, especially to identify to conditions enabling high drying performance.

*3.2.4. Screw speed*

**Screw speed** is a critical parameter that influences both **shear rates** and **residence time**. It must be **sufficiently low** to allow the **drying of BSG**, but **high enough** to ensure **effective shear to grind BSG** and to prevent accumulation of BSG at the entrance of the extruder. The extruder used can reach a maximum of 680 rpm. Here, three screw speeds were evaluated: **100 rpm, 250 rpm**, and **450 rpm**.

Figure 4.4 displays the **residence time of BSG** inside the extruder as function of the **screw speed**. A clear **inverse relationship** is observed. Residence time decrease with increasing screw speed. At screw speed of **100 rpm**, the average residence time is **38.3 ± 2.1 s** which is **nearly twice as long as for 250 rpm**. However, **250** and **450 rpm** do not seem to differ significantly with an average residence time of **18.5 ± 3.8 s** and **14.3 ± 7.1 s,** respectively. This indicates a plateau in the reduction of residence time beyond a certain screw speed threshold.

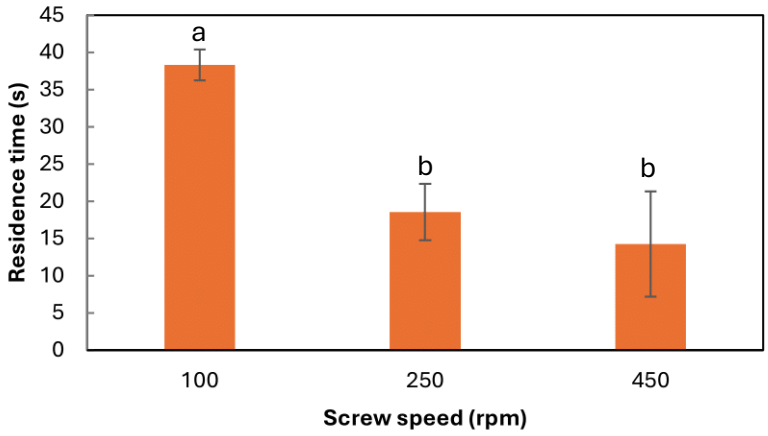


*Figure 4.4: Average residence time recorded as function of screw speed for profile 1, considering all feed rates (10-70%) and all temperatures (110-190°C)*

### 3.2.5. Preliminary results

Figure 4.5 displays **moisture content** of BSG after extrusion using **Profile 1** at **different temperatures, screw speeds** and **feed rates**. It is possible to see that **110 °C** does not permit to sufficiently dry BSG. At **110 °C**, the lowest moisture content reached was **53.9 ± 0.7 %** (wet basis) for a screw speed of **450 rpm** and a feed rate of **10 %**, while the **highest** was **68.9 ± 0.2 %** (wet basis).

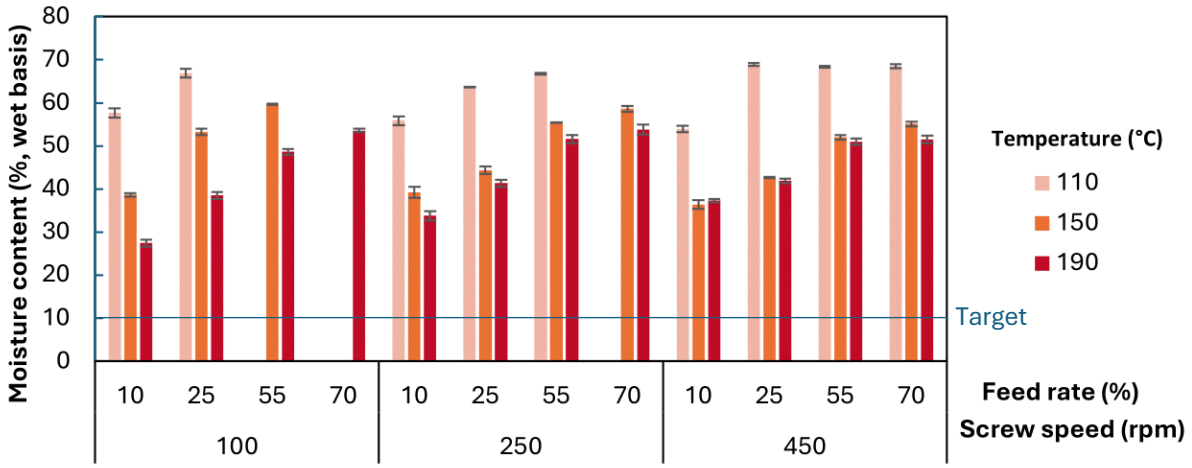


*Figure 4.5: Moisture content (% wet basis) of BSG after extrusion using Screw Profile 1 as a function of screw speed (100, 250, and 450 rpm), feed rate (10, 25, 55, and 70 % motor load), and barrel temperature (110, 150, and 190 °C). Means of triplicates. Initial BSG moisture = 75 % (wet basis).*

It is noteworthy that, as shown in Figure 4.5, moisture content data corresponding to a **feed rate of 55 % at 100 and 250 rpm** and **70 % at 110 °C** could not be obtained because with these settings, the process cannot extrude BSG (the material blocks in the extruder), due to insufficient screw speed compared to feed rate. **Temperature** was also **not high enough** to **dry the input moisture load**, resulting in **water accumulation** at the entrance of the extruder and **instability of the process**.

Looking at results for **150 °C and 190 °C**, it is possible to observe that considering all screw speeds, moisture content increases with feed rate. The **lowest** moisture content achieved was **27.4 ± 0.8 %** (wet basis), being obtained at a feed rate of **10%, 190 °C, 100 rpm,** while the **highest** moisture content is **59.6 ± 0.2 %** (wet basis) at 55 **%, 150 °C and 100 rpm**.

The working window of parameters is represented in Figure 4.6.

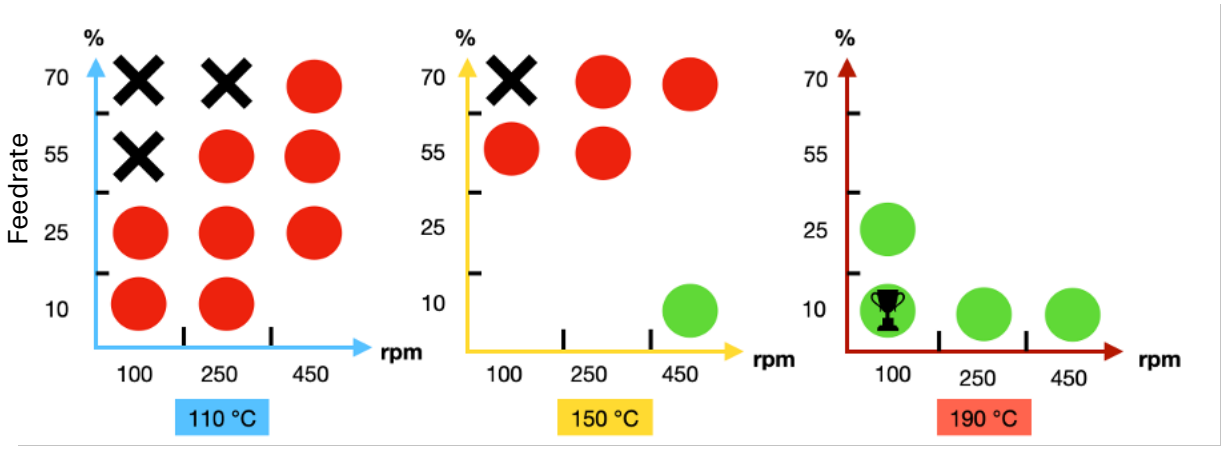


*Figure 4.6: Summary of preliminary process results using Profile 1. Crosses indicate unprocessable parameter combinations, red circles correspond to the highest moisture contents (> 55 %), and green circles are used for the lowest values (<40%).*

### *3.2.6. Conclusions*

To conclude this first set of trials, Figure 4.7 shows the **correlation matrix** between **processing parameters** (temperature, screw speed, feed rates, and residence time) and the **resulting moisture content** of BSG. The matrix helps us to define which parameters have the strongest relationship with moisture content results. Hence, it is apparent from this figure that **temperature** shows the **strongest relationship** with resulting moisture content of BSG, indicating that higher temperatures result in lower moisture levels. Moreover, there is a significant **positive** correlation between **feed rate** and **BSG moisture content**, suggesting that high feed rate prevents drying of BSG. Overall, under the applied conditions, this screw profile did not come close to reaching the first drying objective of 10 % moisture content.

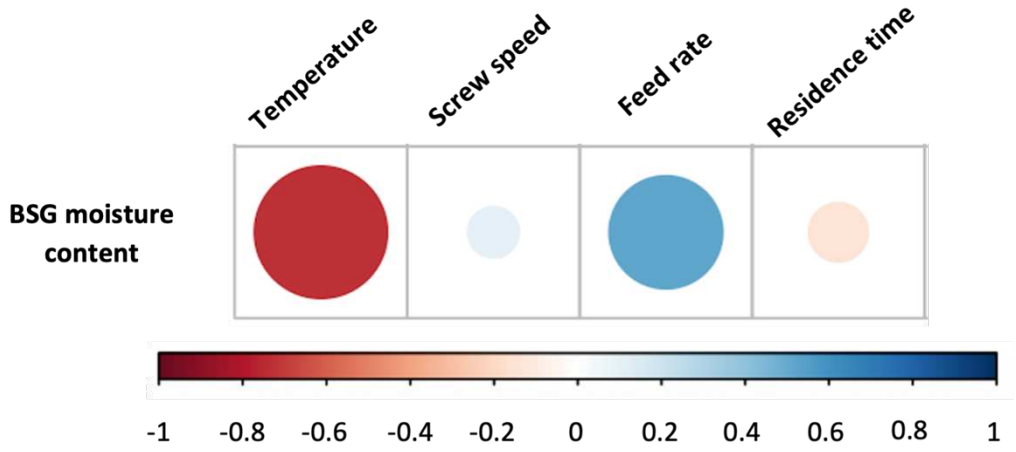


*Figure 4.7: Pearson correlation matrix showing the relationship between processing parameters (Temperature, Screw Speed, Throughput), Residence Time and BSG moisture content for Profile 1. The size and color intensity of the circles indicate the strength and direction of the correlations.*

In summary, these results suggest that **temperature** and **feed rate** are the **most influential parameters to dry BSG**. These findings align with expectations: increasing thermal energy enhances moisture removal, while higher water input (associated with higher feed rate) hinders the drying process. The **lowest temperature** (**110 °C**) proved **insufficient** to reach target moisture content and the **highest feed rates** (**55 and 70 %**) were **not processable** due to BSG accumulation at the inlet of extruder. Moreover, the **screw profile** made of only forward screw elements did not success to achieve moisture content lower than **27.4 ± 0.8 %** (wet basis). Therefore, for the **second set of trials**, selected temperatures were **150 °C** and **190 °C** while feed rates were limited to **10** and **25 %.** Different **screw profiles** were tested to **increase shear and residence time**.

## 3.3. Second set of trials – Modified screw profile

### *3.3.1. Introduction*

In this **second** set of trials, three different screw profiles were developed by **incrementally** adding **grooved** and **full reverse** convoying screw elements to increase **residence time** and improve the capacity of dried BSG to be ground. These profiles were evaluated in order of increasing stringency. A **grooved element** is considered **less stringent** compared to a **full element**.

**All profiles** exhibited the **same structure as Profile 1** (Figure 4.3) with **wide-pitch** screw element at the inlet of the extrusion and following each venting zone, as well as **narrow-pitch** screw elements preceding each venting zone.

*3.3.2. Screw profiles*

For **Profile 2**, displayed in Figure 4.8, **one grooved reverse** screw element of 12.5 mm was added **prior to the second venting zone**. It was chosen to put it prior to the 2nd venting zone and not the first, to avoid any accumulation to close to the feeding zone, thereby avoiding a flow back to the entrance. This addition allows BSG to dry prior to this 2nd venting zone, thereby reducing its density upon reaching 2nd venting zone and preventing accumulation that might occur if this element were positioned before the first venting zone.

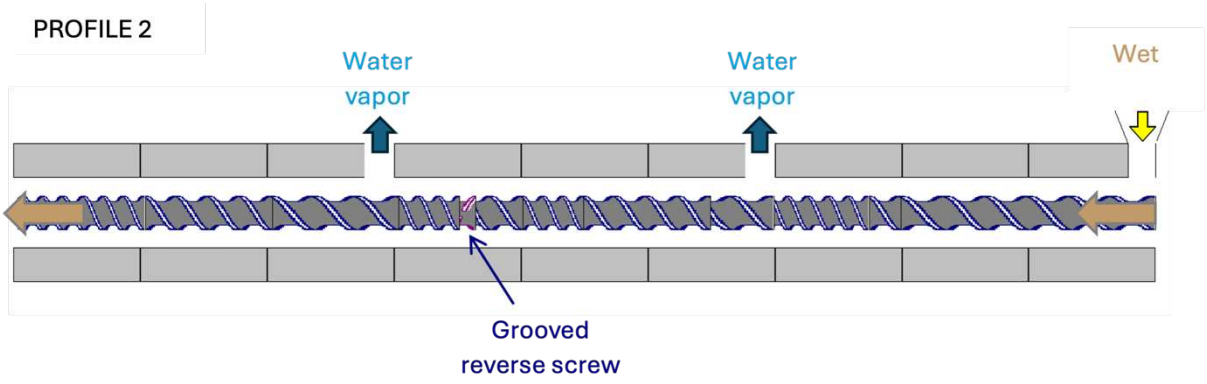


*Figure 4.8: Screw profile 2 of the twin-screw extruder designed to grind and dry BSG incremented by one grooved reverse element*

To further improve drying efficiency, from the profile 2, **a second grooved reverse** conveying screw element of 25 mm was added in Profile 3 (Figure 4.9), this time positioned prior to the **first** venting zone. This modification was motivated by previous observations of **too high remaining moisture content** in BSG at the end of the process and **limited vapor release in the early zones** of the extrusion process. By adding this second screw element, the goal was to increase **pressure** and promote more effective **vapor extraction** through the **first venting zone**.

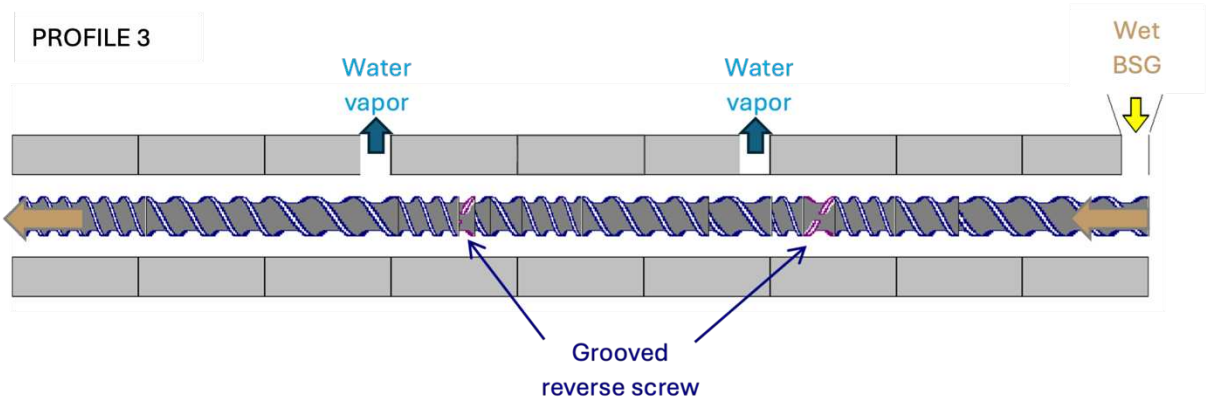


*Figure 4.9: Screw profile 3 of the twin-screw extruder designed to grind and dry BSG incremented by two grooved reverse elements*

To increase even more the **pressure** and **resistance** to the flow, the **first grooved reverse** screw element (in profile 3) was replaced by a **full reverse** screw element in Profile 4, Figure 4.10. To avoid **disrupting** the feeding too much and ensure stable processing, a **shorter reverse** element was chosen to replace the grooved one. This cautious change allowed us to test the effect of reverse flow while limiting the risk of material accumulation or feeding issues at the inlet.

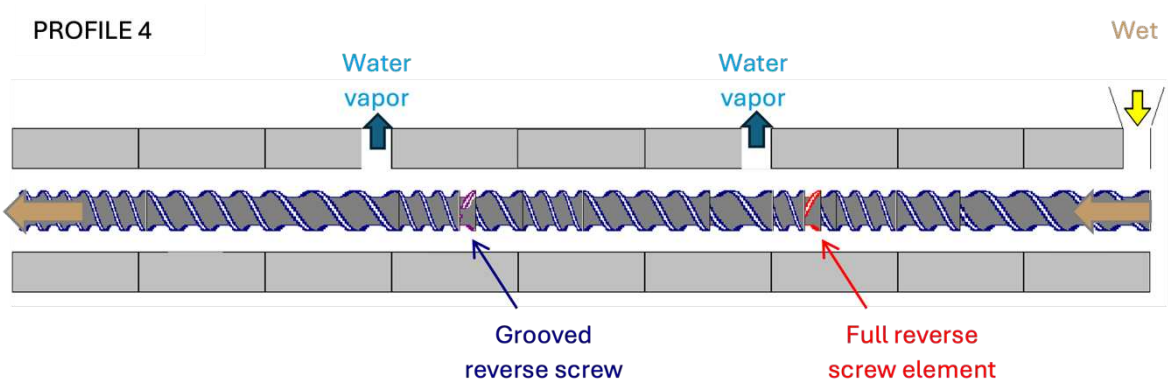


*Figure 4.10: Screw profile 4 of the twin-screw extruder designed to grind and dry BSG incremented by one grooved and one full reverse element*

### *3.3.3. Results*

The first results presented in the section will focus **on processing at 150 °C** as the objective is to identify the **lowest feasible temperature** and to prevent BSG from **thermal damages**. Moreover, conditions that prove effective at 150 °C are expected to remain effective at higher temperatures.

Figure 4.11 displays the **average residence time** at feed rate of **1.82 kg/h (10 %)** and a temperature of **150 °C**, for different screw speeds and for all the screw profiles. As expected, **two trends** are observable:

1- Residence time decreases with increasing screw speeds.

2- Adding reverse screw elements permitted to increase residence time.

This last trend is **amplified at low screw speed** (100 rpm) and less visible at high screw speeds (250 and 450 rpm). It should be noted that, given our limited stock of BSG and the large sample requirements for residence time measurements, this analysis could only be performed once.

At **250 rpm**, we can observe that **Profile 3** seems to have a **longer residence time** which is probably due to the **higher length** of the grooved reverse element compared to the full reverse element of Profile 4. However, at **450 rpm**, **residence times** are much **shorter overall** and there is **less separation between profiles**. At such high screw speed, the extruder barrel is less filled than at lower speeds providing higher freedom for BSG particles, this might restrict the influence of the reverse screw elements.

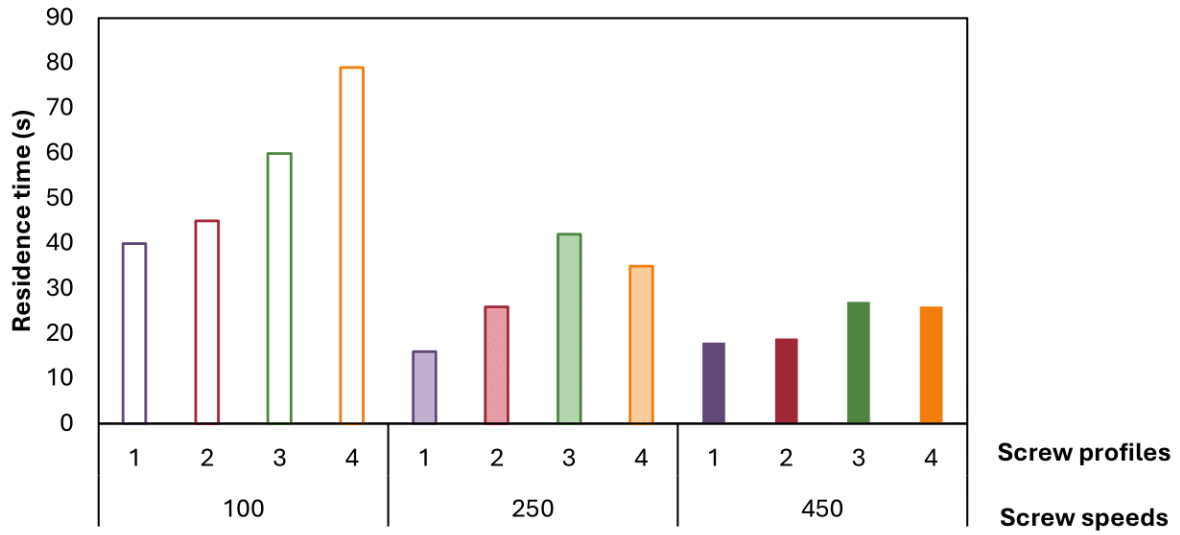


*Figure 4.11: Residence time of BSG at a feed rate of 10 % and 150 °C, for four screw profiles and three screw speeds*

The **primary objective** of extrusion being the **drying of BSG**, we are now going to look at the evolution of **residual moisture content** as function of the **extrusion parameters** on **Figure 4.12**. This figure highlights the **inverse relationship** between **residence time** and **moisture**

**content** across screw profiles in comparison to Figure 4.11. Indeed, as residence time increases with more reverse screw elements, the moisture content of BSG decreases significantly, indicating enhanced drying performance due to longer time under heat.

At low screw speed (**100 rpm**), **moisture content** of BSG decreases with increasing **stringency of the profile** and with increasing residence time.

At medium and high screw speeds, the **moisture content** seems to be **driven by the residence time**.

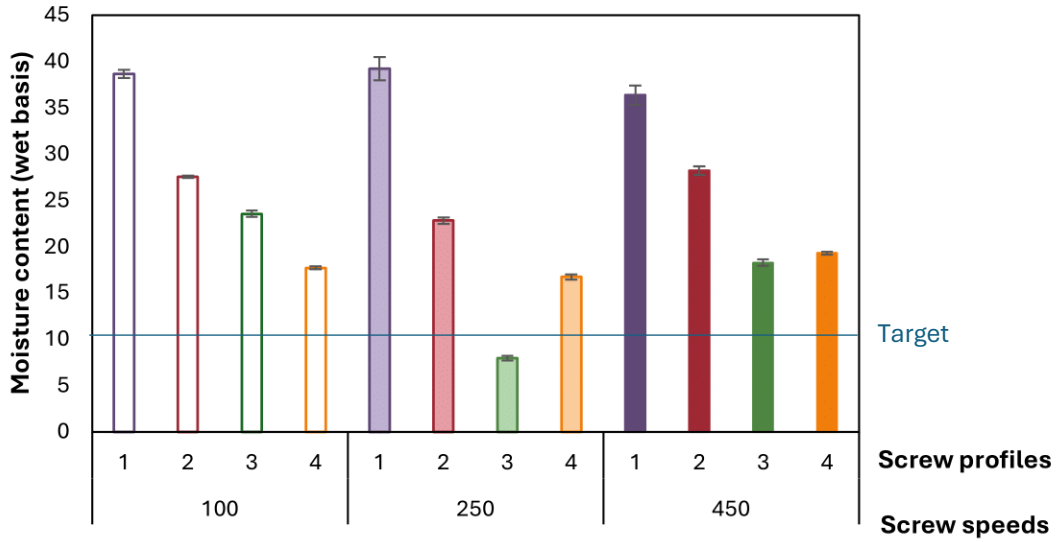


*Figure 4.12: Average moisture content of BSG at a feed rate of 10 % and temperatures of 150 °C, for four screw profiles and three screw speeds*

**Figure 4.13**: Moisture content of BSG vs residence time at 150 °C and a feed rate of 10 %, each shape and color representing a screw profile, the intensity of the color corresponds to the screw speed as displayed in the legend presents a scatterplot illustrating the **relationship between residence time and BSG moisture content** after drying at **150 °C**. This figure summarizes the latest results. For all screw profiles, except Profile 1, the **lowest moisture content** is consistently observed at a screw speed of **250 rpm**. This suggests a balanced influence between residence time and particle reduction associated with mechanical energy dissipation. Other studied also highlighted a similar balance. In their study on extrusion pretreatment of soybeans hulls for fermentable sugars conversion, Yoo *et al.* observed that residence time and mechanical energy input are competing factors. According to them, the

possible reason is that lower screw speed allows more time for thermal degradation and mechanical separation but also results in lower mechanical input and less intensive treatment [276].

While Profile 2, 3 and 4 exhibit the same trend regarding moisture content with lowest point reached at 250 rpm, **Profile 3** seems to exacerbate this trend achieving the **lowest moisture content** recorded at **8.0 ± 0.3 %**. It is significantly lower than the second lowest moisture content reached with Profile 4 at 250 rpm (16.7 ± 0.3 %). This observation highlights the **influence of the screw profile** especially the **length of the reverse screw element**.

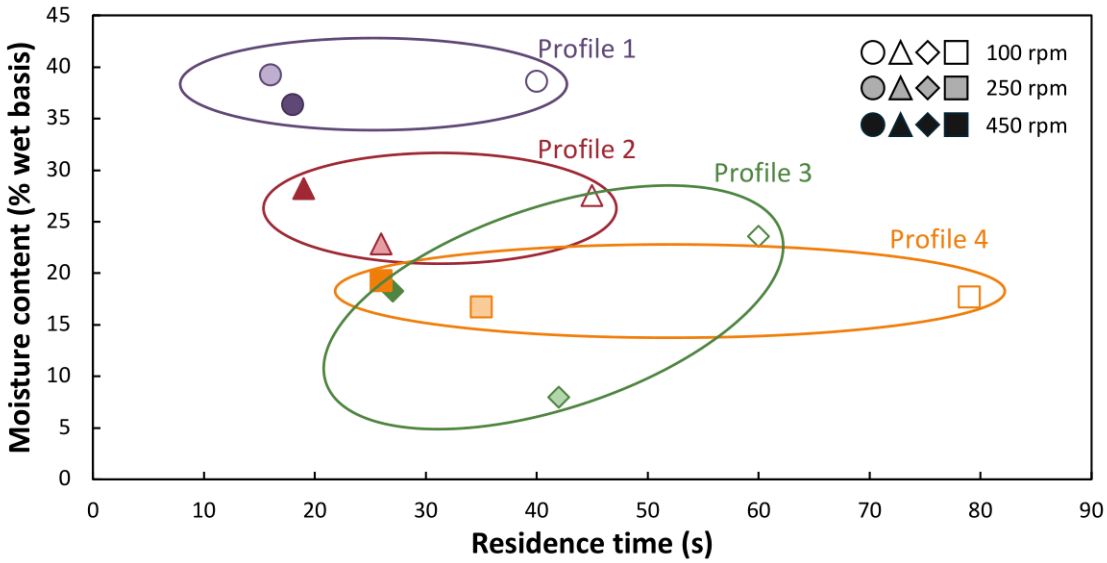


*Figure 4.13: Moisture content of BSG vs residence time at 150 °C and a feed rate of 10 %, each shape and color representing a screw profile, the intensity of the color corresponds to the screw speed as displayed in the legend*

In order, to evaluate whether a **higher efficiency** of the process can be achieved, a **higher feed rate of 25 %** of the motor load was tested at **150 °C** and **190 °C** across all screw speeds.

Figure 4.14: Moisture content of BSG against screw speed for different screw profiles (1,2,3,4) at 150°C (on the left) and 190°C (on the right) for a feed rate of 25% displays **BSG moisture content** obtained after extrusion for the **four screw profiles** at a feed rate **of 4 kg/h** (= 25 %) and two temperatures: **150 °C** and **190 °C**. What stands out in this figure is that at **100 rpm** the **number** of reverse screw elements does not appear to influence the drying performance of BSG, indeed Profile 2, 3 and 4 resulted in similar moisture contents. This suggests that the feed rate is **too high** compared to the **low** screw speed, potentially leading to screw overloading.

At **150 °C**, the trend remains **consistent with** the one observed at **1.8 kg/h feed rate** with **Profile 3** exhibiting the **best drying performance**. However, at **190 °C**, the trend diverges: **Profile 4 shows better drying performance than Profile 3** at both **250 rpm and 450 rpm**.

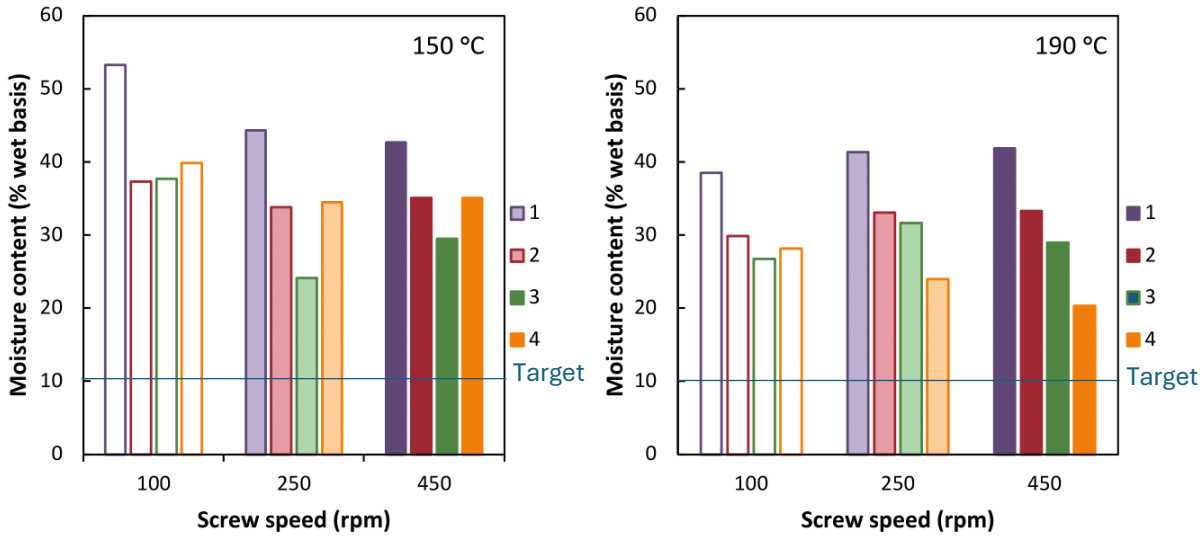


*Figure 4.14: Moisture content of BSG against screw speed for different screw profiles (1,2,3,4) at 150°C (on the left) and 190°C (on the right) for a feed rate of 25%*

As seen in Figure 4.13, the **lowest moisture content** across all tested conditions was **8.0 ± 0.3 %** (wet basis), obtained for **Profile 3** at **250 rpm, 10 % feed rate,** and **150 °C**. In these conditions, the **residence time** was also **the longest** among all profiles. This moisture content is **sufficient** to reach the **first target** of preservability (**10.7 %** wet basis), but still **too high** for direct use in composite production (~3 % wet basis). This could indeed result in lower interfacial adhesion since most of the thermoplastic matrices are hydrophobic. Moreover, the **BSG** was **not ground enough** to be applied effectively as a composite filler **using our method of injection molding** as seen in Figure 4.15. A **powder-like filler** is more favorable in our system, as it ensures processability by enabling passage **through the injection nozzle**. Moreover, the smaller the particles, the higher the contact surface between BSG and matrix is. Although a slight correlation between residence time and moisture reduction was observed, it has also been demonstrated that increasing residence time alone does not systematically lead to lower moisture content within our experimental window. Indeed, shear rate likely plays a significant role in enhancing water removal during extrusion.

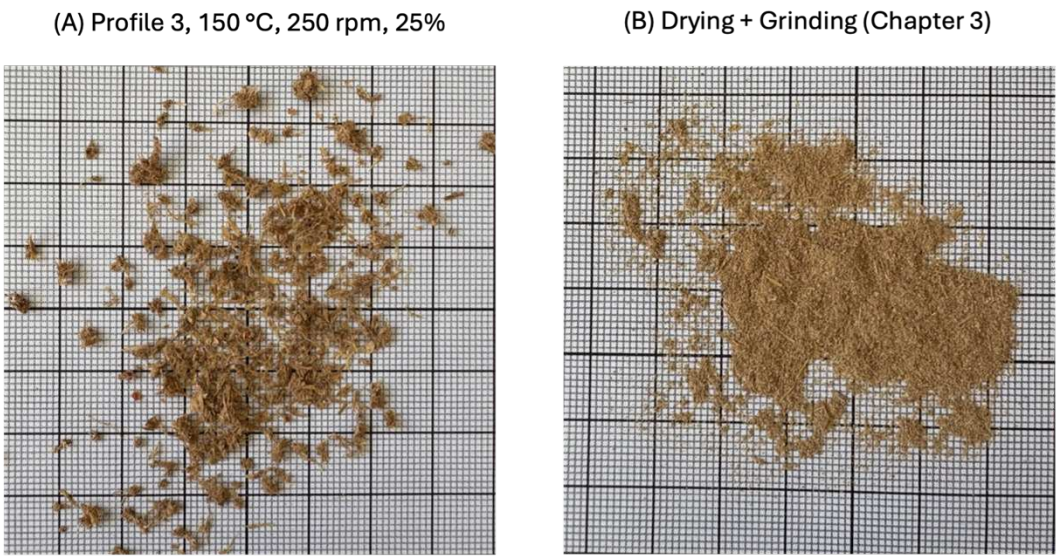


*Figure 4.15: Visual comparison of BSG after processing by two different methods: (A) BSG extruded using Profile 3 at 150 °C, 10 % feed rate, and 250 rpm; (B) BSG dried and ground following the method described in Chapter 3*

Based on these findings, **Profile 3** demonstrated the **most effective drying** performance, while **Profile 4** showed **better performance at higher temperature**. To capitalize on the advantages of both configurations, a **new screw profile** combining the key elements of Profile 3 and Profile 4 was designed. This hybrid profile aims to optimize both **moisture reduction** and **particle size reduction** and will serve as the reference profile for the main following experimental study.

## 4. Extrusion trial methodology

### 4.1. Extrusion profile

Based on the **knowledge** extracted from both sections 3.2. and 3.3. , a **new screw profile**, referred as **Profile 5**, was designed with the objective of **maximizing both drying and grinding**. Like Profile 3, it is constituted by **two grooved reverse** screw elements: one of 12.5 mm located before the second venting zone and one of 25 mm located prior to the first venting zone. The main modification in this profile is the addition of **two full reverse** screw elements of 12.5 mm positioned immediately before each grooved element. These elements are intended to **increase shear rate** and **mechanical stress**, thereby **promoting water extraction** and **grinding**. Screw profile 5 is displayed in Figure 4.16.

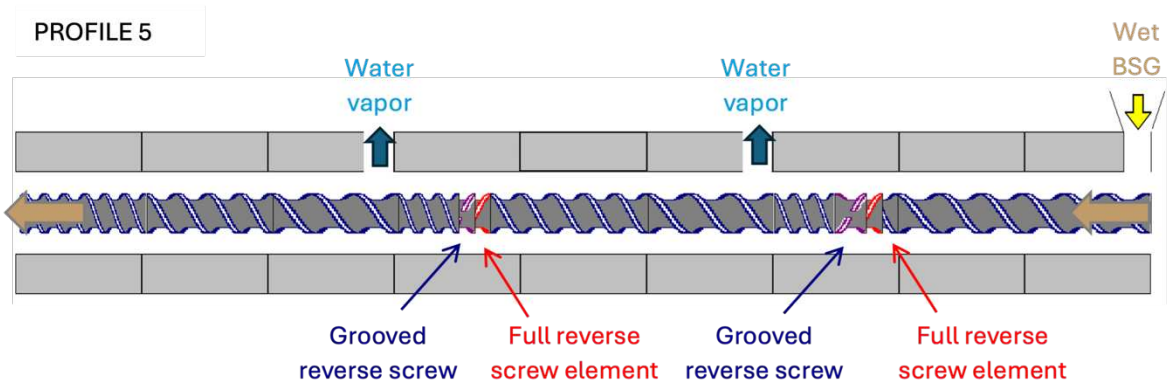


*Figure 4.16: Screw profile 5 of the twin-screw extruder designed to grind and dry BSG incremented by two grooved and two full reverse elements*

## 4.2. Extrusion parameters

For this main study, a **single feed rate** which showed the lowest moisture content was selected. BSG was introduced into the extruder using the volumetric feeder operating at a constant feed rate of **1.82 ± 0.06 kg/h**, corresponding to **10 %**. With both the screw profile and feed rate fixed, **two processing parameters** were varied: **screw speed** and **barrel temperature**. Each of these parameters was tested at **three levels**. Screw speeds were set at **200, 300,** and **400 rpm**, while the barrel temperature was uniformly maintained at **150, 170**, and **190 °C** across all zones. This experimental design resulted in a total of **nine processing conditions**. For each condition, extrusion was carried out for a minimum of 20 minutes following stabilization of the motor load, which was used as an indicator of process stability, before BSG samples were collected.

## 4.3. Effects of the parameters on BSG moisture content

Figure 4.17 shows the **moisture content of BSG** after extrusion drying grinding using profile 5 at different temperatures and different screw speeds. Interestingly, **all parameters** achieved the target moisture content for storage. The **lowest** moisture content **1.57 ± 0.42 %** (wet basis) for **190 °C at 400 rpm** and **the highest** was **4.02 ± 0.52 %** (wet basis) for **150 °C at 300 rpm**. However, except for these two, there is no significant difference across the samples. Therefore, Profile 5 allows us to reach homogenous results across parameters in terms of moisture content. Hence, we now will focus on the characterization of the extruded BSG samples in the following parts.

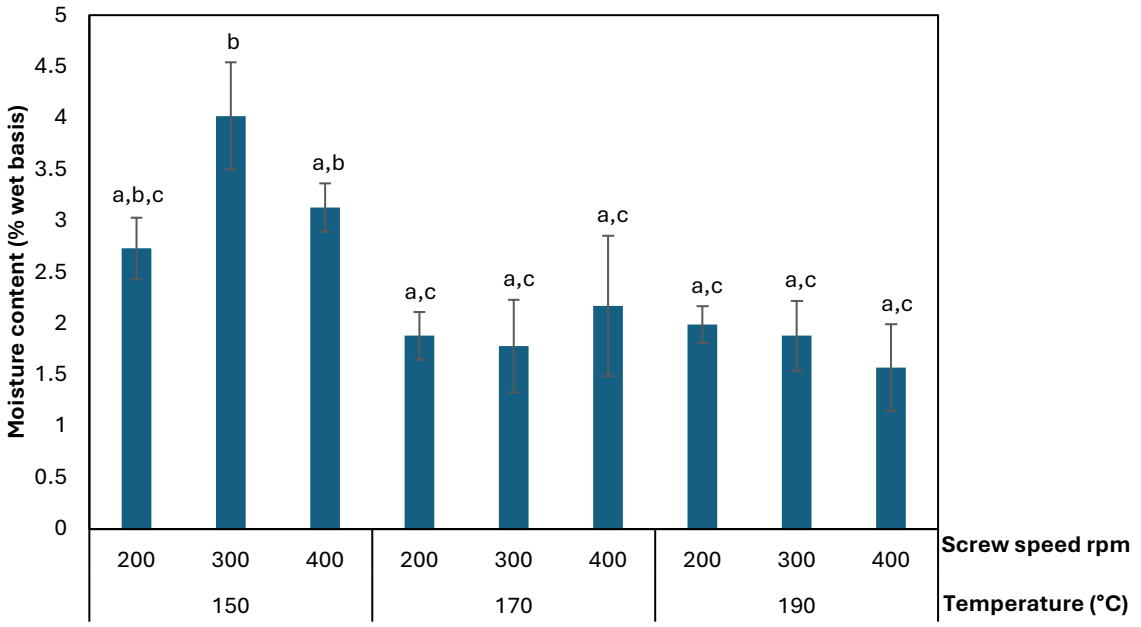


*Figure 4.17: Average moisture content (wet basis) of BSG after extrusion process as function of Temperature (°C) and Screw speed (rpm) at 1.8kg/h using Profile 5*

# 5. Results

## 5.1. Effects of the parameters on Particle Size Distribution (PSD)

### *5.1.1. Particle Size Distribution (PSD)*

In order to define the relevance of the grinding of BSG using extrusion, we will compare the **PSD** of BSG dried and ground **in Chapter 3** using conventional method, referred as **BSGconv** to the PSD of extruded BSG from extrusion process detailed in section 4. , using Profile 5.

**Figure 4.18**: Particle size distribution of BSG dried and ground using method of Chapter 3 next to its SEM image x80 shows the **PSD of BSG** after drying and grinding **using the conventional method of Chapter 3.** What is striking in Figure 4.18: Particle size distribution of BSG dried and ground using method of Chapter 3 next to its SEM image x80 is the **bimodal distribution** of the particles. Two distinct populations can be observed: **smaller particles** and significantly **larger ones**. Additionally, as seen in **SEM picture** (Figure 4.18), while many particles appear **rounded**, a few shows an **elongated shape**. This pattern could be due to inherent heterogeneity of the lignocellulosic biomass. Indeed, as it was seen in Chapter 1, **BSG** consists mainly of residue from the **external layers of barley seeds** and **remnants of embryo** as shown in Chapter 1 (Figure 1.11). Consequently, these components have **different chemical and physical structures** which could result in **different fracture patterns** and grinding behavior.

Another explanation could be linked to the **equipment used to grind**. Shell and Harwood showed that **hammer milling** led to a **broader range of particle size** than other method such as disc milling [277]. This could explain the presence of both fine and coarse particles within the same sample.

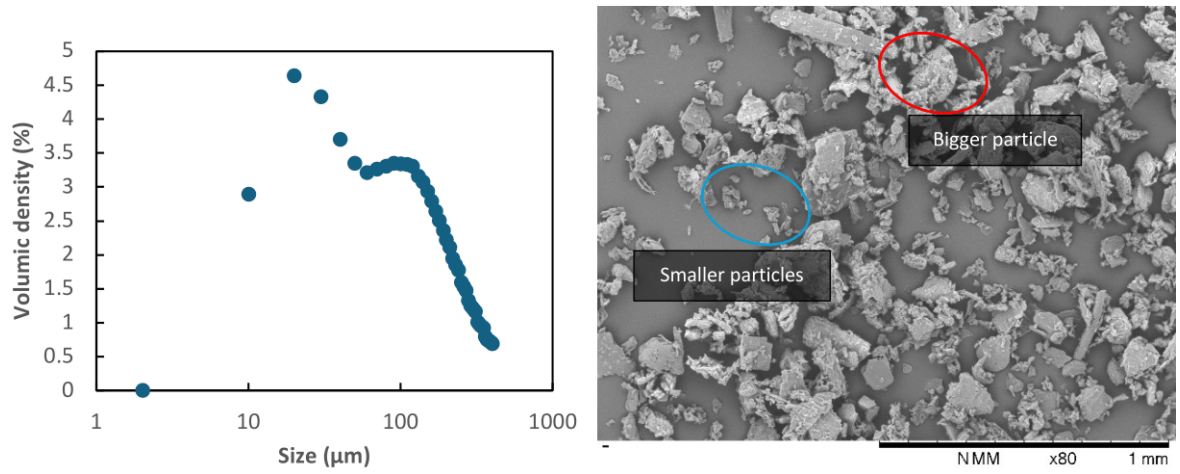


*Figure 4.18: Particle size distribution of BSG dried and ground using method of Chapter 3 next to its SEM image x80*

Figure 4.19 displays the **particle size distribution** of BSG **after extrusion** for each 9 experimental runs. In this figure, they are grouped by extrusion temperature to highlight the influence of screw speed. The **initial hypothesis** was that **screw speed** would have a **greater influence on PSD** than temperature. However, the results of Figure 4.19 and **Table 4.2**, gathering **particles median size** ($D_{50}$) for each condition, do not support this assumption. Across most tested conditions, changes in screw speed do not appear to significantly alter the shape or peak position of the PSD curves.

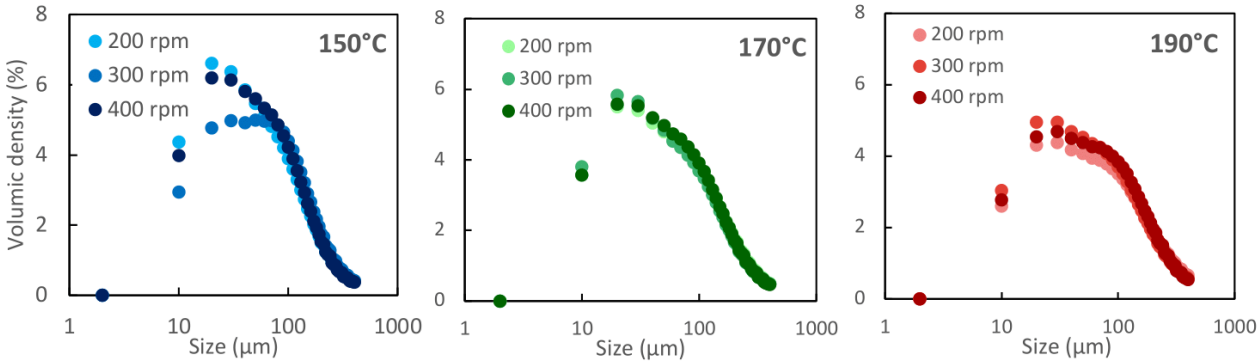


*Figure 4.19: Particle size distribution of extruded BSG at three barrel temperatures (150 °C, 170 °C, and 190 °C) and three screw speeds (200, 300, and 400 rpm) using Profile 5*

Notably, the condition at **150 °C and 300 rpm** shows a **higher $D_{50}$** (**108.8 ± 3.6 µm**) than 200 rpm and 400 rpm at the same temperature (97.1 ± 3.3 µm and 95.8 ± 3.1 µm, respectively). Interestingly, this is also the sample with the highest residual moisture content (4.02 ± 0.52 %), which could have influenced its comminution behavior during extrusion. It has been suggested that **water** could have a **plasticizing effect** on the biomass during milling [124]. Hence, according to Mayer-Laigle *et al.* extensive drying of the biomass may have consequences on mechanical properties of BSG by removing this plasticizing effect making it more brittle and susceptible to comminution [124]. Another explanation could be that **moisture enhances hydrogen bonding** between particles leading to **agglomeration** [105].

Similarly, **at 190 °C**, the particle size distribution obtained **at 200 rpm differs** significantly from the distributions **at 300 and 400 rpm**, indicating that at this high temperature, screw speed begins to have a more marked influence. The possible reasons behind this difference, including thermal and chemical effects, will be discussed later in this section.

The most interesting aspect of all these graphs is that **PSD** is **unimodal**. Indeed, all PSD display only **one peak** with a **maximum** reached around **25 µm**. This suggests that the particles were **ground more uniformly** during the **extrusion process** compared to the method used in Chapter 3, which resulted in a broader, bimodal distribution (Figure 4.18). The **absence** of a second peak indicates **fewer coarse fragments** and a **more homogeneous comminution** of the material. A possible explanation for this might be that BSG undergoes a thermal modification during extrusion which might induce chemical and structural changes within the material.

While the barrel temperatures reached during extrusion (150–190 °C) are slightly **below typical torrefaction ranges** (200–300 °C, [278]), the **elevated pressure** and **oxidative atmosphere** within the extruder may create a thermomechanical environment similar to that of **higher thermal treatments**. Thus, **condensable volatiles** of BSG as well as hemicelluloses, which are less thermally stable as seen in Chapter 3, may have been **degraded.** This can only happen once the water has been removed from BSG which allows particles to reach temperatures above 100 °C. This will be further discussed in 5.3. .

A major change caused by the **degradation of hemicellulose** is the increasing of the **crystallinity of cellulose** due to the relative enrichment of ordered cellulose domains [279]. In their study, Bhuiyan *et al.* investigated how heat treatments under different moisture conditions affect the crystalline structure of cellulose in wood. They showed **that heat treatment** under

**moist environment** significantly **increases cellulose crystallinity** compared to dry conditions in the early stages. They attributed it to the pressure produced by steam leading to low stress conditions in the crystalline and amorphous regions [279]. This supports the idea that **during BSG extrusion**, the combined effect of **heat, moisture, and pressure** may cause **structural rearrangements**, more particularly an increase in cellulose crystallinity. This phenomenon leads to a **more rigid material** and influences the **fracture mechanism**. This could explain the observed shift toward a more uniform particle size distribution.

Repellin *et al.,* studied the torrefaction pretreatment influence on the grinding of raw wood chips. In their study, it was shown that **torrefaction** (in a kiln between 160 °C and 300 °C) **decreases particle size distribution** of wood chips after grinding. They explained it by the **softening of lignin** passing through its glass transition and the stress induced in cellulose released by cracks [280]. In our case, the **uniform** and **unimodal PSD** may reflect **structural changes** induced by combined **thermal** and **mechanical** treatment making BSG more susceptible to **comminution**. As shown in Table 4.2, **all** extrusion treatment led to a significantly **smaller median size of particles** than for the conventional drying and grinding.

Figure 4.20 shows the **PSD** for each 9 runs but this time **grouped by screw speed**, thereby highlighting the **effect of temperature**. For a given screw speed, the same trend is visible, **higher temperature** leads to **bigger particles**. For example, **at 200 rpm**, a temperature of **150 °C** results in particles with a $\boldsymbol{D_{50}}$ of **97.1 ± 3.3 µm** which is significantly **lower than for 190 °C** with a $D_{50}$ of **137.9 ± 4.8 µm**. These findings are contrary to previous studies which have suggested that higher temperature resulted in smaller particle size [105,280,281]. However, it is possible that **Maillard reaction** occurs at higher temperatures due to the high content of **proteins and reducing sugars** in BSG, thereby causing **agglomeration** between small particles. Reducing sugars can represent up to 15 %(m/m) of BSG [103]. The formation of melanoids was observed by Hejna *et al*, who extruded dry BSG at high temperature to grind it [105]. This could result in color change and agglomerations of the particles. We also observed color change of BSG particles at higher temperatures, however the difference is not big enough to visualize it on a picture.

Let us now return to our previous observation regarding the influence of screw speed on PSD at **190 °C**. **Shear rate** seems to **enhance the comminution** of BSG. Indeed, at 190 °C and **200 rpm**, $\boldsymbol{D_{50}}$ is about **137.9 ± 4.8 µm** while it is significantly lower at higher screw speed: **122.8 ± 3.0 µm** and **124.7 ± 2.0 µm** at **300** and **400 rpm**, respectively. It is probable that **higher mechanical shear** promotes the **breakup** of BSG agglomerates.

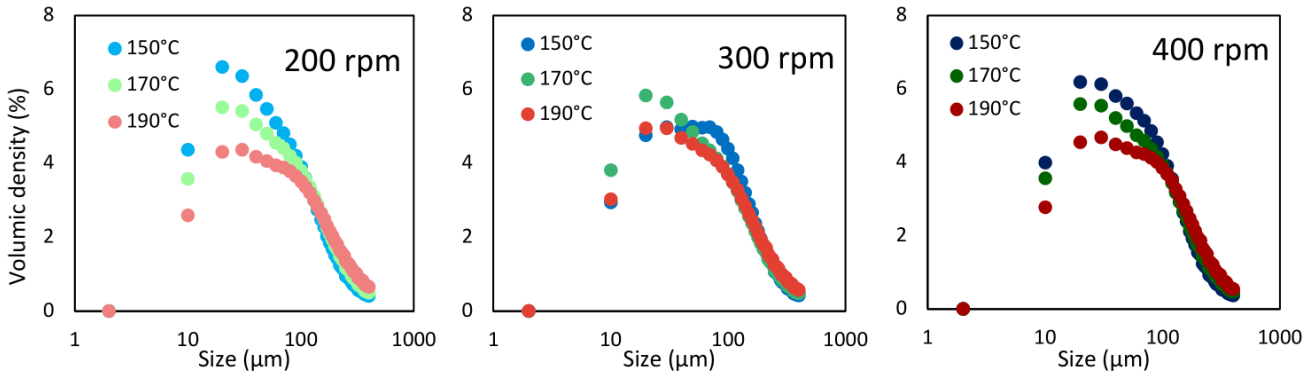


*Figure 4.20: Particle size distribution of extruded BSG at three screw speeds (200, 300, and 400 rpm) and three barrel temperatures (150 °C, 170 °C, and 190 °C) using Profile 5*

*Table 4.2: Median size ($D_{50}$) of BSG particles obtained after extrusion for the 9 experimental runs and after drying and grinding following Chapter 3 method. Different letters represent statistically different values.*

| Temperature (°C) | Screw speed (rpm) | $D_{50}$ (µm) |
|---|---|---|
| 150 | 200 | **97.1**$^{a}$ ± 3.3 |
| | 300 | **108.8**$^{b}$ ± 3.6 |
| | 400 | **95.8**$^{a}$ ± 3.1 |
| 170 | 200 | **113.3**$^{b}$ ± 2.6 |
| | 300 | **111.9**$^{b}$ ± 3.7 |
| | 400 | **109.3**$^{b}$ ± 4.3 |
| 190 | 200 | **137.9**$^{c}$ ± 4.8 |
| | 300 | **122.8**$^{d}$ ± 3.0 |
| | 400 | **124.7**$^{d}$ ± 2.0 |
| BSG conv | | **146.1**$^{e}$ ± 4.0 |

To conclude, **extrusion** allowed us to obtain **finer particles** than when using the **rotor miller** on dry BSG particles. Moreover, compared to the results of Hejna *et al.* whose approach inspired this work, our process achieved significantly **smaller particles** than theirs. They used extrusion on dry particles at 30 °C, 60 °C, 120 °C, and 180 °C. At 30 °C and 60 °C, they observed particles agglomerates bigger than **1200 µm** and for 120 °C and 180 °C they observed a mean particle size of **203 µm and 138 µm** [105]. **Our particles** size between **97.1** and **137.9 µm** which when used in composite promotes better dispersion and higher specific surface.

### 5.1.2. Response surface modelling $D_{50}$ (median size)

Figure 4.21 displays the **response surface model** for the median particle size (**$D_{50}$**) of BSG as a function of extrusion temperature and screw speed. The surface, generated using a second-order polynomial equation, shown in Table 4.3, reveals a **clear downward trend in $D_{50}$ with increasing temperature**. However, it confirms that increasing screw speed helps with BSG particle size reduction. The model fits the experimental data well with a $R^2$ of 0.910 and supports the optimization of process conditions to minimize particle size.

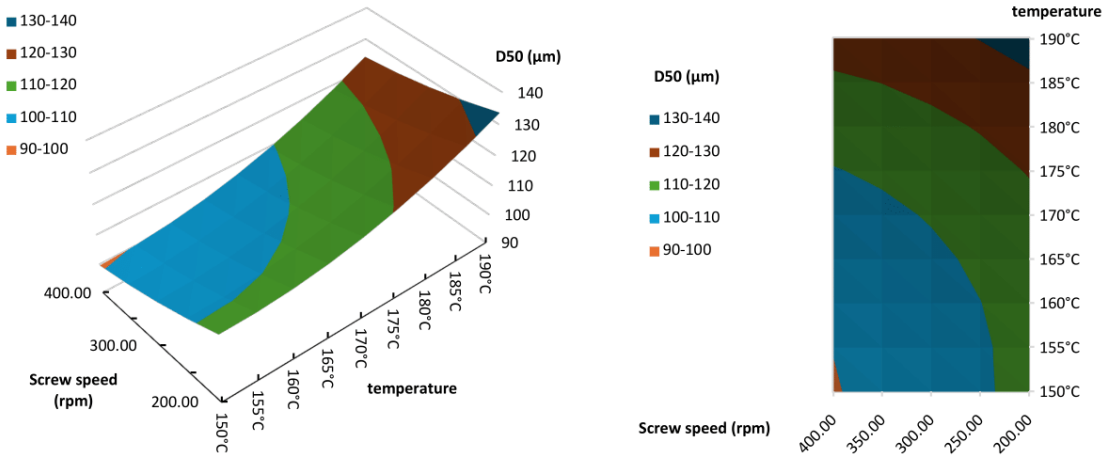


*Figure 4.21: Effect of processing variable conditions (temperature and screw speed) on median size ($D_{50}$) of extruded BSG particles.*

*Table 4.3: Multiple regression equation and regression coefficient of median size (µm) of BSG particles after extrusion for various parameters sets*

| Variable to be predicted | Regression equation | $R^2$ |
|---|---|---|
| $D_{50}$ | $D_{50}$=478.424-4.420*T-0.210*S+0.014*$T^2$ –+11.6*$10^{-5}$*$S^2$ - 48.9*$10^{-5}$*S*T | 0.911 |

*T- temperature; S- screw speed; D50- Median particle size*

## 5.2. Particles aspect (SEM)

Figure 4.22 displays **SEM images** of **BSG** obtained through conventional method used in **Chapter 3** and **extruded BSG at 150 °C and 400 rpm**. These images provide insight into the fracture behavior resulting from each process. On the left, the **conventional grinding** resulted in particles with **cleaner fracture and angular shapes**. At these magnifications, we are able to see long striations on the side of the larger particles, they are indicative of xylem tissues which have higher lignin content [282]. They appear to be more difficult to grind. In contrast **extruded BSG**

(on the right) exhibit markedly different rupture morphology, characterized by **tearing rather than cutting**.

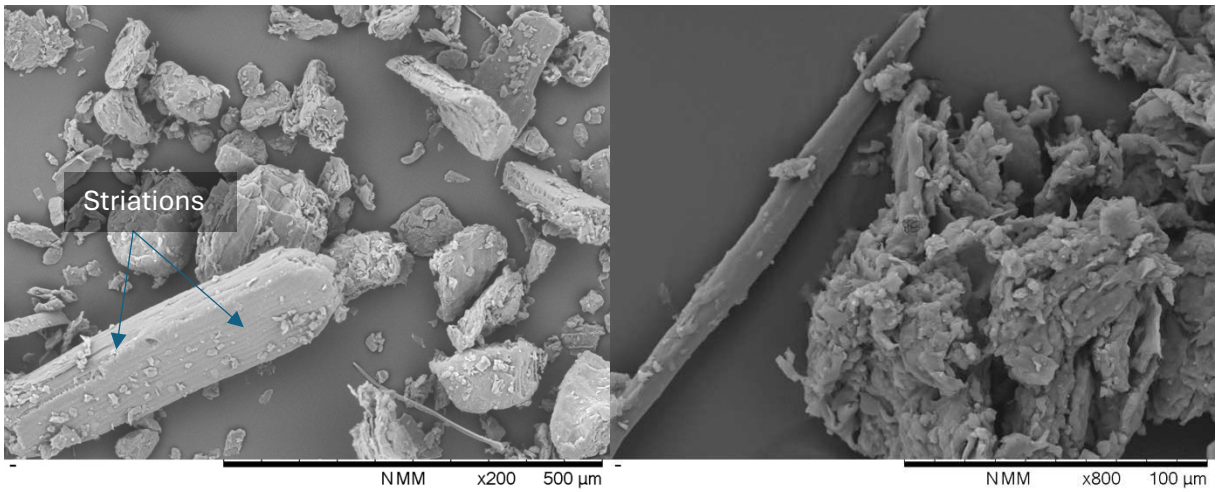


BSG conv Extruded BSG

*Figure 4.22: SEM images of conventional BSG (from chapter 3) (x80 and x200) compared to extruded BSG at 150 °C 400 rpm Profile 5(x80 and x800)*

Not all tested processing conditions are shown here, as many exhibited similar trends. Only representative conditions were selected to illustrate the observations relevant to this study.

Figure 4.23 provides visual evidence of the **fracture behavior** of extruded BSG. On Figure 4.23 a), a **needle-like** fracture pattern, referred to as **defibrillation**, can be observed. This behavior likely originates from cellulose-rich regions, where the elongated molecular arrangement and higher crystallinity promote fracture along the fiber axis. Such anisotropic failure highlights the intrinsic directional brittleness of these domains, which in turn compromises the overall mechanical integrity of the material by favoring premature crack propagation along specific planes. Figure 4.23 b) shows **cracks propagating** at the surface of the particle which may lead to teared smaller particles.

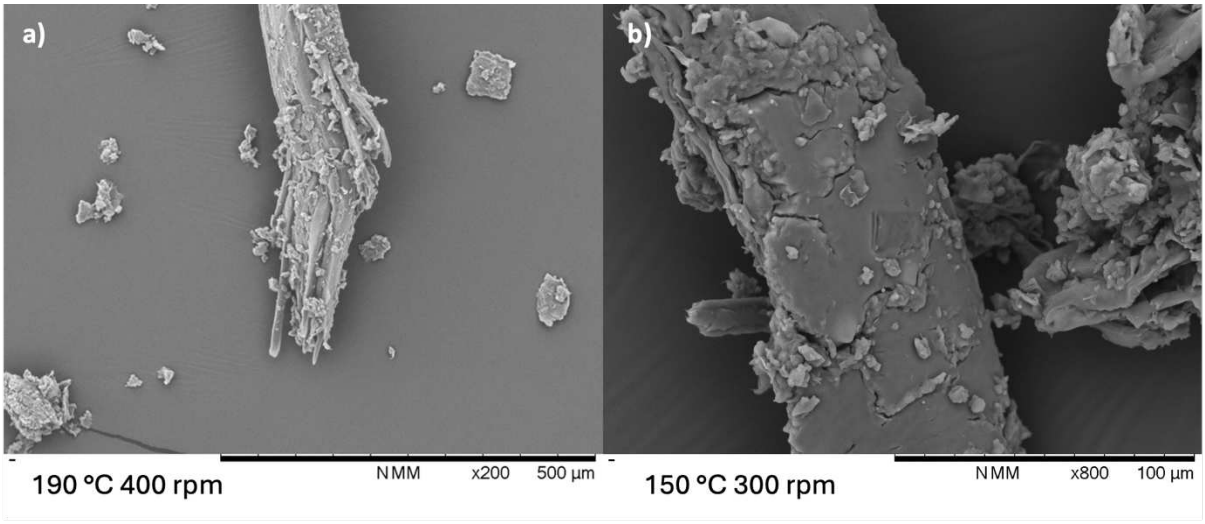


*Figure 4.23:SEM images of extruded BSG using Profile 5 at: a) 190 °C and 400 rpm x 200 b) 150 °C and 300 rpm x800*

Figure 4.24 shows **SEM** pictures of BSG extruded at **150 °C** and **200 rpm** which gave the finest particles. At a magnification of x80, residual cell walls structures are no longer distinguishable as the particles appear very **damaged**. Compared to conventional method of Chapter 3, the **extruded particles** are significantly **smaller** and exhibit a **rougher** surface morphology. This surface roughness increases of the **specific surface area** of the particles which could potentially enhance interfacial bonding in composite application, especially at low filler loadings. This effect is similar to the observed phenomenon in nanocomposites which require lower filler loadings to contribute to improved mechanical reinforcement, even at lower filler loading. This is due to much larger specific surface area of nanofillers compared to micrometric fillers [283].

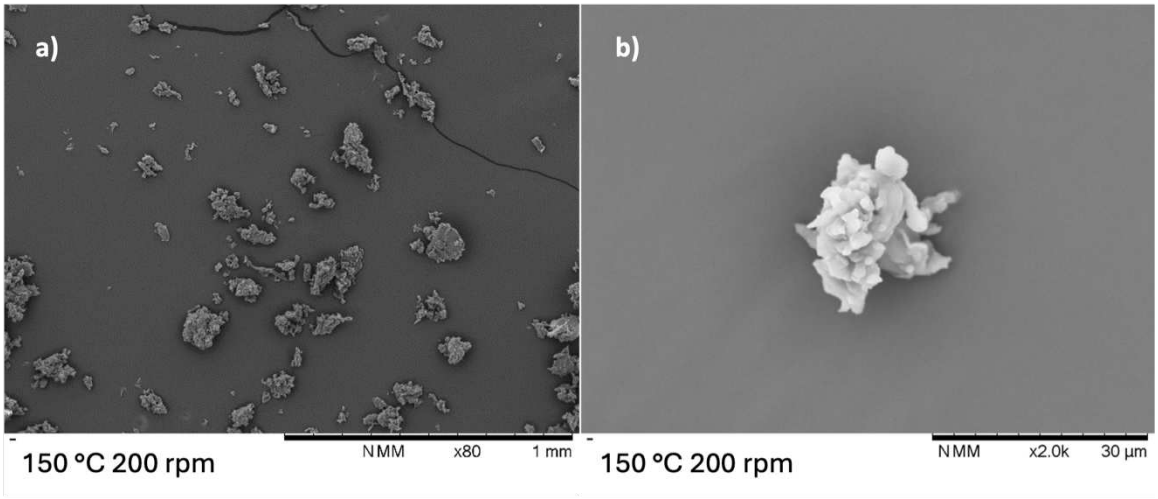


*Figure 4.24: SEM images of extruded BSG at 150 °C, 200 rpm using Profile 5, magnifications a) x80 and b) x2000*

Figure 4.25 presents **SEM pictures** of BSG extruded at **190 °C and 200 rpm** which resulted in the **biggest particles**. As for extruded BSG at 150 °C, particles appear very **damaged**, and their surface are **rough**. However, unlike particles of Figure 4.24, the apparent size of the particles is

larger. Figure 4.25 shows particles **agglomeration**. This observation supports the previous hypothesis of particles agglomeration due to **Maillard reaction**. Indeed, the temperature reached during extrusion may influence the occurrence of Maillard reaction and caramelization, due to the presence of **reducing sugars** and potentially reactive functional groups in lignin [105] which could gain in reactivity due to lignin glass transition temperature passing. These reactions can lead to the formation of high molecular weight compounds such as melanoidins [284], which may increase the **stickiness of the particles**. As a result, this could promote agglomeration phenomena, visible in SEM images as larger, compacted structures.

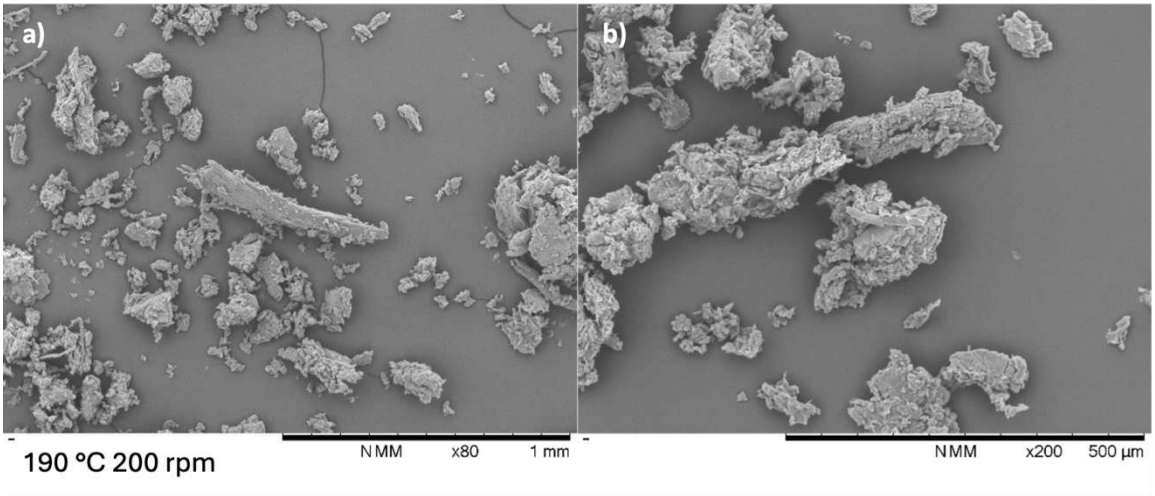


*Figure 4.25: SEM images of extruded BSG at 190 °C, 200 rpm using Profile 5, magnifications a) x80 and b) x200*

In summary, SEM analysis revealed clear morphological differences between conventionally dried and ground BSG and extruded one. **Extruded BSG** displayed more **irregular and teared fractures surfaces** with rougher morphology and in some cases agglomerations. These results were influenced by extrusion parameters (screw speed and temperature). The presence of **needle-like structures** and **surface cracks** suggest an enhanced material brittleness, likely due to structural rearrangements such as lignin softening and cellulose crystallinity.

These morphological and chemical changes induced by the extrusion drying/grinding process may offer advantages for composite applications. The **smaller particle size** could **improve dispersion** within the polymer matrix, while the increased surface roughness may promote **better interfacial adhesion**. Additionally, the chemical modifications induced by extrusion may improve **thermal stability** due to the removal of less stable compounds [285] and reduce **BSG hygroscopicity** by increasing their surface free energy as noticed in numerous

studies [159,278,285]. Therefore, the compatibility of BSG with hydrophobic matrices would be promoted and its shelf life and handling during processing would be improved.

### 5.3. Thermal stability of extruded particles

Figure 4.26 shows the **thermogravimetric analysis** and **derivative** profiles of extruded BSG grouped by screw speed, with key results summarized in Table 4.4. Compared to the conventional method, extrusion process appears to **modify** the **thermal degradation** profile of BSG. Notably, the shoulder at lower temperatures, corresponding to the degradation of the lightest compounds, **shifts towards higher temperatures**, just **after** the main hemicelluloses and celluloses degradation peaks (~298 °C and ~350 °C, respectively), as indicated by **arrows** on Figure 4.26. This shift is attributed to the **degradation of volatile compounds** during extrusion and a relative increase of lignin content.

This is supported by the significant **rise in $T_{1\%}$,** the temperature at which 1 % mass loss occurs. Such effect can be associated with the **reduction** in the content of **low molecular weight compounds**, which may either be degraded of take part in Maillard reactions [88].

It can be noticed that the two sharp peaks related to the degradation of **hemicelluloses and celluloses**, are **not impacted** by the extrusion. Moreover, while extrusion clearly enhances the thermal stability of BSG compared to the conventional method, the extrusion parameters (temperature and screw speed) did **not show a consistent impact** on thermal behavior. This is likely due to the **short residence time** during processing (~70 s), which may have **limited the extent** of chemical transformations. The only notable difference in $T_{1\%}$ were observed with the lowest temperature/shortest time condition (**150 °C – 300 rpm**) and the highest temperature/longest time condition (**190 °C – 200 rpm**), this suggests that **longer exposure** may be required to **impact** significantly BSG **chemical structure**.

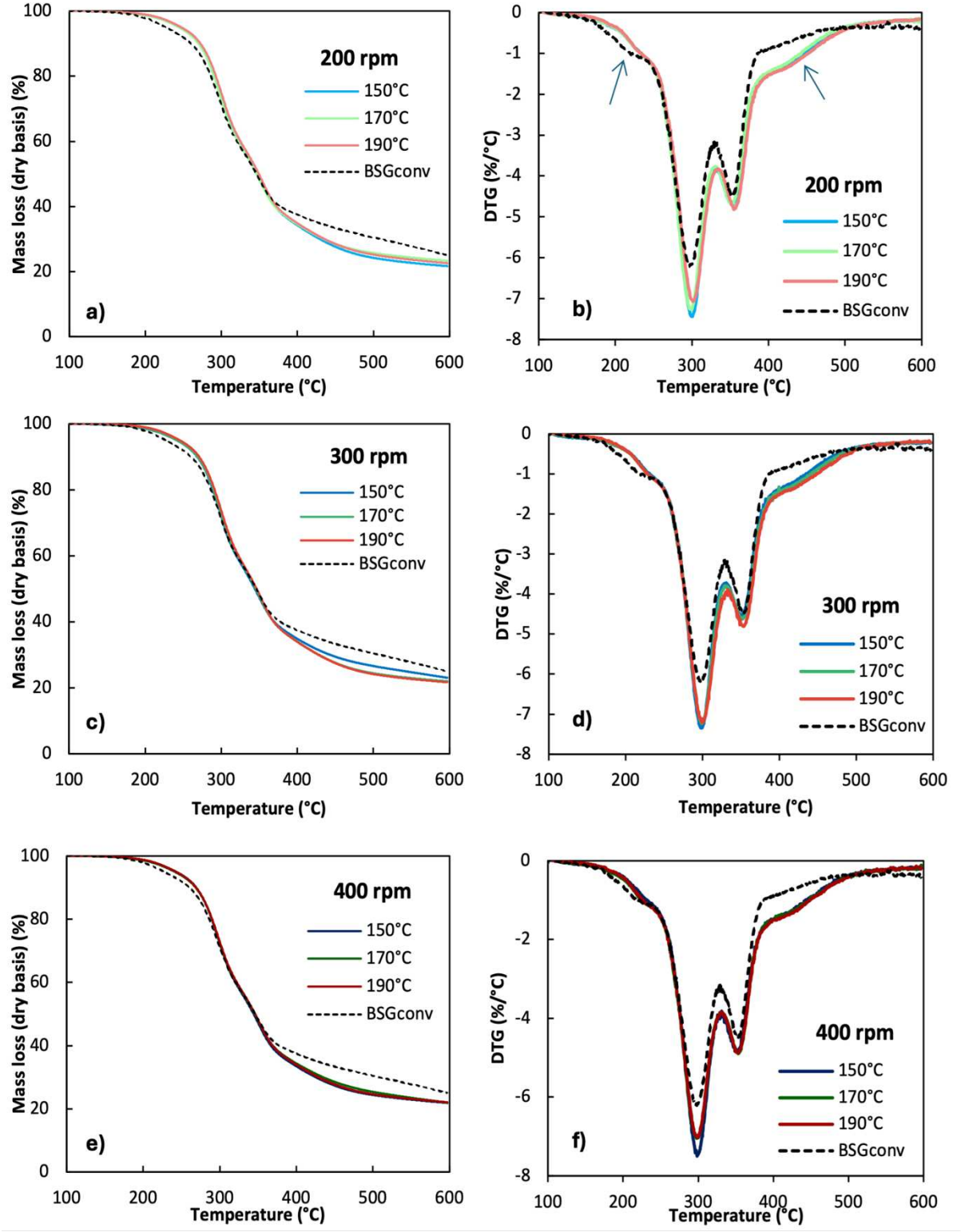


*Figure 4.26: Thermogravimetric curves (a,c,e) and their derivatives (b,d,f) of BSG made with conventional method and extruded BSG with profile 5 at 200 rpm (a,b) ; 300 (c,d) ; 400 rpm (e,f)*

*Table 4.4: Results of thermogravimetric analysis of extruded BSG samples using Profile 5 and BSGconv, different letters mean significative difference*

| Sample | $T_{peak1}$ | $T_{peak2}$ | $T_{1\%}$ | $T_{50\%}$ |
|---|---|---|---|---|
| BSGconv | **297.3**$^{a}$ ± 0.8 | **346.0**$^{a}$ ± 6.5 | **180.0**$^{a}$ ± 2.5 | **345.8**$^{a}$ ± 2.5 |
| BSGext150_200 | **300.9**$^{a}$ ± 1.7 | **353.5**$^{b}$ ± 1.7 | **193.3**$^{bc}$ ± 1.9 | **347.5**$^{a}$ ± 2.5 |
| BSGext150_300 | **298.1**$^{a}$ ± 1.8 | **347.8**$^{b}$ ± 4.5 | **187.7**$^{ab}$ ± 3.5 | **344.0**$^{a}$ ± 2.12 |
| BSGext150_400 | **297.7**$^{a}$ ± 1.1 | **349.8**$^{b}$ ± 1.9 | **189.7**$^{bc}$ ± 3.0 | **344.0**$^{a}$ ± 1.6 |
| BSGext170_200 | **297.7**$^{a}$ ± 1.2 | **350.2**$^{b}$ ± 2.0 | **192.0**$^{bc}$ ± 0.8 | **346.0**$^{a}$ ± 1.1 |
| BSGext170_300 | **298.2**$^{a}$ ± 1.8 | **351.1**$^{b}$ ± 1.2 | **190.8**$^{bc}$ ± 3.7 | **345.5**$^{a}$ ± 2.5 |
| BSGext170_400 | **298.0**$^{a}$ ± 0.9 | **350.8**$^{b}$ ± 3.9 | **189.8**$^{bc}$ ± 2.7 | **345.5**$^{a}$ ± 0.7 |
| BSGext190_200 | **299.1**$^{a}$ ± 1.1 | **352.7**$^{b}$ ± 1.2 | **198.7**$^{c}$ ± 1.6 | **349.2**$^{a}$ ± 2.2 |
| BSGext190_300 | **300.0**$^{a}$ ± 0.3 | **352.8**$^{b}$ ± 0.9 | **198.7**$^{c}$ ± 0.8 | **346.3**$^{a}$ ± 0.6 |
| BSGext190_400 | **298.5**$^{a}$ ± 0.7 | **351.9**$^{b}$ ± 1.0 | **194.2**$^{bc}$ ±1.9 | **346.0**$^{a}$ ±1.1 |

To conclude, this **removal of volatile compounds** during extrusion could still be relevant, firstly to prevent from **moisture uptake during storage** by increasing **hydrophobicity** [278] and secondly during composites processing, as such compounds could otherwise **interact with PLA** promoting **chain scission** as discussed in Chapter 3. Moreover, their presence may lead to **gas release** at the **filler-matrix interface** during compounding as they degrade within the same range of temperatures, potentially compromising interfacial adhesion.

## 5.4. Energy consumption involved in conventional method vs extrusion

### *5.4.1. Introduction*

From the industrial perspective, **energy consumption** is a crucial aspect when evaluating the **feasibility and sustainability** of processing methods. In this section, we compare the **energy requirements** of the conventional **method described in Chapter 3** where BSG was dried in a **ventilated oven** from 78 %(m/m) to 3 %(m/m), then ground using a **rotor hammer mill** with a 0.1 mm screen with those of the **extrusion process**. **Grinding** operation is considered as very **energy intensive**. Therefore, it is of crucial importance to take it into consideration. We begin by analyzing the mechanical energy demand associated with the grinding step.

*5.4.2. Energy required to grind BSG*

The **grinding step** was performed using a RETSCH Ultra Centrifugal Mill ZM 1000. Based on the nominal voltage (U = 230 V), measured current during operation (I = 2.8 A), and estimated (using data of the equipment) power factor (cos(φ) = 0.69), the average power consumption was calculated to be 444 W using Equation 1.

$$P = U \times I \times \cos(\varphi) \quad (4.2)$$

With a processing time of **5 minutes for 200 g of BSG**, this corresponds to a specific mechanical energy of approximately **667 kJ/kg**.

Regarding **extrusion** processing, for the comparison only the **specific mechanical energy (SME)** was considered (and not temperature). SME is defined as the mechanical energy input required to process unit weight of extrudate [130]. SME is calculated using the Equation 2 firstly introduced in Chapter 1. **Except** at the highest screw speed **400 rpm** (900, 720, 828 kJ/kg, highlighted in red, Table 4.5), *SME* values remained **lower** than that of the rotor mill method (667 kJ/kg). The **lowest** extrusion value was recorded for **190 °C at 200 rpm** (**468 kJ/kg**). This corresponds to a **reduction** of almost **30 %** of the energy requirement **compared to the conventional method**.

Contrary to the findings of Hejna *et al*. who studied the grinding of already dried BSG and reported **decreasing energy demand** with **increasing screw speed** due to **reduced residence time** [105], our result show opposite trend. This can be attributed to the **direct linear relationship between SME and screw speed** as can be seen in **Equation 2**. However, when considering **torque** alone, a general **decrease** is observed with **increasing screw speed**, which may effectively reflect **shorter residence time** and consequent **reduced barrel filling** under constant feed rate condition.

$$SME = \frac{1}{Q} \frac{N}{N_{max}} r \frac{C}{C_{max}} W \quad (4.3)$$

With $Q$ the mass feed rate (1.8 kg/h), $N$ is the screw speed, $N_{max}$ is the maximum screw speed (680 rpm), $r$ is the motor efficiency (0.93), $C$ is the torque, $C_{max}$ is the maximum torque (100), and $W$ is the nominal power (9.2 kW).

*Table 4.5: Values of specific mechanical energy required for extrusion drying grinding of BSG under different conditions.*

| Temperature, °C | Screw Speed, rpm | Torque % | *SME* (kWh/kg) | *SME* (kJ/kg) |
|---|---|---|---|---|
| 150 | 200 | 10 | 0.14 | 504 |
| | 300 | 7 | 0.14 | 504 |
| | 400 | 9 | 0.25 | 900 |
| 170 | 200 | 10 | 0.14 | 504 |
| | 300 | 8 | 0.16 | 576 |
| | 400 | 7 | 0.2 | 720 |
| 190 | 200 | 9 | 0.13 | 468 |
| | 300 | 8 | 0.15 | 540 |
| | 400 | 8 | 0.23 | 828 |
| Conventional Mill | | | | 667 |

To conclude at **200 and 300 rpm**, extrusion grinding in terms of mechanical energy offers to **reduce the energy consumption** by **30 %** compared to the **conventional method** (comparing 504 kJ/kg and 667 kJ/kg). Additionally, the presence of the **two venting zones** along the extruder barrel offers an opportunity for **energy recovery**. The **steam** released during extrusion drying could be captured and **reused as part of the heating system**, improving **overall process efficiency** and **cost**.

Considering a **moisture reduction** in extruded BSG **from 78 %** (initial moisture content) **to 3 %** (global final moisture content) and a **feed rate of 1.8 kg/h**, approximately **1.35 kg/h of steam is removed**. Thus, considering the heat of condensation of water which is about **2260 kJ per kg of steam**. Redirecting this heat could contribute to maintaining barrel temperatures, thereby reducing external energy input.

### *5.4.3. Conclusion on energy for grinding*

The extrusion process offers significant practical advantages over the conventional method. In our experimental conditions, the **drying approach** of Chapter 3 required 48 hours to process 2 kg of BSG in thin layers using a 55 L ventilated oven with regular mixing. This corresponds to a **drying rate of 0.042 kg/h**. Moreover, due to slow rate of water removal, recovering and **reusing steam** for energy seems **impractical**. Additionally, in our laboratory scale, the **grinding** was operated per **batch** of 200 g of dry BSG, corresponding to approximately 800 g of wet BSG. A batch of grinding, considering the cleaning took 15 min, yields a rate of **3.2 kg/h** which is significantly **higher** than the grinding rate of **extrusion process**. However, this drying-grinding process (from Chapter 3) contains a limiting step which is the drying due to its significantly higher

duration. This highlights the advantage of extrusion in **integrating both drying and grinding** in a **single operation**.

This single step results in substantial **time savings**, **reduced labor**, and a smaller **spatial footprint** for processing and transport. By reducing BSG particle size and moisture content in one time, extrusion greatly simplifies material handling and storage logistics. In our case, the need to store wet BSG in a freezer added a significant energy requirement and occupied considerable storage space. By **integrating drying and grinding** through extrusion after beer process, it would be possible to **store the extruded BSG** instead, substantially **reducing both the energy required for preservation and the carbon footprint of storage**. This could support the **industrial relevance of extrusion** as a more sustainable approach for BSG valorization.

## 6. Conclusions

This chapter demonstrated that **twin-screw extrusion** is a possible alternative **method** for simultaneously drying and grinding BSG. A **two-step preliminary** study was carried out, first to **refine the extrusion parameters**: temperature and feed rate, and second, to **optimize the screw profile** configuration. As a result, BSG was successfully dried, reaching a moisture content as low as **1.57 %** (at 190 °C, 400 rpm, Profile 5), meeting the requirements of **both storage and composite manufacturing**. Moreover, BSG was successfully ground, with the lowest median size of **95.8 µm** (at 150 °C, 400 rpm, Profile 5), with particles significantly **finer and more uniform** to those obtained with conventional method.

SEM analysis revealed distinct morphological changes, such as **rougher surfaces** and **bimodal fracture patterns** likely resulting from structural modifications which could be lignin softening and cellulose enhanced crystallinity. Signs of **particles agglomeration at higher temperatures**, potentially driven by Maillard reaction products, were observed.

Thermal analysis showed **improved thermal stability** for **extruded BSG** compared to conventional BSG due to **partial removal of the lightest compounds**. This could have advantages during compounding with polymer reducing the risk of unwanted interaction and gas formation at the interface.

From a **laboratory perspective**, extrusion outperformed conventional method in term of operational efficiency. On an **industrial scale**, while mechanical energy consumption for grinding was mainly lower but, in some cases, comparable, the potential of **recovering and reusing steam** released during extrusion could be a **critical advantage**. Furthermore, the process eliminates the need for wet storage, which is energy-intensive and space-consuming,

offering instead the option to store compact, dried material. Moreover, the **extrusion** is a highly **scalable process**, reinforcing its relevance and applicability for industrial scale BSG valorization.

Overall, the twin-screw extrusion process offers not only a technical but also a logistical and energetic advantage, strengthening the potential for BSG upcycling into sustainable, high-performance bio-based materials. Although this chapter focused on the application of extruded BSG in polymer composites, this material presents **valuable opportunity** in **other domains** such as energy sector. Moreover, the extrusion treatment could also be adapted and extended to **reactive extrusion**, paving the way for **biorefinery strategies** such as protein extraction. Given BSG high protein content and the growing demand for plant-based proteins, this strategy offers strong potential for expanding the **valorization of BSG** beyond composites application. The schematic overview of this chapter is in Figure 4.27.

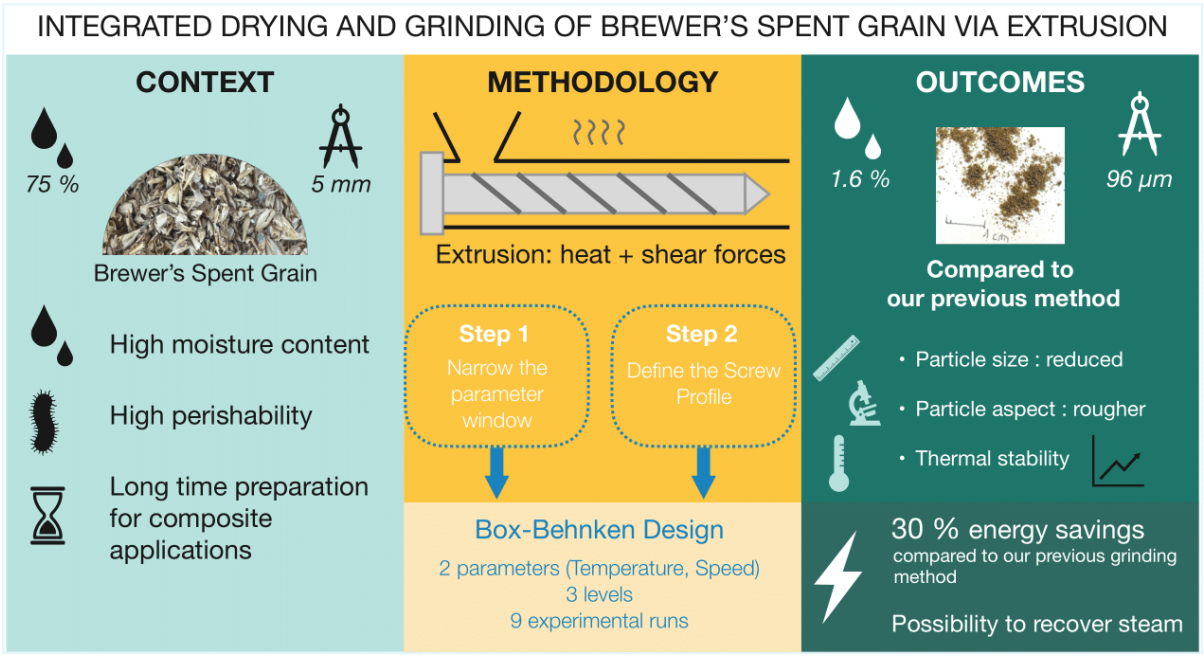


*Figure 4.27: Schematic overview of Chapter 4.*

The **extruded BSG** produced in this study will be further explored in the following chapter, where its performance **as a filler** in polymer composites will be evaluated focusing on its effect on mechanical, thermal, and interfacial properties.

# CHAPTER 5:

## Bridging strategies for composites optimization

# RÉSUMÉ DU CHAPITRE 5

Ce chapitre permet d'associer les connaissances et résultats extraits des chapitres 3 et 4. Il évalue, dans une première partie, le potentiel de la drêche extrudée comme charge dans des composites thermoplastiques, en mettant en lumière l'influence du pré-traitement de la drêche. Dans une seconde partie, l'accent est placé sur le changement d'échelle de la fabrication des composites en passant de l'échelle laboratoire utilisant le mélangeur interne et une presse à injection manuelle à une échelle pilote utilisant l'extrusion et une presse à injecter automatique de taille beaucoup plus conséquente. Les effets des méthodes de mise en forme sur les performances finales des matériaux sont étudiés.

**Première partie** : La drêche retenue pour faire des composites a été extrudée selon trois conditions (150 °C/200 rpm, 170 °C/300 rpm, 190 °C/400 rpm) avant son incorporation dans une matrice polypropylène (PP). Pour la matrice PLA, seule la condition intermédiaire (170 °C/300 rpm) a été retenue. Les formulations ont été mélangées à l'aide d'un mélangeur interne, puis leurs propriétés thermiques, rhéologiques, morphologiques et mécaniques ont été caractérisées. La comparaison entre drêche extrudée et drêche séchée-broyée selon la méthode d'origine montre que l'extrusion modifie la morphologie des particules (surfaces plus rugueuses) et améliore son adhésion avec les matrices. Dans les composites PLA, l'élimination des composés volatils lors de l'extrusion limite la scission des chaînes polymères, ce qui se traduit par des modules rhéologiques plus élevés et une température de transition vitreuse ($T_g$) augmentée, rendant la mise en œuvre plus difficile tout en augmentant la résistance à la traction grâce à une meilleure compatibilité à l'interface. Dans les composites PP, l'effet est moins prononcé sur la $T_g$, mais la résistance à la traction s'améliore sensiblement avec la drêche extrudée, tout en conservant une bonne processabilité, justifiant le choix du PP pour la seconde partie avec le changement d'échelle.

**Seconde partie** : Sur la base des résultats obtenus avec le PP, deux conditions d'extrusion (150 °C/200 rpm et 190 °C/400 rpm) et la méthode d'origine de séchage broyage ont été retenues pour un changement d'échelle. La drêche extrudée a été mélangée avec le PP par extrusion bi-vis (échelle pilote) plutôt que par mélangeur interne. Afin de comparer ces deux méthodes de mélange, les granulés obtenus ont été injectés avec la presse manuelle (le mélangeur ne permettant pas d'avoir assez de matière pour la presse de plus grande taille). La comparaison entre les deux méthodes de mélange a révélé de très faibles différences confirmant la pertinence de l'utilisation du mélangeur interne particulièrement lorsque les quantités de matériaux

disponibles sont faibles. Toutefois, il est nécessaire de préciser que les procédés de mélanges n'ont pas été répliqués, ainsi les interprétations sont à prendre avec précaution. Ensuite, les composites obtenus par extrusion ont été injectés à l'aide d'une presse manuelle de laboratoire et d'une machine d'injection taille pilote/industrielle. L'analyse montre que le procédé d'injection industrielle fournit des pièces plus reproductibles et fiables, alors que l'injection manuelle, limitée par le contrôle des paramètres, entraîne une plus grande variabilité. De grandes différences en terme de cristallinité ont été mise en évidence. Les matériaux injectés manuellement ont montré une plus grande cristallinité probablement due à la trempe nécessaire avant injection puis à la vitesse de refroidissement du moule beaucoup plus faible que dans le cas de l'injection industrielle. Elle reste toutefois une méthode robuste pour les faibles volumes de laboratoire.

Dans l'ensemble, la drêche extrudée apparaît comme une charge durable et prometteuse pour les composites à base de PP, offrant une combinaison intéressante de renforcement mécanique et de facilité de traitement. Les expériences confirment que la morphologie des particules, modifiée par l'extrusion, joue un rôle clé dans les performances des composites, sans toutefois impliquer de modification chimique de la drêche. Le chapitre suivant se concentrera donc sur le traitement chimique de ce résidu de la filière brassicole afin d'approfondir la compréhension de l'influence de la composition et de la surface des particules sur la compatibilité avec les matrices thermoplastiques.

# Chapter 5 : Bridging strategies for composites optimization

## 1. Introduction

This chapter investigates the potential of extruded Brewer's spent grain (BSG) as a bio-based filler for thermoplastic composites with a focus on how **BSG pre-treatment and composite processing methods** influence final material performances.

In the **first part** (Figure 5.1), BSG was extruded under **three different conditions** (150 °C/200 rpm, 170 °C/300 rpm, and 190 °C/400 rpm) before being incorporated into **PP matrix** and under only **one condition** (170 °C/300 rpm) prior to incorporation into **PLA matrix**. For **PP**, we chose to study both the **extreme** and the **intermediate** extrusion conditions. To compare with PP, **one formulation** was investigated for **PLA**, hence we chose the **intermediate** extrusion condition. These formulations were compounded using an **internal mixer**, and their **thermal, rheological, morphological, and mechanical properties** were analysed. This section aims to compare the influence of **extruded** BSG versus conventionally **dried and ground** BSG (BSGconv) on the composite properties and to understand how extrusion affects BSG behavior as a filler within the two different matrices.

In the **second part** (Figure 5.1), based on the results obtained with PP, **two** selected extrusion conditions for drying BSG were further investigated for **scalability**. These extruded BSG were incorporated **only into PP matrix** using **a twin-screw extrusion** process for compounding instead of **internal mixing**. PP was selected instead of PLA, as it offers superior processability under the studied conditions. The **impact of the compounding method** on composites properties is evaluated. Additionally, this part investigates the **effects of injection molding method** by comparing composites molded using a **manual** laboratory press versus an **industrial** injection molding machine.

Figure 5.1 summarizes the workflow overview of these first and second parts.

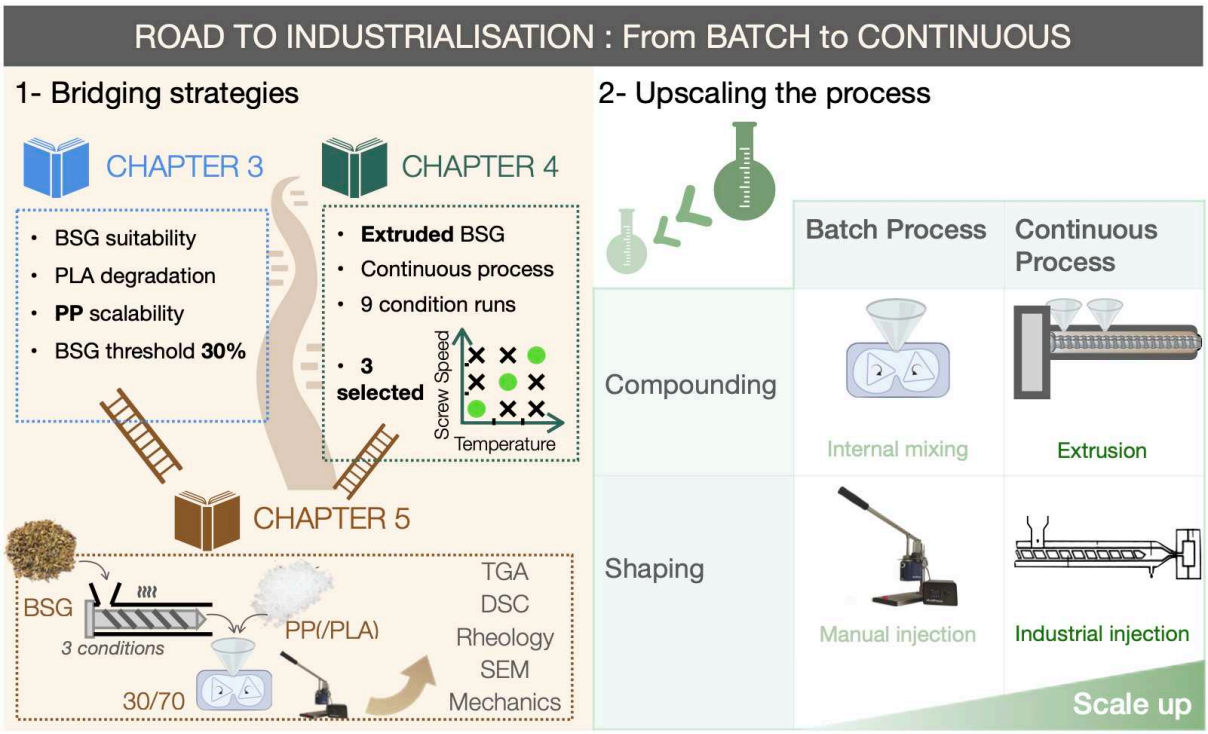


*Figure 5.1: Structure of the Chapter and experimental workflow.*

## 2. Producing composites with extruded BSG via internal mixing

### 2.1. Presentation of the composites

In this part, three extruded BSG using Profile 5 were chosen to be compound with PP at 30 %(m/m): BSGext_150_200, BSGext_170_300, BSGext_190_400. Only BSGext_170_300 was mixed with PLA up to 30 %(m/m). As discussed in the introduction, both extreme and intermediate extrusion conditions of BSG were investigated for compounding with PP to evaluate its wider processing window, whereas for PLA only the intermediate condition was studied, as it could allow for comparison with PP. Table 2.6 in Chapter 2 gathers the formulations made using internal mixing.

### 2.2. Effect of the extruded BSG on PP and PLA composites

#### *2.2.1. Thermal degradation behavior*

Figure 5.2 displays TG and DTG curves of the different composites presented in previous section (2.1. ). Table 5.1 gathers the temperatures reached at maximum mass loss rates for PP and PLA composites.

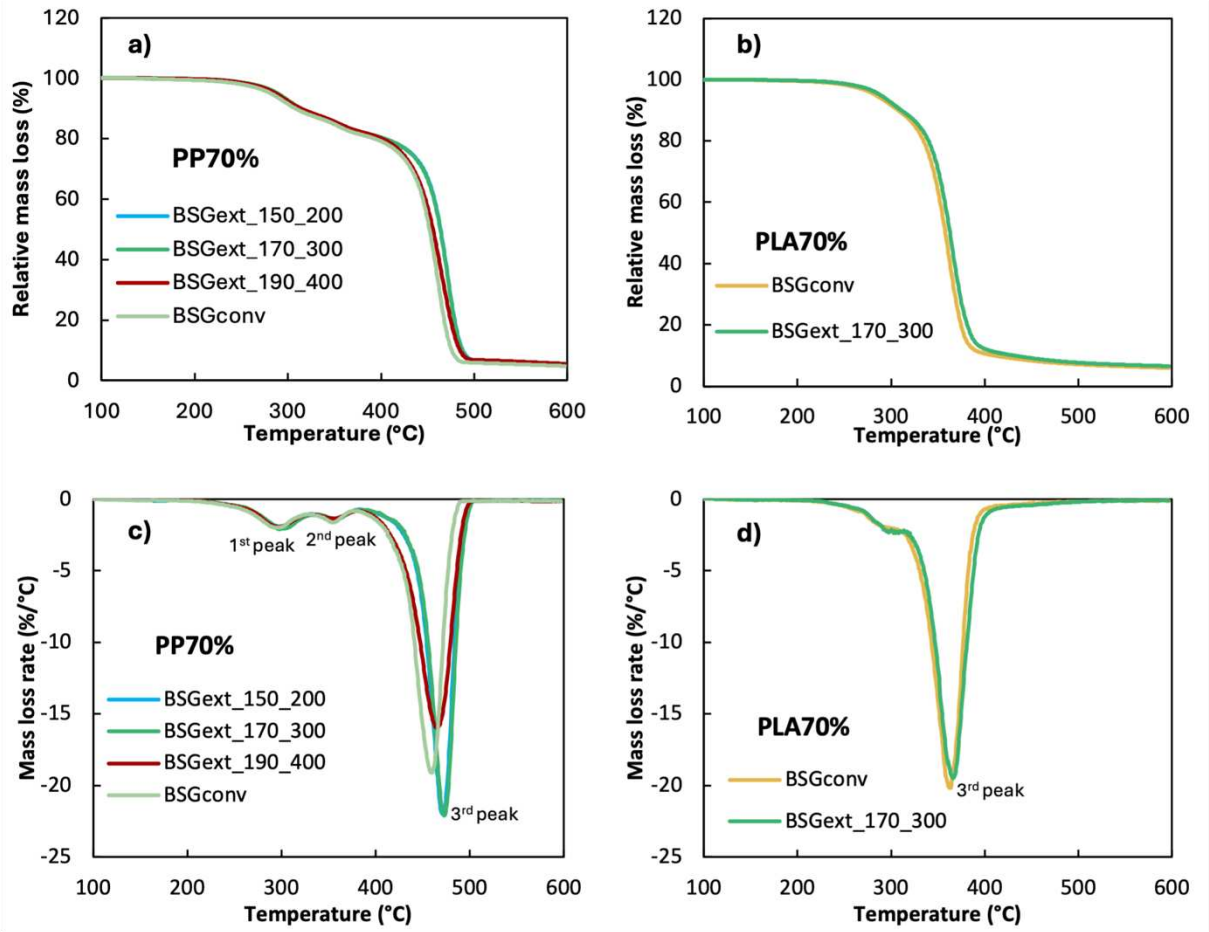


*Figure 5.2: Thermogravimetric analysis of biocomposites made with 30 %(m/m) of extruded BSG (Profile5) or BSG conv with 70 %(m/m) of PP (a,c) or PLA (b,d) (MI 180 °C, 50 rpm, 5 min) TG and DTG curves. Average of three experiments for TG curves and most representative of the three samples for DTG curves.*

The 1st peak and 2nd peak, corresponding to the degradation of hemicelluloses and cellulose, respectively, were already discussed in Chapter 4 and were found not to significantly differ across the different composites as noted in Chapter 2. Therefore, our analysis will focus on the 3rd peak which corresponds to the degradation peak of the polymer matrix. This focus allows us to assess for the impact of the different BSG on PP and PLA thermal degradation behavior.

Analysis of Figure 5.2 reveals a shift towards higher temperature of PP degradation containing extruded BSG, compared to those with BSGconv. Indeed, the degradation peaks of PP in composites with BSG extruded at 150 °C and 170 °C were observed at **471.6 ± 0.7 °C** and **471.8 ± 1.1 °C**, respectively, which are significantly higher than that of PP composites containing BSGconv (**460.7 ± 3.2 °C**). These two curves are overlapping in Figure 5.2.

As discussed, in chapter 3, BSGconv already showed a tendency to improve PP thermal stability, likely by forming a **char layer** that provides a protective effect. However, the extrusion process may enhance this effect by degrading lighter compounds of BSG, thereby increasing **relative carbon content** of BSG which could promote a more **homogeneous char production**.

Moreover, BSG particles extruded at 150 °C and 170 °C were observed to be significantly smaller than BSGconv particles (Figure 5.3). Therefore, these particles show higher interfacial area and likely resulted in improved **dispersion** within PP matrix, contributing to the formation of more **uniform and protective char layer** during thermal degradation.

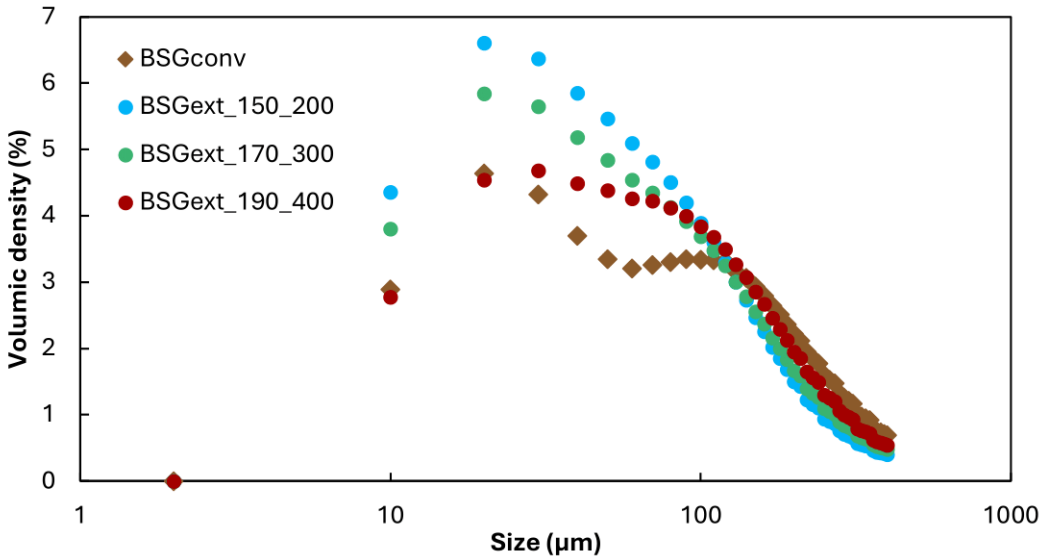


*Figure 5.3: Particle size distribution of BSGconv and BSGext (Profile 5 at 150°C_200rpm, 170°C_300rpm and 190°C_400rpm)*

Additionnaly, PP composites with **BSGext_190_400** exhibited a **lower degradation peak (466.8 ± 3.1 °C)** compared to other PP composites with extruded BSG, and this value is not significantly different from that of PP composites with **BSGconv (460.7 ± 3.2 °C)**. Interestingly, **BSGext_190_400** particles were found to be **significantly larger** than BSG extruded at lower temperatures, and showed **agglomeration phenomena**, as seen in Chapter 4. These observations further support the **dispersion hypothesis**, suggesting that the poorer dispersion of BSGext_190_400 particles within PP matrix may result in **reduced thermal protection**.

This interpretation is further supported by the **larger standard deviations** (Table 5.1) observed for **PP70BSGconv** and **PP70BSGext_190_400**, which are nearly **three times higher** than those of the other PP composites. Such variability likely represents the **inconsistent dispersion** of the larger particles.

Regarding the impact of extruded BSG (**BSGext_170_300**) on the degradation behavior of PLA, Figure 5.2 b,d the TG, DTG curves of PLA composites made with 30 %(m/m) of **BSGext_170_300** or **BSGconv**. As observed in Chapter 3 (and in contrast to the behavior observed in PP composites), **BSGconv** was found to **reduce the thermal stability of PLA**. This effect was attributed to the presence of volatile compounds in BSGconv, which were assumed to interact with PLA chains, potentially causing chain scission. This hypothesis was supported by **SEC analysis**, which indicated a reduction in PLA chain length.

In the present analysis, it is observed that **BSGext_170_300 does not significantly affect the degradation peak** of PLA (**366.2 ± 0.2 °C**) compared to **pure PLA** (**366.4 ± 1.8 °C**). This suggests that the **extrusion process**, by eliminated low molecular weight and volatile components from BSG, might mitigate the negative interactions previously observed during compounding. As a result, the absence of such components likely prevent the premature degradation of PLA, shifting its thermal degradation towards higher temperatures.

*Table 5.1: Temperatures reached at maximum degradation rates for biocomposites made with 30 % (m/m) of extruded BSG or BSGconv and 70 %(m/m) of PP or PLA. The values represent the mean of triplicate measurements, with standard deviations indicated. Different letters indicate statistically significant differences*.*

| Samples | Peak 3 (°C)* |
|---|---|
| PP70BSGext_150_200 | **471.6**$^{a}$ ± 0.7 |
| PP70BSGext_170_300 | **471.8**$^{a}$ ± 1.1 |
| PP70BSGext_190_400 | **466.8**$^{ab}$ ± 3.1 |
| PP70BSGconv | **460.7**$^{b}$ ± 3.2 |
| PP | **444.5** ± 10.2 |
| PLA70BSGext_170_300 | **366.2**$^{c}$ ± 0.2 |
| PLA70BSGconv | **362.6**$^{d}$ ± 0.9 |
| PLA | **366.4** ± 1.8 |

**PP and PLA were excluded from the statistical analysis, as the focus was placed on the different BSG-containing composites.*

To conclude, **extruded BSG appears to further enhance the thermal stability of PP composites**, reinforcing and accentuating the trend previously observed in Chapter 3. In contrast, another **trend** (compared to Chapter 3) **is observed for PLA composites**. Although, these results are not clearly visible in the graph, the results are available in Table 5.1 for

reference. While BSGconv was previously shown to reduce PLA thermal stability, likely due to the release of volatile degradation products, this **effect is no longer evident with extruded BSG**. This suggests that the **extrusion process**, by eliminating the lighter and thermally unstable components of BSG, could **prevent premature PLA degradation** during compounding.

*2.2.2. Thermal transition behavior*

Figure 5.4 displays the DSC curves of PP and PLA composites and Table 5.2 gathers the average key results such as $T_g$, $T_{cc}$, $T_c$, $T_m$ and $\chi_c$ obtained for each composite.

As for Chapter 3, first cooling and second heating curves are analysed, while only second heating cycle of PLA composites is shown because no notable thermal transitions are observed during the cooling of PLA.

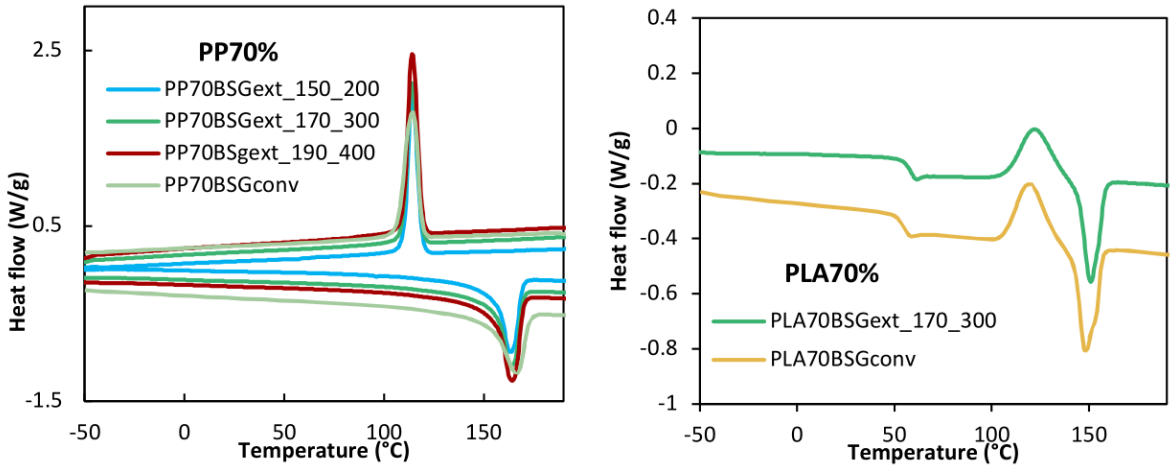


*Figure 5.4: Differential scanning calorimetry curves of injected PP and PLA composites containing 30 %(m/m) of extruded BSG or BSGconv, at 10K/min, under nitrogen atmosphere.*

During cooling, all PP composites exhibited a single crystallization peak which is **not significantly influenced by the type of BSG** used. In all cases, regardless of the process used to obtain BSG, $T_c$ **remained around ~114 °C**, indicating no difference in crystallization behavior due to BSG extrusion. However, this peak is still **shifted to lower temperatures** compared to **pure PP**, occurring at **117 .4 °C**.

As discussed in Chapter 3, **BSGconv** was observed to **hinder PP crystallization** likely due to **physical hinderance effects**, restricting PP chain mobility without specially forming interactions. Since the **volume fraction was mainly kept constant** (with bulk densities and true densities not significantly different) and assuming that no significant chemical interaction is

happening, it is plausible to observe a similar level of hindrance to chain mobility in both extruded and non-extruded BSG composites.

Regarding the **melting temperature** ($T_m$) of PP composites, a similar trend is observed, with **no significative influence from the type of BSG**. However, compared to pure PP, $T_m$ appears **slightly shifted to lower temperatures**. This shift must be cautiously interpreted as it did not reach statistical significance, however it may be attributed to the **hindrance of crystallization**, as previously discussed. When crystallization is hindered, the resulting **crystals could be less stable**, which could **lead to a lower melting temperature**.

The **crystallization rate of PP** appears to be influenced by the **type of BSG**. The highest $\chi_c$ were observed for composites containing BSG extruded at 150 °C and 190 °C, with valued of **47.8 ± 1.7 %** and **48.1 ± 3.4 %**, respectively. Surprisingly the composite with BSG extruded at 170 °C exhibited a lower $\chi_c$ (**39.5 ± 0.6 %**), which was not **significantly different** from that of BSG conv composite (**40.9 ± 2.4 %**) and pure PP (**40.9 ± 1.1 %**).

These observations may be explained by the **particles size** and **dispersion** features. Indeed, smaller particles size like those present in **BSGext_150_200** may be used as more efficient nucleating agent, enhancing crystallization by presenting a **greater number of nucleation sites**. In the case of **BSG_ext_190_400**, although particle size is higher (but still reduced compared to BSGconv), **agglomeration** at the surface was observed (as seen in Chapter 4), this could potentially offer more **nucleation points**. At the contrary, **BSGext_170_300** may **reflect a balance** between particle size reduction and limited agglomeration, leading to a similar crystallization behavior than BSGconv.

In literature, it has been shown that **localized melt flow occurring around a filler**, prior to crystallization, can significantly influence the development of **transcrystalline structures in PP** [6]. Moreover, due to its heterogeneous nature, **BSG could introduce localized thermal gradients**, potentially affecting the crystallization behavior of surrounding PP matrix. However, the **introduction of a filler** like BSG into PP matrix **alters multiple factors simultaneously** which have dissimilar dependence on crystallization. As a result, **separating the individual contributions of these factors may become extremely complex**, making it difficult to attribute crystallization behavior to a single cause.

I the second part of Figure 5.4, we can observe the thermal behavior of PLA composites loaded with 30 %(m/m) of extruded BSG and BSGconv.

Firstly, as presented in Chapter 3, $T_g$ of PLA was observed to **decrease significantly with increasing BSG content** compared to that of **pure PLA** (**59.9 ± 0.7 °C**). This decrease was attributed to two possible mechanisms: either BSG **enhances ductility** by spacing PLA chains apart through physical interactions; or, it increases **free volume** by promoting PLA chain scission, thereby increasing the number of chains ends.

In the present study, the PLA composite containing **extruded BSG** exhibits a **higher $T_g$** (**58.1 ± 0.1 °C**) than that of the composite with BSGconv (**55.5 ± 0.1 °C**). Given that the volume fraction is similar between the two composites (as previously discussed for PP), this observation more strongly supports the second hypothesis. **The lower $T_g$** observed with BSGconv may be due to a **higher chain scission** happening during compounding.

In chapter 3, the **highest** cold crystallization temperature **($T_{cc}$)** was observed for **PLA** composites containing **20 %(m/m) BSGconv**, followed by those with **30 %(m/m) BSGconv** (**120.5 ± 0.3 °C**). In the current study, the composite filled with **extruded BSG** exhibited an even **higher $T_{cc}$** (**122.5 ± 3.0 °C**), while **pure PLA** displayed a **$T_{cc}$ of 115.9 ± 0.9 °C**.

BSG was previously observed to have a **dual effect** on PLA thermal behavior. At **low filler content** (<10 %), **$T_{cc}$** shifted towards **lower temperatures** likely due to shorter PLA chains moving more easily. Then at **intermediate BSG content** (20-30 %), BSGconv was suspected to hinder crystal propagation acting as **a physical barrier**. At even **higher BSG content**, a **percolation phenomenon** may occur where PLA has a similar behavior as seen for lower BSG content, resulting in lower $T_{cc}$.

With this in mind, the even **higher $T_{cc}$ observed for extruded BSG** (**122.5 ± 0.3 °C**) compared to BSGconv (**120.5 ± 0.3 °C**) supports the hypothesis that **filler volume fraction alone hinders crystallization**, as extruded BSG does not seem to promote chain scission in PLA.

Finally, $T_m$ of PLA in the **extruded BSG composite** displays **a single peak**, likely corresponding to the **delayed $T_{cc}$**, similarly to what was observed for PLA composite filled. In contrast, PLA70BSGconv displayed a peak with a shoulder, suggesting a possible overlapping, as discussed in Chapter 3.

The presence of a single melting peak in extruded BSG composite suggests more **thermally stable crystals**, likely crystallized at higher temperatures. This is supported by the significantly **higher melting temperature** of PLA70BSGext_170_300 (**151.3 ± 0.2 °C**) compared to **PLA70BSGconv** (**148.5± 0.2 °C**).

*Table 5.2: DSC data of PP, PLA and their composites with extruded BSG and BSGconv after internal mixing and injection molding. Different letters indicate statistically significant differences between samples.*

| Sample code | $T_g$ (°C) | $T_{cc}$ (°C) | $T_c$ (°C) | $T_m$ (°C) | $\chi_c$ (%) |
|---|---|---|---|---|---|
| PP70BSGext_150_200 | - | - | **113.9**$^{a}$ ± 0.4 | **164.0**$^{a}$ ± 1.0 | **47.8**$^{a}$ ± 1.7 |
| PP70BSGext_170_300 | - | - | **114.1**$^{a}$ ± 0.3 | **164.2**$^{a}$ ± 0.2 | **39.5**$^{b}$ ± 0.6 |
| PP70BSGext_190_400 | - | - | **114.1**$^{a}$ ± 0.2 | **164.4**$^{a}$ ± 0.6 | **48.1**$^{a}$ ± 3.4 |
| PP70BSGconv | - | - | **114.7**$^{a}$ ± 0.4 | **165.6**$^{a}$ ± 1.0 | **40.9**$^{ab}$ ± 2.4 |
| PP | - | - | **117.4** ± 0.5 | **167.0** ± 0.8 | **40.9** ± 1.1 |
| PLA70BSGext_170_300 | **58.1**$^{a}$ ± 0.1 | **122.5**$^{a}$ ± 0.3 | - | **151.3**$^{a}$ ± 0.2 | **3.1** ± 1.1 |
| PLA70BSGconv | **55.5**$^{b}$ ± 0.1 | **120.5**$^{b}$ ± 0.3 | - | **148.5**$^{b}$ ± 0.2 | ~0 |
| PLA | **59.9** ± 0.7 | **115.9** ± 0.9 | - | **150.2** ± 2.3 | 0.6 |

While DSC provides insights into the effect of extruded BSG on the thermal transitions of the composites during and after processing, it does not provide information on the influence on the mechanical response of the material. Therefore, rheological analysis was conducted to investigate the viscoelastic behavior of the composites filled with extruded BSG in the melt state under shear.

*2.2.3. Rheology*

Figure 5.5 displays the evolution of G' and complex viscosity of PP composites with angular frequency.

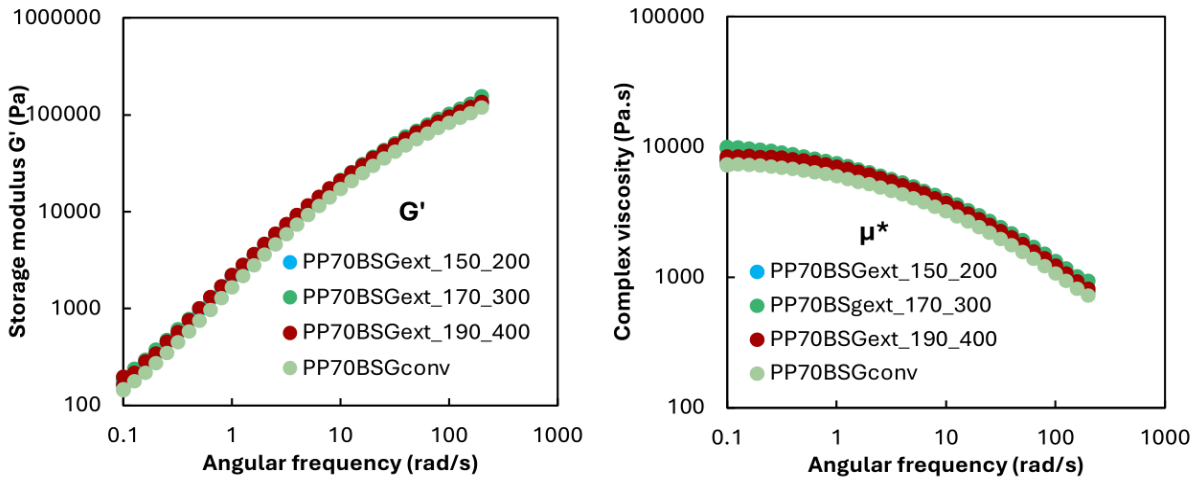


*Figure 5.5: Effect on BSG process on storage modulus and complex viscosity vs. angular frequency (rad/s) in plate-plate rheometer at 180 °C for PP composites processed at 180 °C in internal mixer and injected at 200 °C, plate-plate gap = 2200 µm, plate diameter = 25mm; strain = 0.05 %. Average of three experiments, error bars fall within the symbols.*

In Chapter 3, **BSGconv** was shown to **increase both the storage modulus (*G'*) and complex viscosity** of PP composites, without significantly altering the shape of the curves. This suggested that BSGconv behaves as an **inert filler**, enhancing the overall **solid-like response** of the material due to its volume and solid state rather than specific interactions.

In the present study, the **extrusion of BSG** does not appear to affect much the viscoelastic behavior of the composites. Indeed, ***G'* and *μ** curves of PP composites** containing **30 %(m/m) of extruded BSG** quite overlap with those of **PP70BSGconv,** indicating similar viscoelastic behavior. This observation is consistent with the expectation that filler volume in the case of PP governs the flow properties, as previously discussed. However, to be more precise, the **extruded BSG composites** exhibit slightly **higher values**, suggesting that the **rough surface** of the filler may promote **mechanical interlocking**, which could in turn justify the observed **increase in complex viscosity** and **storage modulus**.

This almost overlapping further confirms that an **equivalent filler volume** was introduced in each composite. This validation is particularly important given that the materials were **compounded based on mass ratios** using the internal mixer, where difference in **filler density** could lead to variations in effective filler volume.

Therefore, the use of **extruded BSG** does not compromise the **viscoelastic response** and confirms that the composites remain **highly processable**. This was also confirmed during manual injection, where no additional effort was required.

Figure 5.6 displays the evolution of *G'*, *G"*, and complex viscosity of PLA composites with angular frequency.

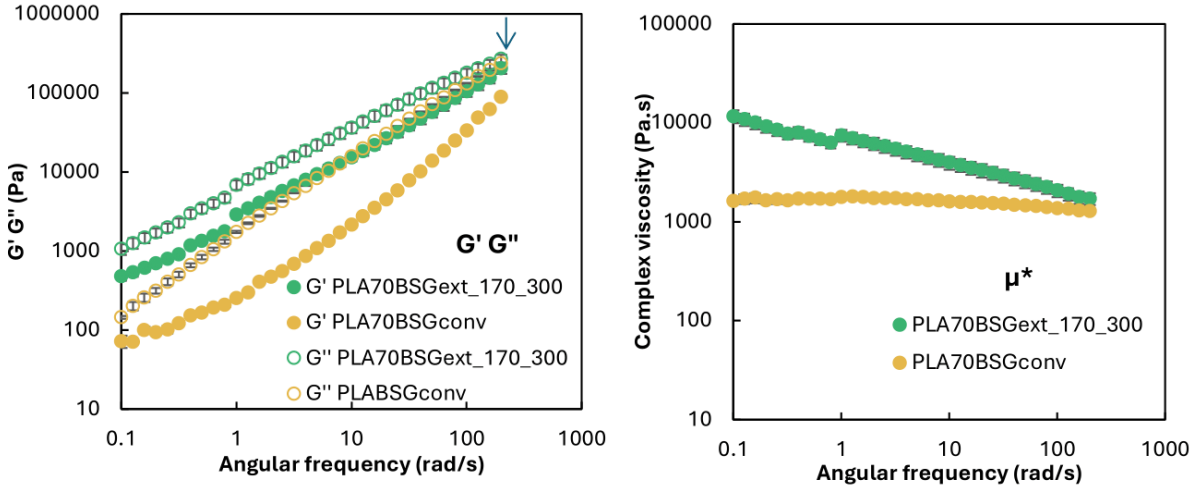


*Figure 5.6: Effect on BSG process on storage modulus, loss modulus and complex viscosity vs. angular frequency (rad/s) in plate-plate rheometer at 180 °C for PLA composites processed at 180 °C in internal mixer and injected at 180 °C, plate-plate gap = 2200 µm, plate diameter = 25 mm, strain= 0.05 % [200-1rad/s] and 0.4% [1-0.1 rad/s]. Average of three experiments, error bars fall within the symbols. Blue arrow indicating crossover point.*

Regarding **PLA composites**, the incorporation of **extruded BSG** resulted in a material with **higher storage modulus** and **complex viscosity** compared to the composites with BSGconv. Regarding complex viscosity, **PLA70BSGconv** displays a **Newtonian plateau** that extends throughout the whole range of frequency. In contrast, **PLA70BSGext_170_300** complex viscosity displays a **transition toward a power-law** behavior at low frequencies. This could indicate that the molten composite system may be **reaching the percolation threshold**. This is also supported by the **flattening of *G'* curve** at low frequencies, characteristic of enhanced filler-matrix interactions or network formation. Moreover, the **crossover point** of **extruded BSG PLA composite** almost appears (marked with an arrow on Figure 5.6 within the frequency range of the study whereas it is **not visible** for **BSGconv PLA composites**. This observation further supports the hypothesis of filler-matrix interactions.

In Chapter 3, it was observed that the incorporation of small amount of BSGconv (10 and 20 %) in PLA resulted in **lower viscoelastic response** due to **chain scission**. The enhanced viscoelastic behavior seen in Figure 5.6 with extruded BSG supports he hypothesis that the extrusion process effectively removes low molecular weight compounds responsible for chain degradation. As a results, **PLA matrix molecular integrity remains intact**. Hence, the current

molten composite system differs a little from the one studied in Chapter 3: the **longer PLA chains** exhibit increased **resistance to flow** and may interact more strongly with the filler. Therefore, PLA chains may be less able to accommodate with the hindrance created by the addition of BSG particles.

*2.2.4. Interface morphology*

Figure 5.7 displays the tensile fracture profiles of PP composites with BSGconv and extruded BSG.

**PPBSGconv** exhibits a section characterized by a **dual behavior**: one region displays **ductile deformation marks,** and the other region revealed a **brittle fracture** pattern. Notably, the brittle region contains very **few particles**. As discussed in Chapter 3, BSG particles were found to act as **stress concentrators**, promoting **localized matrix deformation** around the filler.

In contrast, composites incorporating extruded BSG present a **more homogeneous distribution of the tensile marks** across the fracture surface. This could be due to the **smaller particles size** reached with extrusion, promoting **better dispersion of the particles** within the matrix and thereby, a more **uniform dispersion of the tensile stress**.

Additionally, the number of **voids and particles pulled out** appears to be **independent of the processing method** used to obtain BSG particles. This indicates that **particle-matrix interfacial adhesion** may not be significantly affected by the extrusion process under the tested conditions.

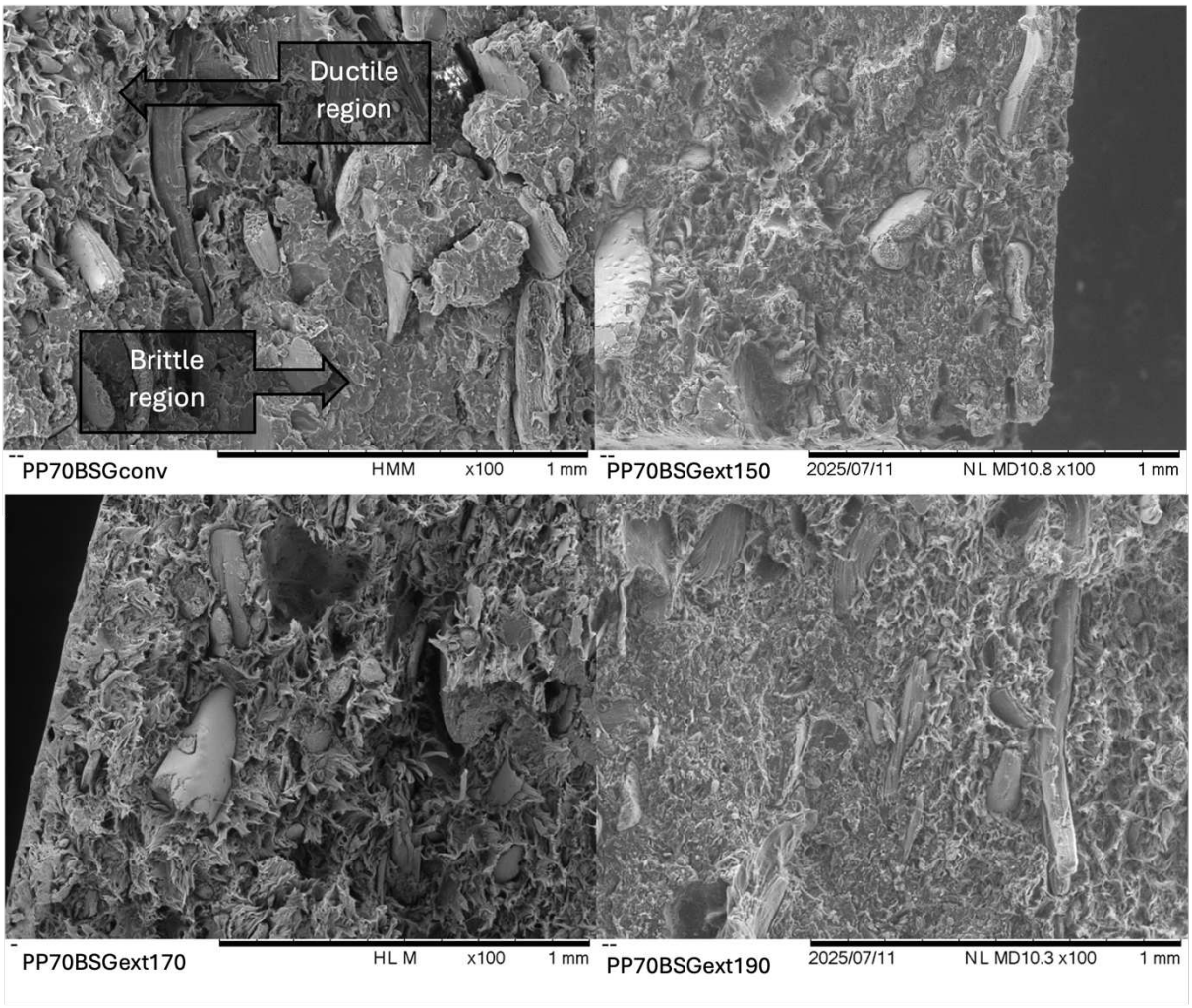


*Figure 5.7: SEM micrographs of PP composites filled with 30 %(m/m) BSGconv and extruded BSG, made with IM 180°C 50 rpm 5 min and injected at 200 °C observation of the tensile fractured cross-section x100*

At higher magnification (Figure 5.8), it becomes possible to observe in greater detail the **surface and aspect of the BSG** particles and their **interfacial behavior** with the PP matrix. In **PP70BSGconv**, the visible particle appears **intact and undamaged** by the internal mixer or the tensile assay.

In contrast, in **PP70BSGext_150_200**, the particle appears **fractured**, this could suggest that the particle **broke during the tensile assay**, possibly due to **some interfacial adhesion** with the matrix.

For **PP70BSGext_170_300** and **PPBSGext_190_400**, the particles seem to be more **embedded into the matrix**, suggesting adhesion or, at minimum, **effective wetting** of the particle surface by the PP. This could be attributed to the **rougher surface of the extruded BSG** (observed in Chapter 4) which provides more mechanical interlocking sites, thereby improving interpenetration at the filler matrix interface [286].

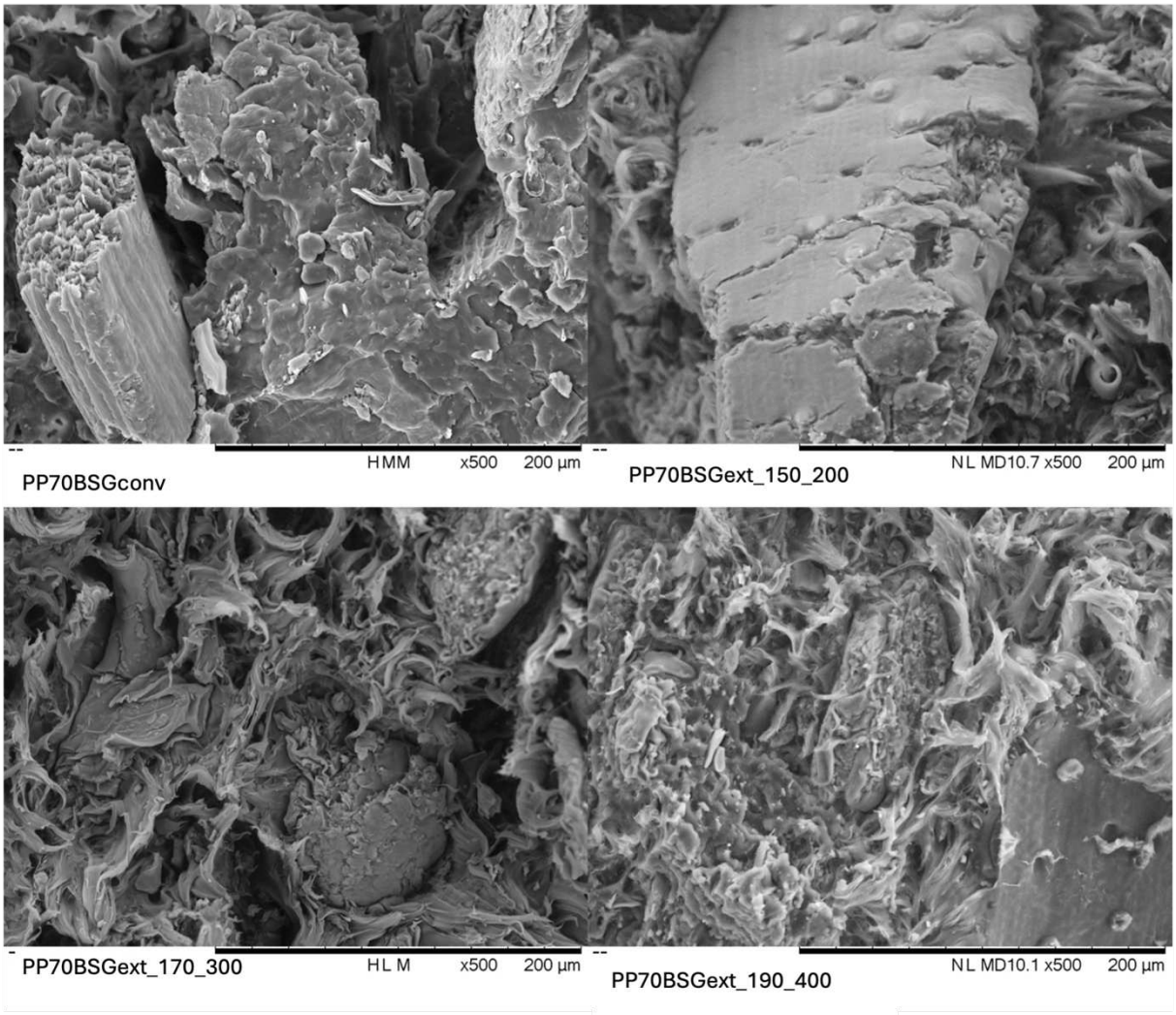


*Figure 5.8: SEM micrographs of PP composites with BSGconv and extruded BSG, observation of the tensile fractured cross-section x500*

Figure 5.9 displays the tensile fracture profiles of PLA composites with BSGconv and extruded BSG at two magnifications: x100 and x500.

What is striking is that the **main difference** between the two composites lies in the **interfacial regions**. In PLA70BSGconv, nearly all the particles are **surrounded by a distinct dark contour**, visible as a black line on the micrographs which corresponds to **voids at the interface** between particle and matrix. This phenomenon becomes even more evident at higher magnification, highlighting the **poor interfacial continuity**.

In **PLA70BSGext_170_300**, these black lines are **less visible** and **thinner** suggesting **better adhesion** or **better coverage** of PLA at the surface of extruded BSG.

A possible explanation for the observation is that, during the compounding, **BSGconv released residual moisture** (~3 %) and **volatiles**, which degrade at temperature below 180 °C. These degradation products may become **trapped in the matrix**, forming interfacial voids or gas pockets around the filler particles. In contrast, **extruded BSG** has already undergone **thermal treatment during extrusion**, during which these volatiles compounds are **partially or fully degraded and eliminated**. As a results, **no significant gas production occurs during compounding** and the interface between matrix and filler remains smaller.

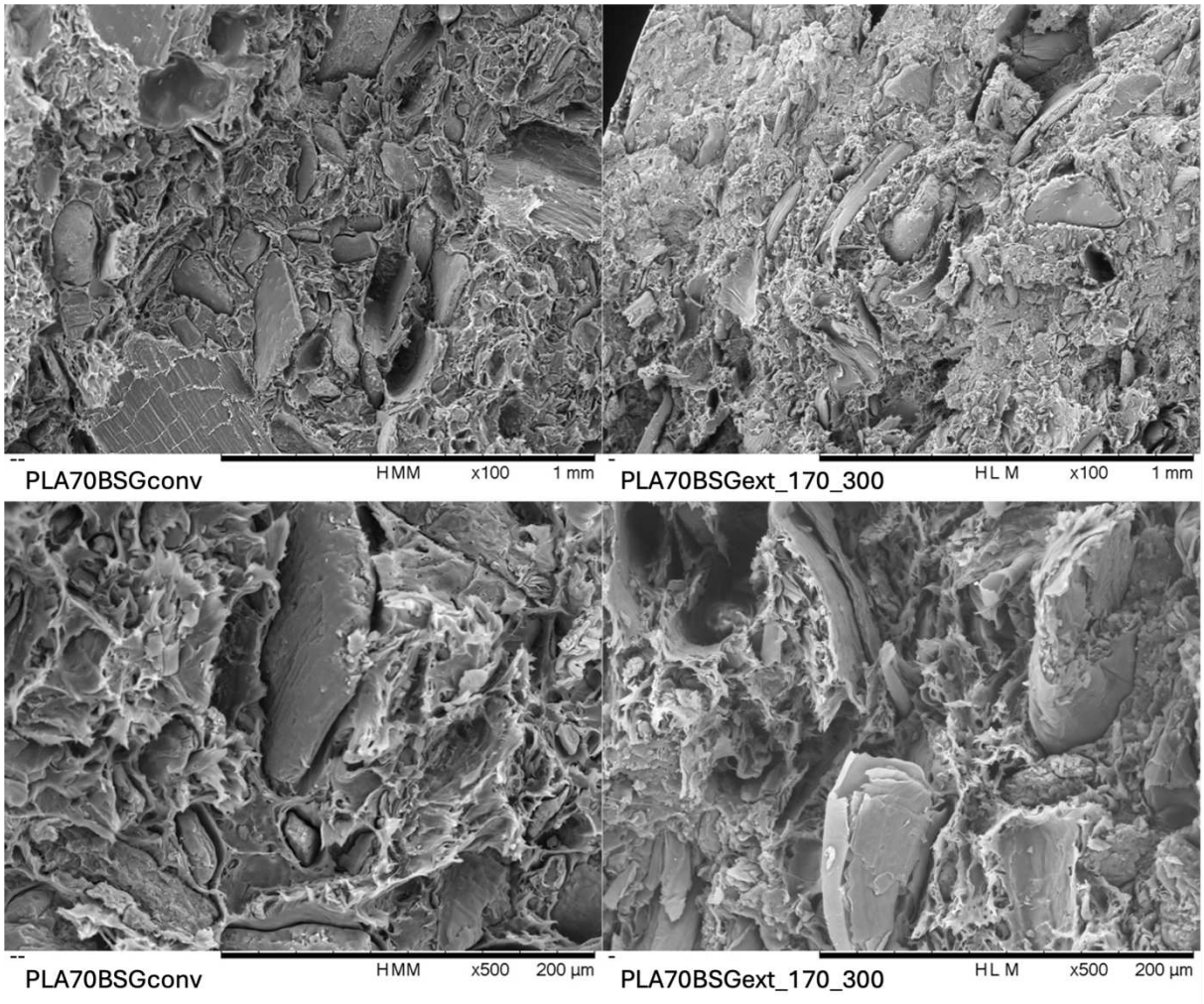


*Figure 5.9: SEM micrographs of PLA composites with BSGconv and extruded BSG, observation of the tensile fractured cross-section x100 and x500*

### *2.2.5. Mechanical testing*

Young's modulus (***YM***) and tensile strength (***TS***) of PP composites with BSGconv and extruded BSG are displayed in Figure 5.10. Again, only composites containing BSG are compared statiscally by pairs, as we are specifically interested in the effect of BSG processing method.

Regarding the elastic modulus, we observe that extruded BSG tends to lower the Young's modulus. Indeed **PP70BSGconv** displays a Young's modulus of **1603.8 ± 26.1 MPa**, whereas PP composite with **BSGext150_200**, **BSGext170_300**, and **BSGext190_400** display lower values of Young's modulus of **1367.5 ± 140.2 MPa**, **1258.7 ± 96.4 MPa**, and **1257.4 ± 153.1 MPa**, respectively. This was not expected since particles surface area is increased which should have led to an increased Young's modulus. The extruded particles have possibly undergone a reduction of their own stiffness during extrusion.

Interestingly, the **reverse trend is observed for tensile strength**, with extruded BSG incresing the tensile strength. **PP70BSGconv** has a tensile strength of **24.3 ± 0.6 MPa,** while **PP70BSGext_150_200** and **PP70BSGext_190_400** reach a tensile strength of **28.0 ± 0.4 MPa** and **28.1 ± 0.4 MPa**, respectively.

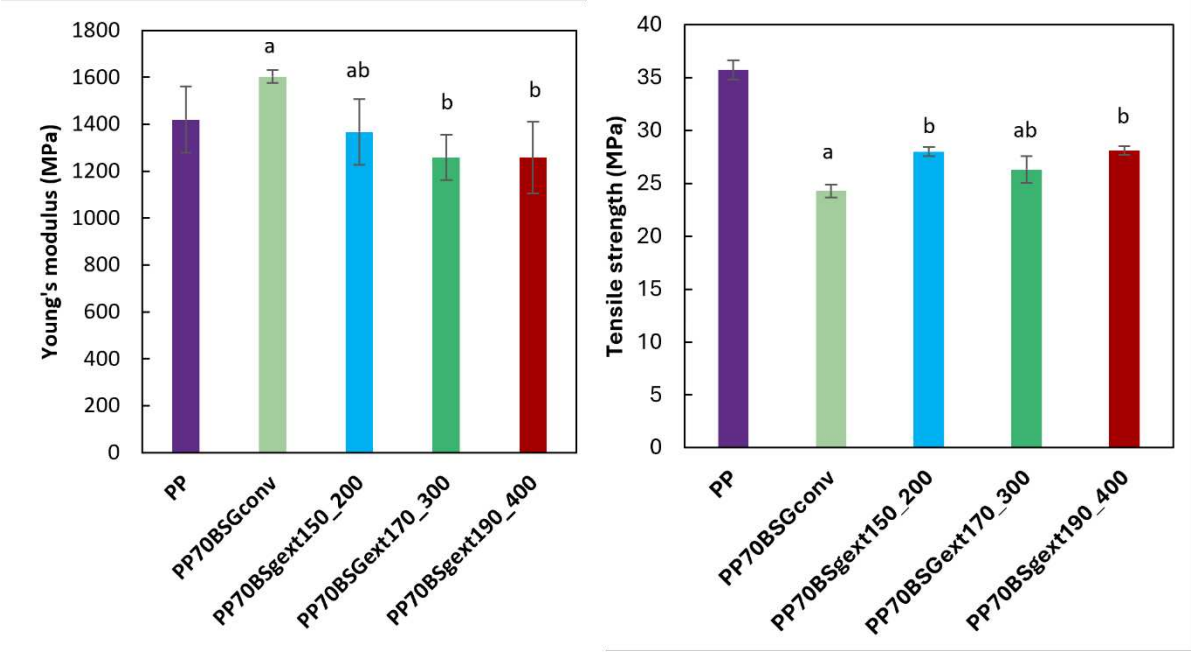


*Figure 5.10: Effect of BSG processing on PP composites (Internal mixing 180 °C 50 rpm 5 min) mechanical properties (Young's modulus and yield tensile strength)*

This apparent contradiction may be partially explained by **SEM observations**, which revealed that **not all the cross section area** of PP70BSGconv **appears to participate in the mechanical load transfer** during tensile testing (strecthing marks not uniformly dispersed within the matrix). This suggests that **only a portion of the section was effectively engaged**. Since tensile strength and Young's modulus are calculated using the total cross-sectional area, **overestimated this area could lead to an underestimation of** tensile strength **and an overestimation of** Young's modulus, because stress is underestimated while strain remains accurately measured.

Therefore, the lower Young's modulus and higher tensile strength of **extruded BSG** composites could reflect a **more uniform stress distribution** across the section likely due to **better particle dispersion** as seen in SEM.

Let's now turn to PLA composites mechanical properties. Young's modulus and tensile strength of PLA composites with BSGconv and extruded BSG are displayed in Figure 5.11.

The extrusion of BSG does not seem to influence the Young's modulus of the composites. Indeed **PLA70BSGconv** exhibits a Young's modulus of **2128.3 ± 95.7 MPa** whereas **PLA70BSGext_170_300** reached a comparable Young's modulus value of **2203.5 ± 139.1 MPa**. However, a clear trend is observed regarding tensile strength, **extruded BSG** seems to **enhance the mechanical performance** of the composites. The same trend was observed by Singh *et al.* who reported a better tensile strength for smaller size of filler in pine cone filled HDPE due to better dispersion of the smaller particles compared to coraser ones [286]. In our case, this improvement may also be attributed to the **better interfacial adhesion** between extruded BSG and PLA, as evidenced by SEM micrograph where **BSG particles appeared more embedded** and showed fewer interfacial voids.

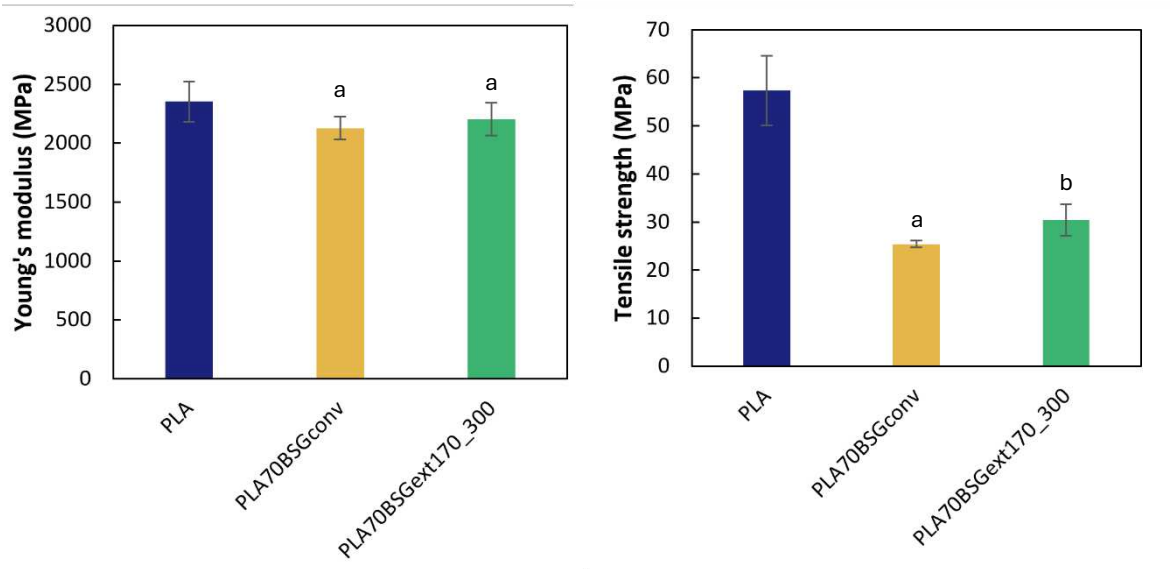


*Figure 5.11: Effect of BSG processing on PLA composites mechanical properties (Young's modulus and yield tensile strength), 2 mm/min.*

While Young's modulus of PP and PLA is **either reduced or remains unchanged** with the addition of extruded BSG compared than with BSGconv, the **tensile strength** was found to **increase** for composite containing **extruded BSG**. This divergence can be explained by the fact that Young's modulus seems governed by the **matrix intrinsic properties**, while tensile strength

might be more sensitive to the **quality of matrix-particle interactions**. Indeed, in their study on natural fibers-PP composites, Serra-parareda *et al.* noted that improving fiber-matrix adhesion has large effects on tensile strength, but that changes in Young's modulus are more predictable from micromechanics using fiber/matrix volume fractions and intrinsic fiber properties, they concluded that modulus is less sensitive to adhesion [287]. Therefore, the observed **increase in tensile strength** might be attributed to the **better dispersion, and good wettability of the fine particles** obtained through extrusion, in contrast to the coarser particles obtained through conventional method.

### 2.3. Conclusion

This part aimed to evaluate the influence of extruded BSG obtained under three different processing conditions, compared to the conventionally dried and ground BSG on **thermal, rheological, morphological, and mechanical properties of PP and PLA composites**. The results highlight that the **extrusion process significantly affects the behavior of BSG** as a filler.

In the case of **PP**, the use of **extruded BSG**, characterized by **finer particles** and **rougher surfaces**, led to **better dispersion and wettability**, as confirmed by SEM observations. These morphological changes contributed to **enhance the thermal stability** of PP composites, likely through the formation of a **more uniform protective char layer**, confirming and accentuating trends observed in Chapter 3. These improved dispersion and rougher surfaces also impacted the crystallization behavior of PP, which resulted in some cases in **enhanced crystallization rates** and **shifted crystallization temperatures**. In r**heology**, all PP composites **exhibited similar behavior** regardless of BSG processing, confirming a consistent filler volume. Mechanical results indicated an **improved tensile strength** with **extruded BSG** likely due to the **more uniform stress distribution** as observed in SEM.

In contrast, for **PLA composites**, **extruded BSG** effects appeared to be driven less by particle morphology and more by the **chemical modifications** associated with the **extrusion process**. Particularly, the **degradation of the lighter components** of BSG during extrusion, and highlighted in TGA, seems to **reduce significantly its interactions with PLA**. Firstly, regarding **thermal degradation behavior**, the extrusion of BSG seemed to **mitigate the degradation effects** caused by least thermally stable compounds present in BSGconv, resulting in **improved thermal stability**. This trend was consistently observed across the results. Additionally, **glass transition temperature** of PLA in composite containing extruded BSG was **shifted towards higher temperatures** compared to composite with BSGconv. This indicates **reduced mobility in PLA chains**, suggesting that **less chain scission** has occurred during internal mixing with

BSGext. This was further supported in rheology, where **PLA composites with extruded BSG** showed a **higher viscoelastic response**, likely due to the presence of **longer PLA chains**. SEM also revealed a significant **reduction of the voids at the interface** between extruded BSG and PLA. This improved adhesion probably contributed to the **improvement of tensile strength** of PLA composites with extruded BSG compared to those with BSGconv.

Overall, **BSG extrusion for drying grinding appears to be a promising method** for **tailoring the properties of BSG as a filler**, especially by improving its morphology and interfacial compatibility, with **distinct impacts depending on the polymer matrix.**

Given the **more consistent improvement** observed in **PP composites**, the next part of this chapter will focus exclusively on PP. This will allow us to further investigate the scalability of this project.

## 3. Upscaling the process

### 3.1. Introduction

This part aims to evaluate the **scalability of this project**, building on the results and strategies developed in the precedent chapters. In this part, the focus is placed on PP matrix only. Hence, two key **scale-up approaches** are evaluated. In the **first section** of this part, the focus is on comparing **PP composites compounding methods**, more specifically **extrusion versus internal mixing**, with all samples shaped using **laboratory injection press**. In the **second section** of this part, focus shifts to the **injection molding process**, **comparing laboratory manual press versus semi-industrial injection press**. In this case, composites pellets are prepared exclusively through extrusion, due to the large material volumes required for semi-industrial processing. Figure 5.12 summarizes the two presented scale-up approaches.

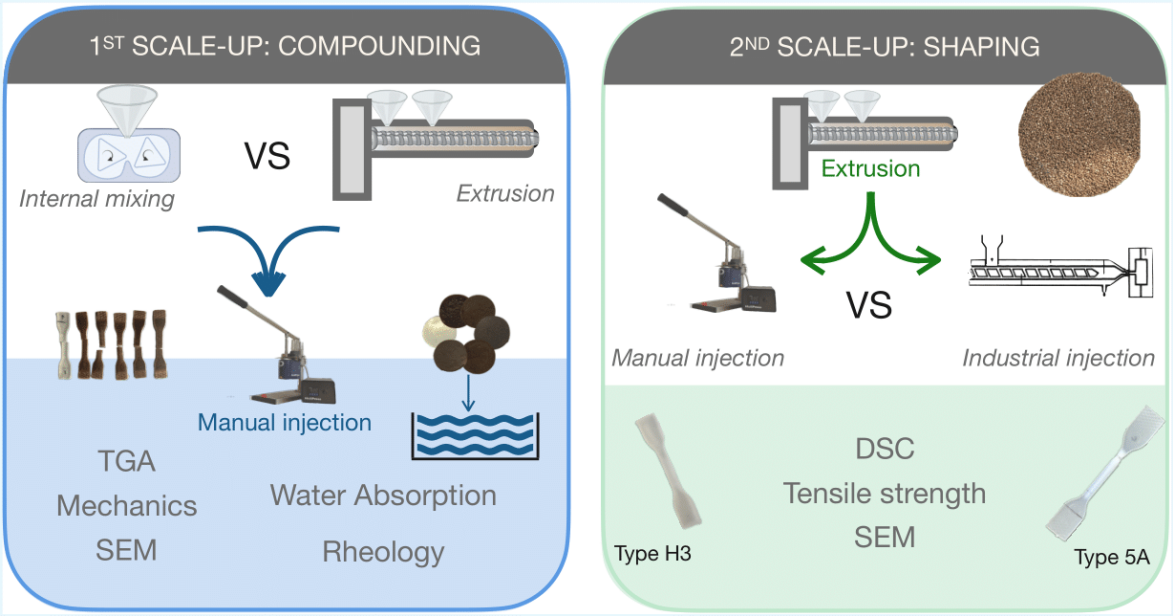


*Figure 5.12: Overview of scale-up approaches evaluated.*

## 3.2. Composites compounding: from internal mixing to extrusion

In this section the scalability of the compounding process in the preparation of the composites is investigated by comparing internal mixing with extrusion. Although internal mixing is a common approach in laboratory research, extrusion provides closer similarity to industrial-scale processes. To allow the comparison, all materials obtained by these methods were shaped using the laboratory injection press.

### *3.2.1. Effects on composites thermal degradation behavior*

Table 5.3 gathers the results of the effects of processing methods on the thermal behavior of PP composites especially temperature reached for the degradation peak of PP.

Figure 5.13 displays the **thermal degradation behavior of PP** obtained through **two different processing methods**: extrusion (PPext) and internal mixing (PPim). One single degradation peak is observed in DTG. PPext reaches its maximum degradation rate at 462.1 ± 0.1 °C while **PPim degrades at slightly higher temperature** of 463.6 ± 0.6 °C. This could be due to **higher shear rates occurring during extrusion** leading to little degradation of the PP chains.

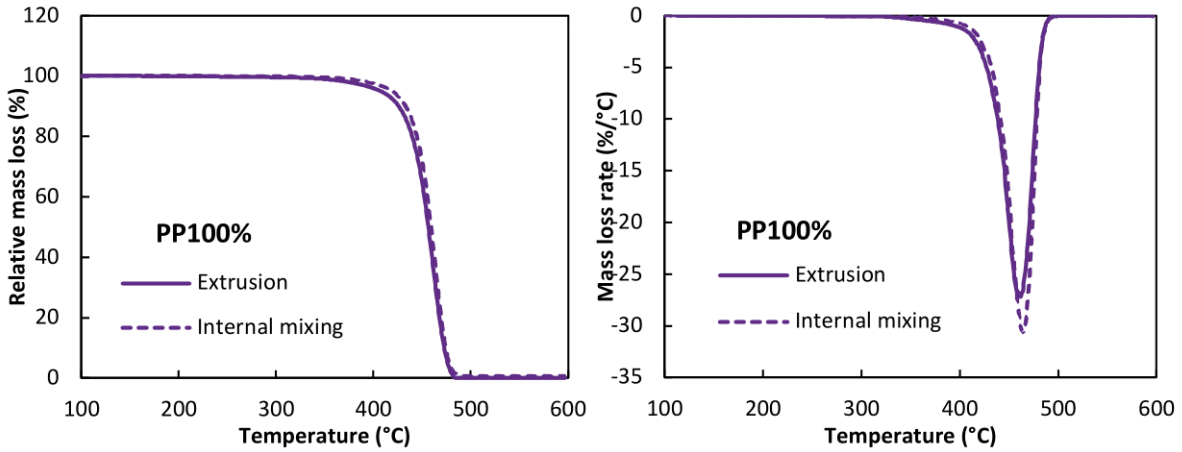


*Figure 5.13: Thermogravimetric analysis of PP obtained through extrusion compared to PP obtained through internal mixing (TG and DTG curves, 10 K/min under nitrogen flow. Average of three experiments.*

Figure 5.14 displays the TG curves of PP composites containing 30 %(m/m) of extruded BSG or BSGconv made via extrusion or via internal mixing. Both methods lead to composites with similar thermal degradation behavior. Looking closer at Table 5.3, no clear trend seems to detach, however extruded composites seem more thermally stable. For instance, PP70BSGconvEXT degrades at **467.6** ± 1.3 °C while PP70BSGconvIM degrades at **460.7** ± 3.2 °C.

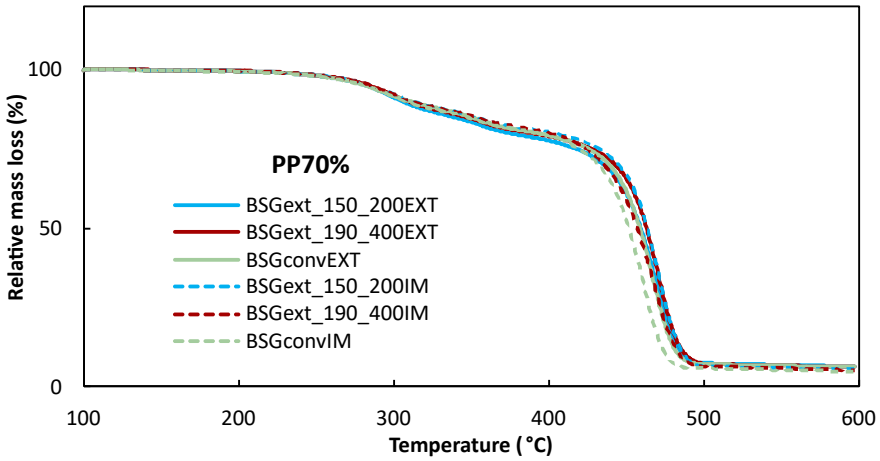


*Figure 5.14: Thermogravimetric analysis of PP composites containing 30 %(m/m) of BSG obtained through extrusion compared to PP composites obtained through internal mixing (180 °C, 50 rpm, 5 min), 10 K/min under nitrogen flow. Average of three experiments.*

*Table 5.3: Temperatures reached at maximum degradation rates for biocomposites made with PP and extruded BSG or BSGconv through two different processing methods (extrusion and internal mixing). The values represent the mean of triplicate measurements, with standard deviations indicated.*

| PP content (%) | Samples | Extrusion compounding Peak 3 (°C) | Internal mixing compounding Peak 3 (°C) |
|---|---|---|---|
| 100 | PP100 | **462.1**[a] ± 0.1 | **463.6**[b] ± 0.6 |
| | PP70BSGext_150_200 | **469.7** ± 2.2 | **471.6** ± 0.7 |
| 70 | PP70BSGext190_400 | **471.7** ± 1.6 | **466.8** ± 3.1 |
| | PP70BSGconv | **467.6** ± 1.3 | **460.7** ± 3.2 |

*3.2.2. Effects on rheological properties*

Regarding rheological properties, Figure 5.15 shows the **viscoelastic behavior** of **PP composites** containing BSG processed under different conditions and compounded using either **internal mixing (IM)** or **extrusion (EXT)**. Each subplot shows either the **storage modulus (*G'*)** (a and b) or **complex viscosity** $|\mu^*|$ (c and d) as a function of angular frequency.

In both internal mixing (Figure 5.15 a and c) and extrusion (Figure 5.15 b and d), *G'* and $\mu^*$ curves are **closely overlapping**, with little difference in complex viscosity for extruded BSG, as previously discussed. This indicates that **filler content** is **well controlled** and consistent across the samples.

In both compounding methods, **PP70BSGext_190_400** appears to show **slightly higher viscoelastic response**. It is particularly highlighted in Figure 5.15 d) for **extrusion**. Indeed, the complex viscosity observed for **PP70BSGext_190_400EXT** is of **10761 ± 577 Pa.s** at the **low frequency plateau** whereas for **PPBSGext_150_200EXT** it is at **7901 ± 841 Pa.s** and **8049 ± 393 Pa.s** for **PP70BSGconvEXT**. This could be attributed to the **agglomeration of particles** of BSGext190_400 or to the **rougher surface** of the particles as observed in Chapter 4 that could promote more **mechanical interlocking** with the matrix and thereby more **resistance to the flow**.

To conclude, the **processability of the composites remains good** regardless of the method used, which is important when considering scaling up.

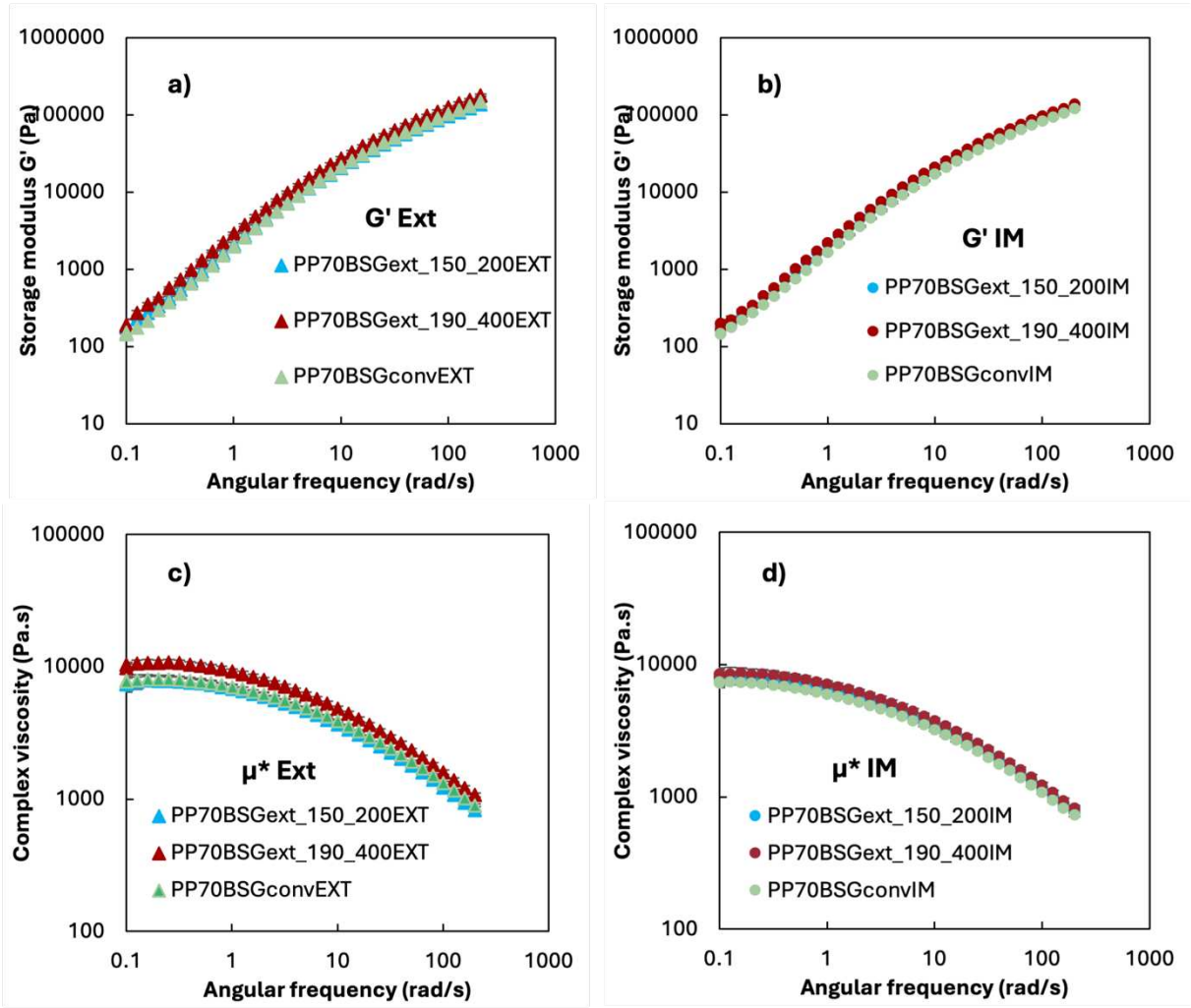


*Figure 5.15: Effects of compounding method (internal mixing a) c) or extrusion b) d)) on storage modulus (Pa) (a,b) and complex viscosity (Pa.s) (c,d) vs. angular frequency (rad/s) in plate rheometer at 180°C for Polypropylene (PP) composites made with 30 % of different BSG injected at 200 °C using laboratory press, plate-plate gap = 2200 µm, plate diameter = 25 mm, strain 0.05%. Average of three experiments*

### *3.2.3. Interfacial and cross-section structure*

In this section, tensile section profiles of PP composites are compared according to the compounding method used to obtain them. To facilitate comparison, SEM micrographs are grouped by four, on the **left** images of **extruded** composites at two magnifications (x**100** and x**500**) and on the **right** images of **internally mixed** composites at the same magnifications.

Figure 5.16 displays the tensile fracture profiles of **PP70BSGconv** compounded with either extrusion (PP70BSGconvEXT) or internal mixing (PP70BSGconvIM) at two magnifications: x100 and x500.

In both compounding methods, fillers **pull-out and voids** are observed which suggest **limited interfacial adhesion** between BSG and PP matrix for both methods. What differs in both

methods is the dispersion and intensity of **stretching marks**. Indeed, composites prepared via **extrusion** seems to exhibit **more uniform and continuous stretching marks**. In contrast, composites made with **internal mixing** as discussed previously show **localized regions** where the fracture has a more **brittle behavior**. This suggests less efficient stress transfer and different dispersion.

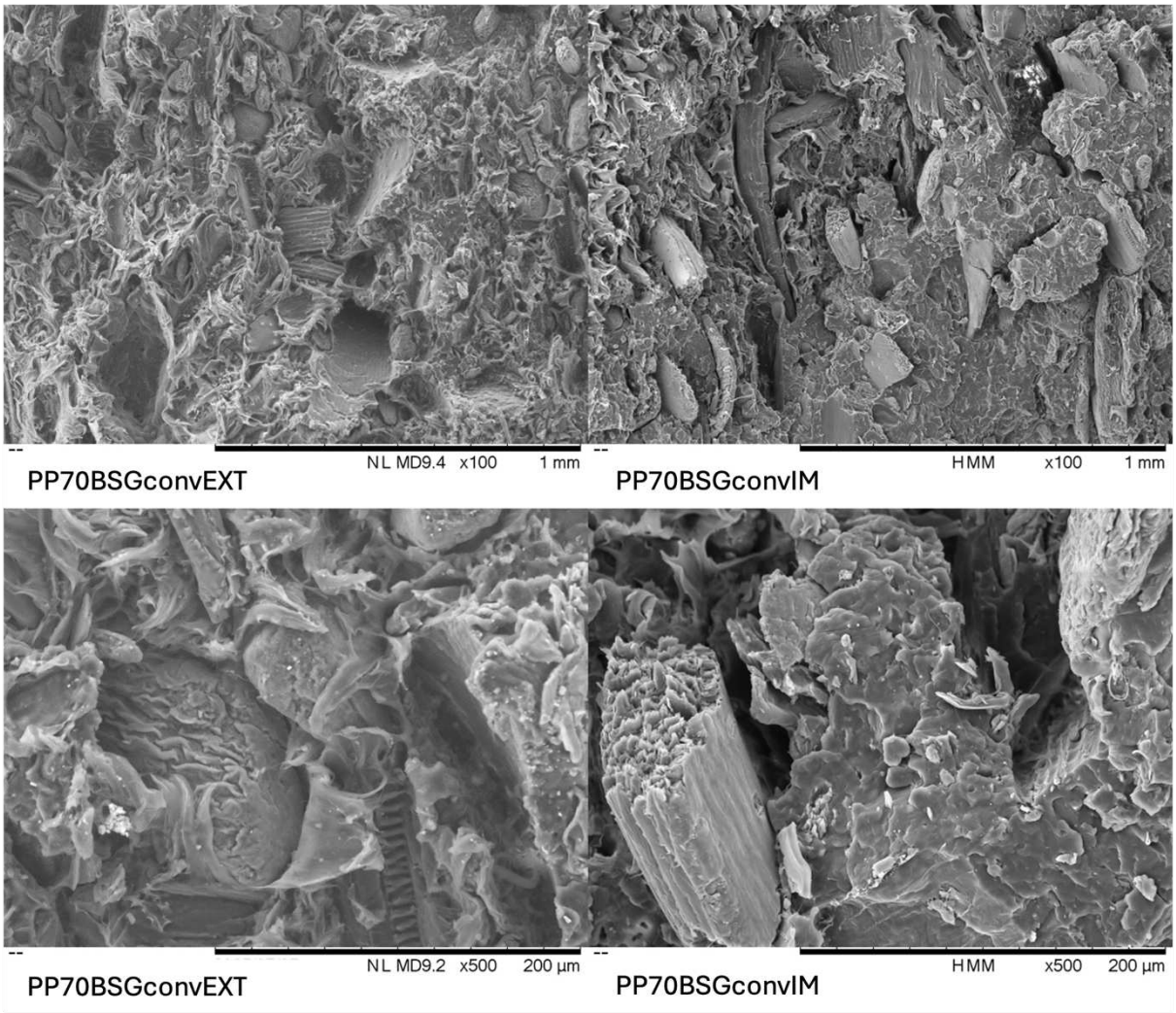


*Figure 5.16: SEM micrographs of PP70BSGconv composites compounded using either extrusion or internal mixing, observation of the tensile fractured cross-section x100 and x500*

Figure 5.17 displays the tensile fracture profiles of **PP70BSGext_150_200** compounded with either extrusion (PP70BSG150EXT) or internal mixing (PP70BSG150IM) at two magnifications: x100 and x500.

In both compounding methods, **no major morphological changes** are observed. The SEM reveals similar fracture pattern considering filler pull-out and matrix deformation. This suggests comparable stress transfer and dispersion. On **PP70BSGext150EXT**, particles seem to be **well embedded** into the PP matrix with **better wetting of PP**.

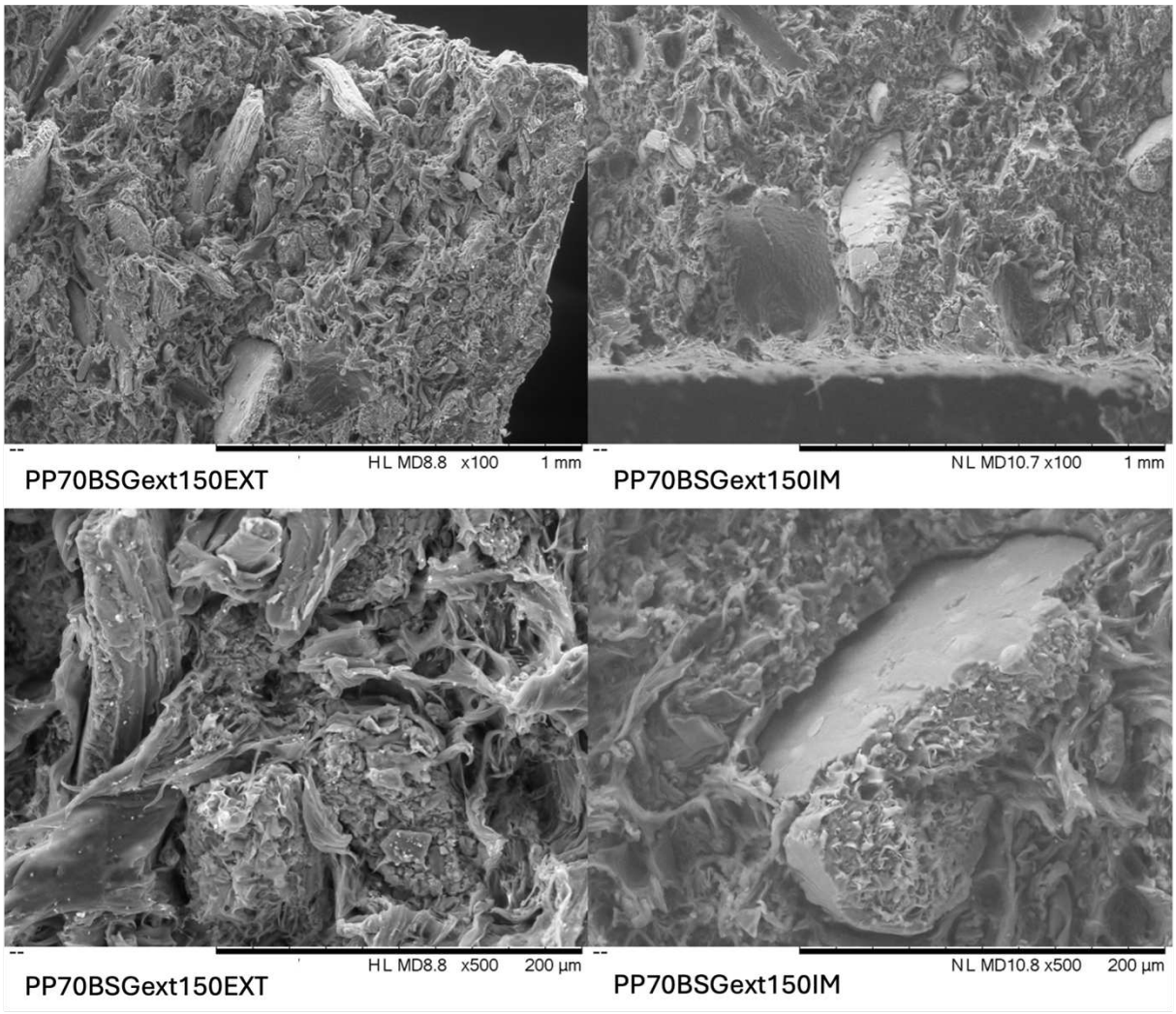


*Figure 5.17: SEM micrographs of PP70BSGext150 composites compounded using either extrusion or internal mixing, observation of the tensile fractured cross-section x100 and x500*

Figure 5.18 displays the tensile fracture profiles of **PP70BSGext_190_400** compounded with either extrusion (PP70BSG190EXT) or internal mixing (PP70BSG190IM) at two magnifications: x100 and x500.

For the composites containing extruded BSG processed at 190 °C and 400 rpm and especially on the cross-section profile of **PP70BSGext190EXT**, different features are observed. At higher magnification (x500) for the extruded composite, longitudinal and transversal fractures are observed, likely induced by the stringent extrusion conditions occurring during

compounding. One particle appears fractured (highlighted by arrows), which may have occurred either during tensile test, thereby suggesting little interfacial adhesion, or during extrusion compounding which may be mechanically aggressive towards BSG particles which are already dry and potentially more fragile after extrusion pretreatment. These partial fractures and fiber folding can create additional voids within the matrix due to the resulting folding.

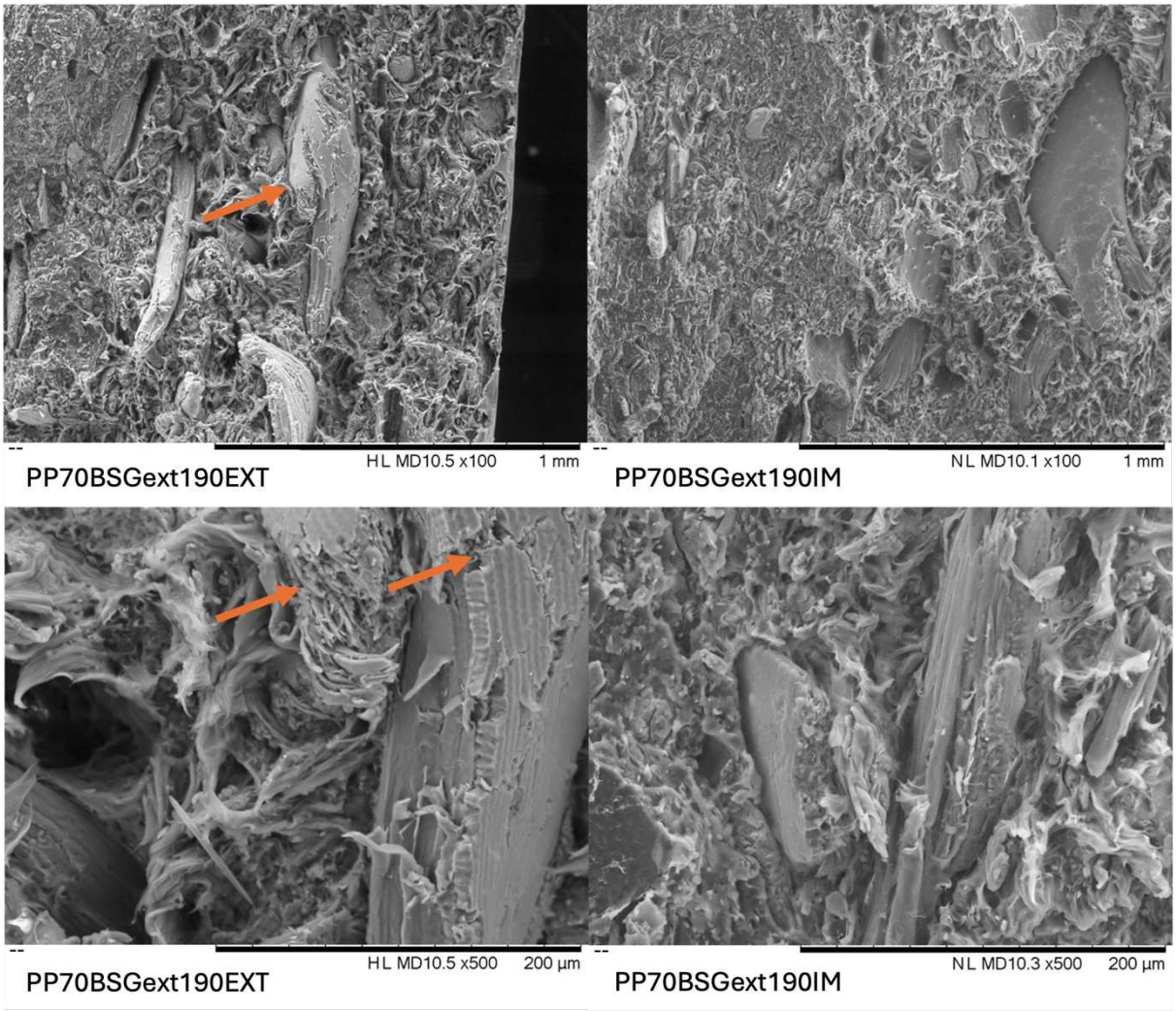


*Figure 5.18: SEM micrographs of PP70BSGext190 composites compounded using either extrusion or internal mixing, observation of the tensile fractured cross-section x100 and x500*

To conclude, in the case of **BSGconv**, some **differences** between the compounding methods were observed, with **internal mixed** composites showing brittle regions suggesting a **limited stress transfer** and **less homogeneous** mixing compared to extrusion. For **BSGext190** composites, the particles appeared **more damaged** in the case of **extrusion** compounding suggesting that **shear forces** during extrusion were **higher** compared to internal mixing. This

observation was less visible with BSGext150 composite probably because the particles were less fragile because less damaged during extrusion drying-grinding.

### *3.2.4. Mechanical properties*

Table 5.4 gathers the results of tensile tests for each PP composites with statistical results focusing on comparing both compounding methods (extrusion and internal mixing).

Figure 5.19 displays Young's modulus of PP composites containing BSG processed under different conditions and compounded using either **internal mixing (IM)** or **extrusion (EXT)**. **PPEXT** and **PPIM** display a **similar Young's modulus**, indicated that **both compounding methods do not seem to alter PP** elastic response to mechanical stress. Some differences are observed in PP composites containing BSGconv. **PP70BSGconv** exhibits a significantly higher modulus when compounded by internal mixing (**1603 ± 26 MPa**) compared to extrusion (**1283 ± 72 MPa**), suggesting that internal mixing promotes a stiffer composite when BGSconv is used. This reflects the behavior seen in SEM images with the brittle regions for PP70BSGconvIM. Conversely, for **PP70BSGext_150_200** and **PP70BSGext_190_400**, **no significant difference** in modulus were observed between the two methods, although a **slight trend toward higher stiffness** is seen for compounding using **internal mixing.** However, at this stage, these are only possible interpretations, and the processing step needs to be reproduced. At present, the standard deviation refers only to the different analyses carried out on a single processed batch.

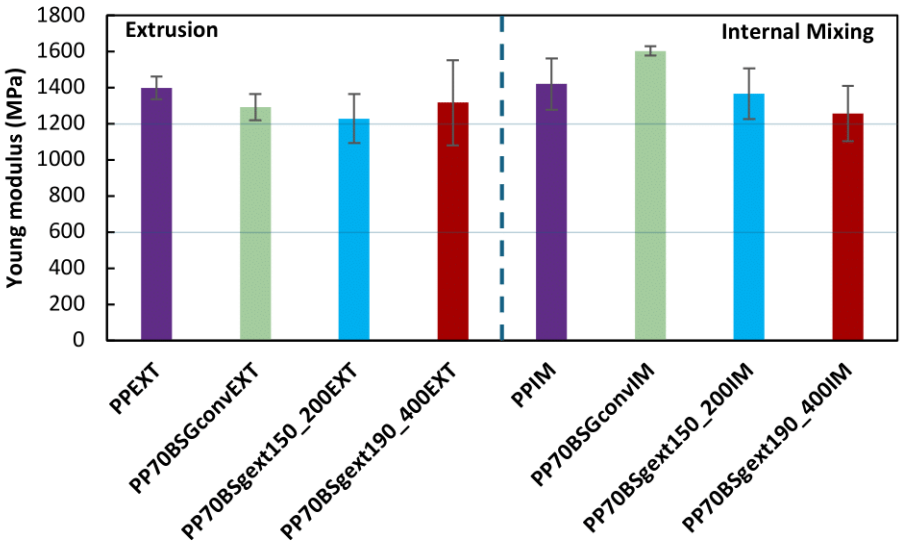


*Figure 5.19: Comparison of Young's modulus for different processing methods in PP composites containing 30% of BSG (conv or extruded). Average of five experiments.*

Figure 5.20 presents the **maximum tensile strength** obtained for PP composites. PP composites containing **extruded BSG**, especially **PP70BSGext_190_400**, demonstrated significantly **higher strength** when compounded by **internal mixing** (**28.0 ± 0.4 MPa**) than by extrusion (**25.5 ± 1.0 MPa**).

Interestingly, for **PP70BSGconv**, the **trend is reversed** with **extrusion** yielding **higher strength** (**26.0 ± 1.0 MPa**) than internal mixing (**24.3 ± 0.6 MPa**). These variations could be explained by differences in **filler dispersion**, or **wetting behavior of the PP** that could be different according to the compounding method. Moreover, the fibers appeared more damaged using extrusion compounding which may reduce their mechanical performance. Again, at this stage, the standard deviation refers only to the different analyses carried out on a single processed batch.

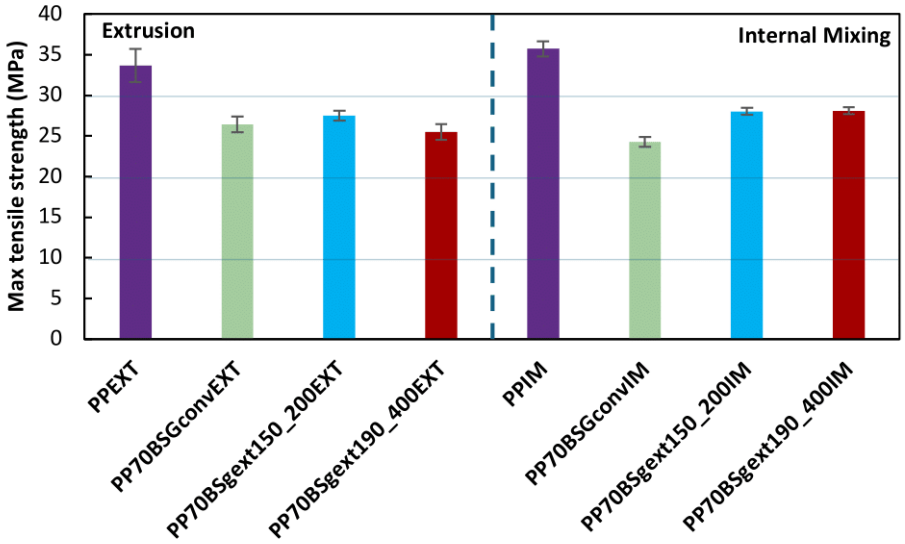


*Figure 5.20: Comparison of maximum tensile strength for different processing methods in PP composites containing 30 % of BSG (conv or extruded). Average of five experiments.*

*Table 5.4: Mechanical tensile test results for PP composites comparing two compounding methods. Average of five replicates. Statistical tests were performed pairwise according to the compounding method. Different letters within a row indicate statistically significant differences ($p < 0.05$).*

| Sample code | Young's modulus (MPa) | | Tensile strength (MPa) | |
|---|---|---|---|---|
| | Extrusion | Internal mixing | Extrusion | Internal mixing |
| PP | **1398**$^{a}$ ± 63 | **1420**$^{a}$ ±141 | **33.7**$^{a}$ ± 2.0 | **35.8**$^{a}$ ± 0.9 |
| PP70BSGconv | **1283**$^{a}$ ± 72 | **1603**$^{b}$ ± 26 | **26.4**$^{a}$ ± 1.0 | **24.3**$^{b}$ ± 0.6 |
| PP70BSGext_150_200 | **1229**$^{a}$ ± 135 | **1368**$^{a}$ ± 140 | **27.5**$^{a}$ ± 0.6 | **28.0**$^{a}$ ± 0.4 |
| PP70BSGext_190_400 | **1317**$^{a}$ ± 140 | **1257**$^{a}$ ±153 | **25.5**$^{a}$ ± 1.0 | **28.1**$^{b}$ ± 0.4 |

In addition to their mechanical behavior, the long-term performance, and application of composites is also linked to their interaction with water. For this reason, the **water uptake** characteristics of the materials were studied, first by **comparing the two compounding methods** to evaluate their impact on barrier properties, and then, by looking at the **influence of BSG extrusion** (drying-grinding) on water-related performance of their composite. This last point was not considered in the first part of this chapter, since that section focused exclusively on internally mixed composites, whereas here the composite made with extruded BSG for water absorption experiments were extruded for compounding. Hence, it was chosen to discuss the results in this following part.

*3.2.5. Liquid water swelling behavior*

In this section, the **water absorption behavior** of composites immersed into water is investigated. As in Chapter 3, the water uptake experiment could not be extended to reach a stable mass due to the visible growth of microorganisms on the sample surface.

The first part is dedicated to compare the effects of **compounding method** on water sorption by comparing **pure PP** and **PP filled with 30 %(m/m) of BSGconv**, each prepared either by **extrusion** or **internal mixing**. All composites were shaped into circular specimens using laboratory injection press. The evolution of water sorption over time for these samples is displayed in Figure 5.21.

In Figure 5.21, the water sorption behavior of the samples shows **similar trends regardless of the compounding method**. For **pure PP**, a small and rapid increase in water absorption within two days is observed. After three days, **PPIM** shows a slightly higher water uptake than **extruded PP**, however the difference remains minimal.

In contrast, when **BSGconv** is added to the formulation, the **extruded composites** exhibit a **higher water sorption** (**2.67 ± 0.10 %**, at 9 days) compared to the ones obtained with **internal mixing** (**2.30 ± 0.05 %**, at 9 days). This result corroborates with previous mechanical observations where **PP70BSGconvIM** showed a **higher elastic modulus** than **PP70BSGconvEXT**, illustrating **higher stiffness**. A stiffer material is likely to deform less under the pressure applied by swelling fillers. Indeed, it has been shown in literature that the increase in matrix stiffness implies a reduction in water uptake and sorption kinetics [288]. Hence, in our case it could **potentially limit BSG swelling** and consequently **reducing water uptake**.

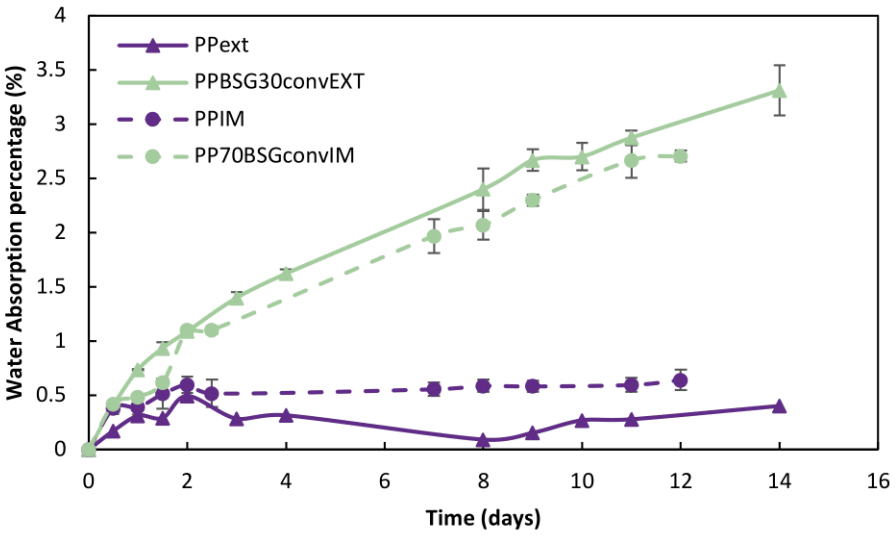


*Figure 5.21: Effect of compounding method on water absorption of PP and PP composites containing 30% of BSGconv and injected with laboratory press, means of two replicates.*

The second part of this section focuses only on **composites produced by extrusion**, with the objective of assessing the **influence of BSG processing method** on **water absorption** behavior. In this part, PP composites containing 30 %(m/m) of either extruded BSG or BSGconv were prepared and shaped into circular mold using laboratory injection press.

The evolution of water sorption over time for these composites is displayed in Figure 5.22.

After 14 days of immersion, a clear trend is observed. **PP70BSGconv** and **PP70BSGext150** show **similar levels of water uptake**, reaching **3.31 ± 0.23 %** and **3.10 ± 0.03 %**, respectively. In contrast, **PP70BSGext190** has a markedly higher water uptake of **4.25 ± 0.13 %**. As discussed in Section 3.2.3. of this Chapter, **BSGext190_400 particles show partial fracture** within its structure, likely due to harsh processing compounding conditions coupled with fragility of the filler caused by extrusion pretreatment. These incomplete fractures could lead to the formation of **internal voids within the composites**. During water immersion, such voids can increase water uptake by serving as **reservoir for water molecules**, thereby increasing the overall **water swelling capacity of the filler**. This capillarity phenomenon could explain the higher water absorption observed for PP70BSGext190.

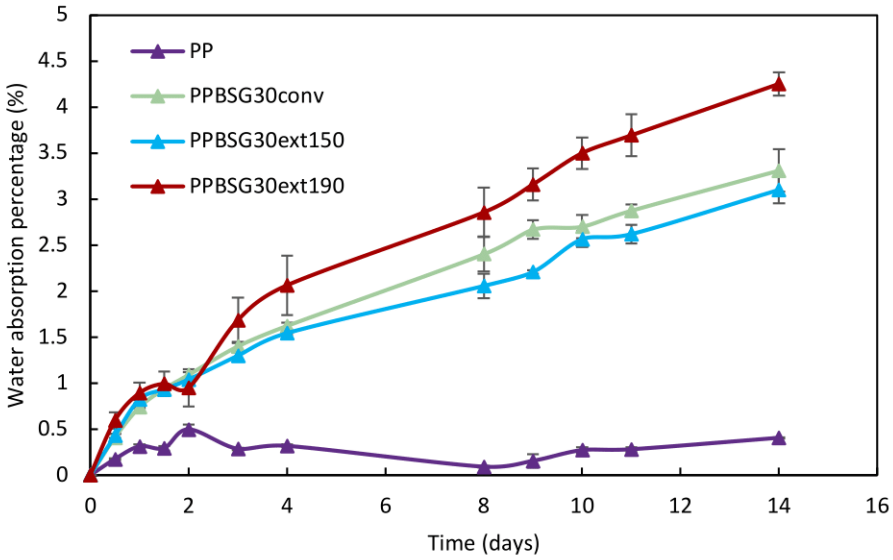


*Figure 5.22: Effect of processing methods to obtain BSG on water absorption of extruded PP composites containing 30% of BSG and injected with laboratory press, means of two replicates.*

### *3.2.6. Conclusion*

This section aimed to **evaluate the compounding method** (extrusion versus internal mixing) on the thermal, rheological mechanical structure and water absorption of injected PP composites made with 30 %(m/m) of extruded BSG and BSGconv.

Across the different results, **Internal mixing** proved to be a **reliable and representative laboratory-scale compounding method**, especially when only small and limited amounts of material are available. The results showed that the **properties of composites obtained via internal mixing are consistent** with those from **extrusion**, making it a valuable approximation of larger-scale process such as extrusion. This validates its use for early-stage research while extrusion is a preferred method for scalability and industrial application.

## 3.3. Composites injection: from manual injection press to industrial injection press

### *3.3.1. Introduction*

Following the evaluation of the compounding methods this section focuses on the **injection process** itself. The goal is to compare the **effects of the injection technique**, more specifically a laboratory manual injection press versus a semi-industrial injection press.

During almost the entire project, the **laboratory injection press** was used because internal mixing produced **limited material quantities** (about 50 g per batch), which were insufficient to use the **semi-industrial injection press** that requires at least 400 g of material to operate. Moreover, due to pressure limitations, the laboratory press did not allow for direct production of dog-boned shape specimens that were cut from injected rectangle shapes, which might affect quality. The semi-industrial process can help us to inject specimen in this form directly.

The two injection processes differ significantly in terms of operating parameters, which can influence the final properties of the composite specimens. Table 5.5 presents the parameters of both injection techniques. The **laboratory injection press** relies on **manually applied pressure** which is inherently inconsistent and lower than the pressure of industrial settings. Moreover, the injection time is slower, approximately 5 sec for one specimen and there is **no measurable holding pressure step**. The mold temperature is also maintained at 125 °C to facilitate the flow of PP inside. In contrast, the **semi-industrial injection press** operates under automated pressure control (~50 bar) with a **faster injection speed** (100 mm/s) and a controlled holding pressure step (25 bar for 10 s). The mold temperature is set at 20 °C. The sustained holding pressure allows for a **better mold filling** with less bubbles and polymer retractation. These conditions allow for direct dog-bone shape specimen injection.

These differences can therefore significantly affect the **structure, crystallization, and mechanical properties** of the PP composites.

*Table 5.5: Comparison between laboratory and semi-industrial injection presses used for PP composite processing.*

| Parameter | Laboratory injection press | Semi-industrial injection press |
|---|---|---|
| **Pressure Application** | Manual | 50 bar |
| **Injection speed** | ~5 mm/s | 100 mm/s |
| **Holding pressure** | None | 25 bar during 10 s |
| **Mold Temperature** | 125 °C | 20 °C |
| **Specimen geometry** | Rectangle, dog-bones cut after | Dog-bone mold |
| **Volume requirement** | Small batch ~6 g | Large batch ~400 g |
| **Material source** | Internal mixing/extrusion | Extrusion |

*3.3.2. Effects on transition temperature (DSC)*

As emphasized in the introduction, the main differences between the injection processes lie in the applied **temperatures, shear stress** and in the **cooling rates**. These parameters have been shown to strongly influence the **crystalline structure** of polymers [6,289,290]. Therefore, DSC experiments are particularly relevant to investigate the effect of both injection methods on our composites.

In this section, particular attention is given to the **first heating ramp**, as it provides insights into the **crystalline state of the composites after being injected** via the two different methods. This comparison is relevant since the **manual injection press** involves PP being melt during a **longer time** (6 min) and cools down from 125 °C to room temperature inside the mold whereas **industrial press** operates at lower mold temperature (20 °C) which involves a **much faster cooling.**

Figure 5.23 displays the 1st heating step of **DSC thermograms** of pure PP and PP composites with 30 %(m/m) of BSGconv injected via the two presented methods.

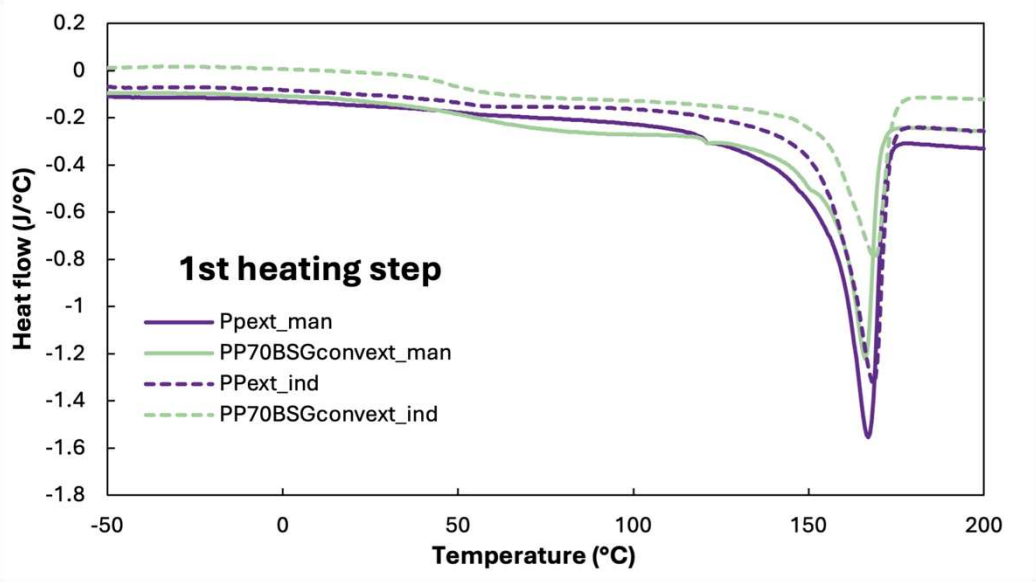


*Figure 5.23: Differential scanning calorimetry curves of extruded pure PP and PP composites containing 30 %(m/m) of BSGconv, comparison of the injection method, at 10 K/min, under nitrogen atmosphere.*

During **1st heating step**, the **melting temperature** ($T_{m1}$) and the **degree of crystallinity** ($\chi_{c1}$) of the composites after injection were determined.

Looking at this **1st heating step**, a **broad endothermic peak**, beginning at 50 °C, is observed in both curves of **PP70BSGconvEXT**. This peak likely corresponds to the **evaporation of the residual moisture** contained by BSG particles (about **1.5 %(m/m)** according to TGA results). Since the residence time during extrusion is much shorter than that of internal mixing, the residual moisture has less time to evaporate. As a result, a larger peak is observed for the extruded composites in DSC. As expected, such endothermic peaks do not appear on pure PP curves as they do not contain enough residual water, approximately **0.5 %(m/m)**. However, it can also be induced by less stable crystals formed after the injection molding.

Moreover, on this **1st heating step**, **two groups** are detaching, depending on the **injection method**. (PPext_ind, PP70BSGconvEXT_ind). Samples injected with the **laboratory press** (PPext_man, PP70BSGconvEXT_man) **melt earlier** (**166.8 ± 0.5 °C** and **166.1 ± 0.3 °C**) compared to the samples industrially injected (**168.6 ± 0.5 °C** and **168.6 ± 0.4 °C**). Additionally, **manually injected specimens** show a significantly **higher degree of crystallinity**: **+10 % for pure PP** and **+5 % for composites containing BSG**, relative to industrially injected samples.

These differences are strongly related to the **processing conditions**. The **mold temperature** used with laboratory press (**125 °C**) is set above the material's **crystallization temperatures** (**114.8 °C-118.3 °C**, Table 5.6), providing good conditions for **crystal growth during cooling**. Moreover, the **longer residence time at 200 °C** (6 min) in the manual press may act as a **thermal annealing step** generating relaxation and molecular rearrangement [291], promoting **higher crystallinity**. This is consistent with the findings of Parenteau *et al*. who demonstrated that **annealing PP at temperatures above 150 °C** enhances its crystallinity [292]. In contrast, the **faster cooling** induced by the **lower mold temperature** (**20 °C**) of the industrial press likely limits crystallization.

*Table 5.6: DSC data of extruded PP and PP composites with 30 %(m/m) of BSGconv, comparison of injection methods (manual (man) vs industrial (ind) with subscript "1" for 1st heating step. Different letters indicate statistically significant differences between samples.*

| Sample code | $T_{m1}$ (°C) | $\chi c_1$ (%) |
|---|---|---|
| PPext_man | **166.8**$^{a}$ ± 0.5 | **46.0**$^{a}$ ± 1.0 |
| PPext_ind | **168.6**$^{b}$ ± 0.4 | **35.7**$^{bc}$ ± 1.9 |
| PP70BSGconvEXT_man | **166.1**$^{a}$ ± 0.3 | **42.1**$^{ab}$ ± 3.4 |
| PP70BSGconvEXT_ind | **168.6**$^{b}$ ± 0.5 | **37.1**$^{c}$ ± 1.8 |

*3.3.3. Effects on interfacial structure*

In this part, we will compare the **internal structure** of fully lab-scale processed samples (internal mixing + manual injection) with the structure of fully industrial-scale processed samples (extrusion + industrial injection), focusing **on pure PP and PP filled with 30 %(m/m) of BSGconv**. To observe their morphology, the samples were **cryo-fractured**, and the resulting cross-sections are shown Figure 5.24.

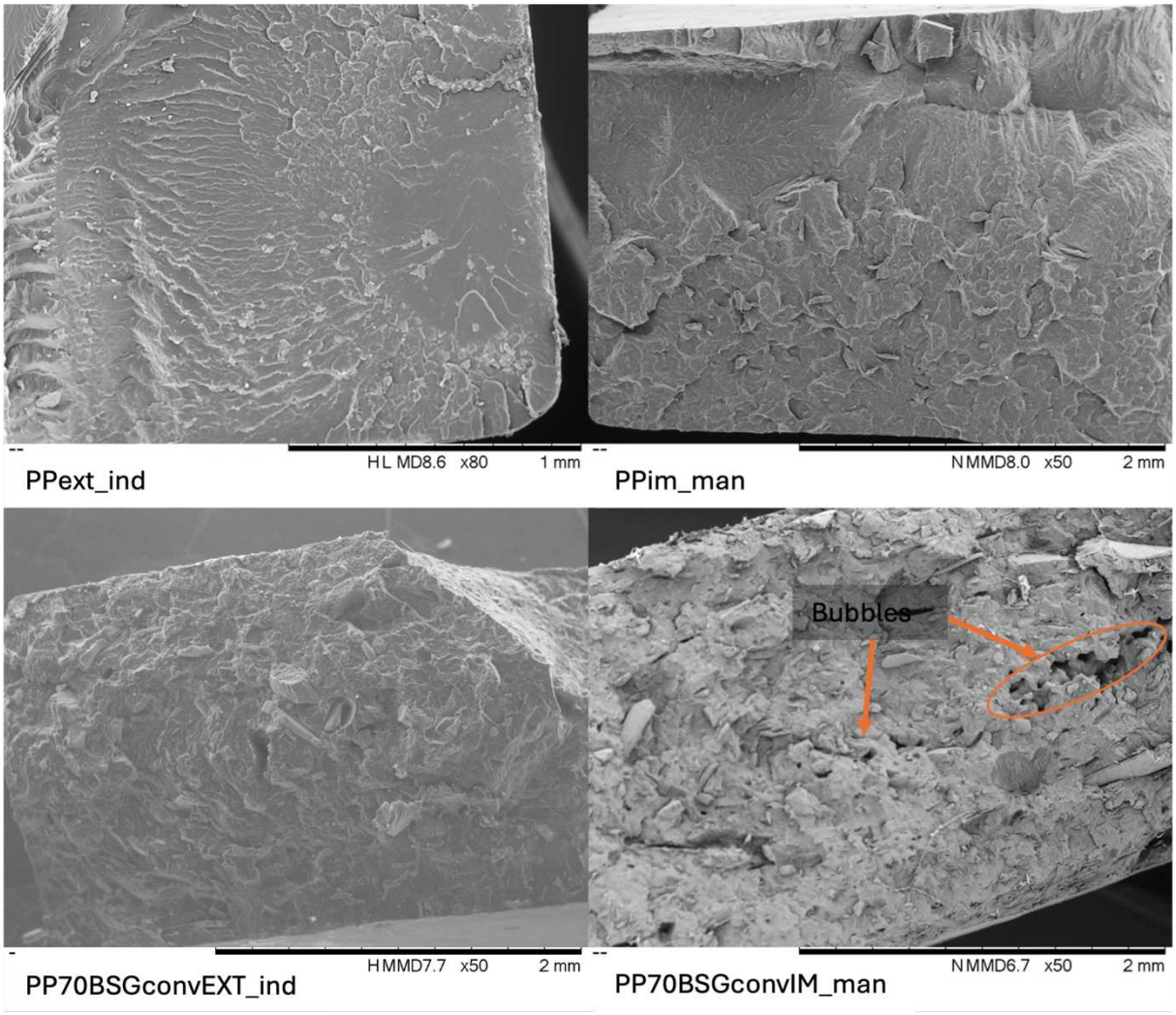


*Figure 5.24: Comparison of the cross-fractured surface of pure PP and PP composites filled with 30 %(m/m) of BSG conv obtained with two different methods (1-extrusion + industrial injection ; 2- Internal mixing + manual injection)*

For **pure PP**, the macrostructure reveals notable differences between the two processes. **PPext_ind** exhibits a **smoother and more uniform surface** where as **PPim_man** shows a more heterogeneous structure, likely resulting from the **manual injection**, where **pressure is applied inconsistently** throughout the injection time. This inconsistency can affect the flow and solidification leading to formation of layered structures.

Moreover, when looking at **PP composites filled with BSG**, the differences are more pronounced. Manually injected sample (**PP70BSGconvIM_man**) shows the presence of **bubbles** within the matrix represented by little dark spots highlighted on the figures with arrows and circles. These are not observed for **PP70BSGconvEXT_ind**. This observation may be attributed to the **maintained pressure and time** used in the **semi-industrial injection process** which likely helps to **minimize air entrapment**, resulting in denser mold filling.

At this point, it is important to note that, throughout this PhD project, all specimens with visible defaults (such as those with bubbles and voids) were systematically removed from mechanical or thermal testing. This example shown here is a rare one and was kept for microstructural analysis as it helps to illustrate the limitations and the more variable conditions of the manual injection.

**Tensile fractured sections** further highlight the differences between industrial and manual injection molding. Indeed, **industrially injected composites** exhibit a **greater elongation** compared to composites obtained via manual injection. In fact, for PPext_ind, the elongation was very high and generated delamination, therefore it was not possible to recover a representative section for SEM (Figure 5.25).Therefore, due to this elongation the tensile test speed for industrially injected specimens has to be adjusted from **2 mm/min to 5 mm/min** to allow for accurate testing.




*Figure 5.25: Picture of extruded PP specimens from two different injection methods after tensile test*

Figure 5.26 displays the tensile fractured surface of **extruded** PP composites filled with 30 %(m/m) of BSGconv obtained via either industrial injection (left) of manual injection (right) at two magnifications (x80 and x200).

Observing Figure 5.26, a clear distinction emerges between the two processing methods. All **industrially injected composites show significantly longer and pronounced stretching**

**marks compared to the manually injected composites**. This could be attributed to the more uniform mold filling of industrial injection.

Additionally, since PP is a **semi-crystalline polymer**, microstructural factors likely play a role in this divergence. While a **lower crystallinity** has been associated with greater ductility and elongation [292,293] the **type of crystalline structures** may also be important to consider. **β-phase spherulites** in PP are known to promote **plastic deformation** and enhance strain. Their formation is also more likely to occur **under conditions of high shear rates** [6].These conditions are also more likely to occur during industrial injection molding due to **higher speed of injection and higher pressure**. Therefore, the combination of **lower crystallinity** and **possible presence of β-crystals** could contribute to the observed **enhanced ductility of the PP**.

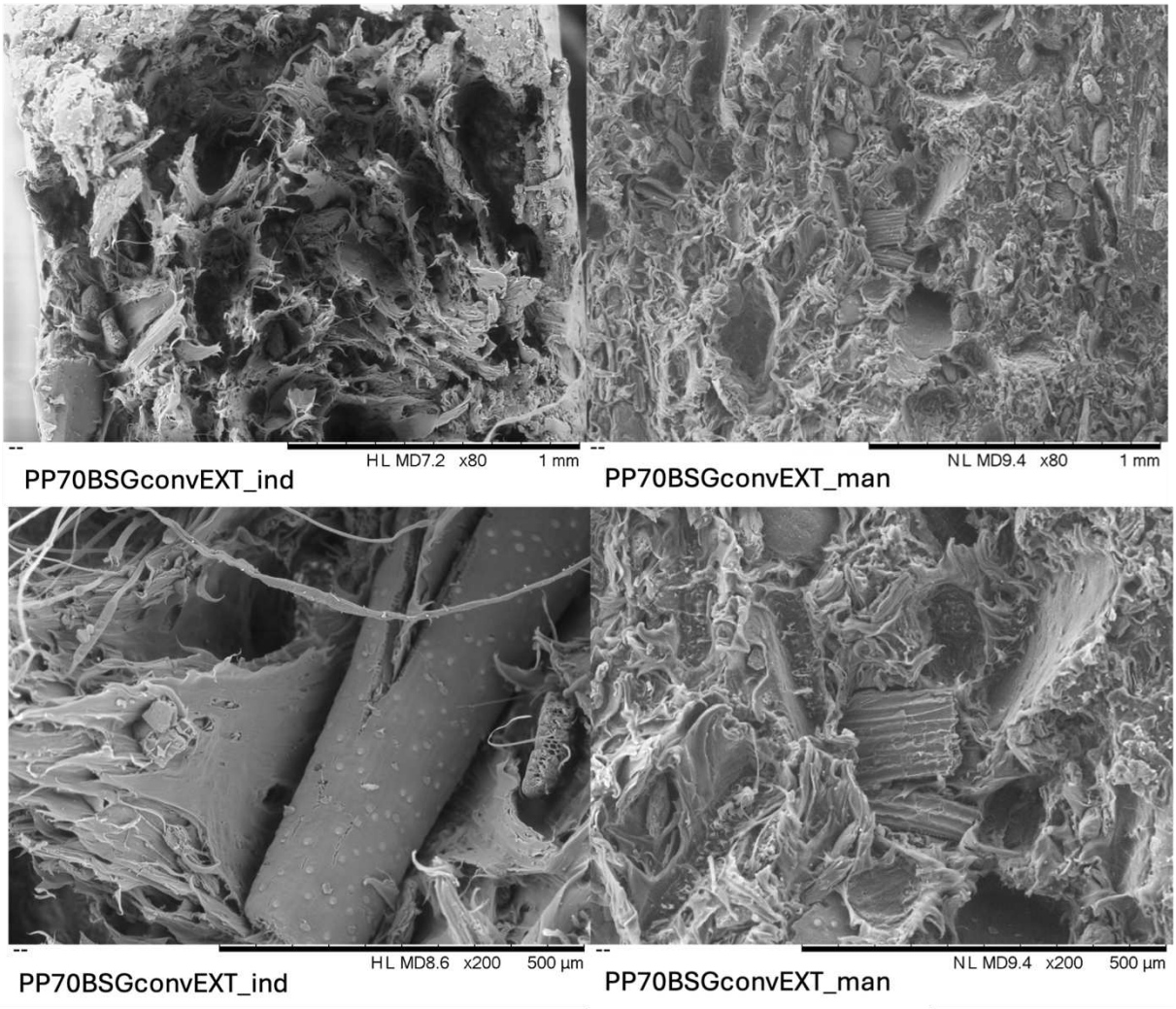


*Figure 5.26: SEM micrographs of extruded PP composites filled with 30 %(m/m) of BSG injected using either industrial or manual injection press, observation of the tensile fractured cross-section x80 and x200*

*3.3.4. Effects on mechanical behavior*

In this section, **two different specimen geometries** were used due to constraints of each injection methods. Specimens **produced using the laboratory injection pressed** were cut from injected rectangles resulting in smaller dog-bone shapes with shorter gauge length (Figure 5.27,b), whereas the semi-industrial injection press permits the obtention of bigger dog-bone specimens (Figure 5.27,a).

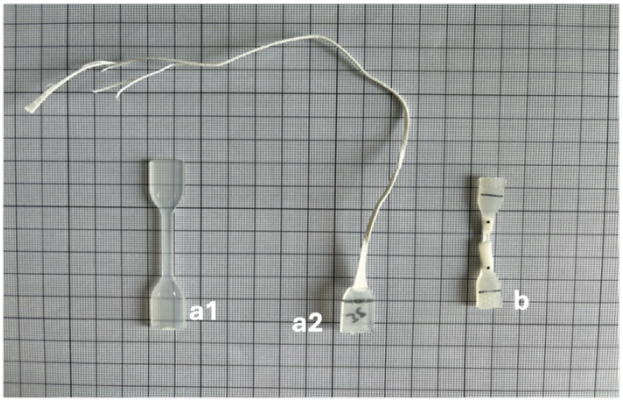


*Figure 5.27: Tensile test specimens obtained from two different injection molding process after industrial injection before (a1) and after tensile test (a2); after manual injection and after tensile test (b)*

As a result, the strain distribution, and gauge length differ between the two types of specimens, making the **comparison** of **strain-dependant parameters** such as strain at break and **Young's modulus unreliable** across the two injection methods. Moreover, the **testing speed** had to be adapted to ensure fracture within the required time range, which was not identical for both specimen geometries as seen during experimentation. Nonetheless, a comparison within the same method as in Chapter 3 remains valid since all specimens share the same shape and testing conditions. In this section, we will focus on the comparison of tensile strength at yield.

Firstly, it is worth noting that even though the strain will not be compared, from a macroscopic (Figure 5.27) and microscopic (Figure 5.26) point of view, the elongation at break was clearly higher for specimens obtained with the industrial injection press. This is either due to the more uniformity and higher pressure of the injection or due to the lower crystallinity and type of crystals of the composites as discussed previously.

Figure 5.28 displays the tensile strength (***TS***) of extruded pure PP and PP composites obtained using the two presented injection methods. Surprisingly the ***TS* was more influenced by the addition of BSG than the injection method**, despite the notable difference in crystallinity degree.

As previously discussed, **many competing factors** (such as crystallinity, filler dispersion, injection shear rates, potential voids creation, etc.) can simultaneously influence the tensile behavior of the material, thereby, **counterbalancing effect** and **minimizing observed differences** between injection methods.

Pure PP injected via semi-industrial method (**PPext_ind**) showed a *TS* of **33.8 ± 1.5 MPa** while **PPext_man** exhibits a very similar *TS* of **33.7 ± 2.3 MPa**. For the filled PP, the industrially injected showed a max *TS* of **27.6 ± 0.9 MPa** while the manual injected showed a *TS* of **26.4 ± 1.1 MPa**.

These results could suggest that either the manual injection remains a valid approach especially when material quantity is limited or that different factors impact the others, resulting in comparable tensile strength values. However, it is important to note that tensile strain behavior was markedly different between the two methods, as observed both macroscopically and with SEM.

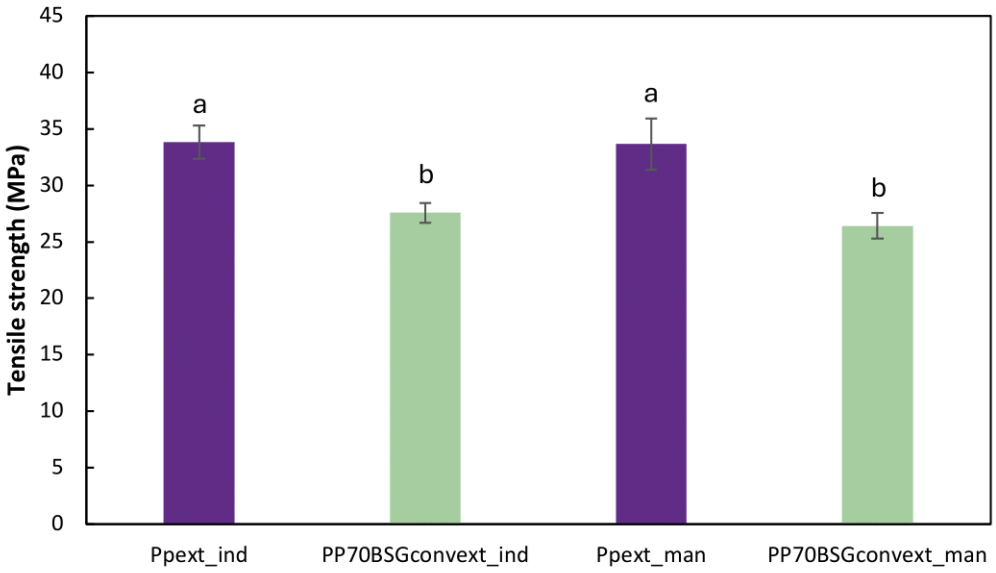


*Figure 5.28: Tensile strength of extruded pure PP and PP composites injected via two methods. Different letters indicate statistically different TS.*

### 3.4. Conclusion about injection methods

As expected, the comparison between **manual laboratory injection and semi-industrial injection molding** highlights several differences and implications for the processing of PP and PP-BSG composites. Although both methods produced materials with **comparable tensile strength**, significant differences were observed in **thermal/crystalline properties, internal structure, and strain behavior**.

The **semi-industrial injection method** allowed us to obtain directly injected dog-bone specimens due to higher pressure and maintaining pressure and time. These conditions addition to the faster cooling resulted in **lower crystallinity** and **greater elongation** of the material, potentially due to differences in crystals structure and shear-induced crystal formation. In contrast, the **manual injection molding** led to **higher crystallinity** likely caused by the **longer melt time** and **slower cooling speed**. While perfectly suited for small batches, it resulted **in more variability and defects** within specimen samples.

To conclude, these results confirms that **manual injection remains a valid lab-scale process** when material is limited. However, semi-industrial injection offers better consistency and reliability regarding the production of specimens.

## 4. Conclusions

This chapter highlighted how both BSG pretreatment (extrusion vs conventional method) and processing methods influence the final properties and potential of our thermoplastic composites. In the first part, **extrusion** was shown to be an **effective pre-treatment** for BSG, modifying its morphology (rougher surface) and improving its interfacial compatibility with the thermoplastic matrices. For **PLA**, extrusion also confirmed the **role of volatiles compounds** in promoting PLA **chain scission**: by eliminating them PLA composites exhibited **higher rheological moduli** and higher $T_g$ reflecting the lower mobility of the chain and making **processability harder**. This was less visible for the same loading of extruded BSG in PP composites. However, PLA composites showed **higher tensile strength** due to better interfacial compatibility. For **PP**, the results were particularly **consistent** with the obtention of **better tensile strength** in the case of extruded BSG, while the processability of the composites remained good which motivated the focus on **PP for scalability**.

The second part showed that the compounding and the shaping process play a significant role in composites performance. While **internal mixing** proved to be a **reliable and**

**representative laboratory-scale compounding method**, especially when only small and limited amounts of material are available, **industrial injection** provided more **reliable** and reproducible specimens compared to manual injection. Indeed, the **lack of control** over manual injection parameters rendered its utilization more variable.

Figure 5.29 summarizes the main outcomes of this chapter.

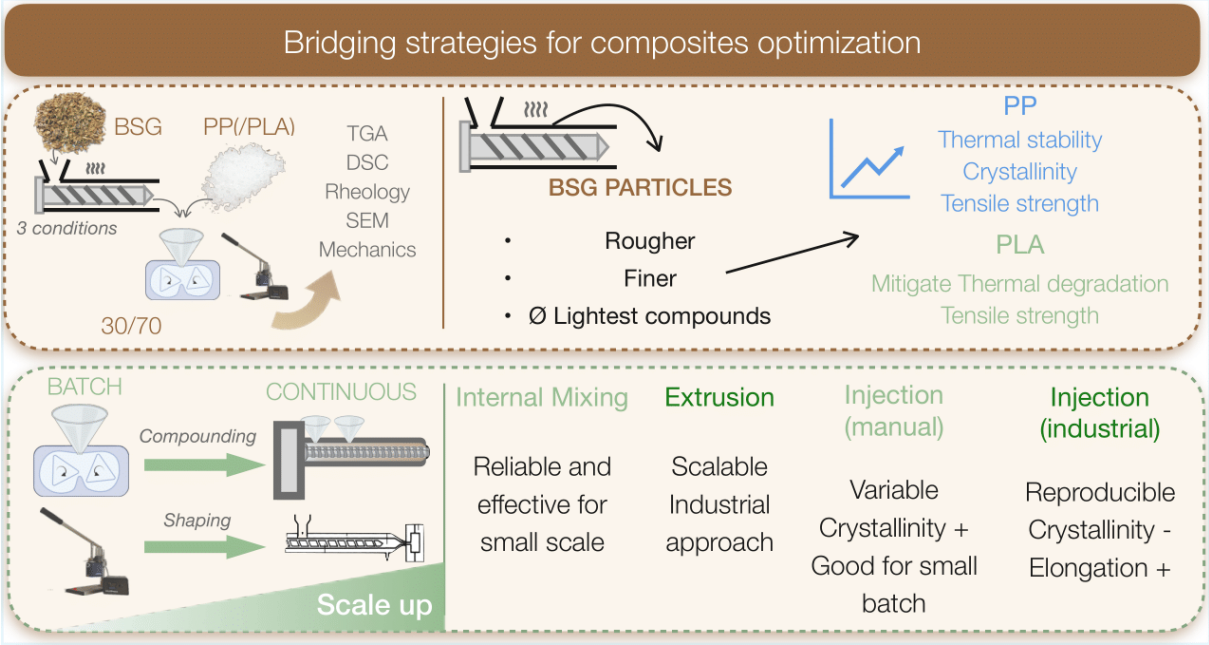


*Figure 5.29: Schematic overview of Chapter 5.*

Overall, the results presented extruded BSG as a promising, sustainable filler for PP composites and demonstrate viable pathways for scaling from laboratory to semi-industrial conditions, a crucial step towards their future implementation in real applications. While this chapter highlighted the role of filler morphology in composites performance, its main purpose was not to address filler modification. Next chapter will help us to dig into our understanding of the influence of filler morphology and composition on thermoplastic matrix by explicitly focusing on chemical treatment of BSG, making its impact on compatibility and BSG-matrix interactions the main objective.

# CHAPTER 6:

# Alkaline treatment of BSG to improve interfacial adhesion with polymer matrices

# RÉSUMÉ DU CHAPITRE 6

L'un des principaux obstacles rencontrés dans cette thèse est la mauvaise adhésion entre la drêche et les matrices thermoplastiques (PP et PLA). Cette incompatibilité, due à la différence de composition chimique entre les charges lignocellulosiques (majoritairement hydrophiles) et les polymères hydrophobes, limite le transfert des contraintes mécaniques ce qui conduit à de mauvaises propriétés mécaniques. Afin d'améliorer l'adhésion à l'interface, nous avons étudié le traitement alcalin (ou mercerisation) de la drêche dans différentes conditions de durée et de température, tout en maintenant constante la concentration en NaOH (5 % m/m) et le rapport biomasse/solution.

**Première partie** : La drêche séchée mais non-broyée a été traitée à 5 % NaOH pendant 30 min, 1 h, 4 h et 8 h à 25 °C et à 70 °C (sauf 8 h à 70 °C en raison de contraintes liées à l'équipement). Les caractéristiques chimiques, la morphologie et l'aspect de surface des particules ont été évalués après broyage par FTIR, TGA et SEM. Le traitement le plus sévère (4 h / 70 °C) a entraîné une élimination progressive des lignines, des hémicelluloses, des protéines et des pectines. L'analyse FTIR confirme la disparition ou diminution des bandes caractéristiques des lignines et de l'hémicellulose. Une plus grande stabilité thermique est mise en évidence par TGA qui montre un pic de dégradation unique confirmant l'élimination d'une grande partie des hémicelluloses, extractibles et lignines. Le SEM révèle une augmentation visuelle du rapport de forme avec une défibrillation partielle de la cellulose et une rugosité de surface accrue, favorable au crochetage mécanique de la matrice pendant le mélange.

**Seconde partie** : La drêche traitée avec les conditions les plus drastiques (4h / 70°C) (**BSGNaOH**) a été incorporée dans des matrices PP et PLA à des charges de 10 % et 30 % (m/m) par mélangeur interne, suivi d'un moulage par injection manuelle. Les composites ont été caractérisés thermiquement, rhéologiquement, morphologiquement, mécaniquement et selon leur propension à l'absorption d'eau. La drêche traitée augmente la viscosité des composites obtenus et leur module élastique, surtout à 30 % de charge, ce qui dépasse la fraction maximale de compactage et empêche l'injection du PLA à ce niveau. La température de transition vitreuse ($T_g$) du PLA reste inchangée avec BSGNaOH (contrairement à une diminution observée avec la drêche d'origine), indiquant la suppression des composés responsables de la scission des chaînes polymériques. Les performances mécaniques s'améliorent modestement, la résistance à la traction augmente avec la charge de BSGNaOH, tandis que le module d'élasticité reste

stable. L'analyse SEM montre une réduction du vide à l'interface drêche-matrice et un meilleur contact.

Le traitement alcalin à 70 °C pendant 4 h avec 5 % NaOH constitue un compromis optimal entre modification morphologique et préservation de l'intégrité cellulaire des drêches, les rendant aptes à renforcer les composites PP et PLA. Cette stratégie chimique pallie le défaut d'adhérence récurrent dans les travaux précédents, améliore la stabilité thermique du remplissage et ouvre la voie à une valorisation à plus grande échelle des drêches comme charge répondant aux objectifs de développement durable.

# Chapter 6 : Alkaline Treatment of BSG to improve interfacial adhesion with polymer matrices

## 1. Introduction

Throughout this work, a recurring challenge has been the lack of adhesion between BSG and thermoplastic polymer matrices (PP and PLA). The chemical composition of lignocellulosic material and thermoplastic polymer matrix are different which complicates interfacial compatibility. This causes ineffective stress transfer throughout the interface of the composites which results in, among other, poor mechanical properties.

Therefore, to make lignocellulosic filler compatible with the matrix in order to use them as reinforcement in composite materials, chemical modifications can be carried out. The mechanical properties of natural filler composites are strongly influenced by the adhesion between the constituents, aspect ratio and surface morphology. Among the primary constituents of natural fillers, cellulose is mainly responsible for their mechanical properties. Chemical treatments of the filler aim to improve aspect ratio by removing amorphous constituents such as lignin and hemicellulose which reduces the diameter of the fiber. These modifications also aim to enhance dimensional stability by decreasing moisture content and hydrophilicity of the fibers. Moreover, better division of the fiber bundles promotes the availability of sites for interaction with the hydrophobic matrix. Additionally, such treatments can significantly alter the surface morphology of the filler, improving mechanical interlocking and overall interface bonding.

Among all chemical treatments that have been introduced in literature chapter, this chapter focuses on **alkaline treatment** (mercerization) of BSG under various conditions. Indeed, it is widely seen as the chemical treatment method of choice because of its combination of effectiveness, simplicity, and relative low cost. In the first part, we investigate the effects of **treatment time and temperature** (while keeping alkali concentration and alkali/biomass proportion constant) on BSG **structural characteristic, aspect ratio and surface morphology**. In the second part, a selected treatment condition is used to prepare treated BSG in bigger volume to incorporate it in composites with **polypropylene** and **polylactic acid** at **10 %(m/m)** and **30 %(m/m)** filler content. Filler loadings of 10 % and 30 % were selected to represent, respectively, a low incorporation level that maintains good processability and a higher level that approaches the practical upper limit for BSG-filled PLA composites as highlighted in Chapter 3. These composites are then characterized in terms of **thermal, rheological, morphological,**

**mechanical and water absorption** properties. Figure 6.1 displays the experimental workflow just described.

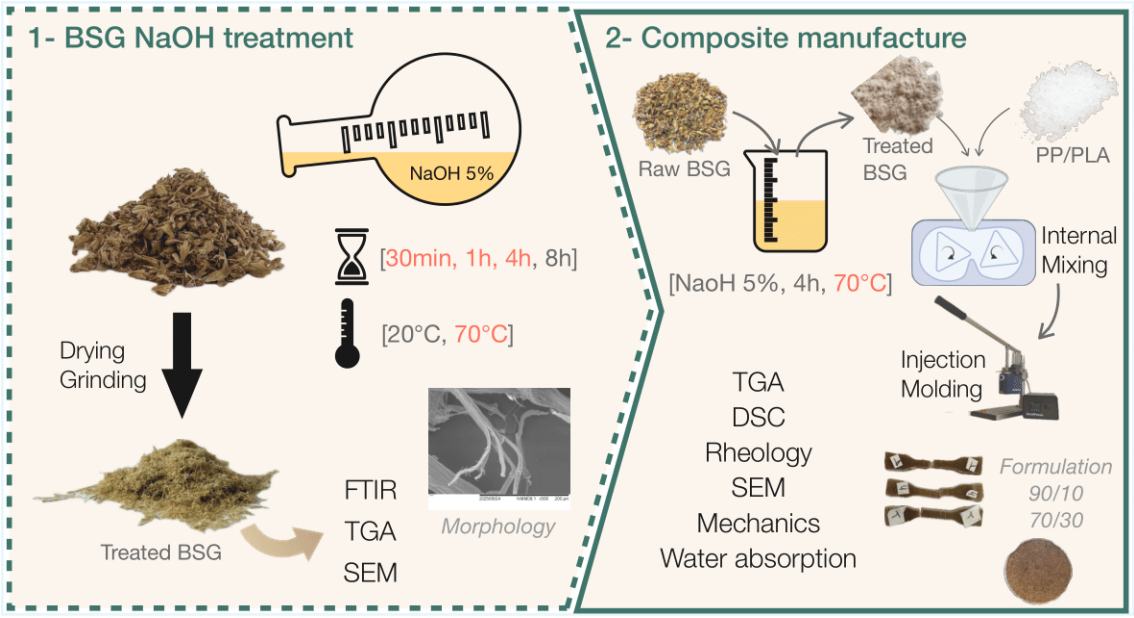


*Figure 6.1: Structure of the Chapter and experimental workflow.*

## 2. BSG NaOH treatment

### 2.1. Introduction

In this part, alkaline treatment is performed on BSG particles in order to remove non-cellulosic components as shown in Figure 6.2. Hence, raw dry BSG particles were subjected to a 5 % alkali (NaOH) solution treatment for 30 min, 1 h, 4 h, and 8 h at ambient temperature and at 70 °C except for 8 h which was not conducted due to equipment constraints. Moreover, the 4-hour treatment at 70 °C already demonstrated good results, therefore an 8-hour treatment was unnecessary as it could potentially lead to cellulose degradation. In the same way, a 5 % alkali solution was selected, as literature reports that higher concentrations cause severe filler degradation, which reduces its mechanical strength [175,176]. Moreover, 70 °C was chosen as the second treatment temperature, since previous studies on alkaline treatment combined with heating typically employed temperatures in the range of 60–100 °C [179,180,182]. To prevent filtration issues, alkaline treatment was conducted on dry BSG before grinding. When BSG was ground first, the resulting mixture was too viscous for efficient filtration. After treatment, BSG was washed with distilled water until pH reached 7, dried and ground using the hammer miller. The effects of the treatment's conditions on BSG morphology and composition were studied with FTIR, TGA, and SEM.

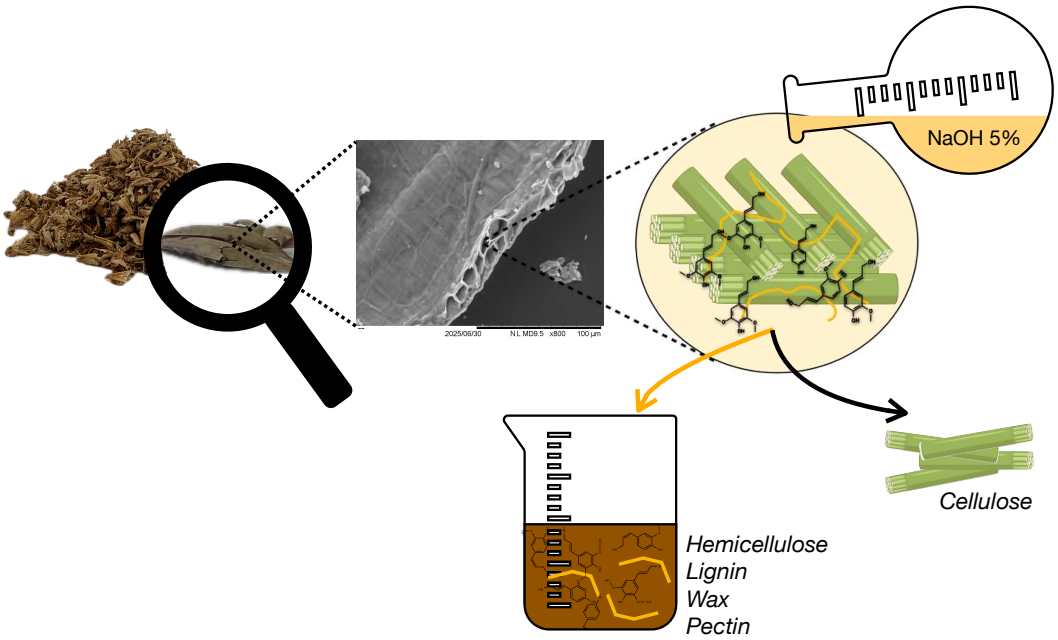


*Figure 6.2: Alkali pretreatment of BSG particles*

### 2.2. Effect of the treatment on BSG chemical functions

Fourier transform infrared spectroscopy (**FTIR**) is a commonly used analytical technique for rapidly assessing the **chemical structure** of lignocellulosic constituents. It provides information on the functional groups present, making it particularly useful for monitoring chemical changes that occur during treatment. Therefore, FTIR was selected to have a rapid insight of the **modifications occurring in BSG** under various **alkaline treatment conditions**.

Firstly, the **FTIR spectrum of untreated BSG** (BSGconv) was studied and compared to the reference spectra of its main different constituents (**lignin, cellulose, and holocellulose**) to identify the **characteristic absorption bands**. The reference spectra were extracted from the study of Cheng *et al*. [208]. Since **holocellulose** corresponds to the mix of **cellulose and hemicellulose**, comparing it with pure cellulose spectrum enabled us to deduce the **spectral contribution of hemicellulose**. This approach allowed us to set the basis for understanding how alkaline treatment works on BSG.

Figure 6.3 displays the **FTIR spectra** of **lignin, cellulose and holocellulose** extracted from Cheng *et al*. study [208] along with **untreated BSG** from our study. Table 6.1 gathers the main **absorption bands** and their **corresponding assignments**. As expected **BSG spectrum** contains features representative of all **three main lignocellulosic components**. Moreover, as highlighted in literature [90,294], BSG contains a significant amount of proteins, the alkali treatment is expected to reduce the content of proteins.

The large stretching signal at **3300 $cm^{-1}$** corresponds to the presence of **hydroxyl groups and amine groups**, commonly found in **cellulose** and **hemicellulose** structures [295]. This stretching band also appears in the **lignin spectrum** which is consistent with the **abundant hydroxyl groups** and **phenolic** structures present in lignins structures.

At **2900 $cm^{1}$**, a stretching band is observed, which is related to **the asymmetric stretch of the $CH_2$** functional groups which are characteristic of **polysaccharides compounds** in BSG according to Naibaho *et al.*, [295]. However, we can observe that this **double peak** is also observed in **lignin spectrum**. These bands have been previously observed in lignin extracted from **hemp, jute and flax**, and related to the **C-H stretching in aliphatic methylene** group, likely originating from **fatty acid** present in the lignin preparations [296].

The band at **1734 $cm^{-1}$** appears in both **holocellulose** and **BSG spectra**, but is **absent from cellulose and lignin** spectra, suggesting that it likely belongs to **hemicellulose spectra**. It has been attributed to the **ester and carboxylic bonds** in **hemicellulose** [208,297] It may also be representative of other **non-cellulosic components** such as **pectins** [182].

From **1684 to 1621 $cm^{-1}$**, a wide band is observed, it is related to the different structure of **BSG proteins** such as **ß-turns**, **α-helix**, and **intra-/inter-molecular ß-sheets**, the last one being more represented as they are associated with aggregate formation [298]. In the brewing process, proteins typically unfold, leading to a reduction in native barley protein structures like intramolecular β-sheets and α-helices, while simultaneously increasing the formation of intermolecular β-sheets [298].

The **O-H bending vibration at 1636 $cm^{-1}$** and **glucose ring vibrations at 1110 $cm^{-1}$** are attributed to **cellulose** functional groups. In contrast, bands at **1603 and 1509 $cm^{-1}$** were **characteristic of lignin benzene ring** stretch vibrations [208].

Since the main objective of the **alkaline treatment** is to **remove hemicellulose and lignins**, the following FTIR spectra will focus on **monitoring the presence of bands associated with these components** to assess the **effectiveness of the treatment**.

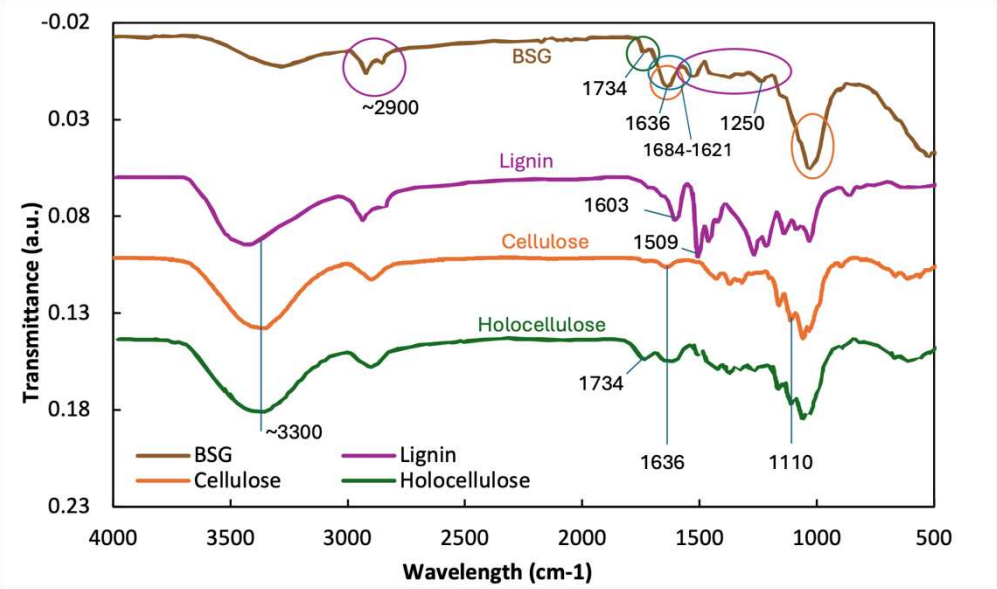


*Figure 6.3: FTIR spectra of our BSG and lignin, cellulose and holocellulose extracted from [208] (4000 to 500 $cm^{-1}$)*

*Table 6.1: Assignments of FTIR peaks in BSG, lignin, cellulose and holocellulose samples [208,295–298].*

| Wavelength ($cm^{-1}$) | Assignment | Component |
|---|---|---|
| 3300 | Stretching vibration of hydroxyl group of hydrogen bond | Hemicellulose, Cellulose |
| 2900 | Asymmetric stretching of $CH_2$ group | Polysaccharides of BSG, lignin |
| 1734 | Ester and carboxylic groups | Hemicellulose, pectins |
| 1636 | Bending vibration of O-H | Cellulose |
| 1684-1621 | β-turns intra/inter molecular β-sheets α-helix | Proteins |
| 1603 | Stretching vibrations of C=C | Lignin (aromatic structure) |
| 1509 | Stretching vibrations of benzene ring | Lignin (aromatic structure) |
| 1250 | Stretching vibration of C=O acetyl | Lignin |
| 1110 | Stretching vibrations of glucose ring | Cellulose |
| 1030 | Stretching vibration of C-O | Cellulose, Hemicellulose |

Figure 6.4 displays the spectra of **untreated BSG and treated BSG** at two different temperatures: **room temperature** (Figure 6.4, a) and **70 °C** (Figure 6.4,b).

The treated BSG at **room temperature** show **a notable change** in the **1500-1200 $cm^{-1}$ region** with principally the **disappearance** of the band at **1250 $cm^{-1}$**. This band has been reported to

**gradually disappear after acid bleaching and NaOH treatment**, confirming the **partial removal of the lignin and hemicellulose** [182,299].

However, most of the **bands** corresponding **to lignin and hemicellulose** chemical structure are still present in the **spectra of BSG treated at room temperature** (Figure 6.4, a). This suggests that **low-temperature treatment** was **not sufficient to fully remove these components**.

However, at **70 °C**, an additional change is observed in the **lignin-related bands** as early as **30 minutes** of the **alkaline treatment**. Indeed, the band at **1509 cm$^{-1}$** which is representative of **benzene ring vibrations** of lignin **is missing** in spectra of treated BSG at **70 °C**. This indicates a **more effective removal of lignin** compared to the room temperature treatment.

Among all our tested conditions, the combination which leads to the **elimination** of a higher number of **lignin and hemicellulose related bands** appears to be **4 hours at 70 °C**. In these conditions, the **double peak** observed at **2900 cm$^{-1}$** merged into a single band. This behavior has been observed by Orue *et al.*, for walnut shells powder treated with **7.5 %(m/m) NaOH at 100 °C for 90 min** [182].

Additionally, the **band at 1734 cm$^{-1}$** attributed to **ester and carboxyl groups in hemicellulose disappeared** after alkaline treatment. This observation aligns with the findings of Laaziz *et al.* who reported a similar behavior for argan nutshell after a **24 h treatment with 8 %(m/m) NaOH at room temperature** [300].

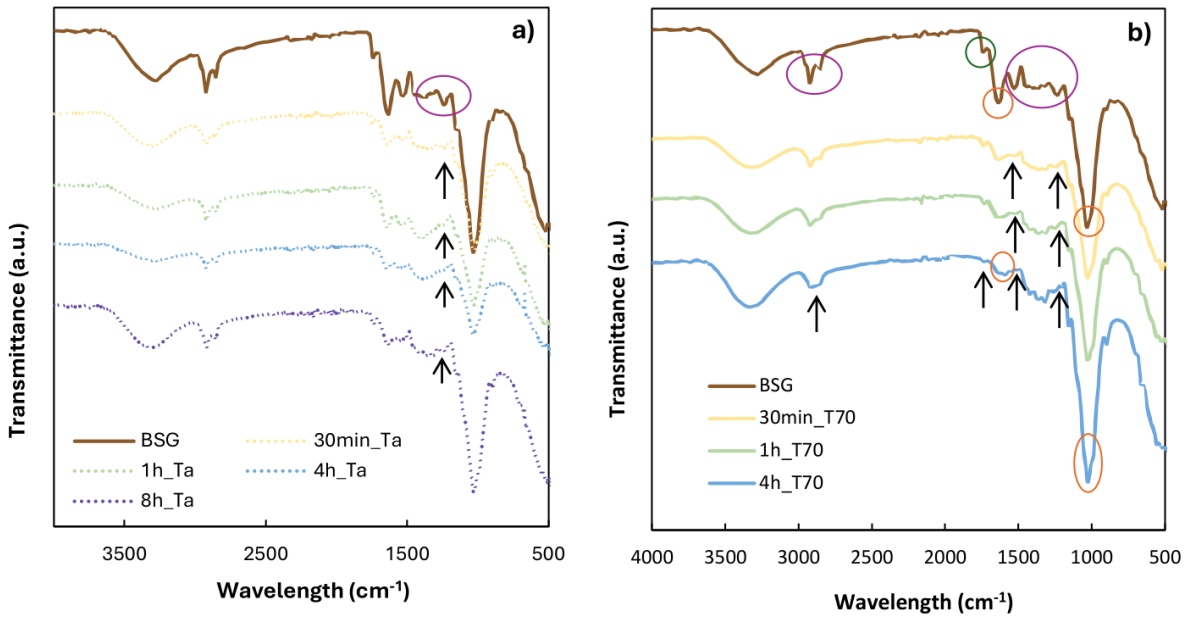


*Figure 6.4: FTIR profiles of untreated BSG and after treatment a) at ambiant temperature b) at 70 °C, circle showing the zones of interest purple for lignin, orange for cellulose and green for hemicellulose belonging bands and arrows showing missing bands.*

FTIR analysis is useful to identify qualitative chemical changes in BSG after alkaline treatment such as the removal of lignin and hemicellulose functional groups. However, while FTIR highlights the presence or disappearance of specific bonds, it remains in general qualitative. Thus, TGA will provide us complementary information on the indicative composition of treated samples, offering a supplementary indication of the extent of component removal. Therefore, the combination of FTIR and TGA allows a more complete evaluation of alkaline treatment effects.

### 2.3. Effect of the treatment on BSG thermal stability

**Thermogravimetric analysis** was carried out to investigate the **thermal stability** of the **untreated** and **treated BSG**, and to **identify and quantify the degradation steps** corresponding to the main lignocellulosic components.

The **thermogravimetric behavior of BSGconv** was previously discussed in **Chapter 3,** Figure 3.5. The TGA curve revealed **three main degradation zones**. **Two sharp peaks** were observed: the **first one** corresponds to the degradation of **hemicellulose** and **second one** to the degradation of **cellulose**. These peaks were surrounded by two shoulders forming a **wider peak** occurring in the background related to the degradation of **extractives and lignin**. The **first shoulder** appearing at lower temperatures corresponds to the **lightest compounds** degraded and the **second shoulder** to more **thermally stable** components such as lignin.

In Figure 6.5, the **thermal degradation behavior** of **treated BSG** shows, as expected, significant differences compared to **untreated BSG**. Even under the **mildest treatment** (30 min at room temperature), the **first shoulder** (~175 °C), previously associated to the degradation of **extractives,** has **disappeared**.

Additionally, the **two sharp peaks**, observed in the untreated BSG degradation profile, corresponding to **hemicellulose and cellulose**, **merged into a single sharp peak.** This peak is likely associated to the degradation during the alkaline treatment of **weakly bound hemicellulose**, probably the less integrated to the cellulose network.

Moreover, this **main degradation peak** observed for treated BSG is **slightly shift towards lower temperatures**. This observation suggests that **alkali treatment** could have partially **degraded cellulose chains**. This is consistent with the findings of other studies [182,300].

For all **sample treated at room temperature**, **the merged degradation peak** is **as large as the two sharp peaks** of untreated BSG suggesting that **hemicellulose is still present**.

Finally, for all the **samples treated at room temperature**, the **2nd shoulder** less predominant in BSGconv is **increased**. This is due to the **relative increase of the lignin** as hemicellulose is progressively removed, increasing the proportional contribution of lignin in the degradation profile.

At the treatments conducted at **70 °C**, a **similar trend** as with room temperature is observed. The **disappearance of the first shoulder** confirms that the **extractives** and **probably proteins** were successfully removed. Moreover, the **merging of the two sharp peaks into a single one** is again observed, indicated that hemicellulose degradation overlaps with early cellulose degradation. These results suggest that **1 hour of alkaline treatment at 70 °C is as effective as 8 hours at room temperature** in removing the less stable components of BSG.

Finally, the **most effective treatment condition** in order to clean and degum the fibers was observed at **4h at 70 °C.** In this sample, **the main peak is shifted toward higher temperatures,** suggesting that most of the **hemicellulose has been removed**, and only the **more stable cellulose remains**. However, according to Wang *et al.*, no extraction method such as alkali treatment have been reported to extract all hemicellulose polysaccharides from biomass, because hemicellulose is prone to decompose [158]. Thus, this could explain the fact that the peak start at lower temperatures. Moreover, it is the only condition where the **second shoulder**, corresponding to the presence of the lignin, disappeared. This suggests that lignin content has been significantly reduced, highlighting the effectiveness of the treatment

Overall, the **4-hour treatment at 70 °C** results in a more thermally **stable and purified BSG**, characterized by the removal of extractives, hemicellulose, and lignin leaving a **cellulose-rich structure**.

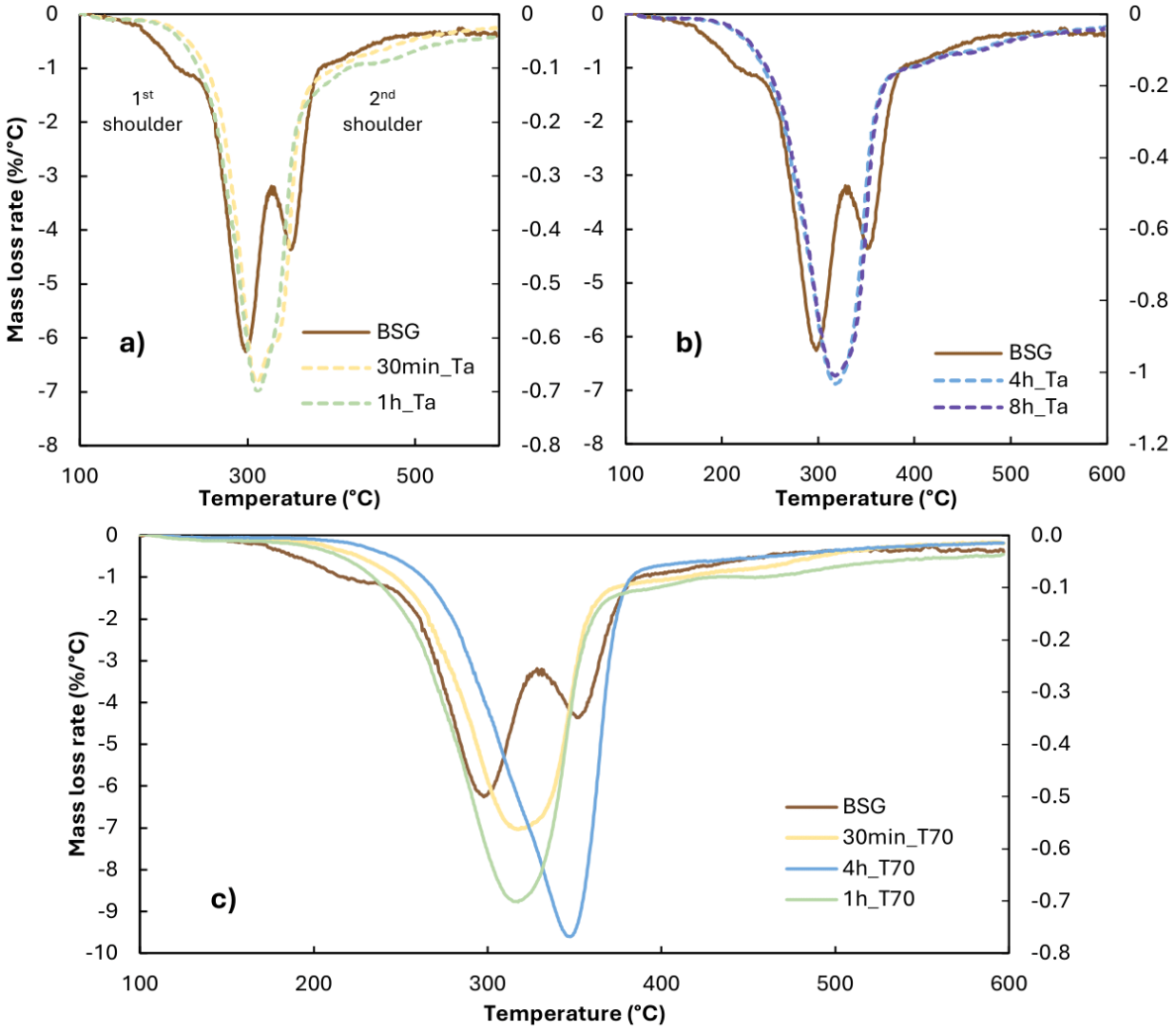


*Figure 6.5: Derivative thermogravimetric curves of untreated and treated BSG at ambiant temperature (a) 30min and 1h and b) 4h and 8h) and at 70 °C (c). Average of three experiments.*

Let's turn to the evaluation of the effect of the treatment on the morphology of the particles.

## 2.4. Effect of the treatment on BSG particles' aspect

**SEM** was performed to examine the effect of the **alkaline treatment conditions** on the **surface morphology and aspect ratio of BSG** particles. As shown in Figure 6.7, the morphological changes vary depending on the **treatment duration** and **temperature**.

To provide an initial comparison, the morphology of raw, untreated, and alkali-treated BSG was investigated before focusing on the effect of alkali treatment on ground particles. Hence, Figure 6.6 displays SEM images of (a) Untreated BSG before grinding, (b) Untreated BSG after

grinding, (c) Alkali-treated (4h-70°C) BSG before grinding, and (d) alkali-treated (4h-70°C) BSG after grinding.

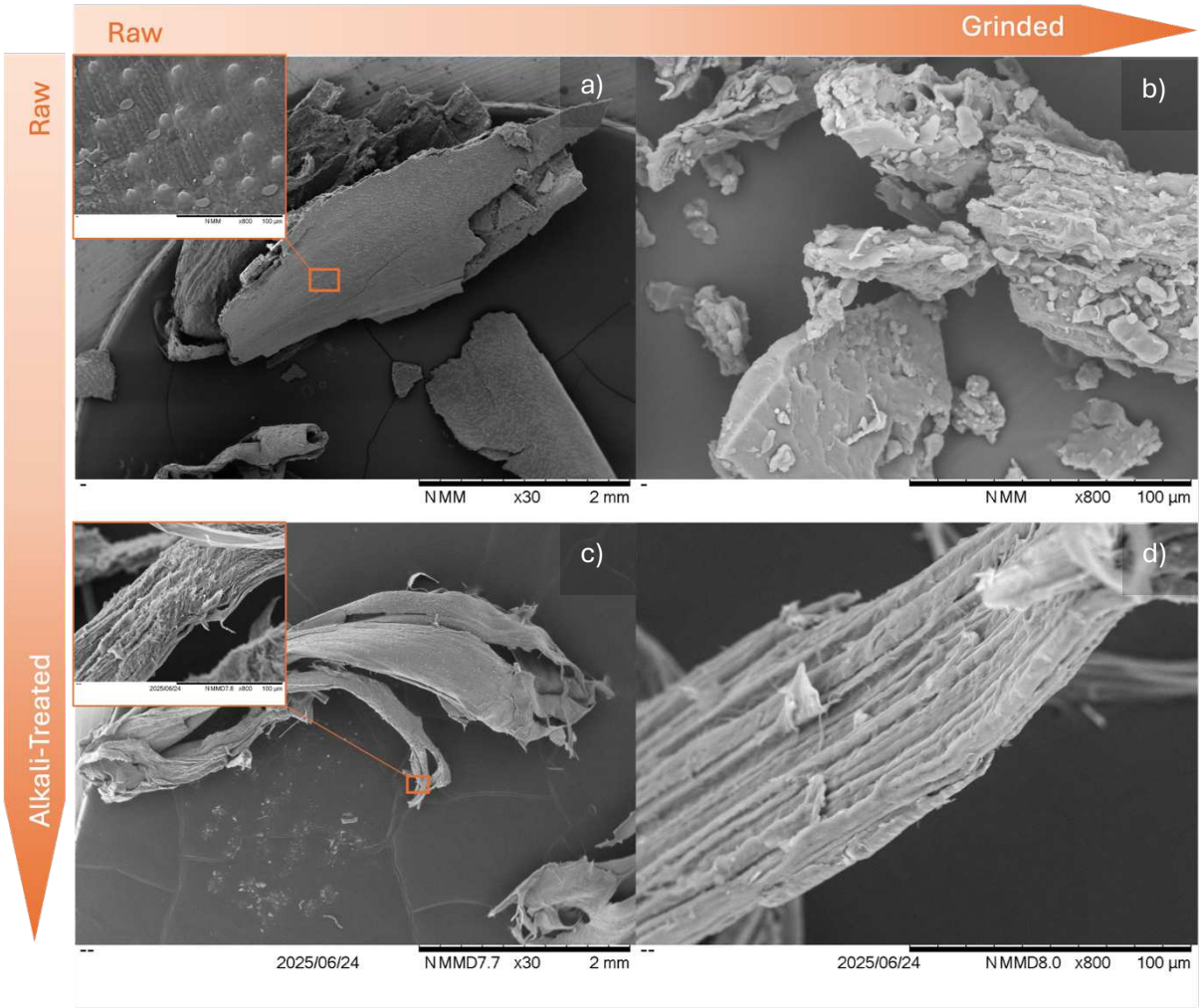


*Figure 6.6: SEM images of (a) Raw BSG before grinding x30 and x800, (b) Untreated BSG after grinding x800, (c) Alkali-treated (4 h-70 °C) BSG before grinding x30 and x800, and (d) alkali-treated (4 h-70 °C) BSG after grinding x800*

In the SEM images of raw, unground BSG (Figure 6.6a), the particles exhibit **smooth and compact** surfaces, with no evidence of defibrillation or fine particles on the surface. After grinding, untreated BSG (Figure 6.6b) displays particles with low aspect ratio whose surfaces are partially covered with small agglomerates. Beneath these fine particles, the bigger particles surface remains comparatively smooth, indicating that grinding alone does not significantly modify the surface morphology.

In contrast, alkali treated BSG prior to grinding (Figure 6.6c) shows a markedly different morphology, the surfaces show clear **striations** and exposed fibrous structures which is consistent with the removal of binding components such as hemicellulose and lignin during

alkaline treatment. It is possible to observe partial **defibrillation**. Such morphology has also been observed by Mussatto *et al.* on BSG treated with soda (2 %, 120 °C, 30 min) [187].

Following grinding of the alkali-treated BSG Figure 6.6d), the particles keep the **rough** and **striated** surfaces, suggesting that the morphological changes induced by alkali treatment are not eliminated by the following grinding step. Moreover, the treated and ground particles exhibit an increased aspect ratio compared to the ground untreated ones.

As BSG will be incorporated into composites in its ground form, the following observations focus on the morphology of ground particles after the different alkali treatments.

On Figure 6.7, at **30 min of alkali treatment and room temperature**, the particles surfaces appear **slightly altered**, with visible **striations** and a **rougher texture** attributed to the partial degradation of the surface components. In contrast, for the same treatment duration at **70 °C**, more pronounced changes are observed. Early **signs of bundles degumming** are observed with **cellulose bundles beginning to detach** (highlighted in red in Figure 6.7). A **similar degree of degradation** at room temperature is only observed **after 4 hours** of alkaline treatment, confirming the more **aggressive** effect of NaOH under higher temperature.

Compared to the untreated BSG particles, **minimal agglomeration** is observed at the surface of the treated particles. One hypothesis is that **very small particles**, which typically contributes to the agglomeration at the surface, **were removed** during the filtration step following alkaline treatment. However, since **milling step** is done **after** treatment, this explanation is less likely. Moreover, Figure 6.6 shows no visible agglomeration at the surface of BSG before grinding. Another reason could be that the **removal of extractives with polar functional groups** could **reduce the electrostatic interactions** between particles. Additionally, **alkaline treatment altering the internal structure** of BGS could lead to a **different fracture pattern** during milling. Therefore, this could result in **the formation of fewer fine particles**, thereby contributing to the **reduction of agglomeration** at particles surface.

The most pronounced changes are seen after **4 hours at 70 °C**. In this case, particles appear **highly damaged** with a clear **separation** of the cellulose bundles. The removal of hemicellulose and lignin, which act as **binding agents** [143,144], results in **less packed fibers**. This observation further supports our previous hypothesis presented in Chapter 4, that **needle-like BSG particles are cellulose rich**.

Finally, we initially considered the possibility that **treating raw BSG prior to milling** might **negate** the treatment's impact on particle surface morphology. However, the **SEM images**

clearly showed that the **surface modifications** are preserved, thereby confirming the effectiveness of the treatment.

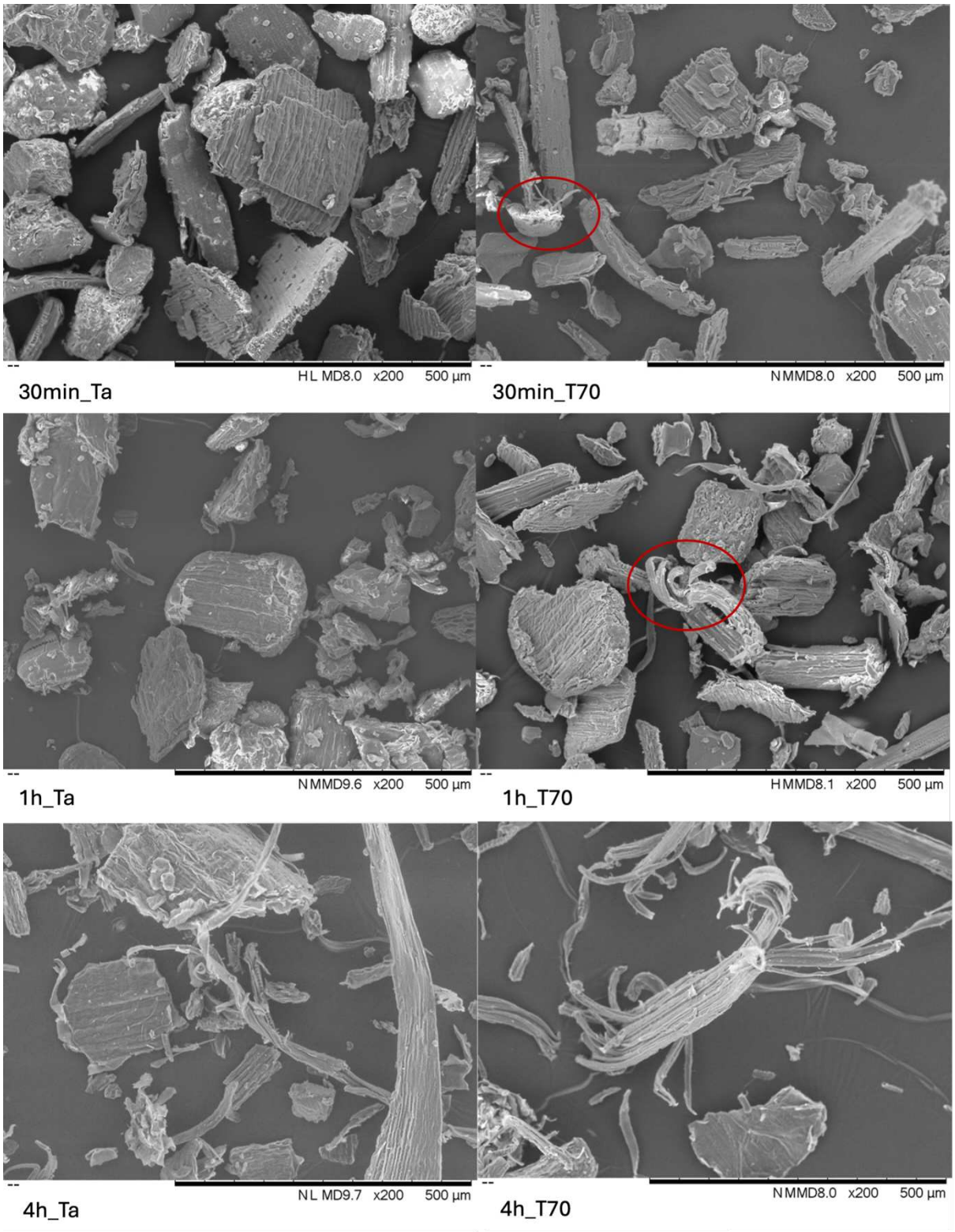


*Figure 6.7: SEM images of treated BSG particles at two temperatures (room temperature and 70 °C and three different times (30 min, 1h and 4h) after grinding x200*

As highlighted earlier, **chemical treatments** are used to modify filler **surface morphology** to create **rougher surfaces and sites for interactions.**

To gain insight into these morphological changes, Figure 6.8 gathers **SEM images at lower magnifications** for three selected samples: **BSGconv**, of BSG after the mildest treatment (**30 min at room temperature**) and after the most aggressive treatment (**4 h at 70 °C**).

In the case of **BGSconv**, the particles exhibit mostly **rounded shapes** and a **broad particle size distribution** which we discussed in Chapter 4. **Numerous fine particles** are visible and often agglomerating at the surface of bigger particles.

For the **mild treatment** at room temperature (30 min), particles remain predominantly rounded, and **few fine particles**.

In contrast, BSG treated at **70 °C for 4 hours** exhibits a significantly higher aspect ratio, characterized by very elongated **fiber-like particles** and extensive of **defibrillations of the bundles**. This morphology is consistent with a more advanced removal of the hemicellulose and lignin, which normally bind the cellulose fibrils. Moreover, the **few fine particles** observed seem also elongated, this suggests a possible change in the **fracture pattern** possibly related to the chemical composition of the particles.

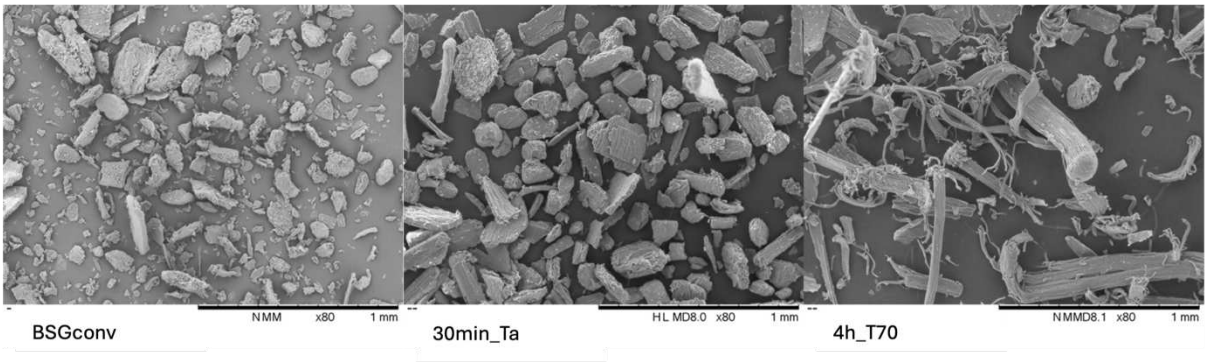


*Figure 6.8: SEM images of BSG conv and treated BSG particles at two temperatures (room temperature and 70 °C and two times 30min and 4h after milling x80*

Together these changes support the conclusion that alkaline treatment of BSG under the most severe conditions we evaluated is effective for producing cellulose-rich particles with high aspect ratio which is favorable for mechanical properties of a composites.

### 2.5. Conclusion

To conclude, the alkaline treatment of BGS using 5 % NaOH solution led to significant modifications in its chemical composition, thermal behavior, and morphological structure. As confirmed by FTIR analysis, the progressive removal of non-cellulosic components (hemicellulose and lignin but also probably pectins) was achieved by increasing treatment time and temperature. The reduction of lignin and hemicellulose absorption bands of FTIR, especially under the most severe conditions (4 h, 70 °C) indicates significant modifications of the lignocellulosic material. This observation was supported by TGA with the formation of one main degradation peak likely indicating the presence of a limited number of components. The progressive removal of non-cellulosic components has also been observed in SEM. Treated BSG exhibit rougher surface, partial defibrillation, and higher aspect ratio as seen in literature. In some areas, bundles of cellulose appear which likely increase the potential for mechanical interlocking with the polymer matrix. Such morphological changes along with removal of hydrophilic components improve the reactivity of fibers toward polymer matrix. These changes are expected to enhance interfacial adhesion through a combination of mechanical interlocking due to higher aspect ratio a rougher surface and physico-chemical interactions.

Therefore, the alkaline treatment condition of **4 hours at 70 °C** was selected for composites processing as it produced a suitable filler for reinforcing application.

## 3. Composites manufacture

### 3.1. Introduction

The incorporation of natural fillers such as BSG into thermoplastic matrices like PLA and PP represents a promising approach toward developing more sustainable composite and valorizing lignocellulosic by-product. However, these fillers face well-known limitations, especially the poor adhesion with hydrophobic matrices. This issue of weak interfacial bonding has been a recurring observation throughout this PhD work and is widely reported in the literature.

To address this, in this part BSG treated for 4 h at 70 °C with 5 % NaOH solution was mixed with PP and PLA at 10 and 30 %(m/m) using internal mixing. From this point forward, **treated BSG using these conditions** will be referred to as **BSGNaOH**. Accordingly, composites with **10 %(m/m) of BSGNaOH** will be named as **PLA90BGSNaOH** and **PP90BSGNaOH**, while those with **30 %(m/m) BSGNaOH** will be referred to as **PLA70BSGNaOH** and **PP70BSGNaOH**. The effect of alkaline treatment of BSG on these composites' mechanical, physical, thermal and morphological properties are evaluated.

### 3.2. BSG density

The removal of low-density components such as lignin and hemicellulose is likely to result in an increase in the density of the BSG [301]. Since the composites are formulated based on mass ratios until now, it is important to determine the **new density of BSGNaOH.** This allows for more **meaningful comparison** based on the **volume ratio of BSG** in the composites, which is in some cases more relevant, as composite properties are often strongly influenced by the **volume occupied by the filler** rather than the mass.

A visual comparison of **BSGNaOH** and **BSGconv,** as seen in Figure 6.9, highlights the impact of the alkaline treatment and milling on the **macroscopic aspect ratio** and **bulk density** of the particles. After treatment **BSGNaOH** appears significantly **fluffier** and more **voluminous**, suggesting a less dense, more fibrous structure. In contrast, **BSGconv** particles are more **densely packed**, with a compact appearance. These visual differences reveal the structural changes induced by the removal of lignin and hemicellulose. Moreover, lignin is a colored compounds of natural fibers [302], hence its removal results in a lighter color of treated BSG. After soda pulping process of BSG (2 %, 120 °C, 90 min), Mussatto *et al*. obtained a material with very similar appearance and color. Their BSG was highly discolored due to the high lignin removal of 90.2 %(m/m) [187].




*Figure 6.9: Visual comparison of ground BSG after alkaline treatment (4h-70°C) and BSGconv*

The results of **bulk density**, **true density**, and **maximum packing fraction** are reported in Table 6.2. As expected, **BSGNaOH** exhibits a much **lower bulk density** (0.230 ± 0.001 g/cm$^3$) compared to **BSGconv** (0.540 ± 0.016 g/cm$^3$), confirming the **fluffier and more expanded structure** observed visually in Figure 6.9: Visual comparison of ground BSG after alkaline treatment (4h-70°C) and BSGconv. However, the **true density** of BSGNaOH (1.592 ± 0.196 g/cm$^3$) is **higher** than that of BSGconv (1.353 ± 0.019 g/cm$^3$), which is consistent with

the **removal of lower-density components** such as lignin and hemicellulose. For comparison, the true density of lignin is reported between 1.350 and 1.500 g/cm$^3$ [303] while microcrystalline cellulose density ranges from 1.512 to 1.668 g/cm$^3$, depending on its crystallinity [304].

Our results are consistent with Naihabo *et al.*, who reported BSG bulk densities after grinding between **0.320 and 0.495 g/cm$^3$** and true densities from **1.318 to 1.392 g/cm$^3$**, depending on brewery origin [295].

Interestingly, the **maximum packing fraction** of BSGconv (0.399 ± 0.013), calculated using Equation 1.3 (in Chapter 3), is **significantly higher** than that of BSGNaOH (0.145 ± 0.018), suggesting that **although treated BSG has a higher true density, its fluffy and irregular structure reduces its ability to pack efficiently**. This is consistent with the visual observation of treated BSG appearing more expanded and less compact, likely due to fibrillation and the opening of bundles during treatment visible in SEM images. Moreover, experimental data have demonstrated that the maximum packing fraction decreases as aspect ratio of the filler increases [305,306].

*Table 6.2: Bulk and true densities of BSGNaOH and BSGconv with their calculated maximum packing fraction. Different letters mean statistical differences.*

| Sample | Bulk density (g/cm$^3$) | True density (g/cm$^3$) | Max pack fraction |
|---|---|---|---|
| **BSGNaOH** | **0.230**$^a$ ± 0.001 | **1.592**$^a$ ± 0.196 | **0.145** ± 0.018 |
| **BSGconv** | **0.540**$^b$ ± 0.016 | **1.353**$^a$ ± 0.019 | **0.399** ± 0.013 |

This changes in BSG density will affect the volume of BSG that we introduce in the composite materials. Thereby, the corresponding volume ratios have been calculated and summarized in Table 2.9 of Chapter 2.

### 3.3. Effect of the treatment on composites thermal stability

In Chapter 3, it was observed that BSG exhibited a **protective effect on PP** and a **catalytic effect on PLA** thermal degradation. This behavior was attributed to the relative thermal degradation temperatures: **PLA** degrades around **366.4 °C** which is close to the thermal degradation ranges of **hemicellulose** and **cellulose** (**297.6 °C** and **347.1 °C**, respectively). The degradation of **volatile products of BSG** could **interact** with PLA molecules, thereby triggering and enhancing PLA degradation and **shifting its degradation peak** towards lower temperatures. In contrast, **PP** degrades at a significantly higher temperature (**444.5 °C**) which is far beyond the decomposition of lignocellulosic products (except for lignin which degrades over a broad range

of temperatures). As a result, the **char layer** formed from BSG before PP degradation temperature could serve as **protective barrier** surrounding PP matrix and delaying PP degradation.

Thermogravimetric profiles of PP and PLA composites made with BSGNaOH and BSGconv are shown in Figure 6.10. On this figure, we can observe that the trends of Chapter 3 not only remain but are exacerbated with the addition of treated BSG. The peak values are displayed in Table 6.3.

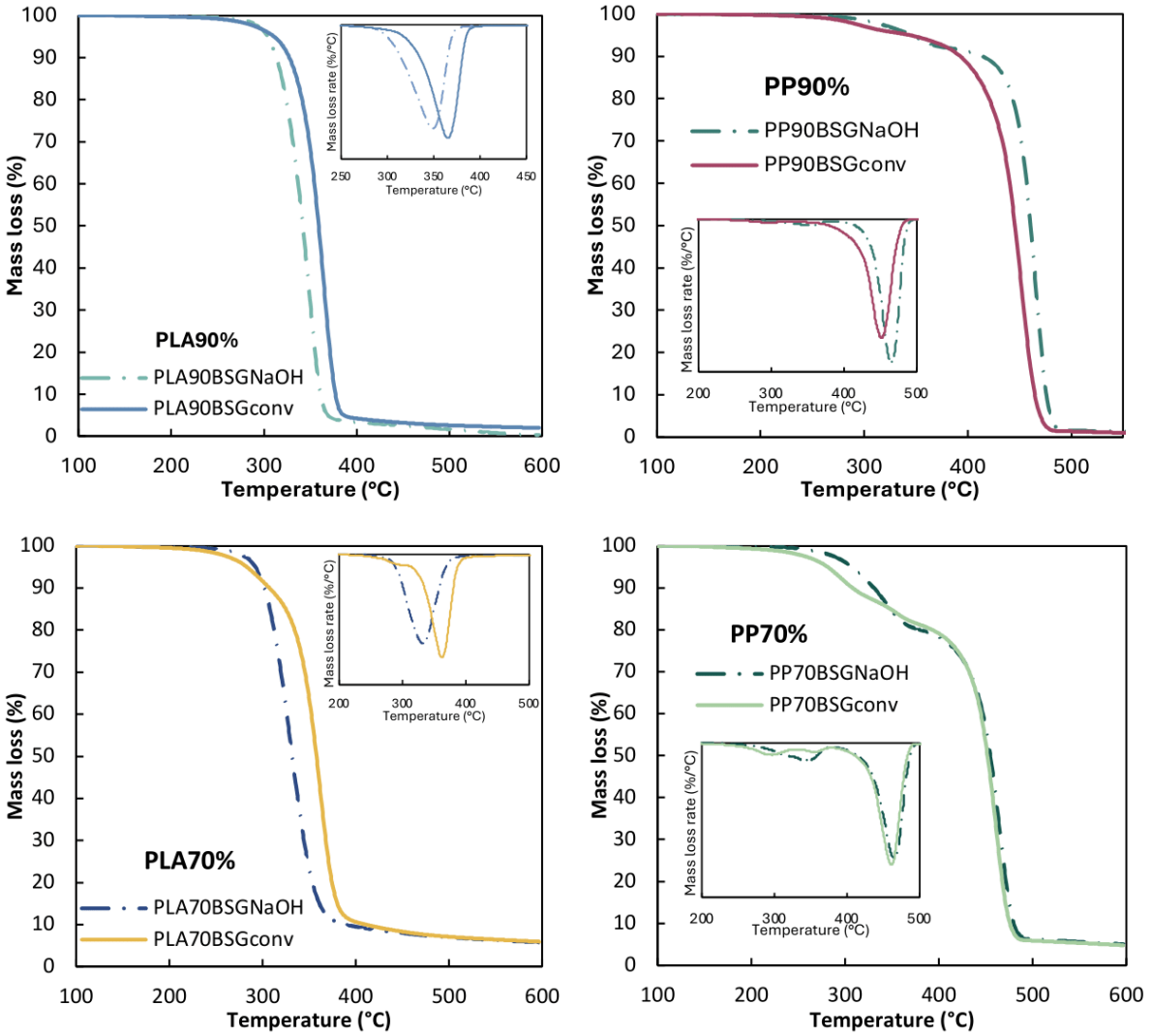


*Figure 6.10: Thermogravimetric analysis of PP and PLA biocomposites made with 10 %(m/m) and 30 %(m/m) of traited BSG and BSGconv. TG and DTG curves. Average of three experiments for TG curves and most representative of the three samples for DTG curves.*

PLA degradation peak is shifted to lower temperatures for both formulations including BSGNaOH. As for BSGconv, BSGNaOH seems to catalyse the degradation of PLA. This **catalytic effect of lignocellulosic biomass on PLA** can be explained by considering the degradation

pathways of both materials. As observed previously, the degradation of BSGNaOH extends from **270 °C to 380 °C** which suggests the presence of some remaining hemicellulose components along with cellulose. In their review article, Wang *et al.* showed that the pyrolysis of lignocellulosic biomass produces a wide range of low-molecular weight compounds, such as acetic acid, furans, aldehydes and other oxygenated volatiles [158]. Moreover, some of these products such as **acetic acid, phenolic compounds, or aldehydes** are typically released in the ~350 °C area [307], overlapping with the degradation window of PLA. On the other side, Li *et al.* highlighted that PLA is particularly sensitive to **acid- or alcohol-catalysed hydrolysis and transesterification reactions**, which initiate **depolymerization** by cleaving the ester backbone [308]. Consequently, in PLA composites, the volatiles emitted by BSG during heating can accelerate PLA degradation through **acid-catalyzed chain scission**, reducing its thermal stability. Moreover, some **residual $Na^+$** from the alkaline treatment might remain and could **catalyse the reactions of both lignocellulosic biomass and PLA** [158,308].

**In contrast** to PLA**, PP** shows a **more delayed degradation peak** in the formulation with **10 %(m/m) of BSGNaOH** compared to the one with BSGconv, suggesting an improved thermal barrier. However, this **delay is not observed for the formulation with 30 %(m/m) of BSGNaOH** where the degradation peak of PP remains statistically similar to the one of BSGconv composite. This suggests that protective effect of BSG char is not linearly proportional to the BSG content in the case of BSGNaOH.

*Table 6.3: Temperatures reached at maximum degradation rates for biocomposites made with 30 %(m/m) and 10 %(m/m) of alkali-treated BSG 70 %(m/m) and 90 %(m/m) of PP or PLA. The values represent the mean of triplicate measurements, with standard deviations indicated. Different letters indicate statistically significant differences*.*

| Samples | Peak 3 (°C)* |
|---|---|
| PP90BSGNaOH | **466.3**[a] ± 0.7 |
| PP90BSGconv | **452.5**[b] ± 3.2 |
| PP70BSGNaOH | **464.8**[a] ± 3.0 |
| PP70BSGconv | **460.7**[a] ± 3.2 |
| PP | **444.5** ± 10.2 |
| PLA90BSGNaOH | **349.1**[a] ± 2.0 |
| PLA90BSGconv | **364.95**[b] ± 1.4 |
| PLA70BSGNaoH | **332.4**[a] ± 1.1 |
| PLA70BSGconv | **362.6**[b] ± 0.9 |
| PLA | **366.4** ± 1.8 |

From TGA results, it is evident that treated BSG interacts more with PLA than with PP suggesting improved compatibility during heating. Given its thermal behavior, it could be expected to see similar interactions in rheological behavior. Therefore, the following part of this chapter moves on to describe in greater detail the rheological behavior of treated BSG composites.

### 3.4. Effect of the treatment on composites rheological behavior

As discussed in Chapter 3, the **volume fraction** of the filler, and more particularly, its **maximum packing fraction**, plays crucial role in understanding the **rheological behavior** of the composites. Additionally, the **aspect ratio of the particles** is a very important parameter, as higher aspect ratio leads to an increase of the **effective volume fraction**. As a result, the **friction** between particle and particle-polymer increases, which increases the **energy dissipation**, and consequently **higher melt viscosity and modulus** are observed.

Furthermore, a **rough surface**, as discussed previously, can promote **mechanical interlocking** between particle and matrix but also between particles which thereby increases the friction, contributing to the same rheological effect with more energy dissipation and higher melt viscosity and modulus. Finally, it is important to note that a **lower maximum packing** fraction leads to a consequent **decrease of the percolation threshold** [202].

To better understand the impact of the **increased aspect ratio** of **BSGNaOH** particles and the interactions occurring between **BSGNaOH** and the polymer chains in our biocomposites, we examined their **storage modulus** (*G'*) and **complex viscosity (**$|\boldsymbol{\mu}^*|$**)** in the molten state.

Figure 6.11 presents the evolution of ***G', G"*** and $|\boldsymbol{\mu}^*|$ with angular frequency ($\omega$) for **PP and PLA based composites** filled with either **BSGconv** or **BSGNaOH**, at two filler contents (10 %(m/m) and 30 %(m/m)).

What is striking is that incorporating **30 %(m/m) of BSGNaOH** resulted **in significant increase in both storage modulus** and **complex viscosity** in both polymer systems. The complex viscosity curves showed markedly different shape, with the **disappearance** of the Newtonian plateau **at low frequencies**. Such behavior indicates molten composites system **reaching the percolation threshold**, as discussed in Chapter 3.

This behavior aligns with our expectations, as the **maximum packing fraction** for BSGNaOH (**0.145**) is exceeded in the **PP70BSGNaOH** (**0.195**) and **PLA70BSGNaOH** (**0.250**) composites. In Chapter 3, PP70BSGconv and PLA70BSGconv remained below the maximum packing fraction.

These results strongly support the idea that the **aspect ratio** and **morphological characteristics** of the fibers are important **drivers** of the rheological behavior, particularly in increasing the **effective volume fraction** as discussed previously.

Composites containing **10 %(m/m) BSGNaOH** exhibit a rheological behavior comparable to that of composites with **30 %(m/m) BSG conv** in their respective polymer system. This result is consistent with expectations, as the **maximum packing fraction** is again of great importance in the rheology of highly filled systems. Indeed, according to Rueda, this parameter appears in most mathematical models that attempt to predict the viscosity of highly filled systems in the form $\Phi/\Phi_m$ [309].

As discussed in Chapter 3, the volume fraction of the filler was identified as a key factor governing composite behavior. However, these new results clearly show that volume fraction alone is not sufficient to predict rheological response. Indeed, despite their similar rheological behavior **PP90BSGNaOH** and **PP70BSGconv** have different volume fractions (0.059 and 0.224, respectively). Therefore, the position of the composites system relative to its maximum packing fraction ($\Phi/\Phi_m$) must also be considered.

Applying the Rueda's analysis [309], we find that for **PP90BSGNaOH**, $\Phi/\Phi_m$ = **0.4**, while for **PP70BSGconv**, this ratio is about **0.56**. This variation may account for the minor differences observed in the complex viscosity curves, with PP90BSGNaOH showing slightly lower values.

Similarly, **PLA90BSGNaOH** yields $\Phi/\Phi_m$ **= 0.56** compared to **0.71** for **PLA70BSGconv**, this difference accounts for the little change in the storage modulus curves, where PLA70BSGconv begins to show a low-frequency plateau indicative of network formation or particles percolation, while **PLA90BSGNaOH** does not.

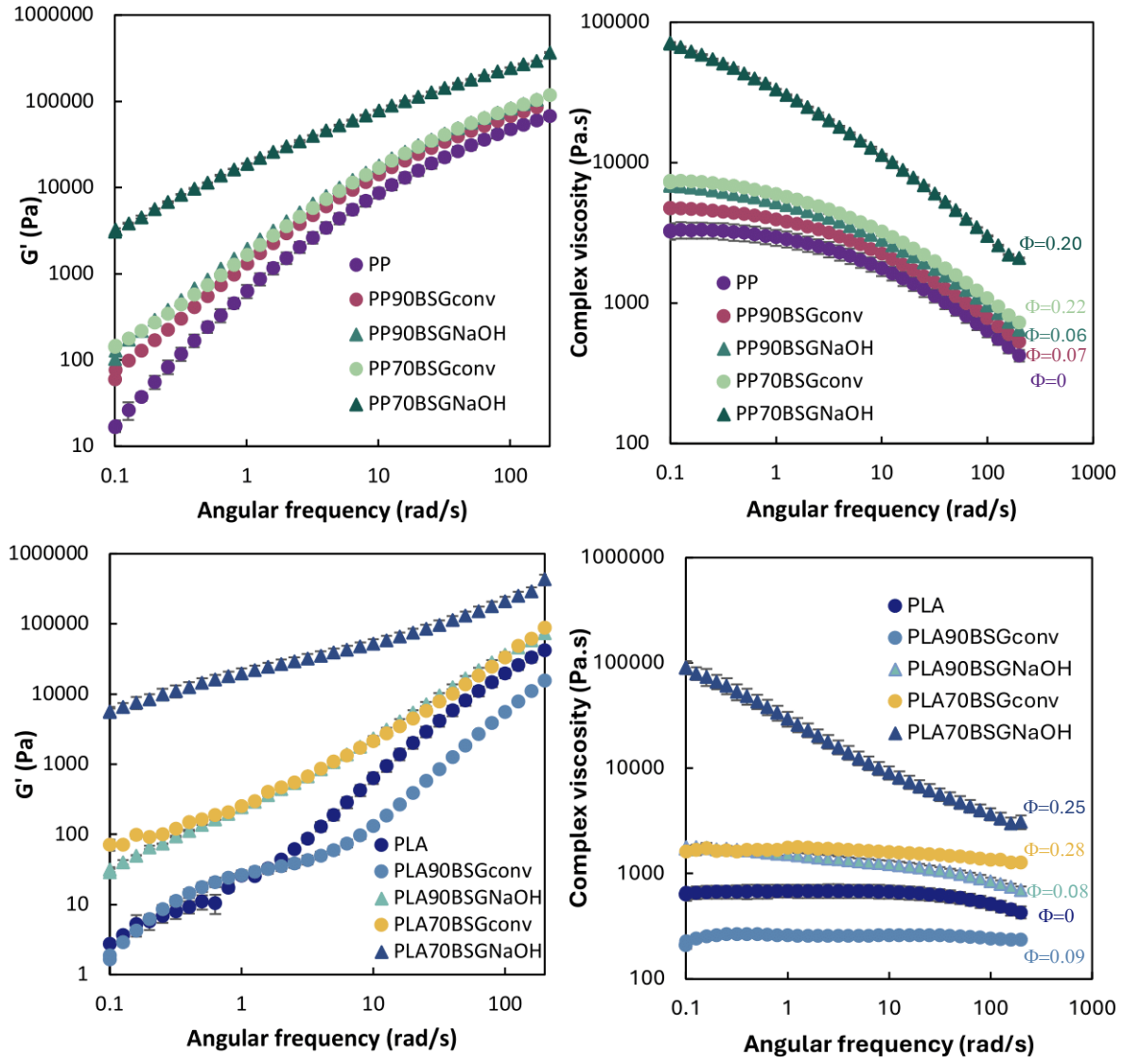


*Figure 6.11: Effect of BSG alkaline treatment on storage modulus (G') and complex viscosity vs angular frequency in plate rheometer at 180 °C for PLA and PP composites processed at 180 °C in internal mixer and injected at 180 °C and 200 °C respectively, = volume fraction of BSG, plate-plate gap = 2200 µm, plate diameter = 25 mm, strain = 10 % for PP, PP90BSGconv, PLA and PLA90BSGconv, and 0.05 % for composites with BSGNaOH and 30 % (m/m) BSG. Average of three experiments.*

The alkaline treatment strongly influences the degree of interactions occurring in the molten composite system as evidence by a global increase in the rheological moduli, a flattening of the *G'* curves, and the disappearance of the Newtonian plateau in complex viscosity. All of these traducing an increased number of interactions (filler-filler and filler-matrix) in the case of treated BSG compared to the untreated one. Moreover, BSGNaOH has a much stronger effect on PLA90BSGNaOH than on PP90BSGNaOH, and the response also differs from that of PP70BSGconv, despite an identical $\Phi/\Phi_m$ ratio (0.56). This more pronounced rheological impact in PLA90BSGNaOH aligns with the behavior observed in TGA.

These interactions and the hindering of BSG on the polymer chains might have some effect on the thermal transitions of our composites. Hence, DSC analysis was carried out on our samples to assess treated BSG effects on the thermal behavior of the composites.

### 3.5. Effect of the treatment on composites thermal transitions

**DSC analyses** were carried out to determine **characteristic temperatures** and obtain information on the effect of **BSG treatment** on the **microstructure** of the different formulations. Figure 6.12 shows the DSC curves of PP and PLA composites made with BSGconv and BSGNaOH.

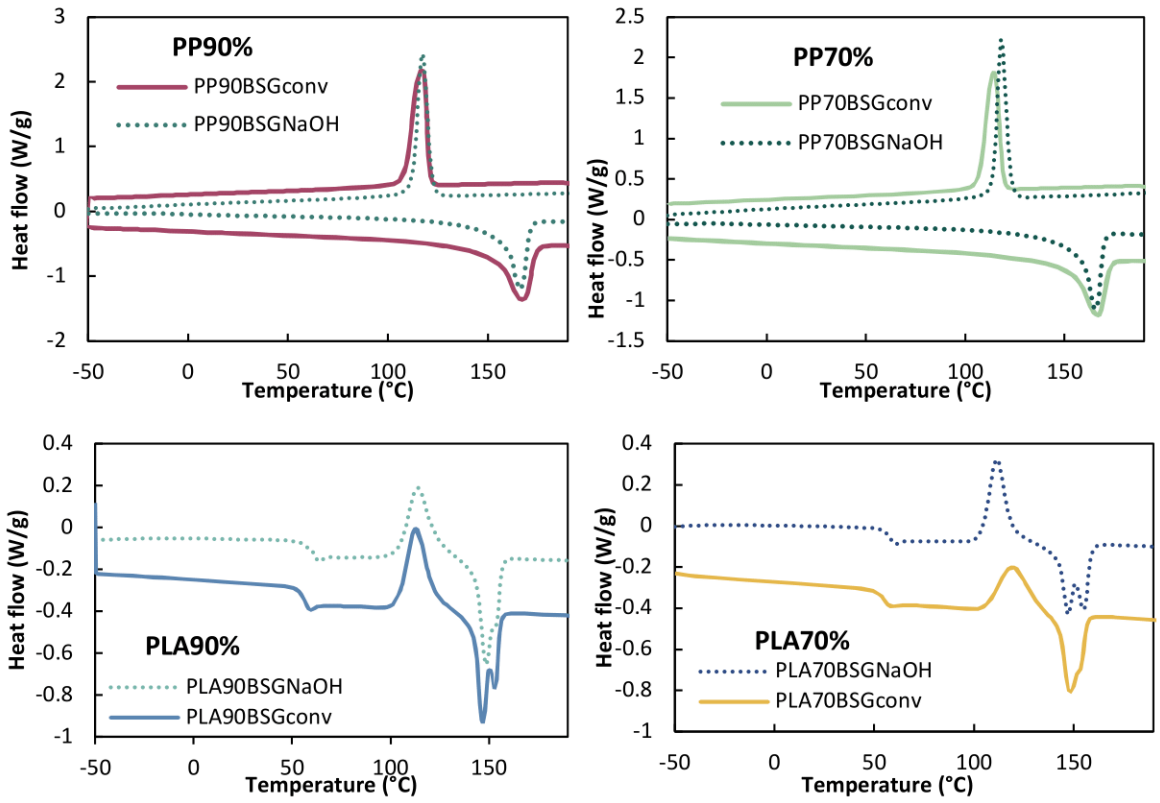


*Figure 6.12: DSC curves of injected PP, PLA composite with BSGconv and BSGNaOH (10 %(m/m) and 30 %(m/m)) at 10 K/min under nitrogen flow.*

Table 6.4 presents the results of measured $T_c$, $T_m$, $T_{cc}$, $T_g$ **and** $\chi_c$ for the **BSGconv** and **BSGNaOH** composites.

In Chapter 3, it was observed that **BSG tends to decrease the $T_c$ of PP composites**, thereby hindering the crystallization likely through a **physical hindrance effect** or a **thermal gradient** induced by the filler insulating the surrounding PP chains, as further discussed in Chapter 5.

However, in Figure 6.12, the addition of **BSGNaOH into PP composites** is found to **facilitate crystallization**, as indicated by the shift of crystallization peak towards higher temperatures. For instance, **PP70BSGNaOH** exhibits a $T_c$ **of 117.9 ± 0.4 °C**, compared to **114.7 ± 0.4 °C** for

**PP70BSGconv**. This observation could be attributed to the **rougher surface** and **higher aspect ratio** of BSGNaOH particles, which **increases the shear rates** at the interface during compounding as evidenced by rheological behavior where complex viscosity is significantly increased in the case of composites filler with treated BSG. As discussed in Chapter 5, increased shear rates can **promote crystallinity at the filler-matrix interface**, potentially propagating into the surrounding polymer matrix, thereby accelerating crystallization despite the filler volume hindrance.

Regarding melting temperature, although the comparison of $T_m$ **did not reach statistical significance**, the trend observed previously in Chapter 3, is maintained: increasing filler content has a slight **negative impact** on $\boldsymbol{T_m}$, with pure PP melting at ~167 °C, PP filled with 10 %(m/m) BSG (treated or untreated) around ~166 °C and PP filled with 30 %(m/m) BSG around 165.5 °C.

In Chapter 3, the $\boldsymbol{T_g}$ was found particularly **indicative of PLA chains length**. The incorporation of **BSGconv led a significant decrease of the** $\boldsymbol{T_g}$ of the composites, attributed to reduction of PLA chains length, which increased their mobility and, consequently, ductility. In contrast, as shown in Figure 6.12, the incorporation of **BSGNaOH does not appears to affect** $\boldsymbol{T_g}$ **of the composite**. This suggests that **BSGNaOH did not induce PLA chains scission**, compared to the untreated BSG. This difference can be attributed to the **removal of early-degrading components** during alkaline treatment, as evidence by the **TGA profiles**, also observed in the case of extruded BSG- PLA composites in Chapter 5. Indeed, removing these lightest compounds eliminates the likely source of PLA catalytic degradation during compounding.

The $\boldsymbol{T_{cc}}$ of PLA was previously found to reflect the dual response of the composite to the addition of BSG. On one hand, $\boldsymbol{T_{cc}}$ **was observed to be lowered due to increased PLA chains mobility** (due to chain scission); on the other hand, BSG could **physically hinders crystals propagation**, delaying $T_{cc}$. This double effect resulted in **a maximum** $\boldsymbol{T_{cc}}$ observed at **intermediate filler content**. In the present case, where **BSGNaOH does not seem to induce chain scission** (as suggested by $T_g$ stability), $T_{cc}$ is expected to be **primarily driven by physical hindrance**. However, **surface roughness and increased number of reactive sites** of BGSNaOH (resulting from the alkaline treatment) could promote crystals propagation, thereby having a competing effect.

As shown in

Table 6.4, **PLA90BSGNaOH** and **PLA90BSGconv** exhibit statistically **similar** $\boldsymbol{T_{cc}}$ values, though a slight increase is observed for PLA90BSGNaOH (**114.1 ± 0.4 °C**) compared to

PLA90BSGconv (**113.4 ± 0.3 °C**). Interestingly, at higher filler content, **PLABSGNaOH appears to crystallize at lower temperature than PLA90BSGconv**. This suggests that the rougher surface of BSGNaOH and the higher number of reactive sites may facilitate crystal propagation despite the higher filler content.

Finally, the **melting behavior of both PLA composites containing BGSNaOH presents a double melting peak**, although it is more overlapped in the case of **PLA90BSGNaOH**. This subtle distinction could reflect **difference in cold crystallization behavior**, reinforcing the previously discussed trend. The behavior observed for PLA70BSGNaOH aligns with previous hypothesis suggested in Chapter 3 that when $T_{cc}$ **> 120°C,** the two melting peaks tend to merge. Here **PLA70BSGNaOH** exhibits a $T_{cc}$ of **118°C** which remains below this threshold, resulting in **two melting peaks**.

In contrast, for **PLA90BSGNaOH**, the melting behavior suggests the formation of **predominantly more stable crystalline structures**, as evidenced by the dominance of the lower-temperature melting peak. This supports the idea that the **BSGNaOH particles** may have promoted **more uniform or stable crystal growth**.

*Table 6.4: DSC data of PP, PLA and their composites with BSGNaOH and BSGconv after internal mixing and laboratory injection molding. Different letters inidcate statistically significant differences between samples.*

| Sample code | $T_g$ (°C) | $T_{cc}$ (°C) | $T_c$ (°C) | $T_m$ (°C) | $\chi_c$ (%) |
|---|---|---|---|---|---|
| PP90BSGNaoH | - | - | **117.5**$^{a}$ ± 0.2 | **166.0**$^{a}$ ± 0.3 | **41.2**$^{a}$ ± 3.1 |
| PP90BSGconv | - | - | **117.5**$^{a}$ ± 0.4 | **166.2**$^{a}$ ± 1.0 | **42.8**$^{a}$ ± 0.7 |
| PP70BSGNaoH | - | - | **117.9**$^{a}$ ± 0.4 | **165.5**$^{a}$ ± 0.3 | **39.6**$^{a}$ ± 2.1 |
| PP70BSGconv | - | - | **114.7**$^{b}$ ± 0.4 | **165.6**$^{a}$ ± 1.0 | **40.9**$^{a}$ ± 2.4 |
| PP | - | - | **117.4** ± 0.5 | **167.0** ± 0.8 | **40.9** ± 1.1 |
| PLA90BSGNaOH | **61.1**$^{a}$ ± 1.0 | **114.1**$^{a}$ ± 0.4 | - | **149.0**$^{ab}$ ± 0.5 | ~0 |
| PLA90BSGconv | **57.3**$^{b}$ ± 0.3 | **113.4**$^{a}$ ± 0.3 | - | **147.3**$^{c}$ ± 0.5 | ~0 |
| PLA70BSGNaoH | **60.5**$^{a}$ ± 0.1 | **118.6**$^{b}$ ± 0.3 | - | **150.2**$^{a}$ ± 0.3 | ~0 |
| PLA70BSGconv | **55.5**$^{c}$ ± 0.1 | **120.5**$^{c}$ ± 0.3 | - | **148.5**$^{bc}$ ± 0.2 | ~0 |
| PLA | **59.9** ± 0.7 | **115.9** ± 0.9 | - | **150.2** ± 2.3 | 0.6 |

The section that follows explores the microstructure of the composites made with treated BSG.

### 3.6. Effect of the treatment on composites morphology

Examination of the **rupture facies** of both PLA and PP composites filled with BSGNaOH reveals insights into the interfacial adhesion between treated BSG particles and both matrices.

Figure 6.13 shows the SEM micrographs of the cryo-fractured surfaces of PP and PLA composites filled with BSGNaOH. In the low filled composites (PP90BSGNaOH and PLA90BSGNaOH), the compatibility appears improved with no evidence of voids at the interface of filler-matrix, suggesting improved adhesion when using treated BSG for both polymer matrix. At higher filler loading (PP7BSGNaOH and PLA70BSGNaOH), it is visible and especially of PLA that BSG loading is over the maximum packing fraction, it is possible to observe polymer clusters trapped within BSG filler network. In the case of PP, this effect is less evident, as the matrix seems to continuously surround BSGNaOH particles. However, filler-filler interactions between BSGNaOH particles are still observed due to high filler content.

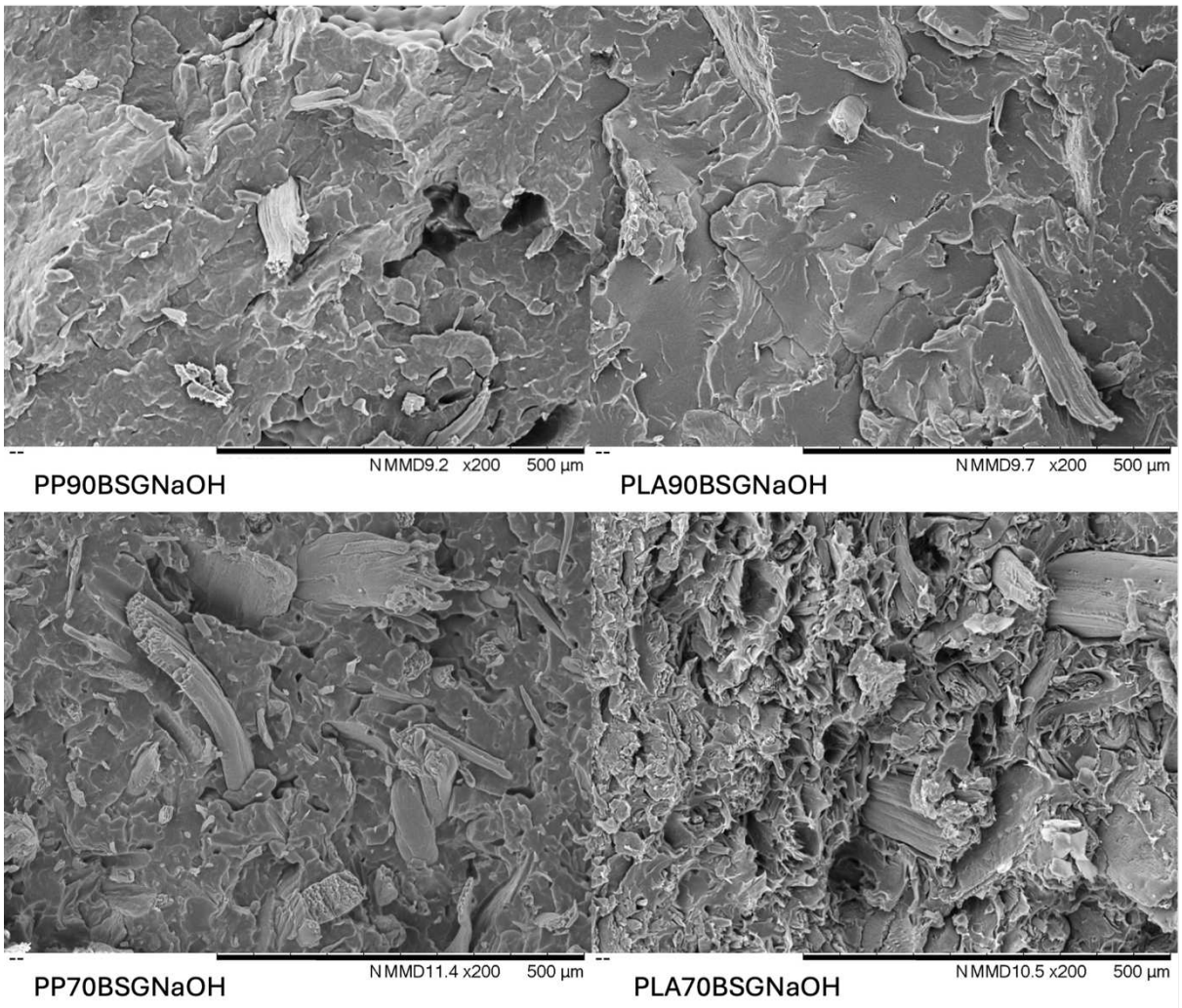


*Figure 6.13: SEM images of PP and PLA composites with BSGNaOH (internal mixing 180 °C, 50 rpm, 5 min + injection molding lab press 200 °C for PP and 180 °C for PLA), cryofractured surface, x200*

Figure 6.14 displays SEM micrographs of the tensile-fractured surfaces of PP90BSGNaOH, PLA90BSGNaOH, and PP70BSGNaOH. Unfortunately, tensile fractured surface of PLA70BSGNaOH could not be obtained because the injection of the tensile specimen was not technically feasible. These limitations are discussed in the following section.

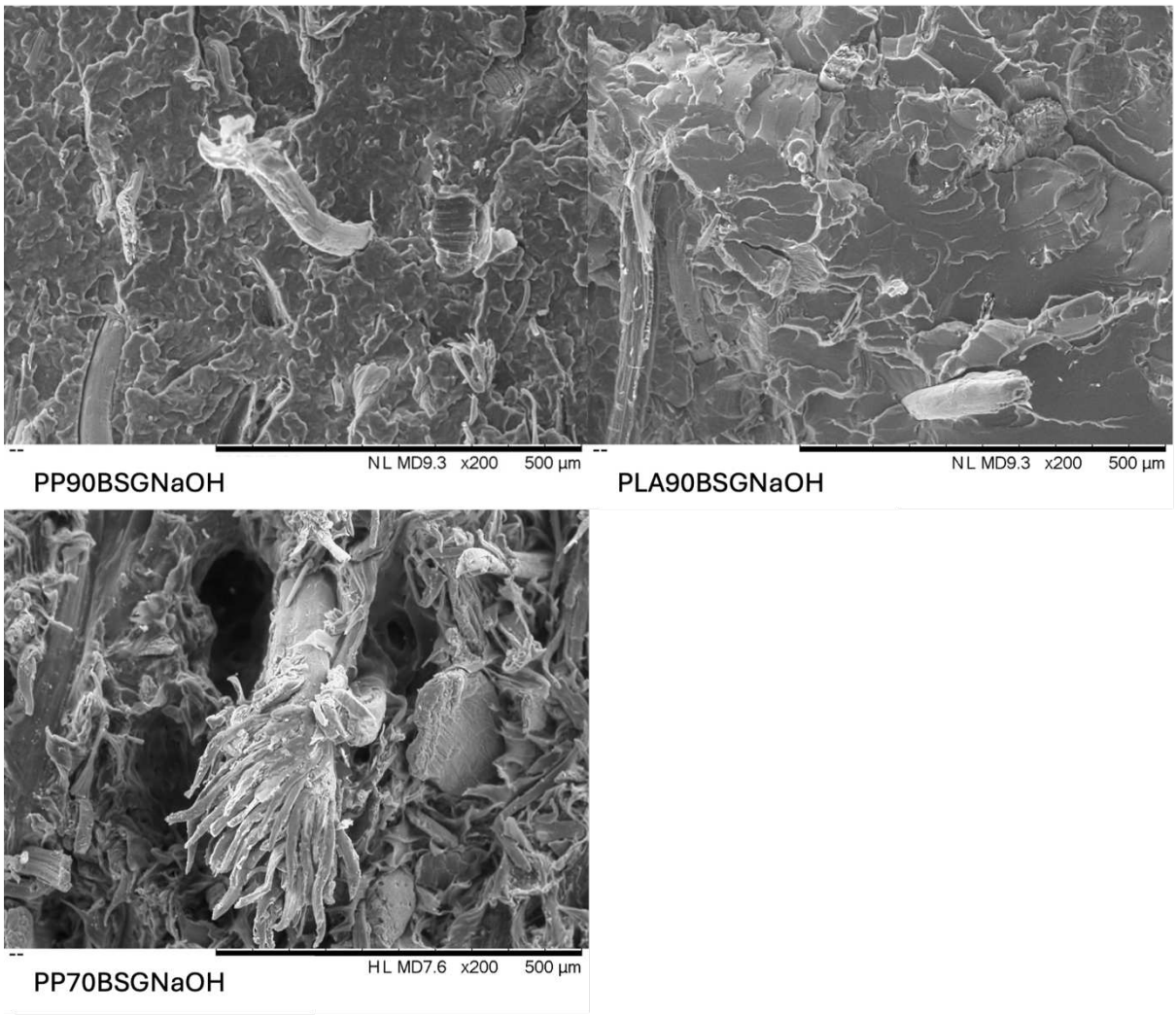


*Figure 6.14: SEM images of PP and PLA composites with BSGNaOH (internal mixing 180 °C, 50 rpm, 5 min + injection molding lab press 200 °C for PP and 180 °C for PLA), tensile fractured surface, except for PLA70BSGNaOH x200*

On Figure 6.14, both PP90BSGNaOH and PLA90BSGNaOH exhibit a **brittle fracture** with absence of stretching marks or ductile deformation marks. While this behavior is unusual for PP, it was also observed in Chapter 5 with samples shaped with laboratory press. In both composites, the BSGNaOH particles appear to be **well wetted by the matrices** with minimal voids at the interface, suggesting relatively good adhesion at low filler content.

In the case of **PP70BSGNaOH**, some fiber pull-out is visible, indicating that although the matrix still wets the treated BSG, interfacial bonding is sometime weaker, possibly due to the

very high filler volume content. This implies that even though the adhesion is better, having too many particles in contact could results in bad mechanical properties.

### 3.7. Effect of the treatment on composites tensile properties

Before discussing the mechanical properties of the composites, it is important to note that **PLA70BSGNaOH could not be injected using the laboratory press**. The composite exhibited **high flow hindrance**, mostly likely due to the high aspect ratio and the fact that it exceeded max packing fraction, which significantly increased melt viscosity and prevented from adequate flow under the tested injection conditions. This observation is supported by the rheological results, where PLA70BSGNaOH demonstrated a highly percolated structure and high resistance to flow.

Figure 6.15 and Figure 6.16 present the Young's modulus and max tensile strength, respectively, obtained for PP and PLA composites including treated or untreated BSG. Table 6.5 summarizes the Young's modulus and tensile strength at yield for PP and PLA composites with 10 %(m/m) and 30 %(m/m) filler content, comparing the performance of **alkali-treated BSG (BSGNaOH)** and **conventional BSG (BSGconv)**.

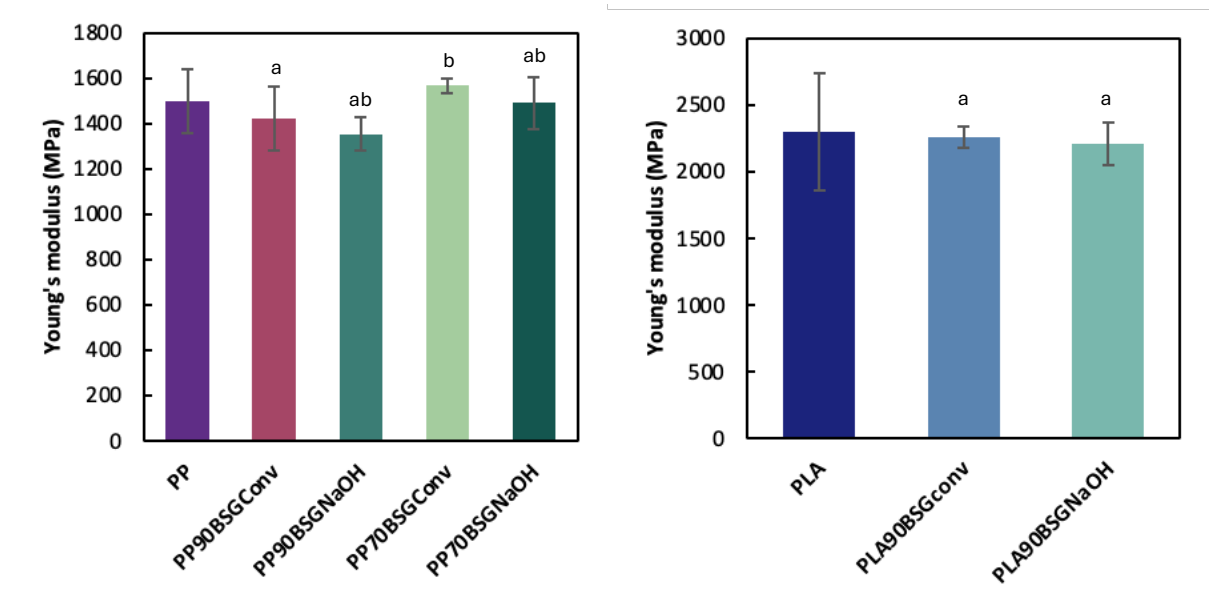


*Figure 6.15: Comparison of Young's modulus for PP and PLA composites with untreated and alkaline treated BGS. Average of at least 3 replicates at 2 mm/min.*

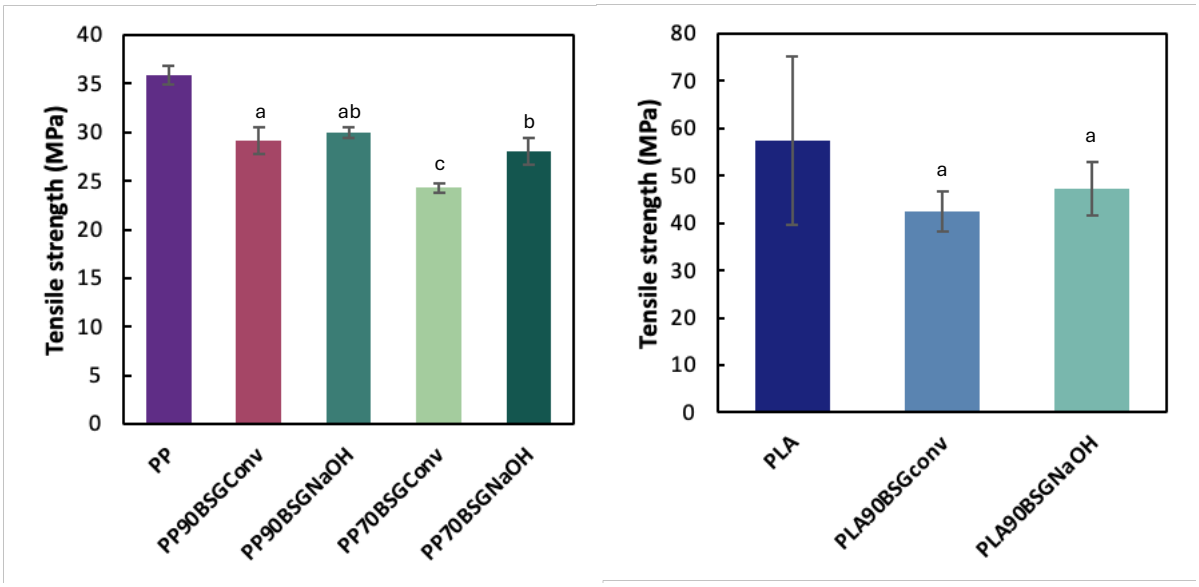


*Figure 6.16: Comparison of max tensile strength for PP and PLA composites with untreated and alkaline treated BGS. Average of at least 3 replicates. 2 mm/min.*

As observed in Chapter 3, Young's modulus of the composites is not significantly affected by the addition of BSG whether being treated or untreated. However, differences emerge when looking at ***TS***. At low filler content (10 %), PP composites show comparable *TS* values (30.0 ± 0.5 MPa for PP90BSGNaOH and 30.6 ± 3.6 MPa for PP90BSGconv). This similarity could be attributed to the **very low volume fraction** BSGNaOH (5.9 vol.%), which limits its reinforcing effect and contribution to stress transfer.

In contrast, at higher filler content, the impact of the alkaline treatment becomes more apparent. Indeed, **PP70BSGNaOH exhibits a higher *TS* than PP70BSGconv, 28.04 ± 1.2 MPa** compared to **24.3 ± 0.5 MPa**, respectively. These results suggest that **alkaline treatment improved interfacial adhesion** between BSG particles and the matrix as seen on SEM images, thereby enhancing mechanical performance.

For **PLA composites**, although the standard deviations are relatively high, there is a consistent trend toward improved tensile strength, when incorporating BSGNaOH into PLA matrix. Indeed, **PLA90BSGNaOH** exhibited a *TS* of **47.2 ± 4.7 MPa** compared to **42.4 ± 6.9 MPa** for **PLA90BSGconv**. This further support the idea that alkaline treatment enhances adhesion and promote better mechanical performances.

*Table 6.5: Mechanical tensile test results for PP and PP composites with untreated and alkaline treated BSG. Average of at least 3 replicates. 2 mm/min. Different letters indicate statistically significant differences (p-value < 0.05)*

| Sample code | Young's modulus (MPa) | Tensile strength at yield (MPa) |
|---|---|---|
| PP90BSGNaoH | **1351.9**[a] ± 65.3 | **30.0**[a] ± 0.5 |
| PP90BSGconv | **1421**[ab] ± 221 | **30.6**[ab] ± 3.6 |
| PP70BSGNaoH | **1490.6**[ab] ± 98.8 | **28.04**[b] ± 1.2 |
| PP70BSGconv | **1567**[b] ± 42 | **24.3**[c] ± 0.5 |
| PP | **1497** ± 140 | **35.75** ± 1.0 |
| PLA90BSGNaOH | **2208**[a] ± 131.4 | **47.2**[a] ± 4.5 |
| PLA90BSGconv | **2262**[a] ± 128 | **42.4**[a] ± 6.9 |
| PLA | **2301** ± 442 | **57.4** ± 17.8 |

Beyond mechanical performance, the durability and the application of composites is also strongly influenced by their interaction with water. Therefore, the water absorption behavior of the materials was investigated.

### 3.8. Effect of the treatment on composites water absorption behavior

Figure 6.17 displays the water absorption kinetics for **PP and PLA composites** filled with **BSGconv**, along with those filled with **10** and **30 %(m/m) of BSGNaOH**. After 21 days, the **total water uptake** for composites with BSGconv is **similar** to that of their counterparts with BSGNaOH. For instance, **PP70BSGconv** exhibited a water uptake of **3.79 ± 0.01 %(m/m)** compared to **4.01 ± 0.08 %(m/m)** for **PP70BSGNaOH**. Similarly, **PLA70BSGconv** had a water absorption of **11.88 ± 0.59 %(m/m)** compared to **10.40 ± 0.49 %(m/m)** for **PLA70BSGNaOH**.

Interestingly, the **water absorption in the first days** is higher for both composite containing **30 %(m/m) BSGNaOH**, despite their lower **volume content** compared to their BSGconv-composites counterparts (**PLA70BSGconv** and **PP70BSGconv**). This behavior could be explained by the fact that these composites **exceeded their maximum packing fraction** calculated for **BSGNaOH** (0.145), as previously discussed. In such cases, filler particles may not be sufficiently wetted by the polymer matrix, leaving them **directly exposed to water**, this has a particularly significant impact in the early stages of immersion. This mechanism was also observed in **composites filled with 50 %(m/m) of BSGconv** (Figure 3.22) which also exceeded their maximum packing fractions and exhibited similar water uptake behavior in the early stages of the experiment which suggests that physical interactions between fibers enhance the water diffusion through the composite.

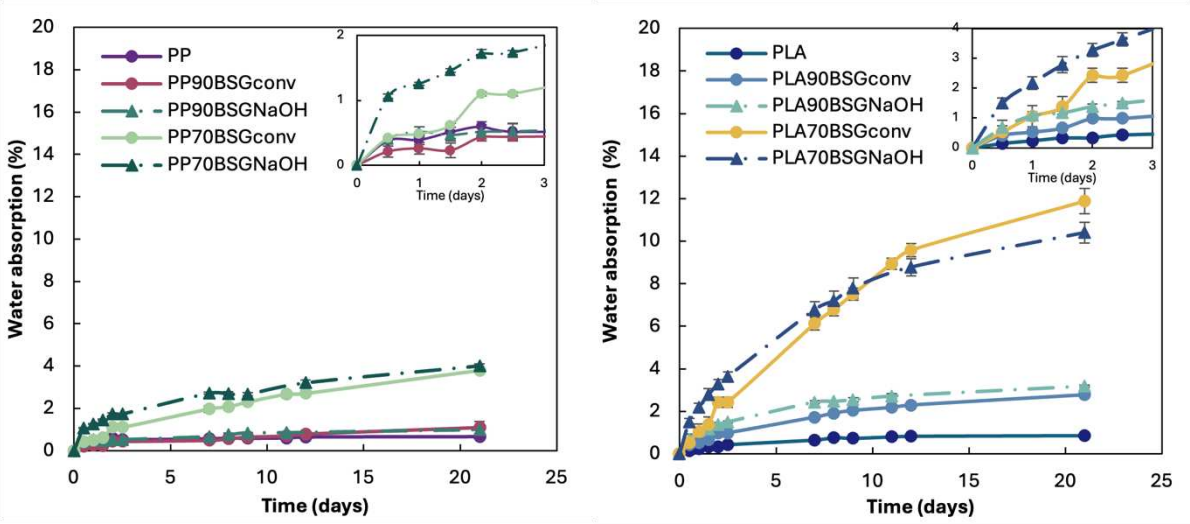


*Figure 6.17: Water absorption curves for PP and PLA composites with BSGconv and BSGNaOH drown in water at room temperature, means of duplicates.*

### 3.9. Conclusion on the composite manufacture with treated BSG

In this part, PLA and PP composites were prepared using the selected alkali treated BSG of the first part of this chapter. In this work, the composites were produced by internal mixing followed by laboratory injection molding. The experimental results revealed that the alkaline treatment significantly altered BGS morphology and chemical composition by removing lignin and part of the hemicellulose, which influenced the thermal properties of the matrix and enhanced interfacial adhesion as observed by SEM characterization. Notably, the enhanced adhesion resulted in higher tensile strength for composites including treated BSG. Moreover, this study highlighted the particular importance of **maximum packing fraction** and **particle aspect ratio** in driving rheological and water absorption properties of both PP and PLA systems. Indeed, while we knew to both mass and volume contents of BSG and could anticipate trends accordingly, it was the relative percentage of maximum packing fraction that proved most explicative of the composite behavior.

## 4. Conclusion

The aim of this chapter was to fill the gap caused by the lack of adhesion between BSG and both our matrices, and to enhance the potential of BSG as a reinforcing filler. Exploring different time and temperature conditions of alkaline treatments allowed us to successfully obtain BSG degummed BSG particles. Indeed, alkaline treatment conducted at 70 °C for 4 hours proved effective in modifying the morphology and composition of BSG by removing lignin and part of the hemicellulose as evidence in FTIR and TGA. This resulted in fibers with higher aspect ratio, rougher surfaces with visible separated bundles of cellulose.

Treated BSG under the most aggressive conditions was incorporated in PLA and PP matrices at 10 and 30 %(m/m) loadings. These modifications impacted a wide range of composites properties. It turned out that 30 %(m/m) was exceeded the maximum packing fraction for treated BSG which resulted in lower wetting of the fillers. Especially, incorporation of the treated BSG led to higher melt viscosity and storage modulus in the molten state, particularly at higher loadings, highlighting the critical influence of aspect ratio and $\Phi/\Phi_m$ ratio. This flow hindrance made impossible the injection of the PLA filler with 30 %(m/m) of treated BSG.

DSC showed that $T_g$ of composites with BSGNaOH was not affected compared to pure PLA whereas $T_g$ of composites with BSGconv was reduced. As literature says that $T_g$ is closely related to molecular weight [34], it suggests that alkaline treatment likely removed the compounds responsible for the chain scission in PLA during compounding. Mechanically, while Young's modulus remained mostly unaffected, tensile strength was slightly improved at higher BSGNaOH content confirming better matrix–filler adhesion. Additionally, SEM analysis supported these findings, showing fewer interfacial voids and stronger filler–matrix contact.

Figure 6.18 summarizes the main outcomes of this chapter.

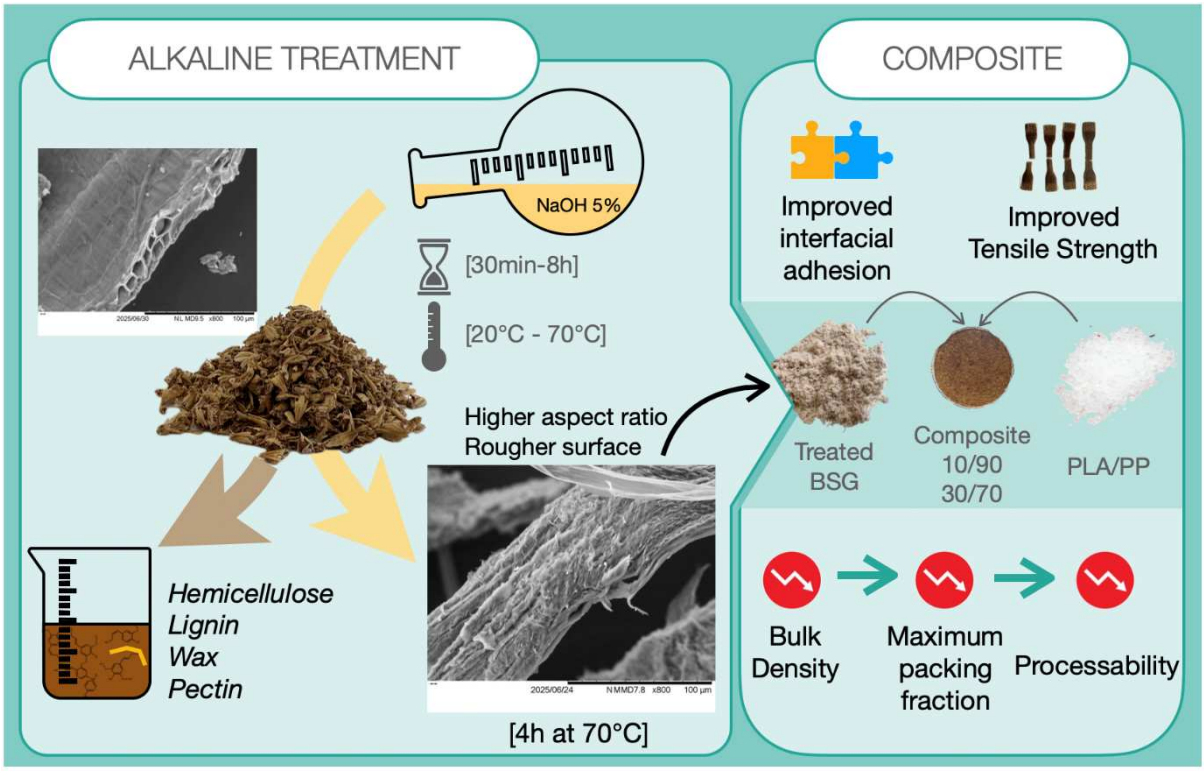


*Figure 6.18: Schematic overview of Chapter 6.*

In summary, alkaline treatment significantly enhanced the reinforcing potential of BSG by improving its compatibility and interaction with both PLA and PP matrices. Notably, the effect of the treatment was more evident in PLA composites. This chapter revealed the importance of considering not only filler content, but also morphological parameters and packing behavior, to fully exploit lignocellulosic fillers in composite systems.

# CONCLUSIONS

## General conclusion (EN)

At a time when global demand for sustainable materials continues to rise, natural fiber-based composites are attracting increasing interest from both industry and the public for the development of environmentally friendly materials. As awareness of energy efficiency and environmental preservation grows, it is particularly desirable that today's composites be derived from renewable, recyclable, or reusable sources. Composites made from natural fillers and thermoplastic polymers stand out for their advantages: low cost, satisfactory performance, ease of modification, and, above all, environmental friendliness. The properties of these composites can be significantly improved through surface modifications of the fibers or chemical treatments that enhance adhesion between the filler and the matrix. When optimally designed, such composites can rival traditional ones, and their market share is expected to expand thanks to these benefits.

This thesis is set in the context of developing more sustainable composite materials, aiming to valorize an abundant and underexploited agro-industrial co-product (BSG) as a filler for thermoplastic matrices. The main objective was to assess the potential of BSG as a filler and to propose technical solutions to overcome challenges related to its perishability, preparation, and limited compatibility with PP and PLA matrices.

**Chapter 1** established the state of the art on biocomposites and highlighted the main challenges related to the use of BSG, including its high moisture content, susceptibility to microbial degradation, limited compatibility with hydrophobic matrices, and the influence of its particle morphology (similar to that of other lignocellulosic fillers) on the final composite properties. The chapter also identified key research directions, notably the optimization of drying and grinding processes, the improvement of matrix-filler adhesion through chemical treatments, and the scale-up of processing methods from laboratory to pilot scale for industrial valorization.

**Chapter 3** demonstrated that BSG can be successfully incorporated into PLA and PP composites using an internal mixer, followed by injection molding. The behavior of BSG varied depending on the matrix: in PP, it acted as a thermal barrier, delaying degradation; whereas in PLA, it promoted degradation and influenced the rheological and mechanical properties. Despite limited interfacial adhesion and higher water absorption in PLA, the composites maintained a stable elastic modulus, indicating consistent behavior under mechanical stress, and offered an appealing balance between performance, low cost, and sustainability.

**Chapter 4** showed that twin-screw extrusion is an effective method for continuously drying and grinding BSG, offering technical, energetic, and logistical advantages over the laboratory method previously used. Extrusion produced finer, more uniform, and thermally stable particles. Scaling up this process to increase throughput is feasible. Moreover, this approach opens perspectives beyond composite applications, including protein valorization via reactive extrusion or expansion toward biorefinery processes. It could also enable *in situ* treatment of BSG during drying and grinding.

**Chapter 5** highlighted the importance of BSG pre-treatment and processing methods on composite performance. Extrusion of BSG improved interfacial compatibility and mechanical strength, especially in PP, while enabling scale-up to pilot-scale conditions. The study confirmed the influence of particle morphology on final composite performance and emphasized the need for further optimization for each matrix and process. It is worth noting that, due to equipment and time limitations, compounding processes (extrusion vs internal mixing) were not replicated, which must be addressed in future studies to assess reproducibility and optimize the process for robust large-scale applications.

Finally, **Chapter 6** focused on improving BSG-matrix adhesion through alkaline treatment (mercerization). This treatment effectively cleaned the fibers by removing binding compounds such as lignin, waxes, proteins, and hemicelluloses, thereby increasing fiber aspect ratio, roughness, and reactivity with the matrix. The incorporation of treated BSG improved interfacial adhesion, leading to a slight increase in tensile strength and fewer microvoids observed under SEM. However, limitations remained for high filler contents, particularly in PLA, where injection molding became difficult at 30 %. This chapter also underscored the importance of the maximum packing fraction in determining rheological, mechanical, and water absorption properties.

Overall, this thesis demonstrated that brewers' spent grain is a promising, low-cost, and sustainable filler for thermoplastic composites, provided that its preparation, morphology, and interactions with the matrix are properly controlled. The work contributes valuable knowledge to the formulation-processing-properties triad, paving the way for industrial applications and broader valorization of BSG.

**Perspectives:**

(i) Extend testing to other bio-based or recycled matrices.

(ii) Optimize BSG pre-treatment by extrusion under new conditions to reduce processing temperature while maintaining efficient drying.

(iii) Develop and validate the reproducibility of pilot-scale processes to confirm industrial feasibility.

(iv) Further optimize chemical treatments to enhance matrix–filler adhesion.

(v) Develop *in situ* treatment of brewers' spent grain using reactive extrusion.

(vi) Conduct life cycle assessment (LCA) of BSG-based composites to confirm their environmental and economic benefits.

(vii) Explore other valorization routes for BSG, including biorefinery processes and protein extraction.

In summary, this work contributes to the valorization of a major agro-industrial by-product and proposes an integrated approach to designing high-performance, sustainable biocomposites suitable for real-world applications.

# Conclusion générale (FR)

À l'heure où la demande mondiale en matériaux durables ne cesse d'augmenter, les composites à base de fibres naturelles connaissent un intérêt croissant des industriels et du grand public pour le développement de matériaux respectueux de l'environnement. Alors que l'attention portée à l'efficacité énergétique et à la préservation de l'environnement ne cesse d'augmenter, il est particulièrement souhaitable que les composites développés aujourd'hui proviennent de sources renouvelables, recyclables et réutilisables. Les composites à base de charges naturelles et de polymères thermoplastiques se distinguent par leurs avantages : coût réduit, performances satisfaisantes, facilité de modification, et surtout respect de l'environnement. Les propriétés de ces composites peuvent être significativement améliorées grâce à des modifications de surface des fibres ou à des traitements chimiques favorisant l'adhésion entre charge et matrice. Lorsqu'ils sont conçus de manière optimale, ces composites peuvent rivaliser avec les matériaux composites traditionnels, et leur part de marché est appelée à croître, portée par ces avantages.

Cette thèse s'inscrit donc dans le contexte du développement de matériaux composites plus durables, visant à valoriser un coproduit agro-industriel abondant et sous-exploité, les drêches de brasserie (BSG), en tant que charge pour des matrices thermoplastiques. L'objectif principal était d'évaluer le potentiel des drêches en tant que charge et de proposer des solutions techniques pour lever les verrous liés à sa périssabilité, sa préparation et sa faible compatibilité avec les matrices PP et PLA.

Le chapitre 1 a permis d'établir l'état de l'art sur les biocomposites et de mettre en évidence les principaux défis liés à l'utilisation des drêches, notamment sa forte teneur en eau, sa sensibilité aux attaques microbiennes, sa compatibilité limitée avec les matrices hydrophobes, et ou encore l'impact de sa morphologie particulaire (similaire à toute charge lignocellulosique de même aspect) sur les propriétés finales des composites. Ce chapitre a également permis d'identifier les axes de recherche nécessaires, notamment l'optimisation du séchage et du broyage, l'amélioration de l'adhésion matrice–charge par traitements chimiques, et le changement d'échelle des procédés, de laboratoire à pilote, pour une valorisation industrielle.

Le chapitre 2 a établi les bases expérimentales de ce travail de recherche.

Le chapitre 3 a montré que les drêches pouvaient être intégrées avec succès dans des composites PLA et PP en utilisant un mélangeur interne puis mises en forme à l'aide d'un

procédé d'injection. Les drêches ont montré un comportement contrasté selon la matrice. Si elles agissaient comme un isolant thermique dans le PP, retardant sa dégradation, elles favorisaient la dégradation du PLA et influençaient ses propriétés rhéologiques et mécaniques. Malgré une adhésion interfaciale limitée et une absorption d'eau plus marquée dans le PLA, les composites ont conservé un module élastique stable traduisant un comportement invariable lors d'un stress mécanique et offrent un compromis intéressant entre performance, faible coût et respect de l'environnement.

Le chapitre 4 a démontré que l'extrusion bi-vis constituait une méthode efficace pour sécher et broyer les drêches de manière continue, avec des avantages tant techniques qu'énergétiques et logistiques par rapport à la méthode laboratoire que nous utilisions. L'extrusion a permis d'obtenir des particules plus fines, plus uniformes et thermiquement stables. Il est possible d'imaginer cette même production à plus grande échelle afin d'augmenter les quantités et débits. Ce procédé ouvre également des perspectives au-delà d'une utilisation des drêches pour application composites, notamment dans la valorisation protéique par extrusion réactive ou l'extension vers des procédés de bioraffinerie. Il serait envisageable de traiter les drêche *in situ* lors du séchage et du broyage par extrusion.

Le chapitre 5 a mis en évidence l'importance du prétraitement des drêches et des méthodes de mise en forme sur les performances des composites. L'extrusion des drêches améliore la compatibilité interfaciale et la résistance mécanique, en particulier dans le PP, tout en permettant une montée en échelle vers des conditions pilotes. Le rôle de la morphologie des particules dans les performances finales des composites a été confirmé, et l'étude a souligné la nécessité de poursuivre l'optimisation pour chaque matrice et procédé. De plus, il convient de noter que lors de leur comparaison, les procédés de mélange (extrusion et mélangeur interne) n'ont pas été répliqués, faute de matériel et de temps. Cette limitation devra absolument être prise en compte dans les perspectives futures, afin d'évaluer la reproductibilité et l'optimisation du procédé pour une application à plus grande échelle plus robuste.

Enfin, le chapitre 6 a abordé l'amélioration de l'adhésion drêche-matrice par traitement alcalin. La mercerisation a permis de nettoyer les fibres de la drêche en retirant les composés liants tels que les lignines, cires, protéines et hémicelluloses, augmentant l'aspect ratio des fibres, leur rugosité et leur réactivité vis-à-vis de la matrice. L'incorporation des drêches traitées a amélioré visuellement l'adhésion interfaciale, entraînant une légère augmentation de la résistance à la traction et moins de micro-vides visibles au microscope électronique. Cependant, des limitations subsistent pour des charges élevées, notamment dans le PLA, où

l'injection devient difficile à 30 %. Ce chapitre a pu mettre en évidence l'importance du taux d'empilement maximale des charges (*maximum packing fraction*) concernant les propriétés rhéologiques mécaniques et relative à l'absorption d'eau.

Dans l'ensemble, cette thèse a démontré que les drêches de brasserie représentent une charge prometteuse, peu coûteuse et durable pour des composites thermoplastiques, à condition de maîtriser sa préparation, sa morphologie et ses interactions avec la matrice. Les travaux réalisés apportent une pierre supplémentaire à l'édifice que constituent les connaissances sur le triptyque formulation–procédé–propriétés ouvrant la voie à des applications industrielles et à une valorisation élargie du BSG.

**Perspectives :**

(i) Étendre les essais à d'autres matrices biosourcées ou recyclées.

(ii) Optimiser le prétraitement des drêches par extrusion en explorant de nouvelles conditions afin d'abaisser les températures tout en séchant efficacement.

(iii) Développer et valider la réplicabilité des procédés pilotes pour valider la faisabilité industrielle.

(iv) Optimiser de manière plus fine des traitements chimiques pour améliorer encore l'adhésion matrice-charge.

(v) Développer un traitement in situ des drêches de brasserie en utilisant l'extrusion réactive.

(vi) Évaluer le cycle de vie complet des composites à base de drêches de brasserie afin de confirmer leur intérêt environnemental et économique.

(vii) Explorer d'autres voies de valorisation du BSG, notamment dans les procédés de bioraffinerie et l'extraction de protéines.

Ainsi, ce travail contribue à la valorisation d'un coproduit agro-industriel majeur et propose une approche intégrée pour concevoir des biocomposites performants, durables et adaptés à des applications réelles.

# REFERENCES

# References

[1] Abdollahiparsa H, Shahmirzaloo A, Teuffel P, Blok R. A review of recent developments in structural applications of natural fiber-Reinforced composites (NFRCs). Composites and Advanced Materials 2023;32. https://doi.org/10.1177/26349833221147540.

[2] Faruk O, Bledzki AK, Fink HP, Sain M. Biocomposites reinforced with natural fibers: 2000–2010. Prog Polym Sci 2012;37:1552–96. https://doi.org/10.1016/J.PROGPOLYMSCI.2012.04.003.

[3] Ku H, Wang H, Pattarachaiyakoop N, Trada M. A review on the tensile properties of natural fiber reinforced polymer composites. Compos B Eng 2011;42:856–73. https://doi.org/10.1016/J.COMPOSITESB.2011.01.010.

[4] Oksman K, Skrifvars M, Selin JF. Natural fibres as reinforcement in polylactic acid (PLA) composites. Compos Sci Technol 2003;63:1317–24. https://doi.org/10.1016/S0266-3538(03)00103-9.

[5] Jawaid, Mohammad & Sapuan, S. & Alothman, Othman. Green Biocomposites: Manufacturing and Properties. 2016. 10.1007/978-3-319-46610-1.

[6] FÜZESSÉRY S. Polypropylènes PP. Plastiques et Composites 1991. https://doi.org/10.51257/a-v1-a3320.

[7] Phung TK, Pham TLM, Vu KB, Busca G. (Bio)Propylene production processes: A critical review. J Environ Chem Eng 2021;9:105673. https://doi.org/10.1016/J.JECE.2021.105673.

[8] Narita N, Sagisaka M, Inaba A. Life cycle inventory analysis of CO2 emissions: Manufacturing commodity plastics in Japan. International Journal of Life Cycle Assessment 2002;7:277–82. https://doi.org/10.1007/BF02978888/METRICS.

[9] Alsabri A, Tahir F, Al-Ghamdi SG. Environmental impacts of polypropylene (PP) production and prospects of its recycling in the GCC region. Mater Today Proc 2022;56:2245–51. https://doi.org/10.1016/J.MATPR.2021.11.574.

[10] Galve JE, Elduque D, Pina C, Javierre C. Life Cycle Assessment of a Plastic Part Injected with Recycled Polypropylene: A Comparison with Alternative Virgin Materials. International Journal of Precision Engineering and Manufacturing - Green Technology 2022;9:919–32. https://doi.org/10.1007/S40684-021-00363-2/METRICS.

[11] Zhang H, Xiao R, Jin B, Xiao G, Chen R. Biomass catalytic pyrolysis to produce olefins and aromatics with a physically mixed catalyst. Bioresour Technol 2013;140:256–62. https://doi.org/10.1016/J.BIORTECH.2013.04.094.

[12] DUVAL C. Polypropylènes (PP). Plastiques et Composites 2004. https://doi.org/10.51257/A-V1-AM3320.

[13] Pukanszky B, Gibson AG, Matsuoka T, Karger-Kocsis J, Berglund LA, Ericson ML, et al. Polypropylene Structure, blends and Composites. Dordrecht: Springer Netherlands; 1995. https://doi.org/10.1007/978-94-011-0523-1.

[14] Trotignon J -P, Verdu J. Skin-core structure–fatigue behavior relationships for injection-molded parts of polypropylene. I. Influence of molecular weight and injection conditions

on the morphology. J Appl Polym Sci 1987;34:1–18. https://doi.org/10.1002/APP.1987.070340101.

[15] Rivera-Armenta JL, Salazar-Cruz BA, Espindola-Flores AC, Villarreal-Lucio DS, De León-Almazán CM, Estrada-Martinez J. Thermal and Thermomechanical Characterization of Polypropylene-Seed Shell Particles Composites. Applied Sciences 2022, Vol 12, Page 8336 2022;12:8336. https://doi.org/10.3390/APP12168336.

[16] Hansen B, Borsoi C, Dahlem Júnior MA, Catto AL. Thermal and thermo-mechanical properties of polypropylene composites using yerba mate residues as reinforcing filler. Ind Crops Prod 2019;140:111696. https://doi.org/10.1016/J.INDCROP.2019.111696.

[17] Gabrielli S, Caviglia M, Pastore G, Marcantoni E, Nobili F, Bottoni L, et al. Chemical, Thermal and Mechanical Characterization of Licorice Root, Willow, Holm Oak, and Palm Leaf Waste Incorporated into Maleated Polypropylene (MAPP). Polymers (Basel) 2022;14. https://doi.org/10.3390/POLYM14204348.

[18] Panthapulakkal S, Zereshkian A, Sain M. Preparation and characterization of wheat straw fibers for reinforcing application in injection molded thermoplastic composites. Bioresour Technol 2006;97:265–72. https://doi.org/10.1016/j.biortech.2005.02.043.

[19] Núñez-Decap M, Wechsler-Pizarro A, Vidal-Vega M. Mechanical, physical, thermal and morphological properties of polypropylene composite materials developed with particles of peach and cherry stones. Sustainable Materials and Technologies 2021;29. https://doi.org/10.1016/j.susmat.2021.e00300.

[20] Luz SM, Gonçalves AR, Del'Arco AP. Mechanical behavior and microstructural analysis of sugarcane bagasse fibers reinforced polypropylene composites. Compos Part A Appl Sci Manuf 2007;38:1455–61. https://doi.org/10.1016/J.COMPOSITESA.2007.01.014.

[21] Yiga VA, Pagel S, Lubwama M, Epple S, Olupot PW, Bonten C. Development of fiber-reinforced polypropylene with NaOH pretreated rice and coffee husks as fillers: Mechanical and thermal properties. Journal of Thermoplastic Composite Materials 2020;33:1269–91. https://doi.org/10.1177/0892705718823255/ASSET/3E546A3F-BC8C-4726-B818-CB869D36B231/ASSETS/IMAGES/LARGE/10.1177_0892705718823255-FIG16.JPG.

[22] Cheremisinoff NP. P. Condensed Encyclopedia of Polymer Engineering Terms 2001:200–55. https://doi.org/10.1016/B978-0-08-050282-3.50021-4.

[23] ChemAnalyst. Polypropylene (PP) Market Analysis: Plant capacity, Production, Process, Technology, Operating efficiency, demand & supply, End-use, foreign trade, Sales channel, Regional demand, Company share, 2015-2035 2025.

[24] Wang S, Muiruri JK, Soo XYD, Liu S, Thitsartarn W, Tan BH, et al. Bio-Polypropylene and Polypropylene-based Biocomposites: Solutions for a Sustainable Future. Chem Asian J 2023;18. https://doi.org/10.1002/ASIA.202200972.

[25] Garlotta D. A literature review of poly(lactic acid). J Polym Environ 2001;9:63–84. https://doi.org/10.1023/A:1020200822435/METRICS.

[26] Lunt J. Large-scale production, properties and commercial applications of polylactic acid polymers. Polym Degrad Stab 1998;59:145–52. https://doi.org/10.1016/S0141-3910(97)00148-1.

[27] Velghe I, Buffel B, Vandeginste V, Thielemans W, Desplentere F. Review on the Degradation of Poly(lactic acid) during Melt Processing. Polymers (Basel) 2023;15. https://doi.org/10.3390/POLYM15092047.

[28] Dreier J, Brütting C, Ruckdäschel H, Altstädt V, Bonten C. Investigation of the Thermal and Hydrolytic Degradation of Polylactide during Autoclave Foaming. Polymers (Basel) 2021;13. https://doi.org/10.3390/POLYM13162624.

[29] Oliveira M, Santos E, Araújo A, Fechine GJM, Machado A V., Botelho G. The role of shear and stabilizer on PLA degradation. Polym Test 2016;51:109–16. https://doi.org/10.1016/J.POLYMERTESTING.2016.03.005.

[30] Brüster B, Addiego F, Hassouna F, Ruch D, Raquez JM, Dubois P. Thermo-mechanical degradation of plasticized poly(lactide) after multiple reprocessing to simulate recycling: Multi-scale analysis and underlying mechanisms. Polym Degrad Stab 2016;131:132–44. https://doi.org/10.1016/J.POLYMDEGRADSTAB.2016.07.017.

[31] Botta L, Scaffaro R, Sutera F, Mistretta MC. Reprocessing of PLA/Graphene Nanoplatelets Nanocomposites. Polymers (Basel) 2017;10. https://doi.org/10.3390/POLYM10010018.

[32] Lv Y, Chen J, Xu W, Kong M. Multiscale analysis on multiextruded poly(lactic acid)/organoclay nanocomposites: Insights into the underlying mechanisms of thermomechanical degradation. Polym Adv Technol 2020;31:2742–51. https://doi.org/10.1002/PAT.5001.

[33] Agüero A, Morcillo M del C, Quiles-Carrillo L, Balart R, Boronat T, Lascano D, et al. Study of the Influence of the Reprocessing Cycles on the Final Properties of Polylactide Pieces Obtained by Injection Molding. Polymers (Basel) 2019;11. https://doi.org/10.3390/POLYM11121908.

[34] Jamshidi K, Hyon SH, Ikada Y. Thermal characterization of polylactides. Polymer (Guildf) 1988;29:2229–34. https://doi.org/10.1016/0032-3861(88)90116-4.

[35] Pan P, Kai W, Zhu B, Dong T, Inoue Y. Polymorphous crystallization and multiple melting behavior of poly(L-lactide): Molecular weight dependence. Macromolecules 2007;40:6898–905. https://doi.org/10.1021/ma071258d.

[36] Drieskens M, Peeters R, Mullens J, Franco D, Iemstra PJ, Hristova-Bogaerds DG. Structure versus properties relationship of poly(lactic acid). I. Effect of crystallinity on barrier properties. J Polym Sci B Polym Phys 2009;47:2247–58. https://doi.org/10.1002/POLB.21822.

[37] Li S, McCarthy S. Influence of crystallinity and stereochemistry on the enzymatic degradation of poly(lactide)s. Macromolecules 1999;32:4454–6. https://doi.org/10.1021/MA990117B/ASSET/IMAGES/LARGE/MA990117BF00003.JPEG.

[38] Litauszki K, Petrény R, Haramia Z, Mészáros L. Combined effects of plasticizers and D-lactide content on the mechanical and morphological behavior of polylactic acid. Heliyon 2023;9. https://doi.org/10.1016/J.HELIYON.2023.E14674.

[39] Saeidlou S, Huneault MA, Li H, Park CB. Poly(lactic acid) crystallization. Prog Polym Sci 2012;37:1657–77. https://doi.org/10.1016/j.progpolymsci.2012.07.005.

[40] Zhang J, Tashiro K, Tsuji H, Domb AJ. Disorder-to-order phase transition and multiple melting behavior of poly(L-lactide) investigated by simultaneous measurements of WAXD and DSC. Macromolecules 2008;41:1352–7. https://doi.org/10.1021/MA0706071/ASSET/IMAGES/LARGE/MA0706071F00011.JPEG.

[41] Kawai T, Rahman N, Matsuba G, Nishida K, Kanaya T, Nakano M, et al. Crystallization and melting behavior of poly (L-lactic acid). Macromolecules 2007;40:9463–9. https://doi.org/10.1021/MA070082C/ASSET/IMAGES/LARGE/MA070082CF00013.JPEG.

[42] Cartier L, Okihara T, Ikada Y, Tsuji H, Puiggali J, Lotz B. Epitaxial crystallization and crystalline polymorphism of polylactides. Polymer (Guildf) 2000;41:8909–19. https://doi.org/10.1016/S0032-3861(00)00234-2.

[43] Selke SE, Wichman I. Wood fiber/polyolefin composites. Compos Part A Appl Sci Manuf 2004;35:321–6. https://doi.org/10.1016/J.COMPOSITESA.2003.09.010.

[44] Kervran M, Vagner C, Cochez M, Ponçot M, Saeb MR, Vahabi H. Thermal degradation of polylactic acid (PLA)/polyhydroxybutyrate (PHB) blends: A systematic review. Polym Degrad Stab 2022;201:109995. https://doi.org/10.1016/J.POLYMDEGRADSTAB.2022.109995.

[45] De Vlieger JJ. Green plastics for food packaging. Novel Food Packaging Techniques 2003:519–34. https://doi.org/10.1533/9781855737020.4.519.

[46] Sutivisedsak N, Cheng HN, Dowd MK, Selling GW, Biswas A. Evaluation of cotton byproducts as fillers for poly(lactic acid) and low density polyethylene. Ind Crops Prod 2012;36:127–34. https://doi.org/10.1016/j.indcrop.2011.08.016.

[47] Kim KW, Lee BH, Kim HJ, Sriroth K, Dorgan JR. Thermal and mechanical properties of cassava and pineapple flours-filled PLA bio-composites. J Therm Anal Calorim, vol. 108, 2012, p. 1131–9. https://doi.org/10.1007/s10973-011-1350-y.

[48] Kim KW, Lee BH, Kim HJ, Sriroth K, Dorgan JR. Thermal and mechanical properties of cassava and pineapple flours-filled PLA bio-composites. J Therm Anal Calorim, vol. 108, 2012, p. 1131–9. https://doi.org/10.1007/s10973-011-1350-y.

[49] Yew GH, Mohd Yusof AM, Mohd Ishak ZA, Ishiaku US. Water absorption and enzymatic degradation of poly(lactic acid)/rice starch composites. Polym Degrad Stab 2005;90:488–500. https://doi.org/10.1016/J.POLYMDEGRADSTAB.2005.04.006.

[50] European Bioplastics. Bioplastics Market Development Update 2024 2024.

[51] Rowell RM. Challenges in biomass - Thermoplastic composites. J Polym Environ 2007;15:229–35. https://doi.org/10.1007/s10924-007-0069-0.

[52] Yussuf AA, Massoumi I, Hassan A. Comparison of polylactic Acid/Kenaf and polylactic Acid/Rise husk composites: The influence of the natural fibers on the mechanical,

thermal and biodegradability properties. J Polym Environ 2010;18:422–9. https://doi.org/10.1007/s10924-010-0185-0.

[53] Finkenstadt VL, Liu LS, Willett JL. Evaluation of poly(lactic acid) and sugar beet pulp green composites. J Polym Environ 2007;15:1–6. https://doi.org/10.1007/s10924-006-0038-z.

[54] Pilla S, Gong S, O'Neill E, Rowell RM, Krzysik AM. Polylactide-pine wood flour composites. Polym Eng Sci 2008;48:578–87. https://doi.org/10.1002/pen.20971.

[55] Arib RMN, Sapuan SM, Ahmad MMHM, Paridah MT, Khairul Zaman HMD. Mechanical properties of pineapple leaf fibre reinforced polypropylene composites. Mater Des 2006;27:391–6. https://doi.org/10.1016/j.matdes.2004.11.009.

[56] Zampaloni M, Pourboghrat F, Yankovich SA, Rodgers BN, Moore J, Drzal LT, et al. Kenaf natural fiber reinforced polypropylene composites: A discussion on manufacturing problems and solutions. Compos Part A Appl Sci Manuf 2007;38:1569–80. https://doi.org/10.1016/j.compositesa.2007.01.001.

[57] Taflick T, Maich ÉG, Dias Ferreira L, Bica CID, Rodrigues SRS, Nachtigall SMB. Acacia bark residues as filler in polypropylene composites. Polimeros 2015;25:289–95. https://doi.org/10.1590/0104-1428.1840.

[58] Panthapulakkal S, Zereshkian A, Sain M. Preparation and characterization of wheat straw fibers for reinforcing application in injection molded thermoplastic composites. Bioresour Technol 2006;97:265–72. https://doi.org/10.1016/j.biortech.2005.02.043.

[59] Jaszkiewicz A, Meljon A, Bledzki AK, Radwanski M. Gaining knowledge on the processability of PLA-based short-fibre compounds - A comprehensive comparison with their PP counterparts. Compos Part A Appl Sci Manuf 2016;83:140–51. https://doi.org/10.1016/j.compositesa.2015.09.022.

[60] Mofokeng JP, Luyt AS, Tábi T, Kovács J. Comparison of injection moulded, natural fibre-reinforced composites with PP and PLA as matrices. Journal of Thermoplastic Composite Materials 2012;25:927–48. https://doi.org/10.1177/0892705711423291.

[61] Liu R, Peng Y, Cao J, Chen Y. Comparison on properties of lignocellulosic flour/polymer composites by using wood, cellulose, and lignin flours as fillers. Compos Sci Technol 2014;103:1–7. https://doi.org/10.1016/j.compscitech.2014.08.005.

[62] Bledzki AK, Jaszkiewicz A. Mechanical performance of biocomposites based on PLA and PHBV reinforced with natural fibres - A comparative study to PP. Compos Sci Technol 2010;70:1687–96. https://doi.org/10.1016/j.compscitech.2010.06.005.

[63] Bensaude-Vincent. (PDF) Eloge du mixte 2020. https://www.researchgate.net/publication/339722398_Eloge_du_mixte (accessed September 27, 2025).

[64] Satyanarayana KG, Arizaga GGC, Wypych F. Biodegradable composites based on lignocellulosic fibers—An overview. Prog Polym Sci 2009;34:982–1021. https://doi.org/10.1016/J.PROGPOLYMSCI.2008.12.002.

[65] Hamim HR, Hasan T, Shahriar F, Chowdhury SR, Rahman MA, Nasim M, et al. Basalt-silk fiber reinforced PLA composites: Effect of graphene fillers and stacking sequence.

Composites Part C: Open Access 2025;16:100564. https://doi.org/10.1016/J.JCOMC.2025.100564.

[66] Reinders MJ, Onwezen MC, Meeusen MJG. Can bio-based attributes upgrade a brand? How partial and full use of bio-based materials affects the purchase intention of brands. J Clean Prod 2017;162:1169–79. https://doi.org/10.1016/J.JCLEPRO.2017.06.126.

[67] Jawaid M, Sapuan M, Othman S, Alothman Editors Y. Green Energy and Technology Green Biocomposites Design and Applications. n.d.

[68] Gaffey J, McMahon H, Marsh E, Vehmas K, Kymäläinen T, Vos J. Understanding Consumer Perspectives of Bio-Based Products—A Comparative Case Study from Ireland and The Netherlands. Sustainability 2021, Vol 13, Page 6062 2021;13:6062. https://doi.org/10.3390/SU13116062.

[69] Allison AL, Lorencatto F, Michie S, Miodownik M. Barriers and Enablers to Buying Biodegradable and Compostable Plastic Packaging. Sustainability 2021, Vol 13, Page 1463 2021;13:1463. https://doi.org/10.3390/SU13031463.

[70] Genencor Household Sustainability Index: Consumer attitudes and adoption of biobased products. Industrial Biotechnology 2011;7:279–85. https://doi.org/10.1089/IND.2011.7.279/ASSET/IND.2011.7.279.FP.PNG_V03.

[71] Scherer C, Emberger-Klein A, Menrad K. Biogenic product alternatives for children: Consumer preferences for a set of sand toys made of bio-based plastic. Sustain Prod Consum 2017;10:1–14. https://doi.org/10.1016/J.SPC.2016.11.001.

[72] The business research company. Report from the Business Research Company (natural fibers global report (2025) 2025.

[73] Radzi MKFM, Muhamad N, Akhtar MN, Razak Z, Mohd Foudzi F. The effect of kenaf filler reinforcement on the mechanical and physical properties of injection moulded polypropylene composites. Sains Malays 2018;47:367–76. https://doi.org/10.17576/jsm-2018-4702-19.

[74] Teramoto N, Urata K, Ozawa K, Shibata M. Biodegradation of aliphatic polyester composites reinforced by abaca fiber. Polym Degrad Stab 2004;86:401–9. https://doi.org/10.1016/j.polymdegradstab.2004.04.026.

[75] Hu R, Lim JK. Fabrication and mechanical properties of completely biodegradable hemp fiber reinforced polylactic acid composites. J Compos Mater 2007;41:1655–69. https://doi.org/10.1177/0021998306069878.

[76] Yussuf AA, Massoumi I, Hassan A. Comparison of polylactic Acid/Kenaf and polylactic Acid/Rise husk composites: The influence of the natural fibers on the mechanical, thermal and biodegradability properties. J Polym Environ 2010;18:422–9. https://doi.org/10.1007/s10924-010-0185-0.

[77] Naghmouchi I, Mutjé P, Boufi S. Olive stones flour as reinforcement in polypropylene composites: A step forward in the valorization of the solid waste from the olive oil industry. Ind Crops Prod 2014;72:183–91. https://doi.org/10.1016/j.indcrop.2014.11.051.

[78] Merijs-Meri R, Zicans J, Ivanova T, Bochkov I, Varkale M, Franciszczak P, et al. Development and Characterization of Grain Husks Derived Lignocellulose Filler Containing Polypropylene Composites. Polym Eng Sci 2019;59:2467–73. https://doi.org/10.1002/pen.25245.

[79] Bledzki AK, Mamun AA, Volk J. Barley husk and coconut shell reinforced polypropylene composites: The effect of fibre physical, chemical and surface properties. Compos Sci Technol 2010;70:840–6. https://doi.org/10.1016/j.compscitech.2010.01.022.

[80] Nunes LJR, De Oliveira Matias JC, Da Silva Catalão JP. Introduction. Torrefaction of Biomass for Energy Applications 2018:1–43. https://doi.org/10.1016/B978-0-12-809462-4.00001-8.

[81] Liu Y, Guan Y, Li Y, Zhai J, Li X, Lin J. Rheological/crystallization behavior of PP/graphite nanosheet composites and performance of microcellular foaming plastics. Composites Communications 2022;32. https://doi.org/10.1016/j.coco.2022.101133.

[82] Georgopoulos ST, Tarantili PA, Avgerinos E, Andreopoulos AG, Koukios EG. Thermoplastic polymers reinforced with fibrous agricultural residues. Polym Degrad Stab 2005;90:303–12. https://doi.org/10.1016/J.POLYMDEGRADSTAB.2005.02.020.

[83] Lezak E, Kulinski Z, Masirek R, Piorkowska E, Pracella M, Gadzinowska K. Mechanical and thermal properties of green polylactide composites with natural fillers. Macromol Biosci 2008;8:1190–200. https://doi.org/10.1002/MABI.200800040.

[84] Bharath KN, Basavarajappa S. Applications of biocomposite materials based on natural fibers from renewable resources: A review. Science and Engineering of Composite Materials 2016;23:123–33. https://doi.org/10.1515/SECM-2014-0088/ASSET/GRAPHIC/J_SECM-2014-0088_FIG_018.JPG.

[85] Mallawarachchi KS, Bandara LRLM, Dilshan SKDHS, Ariyadasa TU, Gunawardena SHP. Optimization of mashing process in beer production using rice as an adjunct. 2nd International Moratuwa Engineering Research Conference, MERCon 2016 2016:289–92. https://doi.org/10.1109/MERCON.2016.7480155.

[86] Lloyd WJW. ADJUNCTS. Journal of the Institute of Brewing 1986;92:336–45. https://doi.org/10.1002/J.2050-0416.1986.TB04420.X.

[87] Poelmans E, Swinnen JFM. From Monasteries to Multinationals (and Back): A Historical Review of the Beer Economy. SSRN Electronic Journal 2011. https://doi.org/10.2139/SSRN.1995425.

[88] Hejna A, Marć M, Kowalkowska-Zedler D, Pladzyk A, Barczewski M. Insights into the Thermo-Mechanical Treatment of Brewers' Spent Grain as a Potential Filler for Polymer Composites. Polymers (Basel) 2021;13. https://doi.org/10.3390/POLYM13060879.

[89] Qazanfarzadeh Z, Ganesan AR, Mariniello L, Conterno L, Kumaravel V. Valorization of brewer's spent grain for sustainable food packaging. J Clean Prod 2023;385:135726. https://doi.org/10.1016/J.JCLEPRO.2022.135726.

[90] Mussatto SI. Brewer's spent grain: a valuable feedstock for industrial applications. J Sci Food Agric 2014;94:1264–75. https://doi.org/10.1002/JSFA.6486.

[91] Aradwad P, Raut S, Abdelfattah A, Rauh C, Sturm B. Brewer's spent grain: Unveiling innovative applications in the food and packaging industry. Compr Rev Food Sci Food Saf 2025;24. https://doi.org/10.1111/1541-4337.70150.

[92] Buffington J, Buffington J. The Economic Potential of Brewer's Spent Grain (BSG) as a Biomass Feedstock. Advances in Chemical Engineering and Science 2014;4:308–18. https://doi.org/10.4236/ACES.2014.43034.

[93] Stojceska V, Ainsworth P, Plunkett A, Ibanoğlu S. The recycling of brewer's processing by-product into ready-to-eat snacks using extrusion technology. J Cereal Sci 2008;47:469–79. https://doi.org/10.1016/J.JCS.2007.05.016.

[94] Kavalopoulos M, Stoumpou V, Christofi A, Mai S, Barampouti EM, Moustakas K, et al. Sustainable valorisation pathways mitigating environmental pollution from brewers' spent grains. Environ Pollut 2021;270. https://doi.org/10.1016/J.ENVPOL.2020.116069.

[95] Mussatto SI, Roberto IC. Chemical characterization and liberation of pentose sugars from brewer's spent grain. Journal of Chemical Technology and Biotechnology 2006;81:268–74. https://doi.org/10.1002/jctb.1374.

[96] Jay AJ, Parker ML, Faulks R, Husband F, Wilde P, Smith AC, et al. A systematic micro-dissection of brewers' spent grain. J Cereal Sci 2008;47:357–64. https://doi.org/10.1016/J.JCS.2007.05.006.

[97] Jin Z, Lan Y, Ohm JB, Gillespie J, Schwarz P, Chen B. Physicochemical composition, fermentable sugars, free amino acids, phenolics, and minerals in brewers' spent grains obtained from craft brewing operations. J Cereal Sci 2022;104:103413. https://doi.org/10.1016/J.JCS.2022.103413.

[98] Virdi AS, Mahajan A, Devraj M, Sanghi R. Brewers' spent grains: Techno-functional challenges and opportunity in the valorization for food products. LWT 2025;227:117785. https://doi.org/10.1016/J.LWT.2025.117785.

[99] Kanauchi O, Mitsuyama K, Araki Y. Development of a Functional Germinated Barley Foodstuff from Brewer's Spent Grain for the Treatment of Ulcerative Colitis. Journal of the American Society of Brewing Chemists 2001;59:59–62. https://doi.org/10.1094/ASBCJ-59-0059.

[100] Carvalheiro F, Esteves MP, Parajó JC, Pereira H, Gírio FM. Production of oligosaccharides by autohydrolysis of brewery's spent grain. Bioresour Technol 2004;91:93–100. https://doi.org/10.1016/S0960-8524(03)00148-2.

[101] Silva JP, Sousa S, Rodrigues J, Antunes H, Porter JJ, Gonçalves I, et al. Adsorption of acid orange 7 dye in aqueous solutions by spent brewery grains. Sep Purif Technol 2004;40:309–15. https://doi.org/10.1016/j.seppur.2004.03.010.

[102] Meneses NGT, Martins S, Teixeira JA, Mussatto SI. Influence of extraction solvents on the recovery of antioxidant phenolic compounds from brewer's spent grains. Sep Purif Technol 2013;108:152–8. https://doi.org/10.1016/j.seppur.2013.02.015.

[103] Waters DM, Jacob F, Titze J, Arendt EK, Zannini E. Fibre, protein and mineral fortification of wheat bread through milled and fermented brewer's spent grain enrichment.

European Food Research and Technology 2012;235:767–78. https://doi.org/10.1007/s00217-012-1805-9.

[104] Lynch KM, Steffen EJ, Arendt EK. Brewers' spent grain: a review with an emphasis on food and health. Journal of the Institute of Brewing 2016;122:553–68. https://doi.org/10.1002/JIB.363.

[105] Hejna A, Barczewski M, Skórczewska K, Szulc J, Chmielnicki B, Korol J, et al. Sustainable upcycling of brewers' spent grain by thermo-mechanical treatment in twin-screw extruder. J Clean Prod 2021;285. https://doi.org/10.1016/j.jclepro.2020.124839.

[106] Hejna A, Formela K, Saeb MR. Processing, mechanical and thermal behavior assessments of polycaprolactone/agricultural wastes biocomposites. Ind Crops Prod 2015;76:725–33. https://doi.org/10.1016/J.INDCROP.2015.07.049.

[107] Berthet MA, Angellier-Coussy H, Machado D, Hilliou L, Staebler A, Vicente A, et al. Exploring the potentialities of using lignocellulosic fibres derived from three food by-products as constituents of biocomposites for food packaging. Ind Crops Prod 2015;69:110–22. https://doi.org/10.1016/j.indcrop.2015.01.028.

[108] Cunha M, Berthet MA, Pereira R, Covas JA, Vicente AA, Hilliou L. Development of polyhydroxyalkanoate/beer spent grain fibers composites for film blowing applications. Polym Compos 2015;36:1859–65. https://doi.org/10.1002/pc.23093.

[109] Hejna A, Haponiuk J, Piszczyk Ł, Klein M, Formela K. Performance properties of rigid polyurethane-polyisocyanurate/brewers' spent grain foamed composites as function of isocyanate index. E-Polymers 2017;17:427–37. https://doi.org/10.1515/epoly-2017-0012.

[110] Formela K, Hejna A, Zedler Ł, Przybysz M, Ryl J, Saeb MR, et al. Structural, thermal and physico-mechanical properties of polyurethane/brewers' spent grain composite foams modified with ground tire rubber. Ind Crops Prod 2017;108:844–52. https://doi.org/10.1016/j.indcrop.2017.07.047.

[111] Zedler Ł, Colom X, Saeb MR, Formela K. Preparation and characterization of natural rubber composites highly filled with brewers' spent grain/ground tire rubber hybrid reinforcement. Compos B Eng 2018;145:182–8. https://doi.org/10.1016/j.compositesb.2018.03.024.

[112] Bledzki AK, Mamun AA, Volk J. Barley husk and coconut shell reinforced polypropylene composites: The effect of fibre physical, chemical and surface properties. Compos Sci Technol 2010;70:840–6. https://doi.org/10.1016/j.compscitech.2010.01.022.

[113] Gholampour A, Ozbakkaloglu T. A review of natural fiber composites: properties, modification and processing techniques, characterization, applications. J Mater Sci 2020;55:829–92. https://doi.org/10.1007/S10853-019-03990-Y/TABLES/23.

[114] Yi J, Li X, He J, Duan X. Drying efficiency and product quality of biomass drying: a review. Drying Technology 2020;38:2039–54. https://doi.org/10.1080/07373937.2019.1628772.

[115] Sahni EK, Chaudhuri B. Contact drying: a review of experimental and mechanistic modeling approaches. Int J Pharm 2012;434:334–48. https://doi.org/10.1016/J.IJPHARM.2012.06.010.

[116] Gómez-de la Cruz FJ, Palomar-Torres A, Pérez-Latorre FJ, Cruz-Peragón F. Convective drying of mango stone for use as biomass. Environ Res 2023;227:115742. https://doi.org/10.1016/J.ENVRES.2023.115742.

[117] EL-Mesery HS, El-khawaga SE. Drying process on biomass: Evaluation of the drying performance and energy analysis of different dryers. Case Studies in Thermal Engineering 2022;33:101953. https://doi.org/10.1016/J.CSITE.2022.101953.

[118] Romdhana H, Bonazzi C, Esteban-Decloux M. Superheated Steam Drying: An Overview of Pilot and Industrial Dryers with a Focus on Energy Efficiency. Drying Technology 2015;33:1255–74. https://doi.org/10.1080/07373937.2015.1025139.

[119] Mayer-Laigle C, Blanc N, Rajaonarivony RK, Rouau X. Comminution of Dry Lignocellulosic Biomass, a Review: Part I. From Fundamental Mechanisms to Milling Behaviour. Bioengineering (Basel) 2018;5. https://doi.org/10.3390/BIOENGINEERING5020041.

[120] Kaya E, Hogg R, Kumar SR. Particle Shape Modification in Comminution. KONA Powder and Particle Journal 2002;20:188–95. https://doi.org/10.14356/KONA.2002021.

[121] Tannous K, Lam PS, Sokhansanj S, Grace JR. Physical Properties for Flow Characterization of Ground Biomass from Douglas Fir Wood. Particulate Science and Technology 2013;31:291–300. https://doi.org/10.1080/02726351.2012.732676.

[122] Zykova AK, Pantyukhov P V., Kolesnikova NN, Popov AA, Olkhov AA. Influence of particle size on water absorption capacity and mechanical properties of polyethylene-wood flour composites. AIP Conf Proc 2015;1683. https://doi.org/10.1063/1.4932932.

[123] Barakat A, de Vries H, Rouau X. Dry fractionation process as an important step in current and future lignocellulose biorefineries: a review. Bioresour Technol 2013;134:362–73. https://doi.org/10.1016/J.BIORTECH.2013.01.169.

[124] Mayer-Laigle C, Rajaonarivony RK, Blanc N, Rouau X. Comminution of Dry Lignocellulosic Biomass: Part II. Technologies, Improvement of Milling Performances, and Security Issues. Bioengineering (Basel) 2018;5. https://doi.org/10.3390/bioengineering5030050.

[125] Mani S, Tabil LG, Sokhansanj S. Grinding performance and physical properties of wheat and barley straws, corn stover and switchgrass. Biomass Bioenergy 2004;27:339–52. https://doi.org/10.1016/J.BIOMBIOE.2004.03.007.

[126] Kratky L, Jirout T. Biomass Size Reduction Machines for Enhancing Biogas Production. Chem Eng Technol 2011;34:391–9. https://doi.org/10.1002/CEAT.201000357.

[127] Tavakoli H, Mohtasebi S, Jafari A. Physical and mechanical properties of wheat straw as influenced by moisture content. Int. Agrophys. 2009;23(2):175–81.

[128] Kocaefe D, Poncsak S, Boluk Y. Thermal treatment of aspen. Bioresources 2008;3:517–37.

[129] N'Diaye S, Rigal L, Larocque P, Vidal PF. Extraction of hemicelluloses from poplar, Populus tremuloides, using an extruder-type twin-screw reactor: A feasibility study. Bioresour Technol 1996;57:61–7. https://doi.org/10.1016/0960-8524(96)00041-7.

[130] Karunanithy C, Muthukumarappan K, Gu T, Karunanithy C, Muthukumarappan K. Thermo-Mechanical Pretreatment of Feedstocks 2013:31–65. https://doi.org/10.1007/978-94-007-6052-3_2.

[131] Zhang S, Keshwani DR, Xu Y, Hanna MA. Alkali combined extrusion pretreatment of corn stover to enhance enzyme saccharification. Ind Crops Prod 2012;37:352–7. https://doi.org/10.1016/J.INDCROP.2011.12.001.

[132] Duque A, Manzanares P, Ballesteros M. Extrusion as a pretreatment for lignocellulosic biomass: Fundamentals and applications. Renew Energy 2017;114:1427–41. https://doi.org/10.1016/J.RENENE.2017.06.050.

[133] Berzin F, Tara A, Tighzert L, Vergnes B. Importance of coupling between specific energy and viscosity in the modeling of twin screw extrusion of starchy products. Polym Eng Sci 2010;50:1758–66. https://doi.org/10.1002/PEN.21702.

[134] Arranz JI, Miranda MT, Sepúlveda FJ, Montero I, Rojas CV. Analysis of Drying of Brewers' Spent Grain, MDPI AG; 2018, p. 1467. https://doi.org/10.3390/proceedings2231467.

[135] Santos M V., Ranalli N, Orjuela-Palacio J, Zaritzky N. Brewers spent grain drying: Drying kinetics, moisture sorption isotherms, bioactive compounds stability and Bacillus cereus lethality during thermal treatment. J Food Eng 2024;364. https://doi.org/10.1016/j.jfoodeng.2023.111796.

[136] Mallen E, Najdanovic-Visak V. Brewers' spent grains: Drying kinetics and biodiesel production. Bioresour Technol Rep 2018;1:16–23. https://doi.org/10.1016/J.BITEB.2018.01.005.

[137] Stroem LK, Desai DK, Hoadley AFA. Superheated steam drying of Brewer's spent grain in a rotary drum. Advanced Powder Technology 2009;20:240–4. https://doi.org/10.1016/J.APT.2009.03.009.

[138] Santos M, Jiménez JJ, Bartolomé B, Gómez-Cordovés C, Del Nozal MJ. Variability of brewer's spent grain within a brewery. Food Chem 2003;80:17–21. https://doi.org/10.1016/S0308-8146(02)00229-7.

[139] Capossio JP, Fabani MP, Reyes-Urrutia A, Torres-Sciancalepore R, Deng Y, Baeyens J, et al. Sustainable Solar Drying of Brewer's Spent Grains: A Comparison with Conventional Electric Convective Drying. Processes 2022, Vol 10, Page 339 2022;10:339. https://doi.org/10.3390/PR10020339.

[140] Tang Z, Cenkowski S, Izydorczyk M. Thin-layer drying of spent grains in superheated steam. J Food Eng 2005;67:457–65. https://doi.org/10.1016/J.JFOODENG.2004.04.040.

[141] Thai S, Avena-Bustillos RJ, Alves P, Pan J, Osorio-Ruiz A, Miller J, et al. Influence of drying methods on health indicators of brewers spent grain for potential upcycling into food products. Applied Food Research 2022;2:100052. https://doi.org/10.1016/J.AFRES.2022.100052.

[142] Shahzad A, Teacă CA, Tanasă F. Natural fibers and surface treatment methods. Surface Treatment Methods of Natural Fibres and Their Effects on Biocomposites 2022:1–18. https://doi.org/10.1016/B978-0-12-821863-1.00001-6.

[143] Kabir MM, Wang H, Lau KT, Cardona F. Chemical treatments on plant-based natural fibre reinforced polymer composites: An overview. Compos B Eng 2012;43:2883–92. https://doi.org/10.1016/J.COMPOSITESB.2012.04.053.

[144] Hasan A, Rabbi MS, Maruf Billah M. Making the lignocellulosic fibers chemically compatible for composite: A comprehensive review. Cleaner Materials 2022;4:100078. https://doi.org/10.1016/J.CLEMA.2022.100078.

[145] Werchefani M, Lacoste C, Belguith H, Gargouri A, Bradai C. Effect of chemical and enzymatic treatments of alfa fibers on polylactic acid bio-composites properties. J Compos Mater 2020;54:4959–67. https://doi.org/10.1177/0021998320941579.

[146] Li X, Tabil LG, Panigrahi S. Chemical treatments of natural fiber for use in natural fiber-reinforced composites: A review. J Polym Environ 2007;15:25–33. https://doi.org/10.1007/S10924-006-0042-3/FIGURES/3.

[147] Kalia S, Kaith BS, Kaur I. Pretreatments of natural fibers and their application as reinforcing material in polymer composites—A review. Polym Eng Sci 2009;49:1253–72. https://doi.org/10.1002/PEN.21328.

[148] Zhou Y, Fan M, Chen L. Interface and bonding mechanisms of plant fibre composites: An overview. Compos B Eng 2016;101:31–45. https://doi.org/10.1016/J.COMPOSITESB.2016.06.055.

[149] Mohanty AK, Misra M, Drzal LT. Surface modifications of natural fibers and performance of the resulting biocomposites: An overview. Compos Interfaces 2001;8:313–43. https://doi.org/10.1163/156855401753255422.

[150] Huda MS, Drzal LT, Mohanty AK, Misra M. Chopped glass and recycled newspaper as reinforcement fibers in injection molded poly(lactic acid) (PLA) composites: A comparative study. Compos Sci Technol 2006;66:1813–24. https://doi.org/10.1016/j.compscitech.2005.10.015.

[151] Le Moigne N, Otazaghine B, Corn S, Angellier-Coussy H, Bergeret A. Surfaces and Interfaces in Natural Fibre Reinforced Composites 2018:136. https://doi.org/10.1007/978-3-319-71410-3.

[152] Akin DE, Gamble GR, Morrison H, Rigsby LL, Dodd RB. Chemical and Structural Analysis of Fibre and Core Tissues from Flax? vol. 72. 1996.

[153] Md. Tahir P, Ahmed AB, SaifulAzry SOA, Ahmed Z. Retting process of some bast plant fibres and its effect on fibre quality: A review. Bioresources 2011;6:5260–81. https://doi.org/10.15376/BIORES.6.4.5260-5281.

[154] Mukhopadhyay S, Fangueiro R. Physical Modification of Natural Fibers and Thermoplastic Films for Composites — A Review. Journal of Thermoplastic Composite Materials 2009;22:135–62. https://doi.org/10.1177/0892705708091860.

[155] Gupta US, Dhamarikar M, Dharkar A, Chaturvedi S, Tiwari S, Namdeo R. Surface modification of banana fiber: A review. Mater Today Proc 2021;43:904–15. https://doi.org/10.1016/J.MATPR.2020.07.217.

[156] Yildiz S, Gümüşkaya E. The effects of thermal modification on crystalline structure of cellulose in soft and hardwood. Build Environ 2007;42:62–7. https://doi.org/10.1016/J.BUILDENV.2005.07.009.

[157] Wang S, Dai G, Yang H, Luo Z. Lignocellulosic biomass pyrolysis mechanism: A state-of-the-art review. Prog Energy Combust Sci 2017;62:33–86. https://doi.org/10.1016/J.PECS.2017.05.004.

[158] Wang S, Dai G, Yang H, Luo Z. Lignocellulosic biomass pyrolysis mechanism: A state-of-the-art review. Prog Energy Combust Sci 2017;62:33–86. https://doi.org/10.1016/J.PECS.2017.05.004.

[159] Kaboorani A, Faezipour M, Ebrahimi G. Feasibility of Using Heat Treated Wood in Wood/Thermoplastic Composites. Journal of Reinforced Plastics and Composites 2008;27:1689–99. https://doi.org/10.1177/0731684407084207.

[160] Young RA. Activation and Characterization of Fiber Surfaces for Composites 1992:115–35. https://doi.org/10.1021/BK-1992-0476.CH009.

[161] Tanasă F, Nechifor M, Teacă CA, Stanciu MC. Physical methods for the modification of the natural fibers surfaces. Surface Treatment Methods of Natural Fibres and Their Effects on Biocomposites 2022:125–46. https://doi.org/10.1016/B978-0-12-821863-1.00006-5.

[162] Zhou Z, Liu X, Hu B, Wang J, Xin D, Wang Z, et al. Hydrophobic surface modification of ramie fibers with ethanol pretreatment and atmospheric pressure plasma treatment. Surf Coat Technol 2011;205:4205–10. https://doi.org/10.1016/J.SURFCOAT.2011.03.022.

[163] Gibeop N, Lee DW, Prasad CV, Toru F, Kim BS, Song J Il. Effect of plasma treatment on mechanical properties of jute fiber/poly (lactic acid) biodegradable composites. Advanced Composite Materials 2013;22:389–99. https://doi.org/10.1080/09243046.2013.843814.

[164] Li Y, Sun J, Cheng P, Jiang Y, Zhou Z, Zhang Q, et al. Aging of hydrophobized surfaces of ramie fibers induced by atmospheric pressure plasma treatment with ethanol pretreatment. J Adhes Sci Technol 2013;27:2387–97. https://doi.org/10.1080/01694243.2013.777321.

[165] Choudhury MR, Debnath K. Analysis of tensile failure load of single-lap green composite specimen welded by high-frequency ultrasonic vibration. Mater Today Proc 2020;28:739–44. https://doi.org/10.1016/J.MATPR.2019.12.290.

[166] Saleem Z, Rennebaum H, Pudel F, Grimm E. Treating bast fibres with pectinase improves mechanical characteristics of reinforced thermoplastic composites. Compos Sci Technol 2008;68:471–6. https://doi.org/10.1016/J.COMPSCITECH.2007.06.005.

[167] Stuart T, Liu Q, Hughes M, McCall RD, Sharma HSS, Norton A. Structural biocomposites from flax—Part I: Effect of bio-technical fibre modification on composite properties. Compos Part A Appl Sci Manuf 2006;37:393–404. https://doi.org/10.1016/J.COMPOSITESA.2005.06.002.

[168] Bledzki AK, Mamun AA, Lucka-Gabor M, Gutowski VS. The effects of acetylation on properties of flax fibre and its polypropylene composites. Express Polym Lett 2008;2:413–22. https://doi.org/10.3144/expresspolymlett.2008.50.

[169] Herbst G, Aguado RJ, Tarrés Q, Corazza ML, Ramos LP, Mutjé P, et al. Silane-modified high-yield lignocellulosic fibers as reinforcement of polylactic acid: Enhancement of interfacial adhesion for high-performance biocomposites. Ind Crops Prod 2024;218:119027. https://doi.org/10.1016/J.INDCROP.2024.119027.

[170] George J, Sreekala MS, Thomas S. A review on interface modification and characterization of natural fiber reinforced plastic composites. Polym Eng Sci 2001;41:1471–85. https://doi.org/10.1002/PEN.10846.

[171] Mishra, P. K., Gregor, T., and Wimmer, R. Utilising brewer's spent grain as a source of cellulose nanofibres following separation of protein-based biomass. *BioRes.* 2017;12(1), 107-116.

[172] Paul SA, Pothan LA, Thomas S. Advances in the Characterization of Interfaces of Lignocellulosic Fiber Reinforced Composites. Characterization of Lignocellulosic Materials 2009:249–74. https://doi.org/10.1002/9781444305425.CH14.

[173] Magagula SI, Mochane MJ, Lenetha GG, Sefadi JS, Mokhothu TH, Mokhena TC. The effect of alkaline treatment on natural fibers/biopolymer composites. Surface Treatment Methods of Natural Fibres and Their Effects on Biocomposites 2022:19–45. https://doi.org/10.1016/B978-0-12-821863-1.00002-8.

[174] Sahu P, Gupta MK. A review on the properties of natural fibres and its bio-composites: Effect of alkali treatment. Proceedings of the Institution of Mechanical Engineers, Part L: Journal of Materials: Design and Applications 2020;234:198–217. https://doi.org/10.1177/1464420719875163.

[175] Chandrasekar M, Ishak MR, Sapuan SM, Leman Z, Jawaid M. A review on the characterisation of natural fibres and their composites after alkali treatment and water absorption. Plastics, Rubber and Composites 2017;46:119–36. https://doi.org/10.1080/14658011.2017.1298550.

[176] Obi Reddy K, Uma Maheswari C, Shukla M, Song JI, Varada Rajulu A. Tensile and structural characterization of alkali treated Borassus fruit fine fibers. Compos B Eng 2013;44:433–8. https://doi.org/10.1016/J.COMPOSITESB.2012.04.075.

[177] Mishra S, Mohanty AK, Drzal LT, Misra M, Parija S, Nayak SK, et al. Studies on mechanical performance of biofibre/glass reinforced polyester hybrid composites. Compos Sci Technol 2003;63:1377–85. https://doi.org/10.1016/S0266-3538(03)00084-8.

[178] Wong KJ, Yousif BF, Low KO. The effects of alkali treatment on the interfacial adhesion of bamboo fibres. Proceedings of the Institution of Mechanical Engineers, Part L: Journal of Materials: Design and Applications 2010;224:139–48. https://doi.org/10.1243/14644207JMDA304.

[179] Rabbani FA, Sulaiman M, Tabasum F, Yasin S, Iqbal T, Shahbaz M, et al. Investigation of tribo-mechanical performance of alkali treated rice-husk and polypropylene-random-copolymer based biocomposites. Heliyon 2023;9. https://doi.org/10.1016/J.HELIYON.2023.E22028.

[180] Kamarudin SH, Abdullah LC, Aung MM, Ratnam CT, Jusoh Talib ER. A study of mechanical and morphological properties of PLA based biocomposites prepared with EJO vegetable oil based plasticiser and kenaf fibres. Mater Res Express 2018;5:085314. https://doi.org/10.1088/2053-1591/AABB89.

[181] El-Abbassi FE, Assarar M, Ayad R, Lamdouar N. Effect of alkali treatment on Alfa fibre as reinforcement for polypropylene based eco-composites: Mechanical behaviour and water ageing. Compos Struct 2015;133:451–7. https://doi.org/10.1016/J.COMPSTRUCT.2015.07.112.

[182] Orue A, Eceiza A, Arbelaiz A. The use of alkali treated walnut shells as filler in plasticized poly(lactic acid) matrix composites. Ind Crops Prod 2020;145:111993. https://doi.org/10.1016/J.INDCROP.2019.111993.

[183] Jacob M, Thomas S, Varughese KT. Mechanical properties of sisal/oil palm hybrid fiber reinforced natural rubber composites. Compos Sci Technol 2004;64:955–65. https://doi.org/10.1016/S0266-3538(03)00261-6.

[184] Anuar H, Rahman NAA, Manshor MR, Alli YA, Alimi OA, Alif F, et al. Novel soda lignin/PLA/EPO biocomposite: A promising and sustainable material for 3D printing filament. Mater Today Commun 2023;35. https://doi.org/10.1016/j.mtcomm.2023.106093.

[185] Aydın M, Tozlu H, Kemaloglu S, Aytac A, Ozkoc G. Effects of Alkali Treatment on the Properties of Short Flax Fiber-Poly(Lactic Acid) Eco-Composites. J Polym Environ 2011;19:11–7. https://doi.org/10.1007/S10924-010-0233-9/FIGURES/10.

[186] Dos Santos DM, De Lacerda Bukzem A, Ascheri DPR, Signini R, De Aquino GLB. Microwave-assisted carboxymethylation of cellulose extracted from brewer's spent grain. Carbohydr Polym 2015;131:125–33. https://doi.org/10.1016/J.CARBPOL.2015.05.051.

[187] Mussatto SI, Dragone G, Rocha GJM, Roberto IC. Optimum operating conditions for brewer's spent grain soda pulping. Carbohydr Polym 2006;64:22–8. https://doi.org/10.1016/J.CARBPOL.2005.10.033.

[188] Moreirinha C, Vilela C, Silva NHCS, Pinto RJB, Almeida A, Rocha MAM, et al. Antioxidant and antimicrobial films based on brewers spent grain arabinoxylans, nanocellulose and feruloylated compounds for active packaging. Food Hydrocoll 2020;108:105836. https://doi.org/10.1016/J.FOODHYD.2020.105836.

[189] Reis SF, Coelho E, Coimbra MA, Abu-Ghannam N. Influence of grain particle sizes on the structure of arabinoxylans from brewer's spent grain. Carbohydr Polym 2015;130:222–6. https://doi.org/10.1016/J.CARBPOL.2015.05.031.

[190] Hejna A, Barczewski M, Kosmela P, Mysiukiewicz O, Sulima P, Przyborowski JA, et al. Mater-Bi/Brewers' Spent Grain Biocomposites-Novel Approach to Plant-Based Waste Filler Treatment by Highly Efficient Thermomechanical and Chemical Methods. Materials (Basel) 2022;15. https://doi.org/10.3390/MA15207099.

[191] Fowler PA, Hughes JM, Elias RM. Biocomposites: technology, environmental credentials and market forces. J Sci Food Agric 2006;86:1781–9. https://doi.org/10.1002/JSFA.2558.

[192] Alves TS, Silva Neto JE, Silva SML, Carvalho LH, Canedo EL. Process simulation of laboratory internal mixers. Polym Test 2016;50:94–100. https://doi.org/10.1016/J.POLYMERTESTING.2016.01.002.

[193] Shih YF, Huang CC. Polylactic acid (PLA)/banana fiber (BF) biodegradable green composites. Journal of Polymer Research 2011;18:2335–40. https://doi.org/10.1007/S10965-011-9646-Y/FIGURES/4.

[194] Gallos A, Paës G, Allais F, Beaugrand J. Lignocellulosic fibers: a critical review of the extrusion process for enhancement of the properties of natural fiber composites. RSC Adv 2017;7:34638–54. https://doi.org/10.1039/C7RA05240E.

[195] Sawpan MA, Pickering KL, Fernyhough A. Improvement of mechanical performance of industrial hemp fibre reinforced polylactide biocomposites. Compos Part A Appl Sci Manuf 2011;42:310–9. https://doi.org/10.1016/J.COMPOSITESA.2010.12.004.

[196] Gamon G, Evon P, Rigal L. Twin-screw extrusion impact on natural fibre morphology and material properties in poly(lactic acid) based biocomposites. Ind Crops Prod 2013;46:173–85. https://doi.org/10.1016/J.INDCROP.2013.01.026.

[197] Cisneros FH, Kokini JL. A generalized theory linking barrel fill length and air bubble entrapment during extrusion of starch. J Food Eng 2002;51:139–49. https://doi.org/10.1016/S0260-8774(01)00050-4.

[198] Bledzki AK, Franciszczak P, Osman Z, Elbadawi M. Polypropylene biocomposites reinforced with softwood, abaca, jute, and kenaf fibers. Ind Crops Prod 2015;70:91–9. https://doi.org/10.1016/J.INDCROP.2015.03.013.

[199] Zouari M, Devallance DB, Marrot L. Effect of Biochar Addition on Mechanical Properties, Thermal Stability, and Water Resistance of Hemp-Polylactic Acid (PLA) Composites. Materials 2022;15. https://doi.org/10.3390/ma15062271.

[200] Koutsomitopoulou AF, Bénézet JC, Bergeret A, Papanicolaou GC. Preparation and characterization of olive pit powder as a filler to PLA-matrix bio-composites. Powder Technol 2014;255:10–6. https://doi.org/10.1016/J.POWTEC.2013.10.047.

[201] Clemons C. Wood-plastic composites in the United States : the interfacing of two industries. Forest Products Journal Vol 52, No 6 (June 2002): Pages 10-18 2002.

[202] Rueda MM, Auscher MC, Fulchiron R, Périé T, Martin G, Sonntag P, et al. Rheology and applications of highly filled polymers: A review of current understanding. Prog Polym Sci 2017;66:22–53. https://doi.org/10.1016/j.progpolymsci.2016.12.007.

[203] Barnes, Howard. A review of the rheology of filled viscoelastic systems. Rheol. 2003;Rev.. 1.

[204] Mayadunne A, Bhattacharya SN, Kosior E. Modelling of packing behavior of irregularly shaped particles dispersed in a polymer matrix. Powder Technol 1996;89:115–27. https://doi.org/10.1016/S0032-5910(96)03155-5.

[205] Zugenmaier P. Materials of cellulose derivatives and fiber-reinforced cellulose-polypropylene composites: Characterization and application. Pure and Applied Chemistry 2006;78:1843–55. https://doi.org/10.1351/PAC200678101843/MACHINEREADABLECITATION/RIS.

[206] Premalal HGB, Ismail H, Baharin A. Effect of Processing Time on the Tensile, Morphological, and Thermal Properties of Rice Husk Powder-Filled Polypropylene Composites. Polym Plast Technol Eng 2003;42:827–51. https://doi.org/10.1081/PPT-120024998.

[207] Dong Y, Ghataura A, Haroosh HJ. Mechanical, thermal, and biodegradable properties of polylactic acid (PLA)/coir fibre biocomposites. Https://DoiOrg/101117/122026927 2013;8793:7–12. https://doi.org/10.1117/12.2026927.

[208] Cheng, Shichao & Huang, Anmin & Wang, Shennan & Zhang, Qiuhui. Effect of Different Heat Treatment Temperatures on the Chemical Composition and Structure of Chinese Fir Wood. Bioresources 2016;4006-4016. 10.15376/biores.11.2.4006-4016.

[209] Zhiltsova T, Campos J, Costa A, Oliveira MSA. Sustainable Polypropylene-Based Composites with Agro-Waste Fillers: Thermal, Morphological, Mechanical Properties and Dimensional Stability. Materials 2024;17:696. https://doi.org/10.3390/MA17030696.

[210] Fayzullin I, Gorbachev A, Volfson S, Zhakypova G, Uderbayev S, Nakyp A, et al. Influence of Different Dosages of Rice Husk Particles on Thermal, Physical, Mechanical and Rheological Properties of Polypropylene-Based Composites. Journal of Composites Science 2025;9:443. https://doi.org/10.3390/JCS9080443/S1.

[211] Tisserat B, Reifschneider L, Carlos López Núñez J, Hughes SR, Selling G, Finkenstadt VL. Coffee tree PP composites. Bioresources 2014;9:4449–67.

[212] Yang HS, Kim HJ, Son J, Park HJ, Lee BJ, Hwang TS. Rice-husk flour filled polypropylene composites; mechanical and morphological study. Compos Struct 2004;63:305–12. https://doi.org/10.1016/S0263-8223(03)00179-X.

[213] Cheng S, Lau K tak, Liu T, Zhao Y, Lam PM, Yin Y. Mechanical and thermal properties of chicken feather fiber/PLA green composites. Compos B Eng 2009;40:650–4. https://doi.org/10.1016/j.compositesb.2009.04.011.

[214] Ahmed S, Jones FR. A review of particulate reinforcement theories for polymer composites. vol. 25. 1990.

[215] Counto UJ. The effect of the elastic modulus of the aggregate on the elastic modulus, creep and creep recovery of concrete. Magazine of Concrete Research 1 September 1964; 16 (48): 129–138. https://doi.org/10.1680/macr.1964.16.48.129

[216] Guth E. Theory of filler reinforcement. J Appl Phys 1945;16:20–5. https://doi.org/10.1063/1.1707495.

[217] M. Mooney,The viscosity of a concentrated suspension of spherical particles,Journal of Colloid Science,Volume 6, Issue 2,1951;ISSN 0095-8522,https://doi.org/10.1016/0095-8522(51)90036-0.

[218] Smallwood HM. Limiting law of the reinforcement of rubber. J Appl Phys 1944;15:758–66. https://doi.org/10.1063/1.1707385.

[219] Brodnyan JG. The Concentration Dependence of the Newtonian Viscosity of Prolate Ellipsoids. Transactions of the Society of Rheology 1959;3:61–8. https://doi.org/10.1122/1.548843.

[220] Kerner EH. The Elastic and Thermo-elastic Properties of Composite Media. Proceedings of the Physical Society B 1956; DOI: 10.1088/0370-1301/69/8/305

[221] Halpin, John C.. Stiffness and Expansion Estimates for Oriented Short Fiber Composites. Journal of Composite Materials 3 1969;732 - 734.

[222] Nielsen LE. Generalized equation for the elastic moduli of composite materials. J Appl Phys 1970;41:4626–7. https://doi.org/10.1063/1.1658506.

[223] Facca AG, Kortschot MT, Yan N. Predicting the elastic modulus of natural fibre reinforced thermoplastics. Compos Part A Appl Sci Manuf 2006;37:1660–71. https://doi.org/10.1016/J.COMPOSITESA.2005.10.006.

[224] Fu SY, Feng XQ, Lauke B, Mai YW. Effects of particle size, particle/matrix interface adhesion and particle loading on mechanical properties of particulate-polymer composites. Compos B Eng 2008;39:933–61. https://doi.org/10.1016/j.compositesb.2008.01.002.

[225] Nielsen LE. Simple theory of stress-strain properties of filled polymers. J Appl Polym Sci 1966;10:97–103. https://doi.org/10.1002/app.1966.070100107.

[226] Nicolais L, Narkis M, Louis S. Stress-Strain Behavior of Styrene-Acrylonitrile/Glass Bead Composites in the Glassy Region. 1971.

[227] Mokhothu TH, Mtibe A, Mokhena TC, Mochane MJ. Influence of silane modification on the properties of natural fibers and its effect on biocomposites. Surface Treatment Methods of Natural Fibres and Their Effects on Biocomposites 2022:67–93. https://doi.org/10.1016/B978-0-12-821863-1.00004-1.

[228] Gamstedt EK. Moisture induced softening and swelling of natural cellulose fibres in composite applications. IOP Conf Ser Mater Sci Eng 2016;139. https://doi.org/10.1088/1757-899X/139/1/012003.

[229] Alomayri T, Assaedi H, Shaikh FUA, Low IM. Effect of water absorption on the mechanical properties of cotton fabric-reinforced geopolymer composites. Journal of Asian Ceramic Societies 2014;2:223–30. https://doi.org/10.1016/J.JASCER.2014.05.005.

[230] Sluiter AD, Templeton DW. Determination of Structural Carbohydrates and Lignin in Biomass: Laboratory Analytical Procedure (LAP) (Revised July 2011). n.d.

[231] Test Method for Tensile Properties of Plastics 2014. https://doi.org/10.1520/D0638-14.

[232] Sobek S, Zeng K, Werle S, Junga R, Sajdak M. Brewer's spent grain pyrolysis kinetics and evolved gas analysis for the sustainable phenolic compounds and fatty acids recovery potential. Renew Energy 2022;199:157–68. https://doi.org/10.1016/j.renene.2022.08.114.

[233] Zhang Q, Shi L, Nie J, Wang H, Yang D. Study on poly(lactic acid)/natural fibers composites. J Appl Polym Sci 2012;125. https://doi.org/10.1002/app.36852.

[234] Wang L, Wang Y nan, Huang Z gang, Weng Y xuan. Heat resistance, crystallization behavior, and mechanical properties of polylactide/nucleating agent composites. Mater Des 2015;66:7–15. https://doi.org/10.1016/j.matdes.2014.10.011.

[235] Blahovec J, Yanniotis S. Gab generalized equation for sorption phenomena. Food Bioproc Tech 2008;1:82–90. https://doi.org/10.1007/S11947-007-0012-3/FIGURES/8.

[236] Bousmina M, Ait-Kadi A, Faisant JB. Determination of shear rate and viscosity from batch mixer data. J Rheol (N Y N Y) 1999;43:415–33. https://doi.org/10.1122/1.551044.

[237] ISO 527-2:2012. Plastics-Determinations of tensile properties - Part 2: Test conditions for moulding and extrusion plastics. 2012.

[238] Inocêncio Silva NF, Soares Filho JE, Cabral Santos TG, da Silva Chagas J, Lucena de Medeiros SAS, Costa Santos EB, et al. Biocomposites based on poly(hydroxybutyrate) and the mesocarp of babassu coconut (Orbignya phalerata Mart.): effect of wax removal and maleic anhydride-modified polyethylene addition. Journal of Materials Research and Technology 2021;15:3161–70. https://doi.org/10.1016/J.JMRT.2021.09.008.

[239] Rueda MM, Fulchiron R, Martin G, Cassagnau P. Rheology of polypropylene filled with short-glass fibers: From low to concentrated filled composites. Eur Polym J 2017;93:167–81. https://doi.org/10.1016/J.EURPOLYMJ.2017.05.025.

[240] Abdoos H, Khorsand H, Yousefi AA. Torque rheometry and rheological analysis of powder–polymer mixture for aluminum powder injection molding. Iranian Polymer Journal (English Edition) 2014;23:745–55. https://doi.org/10.1007/s13726-014-0268-1.

[241] Dolezal PT, Johnson PS. Contribution of Power Profiles to Mixing Efficiency. Rubber Chemistry and Technology 2011;53:252–69. https://doi.org/10.5254/1.3535039.

[242] Carnicer V, Alcázar C, Orts MJ, Sánchez E, Moreno R. Microfluidic rheology: A new approach to measure viscosity of ceramic suspensions at extremely high shear rates. Open Ceramics 2021;5:100052. https://doi.org/10.1016/J.OCERAM.2020.100052.

[243] Agustin-Salazar S, Ricciulli M, Ambrogi V, Cerruti P, Scarinzi G. Effect of thermal annealing and filler ball-milling on the properties of highly filled polylactic acid/pecan nutshell biocomposites. Int J Biol Macromol 2022;200:350–61. https://doi.org/10.1016/J.IJBIOMAC.2021.12.101.

[244] Lv P, Almeida G, Perré P. TGA-FTIR analysis of torrefaction of lignocellulosic components (cellulose, xylan, lignin) in isothermal conditions over a wide range of time durations. Bioresources 2015;10:4239–51. https://doi.org/10.15376/biores.10.3.4239-4251.

[245] Yang H, Yan R, Chen H, Zheng C, Lee DH, Liang DT. In-depth investigation of biomass pyrolysis based on three major components: Hemicellulose, cellulose and lignin. Energy and Fuels 2006;20:388–93. https://doi.org/10.1021/ef0580117.

[246] Inseemeesak B, Siripaiboon C, Somkeattikul K, Attasophonwattana P, Kiatiwat T, Punsuvon V, et al. Biocomposite fabrication from pilot-scale steam-exploded coconut fiber and PLA/PBS with mechanical and thermal characterizations. J Clean Prod 2022;379. https://doi.org/10.1016/j.jclepro.2022.134517.

[247] Rahman NA, Hassan A, Yahya R, Lafia-Araga RA, Hornsby PR. Micro-structural, thermal, and mechanical properties of injection-molded glass fiber/nanoclay/polypropylene composites. Journal of Reinforced Plastics and Composites 2012;31:269–81. https://doi.org/10.1177/0731684411435727.

[248] Mandal DK, Bhunia H, Bajpai PK. Thermal degradation kinetics of PP/PLA nanocomposite blends. Journal of Thermoplastic Composite Materials 2019;32:1714–30. https://doi.org/10.1177/0892705718805130.

[249] Stawski D. The effect of sample weight in thermogravimetric analysis of low viscosity polypropylene in air atmosphere. Polym Test 2009;28:223–5. https://doi.org/10.1016/j.polymertesting.2008.12.003.

[250] Rjeb M, Labzour A, Rjeb A, Sayouri S, Claire Y, Périchaud A. TG and DSC studies of natural and artificial aging of polypropylene. Physica A: Statistical Mechanics and its Applications, vol. 358, Elsevier; 2005, p. 212–7. https://doi.org/10.1016/j.physa.2005.06.023.

[251] Martí-Ferrer F, Vilaplana F, Ribes-Greus A, Benedito-Borrás A, Sanz-Box C. Flour rice husk as filler in block copolymer polypropylene: Effect of different coupling agents. J Appl Polym Sci 2006;99:1823–31. https://doi.org/10.1002/app.22717.

[252] Zhang J, Liang Y, Yan J, Lou J. Study of the molecular weight dependence of glass transition temperature for amorphous poly(l-lactide) by molecular dynamics simulation. Polymer (Guildf) 2007;48:4900–5. https://doi.org/10.1016/j.polymer.2007.06.030.

[253] Di Lorenzo ML. Calorimetric analysis of the multiple melting behavior of poly(L-lactic acid). J Appl Polym Sci 2006;100:3145–51. https://doi.org/10.1002/app.23136.

[254] Guo R, Azaiez J, Bellehumeur C. Rheology of fiber filled polymer melts: Role of fiber-fiber interactions and polymer-fiber coupling. Polym Eng Sci 2005;45:385–99. https://doi.org/10.1002/pen.20285.

[255] Hausnerova B, Honkova N, Kitano T, Saha P. Superposed flow properties of ceramic powder-filled polymer melts. Polym Compos 2009;30:1027–34. https://doi.org/10.1002/pc.20645.

[256] Chae DW, Kim BC. Thermal and rheological properties of highly concentrated PET composites with ferrite nanoparticles. Compos Sci Technol 2007;67:1348–52. https://doi.org/10.1016/j.compscitech.2006.09.018.

[257] Huq AMA, Azaiez J. Effects of length distribution on the steady shear viscosity of semiconcentrated polymer-fiber suspensions. Polym Eng Sci 2005;45:1357–68. https://doi.org/10.1002/pen.20415.

[258] Poslinski AJ, Ryan ME, Gupta RK, Seshadri SG, Frechette FJ. Rheological Behavior of Filled Polymeric Systems I. Yield Stress and Shear-Thinning Effects. J Rheol (N Y N Y) 1988;32:703–35. https://doi.org/10.1122/1.549987.

[259] Ramazani S. A. A, Ait-Kadi A, Grmela M. Rheology of fiber suspensions in viscoelastic media: Experiments and model predictions. J Rheol (N Y N Y) 2001;45:945–62. https://doi.org/10.1122/1.1378026.

[260] Carrot C, Majesté JC, Olalla B, Fulchiron R. On the use of the model proposed by Leonov for the explanation of a secondary plateau of the loss modulus in heterogeneous polymer-filler systems with agglomerates. Rheol Acta 2010;49:513–27. https://doi.org/10.1007/s00397-010-0432-2.

[261] Olalla B, Carrot C, Fulchiron R, Boudimbou I, Peuvrel-Disdier E. Analysis of the influence of polymer viscosity on the dispersion of magnesium hydroxide in a polyolefin matrix. Rheol Acta 2012;51:235–47. https://doi.org/10.1007/s00397-011-0580-z.

[262] Kaully T, Siegmann A, Shacham D. Rheology of highly filled natural CaCO3 composites. II. Effects of solid loading and particle size distribution on rotational rheometry. Polym Compos 2007;28:524–33. https://doi.org/10.1002/pc.20309.

[263] Feger C, Gelorme JD, McGlashan-Powell M, Kalyon DM. Mixing, rheology, and stability of highly filled thermal pastes. IBM J Res Dev 2005;49:699–707. https://doi.org/10.1147/rd.494.0699.

[264] Părpăriţă E, Darie RN, Popescu CM, Uddin MA, Vasile C. Structure-morphology-mechanical properties relationship of some polypropylene/lignocellulosic composites. Mater Des 2014;56:763–72. https://doi.org/10.1016/j.matdes.2013.12.033.

[265] Huda MS, Drzal LT, Misra M, Mohanty AK. Wood-fiber-reinforced poly(lactic acid) composites: Evaluation of the physicomechanical and morphological properties. J Appl Polym Sci 2006;102:4856–69. https://doi.org/10.1002/app.24829.

[266] Hoffmann K, Huber G, Mäder D. Nucleating and clarifying agents for polyolefins. Macromol Symp, vol. 176, John Wiley and Sons Ltd; 2001, p. 83–92. https://doi.org/10.1002/1521-3900(200112)176:1<83::AID-MASY83>3.0.CO;2-N.

[267] Bajpai PK, Singh I, Madaan J. Comparative studies of mechanical and morphological properties of polylactic acid and polypropylene based natural fiber composites. Journal of Reinforced Plastics and Composites 2012;31:1712–24. https://doi.org/10.1177/0731684412447992.

[268] Bax B, Müssig J. Impact and tensile properties of PLA/Cordenka and PLA/flax composites. Compos Sci Technol 2008;68:1601–7. https://doi.org/10.1016/j.compscitech.2008.01.004.

[269] Le Duigou A, Bourmaud A, Davies P, Baley C. Long term immersion in natural seawater of Flax/PLA biocomposite. Ocean Engineering 2014;90:140–8. https://doi.org/10.1016/J.OCEANENG.2014.07.021.

[270] Dönmez Çavdar A, Kalaycioğlu H, Mengeloğlu F. Tea mill waste fibers filled thermoplastic composites: The effects of plastic type and fiber loading. Journal of Reinforced Plastics and Composites 2011;30:833–44. https://doi.org/10.1177/0731684411408752.

[271] Arbelaiz A, Fernández B, Ramos JA, Retegi A, Llano-Ponte R, Mondragon I. Mechanical properties of short flax fibre bundle/polypropylene composites: Influence of matrix/fibre modification, fibre content, water uptake and recycling. Compos Sci Technol 2005;65:1582–92. https://doi.org/10.1016/J.COMPSCITECH.2005.01.008.

[272] Tajvidi M, Ebrahimi G. Water uptake and mechanical characteristics of natural filler–polypropylene composites. J Appl Polym Sci 2003;88:941–6. https://doi.org/10.1002/APP.12029.

[273] Azwa ZN, Yousif BF, Manalo AC, Karunasena W. A review on the degradability of polymeric composites based on natural fibres. Mater Des 2013;47:424–42. https://doi.org/10.1016/J.MATDES.2012.11.025.

[274] Zheng J, Rehmann L. Extrusion pretreatment of lignocellulosic biomass: a review. Int J Mol Sci 2014;15:18967–84. https://doi.org/10.3390/IJMS151018967.

[275] Tapía MS, Alzamora SM, Chirife J. Effects of Water Activity (aw) on Microbial Stability as a Hurdle in Food Preservation. Water Activity in Foods: Fundamentals and Applications 2020:323–55. https://doi.org/10.1002/9781118765982.CH14.

[276] Yoo J, Alavi S, Vadlani P, Amanor-Boadu V. Thermo-mechanical extrusion pretreatment for conversion of soybean hulls to fermentable sugars. Bioresour Technol 2011;102:7583–90. https://doi.org/10.1016/J.BIORTECH.2011.04.092.

[277] Schell DJ, Harwood C. Milling of lignocellulosic biomass - Results of pilot-scale testing. Appl Biochem Biotechnol 1994;45–46:159–68. https://doi.org/10.1007/BF02941795/METRICS.

[278] Berthet MA, Commandré JM, Rouau X, Gontard N, Angellier-Coussy H. Torrefaction treatment of lignocellulosic fibres for improving fibre/matrix adhesion in a biocomposite. Mater Des 2016;92:223–32. https://doi.org/10.1016/J.MATDES.2015.12.034.

[279] Bhuiyan MTR, Hirai N, Sobue N. Changes of crystallinity in wood cellulose by heat treatment under dried and moist conditions. Journal of Wood Science 2000;46:431–6. https://doi.org/10.1007/BF00765800/METRICS.

[280] Repellin V, Govin A, Rolland M, Guyonnet R. Energy requirement for fine grinding of torrefied wood. Biomass Bioenergy 2010;34:923–30. https://doi.org/10.1016/J.BIOMBIOE.2010.01.039.

[281] Saleh SB, Hansen BB, Jensen PA, Dam-Johansen K. Efficient Fuel Pretreatment: Simultaneous Torrefaction and Grinding of Biomass. Energy and Fuels 2013;27:7531–40. https://doi.org/10.1021/EF401787Q.

[282] Bridgeman TG, Darvell LI, Jones JM, Williams PT, Fahmi R, Bridgwater A V., et al. Influence of particle size on the analytical and chemical properties of two energy crops. Fuel 2007;86:60–72. https://doi.org/10.1016/J.FUEL.2006.06.022.

[283] Bindu P, Thomas S. Viscoelastic behavior and reinforcement mechanism in rubber nanocomposites in the vicinity of spherical nanoparticles. J Phys Chem B 2013;117:12632–48. https://doi.org/10.1021/JP4039489.

[284] Hejna A, Barczewski M, Skórczewska K, Szulc J, Chmielnicki B, Korol J, et al. Sustainable upcycling of brewers' spent grain by thermo-mechanical treatment in twin-screw extruder. J Clean Prod 2021;285. https://doi.org/10.1016/j.jclepro.2020.124839.

[285] Odalanowska M, Borysiak S. Influence of wood thermal modification on the supermolecular structure of polypropylene composites. Polym Compos 2021;42:2087–100. https://doi.org/10.1002/PC.25961.

[286] Singh MK, Arora G, Tewari R, Zafar S, Pathak H, Sehgal AK. Effect of pine cone filler particle size and treatment on the performance of recycled thermoplastics reinforced

wood composites. Mater Today Proc 2022;62:7358–63. https://doi.org/10.1016/J.MATPR.2022.02.022.

[287] Serra-parareda F, Vilaseca F, Aguado R, Espinach FX, Tarrés Q, Delgado-aguilar M. Effective Young's Modulus Estimation of Natural Fibers through Micromechanical Models: The Case of Henequen Fibers Reinforced-PP Composites. Polymers 2021, Vol 13, Page 3947 2021;13:3947. https://doi.org/10.3390/POLYM13223947.

[288] Fruleux T, Castro M, Sauleau P, Matsuzaki R, Le Duigou A. Matrix stiffness: A key parameter to control hydro-elasticity and morphing of 3D printed biocomposite. Compos Part A Appl Sci Manuf 2022;156:106882. https://doi.org/10.1016/J.COMPOSITESA.2022.106882.

[289] Yu S, Song S, Gao H, Wang K, Xu L, Guo H, et al. Crystallinity and mechanical properties of polypropylene products foamed by microcellular injection molding process. J Appl Polym Sci 2024;141:e55418. https://doi.org/10.1002/APP.55418.

[290] Mendoza R, Régnier G, Seiler W, Lebrun JL. Spatial distribution of molecular orientation in injection molded iPP: influence of processing conditions. Polymer (Guildf) 2003;44:3363–73. https://doi.org/10.1016/S0032-3861(03)00253-2.

[291] Wang W, Zhao G, Wu X, Zhai Z. The effect of high temperature annealing process on crystallization process of polypropylene, mechanical properties, and surface quality of plastic parts. J Appl Polym Sci 2015;132. https://doi.org/10.1002/APP.42773.

[292] Parenteau T, Ausias G, Grohens Y, Pilvin P. Structure, mechanical properties and modelling of polypropylene for different degrees of crystallinity. Polymer (Guildf) 2012;53:5873–84. https://doi.org/10.1016/J.POLYMER.2012.09.053.

[293] Van Der Wal A, Mulder JJ, Gaymans RJ. Fracture of polypropylene: The effect of crystallinity. Polymer (Guildf) 1998;39:5477–81. https://doi.org/10.1016/S0032-3861(97)10279-8.

[294] Chetrariu A, Dabija A. Brewer's spent grains: Possibilities of valorization, a review. Applied Sciences (Switzerland) 2020;10. https://doi.org/10.3390/app10165619.

[295] Naibaho J, Korzeniowska M. The variability of physico-chemical properties of brewery spent grain from 8 different breweries. Heliyon 2021;7. https://doi.org/10.1016/j.heliyon.2021.e06583.

[296] Boeriu CG, Bravo D, Gosselink RJA, Van Dam JEG. Characterisation of structure-dependent functional properties of lignin with infrared spectroscopy. Ind Crops Prod 2004;20:205–18. https://doi.org/10.1016/J.INDCROP.2004.04.022.

[297] Ribeiro-Sanches MA, Stochi VAL, Borges-Machado AL, Augusto PED, Polachini TC, Telis-Romero J. Valorization of brewer's spent grains (BSG) through alkaline hydrogen peroxide processing: Effect on composition, structure and rheological properties. Food and Bioproducts Processing 2024;147:239–50. https://doi.org/10.1016/J.FBP.2024.07.008.

[298] Chin YL, Keppler JK, Dinani ST, Chen WN, Boom R. Brewers' spent grain proteins: The extraction method determines the functional properties. Innovative Food Science & Emerging Technologies 2024;94:103666. https://doi.org/10.1016/J.IFSET.2024.103666.

[299] Bano S, Negi YS. Studies on cellulose nanocrystals isolated from groundnut shells. Carbohydr Polym 2017;157:1041–9. https://doi.org/10.1016/J.CARBPOL.2016.10.069.

[300] Laaziz SA, Raji M, Hilali E, Essabir H, Rodrigue D, Bouhfid R, et al. Bio-composites based on polylactic acid and argan nut shell: Production and properties. Int J Biol Macromol 2017;104:30–42. https://doi.org/10.1016/J.IJBIOMAC.2017.05.184.

[301] Vishnu Vardhini KJ, Murugan R, Selvi T, Surjit & R. Optimisation of alkali treatment of banana fibres on lignin removal. Indian J Fibre Text Res 2016;41:156–60.

[302] Geremew A, De Winne P, Demissie TA, De Backer H. Surface modification of bamboo fibers through alkaline treatment: Morphological and physical characterization for composite reinforcement. Journal of Engineered Fibers and Fabrics 2024;19. https://doi.org/10.1177/15589250241248764/ASSET/54231434-AA66-4474-BC0F-CCB0790685EA/ASSETS/IMAGES/LARGE/10.1177_15589250241248764-FIG10.JPG.

[303] Malaret F, Nakasu PYS, Verdía Barbará P, Hopson C, Hallett J. Relationship Between Density and Structure of Lignins Obtained from Different Feedstocks Pretreated with Protic Ionic Liquids. Processes 2025;13:1848. https://doi.org/10.3390/PR13061848/S1.

[304] Sun C. True density of microcrystalline cellulose. J Pharm Sci 2005;94:2132–4. https://doi.org/10.1002/JPS.20459.

[305] Kitano T, Kataoka T, Shirota T. An empirical equation of the relative viscosity of polymer melts filled with various inorganic fillers. Rheol Acta 1981;20:207–9. https://doi.org/10.1007/BF01513064/METRICS.

[306] Genovese DB. Shear rheology of hard-sphere, dispersed, and aggregated suspensions, and filler-matrix composites. Adv Colloid Interface Sci 2012;171–172:1–16. https://doi.org/10.1016/J.CIS.2011.12.005.

[307] Peng Y, Wu S. The structural and thermal characteristics of wheat straw hemicellulose. J Anal Appl Pyrolysis 2010;88:134–9. https://doi.org/10.1016/J.JAAP.2010.03.006.

[308] Li YC, Wang S, Qian S, Liu Z, Weng Y, Zhang Y. Depolymerization and Re/Upcycling of Biodegradable PLA Plastics. ACS Omega 2024;9:13509–21. https://doi.org/10.1021/ACSOMEGA.3C08674.

[309] Rueda Martha Margarita Rueda. Rheology and processing of highly filled materials. Materials. Université de Lyon, 2017. English. NNT: 2017LYSE1052. tel-01537585

[310] kasei plastics. https://www.asahi-kasei-plastics.com/en/knowledge-cae/plastics-cae4/ 2025.

[311] HAAKE Practical Approach To Rheology and Rheometry - Schramm | PDF | Viscosity | Shear Stress n.d. https://www.scribd.com/document/57210238/HAAKE-Practical-Approach-to-Rheology-and-Rheometry-Schramm (accessed September 28, 2025).

[312] Mazzanti V, Mollica F. A Review of Wood Polymer Composites Rheology and Its Implications for Processing. Polymers (Basel) 2020;12:1–23. https://doi.org/10.3390/POLYM12102304.

[313] Razavi-Nouri M, Jafarzadeh-Dogouri F, Oromiehie A, Langroudi AE. Mechanical Properties and Water Absorption Behaviour of Chopped Rice Husk Filled Polypropylene Composites. vol. 15. 2006.

# ANNEXES

Distributed by RESINEX

# Braskem PP H357-09RSB

## Braskem Europe GmbH - Homopolymère polypropylène

Thursday, March 3, 2022

### Informations générales

**Description du produit**

BRASKEM H357-09RSB resin is a Polypropylene homopolymer suitable for high output, fast running cast film lines and injection molding processes. BRASKEM Polypropylene H357-09RSB is a controlled rheology resin optimized for easy film winding and cutting as well as good printability after corona treatment. Films based on Braskem Polypropylene H357-09RSB exhibit excellent optical film properties. Braskem Polypropylene H357-09RSB resin contains slip and antiblocking additives.

Applications:

- Food packaging (bakery, snacks)
- Textile packaging (shirts, hosiery, blankets, sweaters)
- Printed materials (books, magazines, journals, stationary)

Process:

- Cast film
- Injection molding

| Généralités | | | |
|---|---|---|---|
| État du matériau | • Commercial : actif | | |
| Disponibilité | • Europe | | |
| Additif | • Antiadhérent | • Glissement | |
| Caractéristiques | • Antibloquant<br>• Effets optiques | • Glissement<br>• Good Printability | • Homopolymère<br>• Rhéologie contrôlée |
| Applications | • Emballage<br>• Emballage alimentaire | • Film<br>• Fournitures de papeterie | • Pellicule moulée |
| Process/Méthode de transformation | • Moulage par injection | • Pellicule moulée | |

### Propriétés ASTM et ISO [1]

| Physique | Valeur nominale | Unité | Méthode de test |
|---|---|---|---|
| Densité | 0.900 | g/cm³ | ISO 1183 |
| Indice de fluidité à chaud en masse (MFR) | | | ISO 1133 |
| 230°C/2,16 kg | 9.5 | g/10 min | |
| **Mécanique** | **Valeur nominale** | **Unité** | **Méthode de test** |
| Contrainte de traction | | | ISO 527-2 |
| Élasticité, Moulé par injection | 33.0 | MPa | |
| Allongement en traction | | | ISO 527-2 |
| Élasticité, Moulé par injection | 10 | % | |
| Module de flexion - Sécant 1 % (Moulé par injection) | 1400 | MPa | ISO 178 |
| **Films** | **Valeur nominale** | **Unité** | **Méthode de test** |
| Épaisseur du film - testée | 50 | µm | |
| Contrainte de traction | | | ISO 527-3 |
| MD : Rupture, 50 µm, Pellicule moulée | 56.0 | MPa | |
| TD : Rupture, 50 µm, Pellicule moulée | 45.0 | MPa | |
| Résistance au choc du mouton (50 µm, Pellicule moulée) | 200 | g | ISO 7765-1 |
| **Choc** | **Valeur nominale** | **Unité** | **Méthode de test** |
| Essai de résilience Charpy avec entaille | | | ISO 179/1eA |
| 23°C, Moulé par injection | 4.0 | kJ/m² | |

WK Name : _____

| t(s) | | | | | | | | | | | | |
|---|---|---|---|---|---|---|---|---|---|---|---|---|
| weight 1st specimen | | | | | | | | | | | | |

NaturePlast
L'évolution naturelle du plastique

*Date de révision : 23/07/2014*

# FICHE TECHNIQUE — NATUREPLAST PLE 001

Poly (Acide Lactique) — Extrusion / Calandrage / Thermoformage

## Propriétés générales

La référence **PLE 001** est une résine thermoplastique de **PLA** (Polylactide) issue de ressources végétales annuellement renouvelables.

Le **PLE 001** est **recyclable**, **compostable** industriellement selon la norme **NF EN 13432:2000** et spécifiquement élaboré pour les applications d'extrusion (film, thermoformage, etc.).

| | Méthode | Unité | Valeur* |
|---|---|---|---|
| **Propriétés Générales** | | | |
| ***Densité*** | ASTM D792 | / | **1,24** |
| ***MFI (210°C ; 2,16 kg)*** | ASTM D1238 | g/10min | **6** |
| ***Propriétés optiques*** | / | / | **Transparent** |
| **Propriétés Thermiques** | | | |
| ***HDT Méthode B120*** | ASTM E2092 | °C | **51** |
| **Propriétés Mécaniques** | | | |
| ***Contrainte de traction au seuil élastique*** | ASTM D882 | MPa | **60** |
| ***Contrainte de traction à rupture*** | ASTM D882 | MPa | **53** |
| ***Allongement en traction à rupture*** | ASTM D882 | % | **6** |
| ***Module d'Young*** | ASTM D882 | MPa | **3 500** |
| ***Choc Izod (entaillé)*** | ASTM D256 | J/m | **16** |

**Valeurs typiques données à titre indicatif ne devant pas être considérées comme des spécifications*

## Stockage et Transformation

Les conditions de séchage et de stockage du **PLE 001**, afin d'obtenir une transformation et des propriétés optimales (i.e. taux d'humidité inférieur à 250 ppm) sont les suivantes :

**NaturePlast**
11 rue Arago ; 14123 IFS ; France / Tel : (+33)2 31 83 50 87 / Fax : (+33)2 31 84 70 98 / www.natureplast.eu
SAS au capital de 174 666 € APE : 4690Z / SIRET : 493 442 891 00047 / TVA : FR 45 49 344 2891

MALT-INFORMATION

# BEST PALE ALE

BESTMALZ

| | |
|---|---|
| THE MALT | **BEST Pale Ale** is an ideal basis for many different styles of English Ale and numerous other beers that require a fuller, golden color and a tangy but also more full-bodied taste. BEST Pale Ale complies with the purity guidelines of the German Reinheitsgebot. |
| USE | For Pale Ale, Kölsch, Pilsner and all other beer styles. |
| RATE | 100 % of the grainbill |
| PACKAGING | In bulk, sacks size 25 kg/55 lbs and 50 kg/110 lbs, super sacks size 500-1,000 kg/1,100-2,200 lbs |
| SHELF LIFE | At least 24 months under dry conditions (max. 20 °C/68 °F, max. 35 % RH). |
| SERVICE | Should you need personal assistance, one of our experts will be happy to advise you. Please do not hesitate to contact us with any questions. Or find more information on our website at www.bestmalz.com. |
| REMARKS | All of our malts are produced in accordance with the purity guidelines of the German Reinheitsgebot of 1516. We use no genetically modified raw materials. Our malts are produced in compliance with all valid food regulations and legal provisions. Of course, absolute compliance with strict statutory limits relating to pesticides, herbicides, fungicides, mycotoxins and nitrosamines is guaranteed. This is checked by independent laboratories on a regular basis.<br>All processes are conducted according to procedures that are stipulated in our quality management system in accordance with the European standard DIN-EN-ISO 9001:2015. This also comprises a HACCP system. Certification of the systems is performed regularly by the LGA InterCert.<br>Malting barley and wheat are natural products. This means that the specifications given here are subject to seasonal variation and are based on a minimum level of quality for the harvested grain. Please find more information on our website at www.bestmalz.com. |

STANDARD MALT SPECIFICATIONS (the values are harvest dependant)

| Specification | Unit | Minimum | Maximum |
|---|---|---|---|
| Moisture content | % | | 4.9 |
| Extract fine grind, dry basis | % | 80.5 | |
| Fine-coarse difference EBC | % | | 2.0 |
| Viscosity (8,6%) | mPa·s | | 1.60 |
| Friability | % | 81.0 | |
| Glassiness | % | | 2.5 |
| Protein, dry basis | % | 9.0 | 11.5 |
| Soluble nitrogen | mg/100g | 610 | 780 |
| Kolbach index | % | 36.0 | 45.0 |
| **Wort color** | **EBC** | **5.0** | **7.0** |
| **Wort color** | **L** | **2.3** | **3.1** |
| Wort pH | | 5.7 | 6.1 |
| Grading > 2,5mm | % | 90.0 | |
| Diastatic power | WK | 250 | |
| ß-Glucan (65°C) | | | 350 |

MADE IN GERMANY

DE-ÖKO-005

PARVE

TÜVRheinland ZERTIFIZIERT Management System ISO 9001:2015 www.tuv.com ID 9108641255

ISO 50001 ENERGY MANAGEMENT

GMO FREE

PALATIA MALZ GMBH • P.O. BOX 10 43 20 • D-69033 HEIDELBERG • GERMANY
T +49 (0)62 21 - 64 66-0 • F +49 (0)62 21 - 64 66-99 • INFO@BESTMALZ.DE • WWW.BESTMALZ.COM

## Composites biosourcés à base de PP, PLA et de drêches de bière : impact des procédés de transormation et de modification sur les propriétés des composites

Cette thèse s'inscrit dans une démarche de valorisation des coproduits agro-industriels à travers le développement de biocomposites à matrices thermoplastiques. Les drêches de brasserie (BSG), principal sous-produit de la filière brassicole, ont été étudiées comme charge lignocellulosique potentielle pour la formulation de composites à base de polypropylène (PP) et d'acide polylactique (PLA). L'objectif principal a été d'évaluer la faisabilité technique et scientifique de cette valorisation, tout en identifiant les leviers d'optimisation à différentes échelles du procédé.

Une première phase bibliographique a permis de cerner les enjeux, les verrous technologiques et les opportunités associées aux biocomposites à fibres naturelles. Dans un second temps, les composites BSG/PP et BSG/PLA ont été élaborés et caractérisés afin d'étudier l'effet de la charge sur leurs propriétés thermiques, mécaniques et rhéologiques. Les résultats ont montré que, si le BSG interagit fortement avec le PLA en accélérant sa dégradation, il agit de manière plus neutre avec le PP, soulignant l'importance du choix de la matrice. Pour répondre aux contraintes de conservation et de mise à l'échelle, un procédé d'extrusion bi-vis a été développé pour assurer le séchage et le broyage continus des drêches, permettant leur incorporation direct dans les matrices thermoplastiques et améliorant à la fois leur stabilité thermique et leur morphologie. Enfin, un traitement alcalin a été utilisé sur les drêches pour renforcer l'adhésion charge-matrice, améliorant ainsi la résistance mécanique et l'adhésion interfaciale des composites.

Dans l'ensemble, ces travaux démontrent le fort potentiel de BSG comme charge durable dans les biocomposites thermoplastiques, et ouvrent la voie à une valorisation à plus grande échelle, contribuant à la transition vers des matériaux répondant aux exigences du développement durable.

Mots-clés : Formulation – Compatibilisation/caractérisation – Extrusion réactive – Valorisation de la biomasse – Composite biosourcé

## Bio-based composites from PP, PLA and brewer's spent grain: impact of processing and modification on composite properties

This PhD work focuses on the valorization of agro-industrial by-products through the development of thermoplastic biocomposites. Brewer's spent grain (BSG), the main by-product of the brewing industry, was investigated as a potential lignocellulosic filler for polypropylene (PP) and polylactic acid (PLA) matrices. The main objective was to assess the technical feasibility and optimization strategies required for large-scale valorization.

A literature review first identified the key challenges and opportunities of natural fiber biocomposites. Then, BSG/PP and BSG/PLA composites were produced and characterized to evaluate the effect of filler content on their thermal, mechanical, and rheological properties. Results revealed opposite behaviors between matrices: BSG interacted with PLA, accelerating its thermal degradation, whereas it acted more inertly with PP, highlighting the influence of polymer nature on composite performance. To overcome storage and scalability limitations, a continuous twin-screw extrusion process was developed for simultaneous drying and grinding of BSG, allowing its direct use into thermoplastic matrices and improving both thermal stability and morphology. Additionally, alkaline treatment was applied to enhance filler-matrix adhesion, leading to better mechanical strength and interfacial adhesion.

Overall, this research demonstrates the high potential of BSG as a sustainable filler for thermoplastic composites and outlines viable strategies to move from laboratory to pilot scale, contributing to the development of environmentally responsible materials.

Key-words: Formulation – Compatibility/Characterization – Reactive extrusion – Biomass valorization – Bio-based composite

***Discipline : GENIE DES PROCEDES***

***Spécialité : Génie des procédés environnementaux***

Université de Reims Champagne-Ardenne

ItheMM – EA 7548

UFR Sciences Exactes et Naturelles
Campus Moulin de la Housse – BP 1039
51687 Reims Cedex 2, FRANCE